1995

Turbulent scalar transport using two-point statistical closure theory

Robert Charles Sanderson
Iowa State University

INFORMATION TO USERS

This manuscript has been reproduced from the microfilm master. UMI films the text directly from the original or copy submitted. Thus, some thesis and dissertation copies are in typewriter face, while others may be from any type of computer printer.

The quality of this reproduction is dependent upon the quality of the copy submitted. Broken or indistinct print, colored or poor quality illustrations and photographs, print bleedthrough, substandard margins, and improper alignment can adversely affect reproduction.

In the unlikely event that the author did not send UMI a complete manuscript and there are missing pages, these will be noted. Also, if unauthorized copyright material had to be removed, a note will indicate the deletion.

Oversize materials (e.g., maps, drawings, charts) are reproduced by sectioning the original, beginning at the upper left-hand corner and continuing from left to right in equal sections with small overlaps. Each original is also photographed in one exposure and is included in reduced form at the back of the book.

Photographs included in the original manuscript have been reproduced xerographically in this copy. Higher quality 6" x 9" black and white photographic prints are available for any photographs or illustrations appearing in this copy for an additional charge. Contact UMI directly to order.

UMI

A Bell & Howell Information Company
300 North Zeeb Road. Ann Arbor. MI 48106-1346 USA
313/761-4700 800/521-0600

Turbulent scalar transport using two–point statistical closure theory

by

Robert Charles Sanderson

A Dissertation Submitted to the

Graduate Faculty in Partial Fulfillment of the

Requirements for the Degree of

DOCTOR OF PHILOSOPHY

Department: Chemical Engineering
Major: Chemical Engineering

Approved:

Signature was redacted for privacy.

In Charge of Major Work

Signature was redacted for privacy.

For the Major Department

Signature was redacted for privacy.

For the Graduate College

Members of the Committee:

Signature was redacted for privacy.

Signature was redacted for privacy.

Signature was redacted for privacy.

Signature was redacted for privacy.

Iowa State University
Ames, Iowa
1995

TABLE OF CONTENTS

LIST OF FIGURES

LIST OF TABLES

ABSTRACT

The turbulent transport of a passive scalar (Corrsin's problem with diffusion) and of an active scalar in stably stratified fluids is studied using linear analysis (rapid distortion theory or RDT), Kraichnan's direct interaction approximation (DIA) and direct numerical simulation (DNS). The results are compared with each other and with laboratory experiments. The numerical results compare favorably with the experiments of Sirivat and Warhaft, Budwig, Tavoularis and Corrsin and Stillinger and Itsweire of van Atta's group. The RDT study reveals that much of the qualitative behavior observed in experiments, such as the tendency for the system to evolve towards some statistically asymptotic state, is embodied in the linear results. Specifically, predictions from the passive scalar linear theory for lengthscale ratios (both integral and microscale) are in good agreement with nonlinear results but the linear values for the scalar transport correlation coefficient contain significant error.

DNS and DIA results are reasonably close for the velocity field and scalar transport with Gaussian initial spectra, but differ significantly for exponential spectra. Although the transport problem is anisotropic, the DIA results using only the first Legendre functions yield integrated results identical to those obtained with two harmonics. Linear and DIA runs show significant dependance of scalar transport upon initial spectral shapes.

The passive scalar transport problem is shown to be equivalent to the sum of an isotropic scalar turbulence problem with the scalar initial conditions of the transport problem and a transport problem with zero initial scalar fluctuations (both with the same velocity fields). The asymptotic state is defined by the zero initial scalar field transport problem while the rate and manner in which the complete problem

approaches this state is strongly affected by the initial scalar field.

The DIA is also used to simulate some experimental decaying turbulence experiments in isotropic velocity fields, passive isotropic scalar fields and transport of a passive scalar by an isotropic velocity field. A rational technique for determining the appropriate nondimensionalization for time is presented and demonstrated. The spectral aspect ratio, the ratio of the integral lengthscale and Taylor microscale, A, is shown, with R_λ, to be important for accurate simulation of the evolution of the isotropic velocity field. For problems involving a scalar field, the ratio of this number for the velocity and scalar fields plays a crucial role in the subsequent evolution of the scalar field.

CHAPTER 1. GENERAL INTRODUCTION AND BACKGROUND

Turbulence is characterized by statistically random fluid motions in three dimensions governed by the Navier–Stokes equations. The strong nonlinearity of turbulent motions renders difficult any mathematical study. In spite of its intractability (or perhaps because of it), turbulence has attracted students from many disciplines. Turbulence is important in such diverse areas as weather forecasting, oceanic studies, chemical reactions in chemical processing and combustion, stellar evolution, aerodynamic performance of ground vehicles, aircraft and rockets, transport of heat and chemical species, magnetohydrodynamics, plasmas necessary for controlled fusion, etc. Much progress has been achieved in the physical understanding of energy transport between different scales of motion, experimental and measurement techniques, interaction of turbulence with other physical phenomena such as mean shear, buoyancy effects, acoustic fields, and its relation to chaos, stability theory, attractors, etc. Mathematical progress has been made in the development of techniques for modeling subgrid turbulence effects, numerical simulation of the governing equations and closure of the statistical moment and probability density function (pdf) governing equations, Nonetheless a great deal of study is needed to attain a thorough understanding of turbulent velocity and scalar fields. This section discusses the experimental and theoretical background of turbulent scalar decay and scalar transport in the presence

of a uniform mean scalar gradient which is the subject of this dissertation.

Large Reynolds Number Isotropic Velocity and Scalar Turbulence

The general topic of this dissertation is numerical analysis of the turbulent transport of a scalar in the presence of a uniform mean scalar gradient, in both neutrally and stably stratifieds fluid, using multi–point statistical moments. Oboukhov [60] and Corrsin [9] extended the studies of Kolmogorov [41] (on turbulence velocity structure functions) and of Batchelor [2] (extending Kolmogorov's work to wavenumber space) of the spectral transport of turbulent kinetic energy in the inertial range of the energy spectrum to the inertial–convective range of a scalar variance (or energy) spectrum and found independently that it also followed a $k^{-5/3}$ law. Batchelor, et al. [3, 4] analyzed the diffusive–convective (e.g., high Pr) and inertial–diffusive (e.g., low Pr) regions of scalar spectra and determined their behavior to be k^{-1} and $k^{-17/3}$ respectively while Gibson [21, 22] determined a k^{-3} regime when considering isoscalar surfaces. Kraichnan [49] and Saffman [65] considered the effects of intermittency and arbitrary orientation of the principal rates of strain and local fluctuating scalar gradients upon the analyses of Batchelor. They determined these influences to be negligible upon the power laws.

A relatively large number of experiments upon isotropic turbulence have detected Kolmogorov's $k^{-5/3}$ spectral regime, many under conditions which clearly do not meet the conditions of his hypotheses. Making measurements of the velocity field in a tidal basin with a channel Reynolds number on the order of 10^8, Grant, Stewart and Moilliet [29] found an inertial spectral subrange which obeyed the $k^{-5/3}$ law for several decades. Gibson and Schwarz [20] measured velocity spectra in a water tunnel

at mesh Reynolds numbers in the range of 20,000–40,000 and confirmed that, as Reynolds number increases, an increasing portion of the energy spectrum behaved as $k^{-5/3}$ and that, using the Kolmogorov nondimensionalization, the high wavenumber spectral ranges collapsed to one universal curve. This latter conclusion was based upon comparison of the water/sea water data of Gibson and Schwarz[20]; Grant, Stewart and Moilliet[30]; and the air data of Stewart and Townsend [74].

Grant, Hughes, Vogel and Moilliet [30], measuring scalar (temperature) spectra in the tidal basin at very high Reynolds numbers found a significant range of diffusive–convective scalar spectrum with a k^{-1} behavior and significant inertial–convective range following a $k^{-5/3}$ power law. Although their data contained significant intermittency, its effects did not materially influence the behavior of their spectral data. Gibson and Schwarz [20] studied conductivity fluctuations (caused by salt and temperature fluctuations) in a water tunnel. Water has a relatively high Schmidt/Prandtl number (approximately 700 and 7 for salt and temperature, respectively) and the scalar (conductivity) spectra displayed both a $k^{-5/3}$ inertial–convective range and a k^{-1} diffusive–convective range. Nye and Brodkey [59] conducted experiments using optical measurements of dye concentrations injected into water flow in a tube (Schmidt number of 4,000, Reynolds number of 50,000). They also found k^{-1} behavior in the concentration spectrum. Clay [12] made temperature measurements in air, water and mercury and observed k^{-1}, $k^{-5/3}$, k^{-3} and $k^{-17/3}$ behavior.

Thus much of the theoretical work concerning the spectral physics of high Reynolds number isotropic turbulence has recieved experimental support and/or verification.

Low Reynolds Number Homogeneous Turbulent Velocity and Scalar Fields

Many of the experiments reported concerning turbulent isotropic velocity and scalar fields have occurred at low microscale Reynolds numbers, i.e., less than 100. This has the dual benefit that the bandwidth of important turbulent lengthscales is narrowed and that the results may be directly compared with those of numerical DNS or closure theory computations. Numerical work has historically been confined to low turbulence Reynolds numbers because of the limitations imposed by computer operations speed and memory size. Although recent developments in computer technology are relaxing these restrictions somewhat, most numerical studies are still conducted at low R_λ but often with enhanced resolution.

Low R_λ isotropic turbulent velocity fields have been studied experimentally since the early 1950's, with early emphasis placed upon developing techniques of flow manipulation to produce the highest quality isotropic turbulence over the longest fraction of the tunnel test section (c.f., Comte–Bellot and Corrsin [7, 8], Grant and Nisbet [28], Kistler and Vrebalovich [40] and Uberoi, et al. [77, 78]) and enhancing the resolution and bandwidth of the instrumentation (c.f., Hinze [38]).

A survey of a number of turbulent velocity experiments was conducted by Mohamed and LaRue [57] with the goal of rationalizing the range of decay exponents observed. Their results for the initial period of decay indicated $n \approx -1.3$ was a reasonable turbulence kinetic energy decay exponent (in x/M). Sirivat and Warhaft [71] report their experimental results at two flow speeds, 3.4 and 6.3 m/s corresponding to microscale Reynolds numbers at $x/M = 100$ of 26.4 and 36.5, respectively. They reported decay exponents, n, of -1.29 and -1.37 for the low and high speed experi-

ments.

The evolution of decaying isotropic scalar turbulence has been studied experimentally by a number of investigators including Mills, Kistler, O'Brien and Corrsin [56], Lin and Lin [53], Yeh and van Atta [83], Sepri [70] and Warhaft and Lumley [80]. As Warhaft and Lumley [80] point out, the scalar energy decay exponent displays a very wide range in these studies, from -0.87 to -3.09. They found that changing grid heating rates altered the scalar field lengthscales and then performed further experiments using the scalar to mechanical lengthscale ratio as the parameter. By so doing they could vary the scalar energy decay exponent from -1.29 to -3.20, thus effectively replicating the previously reported data and providing the rationale for its variance. Mell, Kosály and Riley [54] reported results obtained from DNS computations of a decaying isotropic scalar field with variable scalar to mechanical integral lengthscale ratio. By changing this ratio from 0.2 to 1.25 they were able to achieve scalar energy decay exponents from -2.76 to -2.23. Durbin [18] used his Lagrangian model to model decaying isotropic sclaar turbulence and the effects of initial thermal to mechanical integral lengthscale ratio. He found decay exponents to vary from -1.2 to -2.3 as the lengthscale ratio varied from about 0.20 to 1.75 although the decay exponent appeared to approach an upper asymptotic magnitude at a ratio of approximately 0.40. Eswaran and O'Brien [19] used a physical space model derived from the EDQNM to study decaying isotropic scalar turbulence reported by Sreenivasan, Tavoularis, Henry and Corrsin [73]. The EDQNM model used a simplified eddy diffusivity equation and assumed analytical forms for the velocity field statistics, scaled to provide the correct intensity, lengthscales, etc. Only the scalar equations were numerically solved. They were able to obtain scalar energy decay exponents of -1.34

to -2.14 (integral lengthscale ratios of 0.7 to 1.40) for their modeling of heated grid experiments and -2.05 to -2.27 for the heated screen experiments (integral lengthscale ratios of 0.40 to 0.81).

Isotropic Turbulent Transport of a Passive Scalar

Corrsin [10] first suggested the problem of passive scalar transport in isotropic turbulence with a uniform mean scalar gradient as the simplest possible transport problem which could be realized experimentally and computed using turbulence models, theories or computational techniques for comparison. Corrsin predicted that an initially linear mean scalar gradient would retain its linear form and strength in isotropic turbulence. He also predicted an initially linear growth rate in the scalar variance (scalar "energy") in time in a nondiffusive scalar field. Wiskind [81] performed the first experimental investigation of this problem using a wind tunnel. Although his instrumentation for measuring the turbulent heat transfer lacked the robustness of the velocity and temperature measurement techniques (his evaluation), he confirmed Corrsin's predictions about the mean and turbulent scalar fields. He also made preliminary measurements of the heat transfer correlation coefficient, $\rho_{u\theta}$, of -0.48. The general growth properties of the thermal field were also verified by Alexopoulos and Keffer [1] in wake flow and further studied Venkataramani and Chevray [79] in statistical and probabalistic detail. Venkataramani and Chevray greatly improved the linearity of the mean scalar gradient and reconfirmed the growth characteristics of the scalar variance while measuring the scalar transport correlation coefficient as approximately -0.58.

Further refinements in experimental apparatus were reported by Sirivat and

Warhaft [71] who also studied the effects of initial thermal to velocity integral length-scale ratio upon the evolution of the scalar and scalar transport fields. They used a differentially heated "mandoline" and "toaster" in separate experiments (see Figure 1.1), both of which substantially reduced the scalar transport in the streamwise and cross–stream (normal to the mean scalar gradient) directions at two different mean velocities (R_λ's of about 26 and 36). The initial conditions affected the evolution of the problem but all runs appeared to evolve towards common asymptotic states. Measured scalar transport correlation coefficients were about -0.70 and the eddy diffusivity ratios were of the order of the microscale Reynolds numbers. Budwig, Tavoularis and Corrsin [5] performed experiments similar to those of Sirivat and Warhaft with similar scalar transport results. Gibson and Dakos [27] measured $\rho_{u\theta}$ of -0.625 at R_λ of 42 and a mechanical to thermal timescale ratio approximately 30–50% of that measured by Sirivat and Warhaft [71] and Budwig, Tavoularis and Corrsin [5].

Numerical studies have been few in number. Hill [37] performed DIA computations under scalar conditions similar to those of Wiskind [81] with a stationary velocity field. Due to the limited available computational resources at the time this study was conducted, the velocity field two–point correlation function was assumed to be of several analytical mathematical forms. This permitted the partial analytical integration of the nonlinear DIA terms, thereby reducing the numerical effort for the solution of the nonlinear scalar field terms. In addition, he expanded the average scalar field equations using the perturbation technique to derive an expression for the eddy diffusivity involving the scalar response function and the velocity correlation. This eliminated the requirement for numerical solution of the scalar–velocity

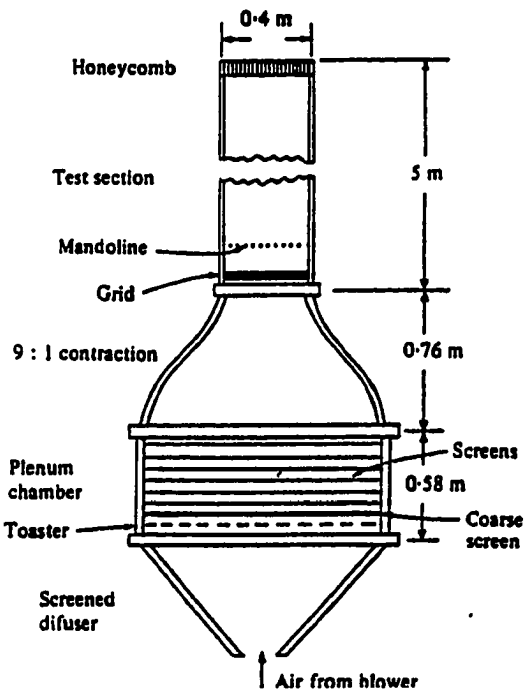

Figure 1.1: Illustration of the experimental configuration for the experiments of Sirivat and Warhaft showing the mandoline and toaster.

covariance and their related response function equations. This reduced the numerical requirements to that of computing only the scalar field variance and response functions. He reported values of the scalar transport correlation coefficient of about -0.3 to -0.4 and eddy diffusivity ratios around 18-26 for R_λ of 29.

Transport of a Scalar in Stably Stratified Turbulence

Stably stratified fluids are characterized by an increasing density in the gravitational direction. Any vertical fluid motions in this situation involve the transformation of kinetic energy into potential energy or vice versa, depending upon the direction involved. Thus, while vertical turbulent fluctuations can induce enhanced scalar transport in that direction, they can also give rise to internal waves which are capable of convecting energy horizontally away from their source while dissipating kinetic energy at a very low rate relative to turbulent flows. Conversely, since these internal waves involve vertical oscillatory motion, they may appear to be turbulent velocity fluctuations in fluid velocity measurements. Thus interpretation of experimental (and perhaps numerical) data in this situation can be difficult and controversial. Using a towed grid in a vertical water tank with neutrally and stably stratified fluid, Dickey and Mellor [17] studied the differences in velocity field evolution induced by stable stratification at a relatively high mesh Reynolds number. They noted that, while the stratified velocity field initially evolved in a manner similar to that of the unstratified case, there was a marked deviation in the decay of kinetic energy at a time corresponding to a critical Richardson number. This value for $Ri_c \equiv (NL/q)_c^2$ was found to be 4.7 ($N \equiv \sqrt{-(g/\rho_o)(d\overline{\rho}/dz)}$ is the Brunt–Väisälä frequency with g the gravitational magnitude, ρ_o a reference density and $d\overline{\rho}/dz$ the

mean density gradient; L is the integral lengthscale and $q^2/2$ is the total turbulence kinetic energy). The interpretation of this result is that at later times in the evolution of the stably stratified cases, the turbulent velocity field had been converted into an internal wave field with correspondingly low dissipation rates.

Gibson [23, 24, 20, 26] has proposed a physical model to determine when stably stratified velocity fields are actively turbulent or dominated by internal waves (he denotes the latter condition "fossil turbulence"). These criteria involve a suitable vertical velocity lengthscale, the Kolmogorov [41] dissipation lengthscale and the Ozmidov [63] lengthscale from which a critical dissipation rate was derived, above which indicated active turbulence. Gibson (c.f., [25, 26]) has applied this to some previous oceanic studies and determined that some were primarily wavelike, not actively turbulent as had been assumed. If this interpretation is correct, it invalidates at least some of the conclusions drawn from the experiments. Thus it is of great interest to more fully understand stably stratified turbulence, internal waves and any interactions they experience. Several water tunnel experiments and numerical studies have been conducted to study this problem.

Stillinger, Helland and van Atta [75] and Itsweire, Helland and van Atta [39] conducted water tunnel tests, varying the turbulence source geometry and the Brunt–Väisälä frequency (N) or strength of the stabilization. Their results lent qualitative support to the results of Gibson although changing the quantitative results. Riley, Metcalfe and Weissman [64], Métais and Herring [55] have conducted DNS computations to simulate the experiments of van Atta's group and were able to show reasonably good qualitative and quantitative agreement. This occurred despite their use of a value for Pr of approximately unity whereas the experiments (being salt in

water) had a value closer to 700. Due to numerical stability considerations, DNS computations are limited to very moderate or low Pr. Sanderson et al. [66, 67, 68] conducted numerical computations of decaying stably stratified turbulence using both DNS and DIA techniques and found good qualitative agreement between DIA and DNS but the DIA required more than the single Legendre coefficient to achieve good quantitative agreement.

Goals of the Dissertation

This dissertation applies the statistical closure theory developed by Robert Kraichnan [42] in the late 1950's known as the direct interaction approximation (DIA) to the problem or turbulent transport of scalars, passive and active in a stably stratified fluid. This is a complete and self-consistent theory which is derived directly from the governing Navier–Stokes equations, applying a few assumptions made about the nature of interactions between scales of motion and utilizing a perturbation technique which perturbs, not from the linear case, but from the fully nonlinear case. The perturbations are expressed in terms of time integrations of response functions acting upon the (assumed) primary forcing functions producing these perturbations. The final step is a partial infinite summation of terms resulting in the expression of the triple moments in the second order moment governing equations in terms of bilinear products of second order moments acted upon by response functions. The resulting theory is a two–point two–time integro–differential description of the evolution of the second order moments containing no arbitrary constants or functions. The DIA is flawed in that it lacks invariance to random Galilean transformations (c.f., Kraichnan [45], Leslie [52]) which results in the prediction of inertial range behavior

of $k^{-3/2}$ rather than the observed and accepted Kolmogorov [41] $k^{-5/3}$ spectral decay (c.f., Kraichnan [43], Leslie [52]). This also results in a singularity in the response function as k approaches zero and a zero radius of convergence at all values of R_λ. Nonetheless it is the exact solution of a model problem which guarantees physicality of the results. More complex variations of this theory employing Lagrangian velocity tracking (for both velocity and strain) have been developed, studied theoretically and numerically implemented (the Lagrangian history direct interaction approximation or LHDIA and strain based Lagrangian history direct interaction approximation or SBLHDIA, c.f., Kraichnan [47, 51], Herring [36]). While these do predict the correct $k^{-5/3}$ inertial range behavior, they lack a physical model and are considerably more complex to compute. Simpler, markovianized theories (e.g., the test field model or TFM of Kraichnan [50], eddy damped quasi-normal markovianized or EDQNM, c.f., Orszag [61], Cambon et al. [6], the renormalized group or RNG of Yakhot and Orszag [82], see also Smith and Reynolds [72], etc.) have been developed but suffer from the need for scaling constants to achieve correct results.

Despite its failings, the DIA remains the complete self–consistent theory of choice for study and comparison with direct numerical simulation (DNS) and experiment. This dissertation utilized the DIA in the study of scalar transport in homogeneous turbulent flow with and without buoyancy effects. These results were then compared with those of DNS and experiment to assess the fidelity of the DIA in computing these problems. Some previous studies have investigated decaying homogeneous velocity and scalar fields using the DIA and compared asymptotic results with experiment and time evolutionary results with DNS and, occasionally, other closure theory results. Comparisons between the DIA and DNS were made by Herring and Kerr [36]

for decaying isotropic turbulent velocity and scalar fields. These were low Reynolds number cases (initial R_λ of 15-30) which highlighted some differences (e.g., development of derivative skewnesses) but showed overall similarity in the evolution of the variances and spectra. Schumann and Herring [69] compared DNS and DIA for the case of initially anisotropic homogeneous turbulent velocity fields. Dannevik [14, 15] used the DIA to computed the evolution of unstably stratified turbulence. He divided the variable functions into "fast moving" and "slow moving" parts and used Padé approximates to compute the time integrals. With this procedure he did exclude some portions of the second order moments and response functions.

Dissertation Organization

The first paper of this dissertation (Chapter 2) considers the question of the differences between stably stratified turbulence and Gibson's [23, 24, 20, 26] "fossil turbulence" by comparing DNS and DIA computations of active scalar transport with various distributions of the initial energy between the vertical and horizontal velocity fields and the initial potential energy field.

The second paper (Chapter 3) deals with DIA studies performed in conjunction with DNS computations and linear rapid distortion theory (RDT) on the isotropic transport of a passive scalar in the presence of a uniform mean scalar gradient. The comparison in this paper of the RDT results with those of DIA and DNS were for the purpose of illustrating the differences induced upon the problem by the nonlinear effects.

The work presented in the third paper (Chapter 4) involves only the DIA and consists of the direct modeling of experimental (in this case all experiments were

conducted in wind tunnels) studies of decaying isotropic turbulent velocity fields reported by Sirivat and Warhaft [71], isotropic decaying passive scalar turbulence of Warhaft and Lumley [80] and evolving homogeneous turbulent transport of a passive scalar in the presence of a uniform mean scalar gradient studied by Sirivat and Warhaft [80]. While a few previous studies (c.f., Eswaran and O'Brien [19], Riley, Metcalfe and Weissman [64], Métais and Herring [55]) have attempted to fit the numerical results of EDQNM, DNS, etc. to experimental evolutionary data, this particular study focuses on predictive, not fitting, activities. In other words, given a sufficiently complete set of experimental data at one point, how must the numerical scheme of choice be initialized and what are the necessary conditions which the numerical results must satisfy at the known experimental data point in order to have confidence in the numerical predictions for any quantities at later points in time (or space in the wind tunnel test section).

Following the last paper is a general summary of the work presented in these three papers. Appendix A contains a summary of the DIA equations for passive scalar transport and the associated geometric coefficients for the nonlinear terms and the linear forcing terms. Appendix B reiterates the geometric coefficients for the nonlinear terms and indicates some of the mathematical relationships between them. Appendix C presents some preliminary numerical comparisons of various geometric coefficients showing that, under conditions of isotropy of the velocity field, they take on values such that higher Legendre coefficients will contribute nothing to the lowest order coefficients, and thus the wavenumber integrated quantities of total scalar transport and scalar energy. Appendix D analytically examines the behavior of the geometric coefficients for the nonlinear terms which also appear in the isotropic scalar

turbulence problem. It is shown that these coefficients in the scalar–velocity covariance equations contribute nothing to higher Legendre coefficients when the velocity field is isotropic. The linear forcing terms also contribute zero to higher harmonics. Although this type of behavior was not proven for the other nonlinear coefficients, these results do suggest that the first associated Legendre function coefficient may be sufficient to completely characterize the angular dependence of the scalar transport field. Finally, Appendix E briefly discusses the details of the $p - q$ wavenumber integration technique. All these appendices support the work presented in the second paper in Chapter 3.

References

[1] Alexopoulos, C.C. and Keffer, J.F.; Turbulent wake in a passively stratified field. Phys. of Fluids, **14**, pp. 216–224, 1971.

[2] Batchelor, G.K.; *The Theory of Homogeneous Turbulence*, Cambridge University Press, London, 1953.

[3] Batchelor, G.K.; Small–scale variation of convected quantities like temperature in turbulent fluid. Part 1. General discussion and the case of small conductivity. J. Fluid Mech., **5**, pp. 113–133, 1959.

[4] Batchelor, G.K., Howells, I.D. and Townsend, A.A.; Small–scale variation of convected quantities like temperature in turbulent fluid. Part 2. The case of large conductivity. J. Fluid Mech., **5**, pp. 134–139, 1959.

[5] Budwig, R., Tavoularis, S. and Corrsin, S.; Temperature fluctuations and heat flux in grid generated isotropic turbulence. J. Fluid Mech., **153**, pp. 441–460, 1985.

[6] Cambon, C., Jeandel, D. and Mathieu, J. Spectral modelling of homogeneous non–isotropic turbulence. J. Fluid Mech., **104**, pp. 247–262, 1981.

[7] Comte–Bellot, G. and Corrsin, S.; The use of a contraction to improve the isotropy of grid–generated turbulence. J. Fluid Mech., **25**, pp. 657–682, 1966.

[8] Comte–Bellot, G. and Corrsin, S.; Simple Eulerian time correlation of full– and narrow–band velocity signals in grid–generated 'isotropic' turbulence., J. Fluid Mech., **48**, pp. 273–337, 1970.

[9] Corrsin, S.; On the spectrum of isotropic temperature fluctuations in an isotropic turbulence. J. Appl. Phys., **22**, pp. 469–473, 1951.

[10] Corrsin, S.; Heat transfer in isotropic turbulence. J. Appl. Phys. **23**, pp. 113–118, 1952.

[11] Chakrabarti, M. Numerical studies of chemical selectivity and heat transfer in decaying homogeneous turbulence. Ph.D. Dissertation, Iowa State University, Ames, Iowa, 1991.

[12] Clay, J.P. *Turbulent mixing of temperature in water, air and mercury.*, Ph.D. dissertation, University of California at San Diego, San Diego, Ca., 1973.

[13] Craya, A. *Contribution a l'Analyse de la Turbulence a des Vitesse Moyennes*, P.S.T. Ministere de l'Air (Fr.), 1958.

[14] Dannevik, W.P.; *Two-point Closure of Covariance Budgets for Turbulent Rayleigh-Benard Convection*, Ph.D. dissertation, St. Louis University, St. Louis, Mo., 1984.

[15] Dannevik, W.P.; Efficient solution of non-Markovian covariance evolution equations in fluid turbulence. J. Sci. Comp., **1**, pp. 151–182, 1986.

[16] Dannevik, W.P., Yakhot, V. and Orszag, S.A.; Analytical theories of turbulence and the ε-expansion, Phys. Fluids, **30**, pp. 2021–2029, 1987.

[17] Dickey, T.D. and Mellor, G.L.; Decaying turbulence in neutral and stratified fluids. J. Fluid Mech., **99**, pp. 13–31, 1980.

[18] Durbin, P.A.; Analysis of the decay of temperature fluctuations in isotropic turbulence. Phys. Fluids, **25**, pp. 1328–1332, 1982.

[19] Eswaran, V. and O'Brien, E.E.; Simulations of scalar mixing in grid turbulence using an eddy-damped closure model. Phys. Fluids A, **1**, pp. 537–548, 1989.

[20] Gibson, C.H. and Schwarz, W.H.; The universal equilibrium spectra of turbulent velocity and scalar fields. J. Fluid Mech., **16**, pp. 365–384, 1963.

[21] Gibson, C.H.; Fine structure of scalar fields mixed by turbulence. I. Zero-gradient points and minimal gradient surfaces. Phys. Fluids, **11**, pp. 2305–2315, 1968.

[22] Gibson, C.H.; Fine structure of scalar fields mixed by turbulence. II. Spectral theory. Phys. Fluids, **11**, pp. 2316–2327, 1968.

[23] Gibson, C.H.; Fossil turbulence and internal waves. in , *Proc. AIP Conf. on Nonlinear Properties of Internal Waves*, ed. Bruce J. West, pp. 159–179, 1981.

[24] Gibson, C.H.; Alternative interpretations for microstructure patches in the thermocline. J. Phys. Oceanogr., **12**, pp. 374–383, 1982.

[25] Gibson, C.H.; Ocean turbulence; big bangs and continuous creation. Ms. submitted to J. Physico Chem. Hydro.

[26] Gibson, C.H.; Internal waves, fossil turbulence, and composite ocean microstructure spectra. J. Fluid Mech., **168**, pp. 89–117, 1986.

[27] Gibson, M.M. and Dakos, T.; Production of temperature fluctuations in grid turbulence: Wiskind's experiment revisited. Exp. in Fluids, **16**, 146–154, 1993.

[28] Grant, H.L. and Nisbet, I.C.T.; The inhomogeneity of grid turbulence, J. Fluid Mech., **2**, pp. 263–272, 1957.

[29] Grant, H.L., Stewart, R.W. and Moilliet, A.; Turbulence spectra from a tidal channel. J. Fluid Mech., **12**, pp. 241–268, 1962.

[30] Grant, H.L., Hughes, B.A., Vogel, W.M. and Moilliet, A.; The spectrum of temperature fluctuations in turbulent flow. J. Fluid Mech., **34**, pp.423–442, 1968.

[31] Herring, J.R.; Approach of axisymmetric turbulence to isotropy. Phys. Fluids **17**, pp. 859–872, 1974.

[32] Herring, J.R. and Kraichnan, R.H.; A numerical comparison of velocity–based and strain–based Lagrangian–history turbulence approximations.; J. Fluid Mech. **91**, pp. 581–597, 1979.

[33] Herring, J.R., Schertzer, D., Lesieur, M., Newman, G.R., Chollet, J.P. and Larcheveque, M.; A comparative assessment of spectral closures as applied to passive scalar diffusion. J. Fluid Mech., **124**, pp. 411–437, 1982.

[34] Métais, O. and Herring, J.R.; Numerical simulations of freely evolvoing turbulence in stably stratified fluids. J. Fluid Mech., **202**, pp. 117–148, 1989.

[35] Herring, J.R. and Métais, O.; Numerical experiments in forced stably stratified turbulence. J. Fluid Mech., **202**, pp. 97–115, 1989.

[36] Herring, J.R. and Kerr, R.M.; Comparison of direct numerical simulations with predictions of two–point closures for isotropic turbulence convecting a passive scalar. J. Fluid Mech., **118**, pp. 205–219, 1982.

[37] Hill, J.C.; Heat transfer in isotropic turbulence.; Chem. Eng. Commun., **12**, pp. 69–96, 1981.

[38] Hinze, J.O. *Turbulence,* 2^{nd} *edition.* McGraw–Hill Book Co., New York, N.Y., 1975.

[39] Itsweire, E.C., Helland K.N. and van Atta, C.W.; Evolution of grid–generated turbulence in a stably stratified fluid. J. Fluid Mech., **162**, pp. 299–338, 1986.

[40] Kistler, A.L. and Vrebalovich, T.; Grid turbulence at large Reynolds numbers, J. Fluid Mech., **26**, pp. 37–47, 1966.

[41] Kolmogorov, A.N.; The local structure of turbulence in incompressible viscous fluid for very large Reynolds numbers. Compte. rendu. Acad. Sci. URSS, **30**, pp. 301, 1941.

[42] Kraichnan, R.H.; Irreversible statistical mechanics of incompressible hydromagnetic turbulence. Phys. Rev. 2, **109**, pp. 1407–1422, 1958.

[43] Kraichnan, R.H.; The structure of turbulence at very high Reynolds numbers, J. of Fluid Mech., **5**, pp. 497–543, 1959.

[44] Kraichnan, R.H.; Dynamics of nonlinear stochastic systems, J. of Math Phys., **2**, pp. 124–148, 1961.

[45] Kraichnan, R.H.; Kolmogorov's hypotheses and Eulerian turbulence theory, Phys. of Fluids, **7**, pp. 1723–1734, 1964.

[46] Kraichnan, R.H.; The direct interaction approximation for shear and thermally driven turbulence. Phys. Fluids., **7**, pp. 1048–1062 ,1964.

[47] Kraichnan, R.H.; Lagrangian–history closure approximation for turbulence. Phys. Fluids., **8**, pp. 575–598 ,1965.

[48] Kraichnan, R.H.; Convergents to turbulence functions. J. Fluid Mech., **41**, pp. 189–217, 1970.

[49] Kraichnan, R.H.; Small–scale structure of a scalar field convected by turbulence. Phys. Fluids, **11**, pp. 945–953, 1968.

[50] Kraichnan, R.H.; An almost markovian Galilean–invariant turbulence model. J. Fluid Mech., **47**, pp. 513–524, 1971.

[51] Kraichnan, R.H. and Herring, J.R.; A strain–based Lagrangian–history turbulence theory.; J. Fluid Mech., **88**, pp. 355–367, 1978.

[52] Leslie, D.C.; *Developments in the theory of turbulence*, Oxford University Press; Oxford, England, 1973.

[53] Lin, S.C. and Lin, S.C.; Study of strong temperature mixing in subsonic grid turbulence. Phys. Fluids, **16**, pp. 1587–1598, 1973.

[54] Mell, W.E., Kosály, G. and Riley, J.J.; The length-scale dependence of scalar mixing. Phys. Fluids A, **3**, pp. 2474–2476, 1991.

[55] Métais, O. and Herring, J.R.; Numerical simulations of freely evolving turbulence in stably stratified fluids., J. Fluid Mech., **202**, pp. 117–148, 1989.

[56] Mills, R.R., Kistler, A.L., O'Brien, V. and Corrsin, S.; Turbulence and temperature fluctuations behind a heated grid. *NACA Note, No. 4288*, 1958.

[57] Mohamed, M.S. and LaRue, J.C.; The decay power lay in grid-generated turbulence. J. Fluid Mech., **219**, pp. 195–214, 1990.

[58] Newman, G.R. and Herring, J.R.; A test field model study of a passive scalar in isotropic turbulence. J. Fluid Mech., **94**, pp. 163–194, 1979.

[59] Nye, J.O. and Brodkey, R.S.; The scalar spectrum in the viscous-convective subrange. J. Fluid Mech., **29**, pp. 151–163, 1967.

[60] Oboukhov, A.M.; Structure of the temperature field in turbulent flows. Izv. Akad. Nauk. SSSR Geogr. i Geofiz., **13**, pp. 58, 1949.

[61] Orszag, S.A.; Analytical theories of turbulence. J. Fluid Mech., **41**, pp. 363–386, 1970.

[62] Orszag, S.A. and Patterson, G.S.; in *Statistical Models and Turbulence.* Springer–Verlag, New York, 1972.

[63] Ozmidov, R.V.; On the turbulent exchange in a stably stratified ocean. Izv., Atmos. and Ocean. Phys. Ser., **1**, pp. 853–860, 1965.

[64] Riley, J.J., Metcalfe, R.W. and Weissman, M.A.; Direct numerical simulations of homogeneous turbulence in density–stratified fluids. , *Proc. AIP Conf. on Nonlinear Properties of Internal Waves*, ed. Bruce J. West, pp. 79–112, 1981.

[65] Saffman, P.G.; On the fine–scale structure of vector fields convected by a turbulent fluid. J. Fluid Mech., **16**, pp. 545–572, 1963.

[66] Sanderson, R.C., Hill, J.C. and Herring, J.R.; Transient behavior of a stably stratified homogeneous turbulent flow. in Advances in Turbulence, G. Comte–Bellot and J. Mathieu, eds., 1987.

[67] Sanderson, R.C. and Hill, J.C.; Dynamics of decaying stably stratified turbulent flow, Presented at the Geophysical Turbulence Symposium of the American Meteorological Society, San Diego, Ca., 1988.

[68] Sanderson, R.C., Leonard, A.D., Herring, J.R. and Hill, J.C.; Fossil and active turbulence. In *Turbulence and Coherent Structures*, M. Lesieur and O. Métais, eds., Kluwer Academic Publishing, 1989.

[69] Schumann, U. and Herring, J.R.; Axisymmetric homogeneous turbulence: A comparison of direct simulations with the direct–interaction approximation., J. Fluid Mech., 76, pp. 755–782, 1976.

[70] Sepri, P.; Two-point turbulence measurements downstream of a heated grid. Phys. Fluids, **19**, pp. 1876–1884, 1976.

[71] Sirivat, A. and Warhaft, Z.; The effect of a passive cross-stream temperature gradient on the evolution of temperature variance and heat flux in grid turbulence. J. Fluid Mech., **128**, pp. 323–346, 1983.

[72] Smith, L.M. and Reynolds, W.C.; On the Yakhot–Orszag renormalization group method for deriving turbulence statistics and models. Phys. Fluids A, **4**, pp 364–390, 1992.

[73] Sreenivasan, K.R., Tavoularis, S., Henry, R. and Corrsin, S.; Temperature fluctuations and scales in grid-generated turbulence. J. Fluid Mech. **100**, pp. 597–621, 1980.

[74] Stewart, R.W. and Townsend, A.A.; Similarity and self-preservation in isotropic turbulence. Phil. Trans. of the Royal Soc. of London A, **243**, pp. 359–386, 1951.

[75] Stillinger, D.C., Helland K.N. and van Atta, C.W.; Experiments on the transition of homogeneous turbulence to internal waves. J. Fluid Mech., **131**, pp. 91–122, 1983.

[76] Thorpe, S.A.; Turbulence and mixing in a Scottish Loch. Phil. Trans. Roy. Soc. of London, Series A, **286**, pp. 125–181, 1977.

[77] Uberoi, M.S.; Energy transfer in isotropic turbulence. Phys. Fluids, **6**, pp. 1048–1056, 1963.

[78] Uberoi, M.S. and Wallis, S.; Small axisymmetric contraction of grid turbulence. J. Fluid Mech., **24**, pp. 539–543, 1966.

[79] Venkataramani, K.S. and Chevray, R.; Statistical features of heat transfer in grid–generated turbulence: constant–gradient case. J. Fluid Mech., **86**, pp. 513–543, 1978.

[80] Warhaft, Z. and Lumley, J.L.; An experimental study of the decay of temperature fluctuations in grid–generated turbulence. J. Fluid Mech., **88**, pp. 659–684, 1978.

[81] Wiskind, H.K.; A uniform gradient turbulent transport experiment. J. Geophys. Res., **67**, pp. 3033–3048, 1962.

[82] Yakhot, V. and Orszag, S.A.; Renormalization group analysis of turbulence. I. Basic Theory, J. Sci. Comp., **1**, pp. 3–51, 1986.

[83] Yeh, T.T. and van Atta, C.W.; Spectral transfer of scalar and velocity fields in heated–grid turbulence. J. Fluid Mech., **58**, pp. 233–261, 1973.

CHAPTER 2. FOSSIL AND ACTIVE TURBULENCE

A paper published in *Turbulence and Coherent Structures*, M. Lesieur and O. Métais, eds., Kluwer Academic Publishers [1]

Robert C. Sanderson [2], Andy D. Leonard [3], Jackson R. Herring [4] and James C. Hill [5]

Introduction

Stably stratified turbulence is commonly encountered in geophysical flows and can dramatically alter the evolutionary characteristics of the turbulence by introducing oscillatory behavior in both the scalar and velocity transport fields. Although only velocities in the vertical direction are subject to buoyancy forces, the horizontal components are also affected through nonlinear interaction with the vertical velocity components. If the length scales of the velocity field are small relative to those at which the buoyancy forces become strong, the turbulence is classified as "active" by Gibson [2]. In buoyancy-dominated turbulence, some or all motions have inertial

[2]APTEK, Inc., Colorado Springs, Co. 80906
[3]CFD Research Corp., Huntsville, Al. 35805
[4]National Center for Atmospheric Research, Boulder, Co. 80307
[5]Dept. of Chemical Engineering, Iowa State University, Ames, Ia. 50011

forces less than or equal to buoyant forces. There is also reduced turbulent scalar transport and dissipation compared with active turbulence of similar total energy. These ideas have been used by Gibson [2] in his physical modeling of this problem to derive criteria for discriminating stably stratified turbulent flow which is buoyancy-dominated from inertially-dominated (active) turbulence. His results have received support from the experimental studies of Stillinger et al. [13] and Itsweire et al. [4].

Fossil turbulence has been defined in several ways, as discussed by Gibson [2]. One definition is that it is a passive scalar field containing spatial deviations from the mean which remain after the turbulent motions of the fluid have disappeared due to viscous dissipation. The scalar field fluctuations are thus the remains or fossilized remnants created by the defunct turbulent velocity field. This situation is most easily envisioned in high Prandtl or Schmidt number fluids (e.g. sea water) in which scalar fluctuations diffuse very slowly. This definition is subject to some objections, as turbulence is generally considered to be a dynamic process, not a static scalar field. Secondly, it is somewhat restrictive in that velocity fields which occur in stably stratified fluids may become dominated by buoyancy forces to the point that they no longer possess the mixing and eddy-dissipative properties normally associated with nonstratified flows having the same energy content. In this sense they may be considered to be the dynamic remnants or fossils of the original turbulence (Gibson [2]). This paper will use this latter definition in a theoretical and numerical investigation of the characteristics of dynamic turbulence which is strongly buoyancy-dominated.

Problem Statement and Linear Theory

The problem to be addressed is incompressible homogeneous axisymmetric turbulence with a uniform mean scalar gradient in the vertical direction, leading to stable stratification. The buoyancy forces are assumed to obey the linear Boussinesq approximation. The resulting equations governing the fluctuating velocity and scalar fields are

$$\left(\frac{d}{dt}+\nu k^2\right)u_i(\mathbf{k},t)-\beta g n_i\vartheta(\mathbf{k},t)=-\frac{\imath}{2}P_{imn}(\mathbf{k})\sum_{\mathbf{p}+\mathbf{q}=\mathbf{k}}u_m(\mathbf{p},t)u_n(\mathbf{q},t) \tag{2.1}$$

$$\left(\frac{d}{dt}+\alpha k^2\right)\vartheta(\mathbf{k},t)+an_iu_i(\mathbf{k},t)=-\imath\mathbf{k}_m\sum_{\mathbf{p}+\mathbf{q}=\mathbf{k}}u_m(\mathbf{p},t)\vartheta(\mathbf{q},t) \tag{2.2}$$

with

$$P_{imn}(\mathbf{k})=k_mP_{in}(\mathbf{k})+k_nP_{im}(\mathbf{k})\;;\;\;P_{im}(\mathbf{k})=\delta_{im}-\frac{k_ik_m}{k^2}. \tag{2.3}$$

In this paper we define

$$N\equiv\sqrt{a\beta g} \tag{2.4}$$

as the Brunt-Väisälä frequency, with a the magnitude of the scalar gradient, β the volumetric expansion coefficient, and g the gravitational constant. The unit vector n_i is in the direction of the mean scalar gradient a. The mean scalar gradient, represented by the an_iu_i term in equation (2.2), is assumed to be unaffected by the turbulence, thus leading to a constant Brunt-Väisälä frequency. It should be noted here that the Boussinesq buoyancy term in equation (2.1) is an additional (linear) force which is added to the standard Navier-Stokes equations to describe the buoyancy forces, and the an_iu_i term in equation (2.2) comes from the nonlinear scalar convection term but is linear because of the uniformity of the mean scalar gradient. The energy interchange between the kinetic and potential energy fields

in this problem is primarily a linear process with the nonlinearities confined to the inertial convection of energy from one wavenumber to another.

Due to the linearity of the forcing terms in equations (2.1) and (2.2), insight into the behavior of the system may be obtained using (linear) rapid distortion theory (RDT). The linearized nondimensional two-point single-time correlation equations for nonzero initial total kinetic energy are

$$\left(\frac{d}{dt}+\frac{2k^2}{R_\lambda}\right)U_{ij}(\mathbf{k},t)-N^{*2}n_i\left[U_{\theta j}(\mathbf{k},t)+U_{j\theta}(-\mathbf{k},t)\right]=0 \tag{2.5}$$

$$\left(\frac{d}{dt}+\frac{(1+\mathrm{Pr})k^2}{\mathrm{Pr}\,R_\lambda}\right)U_{i\theta}(\mathbf{k},t)+n_jU_{ij}(\mathbf{k},t)-N^{*2}n_iU_{\theta\theta}(\mathbf{k},t)=0 \tag{2.6}$$

$$\left(\frac{d}{dt}+\frac{2k^2}{\mathrm{Pr}\,R_\lambda}\right)U_{\theta\theta}(\mathbf{k},t)+n_i\left[U_{i\theta}(\mathbf{k},t)+U_{\theta i}(-\mathbf{k},t)\right]=0 \tag{2.7}$$

with the equation for $U_{\theta i}(\mathbf{k},t)$ identical to equation (2.6) and where the following definitions are used:

$$U_{\iota\kappa}(\mathbf{k},t)\equiv\langle\hat{u}_\iota(\mathbf{k},t)\hat{u}_\kappa(-\mathbf{k},t)\rangle;\ \iota,\kappa\ =\ 1,2,3,\theta \tag{2.8}$$

with $\hat{u}_\kappa(\mathbf{k},t)$ or $\hat{u}_\iota(\mathbf{k},t)$ given by

$$\hat{u}_\kappa(\mathbf{k},t)\ =\ u_\kappa(\mathbf{k},t)/u_\mathrm{o},\quad \text{for } \kappa=1,2,\text{ or } 3 \tag{2.9}$$

$$=\ \vartheta(\mathbf{k},t)/a\lambda_\mathrm{o},\quad \text{for } \kappa=\theta. \tag{2.10}$$

Equivalently, the potential energy spectrum $P(\mathbf{k},t)\equiv U_{\theta\theta}(\mathbf{k},t)N^{*2}/2$ may be used in place of $U_{\theta\theta}$. In equations (2.5) through (2.7), $R_\lambda\equiv u_\mathrm{o}\lambda_\mathrm{o}/\nu$, $\mathrm{Pr}\equiv\nu/\alpha$, and $N^*\equiv N\lambda_\mathrm{o}/u_\mathrm{o}$, with u_o the initial turbulence intensity and λ_o the initial Taylor velocity microscale. The eigenvalues ξ_i corresponding to equations (2.5) through (2.7) and the equation for $U_{\theta i}(\mathbf{k},t)$ are

$$\xi_1=\xi_2=-\frac{(1+\mathrm{Pr})k^2}{\mathrm{Pr}\,R_\lambda} \tag{2.11}$$

$$\xi_3, \xi_4 = -\left(\frac{1+\mathrm{Pr}}{\mathrm{Pr}\,R_\lambda}\right)k^2 \mp \sqrt{\left(\frac{\mathrm{Pr}-1}{\mathrm{Pr}\,R_\lambda}\right)^2 k^4 - 4\left(\frac{N\lambda_o}{u_o}\right)^2}. \tag{2.12}$$

If $N=0$ the last two eigenvalues reduce to their isotropic form:

$$\xi_3 = -\frac{2}{R_\lambda}k^2 \text{ and } \xi_4 = -\frac{2}{\mathrm{Pr}\,R_\lambda}k^2. \tag{2.13}$$

The eigenvalues ξ_1 and ξ_2 are associated with the scalar transport field $\langle u\theta \rangle$, ξ_3 corresponds with the velocity field and ξ_4 with the scalar or potential energy field. The eigenvalues ξ_1 and ξ_2 are always real and thus indicate purely dissipative behavior of the $\langle u\theta \rangle$ field, while the nature of ξ_3 and ξ_4 depends upon the sign of the discriminant in equation (2.12). A non-negative discriminant indicates behavior which is dissipative but modified from the isotropic form. Negativity of the discriminant introduces oscillatory behavior into the problem.

The negativity of the discriminant is wavenumber dependent. As the wavenumber k increases from zero, the discriminant approaches zero, which occurs at a wavenumber value k_o of

$$k_o = \sqrt{\frac{2N^* \mathrm{Pr}\,R_\lambda}{|1-\mathrm{Pr}|}}. \tag{2.14}$$

For wavenumbers greater than k_o the discriminant will be positive and the integrating factors are strictly dissipative (although changed from their passive scalar values), while for wavenumbers smaller than k_o the integrating factors will consist of a dissipative real part and an oscillatory imaginary part. The dissipative part (the first term in equation (2.12)) is the arithmetic mean of the eigenvalues for the passive scalar case. The imaginary part results in oscillatory terms with frequency dependent upon wavenumber.

Figure 2.1 compares the wavenumber dependence of the magnitude of the imaginary part of the eigenvalues (equation (2.12)), or the radial frequency of the resulting

sinusoidal (and cosinusoidal) terms, with a typical initial kinetic energy spectrum. The hydrodynamic conditions are similar to the initial conditions of Métais and Herring [9] but with Pr = 0.7 and 200. Because the oscillatory frequency is close to the $k = 0$ value over the energy-containing range of the spectrum, it appears that any activeness of the turbulence in the sense of Gibson [2] would be due to the initial conditions and tend to disappear in time. Itsweire et al. [4] reported this to be the case for their experiments.

The linear integrating factors are formed by taking the exponential of the eigenvalues multiplied by the time at which the solution is desired. The part of the integrating factors corresponding to the real parts of the eigenvalues we designate the dissipative part, while that due to the imaginary portions we call the oscillatory part. Figure 2.2 shows the equality of the scalar and velocity dissipation integrating factors for wavenumbers up to k_o, after which they diverge and approach their passive scalar values with increasing k. The consequences of this behavior (for Pr < 1) are that energy dissipation in the velocity field is, for given spectral levels, increased from passive scalar levels in the lower wavenumber range, while that for the scalar or potential energy field is decreased. For Prandtl numbers greater than unity this behavior is reversed, as is evident in the figure.

Understanding the interaction of these linear effects with nonlinear advection requires the solution of the full nonlinear equations. Sanderson et al. [10] used the direct interaction approximation (DIA) of Kraichnan [5, 44] to study stably stratified turbulence and make qualitative comparisons with the work of Stillinger et al. [13]. The DIA was also compared by Sanderson and Hill [11] with the direct numerical simulations (DNS) of Métais and Herring [9] and the experiments of Itsweire et

al. [4]. Based upon the success of this previous work the present paper compares the DIA predictions with those of DNS for the cases of active and strongly buoyancy-dominated ("fossil") turbulence.

Numerical Methodology

The full nonlinear governing equations were solved numerically using direct numerical simulation and the direct interaction approximation. The code used for the DNS is a modified version of the pseudo-spectral code developed by R.M. Kerr which employs a third order Runge-Kutta time integration scheme. DNS was used only for computations at Prandtl numbers near unity, while the DIA was used for these conditions as well as at high Pr.

The DIA was derived following Kraichnan [7] for thermally driven turbulence. The tensor correlations were reexpressed in terms of their eigenfunctions. Variation with angle θ between the wavenumber vector $\mathbf{k}$ and the direction $\mathbf{n}$ of the mean scalar gradient was represented by a Legendre series expansion, following Craya [1] and Herring [3]. For the velocity-velocity correlation, e.g., we have

$$U_{ij}(\mathbf{k},t,t') = \sum_{\lambda=1}^{2}\sum_{l=0}^{\infty}\varphi_l^{\lambda}(k,t,t')P_l(\mu_k)e_i^{\lambda}(\mathbf{k})e_j^{\lambda}(\mathbf{k}), \tag{2.15}$$

where $i,\ j\ =\ 1,2,\text{or } 3$ and

$$\mathbf{e}^1(\mathbf{k}) \equiv \frac{\mathbf{k}\times\mathbf{n}}{|\mathbf{k}\times\mathbf{n}|}\ ;\ \mathbf{e}^2(\mathbf{k}) \equiv \frac{\mathbf{k}\times\mathbf{e}^1(\mathbf{k})}{|\mathbf{k}\times\mathbf{e}^1(\mathbf{k})|}\ ;\ \mu_k \equiv \frac{\mathbf{n}\cdot\mathbf{k}}{|\,\mathbf{k}\,|} \tag{2.16}$$

and $P_l(\mu_k)$ is a Legendre polynomial. The first eigenfunction $\varphi^1(k,t,t')$ contains only horizontal velocity components and is thus denoted the vortical component, while the second eigenfunction $\varphi^2(k,t,t')$ contains vertical and horizontal velocity components

Table 2.1: Initial Energy Distributions.

Name	$E_{horiz.}$ or φ_{HH}	$E_{vert.}$ or φ_{VV}	$E_{potential}$
3-D	Nonzero	Nonzero	Zero
2-D	Nonzero	Zero	Nonzero
0-D	Zero	Zero	Nonzero

and is denoted the wave component of the velocity field (see Métais and Herring [9]. The velocity-velocity and scalar-scalar correlations are tensors of even order and so were represented by Legendre polynomials of even order (i.e. $P_l(\mu_k)$ with $l=2m$, $m=0,1,2,...$), and the velocity-scalar and scalar-velocity correlations (vectors) by odd order Legendre functions of the first kind ($P_l^1(\mu_k)$, with $l=2m+1$, $m=0,1,2,...$). The complete listing of the DIA equations will appear in a future paper.

The geometric coefficients were evaluated using the method of residues (Schumann and Herring [12]) while the wavenumber convolution integrals were evaluated using two dimensional tensor B-splines. The time integration of the differential equations was effected by the use of the exact integrating factors (determined by use of the eigenvalues from equations (2.11) and (2.12)) for the linear portion of the equations, analogous to the method outlined in Kraichnan [6].

Both numerical methods employed wavenumbers between 1 and 32. The simulations were performed with a box size of 64^3 while the DIA computations used 18 wavenumbers spaced logarithmically. In keeping with the exploratory nature of this study—as well as to remain within the memory limits of the available computational equipment—the Herring-Craya representations for the correlation and response functions were limited to one Legendre coefficient each.

The initial energy distributions used for the DIA/DNS comparisons are summarized in Table 2.1 with $\varphi_{HH} \equiv \int_0^\infty 2\pi k^2 \varphi_0^{\lambda=1}(k, t{=}0)dk$, $\varphi_{VV} \equiv \int_0^\infty 2\pi k^2 \varphi_0^{\lambda=2}(k, t{=}0)dk$, $E_{\mathbf{horiz.}} \equiv \int_0^\infty \int_{-1}^1 \pi k^2 [U_{11}(\mathrm{k}, t{=}0) + U_{22}(\mathrm{k}, t{=}0)] d\mu_k dk$, $E_{\mathbf{vert.}} \equiv \int_0^\infty \int_{-1}^1 \pi k^2 U_{33}(\mathrm{k}, t{=}0) d\mu_k dk$, and with $E_{\mathbf{potential}} \equiv \int_0^\infty \int_{-1}^1 2\pi k^2 P(\mathrm{k}, t{=}0) d\mu_k dk$. The 3-D case may be active or fossil (buoyancy-dominated) depending upon the hydrodynamic conditions, while the 2-D and 0-D cases are used as idealizations of possible fossil turbulence situations. Although the value of φ_{VV} depends, in general, upon both $E_{\mathbf{horiz.}}$ and $E_{\mathbf{vert.}}$, the lowest order truncation used in this study requires φ_{VV} to be identically zero when $E_{\mathbf{vert.}}$ is zero, i.e. for the 2-D and 0-D initial conditions, thus enabling a direct comparison between the DIA and DNS results for these cases. All nonzero initial energy spectral shapes were of the form ak^3e^{-bk} with a and b constant and peak wavenumber $k = 4.76$, except for the value 3.60 used with the scalar field in the 2-D case. A viscosity value of $\nu = 0.007$ was employed. All results are for Brunt-Väisälä frequencies N of 2π and a Prandtl number of 0.7 unless otherwise noted.

Results and Discussion

The results of the (truncated) DIA theory were assessed by comparing its performance in the three cases of Table 2.1 with those of the DNS. The evolution of total energy (kinetic plus potential) for each of the cases outlined in Table 2.1 is plotted in Figure 2.3 as calculated by the DNS and the DIA computations.

Both techniques yield similar results, although the DIA results are not quite as sensitive to initial conditions as are the DNS results. Both predict decreased rates of total energy dissipation as the turbulence field is reduced in initial importance, i.e. as first the vertical component and then all components are initialized with

zero kinetic energy. This occurs despite the fact that, with Pr = 0.7, the scalar diffusivity is higher than the kinematic viscosity. This attests to the importance, even under strongly buoyancy-dominated conditions, of the nonlinear energy cascade in determining total energy dissipation.

Figure 2.4 compares the predicted evolutions of the half-horizontal energy fields for the DNS and DIA. The 3-D and 2-D cases display reasonably good agreement between the two methods, but significant disagreement occurs in the 0-D case. Although the horizontal velocity field is isotropic in all cases, the 0-D represents an especially severe test of the DIA treatment of the nonlinear terms, since the growth of the horizontal kinetic energy is due solely to nonlinearities. Thus, while some errors in the DIA may not be significant in the 3-D and 2-D cases, they will be quite obvious in the 0-D situation. It is apparent that the truncated Legendre series expansion performs most poorly in the 0-D case. The question of to what degree the inclusion of higher order Legendre functions can improve this performance cannot be answered at this time.

Figures 2.5 and 2.6 compare the results of the two techniques for the potential and vertical kinetic energy histories of the 0-D problem. They are representative of all the cases tested. Again the DIA displays shortcomings in its treatment of nonlinearities, as it tends to oscillate more strongly than the DNS, behaving like the linear problem in that the energies become very nearly zero at their minima. The difference in phase is unexplained at this time but may also be due to the nonlinearities.

Figures 2.7 and 2.8 compare the evolution of the scalar transport eddy diffusivity ratio ($\varepsilon_h/\alpha \equiv -\langle u_3\vartheta\rangle/\alpha a$) and the scalar transport correlation coefficient

($\rho_{u\theta} \equiv \langle u_3\vartheta\rangle/u_3'\vartheta'$), respectively, as computed by the DNS for the three cases of Table 2.1. The large $\rho_{u\theta}$ magnitudes observed in air flow experiments by Lienhard and Van Atta [8] and numerically by Métais and Herring [9] and by Sanderson and Hill [11] are evident in Figure 2.8. Although oscillations of $\rho_{u\theta}$ for the 3-D and 2-D cases are opposite in phase, the differences in amplitude between the two cases are relatively small, apparently due to the presence in both cases of significant amounts of horizontal kinetic energy contributing to the nonlinearities of the problem. The 0-D case displays somewhat stronger oscillations, perhaps due to reduced nonlinearities caused by the low levels of the horizontal velocity field compared with the other cases. The DIA results for these quantities behave in a similar manner but display the same shortcomings as discussed earlier with respect to the half-horizontal kinetic energy field in the 0-D problem.

The DIA also shows some interesting characteristics of the anisotropy of the turbulence. Figure 2.9 shows the evolution of the ratio of the vertical and horizontal DIA eigenfunctions at two wavenumbers in the 3-D case for conditions similar to those used by Métais and Herring [9] ($\mathrm{Pr}=1$, $N=0.98$), in which the initial potential energy field was small but nonzero. The highest wavenumber ($k=29.145$ or $k^*=k\lambda_o=12.15$) is well into the dissipation range, while the lower one ($k = 10.029$ or $k^* = 4.18$) is in the upper end of the energy containing range. Although these experiments showed a transition to buoyancy domination, neither wavenumber exhibits significant anisotropy. To obtain more history with the DIA (which requires all historical values of the variables due to its two time structure), subsequent studies used the higher value of $N=2\pi$.

Figure 2.10 illustrates the DIA eigenfunction ratio for the same two wavenum-

bers at the higher N for a 3-D problem. Significantly more anisotropy, indicated by the deviation of the eigenfunction ratio from unity, is evident at both wavenumbers, especially for k in the energy-containing range, due to the stronger stratification. The corresponding behavior for the high wavenumber under 0-D conditions (all initial energy in the potential field) for Prandtl numbers of 0.7 and 200 is shown in Figure 2.11 and the same for the lower wavenumber in Figure 2.12. Both wavenumbers exhibit significantly stronger oscillations than for the 2-D problem. Although the low Prandtl number case ($\mathrm{Pr} = 0.7$) has oscillatory integrating factors over a wider wavenumber range than does the high Prandtl number case ($\mathrm{Pr} = 200$), the latter case displays stronger high wavenumber oscillations even though oscillations are absent from the linear problem at this Pr.

The enhanced anisotropy of the kinetic energy field in the case of 0-D initial conditions is due to the efficient (linear) transfer of energy from the potential field to the vertical velocity field and the relatively slower nonlinear transfer from the vertical to horizontal velocity components. This is illustrated in Figure 2.13 where the vertical energy, predicted by DNS and normalized with respect to total energy, is plotted as a function of time for the three cases of Table 2.1. The 0-D case experiences oscillations of the largest magnitude. The effectiveness of the linear energy transfer is also reflected in the comparison of the scalar transport correlation coefficients in Figure 2.8. Although the differences are not so pronounced here, the 0-D case exhibits the highest oscillation peaks. With reference to Figure 2.13, it should be pointed out that differences in initial potential energies could account for these variations. However, the differences in initial potential energies are less by a factor of two, while the two vertical energy fields differ in peaks by a factor of approximately three. It

appears that the presence of significant horizontal kinetic energy may act to damp the oscillations in the vertical field by nonlinear energy transfer to and from the vertical modes.

Figures 2.14–2.16 compare typical DNS three-dimensional spectra of the vertical kinetic, half-horizontal, and potential energy fields for the 0-D, 2-D, and 3-D cases at a Prandtl number of 0.7. The figures show that there is more scalar energy at low k in the 0-D and 2-D cases than in the 3-D case. Also, the energy spectra for the 2-D case resemble those of the 0-D case at low k and the 3-D case at high k, probably because of the smaller nonlinear transfer rate in the 0-D case.

Figures 2.17 and 2.18 compare typical spectra from DIA computations for the 0-D case and Prandtl numbers of 0.7 and 200. The vortical eigenfunction (φ_{HH}) spectrum displays a pronounced upward shift in peak wavenumber compared to the wave eigenfunction (φ_{VV}) and potential energy spectra. The shift is not nearly as pronounced with the half-horizontal and vertical kinetic energy spectra, probably due to the clearer distinction between vortical and wave modes in the eigenfunction representation. There is a reversal of relative magnitudes of vertical and potential energies between the DNS and DIA results, possibly because of a phase shift in the energy exchange between these fields, as suggested by Figures 2.5 and 2.6. Increasing the Prandtl number in Figure 2.18 does not significantly affect the low k spectral shapes or relative peaks. This suggests that inferences from the studies of Stillinger, et al. [13] and Itsweire, et al. [4], concerning the large scales of the velocity and scalar fields, may be applied to Prandtl numbers near unity.

Figure 2.19 compares the spectra for the horizontal, vertical and potential energies of the nonlinear DIA and the linear (RDT) problems for $N = 2\pi$. The linear

RDT analysis displays no spectral shift; rather, all of the spectra evolve to the same shape. The shift in the DIA spectrum appears to be a result of stronger nonlinear energy transport up the wavenumber spectrum for the horizontal kinetic energy than for the vertical kinetic and potential energies. Examination of the exact kinetic and potential energy equations suggests a reason for this difference. The equations for a vertically oriented gradient ($n_i = \delta_{i3}$) are

$$\left(\frac{d}{dt} + \frac{2k^2}{R_\lambda}\right) U_{11}(\mathbf{k},t) = -\imath P_{1mn}(\mathbf{k}) \sum_{\mathbf{p}+\mathbf{q}=\mathbf{k}} \langle u_m(\mathbf{p},t) u_n(\mathbf{q},t) u_1(-\mathbf{k},t)\rangle \tag{2.17}$$

$$\left(\frac{d}{dt} + \frac{2k^2}{R_\lambda}\right) U_{33}(\mathbf{k},t) - N^{*2}\left[U_{3\theta}(\mathbf{k},t) + U_{\theta 3}(\mathbf{k},t)\right] = \tag{2.18}$$

$$-\imath P_{3mn}(\mathbf{k}) \sum_{\mathbf{p}+\mathbf{q}=\mathbf{k}} \langle u_m(\mathbf{p},t) u_n(\mathbf{q},t) u_3(-\mathbf{k},t)\rangle \tag{2.19}$$

$$\left(\frac{d}{dt} + \frac{2k^2}{\mathrm{Pr}\, R_\lambda}\right) U_{\theta\theta}(\mathbf{k},t) + \left[U_{\theta 3}(\mathbf{k},t) + U_{3\theta}(\mathbf{k},t)\right] = \tag{2.20}$$

$$-\imath k_m \sum_{\mathbf{p}+\mathbf{q}=\mathbf{k}} \langle u_m(\mathbf{p},t) \vartheta(\mathbf{q},t) \vartheta(-\mathbf{k},t)\rangle, \tag{2.21}$$

with the equation for $U_{22}(\mathbf{k},t)$ similar to that for $U_{11}(\mathbf{k},t)$. The nonlinear terms in equations (2.17) through (2.21) are formed from the product of three dynamical quantities. The third variable is associated with the energy variable for which the equation is derived: $u_1(-\mathbf{k},t)$ for the equation governing $U_{11}(\mathbf{k},t)$, $u_3(-\mathbf{k},t)$ for the equation governing $U_{33}(\mathbf{k},t)$, and $\vartheta(-\mathbf{k},t)$ for the equation governing $U_{\theta\theta}(\mathbf{k},t)$. The stratification reduces the magnitude of the vertical velocity components and scalar variables to values which are generally less than those of the horizontal velocity components. Thus the vertical kinetic and potential energy equations have nonlinear terms whose third factors are reduced in magnitude by the stratification, while the third factors of the horizontal kinetic energy nonlinear terms are the relatively undamped horizontal

velocity components. The nonlinear terms in the potential energy equation contain one velocity factor and two scalar factors and thus are doubly reduced by the stratification. Consequently, the potential and vertical kinetic energies can be expected to behave in a somewhat more linear fashion than does the horizontal kinetic energy.

Conclusions

The truncated DIA tested here appears to predict qualitatively correct behavior of buoyancy-dominated or fossil turbulence but is inadequate for producing reliable quantitative results. It is possible that the angular dependence of the eigenfunctions requires more accurate representation by retaining higher order Legendre functions than used here. The numerical studies of fossil turbulence have shown some interesting dependencies upon the relative energy distributions. These include (1) enhanced oscillations of the scalar transport correlation coefficient and the vertical kinetic energy field, (2) a higher degree of anisotropy (especially at high Prandtl numbers) for the cases with zero initial vertical kinetic energy compared to the case of an isotropic initial velocity field, and (3) a stronger spectral shift of energy to low wavenumbers for the scalar and vertical velocity fields than for the horizontal velocity field. This last effect appears to be due to the repression of the nonlinearities of the scalar and vertical velocity fields by the mean density gradient. The high Pr results indicate little effect of Pr on this peak wavenumber shift, implying a small Pr effect on the large scale motions.

Acknowledgements

The authors are grateful for the support of the Iowa State University Computation Center, the National Center for Supercomputing Applications, the IBM Palo Alto Scientific Center (through the IBM Research Assistance Program), and the National Center for Atmospheric Research which is funded by the National Science Foundation. The authors also appreciate the use of the turbulence simulation code provided by Dr. R.M. Kerr and the assistance of Ms. M. Chakrabarti in carrying out the simulations.

References

[1] Craya, A.; *Contribution a l'Analyse de la Turbulence a des Vitesse Moyennes*, P.S.T. Ministere de l'Air (Fr.), 1958.

[2] Gibson, C.H.; Internal waves, fossil turbulence, and composite ocean microstructure spectra. *J. Fluid Mech.*, **168**, 89–117, 1986.

[3] Herring, J.R.; Approach of axisymmetric turbulence to isotropy. *Phys. Fluids*, **17**, pp. 859–872, 1974.

[4] Itsweire, E.C., Helland, K.N., & Van Atta, C.W.; Evolution of grid-generated turbulence in a stably stratified fluid. *J. Fluid Mech.*, **162**, pp. 299–338, 1986.

[5] Kraichnan, R.H.; The structure of isotropic turbulence at very high Reynolds numbers. *J. Fluid Mech.*, **5**, pp. 497–543, 1959.

[6] Kraichnan, R.H.; Decay of isotropic turbulence in the direct-interaction approximation. *Phys. Fluids*, **7**, pp. 1030–1048, 1964.

[7] Kraichnan, R.H.; Direct-interaction approximation for shear and thermally driven turbulence. *Phys. Fluids*, **7**, pp. 1048–1062, 1964.

[8] Lienhard V, J.H. & Van Atta, C.W.; The decay of turbulence in thermally stratified flow. *J. Fluid Mech.*, **210**, pp. 57–112, 1990.

[9] Métais, O. & Herring, J.R. 1989 Numerical simulations of freely evolving turbulence in stably stratified fluids. *J. Fluid Mech.*, **202**, pp. 117–148, 1989.

[10] Sanderson, R.C., Hill, J.C. and Herring, J.R.; Transient behavior of a stably stratified homogeneous turbulent flow. *Advances in Turbulence*, G. Comte-Bellot & J. Mathieu, eds. Springer-Verlag, Berlin, pp. 184–190, 1986.

[11] Sanderson, R.C. and Hill, J.C.; Dynamics of decaying stably stratified turbulent flow. *Eighth Symposium on Turbulence and Diffusion*(Preprint Volume), American Meteorological Society, Boston, Mass., pp. 53–56, 1988.

[12] Schumann, U. & Herring, J.R.; Axisymmetric homogeneous turbulence: a comparison of direct simulations with the direct–interaction approximation. *J. Fluid Mech.*, **76**, pp. 755–782, 1976.

[13] Stillinger, D.C., Helland, K.N., & Van Atta, C.W.; Experiments on the transition of homogeneous turbulence to internal waves in a stratified fluid. *J. Fluid Mech.*, **131**, pp. 91–122, 1983.

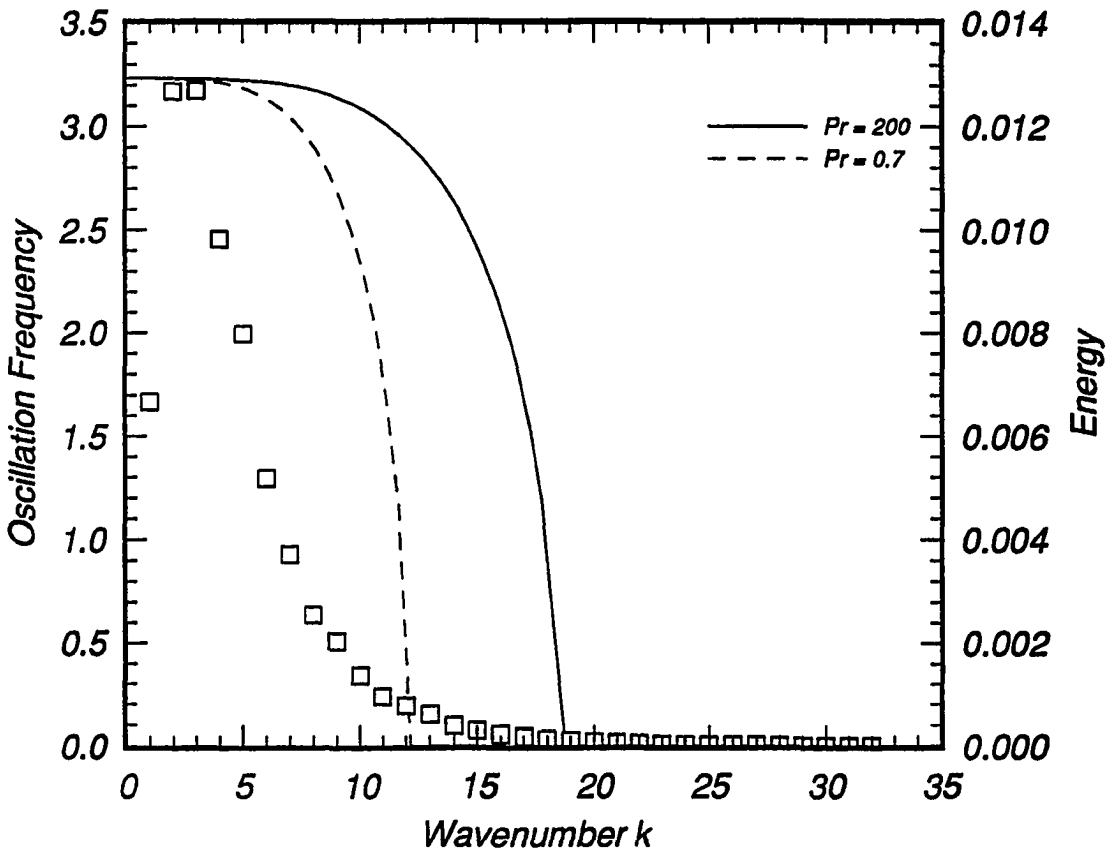

Figure 2.1: Wavenumber dependence of the oscillatory part of the linear eigenvalues (squares represent a typical energy spectrum, lines are oscillation frequencies).

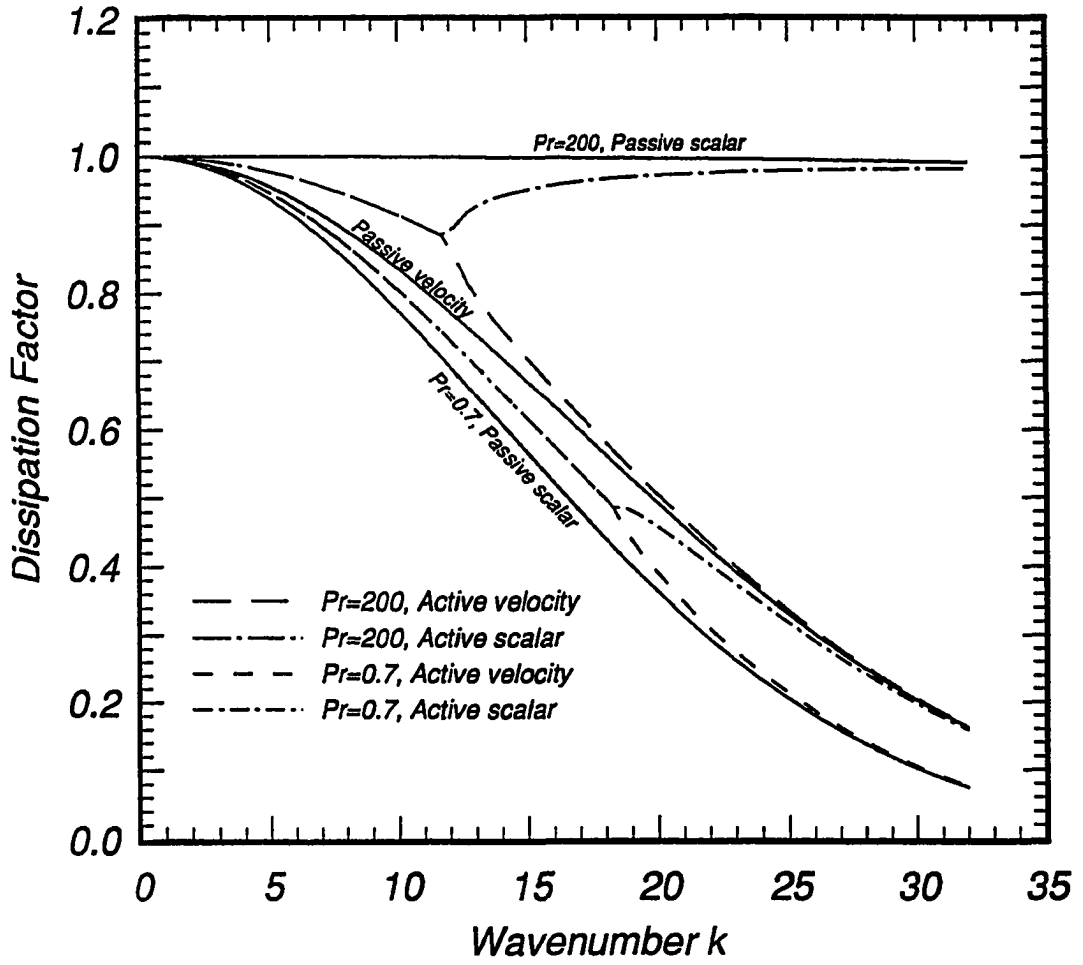

Figure 2.2: Dependence of dissipative part of linear integrating factors upon wavenumber for $\mathrm{Pr} = 0.7$, $N = 2\pi$.

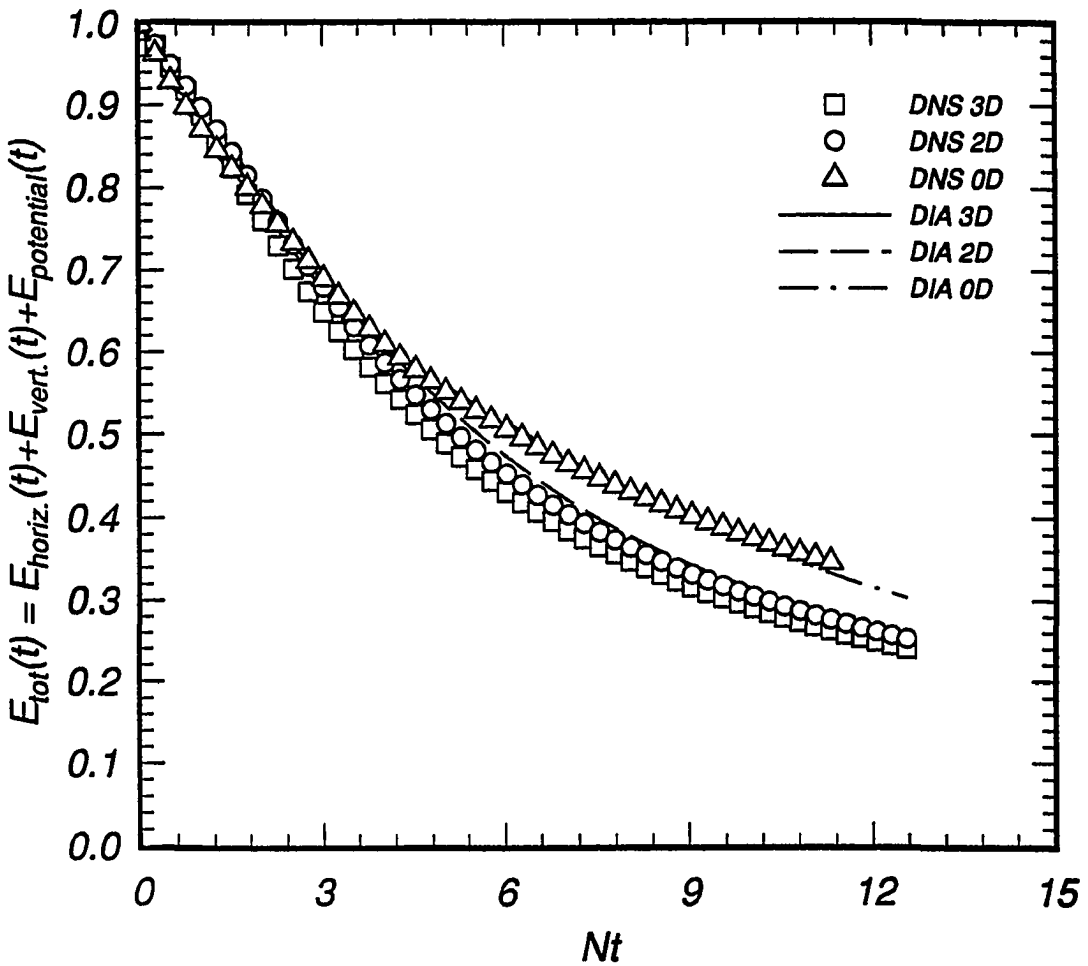

Figure 2.3: Total energy histories for DIA and DNS computations.

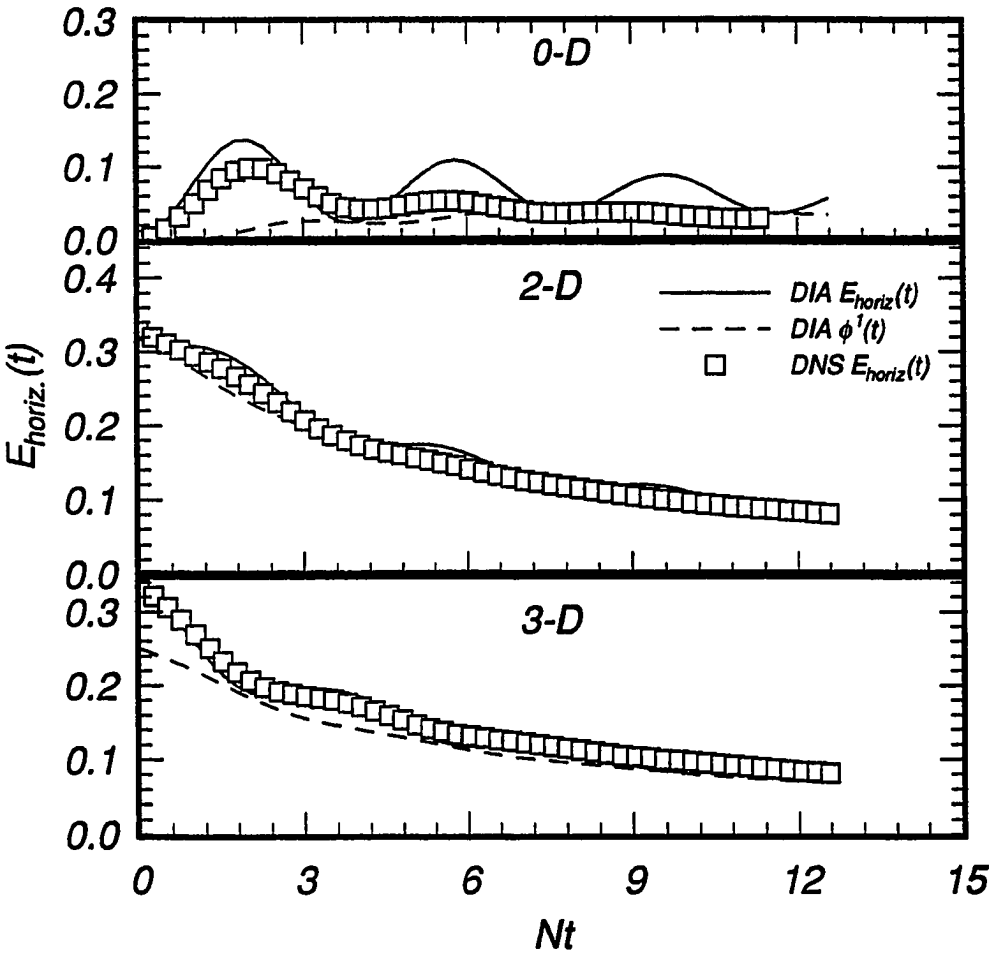

Figure 2.4: Half-horizontal DNS and DIA energy histories for the cases Table 1. For comparison the vortical DIA energy φ_{HH} is indicated by the dashed lines.

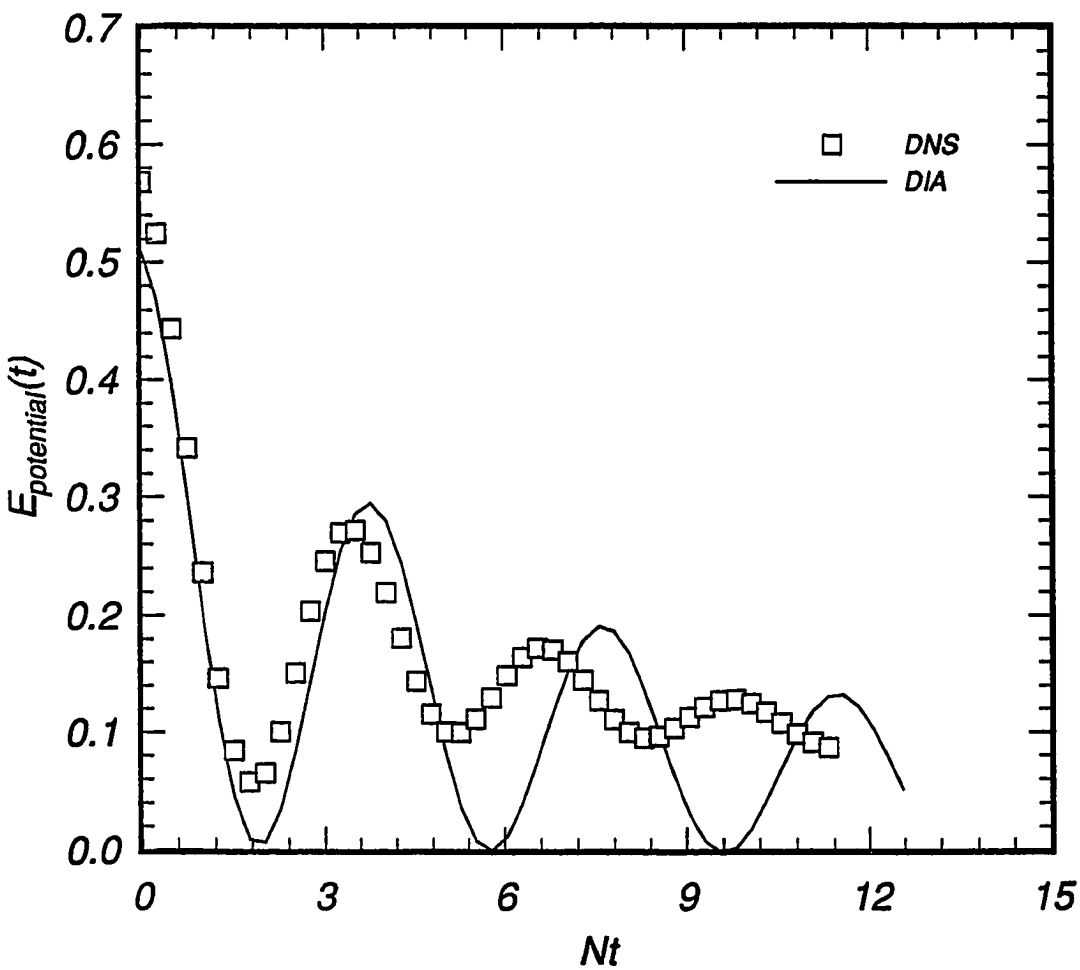

Figure 2.5: Potential energy histories for the 0-D case.

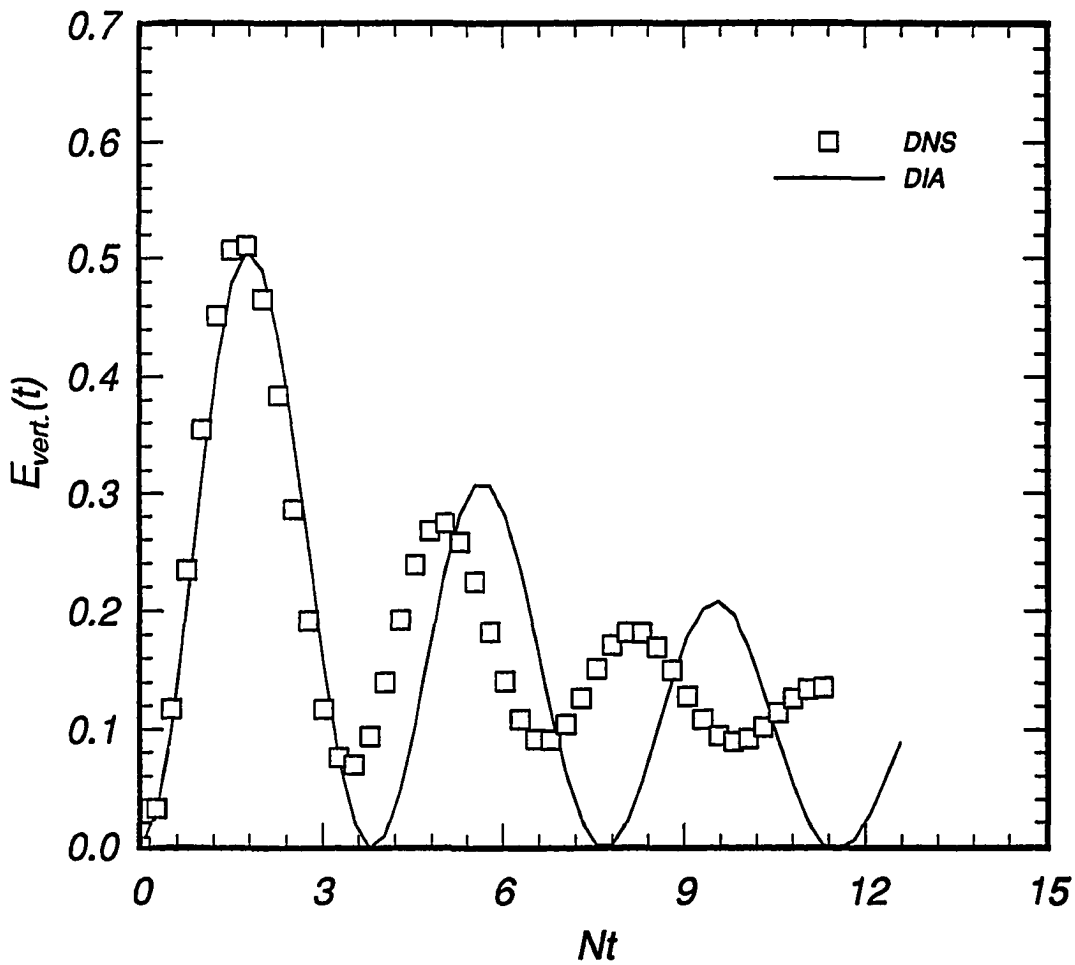

Figure 2.6: Vertical kinetic energy histories for the 0-D case.

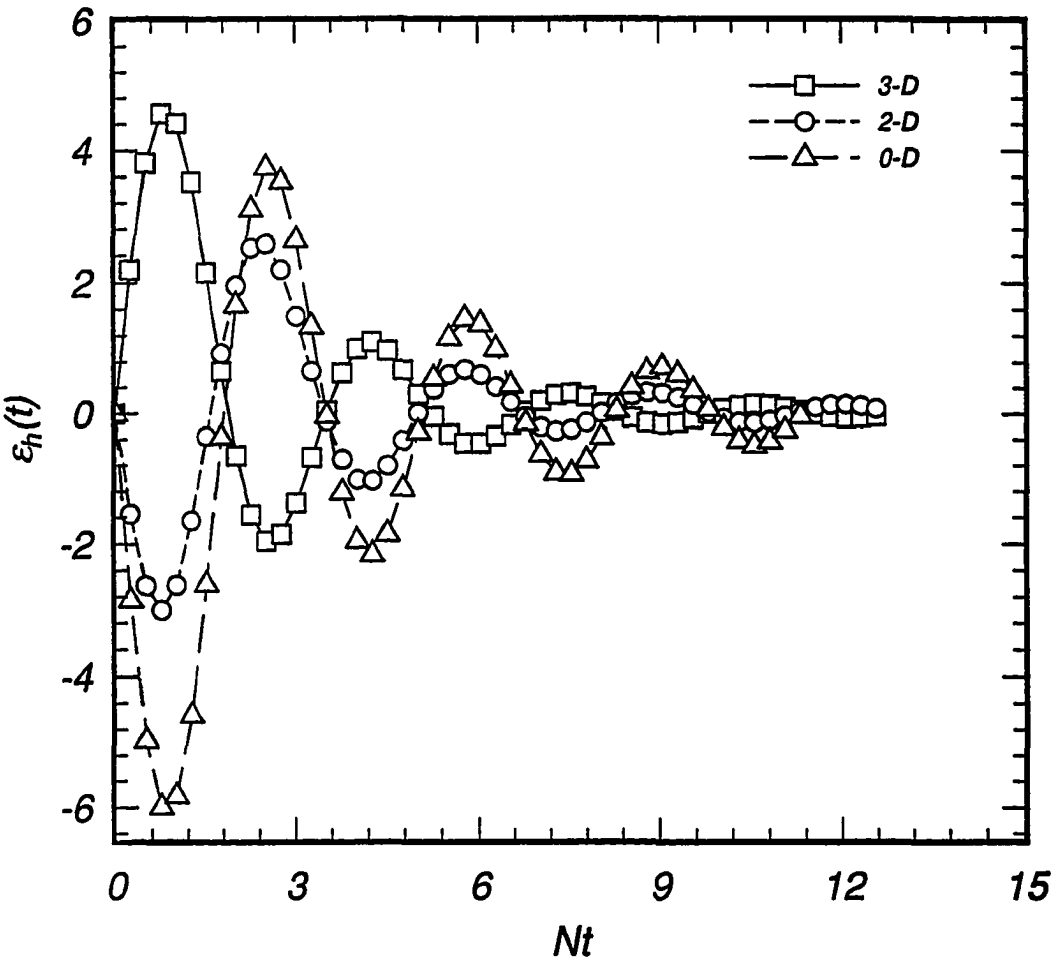

Figure 2.7: DNS eddy diffusivity ratio histories for the cases of Table 1.

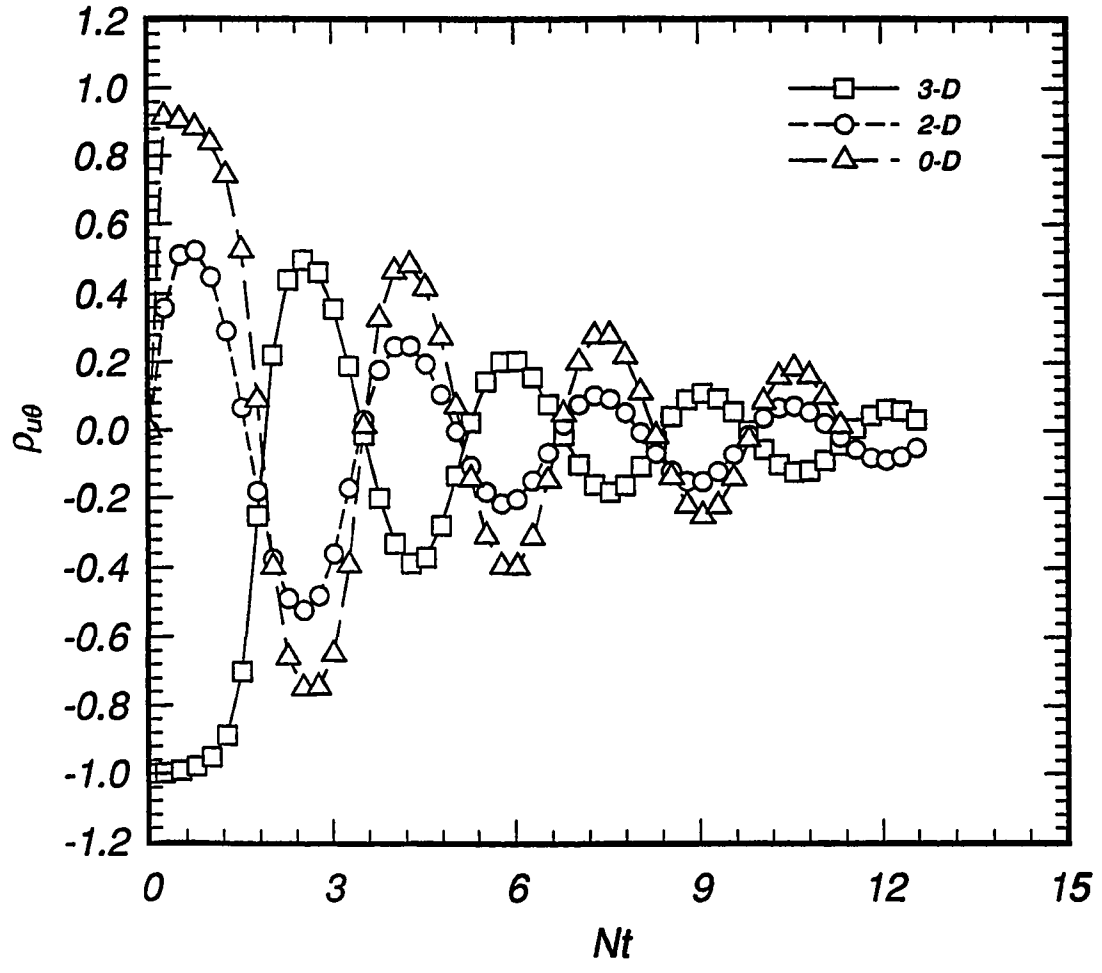

Figure 2.8: DNS histories of scalar transport correlation coefficients for the cases of Table 1.

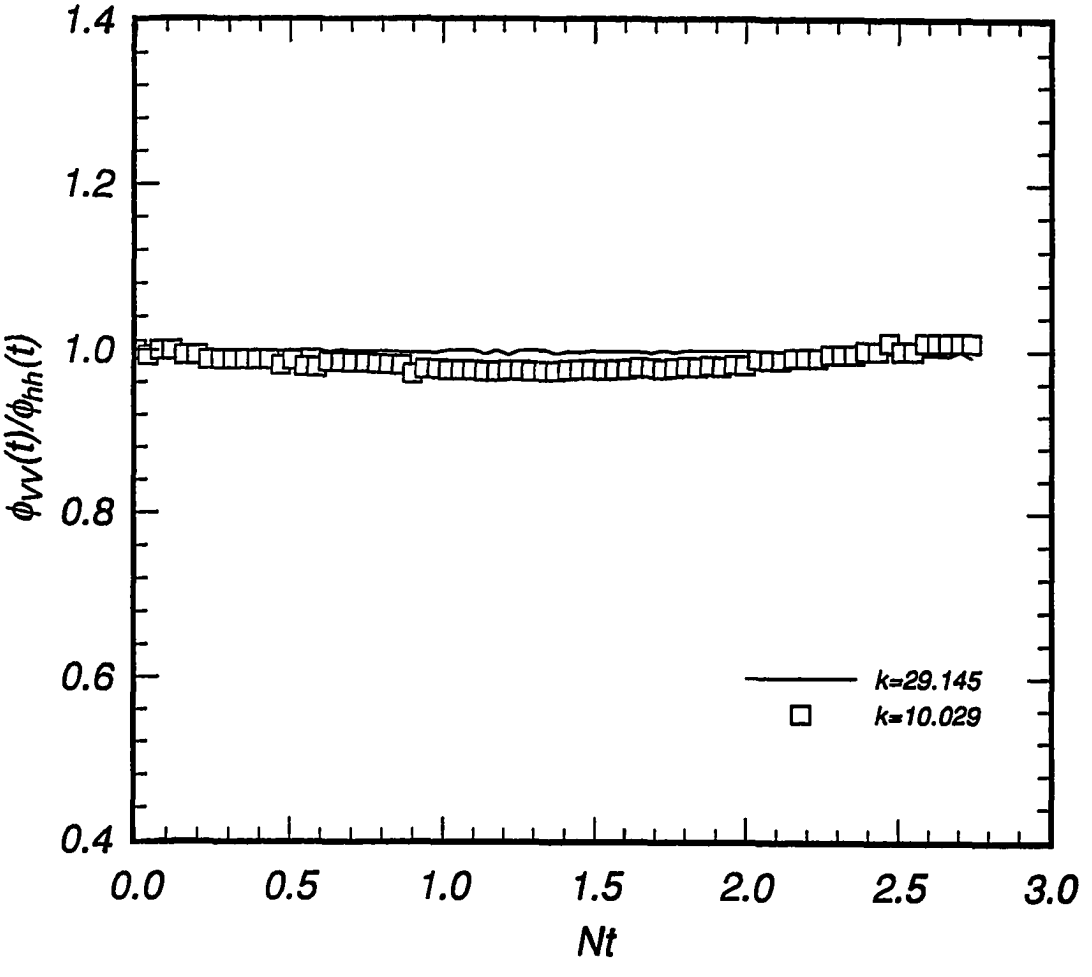

Figure 2.9: Evolution of the DIA eigenfunction ratio $\varphi_0^{\lambda=2}(k,t,t)/\varphi_0^{\lambda=1}(k,t,t)$, for the 3-D case ($N=0.98$).

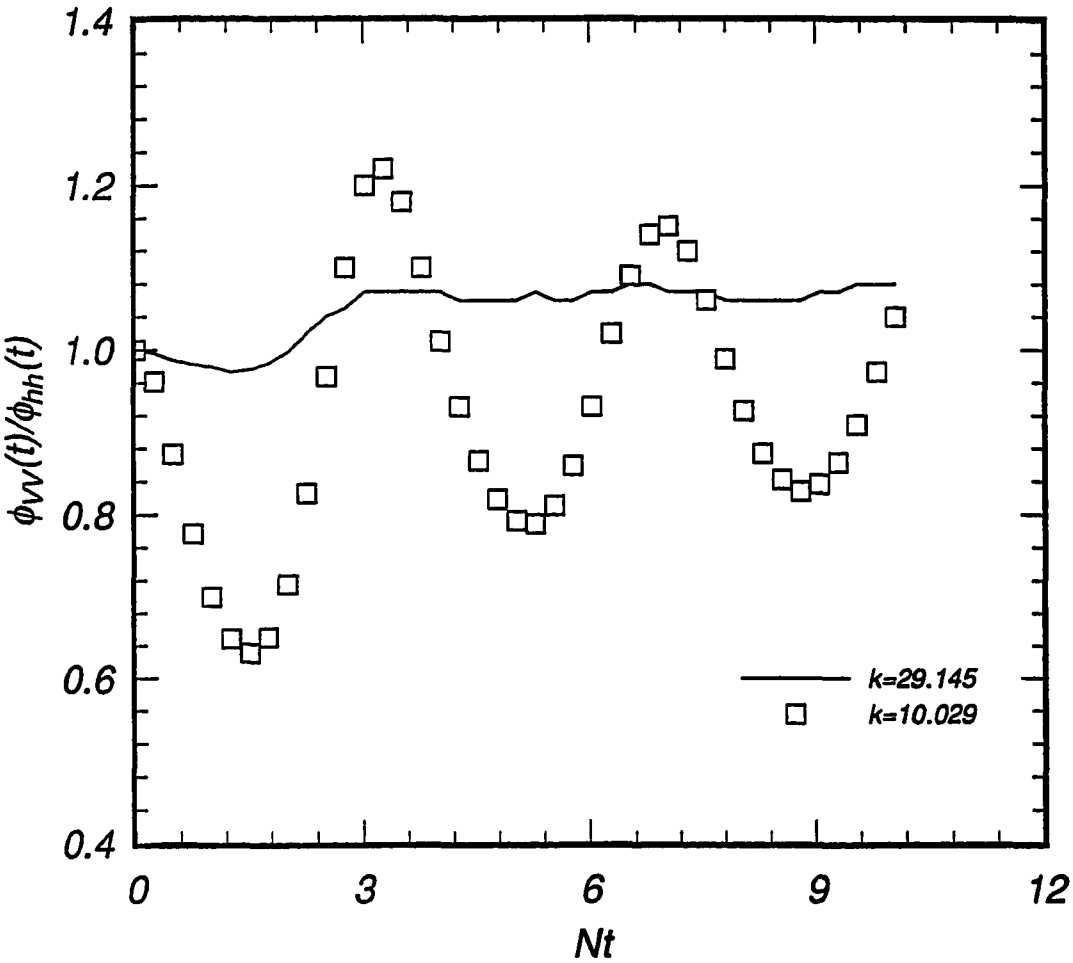

Figure 2.10: Evolution of the DIA eigenfunction ratio for the 3-D case ($N=2\pi$).

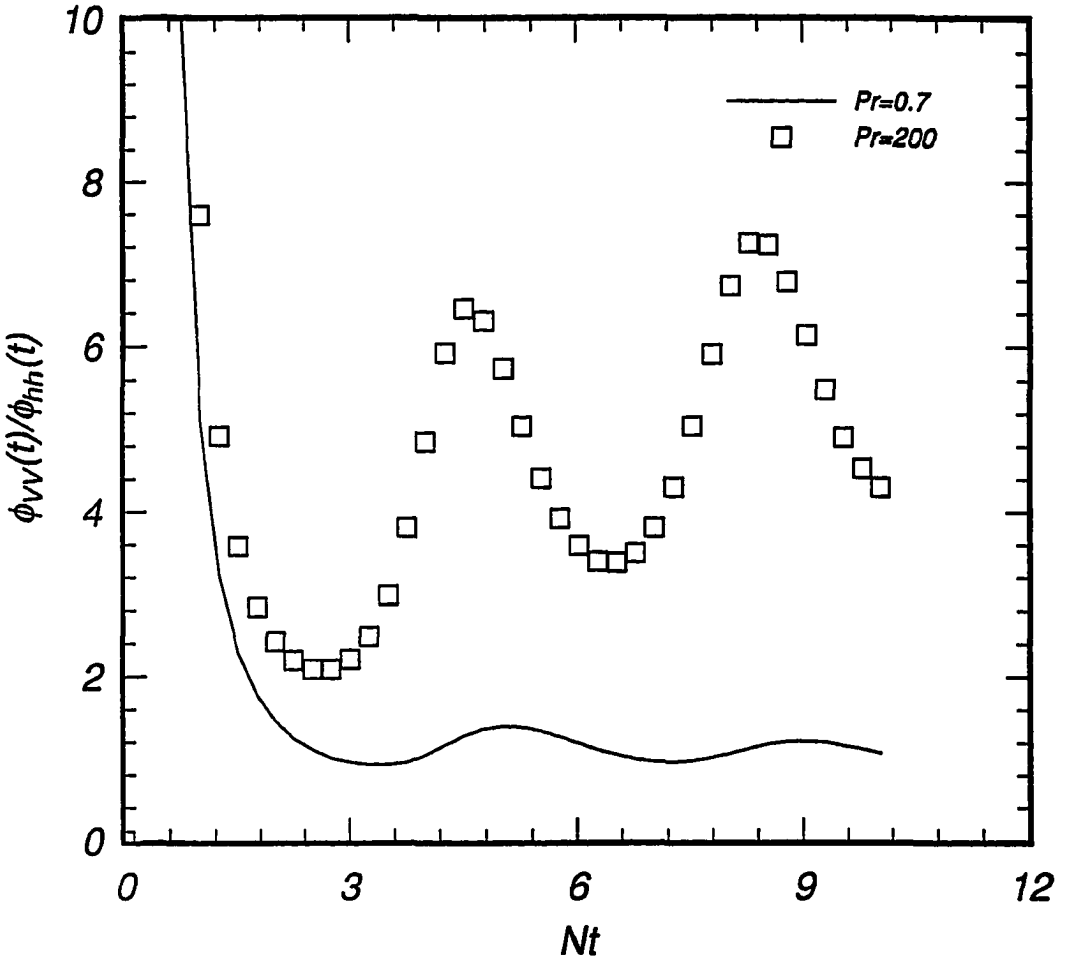

Figure 2.11: Evolution of the DIA eigenfunction ratio for the 0-D case ($N=2\pi, k=29$).

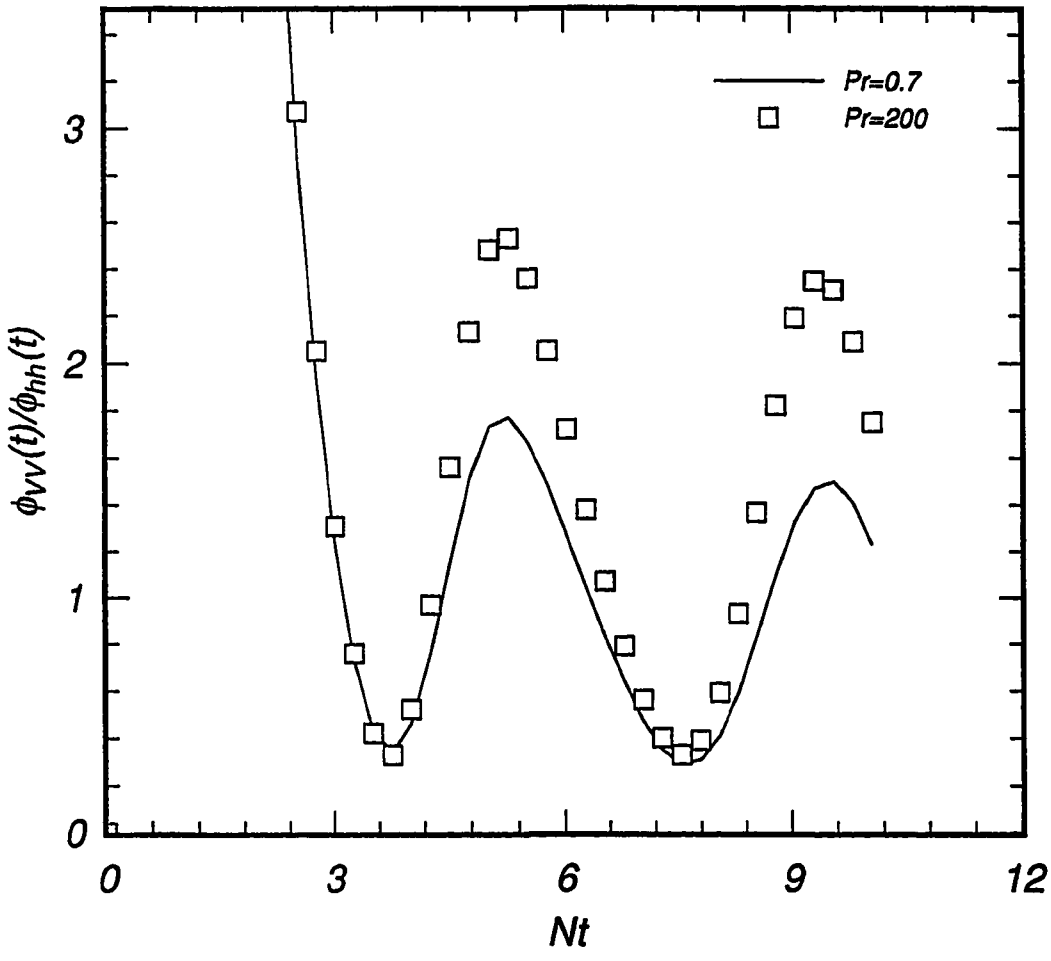

Figure 2.12: Evolution of the DIA eigenfunction ratio for the 0-D case ($N=2\pi, k=10$).

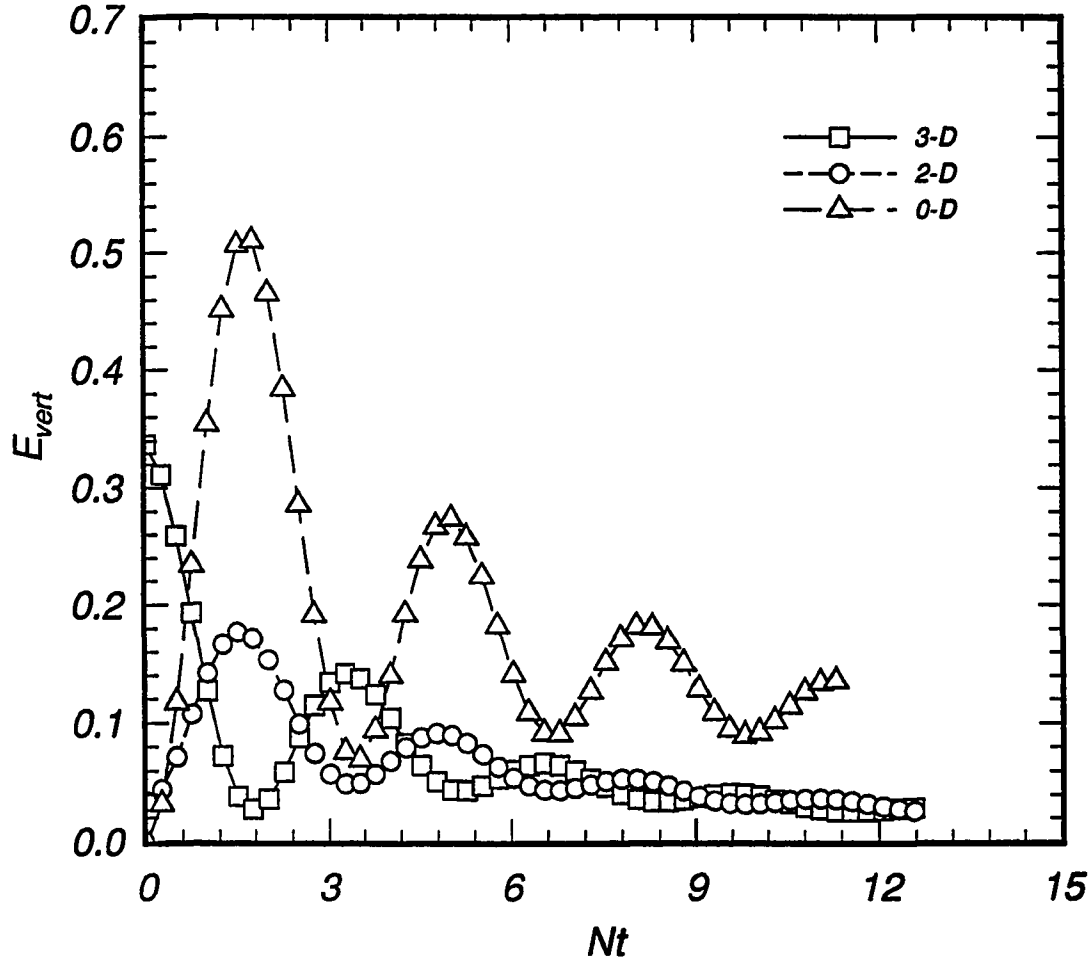

Figure 2.13: Evolution of the vertical kinetic energy (predicted by DNS) for stably stratified turbulence ($N = 2\pi$).

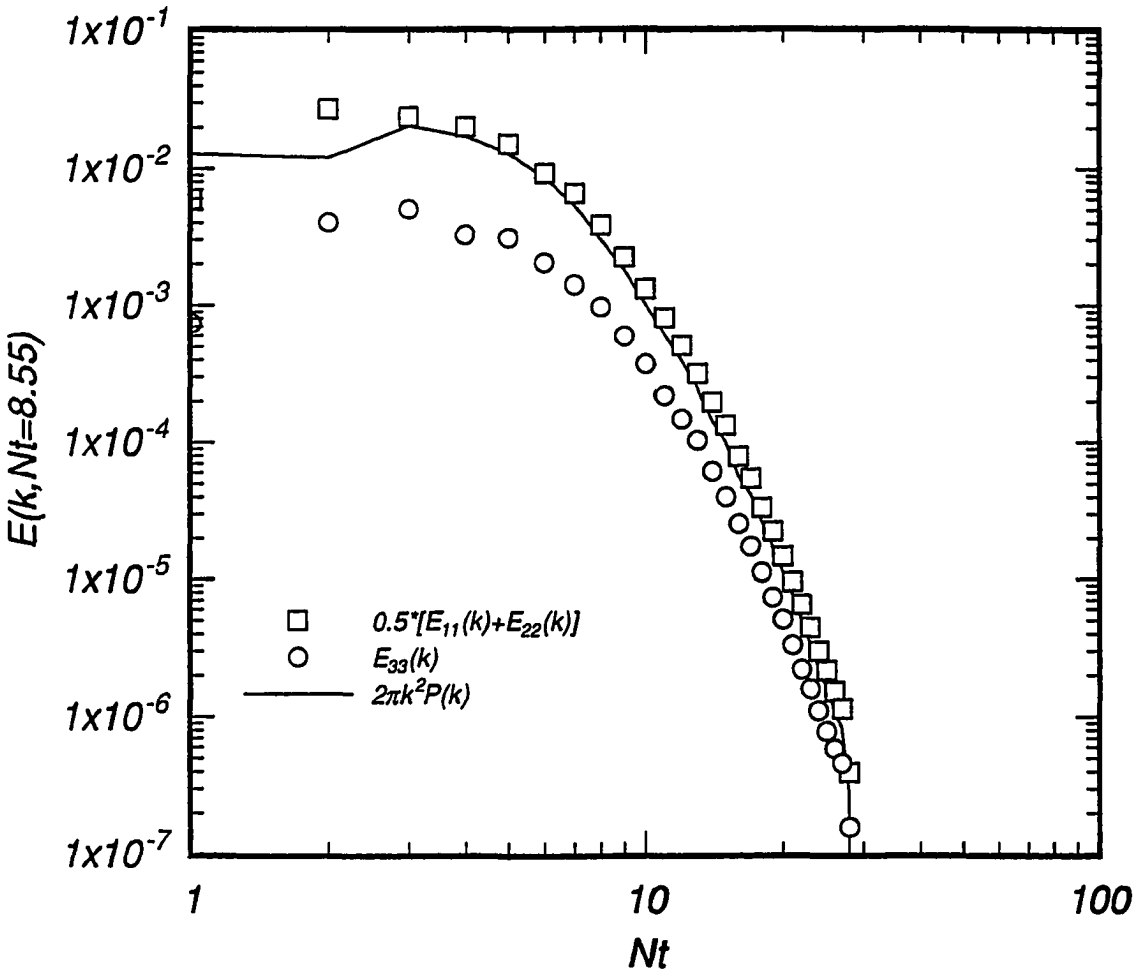

Figure 2.14: DNS energy spectra for the 0-D case ($N=2\pi, \mathrm{Pr}=0.7, Nt=8.55$).

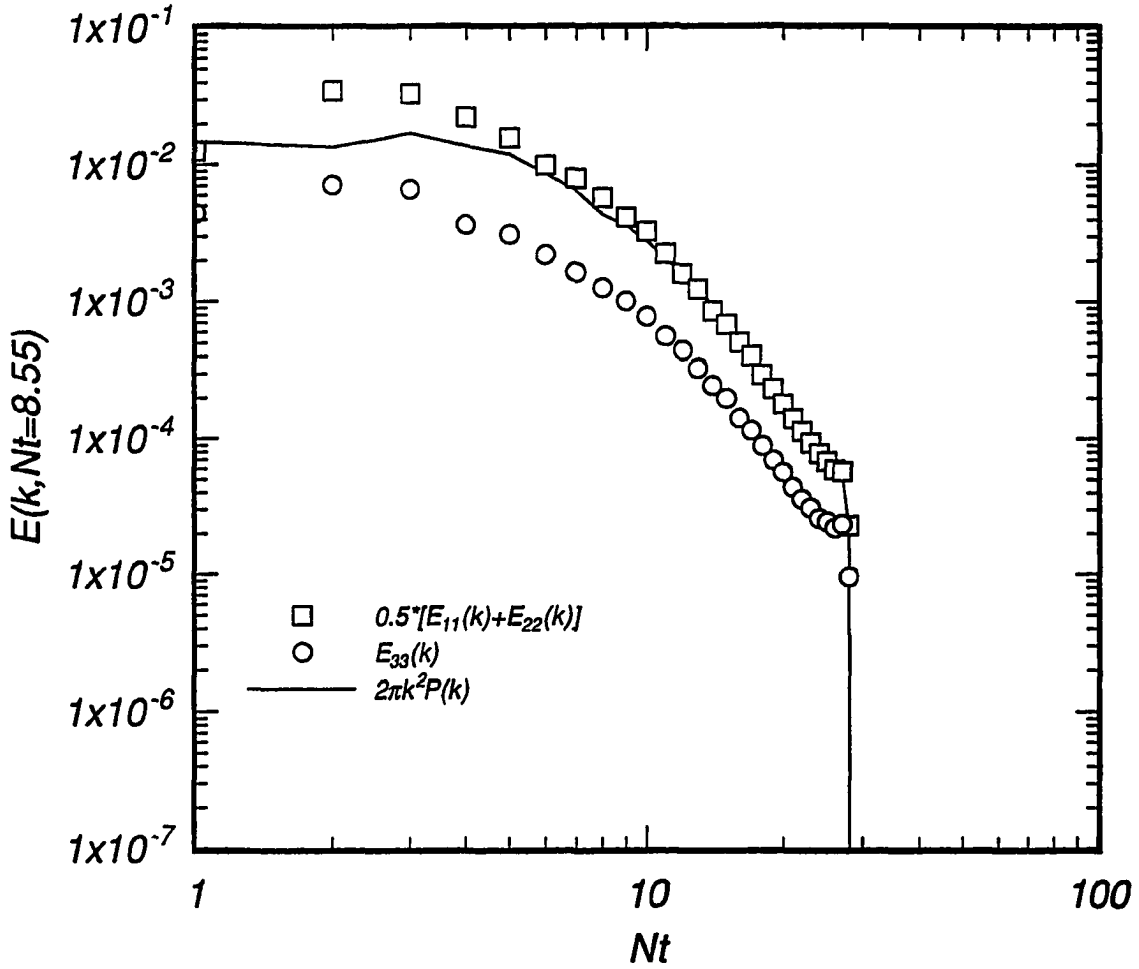

Figure 2.15: DNS energy spectra for the 2-D case ($N=2\pi, \mathrm{Pr}=0.7, Nt=8.55$).

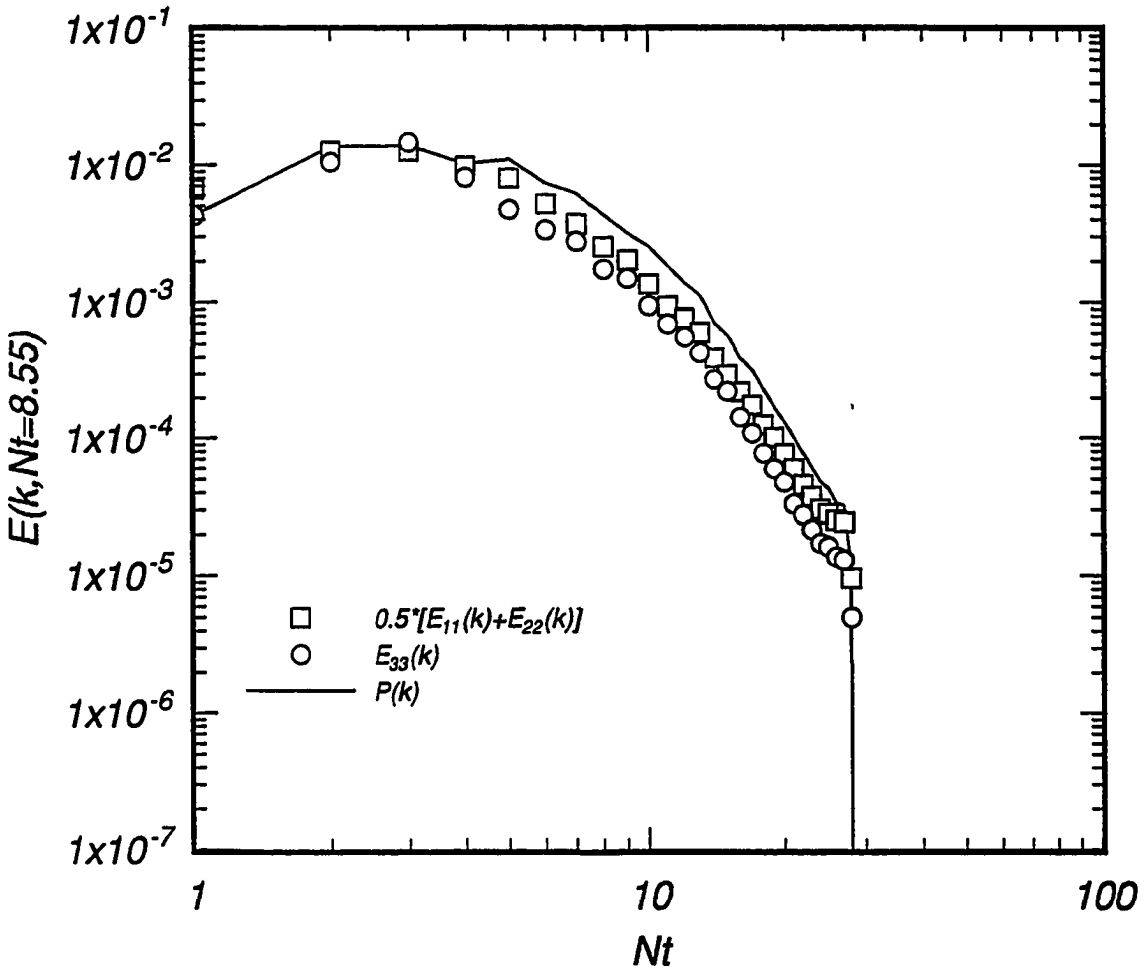

Figure 2.16: DNS energy spectra for the 3-D case ($N=2\pi, \mathrm{Pr}=0.7, Nt=8.55$).

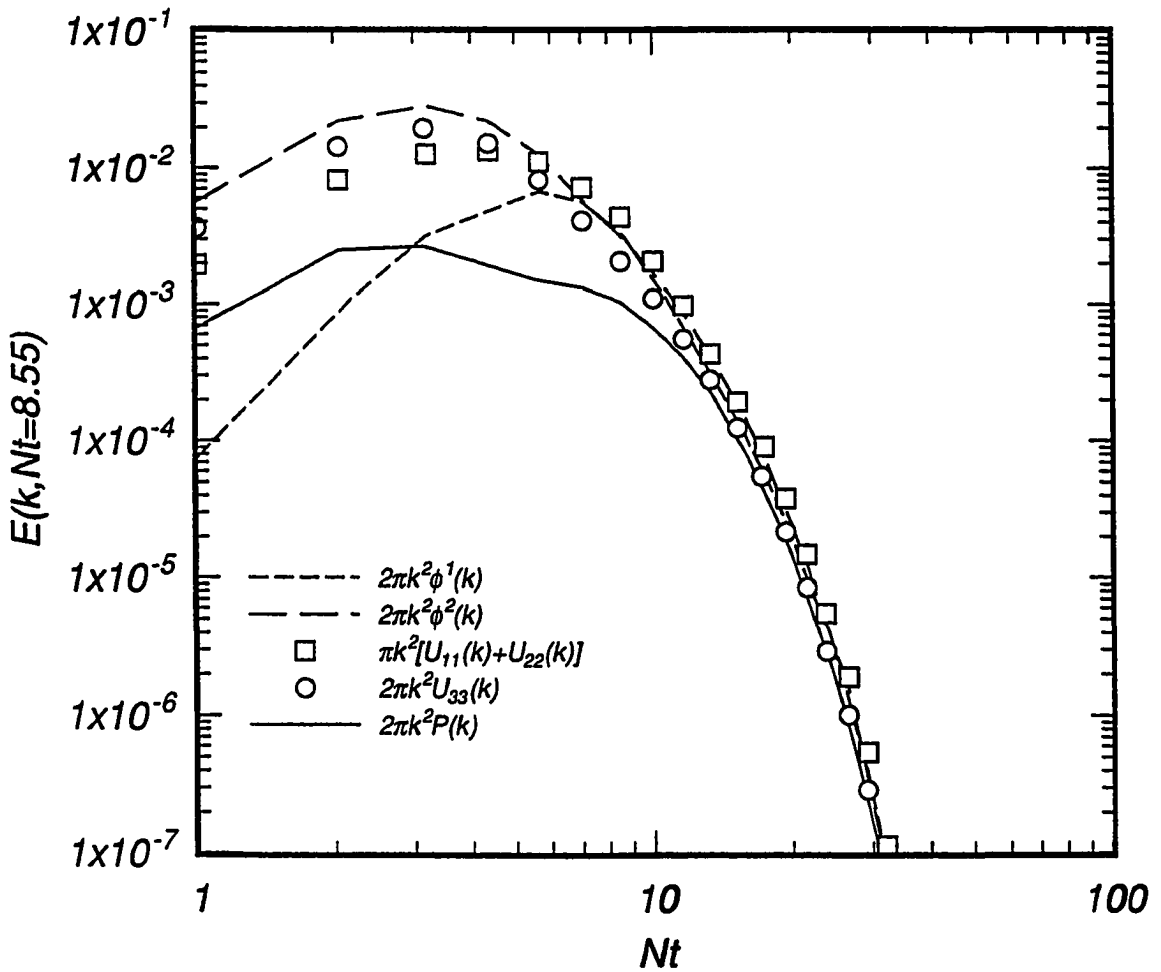

Figure 2.17: DIA energy spectra for the 0-D case ($N=2\pi$, Pr$=0.7$, $Nt=8.55$).

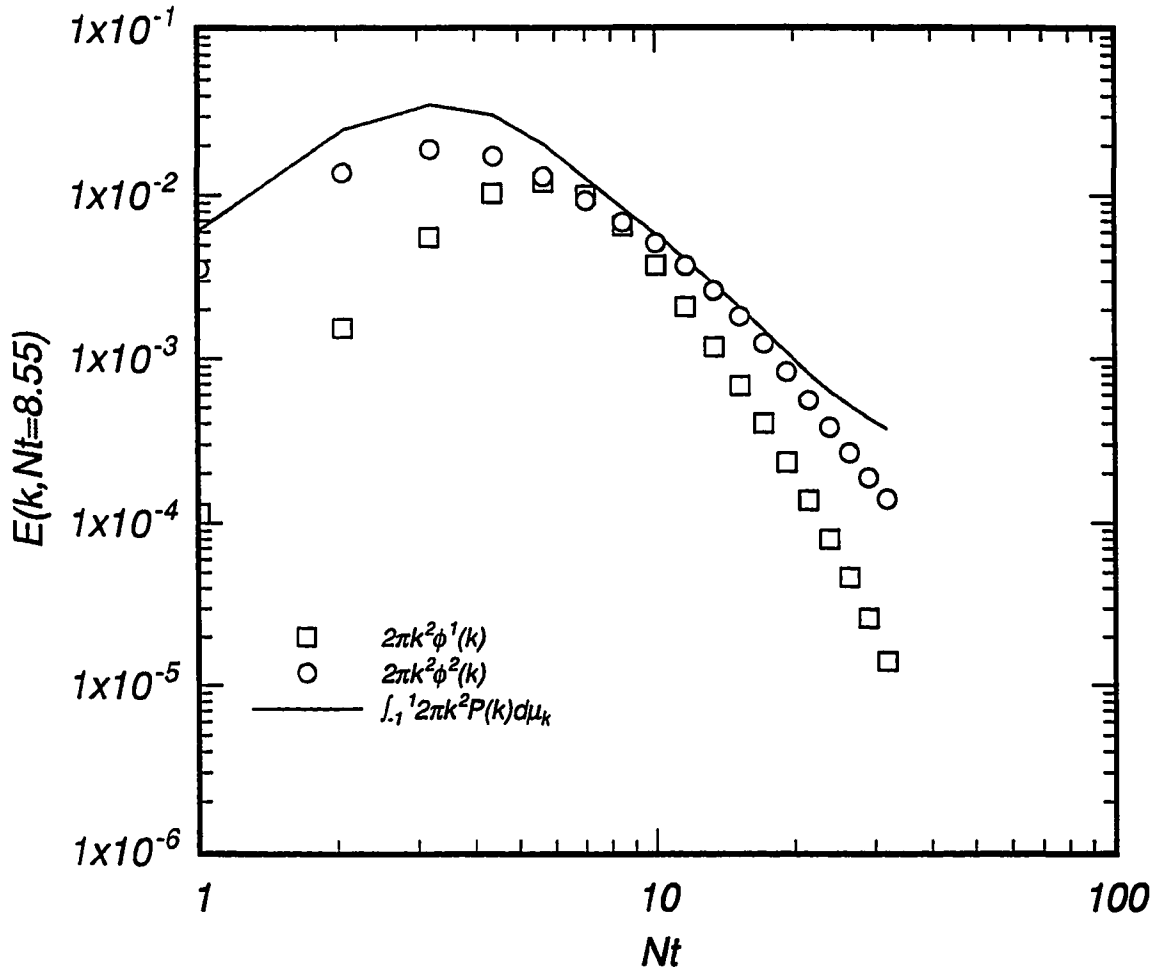

Figure 2.18: DIA energy spectra for the 0-D case ($N=2\pi, \mathrm{Pr}=200, Nt=8.55$).

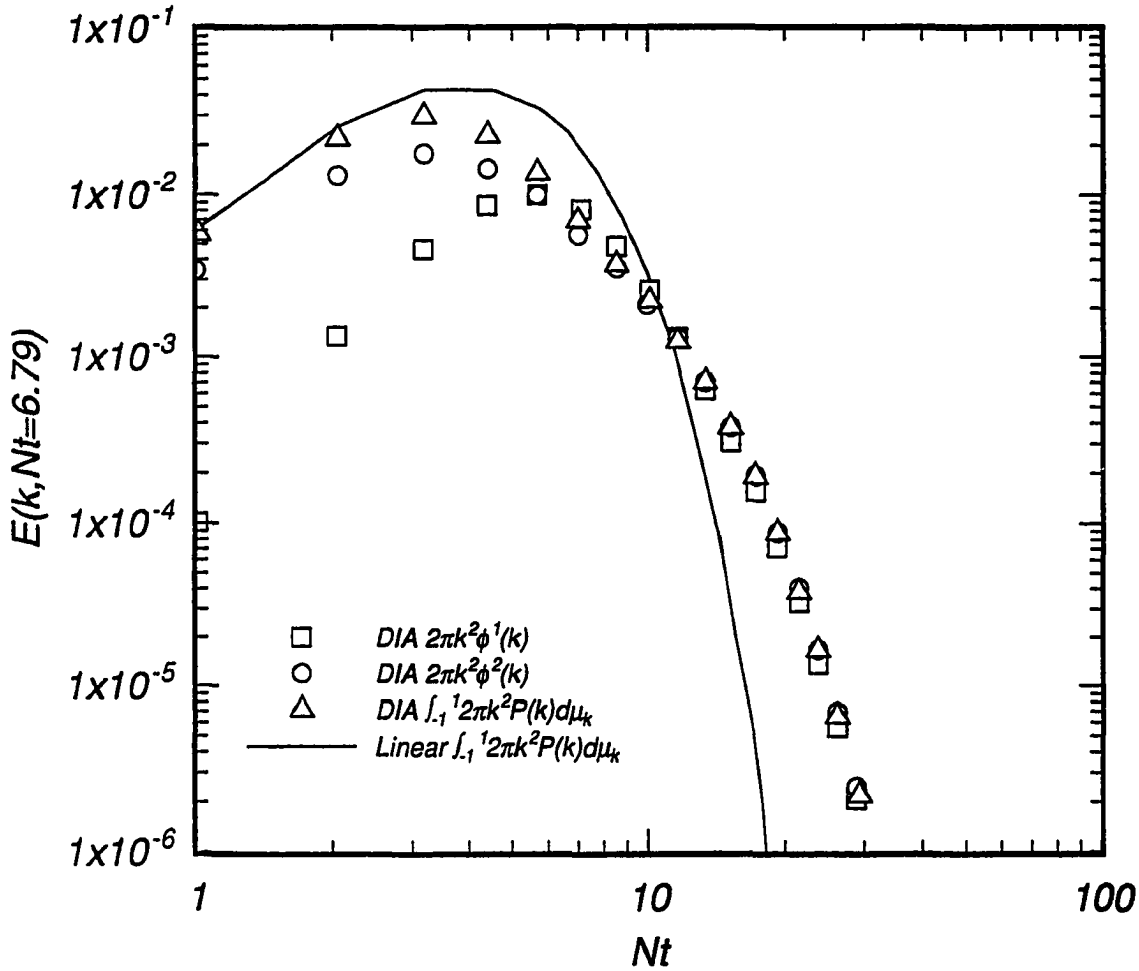

Figure 2.19: Comparison of nonlinear and linear energy spectra for the 0-D case ($N=2\pi, \mathrm{Pr}=0.7, Nt=6.79$).

CHAPTER 3. TURBULENT PASSIVE SCALAR TRANSPORT: ASYMPTOTIC STATES OF EXPERIMENT, RDT, DIA, AND DNS

A paper to be submitted to Physics of Fluids

Robert C. Sanderson, [1] Andy D. Leonard, [2] Robert M. Kerr, [3] and James C. Hill [4]

Abstract

The problem of decaying turbulent passive scalar transport (Corrsin's problem with diffusion) is studied using linear analysis (rapid distortion theory or RDT), Kraichnan's direct interaction approximation (DIA) and direct numerical simulation (DNS) and compared with laboratory experiments. The results from both the DIA and DNS compare favorably with the experiments of Sirivat and Warhaft, and Budwig, Tavoularis and Corrsin both qualitatively and quantitatively. The RDT study reveals that much of the qualitative behavior observed in experiments, such as the tendency for the system to evolve towards some statistically asymptotic state, are embodied in the linear results. Specifically, predictions from the linear theory for lengthscale ratios (both integral and microscale) are in good agreement with nonlin-

[1]Monument, Co. 80132
[2]CFD Research, Corp., Huntsville, Al. 35805
[3]National Center for Atmospheric Research, Boulder, Co. 80307
[4]Iowa State University, Ames, Ia. 50011

ear results but the linear values for the scalar transport correlation coefficient contain significant error.

Agreement between DNS and DIA are reasonbly close for the velocity field and scalar transport with Gaussian initial spectra, but differ significantly for exponential spectra. Linear and DIA runs show significant dependance of scalar transport upon initial spectral shapes. Although the transport problem is anisotropic, it is shown that DIA results using only the first Legendre functions yield integrated results identical to those obtained with two harmonics.

Introduction

The presence of a uniform mean scalar gradient preserves homogeneity while adding a linear source term to the scalar problem. While the linear effects of this term may be predicted in closed form for some spectral shapes, this is not the case when nonlinear convection is included. Thus the need for experiments, both physical and numerical, remains. The first such physical experiments were performed by Wiskind [24]. He confirmed the predictions by Corrsin [4] that 1) an initially uniform mean scalar gradient would retain its profile and magnitude in the presence of isotropic turbulence, and 2) the scalar variance would experience a linear growth rate. Although his instrumentation was not adequate for the accurate measurement of scalar transport, he obtained an eddy diffusivity ratio of about 17 and scalar transfer correlation coefficient of -0.48. Hill [8] performed steady-state DIA computations under the conditions of Wiskind's experiment using assumed analytical velocity field statistics and observed corresponding values of 20-26 and -0.30 to -0.39 depending upon the assumed form of velocity field statistics.

More recent experiments by Sirivat and Warhaft [23] and Budwig, Tavoularis and Corrsin [3] concentrated upon the characterization of evolving low Reynolds number turbulent heat transfer and the effects of the initial thermal to mechanical lengthscale ratio upon the evolution of a turbulent scalar field and associated turbulent scalar transport. They found that the lengthscale ratio influenced the evolution of the scalar field but had minimal late time effects as the turbulent velocity field appeared to bring all initial fields to similar asymptotic states.

The goal of the present work is two–fold. The first task was to perform numerical computations of passive scalar transport at moderate turbulent Reynolds numbers (approximately $R_{\lambda o}$ of 40) using direct numerical simulation (DNS) and the direct interaction approximation (DIA) of Kraichnan [10] under conditions similar to the laboratory experiments of Sirivat and Warhaft [23]. This allows comparison of the numerical techniques with each other and with experiment. The DIA possesses demonstrated deficiencies (i.e. its lack of Galilean invariance with respect to small scale structures convected by random large scale motions) which other newer closure theories do not have (e.g., the test field model (TFM, see Kraichnan [14]) and the eddy damped quasi-normal markovianized (EDQNM, see, e.g., [2]). While these theories are Galilean invariant and predict a $k^{-5/3}$ inertial spectral regime (compared with the $k^{-3/2}$ predicted by the DIA) they require scaling constants provided by comparison with experiment, whereas the DIA is a complete theory with no empirical constants. Thus the use of the DIA constitutes a more rigorous theoretical statistical closure approach. Herring [15] noted that, while Markovianized closures (such as the TFM and EDQNM) display superior accuracy for high R_λ relative to the DIA, the latter performs equally well at low to moderate R_λ which corresponds to the conditions for

this study.

The second task, the various physical mechanisms which participate in the passive scalar transport problem are investigated. The linear mechanisms, scalar and viscous dissipation and the scalar transport term (which is linear due to the uniformity of the mean scalar field gradient) will be studied using linear analysis (hereinafter called rapid distortion theory or RDT, c.f. [22] or [1]) and compared with the nonlinear convective mechanisms.

The spatial turbulence velocity field, $\tilde{u}_i(\mathbf{x},t)$, may be expanded in a discrete Fourier series

$$\tilde{u}_i(\mathbf{x},t) = \sum_{\mathbf{k}} \hat{u}_i(\mathbf{x},t) e^{i\mathbf{k}\cdot\mathbf{x}} \tag{3.1}$$

(c.f., Kraichnan [10]). The nondimensionalized equations (transformed to Fourier space) governing passive scalar transport are:

$$\left(\frac{d}{dt} + \frac{k^2}{R_{\lambda o}}\right) u_i(\mathbf{k},t) = -\frac{\imath}{2} P_{imn}(\mathbf{k}) \sum_{\substack{\Delta \\ \mathbf{p}+\mathbf{q}=\mathbf{k}}} u_m(\mathbf{p},t) u_n(\mathbf{q},t) \tag{3.2}$$

$$\left(\frac{d}{dt} + \frac{k^2}{Pr R_{\lambda o}}\right) \vartheta(\mathbf{k},t) + n_i u_i(\mathbf{k},t) = -\imath k_m \sum_{\substack{\Delta \\ \mathbf{p}+\mathbf{q}=\mathbf{k}}} u_m(\mathbf{p},t) \vartheta(\mathbf{q},t) \tag{3.3}$$

where the variables are defined as (with the caret denoting dimensional variables and subscript o denoting initial time value) :

$$\begin{aligned} R_\lambda(t) &= \frac{\hat{u}(t)\lambda_g}{\nu} \\ Pr &= \frac{\nu}{\alpha} \\ u_i(\mathbf{k},t) &= \frac{\hat{u}_i(\mathbf{k},t)}{\hat{u}_o} \\ \theta(\mathbf{k},t) &= \frac{\hat{\theta}(\mathbf{k},t)}{a\lambda_g} \\ \mathbf{k} &= \hat{\mathbf{k}}\lambda_g \end{aligned}$$

$$
\begin{aligned}
t &= \frac{\hat{t}\hat{u}_o}{\lambda_g} \\
a_i &= an_i \\
P_{imn}(\mathbf{k}) &= k_m P_{in}(\mathbf{k}) + k_n P_{im}(\mathbf{k}) \\
P_{im}(\mathbf{k}) &= \delta_{im} - \frac{k_i k_m}{k^2}
\end{aligned}
$$

where ν is the kinematic viscosity, α is the scalar diffusivity, and **a** is the mean scalar gradient vector. The corresponding governing equations for the two point-single time correlations are

$$\left[\frac{d}{dt} + \frac{2k^2}{R_{\lambda o}}\right] U_{ij}(\mathbf{k},t,t) = -\imath P_{imn}(\mathbf{k}) \sum_{\substack{\Delta \\ \mathbf{p}+\mathbf{q}=\mathbf{k}}} \langle u_m(\mathbf{p},t) u_n(\mathbf{q},t) u_m(-\mathbf{k},t)\rangle \tag{3.4}$$

$$\begin{aligned}
&\left[\frac{d}{dt} + \frac{(1+Pr)k^2}{PrR_{\lambda o}}\right] U_{i\theta}(\mathbf{k},t,t) + n_j U_{ij}(\mathbf{k},t,t) = \\
&\quad -\frac{\imath}{2} P_{imn}(\mathbf{k}) \sum_{\substack{\Delta \\ \mathbf{p}+\mathbf{q}=\mathbf{k}}} \langle u_m(\mathbf{p},t) u_n(\mathbf{q},t) \vartheta(-\mathbf{k},t)\rangle \\
&\quad -\imath k_m \sum_{\substack{\Delta \\ \mathbf{p}+\mathbf{q}=\mathbf{k}}} \langle u_m(-\mathbf{p},t) \vartheta(-\mathbf{q},t) u_i(\mathbf{k},t)\rangle
\end{aligned} \tag{3.5}$$

$$\begin{aligned}
&\left[\frac{d}{dt} + \frac{(1+Pr)k^2}{PrR_{\lambda o}}\right] U_{\theta j}(\mathbf{k},t,t) + n_i U_{ij}(\mathbf{k},t,t) = \\
&\quad -\frac{\imath}{2} P_{jmn}(-\mathbf{k}) \sum_{\substack{\Delta \\ \mathbf{p}+\mathbf{q}=\mathbf{k}}} \langle u_m(-\mathbf{p},t) u_n(-\mathbf{q},t) \vartheta(\mathbf{k},t)\rangle \\
&\quad -\imath k_m \sum_{\substack{\Delta \\ \mathbf{p}+\mathbf{q}=\mathbf{k}}} \langle u_m(\mathbf{p},t) \vartheta(\mathbf{q},t) u_j(-\mathbf{k},t)\rangle
\end{aligned} \tag{3.6}$$

$$\begin{aligned}
&\left[\frac{d}{dt} + \frac{2k^2}{PrR_{\lambda o}}\right] U_{\theta\theta}(\mathbf{k},t,t) + n_i \left(U_{i\theta}(\mathbf{k},t,t) + U_{\theta i}(\mathbf{k},t)\right) = \\
&\quad -2\imath k_m \sum_{\substack{\Delta \\ \mathbf{p}+\mathbf{q}=\mathbf{k}}} \langle u_m(\mathbf{p},t) \vartheta(\mathbf{q},t) \vartheta(-\mathbf{k},t)\rangle
\end{aligned} \tag{3.7}$$

Note that, due to the normalization chosen for the scalar field, the scalar transport term does not involve the gradient magnitude, only its direction. Thus the dimen-

sionless groups which arise from these equations are the turbulent Reynolds number, $R_{\lambda o}$, and the Prandtl number, Pr. The linearized equations (derived by setting the right hand sides of equations (3.4) through (3.7) to zero) are given by equations (3.8).

$$\frac{d}{dt}\begin{bmatrix} U_{ij}(\mathbf{k},t,t) \\ U_{i\theta}(\mathbf{k},t,t) \\ U_{\theta j}(\mathbf{k},t,t) \\ U_{\theta\theta}(\mathbf{k},t,t) \end{bmatrix} = \begin{bmatrix} -\frac{2k^2}{R_{\lambda o}} & 0 & 0 & 0 \\ -n_j & -\frac{(1+Pr)k^2}{PrR_{\lambda o}} & 0 & 0 \\ -n_i & 0 & -\frac{(1+Pr)k^2}{PrR_{\lambda o}} & 0 \\ 0 & -n_i & -n_j & -\frac{2k^2}{PrR_{\lambda o}} \end{bmatrix} \begin{bmatrix} U_{ij}(\mathbf{k},t,t) \\ U_{i\theta}(\mathbf{k},t,t) \\ U_{\theta j}(\mathbf{k},t,t) \\ U_{\theta\theta}(\mathbf{k},t,t) \end{bmatrix} \tag{3.8}$$

When equations (3.8) are solved and integrated with respect to $\mathbf{k}$ for given initial conditions, the scalar and mechanical lengthscales enter the integrated results via specification of the initial spectral peak wavenumbers (see Table 3.2).

Numerical Methodology

The DIA equations were derived by perturbation and expansion from the complete turbulent flow following the development by Kraichnan [10] and Leslie [18] and verified by comparison with the real space DIA equations for shear and thermally driven turbulence reported by Kraichnan [11]. They are listed in Appendices A and B. The statistical functions were represented using an eigenfunction decomposition described by Craya [5] and Herring [15], and the angular dependence of the eigenfunctions was represented using Legendre polynomials for the scalar–scalar and velocity–velocity functions, whereas the scalar–velocity quantities employed associ-

ated Legendre functions in a manner analogous to that of Herring [15], i.e.:

$$
\begin{aligned}
U_{ij}(\mathbf{k},t,t') &\equiv \sum_{\lambda=1}^{2}\varphi_{vv}^{\lambda}(\mathbf{k},t,t')e_i^{\lambda}(\mathbf{k})e_j^{\lambda}(\mathbf{k}) \\
&\equiv \sum_{\lambda=1}^{2}\sum_{l=0}^{\infty}\varphi_{vv,2l}^{\lambda}(k,t,t')P_{2l}(\mu_k)e_i^{\lambda}(\mathbf{k})e_j^{\lambda}(\mathbf{k}) \\
U_{i\theta}(\mathbf{k},t,t') &\equiv \sum_{\lambda=1}^{2}\varphi_{vs}^{\lambda}(\mathbf{k},t,t')e_i^{\lambda}(\mathbf{k}) \\
&\equiv \sum_{\lambda=1}^{2}\sum_{l=1}^{\infty}\varphi_{vs,2l-1}^{\lambda}(k,t,t')P_{2l-1}^{1}(\mu_k)e_i^{\lambda}(\mathbf{k}) \\
U_{\theta j}(\mathbf{k},t,t') &\equiv \sum_{\lambda=1}^{2}\varphi_{sv}^{\lambda}(\mathbf{k},t,t')e_j^{\lambda}(\mathbf{k}) \\
&\equiv \sum_{\lambda=1}^{2}\sum_{l=1}^{\infty}\varphi_{sv,2l-1}^{\lambda}(k,t,t')P_{2l-1}^{1}(\mu_k)e_j^{\lambda}(\mathbf{k}) \\
U_{\theta\theta}(\mathbf{k},t,t') &\equiv \varphi_{ss}(\mathbf{k},t,t') \\
&\equiv \sum_{l=0}^{\infty}\varphi_{ss,2l}(k,t,t')P_{2l}(\mu_k)
\end{aligned}
\tag{3.9}
$$

This representation was previously used in studies of stably stratified turbulence by Sanderson et. al. (see [19, 20, 21]). In this study only the first term of each Legendre series representation is used. This truncation is exact for the velocity field and the scalar–scalar response function (which are isotropic as described by Hill [8]). The scalar–velocity and scalar variance functions are anisotropic and truncation is expected to incur some degree of error.

The numerical code used for the DIA studies employed a predictor–corrector time stepping algorithm with the linear terms treated exactly using an eigenvector analysis analogous to the technique described by Kraichnan [12]. Eighteen wavenumbers were employed with a logarithmic distribution given by

$$k_n = A(e^{Bn} - 1) \tag{3.10}$$

Table 3.1: Wavenumbers used in the DIA computations.

n	1	2	3	4	5	6	7	8	9
k	1.00	2.06	3.20	4.40	5.68	7.04	8.49	10.03	11.67
n	10	11	12	13	14	15	16	17	18
k	13.41	15.26	17.24	19.33	21.56	23.94	26.46	29.15	32.00

with

$$\begin{aligned} A &= 15.70746468 \\ B &= 0.06171955 \\ 1 \leq\ & k \leq 32 \\ 1 \leq\ & n \leq 18 \end{aligned}$$

and listed in Table 3.1. The wavenumber convolution integrals were evaluated using two dimensional tensor B-splines to approximate the geometric coefficients, $A^{\lambda\mu\nu}_{ll'mn}(k,p,q)$, and the statistical function product, e.g., $\varphi^{\mu}(p,t,t')\varphi^{\nu}(q,t,t')$, in the following manner:

$$\begin{aligned} A^{\lambda\mu\nu}_{ll'mn}(k,p,q) &= \sum_{r=1}^{c}\sum_{s=1}^{d} C_{rs}B_r(p)B_s(q) \\ \varphi^{\mu}(p,t,s)\varphi^{\nu}(q,t,s) &= \sum_{t=1}^{e}\sum_{u=1}^{f} C_{tu}B_t(p)B_u(q) \end{aligned}$$

The functions like $B_r(p)$ are one dimensional spline functions of argument p with their bilinear product (e.g., $B_t(p)B_u(q)$) constituting a tensor B-spline function (cf. [6]) and the quantities C_{rs} are the spline function coefficients. The spline functions at the data points may be expressed as follows:

$$A^{\lambda\mu\nu}_{ll'mn}(k,p_I,q_J) = C_{rs}B_{rI}B_{sJ} \tag{3.11}$$

$$\varphi^{\mu}(p_R,t,s)\varphi^{\nu}(q_S,t,s) \;=\; C_{tu}B_{tR}B_{uS} \tag{3.12}$$

where the Einstein summation convention for repeated indices is followed, and

$$B_{rI} \equiv B_r(p_I),$$

and similarly for the other B matrices. Equations (3.11) and (3.12) may be inverted to solve for the coefficients C_{rs} and C_{tu}.

$$\begin{aligned} C_{rs} &= A^{\lambda\mu\nu}_{ll'mn}(k,p_I,q_J)B^{-1}_{sJ}B^{-1}_{rI} \\ C_{tu} &= \varphi^{\mu}(p_R,t,s)\varphi^{\nu}(q_S,t,s)B^{-1}_{uS}B^{-1}_{tR} \end{aligned}$$

The tensor spline functions are multiplied together and integrated analytically. The complete expression is

$$\begin{aligned} &\iint_{\mathbf{p+q=k}} A^{\lambda\mu\nu}_{ll'mn}(k,p,q)\varphi^{\mu}(p,t,s)\varphi^{\nu}(q,t,s)\,dp\,dq = \\ &\quad \sum_{R=1}^{v}\sum_{S=1}^{w} \varphi^{\mu}(p_R,t,s)\varphi^{\nu}(q_S,t,s)B^{-1}_{uS}B^{-1}_{tR}A^{\lambda\mu\nu}_{ll'mn}(k,p_I,q_J)B^{-1}_{sJ}B^{-1}_{rI} \times \\ &\quad \times \iint_{\mathbf{p+q=k}} B_r(p)B_s(q)B_t(p)B_u(q)\,dp\,dq \end{aligned} \tag{3.13}$$

All sums were computed using precomputed geometric coefficient $A^{\lambda\mu\nu}_{ll'mn}(k,p_I,q_J)$ values, with the exception of the R and S sums. The results were stored for use during the DIA computations when the specific values for $\varphi^{\mu}_{ij}(p_R,t,s)$ and $\varphi^{\nu}_{ab}(q_S,t,s)$ are known, multiplied by each other and by the appropriate B-spline coefficients, and then summed over R and S to determine the current value of the pq integral. The time history integrals were evaluated using one dimensional B-splines in a manner analogous to the above method.

Figures 3.2 and 3.3 compare p–q integration results obtained using the B–spline technique described above with those obtained analytically for the isotropic velocity–velocity and scalar–scalar field nonlinear terms. The response functions were assumed

to be unity (i.e., $t = t' \equiv 1$) for ease of the analytical integration while the correlation functions were assumed to be of the form $k^4 e^{-bk^2}$. The figures show close agreement between the two techniques, thus validating the numerical scheme.

The simulations were performed using the pseudo–spectral code of Kerr [9] using a third order Runge–Kutta time integration algorithm. The code was modified to allow the evaluation of the scalar gradient terms by Leonard [17]. A simulation size of 80^3 equidistantly spaced Fourier modes was employed. These simulations were performed on a Cray X–MP at the National Center for Scientific Applications at Urbana, Illinois.

The DIA was initialized by assigning to each wavenumber node the amount of energy defined by the prescribed initial spectra while the DNS was initialized by assigning to each node an independent, uncorrelated, Gaussian amount of energy satisfying the prescribed initial spectra. Initial spectral shapes for both numerical methods were of two types. One (which will be referred to as Gaussian) is that of Kraichnan [13], i.e.

$$E(k, t_o) = 16\sqrt{\frac{2}{\pi}} u_o^2 \frac{k^4}{k_o^5} e^{-2(\frac{k}{k_o})^2} \tag{3.14}$$

where u_o is the initial turbulence intensity and k_o is the peak wavenumber of the spectrum. A second shape (which will be called exponential) is

$$E(k, t_o) = \frac{81}{4} u_o^2 \frac{k^3}{k_o^4} e^{-3\frac{k}{k_o}} \tag{3.15}$$

These two spectra were used to numerically investigate the effects upon the system evolution of different initial spectral conditions.

Results and Discussion

Whereas the governing equations for the turbulent fluctuating velocity and scalar variables are nonlinear, it is instructive to study the simpler linear problem. In this way it possible to separate, at least partially, the linear effects from those due to the nonlinear terms so that the roles of each may be more clearly understood. In the first sub-section the behavior of the linear equations is studied in some detail while in the following sub-sections the nonlinear results are presented, discussed and compared with the linear results and with previous experimental results.

Linear Analysis

The following definitions are used for the energies (with subscript 'v' indicating the velocity field and subscript 'θ' denoting the scalar field):

$$E_{vv}(k,t) \equiv 2\pi k^2 U_{ii}(k,t) \equiv 2\pi k^2 \langle u_i(\mathbf{k},t) u_i(-\mathbf{k},t)\rangle \tag{3.16}$$

$$E_{v\theta}(k,t) \equiv 4\pi k^2 U_{i\vartheta}(k,t) \equiv 4\pi k^2 \langle u_i(\mathbf{k},t) \vartheta(-\mathbf{k},t)\rangle \tag{3.17}$$

$$E_{\theta\theta}(k,t) \equiv 4\pi k^2 U_{\theta\theta}(k,t) \equiv 4\pi k^2 \langle \vartheta(\mathbf{k},t) \vartheta(-\mathbf{k},t)\rangle \tag{3.18}$$

The various lengthscales are now defined as

$$\begin{aligned} L_f &\equiv \frac{\pi}{2u^2} \int_o^\infty \frac{E_{vv}(k)}{k}\, dk \\ &\equiv \frac{3\pi}{4} \int_o^\infty \frac{E_{vv}(k,t)}{k}\, dk \Big/ \int_o^\infty E_{vv}(k,t)\, dk \end{aligned} \tag{3.19}$$

$$\begin{aligned} L_\theta &\equiv \frac{\pi}{2\vartheta^2} \int_o^\infty \frac{E_{\theta\theta}(k)}{k}\, dk \\ &\equiv \frac{\pi}{2} \int_o^\infty \frac{E_{\theta\theta}(k,t)}{k}\, dk \Big/ \int_o^\infty E_{\theta\theta}(k,t)\, dk \end{aligned} \tag{3.20}$$

$$\lambda_g \equiv \sqrt{\frac{15\nu u^2}{\varepsilon_{vv}}}$$

$$\equiv \sqrt{\frac{5\int_o^\infty E_{vv}(k,t)\,dk}{\int_o^\infty k^2 E_{vv}(k,t)\,dk}} \tag{3.21}$$

$$\lambda_\theta \equiv \sqrt{\frac{12\alpha\vartheta^2}{\varepsilon_{\theta\theta}}}$$

$$\equiv \sqrt{\frac{6\int_o^\infty E_{\theta\theta}(k,t)\,dk}{\int_o^\infty k^2 E_{\theta\theta}(k,t)\,dk}} \tag{3.22}$$

The velocity integral lengthscale is longitudinal, consistent with that used by Sirivat and Warhaft while the transverse velocity microscale is used. Equations (3.19) through (3.22) yield the following relationships for the lengthscale ratios:

$$\frac{L_\theta(t)}{L_f(t)} \equiv \frac{2}{3}\left[\frac{\int_0^\infty \frac{E_{\theta\theta}(k,t)}{k}\,dk \int_0^\infty E_{vv}(k,t)\,dk}{\int_0^\infty \frac{E_{vv}(k,t)}{k}\,dk \int_0^\infty E_{\theta\theta}(k,t)\,dk}\right] \tag{3.23}$$

$$\frac{\lambda_\theta(t)}{\lambda_g(t)} \equiv \sqrt{\frac{6}{5}}\left[\frac{\int_0^\infty E_{\theta\theta}(k,t)\,dk \int_0^\infty k^2 E_{vv}(k,t)\,dk}{\int_0^\infty E_{vv}(k,t)\,dk \int_0^\infty k^2 E_{\theta\theta}(k,t)\,dk}\right]^{\frac{1}{2}}. \tag{3.24}$$

Examination of equations (3.23) and (3.24) indicates that the lengthscale ratios are independent of the exact spectral shapes if the scalar and velocity spectra are proportional to each other, i.e. if $E_{\theta\theta}(k,t) = cE_{vv}(k,t)$.

The solutions for equations (3.8) are (with $\Delta t \equiv t - t_o$)

$$E_{vv}(k,t) = E_{vv}(k,t_o)e^{-\frac{2k^2}{R_{\lambda o}}\Delta t} \tag{3.25}$$

$$\begin{aligned} E_{v\theta}(k,t) &= E_{v\theta}(k,t_o)e^{-\frac{(1+Pr)k^2}{PrR_{\lambda o}}\Delta t}+ \\ &+E_{vv}(k,t_o)\left[\frac{2PrR_{\lambda o}}{(1-Pr)k^2}\right]\left[e^{-\frac{(1+Pr)k^2}{PrR_{\lambda o}}\Delta t} - e^{-\frac{2k^2}{R_{\lambda o}}\Delta t}\right] \end{aligned} \tag{3.26}$$

$$\begin{aligned} E_{\theta\theta}(k,t) &= E_{\theta\theta}(k,t_o)e^{-\frac{2k^2}{PrR_{\lambda o}}\Delta t}+ \\ &-E_{v\theta}(k,t_o)\left[\frac{2PrR_{\lambda o}}{(1-Pr)k^2}\right]\left[e^{-\frac{(1+Pr)k^2}{PrR_{\lambda o}}\Delta t} - e^{-\frac{2k^2}{PrR_{\lambda o}}\Delta t}\right]+ \\ &+E_{vv}(k,t_o)\frac{2}{3}\left[\frac{PrR_{\lambda o}}{(1-Pr)k^2}\right]^2\left[e^{-\frac{k^2}{R_{\lambda o}}\Delta t} - e^{-\frac{k^2}{PrR_{\lambda o}}\Delta t}\right]^2 \end{aligned} \tag{3.27}$$

with the equation governing $E_{\theta v}(k,t)$ identical with equation (3.26). If the Gaussian spectral shape (equation (3.14) is used for the initialization of each field with arbitrary

peak spectral wavenumber, these three equations may be integrated with respect to wavenumber k to yield the evolution expressions for the total "energy" of each field (where we define the kinetic energy as $E_{vv}(t) \equiv \int_0^\infty E_{vv}(k,t)\,dk$):

$$E_{vv}(t) = E_{vv}(t_o)\left[1+\frac{k_{ov}^2\,\Delta t}{R_{\lambda o}}\right]^{-\frac{5}{2}} \tag{3.28}$$

$$\begin{aligned} E_{v\theta}(t) = {} & E_{v\theta}(t_o)\left[1+\frac{(1+Pr)k_{ov\theta}^2\,\Delta t}{2PrR_{\lambda o}}\right]^{-\frac{5}{2}} + \\ & + E_{vv}(t_o)\left[\frac{PrR_{\lambda o}}{1-Pr}\right]\left[\frac{8}{9k_{ov}^2}\right]\left\{\left[1+\frac{(1+Pr)k_{ov}^2\,\Delta t}{2PrR_{\lambda o}}\right]^{-\frac{3}{2}} - \left[1+\frac{k_{ov}^2\,\Delta t}{R_{\lambda o}}\right]^{-\frac{3}{2}}\right\} \end{aligned} \tag{3.29}$$

$$\begin{aligned} E_{\theta\theta}(t) = {} & E_{\theta\theta}(t_o)\left[1+\frac{k_{o\theta}^2\,\Delta t}{PrR_{\lambda o}}\right]^{-\frac{5}{2}} + \\ & - E_{v\theta}(t_o)\left[\frac{PrR_{\lambda o}}{1-Pr}\right]\left[\frac{8}{3k_{ov\theta}^2}\right]\left\{\left[1+\frac{(1+Pr)k_{ov\theta}^2\,\Delta t}{2PrR_{\lambda o}}\right]^{-\frac{3}{2}} - \left[1+\frac{k_{ov\theta}^2\,\Delta t}{PrR_{\lambda o}}\right]^{-\frac{3}{2}}\right\} + \\ & + E_{vv}(t_o)\left[\frac{PrR_{\lambda o}}{1-Pr}\right]^2\left[\frac{32}{9k_{ov}^4}\right] \times \\ & \times\left\{\left[1+\frac{k_{ov}^2\,\Delta t}{R_{\lambda o}}\right]^{-\frac{1}{2}} - 2\left[1+\frac{(1+Pr)k_{ov}^2\,\Delta t}{2PrR_{\lambda o}}\right]^{-\frac{1}{2}} + \left[1+\frac{k_{ov}^2\,\Delta t}{PrR_{\lambda o}}\right]^{-\frac{1}{2}}\right\}. \end{aligned} \tag{3.30}$$

For the velocity field, the additional integrals required for the lengthscale ratios are total dissipation ($\varepsilon_{vv}(t)$) and $E_{vv}^L(t)$ ($\equiv \int_0^\infty E_{vv}(k,t)/k\,dk$);

$$\varepsilon_{vv}(t) = \varepsilon_{vv}(t_o)\left[1+\frac{k_{ov}^2}{R_{\lambda o}}\,\Delta t\right]^{-\frac{7}{2}} \tag{3.31}$$

$$E_{vv}^L(t) = E_{vv}^L(t_o)\left[1+\frac{k_{ov}^2}{R_{\lambda o}}\,\Delta t\right]^{-2} \tag{3.32}$$

while those for the scalar field are

$$\begin{aligned} \varepsilon_{\theta\theta}(t) = {} & \varepsilon_{\theta\theta}(t_o)\left[1+\frac{k_{o\theta}^2\,\Delta t}{PrR_{\lambda o}}\right]^{-\frac{7}{2}} + \\ & - E_{v\theta}(t_o)\left[\frac{4}{1-Pr}\right]\left\{\left[1+\frac{(1+Pr)k_{ov\theta}^2\,\Delta t}{2PrR_{\lambda o}}\right]^{-\frac{5}{2}} - \left[1+\frac{k_{ov\theta}^2\,\Delta t}{PrR_{\lambda o}}\right]^{-\frac{5}{2}}\right\} + \end{aligned}$$

Table 3.2: Definition of initial quantities for Gaussian initial spectra.

Field	$E(t_o)$	$\varepsilon(t_o)$	$E^L(t_o)$	$L(t_o)$	$\lambda(t_o)$
Velocity	$\frac{3}{2}$	$\frac{15}{4R_{\lambda o}}k_{ov}^2$	$\frac{2\sqrt{2}}{\sqrt{\pi}k_{ov}}$	$\frac{\sqrt{2\pi}}{k_{ov}}$	$\frac{2}{k_{ov}}$
Scalar	1	$\frac{5k_{o\theta}^2}{2PrR_{\lambda o}}$	$\frac{2\sqrt{2}}{3\sqrt{\pi}k_{o\theta}}$	$\frac{2\sqrt{2\pi}}{3k_{o\theta}}$	$\frac{2}{k_{o\theta}}\sqrt{\frac{6}{5}}$

$$+E_{vv}(t_o)\left[\frac{PrR_{\lambda o}}{(1-Pr)^2}\right]\left[\frac{16}{9k_{ov}^2}\right]\times$$
$$\times\left\{\left[1+\frac{k_{ov}^2\,\Delta t}{R_{\lambda o}}\right]^{-\frac{3}{2}}-2\left[1+\frac{(1+Pr)k_{ov}^2\,\Delta t}{2PrR_{\lambda o}}\right]^{-\frac{3}{2}}+\left[1+\frac{k_{ov}^2\,\Delta t}{PrR_{\lambda o}}\right]^{-\frac{3}{2}}\right\} \tag{3.33}$$

$$E_{\theta\theta}^L(t)=E_{\theta\theta}^L(t_o)\left[1+\frac{k_{os}^2\,\Delta t}{PrR_{\lambda o}}\right]^{-2}+$$
$$-E_{v\theta}(t_o)\left[\frac{PrR_{\lambda o}}{1-Pr}\right]\left[\frac{16}{3}\sqrt{\frac{2}{\pi}}\right]\left\{\left[1+\frac{(1+Pr)k_{ovs}^2\,\Delta t}{2PrR_{\lambda o}}\right]^{-1}-\left[1+\frac{k_{ovs}^2\,\Delta t}{PrR_{\lambda o}}\right]^{-1}\right\}+$$
$$+E_{vv}(t_o)\frac{32}{9k_{ov}^5}\sqrt{\frac{2}{\pi}}\left[\frac{PrR_{\lambda o}}{1-Pr}\right]^2\ln\left\{1+\frac{k_{ov}^4\,\Delta t^2(1-Pr)^2}{4Pr[R_{\lambda o}+k_{ov}^2\,\Delta t][PrR_{\lambda o}+k_{ov}^2\,\Delta t]}\right\} \tag{3.34}$$

The initial values (e.g., $E_{vv}(t_o)$ for each of the above quantities are listed in Table 3.2.

These expressions may now be used to generate the various lengthscales. It can be seen that the second and third terms in equations (3.30), (3.33) and (3.34) are zero at time $\Delta t = 0$. Thus the initial time lengthscales are identical to those for the isotropic turbulent scalar problem with zero mean scalar gradient:

$$\frac{L_\theta(t_o)}{L_f(t_o)} = \frac{2}{3}\left[\frac{k_{ov}}{k_{o\theta}}\right] \tag{3.35}$$

$$\frac{\lambda_\theta(t_o)}{\lambda_g(t_o)} = \sqrt{\frac{6}{5}}\left[\frac{k_{ov}}{k_{o\theta}}\right] \tag{3.36}$$

where it is obvious the relative spectral peaks are important.

The magnitudes of the time function exponents in the third terms of equations (3.30), (3.33) and (3.34) are smaller than those appearing on the remaining terms. Thus at long times the third terms dominate, i.e. the velocity field contributions will overwhelm the initial scalar and scalar transport fields. The various lengthscales at moderate times are thus

$$L_f(t) = L_f(t_o)\left[1+\frac{k_{ov}^2}{R_{\lambda o}}\triangle t\right]^{\frac{1}{2}} \tag{3.37}$$

$$\lambda_g(t) = \lambda_g(t_o)\left[1+\frac{k_{ov}^2}{R_{\lambda o}}\triangle t\right]^{\frac{1}{2}} \tag{3.38}$$

$$L_\theta(t) = \left(\frac{\sqrt{\pi}}{2}\right)\left[\frac{\triangle t}{R_{\lambda o}}\right]^{\frac{1}{2}} F_1(Pr) \tag{3.39}$$

$$\tag{3.40}$$

$$\lambda_\theta(t) = 2\sqrt{6}\left[\frac{\triangle t}{R_{\lambda o}}\right]^{\frac{1}{2}} F_2(Pr) \tag{3.41}$$

with

$$F_1(Pr) \equiv \frac{\sqrt{(1+Pr)}\ln\left[\frac{(1+Pr)^2}{4Pr}\right]}{\sqrt{1+Pr}(1+\sqrt{Pr})-2\sqrt{2Pr}}$$

$$F_2(Pr) \equiv \left[\frac{(1+Pr)\left[(1+\sqrt{Pr})(1+Pr)-2\sqrt{2Pr(1+Pr)}\right]}{(1+Pr\sqrt{Pr})(1+Pr)^2-4Pr\sqrt{2Pr(1+Pr)}}\right]^{\frac{1}{2}}$$

The Taylor microscale Reynolds number evolution is given by

$$R_\lambda(t) = R_\lambda(t_o)\left[1+\frac{k_{ov}^2}{R_{\lambda_o}}\triangle t\right]^{-\frac{3}{4}} \tag{3.42}$$

with

$$R_\lambda(t_o) \equiv R_{\lambda o} \equiv \frac{2}{\nu k_{ov}} \tag{3.43}$$

For long times the lengthscale ratios are:

$$\frac{L_\theta}{L_f} = \frac{1}{2} F_1(Pr) \tag{3.44}$$

$$\frac{\lambda_\theta}{\lambda_g} = \sqrt{6} F_2(Pr) \tag{3.45}$$

These asymptotic values contain no dependence upon the spectral peak wavenumbers. At long times the contribution of the velocity field to the scalar field dominates the scalar field behavior so differences between the spectral peaks of the velocity, scalar transport and scalar fields disappear.

Another quantity of interest is the scalar transport correlation coefficient, $\rho_{u\theta}$. This is defined to be

$$\rho_{u\theta} \equiv \frac{< w\vartheta >}{w'\vartheta'} \tag{3.46}$$

where w is the turbulent velocity in the direction of the mean scalar gradient and a superscript $'$ affixed to a variable denotes the intensity of that turbulent quantity. $< w\vartheta >$ is the scalar–velocity correlation (or turbulent scalar transport) in the direction of the mean scalar gradient. For isotropic passive scalar transport the correlation coefficient is given (for long time t, moderate Pr and zero initial scalar transport) by

$$\lim_{t\to\infty} \rho_{u\theta}(t) = \sqrt{\frac{1}{3}} \frac{2Pr\sqrt{2Pr} - (1+Pr)\sqrt{1+Pr}}{(1+Pr)\left[(1+Pr)(1+\sqrt{Pr}) - 2\sqrt{2Pr(1+Pr)}\right]^{\frac{1}{2}}} \tag{3.47}$$

Thus, with respect to the lengthscale ratios and scalar transport correlation coefficient, the linear case tends towards an asymptotic state determined only by the Prandtl number. As Pr varies over its range, $0 \leq Pr \leq \infty$ it is of interest to determine the asymptotes of $\rho_{u\theta}$. Accordingly:

$$\lim_{Pr\to 0} \rho_{u\theta} = \sqrt{\frac{1}{3}} \frac{0-1}{(1)\left[(1)(1) - 2\sqrt{0}\right]^{\frac{1}{2}}} = -\frac{1}{\sqrt{3}} \tag{3.48}$$

and

$$\lim_{Pr\to\infty} \rho_{u\theta} = \frac{1-2\sqrt{2}}{\sqrt{3}} \left[\frac{R_{\lambda o}}{k_{ov}^2 \, \Delta t} \right]^{\frac{1}{4}} = 0 \tag{3.49}$$

Nonlinear Results

The inclusion of the nonlinear convection terms in the governing equations adds transport of "energy" up the spectrum of each field. This will serve to alter the spectral shapes as well as enhance dissipation of each of the fields. The fields also experience enhanced decorrelation relative to the linear case. The effects of these phenomena upon lengthscale ratios and correlation coefficients will now be investigated. The DIA and DNS predict nearly identical behavior for $R_\lambda(t)$ as shown in Figure 3.4. The evolution of total scalar variance is shown in Figure 3.5 for the case of zero initial scalar fluctuations ($L_\theta(t_o)/L_f(t_o) = 0$). After an initial transient period, the growth is linear, in agreement with Corrsin's predictions and the results of experiments. The simulation results agree with those of the DIA fairly closely except at the last DNS point where it appears that the DNS begins to lag the DIA predictions. The reason for this becomes apparent in the next two figures. The total scalar dissipation as computed by the two techniques is compared in Figure 3.6 and is greater in the case of the DNS than for the DIA. The DNS predicts a higher rate of nonlinear scalar variance transfer to the higher wavenumbers (see Figure 3.7) leading to higher spectral levels at those wavenumbers than does the DIA. This results in an increased rate of scalar dissipation and thus reduced growth of the scalar field in the simulations. This difference may be due to the truncation of the Legendre function series representation for the DIA scalar–velocity and scalar–scalar fields.

The discrepancy between the two numerical methods is most notable in the

predicted eddy diffusivity ratios, for example in Figure 3.8. The DIA results peak at a value of about 25 while the simulation results are lower (approximately 22). Because the scalar transport correlation coefficient normalizes the scalar–velocity correlation with the scalar intensity, the DIA and DNS results for this quantity (Figure 3.9) are quite close. The DIA results follow those of the DNS rather closely for the first eddy turnover time and, while still slowly decreasing in magnitude, level out between -0.7 to -0.8. These results are quite close to those of experiment; eddy diffusivity ratios of 24 to 28 and scalar transport correlation coefficients of -0.7 to -0.8 in the studies of Sirivat and Warhaft [23] and Budwig, et al. [3].

The issue of appropriate numerical initial conditions is difficult to address due to the relative lack of knowledge about the experimental velocity, scalar and scalar transport fields immediately downstream of the turbulence generating grid. The experimental spectra, intensities, etc. are generally unknown as is the degree of inhomogeneity. The initial dissipation rates experienced in most wind tunnels (within a distance of x/M of approximately 30 of the grid) is considerably higher than that seen in numerical work using typical initial spectra. The issue of initial spectra was studied numerically by making comparisons between (isotropic) Gaussian and exponential shapes. The results are illustrated in Figures 3.10, 3.11 and 3.12 (see Table 3.3 for run conditions). Figures 3.10 and 3.11 exhibit the evolution of the DIA and DNS eddy diffusivity ratios. By the end of one eddy turnover time the evolution of the eddy diffusivity ratio computed by DNS is relatively unaffected by the initial spectra used. However the exponential initial spectra lead to values approximately 25% higher (approximately 11.5 and 9.2) than do the Gaussian spectra. The DNS runs only extend to approximately one eddy circulation time while the DIA runs

Table 3.3: Initial conditions and identification for numerical runs.

Run No.	$R_{\lambda o}$	$L_\theta(t_o)/L_f(t_o)$	Spectra	Theories
1	45	0.0	Exponential	DIA/DNS
2	35	1.0	Gaussian	DIA/DNS
3	35	0.5	Gaussian	DIA/DNS
4	35	1.0	Exponential	DIA/DNS
5	35	0.5	Exponential	DIA/DNS
6	45	0.0	Gaussian (vel.)	DIA/RDT
7	45	0.5	Gaussian	DIA/RDT
8	45	1.0	Gaussian	DIA/RDT
9	45	2.0	Gaussian	DIA/RDT
10	45	0.0	Exponential (vel.)	DIA/RDT
11	45	0.5	Exponential	DIA/RDT
12	45	1.0	Exponential	DIA/RDT
13	45	2.0	Exponential	DIA/RDT

are carried out to 8–10 circulation times, thus the long-time behavior of DNS scalar transport is not illustrated. The DNS and DIA eddy diffusivity ratio results with Gaussian initial spectra agree reasonably well although the DIA overpredicts the peak. The exponential results for the eddy diffusivity (Figure 3.10) show considerably more disagreement between the two numerical techniques. At the end of one eddy turnover time, the DIA is predicting values for ε_H roughly 50% higher than does the DNS. This suggests a lower level of nonlinear mixing in the DIA than the DNS, as indicated by the spectral comparison in Figure 3.7. The DIA results do indicate significant long time differences in the evolution of ε_H depending upon the initial spectral shapes. This point will be visited in more detail later.

Figure 3.12 compares directly the evolution of the scalar transport correlation coefficient for the two different spectral shapes. Differences in evolution exist but

are small, and the final values are insensitive to the initial spectral specification. In addition, the DIA results are in closer agreement with those of DNS than was the case for ϵ_{II}. Both this agreement and the insensitivity to initial spectral conditions may be due to the ratio nature of $\rho_{u\theta}$ and a subsequent "cancellation of errors" effect. DIA overprediction of the scalar transport results in values of $< w\vartheta >$ as well as excessive growth of the scalar variance. In $\rho_{u\theta}$, a too large $< w\vartheta >$ in the numerator is counteracted by a too large value for ϑ in the denominator leading to better agreement for $\rho_{u\theta}$ between DIA and DNS than is the case for $< w\vartheta >$ and $E_{\theta\theta}$.

Comparison of Nonlinear and Linear (RDT) Results

Another aspect of the initial condition problem was investigated experimentally by Sirivat and Warhaft [23] and by Budwig, et al. [3]. They studied the effects of changing the initial scalar to velocity lengthscale ratio on the evolution and final states of the turbulent scalar transport quantities. This was accomplished by physically changing the relative sizes of the grids producing the two fields. The subsequent results indicated that, while the evolution of the fields might be significantly affected by the choice of initial lengthscale ratio, the systems evolved towards similar asymptotic states.

This problem was also studied numerically using the DIA and linear (RDT) analysis. The initial lengthscale ratios were varied by changing the relative peak wavenumbers of the initial spectra for the velocity and scalar fields. Again, both exponential and Gaussian initial spectra were used to further study the effects of spectral shapes upon subsequent problem evolution. Figures 3.13 and 3.14 compare

the evolution of the DIA and RDT scalar variance with different initial lengthscale ratios for Gaussian and exponential spectra, respectively. As expected, the growth of the scalar energy in the RDT runs grows far more rapidly than predicted by the DIA. In addition, the RDT runs show enhanced scalar fluctuation levels with increased initial lengthscale ratio ($L_{\theta o}/L_{vo}$). However, after approximately 4–5 eddy turnover times the scalar growth rates are all quite close and not a strong function of $L_{\theta o}/L_{vo}$. The DIA runs exhibit an enhancement of scalar fluctutions with increased $L_{\theta o}/L_{vo}$ but the differences are significantly reduced relative to the RDT case. Although the DIA results display a much stronger evolution towards a similar asymptotic condition, the runs for $L_{\theta o}/L_{vo}$ values of unity or less are more strongly asymptotic than for higher values. These higher $L_{\theta o}/L_{vo}$ runs may approach their asymptotic states more slowly than the runs lower initial lengthscale ratios due to the fact that much of the initial scalar "energy" is at low wavenumbers (i.e., large scales of motion) and is therefore not strongly affected by nonlinear mixing or diffusion. Thus more scalar transport and/or time is required to attain an asymptotic state than is the case for the lower $L_{\theta o}/L_{vo}$ runs. The presence of the DIA nonlinearities decreases the scalar field levels at 8–9 eddy circulation times (one eddy circulation time is given by tu_o/L_{f_o}) by a factor of 4–5.

The effect of the initial spectral shapes upon the growth of the scalar energy is dramatic and displayed by both RDT and DIA computations. The exponential spectra lead to significant and sustained scalar field growth with no signs of abatement throughout the 8–9 eddy circulation times studied. By contrast, the Gaussian RDT runs, while showing continual growth during this time, also exhibits significant abatement of the rate of that growth.

The DIA runs show very slow growth for $L_{\theta o}/L_{vo}$ values of unity or less while the run with $L_{\theta o}/L_{vo}$ of 2 actually has a declining scalar field after brief growth during the first eddy circulation time. Note that the nonlinear exponential scalar fields are all at levels of approximately 30–35 while the DIA Gaussian fields, at the same time, are at 5–6. Thus the exponential runs result in much more scalar growth (even for initially zero scalar fields) than do Gaussian initial conditions.

These runs were conducted with the velocity spectral peak wavenumbers held constant as the spectral shapes were varied. While this introduced different values for L_{fo} these differences were small. The Gaussian spectra, being much more peaked than the exponential, has a higher initial spectral peak value with subsequently sharper declines in wavenumber space as k increases. Thus the spectral gradients (i.e., the derivatives with respect to k) are initially larger for the Gaussian than the exponential spectra. This characteristic may lead to higher nonlinear transport from low to high wavenumbers, thus leading to higher dissipation rates than is the case for the exponential spectrum. As this occurs, the velocity field also nonlinearly mixes the scalar field in an analogous manner, which increases the rate of diffusion of the turbulent scalar field. The scalar to mechanical integral lengthscale ratio also has an effect in determining the spectral position of the scalar energy relative to that of the velocity field. If this ratio is unity, the two spectra essentially lie upon each other. A low ratio indicates the scalar energy is concentrated at wavenumbers in the high k range of the velocity spectrum while a high ratio indicates concentration of scalar energy at wavenumbers in the low k range of the velocity spectrum. Low ratios may indicate a situation in which the scalar energy is not strongly convected by the velocity field as it lies predominantly at wavenumbers in which the velocity

nonlinearities are reduced from their peak. Physically this may correspond to a situation where the scalar field fluctuations are of such small size that the larger velocity fluctuations tend to convect them undistorted and not strain them into smaller scales. Conversely, high ratios indicate the bulk of the scalar energy resides at wavenumbers in the small k range of the velocity spectrum. This exposes nearly all the scalar energy to the strongest nonlinear convection of the velocity field and thus rapid scalar energy diffusion. This corresponds to a physical picture of scalar fluctuations of sizes larger than most of those in the velocity field. This leads to nearly every velocity fluctuation straining the scalar fluctations into smaller sizes and thus may lead to a high rate of scalar energy diffusion. At this point this description is speculative but is consistent with the behavior described above.

The eddy diffusivity ratio (Figures 3.15 and 3.16) displays no sensitivity to the initial lengthscale ratio. The initial velocity and scalar transport fields, Prandtl number, and mean scalar gradient magnitude were the same for each run. Since the initial scalar transport fields were always zero, the RDT cases must have identical ϵ_H since they are always induced by the same velocity field acting upon the same mean scalar gradient. For the DIA runs, any variation from the RDT cases must be due to differences induced by the nonlinear terms in the scalar transport field equations. For these DIA runs those differences appear to be negligible. The initial spectral shapes have a pronounced effect upon the eddy diffusivity. The exponential spectra (Figure 3.15) lead to strongly growing RDT diffusivity ratio while the DIA results peak at approximately 4 circulation times and only slowly decays thereafter. In the Gaussian case (Figure 3.16) the RDT case peaks at about 5–6 circulations times and then begins a significant decay while the DIA peaks shortly after 1 eddy circulation

time and steadily decays afterward. In addition, the magnitudes of the exponential runs (155 RDT and ≈38 DIA) are significantly higher than those of the Gaussian runs (≈60 RDT and ≈20 DIA). These spectrally induced evolutionary differences are directly compared in Figures 3.17 (DIA runs) and 3.18 (linear runs) where the greatly enhanced scalar transport due to the exponential spectral shape is obvious even in the RDT case. The effect of the nonlinear terms is to enhance the dissipation of scalar transport.

The experiments of Sirivat and Warhaft also (nominally) changed only the initial scalar fields while maintaining constant velocity field conditions. However their results display some differences in the behavior of the eddy diffusivity ratio (see Figure 16, Sirivat and Warhaft [23]). This occurred possibly due to different initial scalar transport characteristics induced by altering the temperature field producing grid.

The evolution of the DIA correlation coefficients exhibit significant sensitivity to initial conditions in Figures 3.19 and 3.20. Both the RDT and the DIA results show strongly different evolutions strongly dependent upon initial lengthscale ratio but also display a tendency towards asymptotic states. The RDT runs appear to approach an asymptotic value very near unity with the approach rate inversely related to initial lengthscale ratio. The DIA results behave similarly but the asymptote is significantly different from that of RDT due to decorrelation by the nonlinearities. In both the RDT and DIA runs the asymptotic values appear to be determined by the case with zero initial scalar field. Although the exponential DIA runs tend to have correlation coefficients slightly lower in magnitude than those in the Gaussian runs, both cases result in asymptotic values between approximately -0.7 and -0.8.

Figures 3.21 and 3.22 show the evolution of the DIA scalar to velocity integral

lengthscale ratio. The tendency towards an asymptotic state is strong and universal in Figure 3.21, the exponential case and holds in both the RDT and DIA cases. For the exponential case, the RDT cases evolve to a significantly lower ratio than do the DIA runs (about 0.9 vs. 1.1 at 8–9 turnover times) but all four lengthscale ratio runs are quite close to each other by this time. In the Gaussian cases, the differences between the RDT and DIA results are small and there is a marked difference in the behavior between the runs with initial lengthscale ratios of unity and lower compared with the higher values (true for both RDT and DIA runs) with final values of 0.9 for the lower and 1.0 for the larger initial lengthscale ratios. Thus, while the effects of the nonlinearities in the DIA are to reduce the lengthscale ratio from its RDT values, these effects are strong functions of the initial spectra. Both RDT and DIA runs exhibit the tendency towards asymptotic states observed in experiments. The asymptotic DIA values of 0.9 to 1.0 are at the upper end of the experimental results (about 0.7–0.9) of Sirivat and Warhaft (see [23]).

Use of the various initial lengthscale ratios and initial spectra selected for this study has shown that the DIA and DNS can numerically predict evolutionary behavior similar to that observed experimentally. In addition, the asymptotic values of lengthscale ratios and transport correlation coefficients are in reasonable agreement with those observed experimentally. However, the eddy diffusivity ratio (and subsequently the scalar fluctuation field) is highly dependent upon the initial spectral shape used. The peak values for the DIA eddy diffusivity ratio bracket values reported from experiments. However, the dependency of DIA scalar transport is shown here to be so strongly dependant upon initial spectra that attempting to evaluate the accuracy of the closure theory in predicting scalar transport seen in experiments is be-

Table 3.4: Asymptotic values for Pr of 0.7.

Variable	RDT	DIA	DNS	Experiment
L_θ/L_f	0.73	≈ 0.9	—	0.7 to 0.9
λ_θ/λ_g	1.196	1.2 to 1.4	—	0.9 to 1.2
$\rho_{u\theta}$	-0.99	-0.7 to -0.8	-0.7 to -0.8	-0.7 to -0.8

Table 3.5: Asymptotic values for Pr of 0.5.

Variable	RDT	DIA	DNS	Experiment
L_θ/L_f 0.5	0.80	≈ 0.9	—	—
λ_θ/λ_g	1.296	1.2 to 1.4	—	—
$\rho_{u\theta}$	-0.966	-0.65 to -0.75	—	—

yond the scope of this paper and will be addressed in a future paper. The differences between the exponential and Gaussian velocity spectra are illustrated in Figure 3.23 at three different times during the runs. At early times, the Gaussian spectrum is more strongly peaked with a higher energy content at the peak than the exponential spectrum has. However, the energy content at the lowest two wavenumbers and in the higher wavenumber range is lower than in the exponential case. As time passes, the differences at the low wavenumbers reduce and the Gaussian case loses more energy at the peak and high wavenumbers than does the exponential. Over all time, the exponential case retains higher energy levels at the high wavenumbers.

All fully nonlinear results presented herein were computed with a Prandtl number of 0.7 or (for some DIA runs) 0.5. Tables 3.4, and 3.5 list the lengthscale ratios and transport coefficients from linear and nonlinear computations as well as experiments. The available lengthscale results for all methods are surprisingly close. It should be

noted that the (nonlinear) analysis presented in equations (3.23) and (3.24) predicts an integral lengthscale ratio of 0.67 and microscale ratio of 1.10 which are also in reasonably good agreement with experiment. Thus lengthscale ratios appear to infer more about relative spectral relationships than effects specific to the nonlinearities of the scalar transport problem. Although the range of Pr investigated is small, it still has a significant (if relatively small) effect upon the scalar transport correlation coefficient and the scalar to mechanical microscale ratio.

While the correlation coefficients for the DIA, DNS and experiment are reasonably close, the linear analysis predicts magnitudes which are significantly higher than the nonlinear results. It is apparent that the nonlinearities serve to decorrelate the scalar and velocity fields at Pr of 0.7. From the few results presented here (linear and nonlinear) concerning Prandtl number variation, deviation of Pr from unity also serves to decorrelate these fields by enhancing the differences between the (viscous and conductive) dissipation characteristics of the velocity and scalar fields.

These results indicate that the integral lengthscale and Taylor microscale ratios appear to be reasonably accurately predicted by linear analysis while the correlation coefficient is significantly affected by the presence of nonlinearities.

Higher Legendre Coefficient Results

All the DIA results presented above were obtained using only the first Legendre coefficients for the representation of all turbulence functions. This is exact for the velocity field functions (correlation and response functions) as well as the scalar field response function. However, it can be shown that the linear forcing terms in the scalar variance equation induces an angular dependence which requires the first two

even Legendre polynomials to described completely. While the linear terms induce only sinusoidal angular dependence in the scalar transport field which is completely described by the first associated Legendre function, the presence of the scalar field covariances in the nonlinear terms of the transport equations implies higher order terms may be required to accurately describe these fields.

The effects of including the second Legendre coefficients in DIA computations were studied, and the results are presented in Figures 3.24 and 3.25. The surprising result was that, although the second scalar variance coefficients achieved magnitudes approximately equal but opposite in sign to the first coefficients (as predicted by analysis of the RDT equations), there was no noticeable change in the actual scalar variance. In addition, the scalar transport field develops virtually zero magnitude in the second coefficient, implying that its angular dependence is accurately modeled using only the sinusoidal first associated Legendre function, $P^1(\mu_k)$. In order to ensure the proper working of the DIA code, two other problems were studied. The first was passive scalar transport in anisotropic turbulence. The initial velocity field was anisotropic with 25% of the turbulence energy in the vertical mode and the remainder in the horizontal mode. The comparison of the one and two Legendre coefficient computations shows that inclusion of the higher harmonics reduces scalar transport due to the more accurate representation of the velocity field anisotropy. This is true for both the eddy diffusivity ratio as well as the scalar energy. The final problem is stably stratified turbulence with nonzero initial scalar (i.e., potential energy) field. Here the influence of the second coefficient is dramatic, significantly reducing the magnitude of the scalar field (and scalar transport) oscillations as well as reducing the oscillation period (increasing the frequency). The magnitude of this

effect is sufficient to bring these DIA results into much closer agreement with those of DNS (e.g., see Figure 5 of Sanderson et al. [21]).

These results imply that the DIA code is computing the effects of the second Legendre coefficients correctly and is predicting that the second order coefficients do not affect the integrated scalar transport or scalar field intensity. The results presented above are believed to fairly represent the performance of the DIA in computing turbulent passive scalar transport.

This numerical evidence is satisfactory for illustrating cases where higher Legendre coefficients are necessary. However, it does not explain the mathematical reasons, nor provide physical insight as to why, the passive scalar transport problem requires only one coefficient for complete characterization of the evolution of integrated quantities. Appendix C examines some numerically determined values for selected coefficients, wavenumbers and Legendre coefficients in a preliminary attempt to show that, in the case of isotropic velocity fields, the contributions in the nonlinear terms of each velocity eigenfunction towards building up higher order Legendre coefficients in the velocity–scalar covariance and scalar variance equations cancel each other out. Appendix A investigates analytically the nature of the coefficients for the linear forcing (mean scalar gradient) term and show they contribute to only the first coefficient for the transport (velocity–scalar covariance) equations and only the first two coefficients in the scalar variance equations. Appendix D examines analytically the scalar and scalar transport field nonlinear coefficients which arise in the isotropic scalar turbulence problem. The result is that these DIA coefficients, for the first and second eigenfunctions of the velocity field, are equal in magnitude and opposite in sign for the scalar transport field. Thus for an isotropic velocity field any contributions of the

isotropic part of the scalar transport field to higher harmonics sum to zero. Thus the only way that anisotropy can affect the integrated scalar transport (through these coefficients) is through anisotropy in the initial scalar field, initial transport field (which is normally initialized to zero) or an anisotropic velocity field. This result and those of the one and two coefficient runs suggest that the DIA may possibly predict only one nonzero Legendre coefficient for the scalar transport field and two for the scalar field and raises the question whether this may be also true for the exact problem. This is an area for future investigations.

Conclusions

The DIA and DNS results both appear to predict integrated single time statistics in general qualitative and quantitative agreement with the studies by Sirivat and Warhaft, and Budwig et al. The DIA appears to underpredict the nonlinear scalar transfer, and thus the overall dissipation of scalar energy. This results in overprediction of the growth of the scalar variance and associated scalar transport (as shown in the eddy diffusivity ratio) although the scalar transfer correlation coefficient appears to be reasonably represented. Whether these disagreements are the result of the Legendre series truncations, the closure theory, or both cannot be determined on the basis of this study. Use of two Legendre coefficients did not measurably change the integrated results for the passive scalar transport problem while they significantly altered those for decaying stably stratified turbulence. The only field to develop significant amplitude in the second coefficient was the scalar field. While it is shown that the linear isotropically initiated problem will only develop one coefficient in the velocity and scalar transport fields and two in the scalar field, it is surprising that

the nonlinear terms apparently develop no higher coefficients. It is speculated this may be a reflection of a return to isotropy type of behavior and it is proven that this is true for the case of the isotropic DIA scalar field nonlinear coefficients. While this behavior was not shown to hold for the other DIA nonlinear coefficients, it might and this is an area for future investigation.

The lengthscale studies using the DIA show good qualitative agreement with the results of experiment. Changing the initial value of this quantity affects the initial evolution of the scalar and scalar transfer fields but all problems studied appeared to approach similar asymptotic states. This is in agreement with the experimental results of Sirivat and Warhaft [23] and Budwig, et al. [3].

Comparison of the linear studies with the numerical and experimental work indicates that lengthscale ratios (both integral and dissipation) are surprisingly well predicted using only linear analysis. The scalar transport correlation coefficients cannot be accurately predicted without including the nonlinear terms due to their decorrelating effects. A preliminary linear study of the effect of changing the Prandtl number from close to unity indicates that this appears to enhance decorrelation of the velocity and scalar fields by changing the relative roles of molecular dissipation in these fields.

Acknowledgements

The authors are grateful to the Iowa State University Computation Center and the National Center for Supercomputing Applications for their support of these computations. The first two authors also acknowledge the support of the Exxon Foundation and the first author is grateful for the computional facilities provided by APTEK,

Inc. of Colorado Springs, Colorado.

References

[1] Batchelor, G.K. and Proudman, I. (1954) The effect of rapid distortion of a fluid in turbulent motion. *Q. J. Mech. Appl. Math.* **7**, pp. 83–103.

[2] Cambon, C., Jeandel, D. and Mathieu, J. (1981) Spectral modelling of homogeneous non-isotropic turbulence. *J. Fluid Mech.* **104**, pp. 247–262.

[3] Budwig, R., Tavoularis, S. and Corrsin, S. (1985) Temperature fluctuations and heat flux in grid generated isotropic turbulence with streamwise and transverse mean temperature gradients. *J. Fluid Mech.* **153**, pp. 441–460.

[4] Corrsin, S. (1952) Heat transfer in isotropic turbulence. *J. of Appl. Phys.* **23**, pp. 113–118,.

[5] Craya, A. (1958) *Contribution a l'Analyse de la Turbulence a des Vitesse Moyennes*, P.S.T. Ministere de l'Air (Fr.).

[6] de Boor, Carl. (1977) Package for calculating with B-splines. *SIAM J. Numer. Anal.* **14**, pp. 441–472.

[7] Herring, J.R. (1974) Approach of axisymmetric turbulence to isotropy. *Phys. Fluids* **17**, pp. 859–872.

[8] Hill, J.C. (1981) Heat transfer in isotropic turbulence, *Chem. Eng. Commun.* **12**, pp. 69–96.

[9] Kerr, R.M. (1985) Higher-order derivative correlations and the alignment of small-scale structures in isotropic numerical turbulence. *J. Fluid Mech.* **153**, pp. 31–58.

[10] Kraichnan, R.H. (1959) The structure of isotropic turbulence at very high Reynolds numbers. *J. Fluid Mech.* **5**, pp. 497–543.

[11] Kraichnan, R.H. (1964) Direct-interaction approximation for shear and thermally driven turbulence. *Phys. Fluids* **7**, pp. 1048–1062.

[12] Kraichnan, R.H. (1964) Decay of isotropic turbulence in the direct-interaction approximation. *Phys. Fluids* **7**, pp. 1030–1048.

[13] Kraichnan, R. (1970) Convergents to turbulence functions, *J. Fluid Mech.* **41**, pp. 189–217.

[14] Kraichnan, R. (1971) An almost-Markovian Galilean-invariant turbulence model. *J. Fluid Mech.* **47**, pp. 513–524.

[15] Herring, J.R. (1990) (personal communication).

[16] Schumann, U. and Herring, J.R. (1976) Axisymmetric homogeneous turbulence: a comparison of direct simulations with the direct-interaction approximation. *J. Fluid Mech.* **76**, pp. 755–782.

[17] Leonard, A.D. and Hill, J.C.; Direct numerical simulation of turbulent flows with chemical reaction. J. Sci. Comp., **3**, pp. 25–43, 1988.

[18] Leslie, D.C.; *Developments in the theory of turbulence*, Oxford University Press, London, 1973.

[19] Sanderson, R.C., Hill, J.C. and Herring, J.R. (1987) Transient behavior of a stably stratified homogeneous turbulent flow. In *Advances in Turbulence*, G. Comte-Bellot and J. Mathieu, eds., Springer–Verlag, Berlin.

[20] Sanderson, R.C. and Hill, J.C. (1988) Dynamics of Decaying Stably Stratified Turbulent Flow, *Proc. of the Geophysical Turbulence Symposium of the American Meteorological Society*, San Diego, Ca.

[21] Sanderson, R.C., Leonard, A.D., Herring, J.R. and Hill, J.C. (1989) Fossil and Active Turbulence. In *Turbulence and Coherent Structures*, M. Lesieur and O. Métais, eds., Kluwer Acad. Press.

[22] Savill, A. M. (1987) Recent developments in rapid-distortion theory *Ann. Rev. Fluid Mech.* **19**, pp. 531–575.

[23] Sirivat, A. and Warhaft, Z. (1983) The effect of a passive cross-stream temperature gradient on the evolution of temperature variance and heat flux in grid turbulence. *J. Fluid Mech.* **128**, pp. 323–346.

[24] Wiskind, H.K. (1962) A uniform gradient turbulent transport experiment. *J. Geophys. Res.* **67**, pp. 3033–3048.

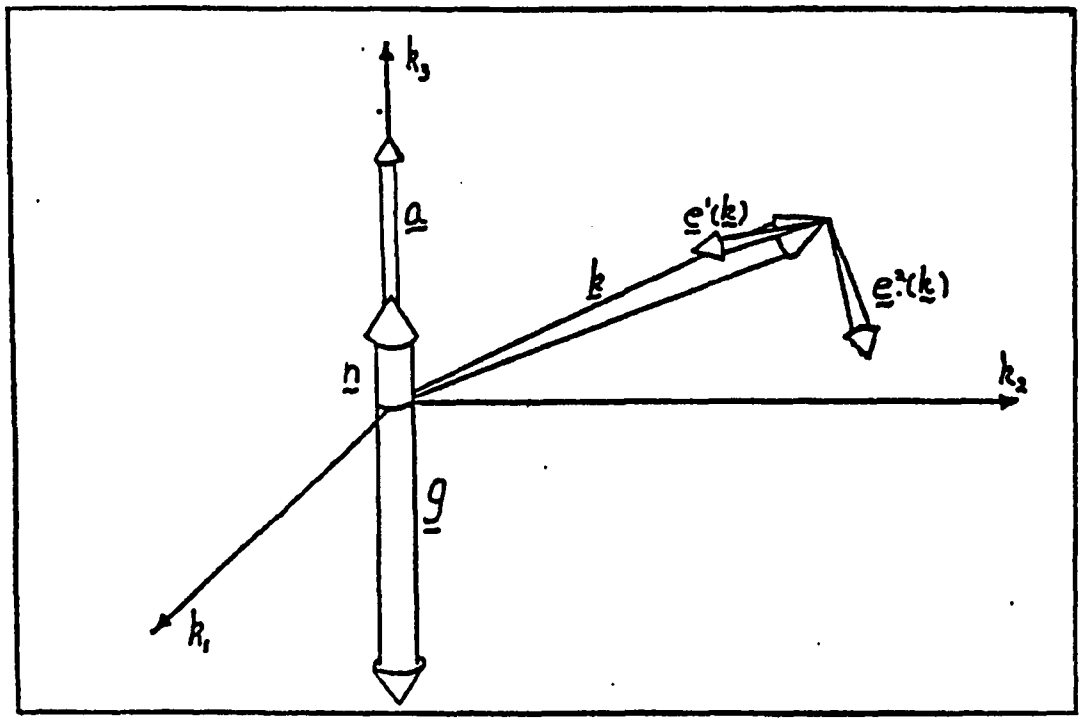

Figure 3.1: Illustration of the geometric relationship between **a**, **n**, **k**, and the eigenvectors $\mathbf{e}^{\lambda}(\mathbf{k})$.

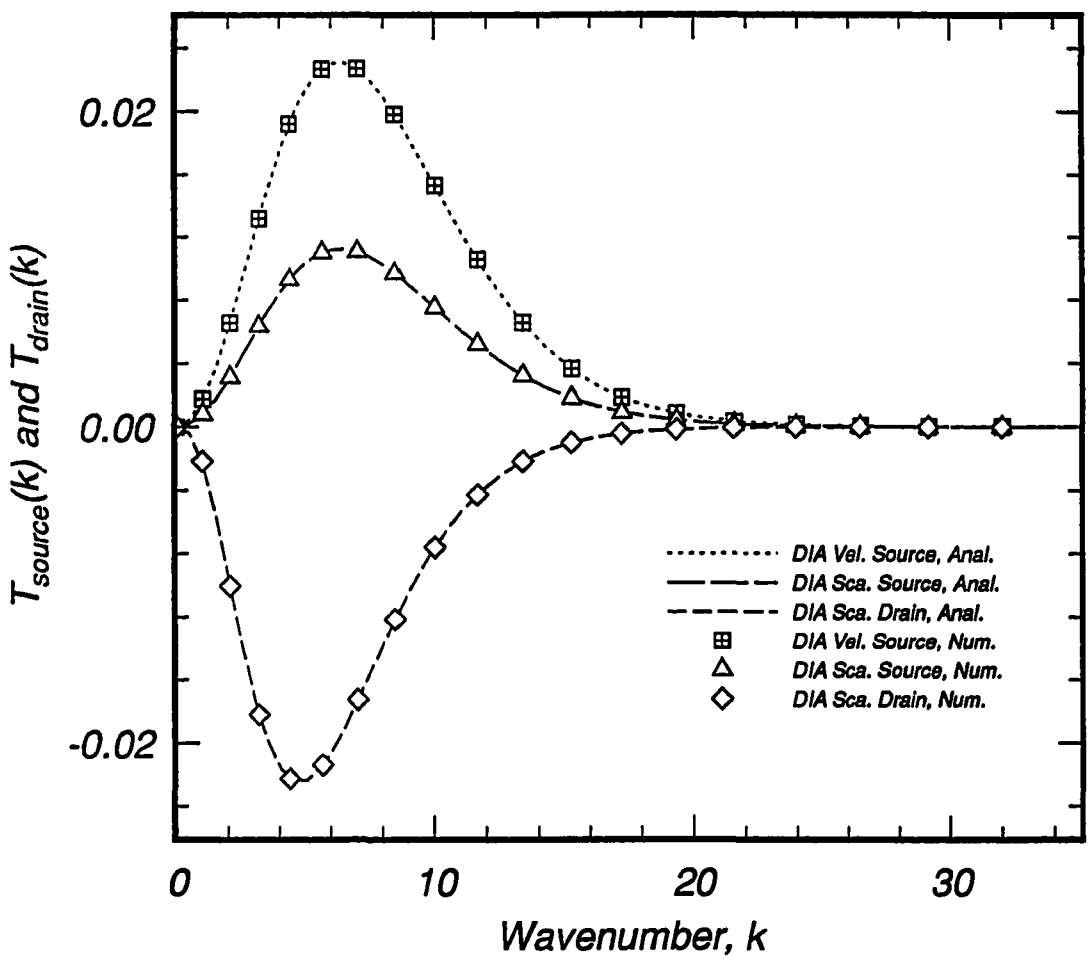

Figure 3.2: Analytic and B-spline numerical p–q integrations of velocity nonlinear terms.

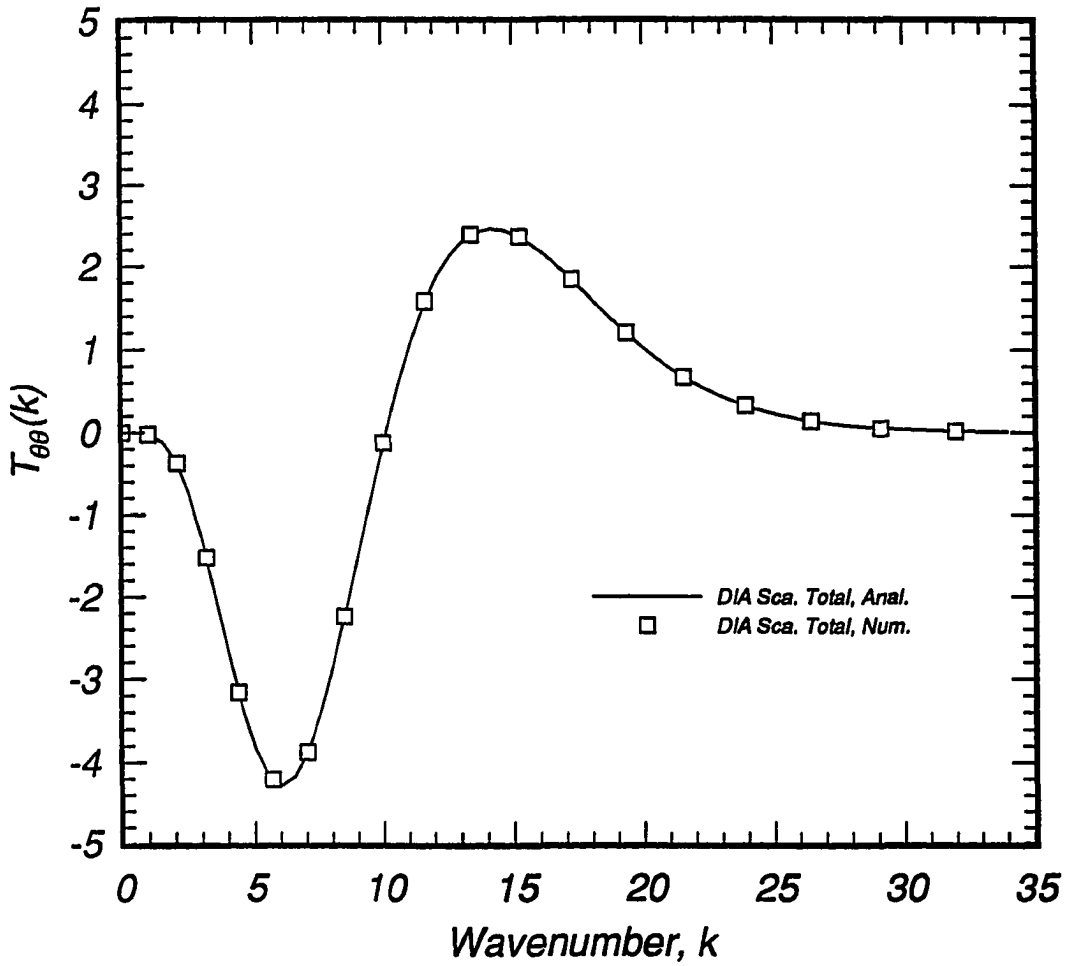

Figure 3.3: Analytic and B-spline numerical p-q integrations of scalar field nonlinear terms.

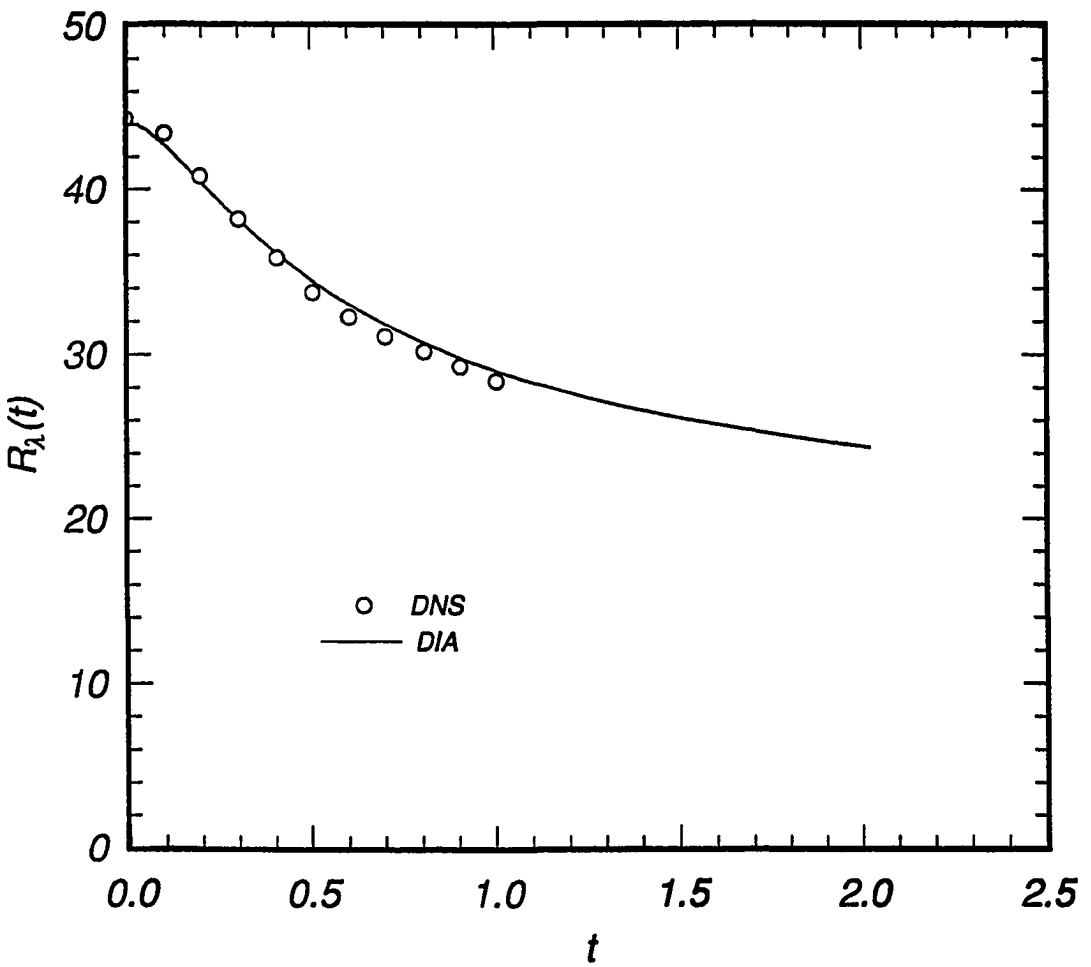

Figure 3.4: Reynolds number evolution as predicted by DIA and DNS for isotropic turbulence.

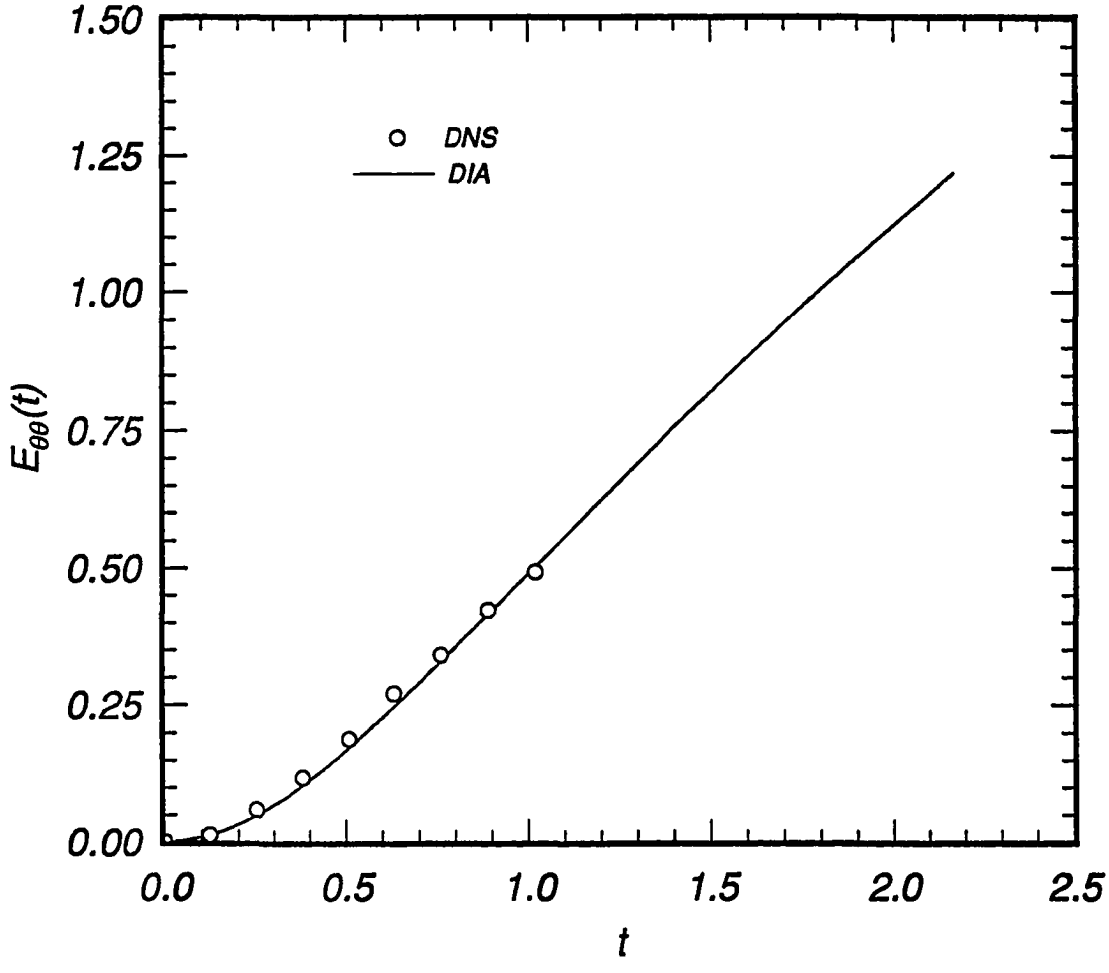

Figure 3.5: Evolution of the scalar energy for DIA and DNS; $R_{\lambda o} = 45$, $Pr = 0.7$, $\vartheta'_o = 0$.

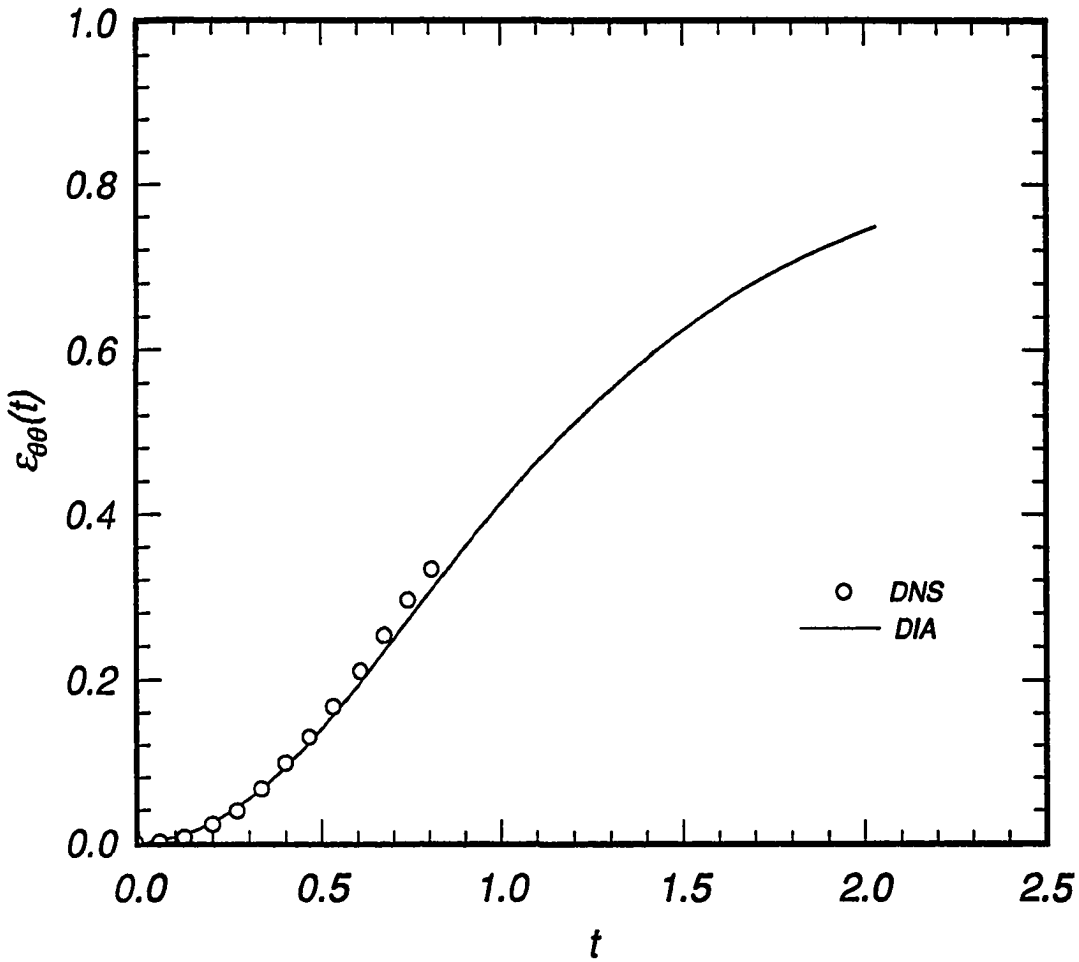

Figure 3.6: Evolution of the scalar dissipation for DIA and DNS; $R_{\lambda o} = 45$, $Pr = 0.7$, $\vartheta'_o = 0$.

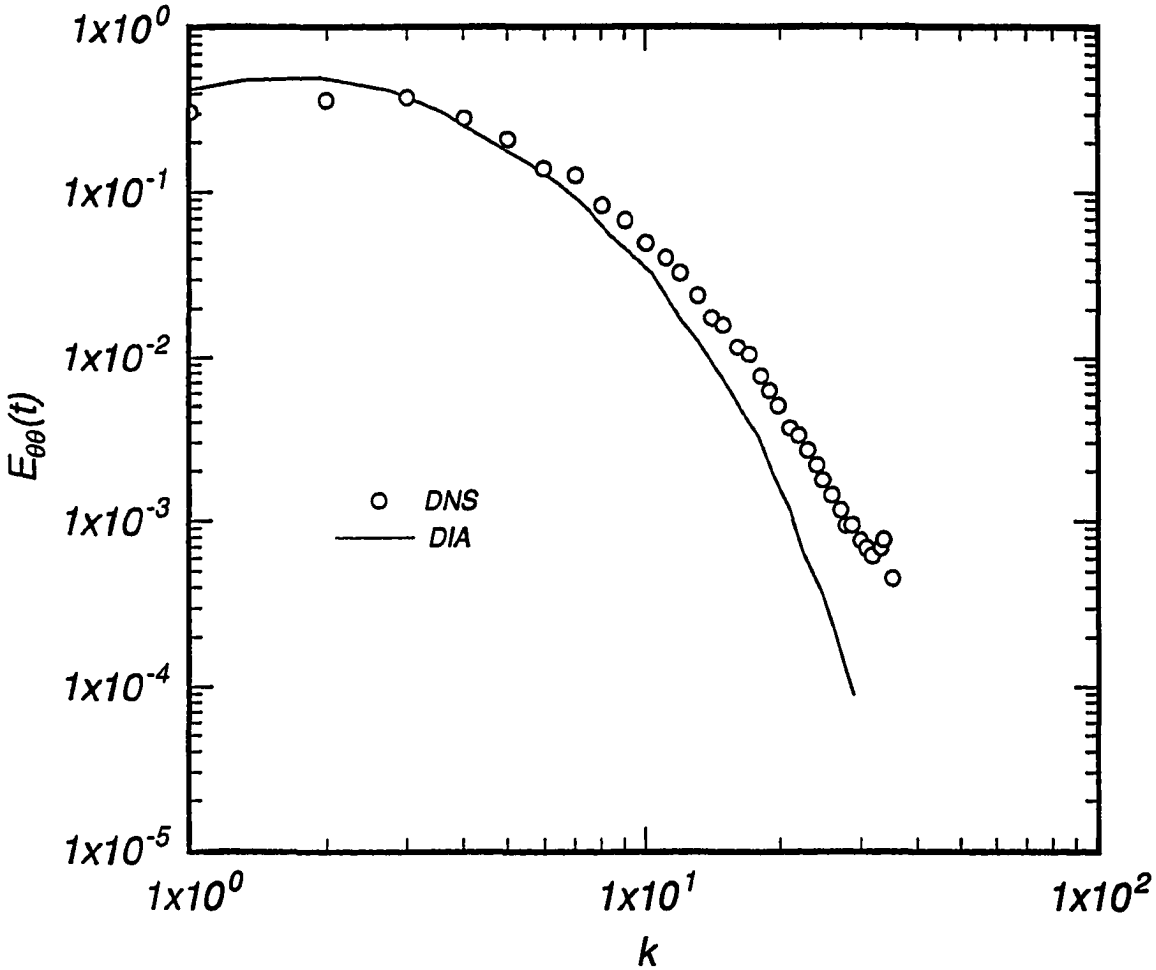

Figure 3.7: Spectra of the scalar energy for DIA and DNS; $R_{\lambda o} = 45$, $Pr = 0.7$, $\vartheta'_o = 0$, $t = 1.02$.

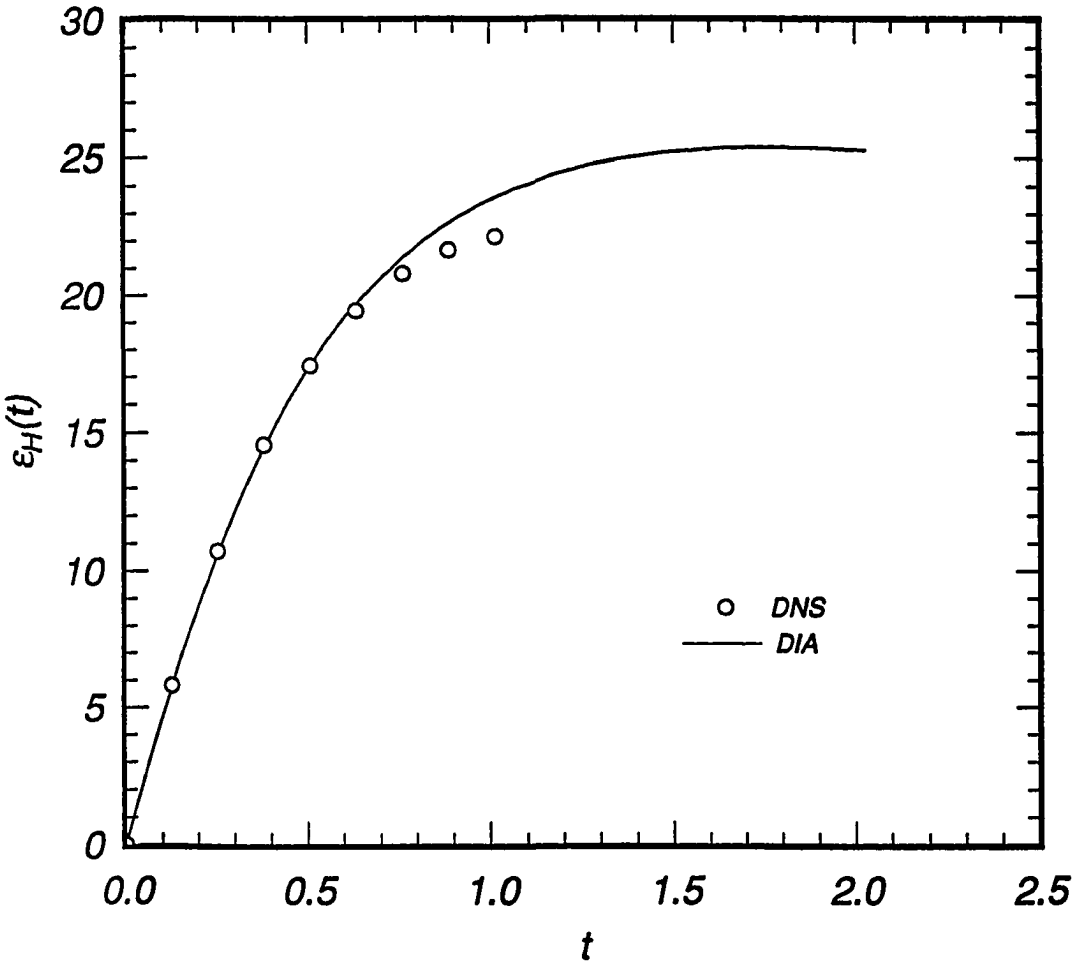

Figure 3.8: Evolution of the eddy diffusivity ratio for DIA and DNS; $R_{\lambda o} = 45$, $Pr = 0.7$, $\vartheta'_o = 0$.

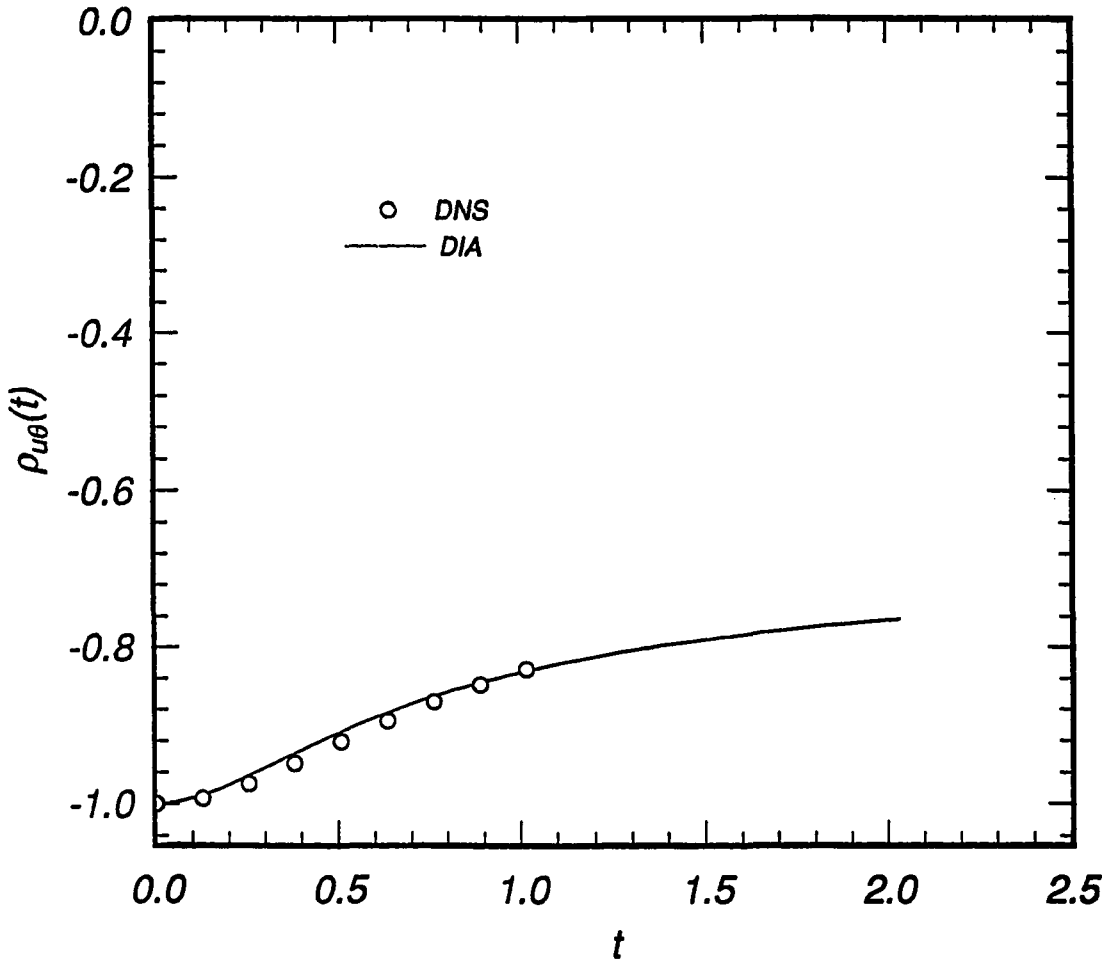

Figure 3.9: Evolution of the scalar transport correlation coefficient for DIA and DNS; $R_{\lambda_o} = 45$, $Pr = 0.7$, $\vartheta'_o = 0$.

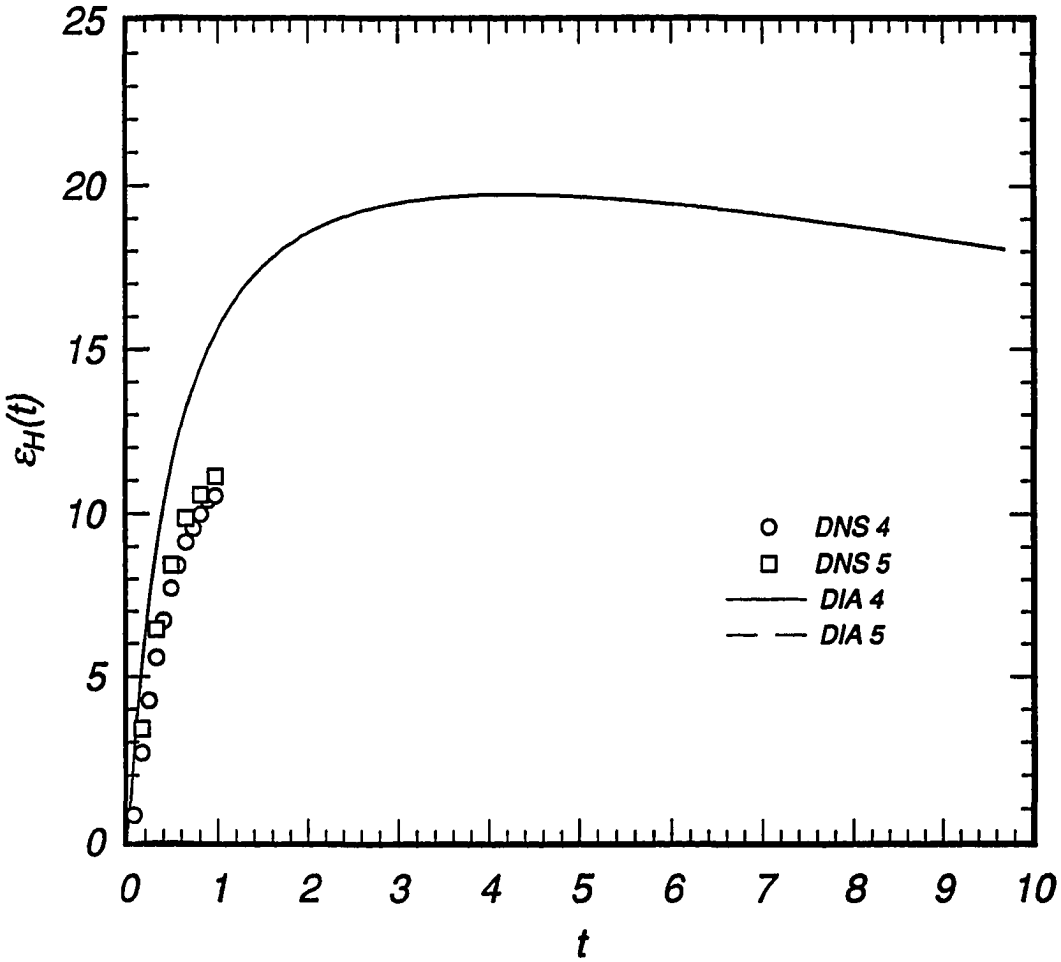

Figure 3.10: Evolution of the eddy diffusivity ratio with exponential initial spectra (see Table 3.3 for run definitions).

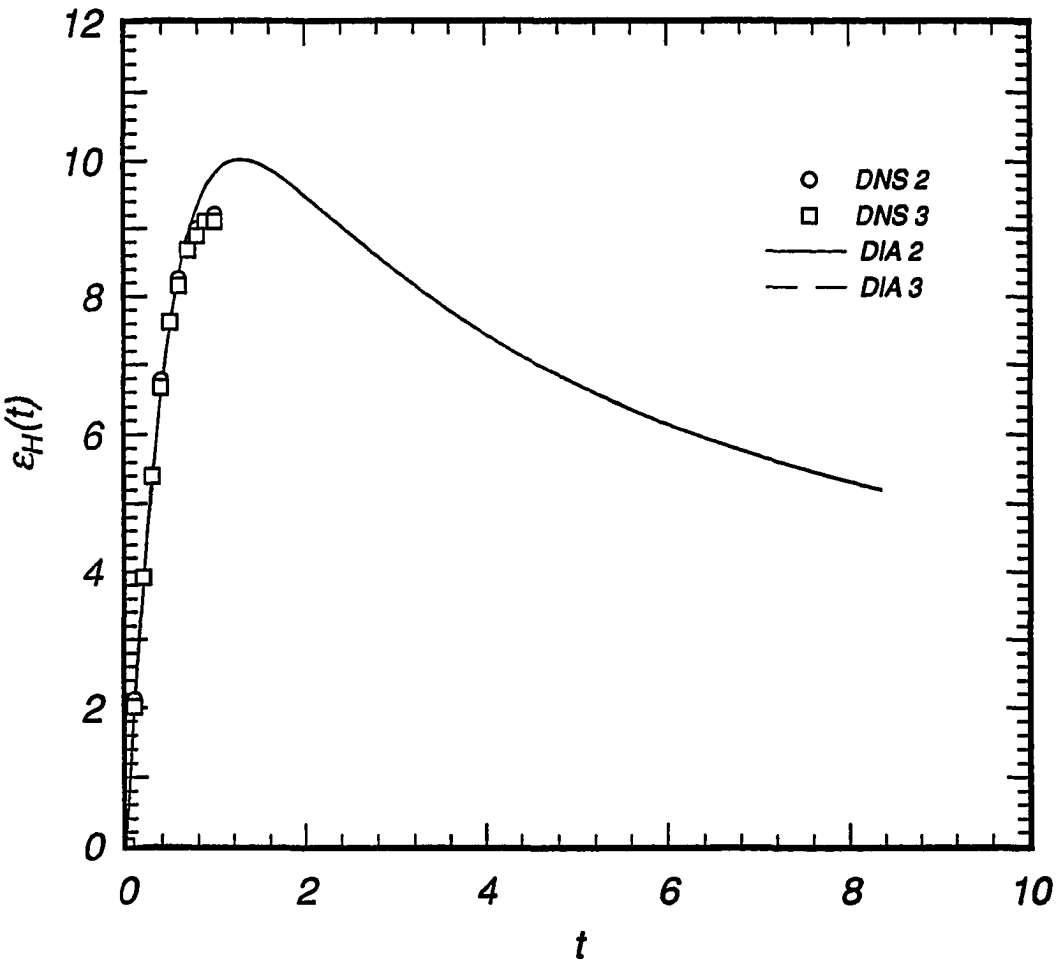

Figure 3.11: Evolution of the eddy diffusivity ratio with Gaussian initial spectra (see Table 3.3 for run definitions).

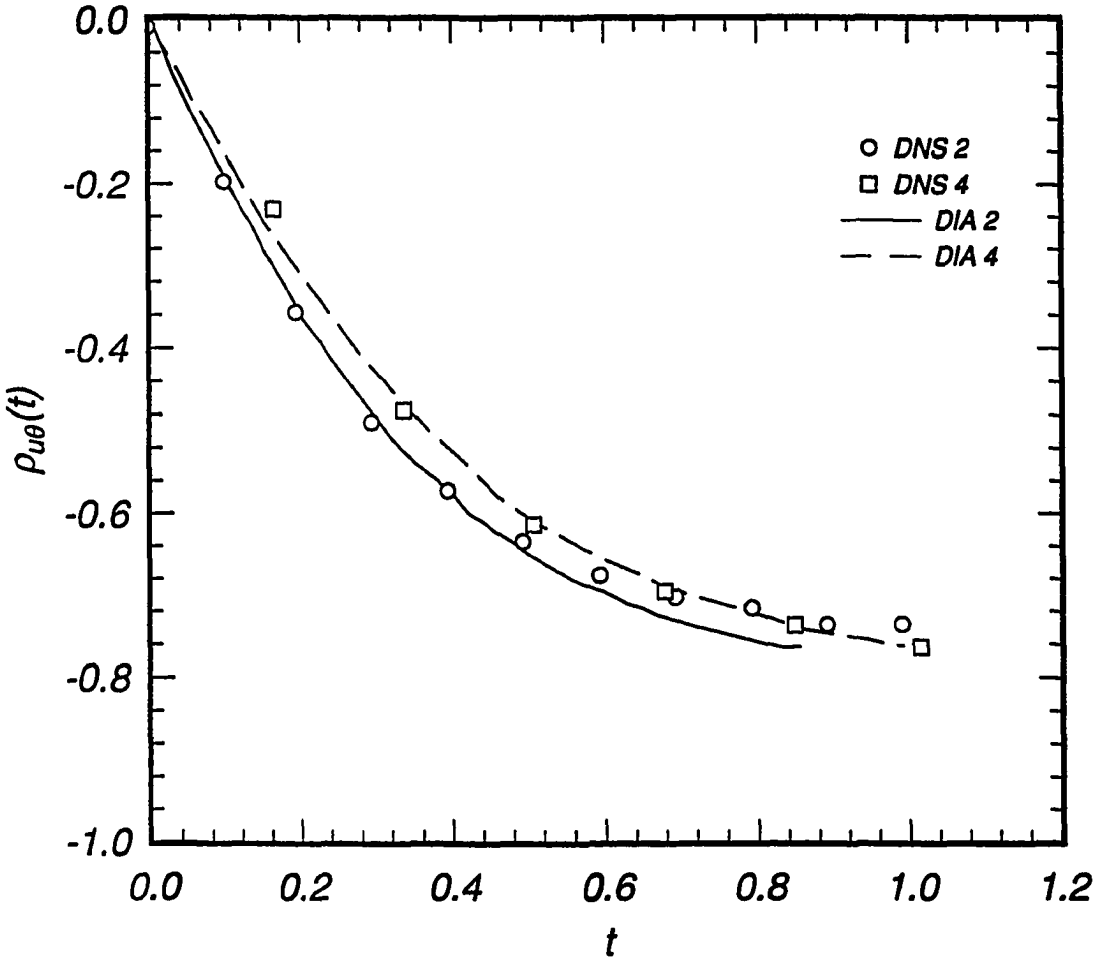

Figure 3.12: Evolution of the correlation coefficient with exponential and Gaussian initial spectra (see Table 3.3 for run definitions).

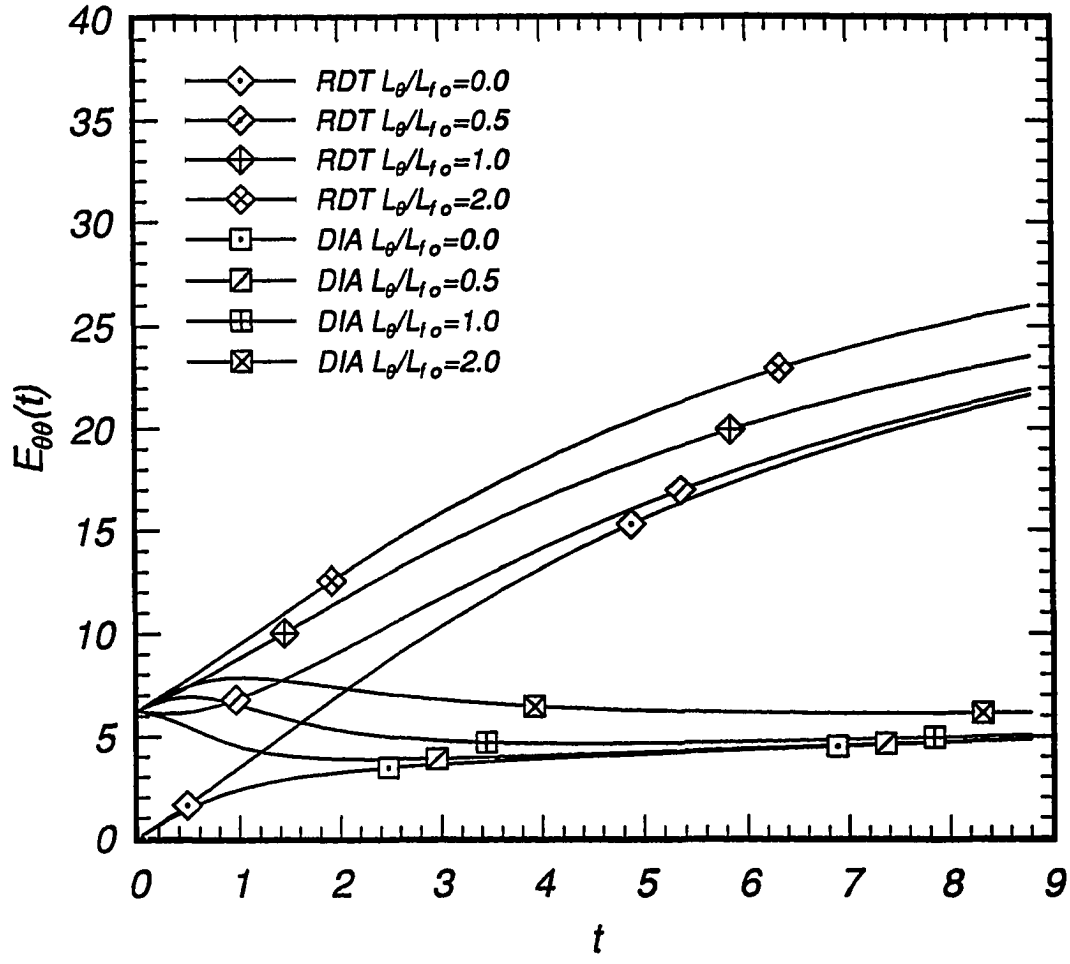

Figure 3.13: Evolution of Gaussian DIA and RDT scalar energy for different initial lengthscale ratios; $R_{\lambda o} = 45$, $Pr = 0.7$.

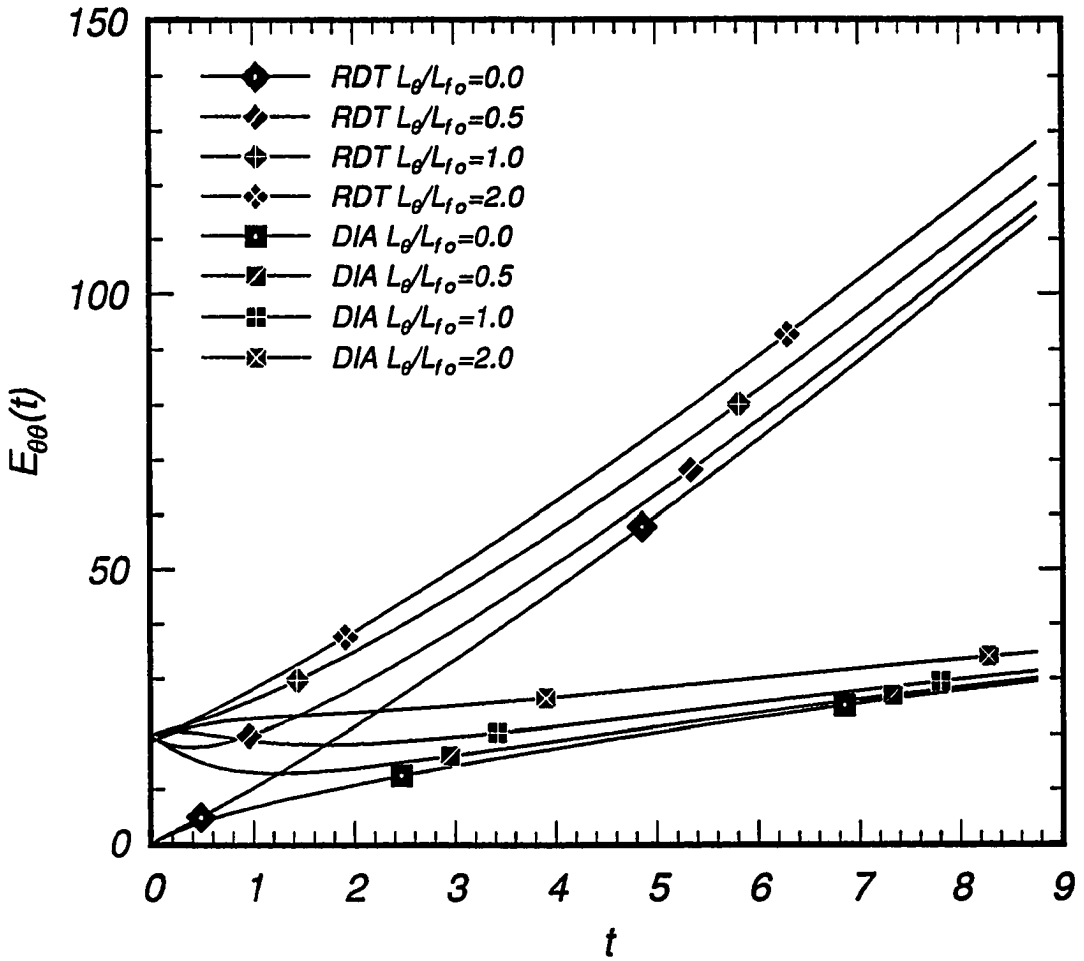

Figure 3.14: Evolution of exponential DIA and RDT scalar energy for different initial lengthscale ratios; $R_{\lambda o} = 45$, $Pr = 0.7$.

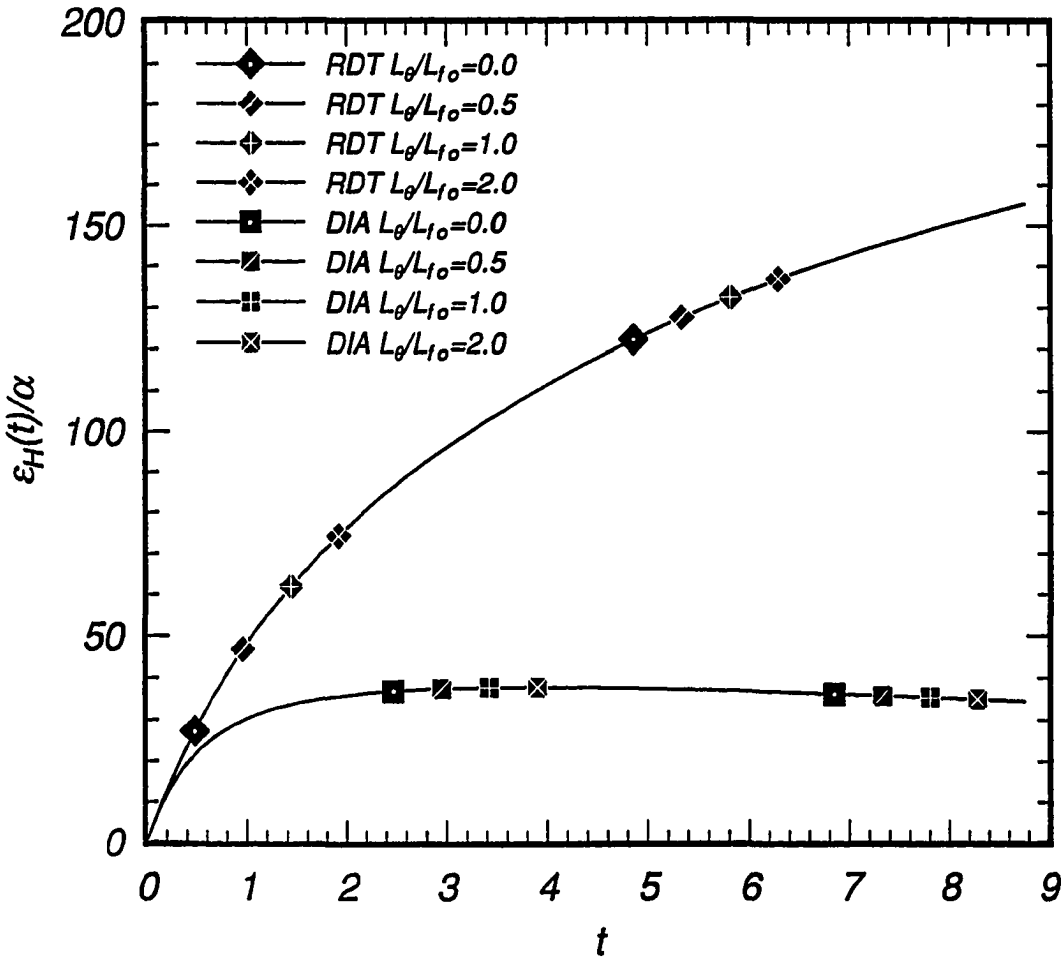

Figure 3.15: Evolution of exponential DIA and RDT eddy diffusivity ratios for different initial lengthscale ratios; $R_{\lambda o} = 45$, $Pr = 0.7$.

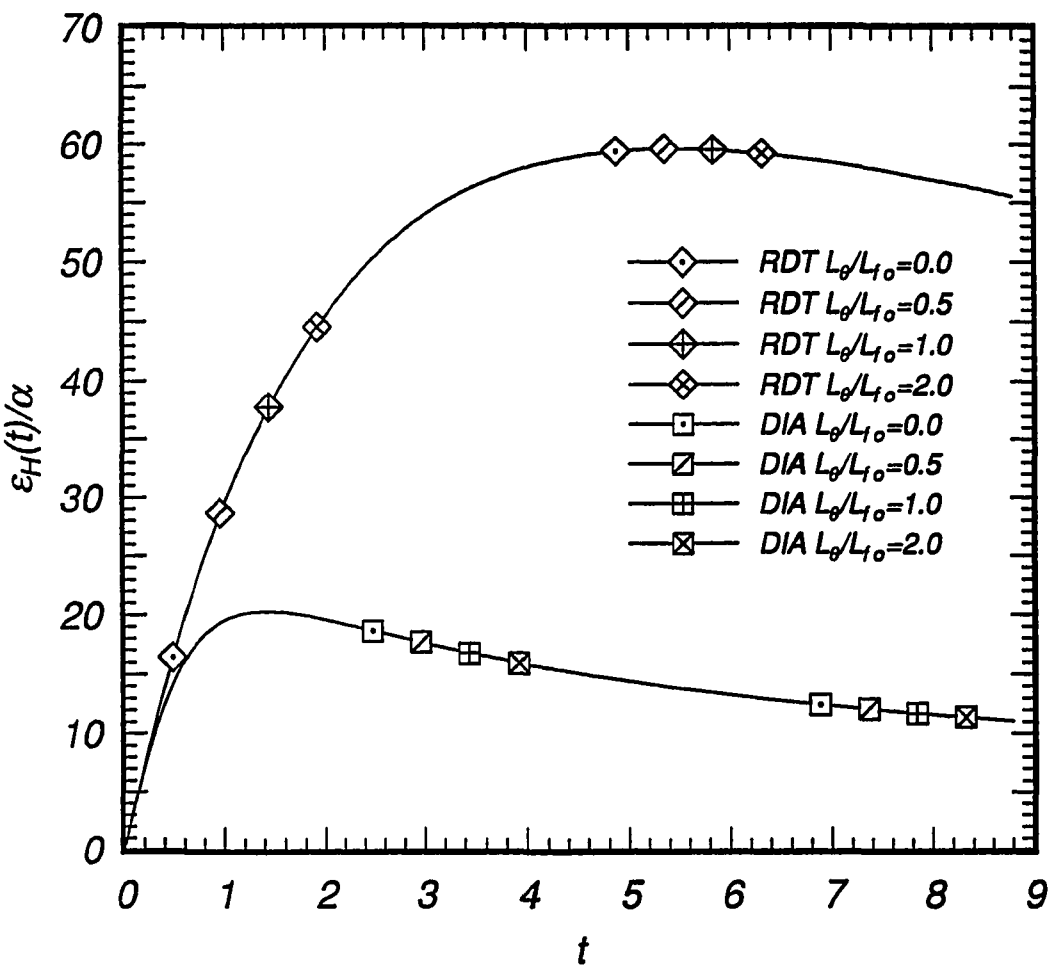

Figure 3.16: Evolution of Gaussian DIA and RDT eddy diffusivity ratios for different initial lengthscale ratios; $R_{\lambda o} = 45$, $Pr = 0.7$.

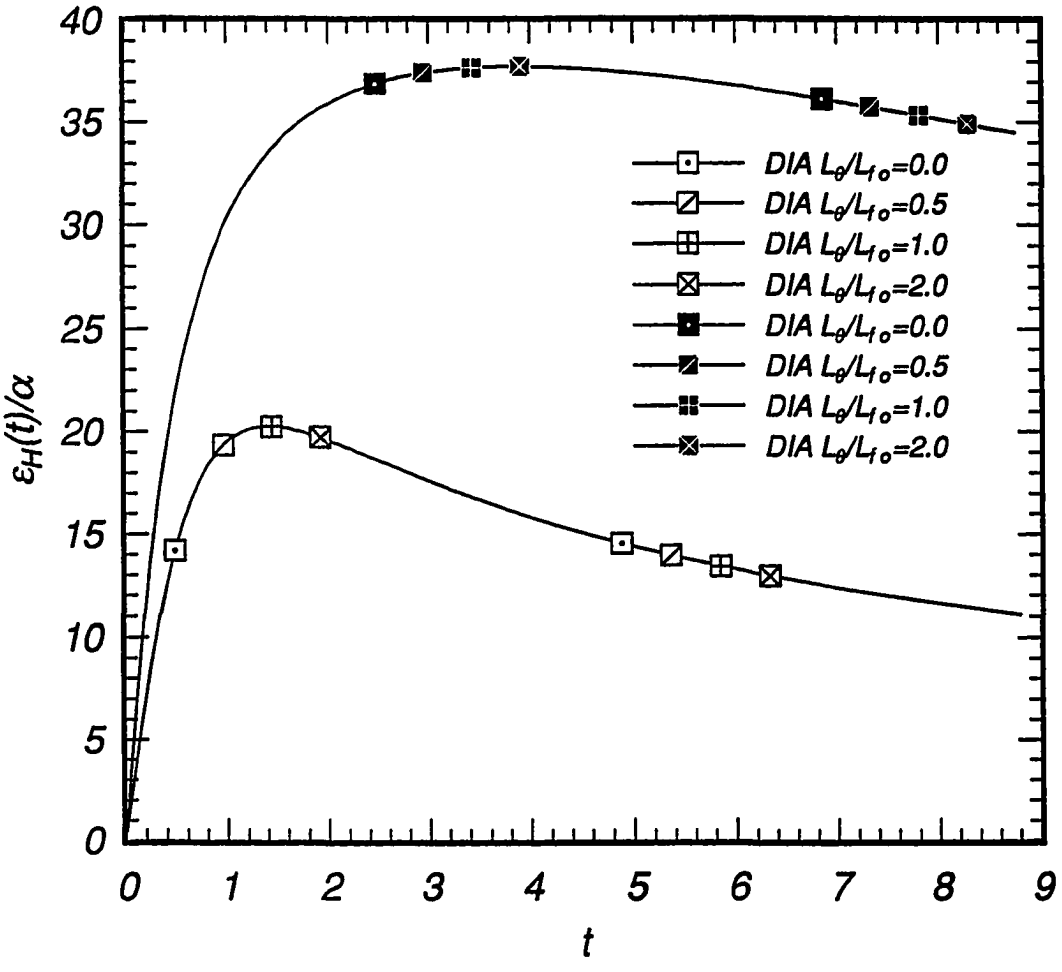

Figure 3.17: Evolution of Gaussian and exponential DIA eddy diffusivity ratios for different initial lengthscale ratios; $R_{\lambda o} = 45$, $Pr = 0.7$.

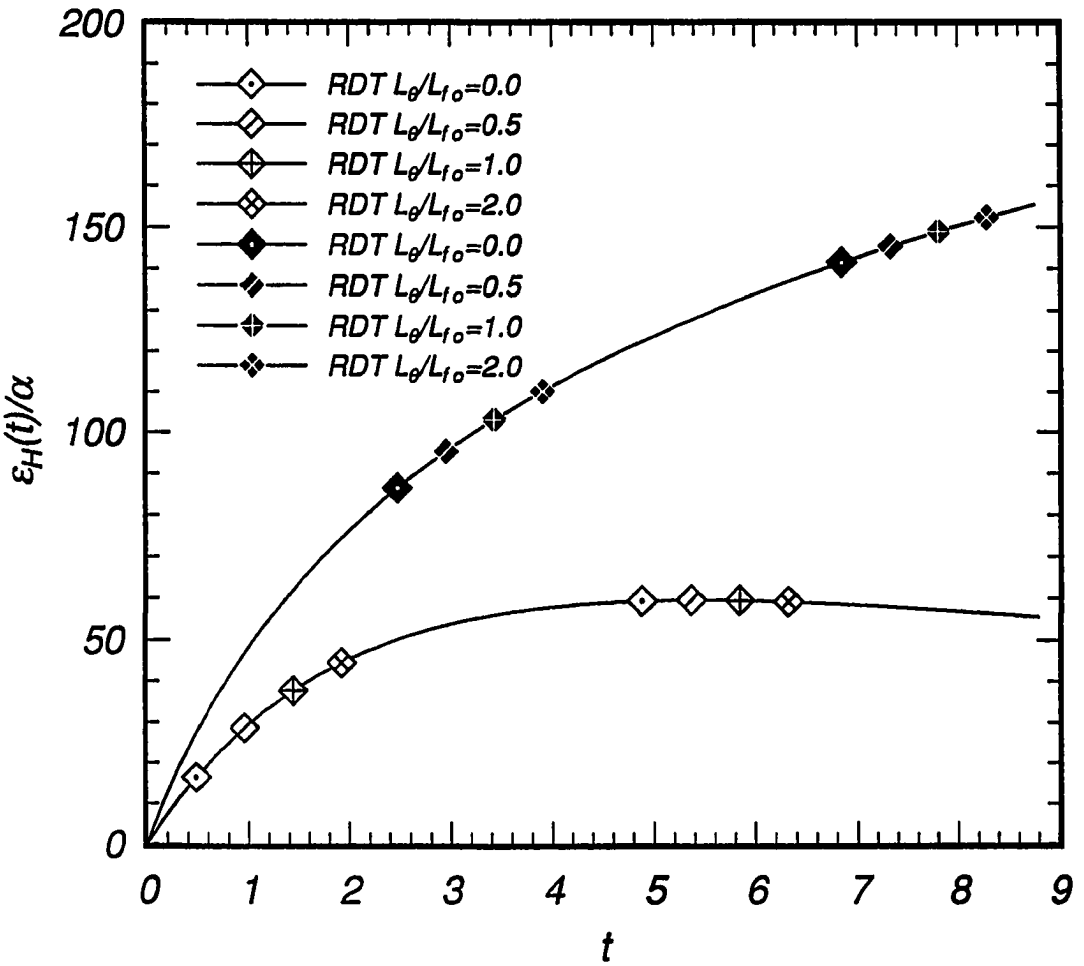

Figure 3.18: Evolution of Gaussian and exponential RDT eddy diffusivity ratios for different initial lengthscale ratios; $R_{\lambda o} = 45$, $Pr = 0.7$.

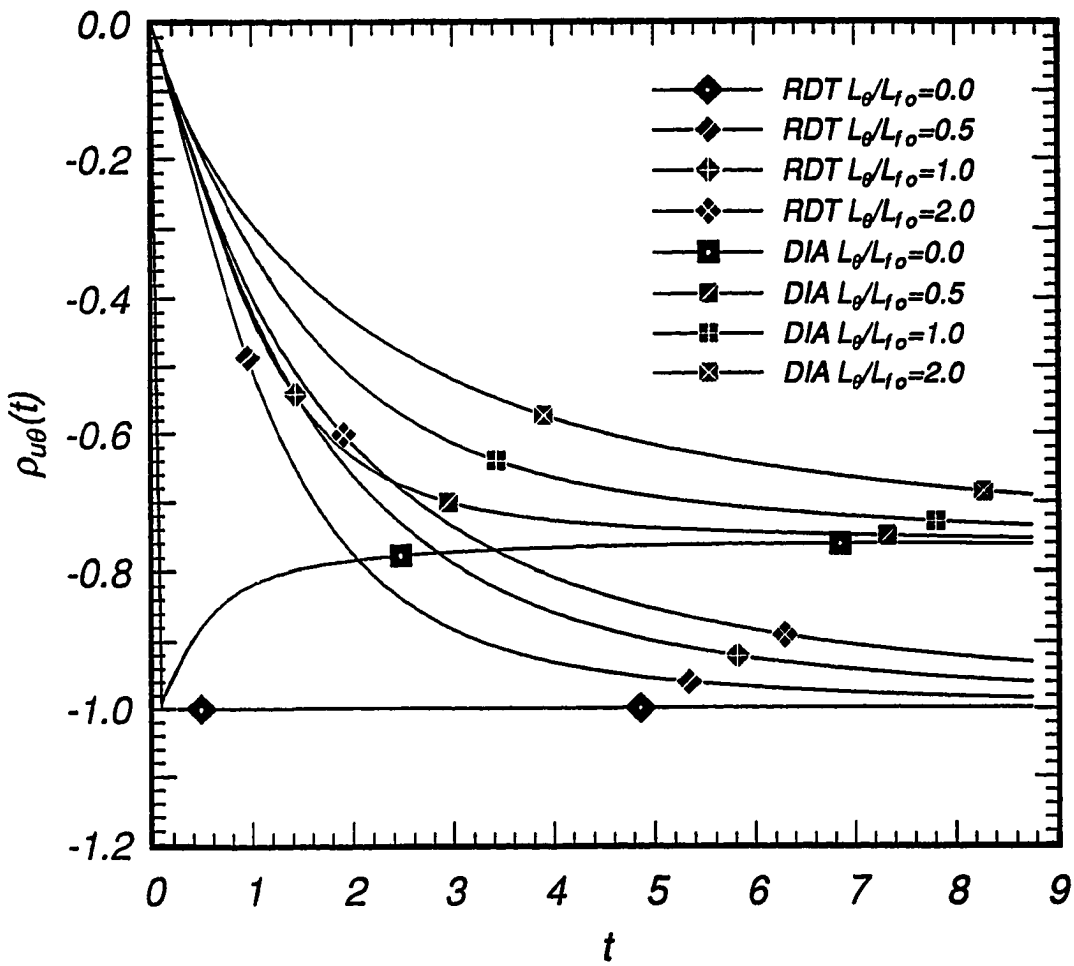

Figure 3.19: Evolution of exponential DIA and RDT correlation coefficients for different initial lengthscale ratios; $R_{\lambda o} = 45$, $Pr = 0.7$.

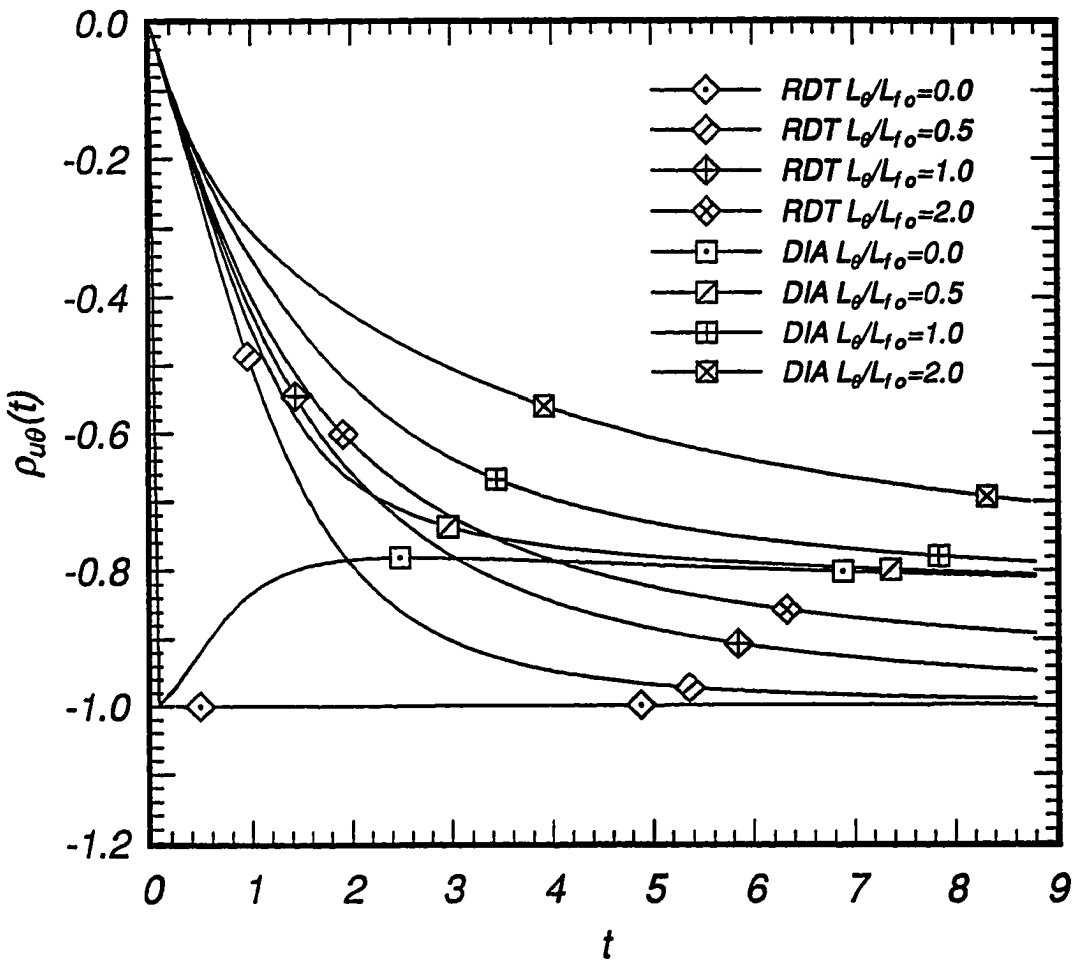

Figure 3.20: Evolution of Gaussian DIA and RDT correlation coefficients for different initial lengthscale ratios; $R_{\lambda o} = 45$, $Pr = 0.7$.

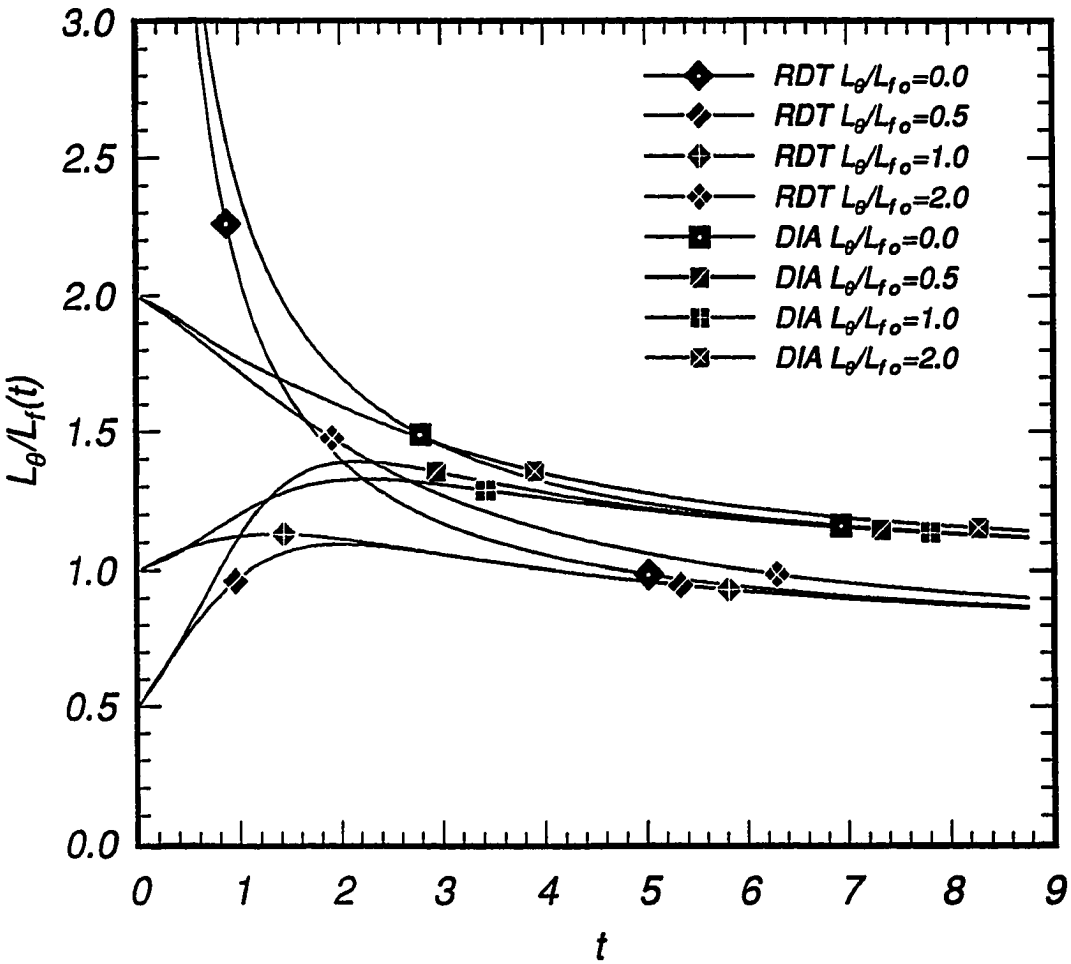

Figure 3.21: Evolution of exponential DIA and RDT integral lengthscale ratios for different initial lengthscale ratios; $R_{\lambda o} = 45$, $Pr = 0.7$.

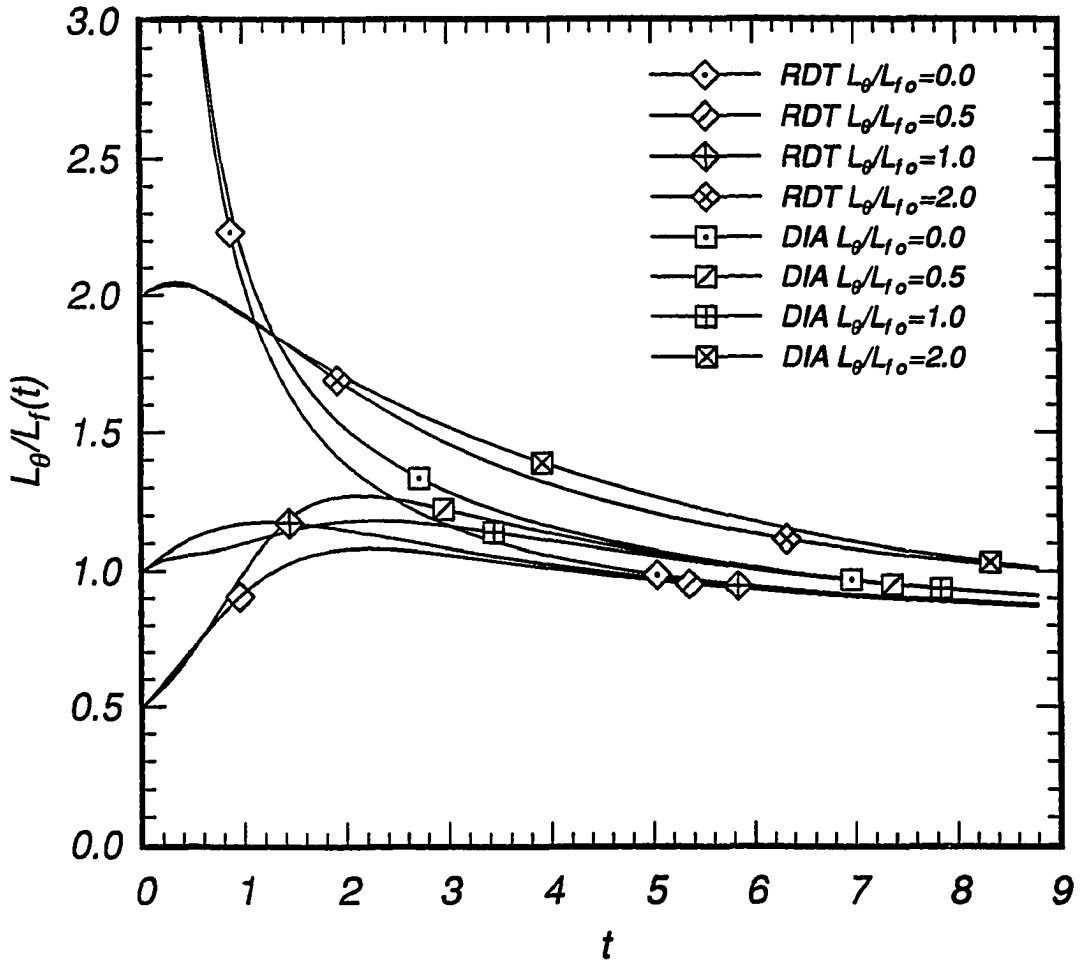

Figure 3.22: Evolution of Gaussian DIA and RDT integral lengthscale ratios for different initial lengthscale ratios; $R_{\lambda o} = 45$, $Pr = 0.7$.

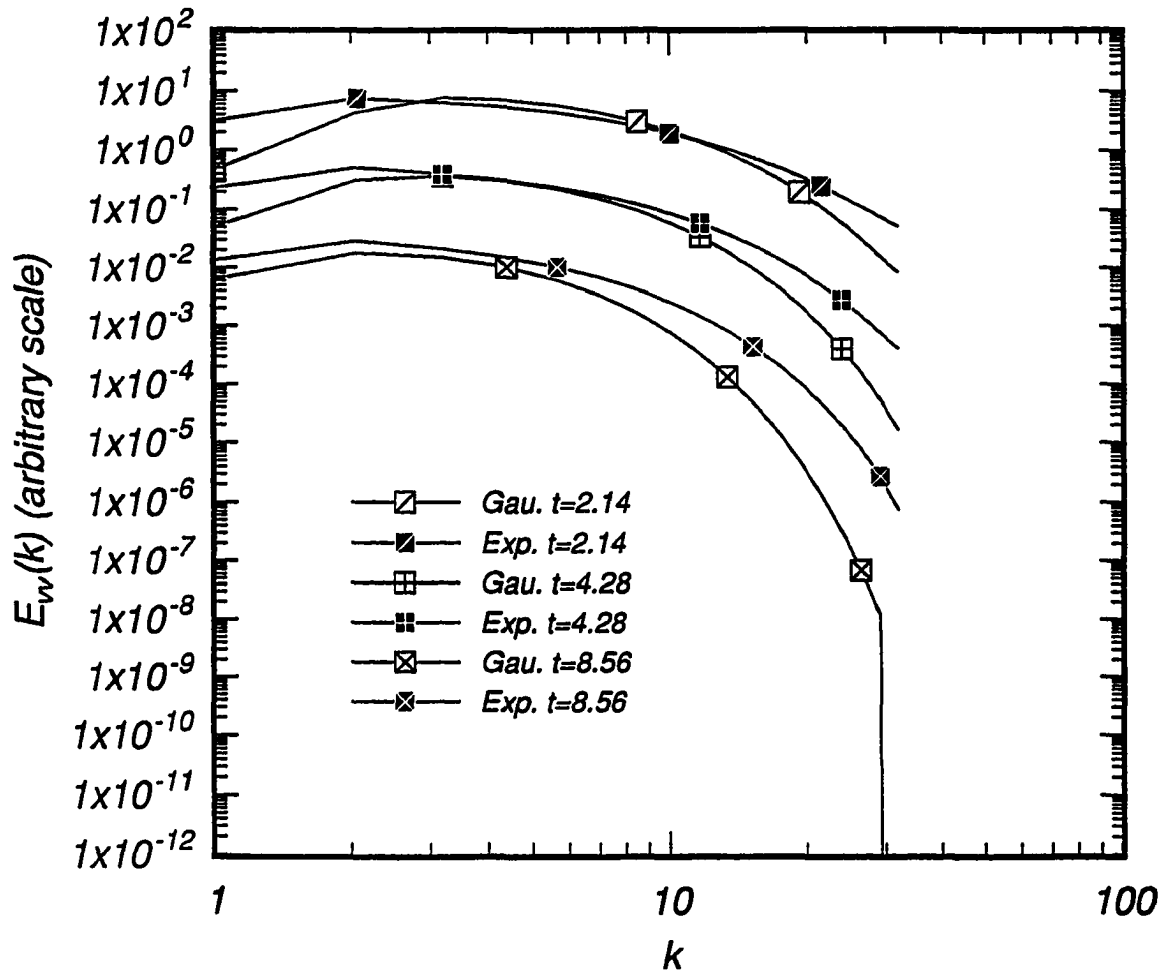

Figure 3.23: Evolution of Gaussian and exponential velocity spectra for $R_{\lambda o} = 45$, $Pr = 0.7$, $L_f/L_{\theta o} = 0$.

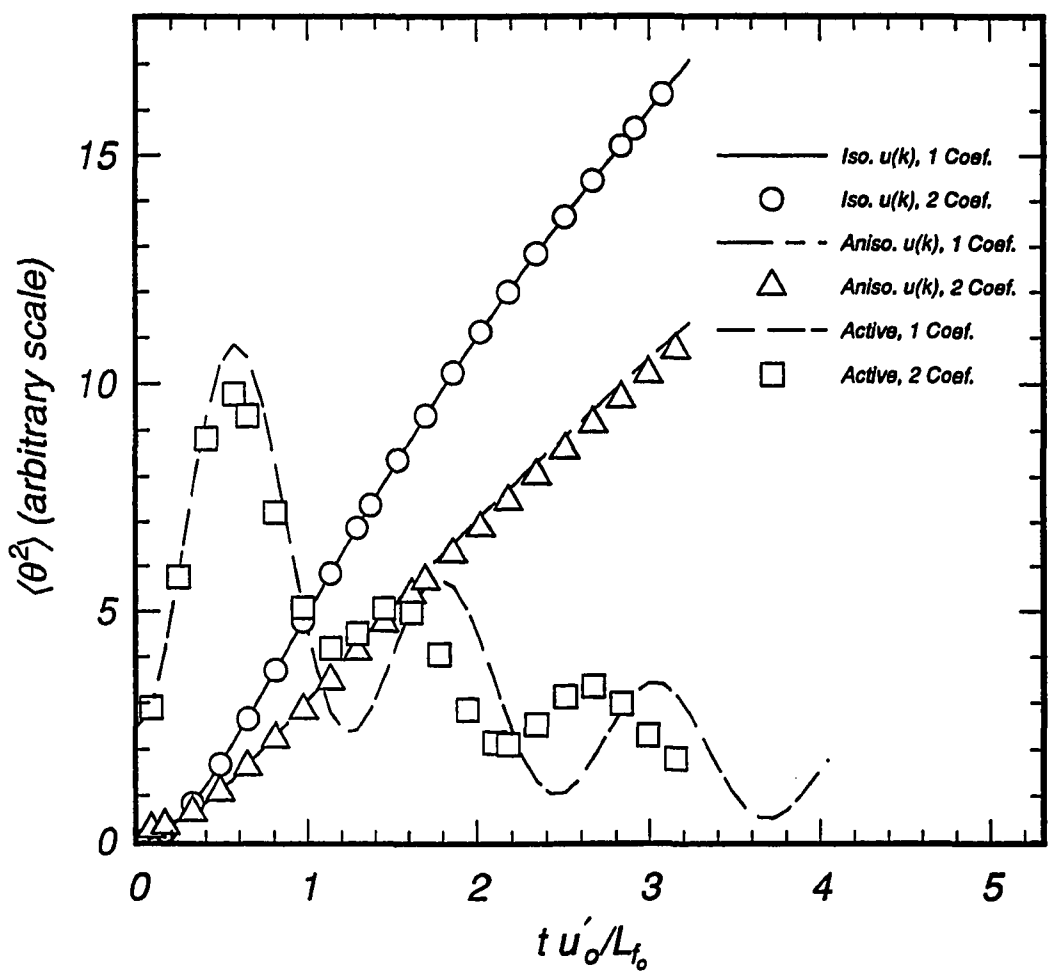

Figure 3.24: Evolution of DIA scalar variance employing one and two Legendre coefficients.

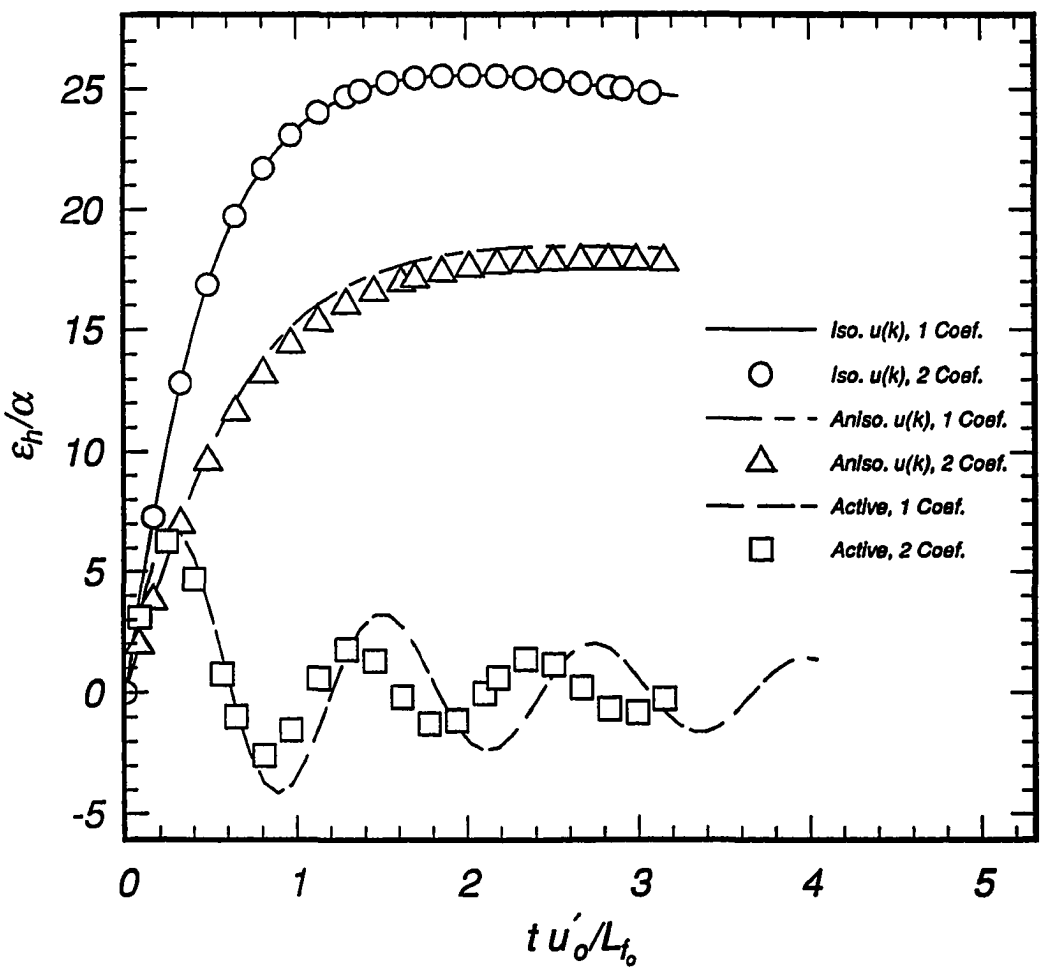

Figure 3.25: Evolution of DIA eddy diffusivity ratio employing one and two Legendre coefficients.

CHAPTER 4. MODELING EXPERIMENTAL PASSIVE SCALAR TRANSPORT USING MULTI-POINT STATISTICAL CLOSURE THEORY

A paper to be submitted to Journal of Fluid Mechanics

Robert C. Sanderson [1] and James C. Hill [2]

Abstract

Two point statistical closure theory, specifically Kraichnan's direct interaction approximation (DIA), was used to model the experimental studies performed by Warhaft and Lumley as well as those of Sirivat and Warhaft of homogeneous turbulent passive scalar fields, with and without transport. The velocity spectral aspect ratio, $A_v \equiv L_f/\lambda_g$, is defined and shown to be an important modeling parameter to obtain numerical results which are dynamically similar to those of experiment. Kinetic energy decay exponents could be varied over a range of -1.16 to -1.60 by simply varying A_v. A methodology for determining appropriate initial conditions for the numerical predictions is outlined. Using primarily the microscale Reynolds number, R_λ, and A_v, the low and high speed velocity field reported by Sirivat and Warhaft

[1]Monument, Co. 80132
[2]Iowa State University, Ames, Ia. 50011

were modeled by the DIA with a satisfactory degree of accuracy, both in the evolution of the kinetic energy and its dissipation.

The turbulent scalar field also possesses an aspect ratio, A_s, whose ratio with that of the velocity field (i.e., A_s/A_v) was shown to have a marked effect upon the evolution of the scalar field, more pronounced than the scalar to velocity integral lengthscale ratio, L_s/L_f. The effects of these ratios upon the scalar field behavior were documented. The passive isotropic turbulent decaying scalar results reported by Warhaft and Lumley (with a velocity field similar to that of the high speed runs of Sirivat and Warhaft) were satisfactorily modeled by the DIA.

The turbulent transport of a passive scalar in the presence of a uniform mean scalar gradient was also studied. It was shown mathematically that this problem (with zero initial scalar transport) decomposes into the sum of an isotropic decaying scalar field with all initial scalar energy and the turbulent transport problem with zero initial scalar field. The effects of changing the integral lengthscale ratio and scalar field intensity were examined and it was shown that, when the velocity field is properly modeled, the DIA can give reasonable quantitative estimates of the scalar transport. However, there appear to still exist problems with the DIA initialization, such as possibly nonzero countergradient scalar transport, which prevent modeling accuracy such as that seen for the isotropic decaying velocity and scalar fields.

Introduction

Theoretical and numerical studies of turbulence have been conducted for well over four decades. These results have been compared with, and sometimes stimulated the design and execution of, experimental studies. Theoretical studies of the

energy spectra of turbulent velocity fields (for a summary see Hinze [26]) include the predictions of Kolmogorov [27] for the spectral shape of turbulence kinetic energy in isotropic turbulence at high Reynolds numbers and those of Corrsin [6], Batchelor et al. [2, 3] and Gibson [15, 16] for the spectral behavior of scalar fields in the various regions (inertial–convective, inertial–diffusive, viscous–convective, viscous–diffusive, etc.). These results spurred the experimental community to devise means for creating nearly isotropic flows and scalar fields as well as the necessary instrumentation to accurately measure turbulence velocity and scalar quantities in an attempt to clarify, verify, or refute the theoretical results. To a surprising extent these theoretical results were confirmed, even though the simplified models used in the theoretical studies failed to include such important features of real turbulence as intermittency. Continued experimentation revealed the existence of, and provided data for, such phenomena as the structure of turbulent boundary layers (e.g., Runstadler streaks, bursting and inflows and other coherent structures), jets, mixing (e.g., of reactants), intermittency of various flows, etc. Further advances in turbulence theory such as the various physical closure theories (DIA, c.f. Kraichnan [28], Leslie[34], Kraichnan's [33] test field model, TFM, eddy damped quasi–normal markovianized closure, EDQNM, c.f. Cambon et al. [5] or Orszag [39], the renormalized group theory, RNG, c.f. Yakhot et al. [50, 16], Smith and Reynolds [46]), and numerical algorithms for computing turbulent flows (e.g., schemes for solving the closure theories, pseudo–spectral methods for direct numerical simulations, large eddy simulations with their associated subgrid models), and the rapidity with which computer hardware has evolved, both in CPU/IO speed and memory capacities, have allowed the numerical investigation and comparison of different theoretical methods as well as various types

of turbulent flows.

Often the goals of the numerical (and theoretical) studies have been restricted to comparison of asymptotic or steady state values of dimensionless quantities (e.g., decay exponents of kinetic and/or scalar energies, eddy diffusivity ratios or time scale ratios). Examples include Hill[25], Sanderson et al.(see Chapter 3 of this thesis) and Chakrabarti [8]. Direct comparisons of numerical/theoretical predictions for the temporal behavior of turbulent flows, especially DNS and closure theories are not common. Some examples include Métais and Herring [22], Riley et al. [41], Sanderson et al. [42, 43, 44], and Eswaran and O'Brien [13].

The transport of a passive scalar with a uniform mean gradient in isotropic turbulence was proposed by Corrsin [7] as the simplest possible turbulent scalar transport problem. He suggested this would be the best transport problem to be used to initially evaluate various turbulence theories and/or models by comparison with experimental data. Corrsin also predicted that an initially uniform mean scalar gradient would remain linear and of constant strength and that the growth of the turbulent scalar intensity would be directly proportional to time. Subsequent laboratory experiments (e.g., Wiskind [49], Alexopoulos and Keffer [1], Venkataramani and Chevray [47], Sirivat and Warhaft [45], Budwig, Tavoularis and Corrsin [4] and Gibson and Dakos [17]) have not only confirmed Corrsin's original predictions but have also provided information on the evolution and the statistics of the scalar and scalar transport fields (including evolution of scalar variance, eddy diffusivity ratio, scalar transport correlation coefficient, and various lengthscales and timescales).

Previous numerical studies of this problem include those of Hill [25], Chasnov [9] and Chakrabarti [8]. The primary thrust of these studies was to numerically in-

vestigate the long time or asymptotic behavior of the system and its dependence upon such initial conditions as initial scalar to velocity lengthscale ratios and initial spectral shape. Although the asymptotic behavior was in generally reasonable qualitative agreement with that of experiment, no effort was made to model the actual experimental evolution.

This study addresses the DIA modeling of the evolution of a decaying isotropic velocity field convecting a passive scalar field with a uniform mean scalar gradient and comparing directly with published experimental data. A methodology for determining appropriate initial conditions (e.g., field intensities, spectral shapes, lengthscale ratios, etc.) is developed to reasonably model a given, evolving turbulence problem.

Some significant problems exist for any effort attempting to simulate real turbulence, even at the relatively low R_λ values found in most laboratory turbulence studies (approximately 20 to 50). Perhaps the most significant and difficult to resolve is that of bandwidth. It has been pointed out (see the discussion in Mell, et al. [35], p. 2475) that the number of degrees of freedom required to accurately simulate turbulence is sufficiently large even at laboratory conditions to preclude accurate simulations with 256^3 points in a DNS computation. A casual perusal of turbulence variance spectra from such studies as Warhaft and Lumley [48], etc. shows they span a wavenumber range of roughly three orders of magnitude. Even a direct numerical simulation of 512^3 spans only two and a half orders of magnitude excluding the truncating effects of dealiasing. Thus, as Mell et al. [35] point out, any numerical "simulation" of laboratory turbulence will be lacking in bandwidth and the results of such attempts must be considered accordingly.

A second problem is that of appropriate initial conditions for the numerical work.

The initial conditions for wind/water tunnel work consist of the highly inhomogeneous wake flows generated by the turbulence producing grid which merge and mix to produce the decaying (relatively) isotropic flows which are then measured and studied. Codes designed to compute homogenous isotropic turbulence usually employ spectral (specifically Fourier transforms) algorithms and are incapable of modeling the wake flows produced by the experimentalist's grid. However, due to the highly nonlinear nature of turbulent flows, there exists reason to believe that the initial conditions (in terms of spectral type) are important only for the initial portion of the computation and their effects are eventually washed out by nonlinear mixing. It is upon this rationale that a number of different initialization schemes have been devised over the past few years.

A number of DNS studies have employed the technique of initializing the velocity field in some manner (often using a Gaussian energy spectrum as outlined by Kraichnan [29, 31] and Orszag and Patterson [40]) and carrying out the computation for a time sufficient to fully develop the nonlinear terms to a point where the evolving spectra exhibit self-similarity (c.f., Métais and Herring [22], Mell, et al. [35], Riley, Metcalfe and Weisman [41], Chakrabarti [8]). The resulting velocity field is then used as the initial velocity field conditions for subsequent scalar studies with or without some appropriate scaling applied. It is thus assumed that the actual initial conditions used in the numerical work have been nonlinearly "forgotten" by the system analagous to the experimental initial conditions being transformed into a relatively isotropic flow by the first measurement station (often at x/M of 40). This is a mathematically and physically satisfying approach and indeed has produced results which are in generally good qualitative, and sometimes good quantitative, agreement with

experimental data. However, previous computations employing direct numerical simulation (DNS) and Kraichnan's direct interaction approximation (DIA, c.f. [28]) have shown that varying the initial spectral shape (exponential vs. Gaussian in Chapter 3 of this thesis) can significantly affect the evolution of decaying turbulence for many eddy circulation times. Thus this topic is not a closed one.

This study seeks to determine a methodology which employs numerical solution of the DIA to simulate the evolution of experimental turbulence, including the decay of an isotropic velocity field (as reported by Sirivat and Warhaft [45]), decaying isotropic scalar turbulence (Warhaft and Lumley [48]) and turbulent transport of a passive scalar in the presence of a uniform mean scalar gradient (Sirivat and Warhaft [45]). Since the goal of turbulence theory is to be predictive, attention will placed upon determining the criteria necessary to ensure the DIA (or other computational technique) will correctly predict the behavior of the real flow given only a single (complete) set of "initial" experimental conditions (e.g., field measurements at the first measurement station).

Comparison of DIA with Experimental Results

Comparisons of DIA and DNS results illuminate the differences between the two theoretical techniques. The goal of analytical and numerical turbulence studies is to gain insight into the physics of real turbulence and to determine improved means for a priori prediction of the behavior of a turbulent system. To this end, DIA studies were performed for direct comparison with experimental studies.

Description of Technique

The nondimensional equations governing the isotropic turbulent velocity field and passive scalar field with uniform mean scalar gradient are:

$$\left(\frac{d}{dt}+\frac{k^2}{R_\lambda}\right)u_i(\mathbf{k},t) = -\frac{\imath}{2}P_{imn}(\mathbf{k})\sum_{\Delta}u_m(\mathbf{p},t)u_n(\mathbf{q},t) \quad (4.1)$$

$$\left(\frac{d}{dt}+\frac{k^2}{PrR_\lambda}\right)\vartheta(\mathbf{k},t)+\frac{a_i}{a}u_i(\mathbf{k},t) = -\imath k_m\sum_{\Delta}u_m(\mathbf{p},t)\vartheta(\mathbf{q},t) \quad (4.2)$$

where

$$\begin{aligned} a &\equiv |\mathbf{a}| \\ u(\mathbf{k},t) &\equiv \frac{\hat{u}((\mathbf{k},t)}{u'_o} \\ \vartheta(\mathbf{k},t) &\equiv \frac{\hat{\vartheta}(\mathbf{k},t)}{a\lambda_{g_o}} \\ k &\equiv \hat{k}\lambda_{g_o} \\ t &\equiv \frac{\hat{t}u'_o}{\lambda_{g_o}} \\ R_\lambda &\equiv \frac{u'\lambda_g}{\nu} \\ Pr &\equiv \frac{\nu}{\alpha} \\ P_{imn}(\mathbf{k}) &\equiv k_nP_{im}(\mathbf{k})+k_mP_{in}(\mathbf{k}) \\ P_{im}(\mathbf{k}) &\equiv \delta_{im}-\frac{k_ik_m}{k^2} \end{aligned}$$

and where

$$\sum_{\Delta}$$

denotes the sum over all wavevectors $\mathbf{p}$ and $\mathbf{q}$ which sum vectorally to $\mathbf{k}$, ν is the kinematic viscosity and α is the scalar diffusivity. The quantity L_{f_o}/u'_o is defined to be an eddy circulation or turnover time and this time is used to nondimensionalize

the graphical evolutionary plots in this paper. The time given by λ_{g_o}/u'_o is used to nondimensionalize the equations of motion as the initial velocity field conditions are stated in terms of R_λ, not R_L. Note that if the magnitude of the mean scalar gradient, a, is set to zero, equation (4.2) reduces to the decaying isotropic scalar turbulence equation.

As mentioned above, a significant problem in attempting direct comparison between the DIA (or other numerical/theoretical techniques) and experiment is the entirely different nature of the initial conditions of the two situations. It is therefore necessary to determine an appropriate methodology which allows the very early time evolution of the numerical computations to achieve a state in dynamic similarity with that reported for the experiments at the earliest (lowest x/M) measurement stations. This will involve determining appropriate initial spectral shapes, integral lengthscales, and initial microscale Reynolds numbers as well as establishing a rational means for aligning and scaling time from the computations with that of experiments. The following sections address these problems for the decaying, isotropic, turbulent velocity field, the decaying, isotropic, turbulent scalar field and the turbulent transport of a passive scalar in the presence of a uniform mean scalar gradient.

The Isotropic Turbulent Velocity Field This study addresses the direct comparison of evolving, decaying turbulence as computed numerically using multi-point statistical theory (specifically the DIA) to that measured in wind tunnels. Due to difficulties previously discussed these may not properly be considered complete simulations. Rather they are studies in how computations may be structured to result, after some initial amount of time, in evolution which is similar to that seen

in experiments. A secondary goal is to study the behavior of the DIA as initial conditions are varied. The results of this work may support an effort to directly simulate experimental turbulence.

In line with this philosophy the goals of the first part of this paper are as follows:

1. Determine appropriate initial velocity field conditions (e.g., initial values for R_λ, k_{v_o}, spectral form, etc.) which will result in evolution of R_λ, kinetic energy, dissipation, lengthscales, etc. similar to those of experimental isotropic velocity fields.

2. Determine required scalar field initial conditions (e.g., initial scalar field intensity, k_{s_o}, spectral form, etc.) which result in good agreement of numerically predicted scalar decay with that of experimental decaying isotropic scalar turbulence.

3. Finally, optimize the above mentioned parameters to give best agreement between DIA velocity, scalar transport and scalar fields and their characteristics with those of experimental passive turbulent scalar transport.

Note that, even if very good agreement between the DIA and experimental results is achieved, this will not necessarily prove the accuracy of the DIA. Rather, it will show that initial conditions exist for the DIA which may yield time evolutionary results in reasonably accurate agreement with the experiments. The initial conditions for some other closure theory (e.g., TFM, RNG or the local energy transport or LET) or other technique (e.g., DNS, large eddy simulation or LES) may differ to achieve agreement due to their differing mathematical natures. The only way to conclusively prove the superior accuracy of one technique over others is to directly simulate the

initial conditions of experiment(s), allow the system to numerically evolve and observe superior agreement in the predicted results with experiment by the one technique over others. This type of comparison is beyond the scope of the present effort. Instead, we seek only to ascertain some "best" initial conditions for the DIA to create an evolutionary environment which closely matches that observed in certain experiments.

In equation 4.1, the velocity field has only one dimensionless number, the microscale Reynolds number R_λ, to use for dynamic modeling. However, two other factors may influence the evolution of the velocity field. These are the initial shape of the energy spectrum and its peak wavenumber k_{v_o}. Various initial spectral shapes have been implemented in previous studies (c.f., Kraichnan [29], Herring and Kerr [24], Riley et al. [41], Sanderson et al. [42, 43, 44], Eswaran and O'Brien [13] etc.) in generally one of two forms; Gaussian ($\propto k^4 \exp^{-2(k/k_o)^2}$, see Kraichnan [29, 31] and Orszag and Patterson [40]) or exponential ($\propto k^n \exp^{-3(k/k_o)}$, n=1,3). Although other initial spectral shapes have been used on occasion (cf. Herring [20], Herring, Schertzer et al. [21], etc.) these two are the primary initializations used. There is no apparent intrinsic reason to use one or the other of these two functional forms (aside from some arguments indicating consistency of the Gaussian shape with the low k spectra measurements and/or theoretical reasonings).

The turbulence spectral shape has been an implicitly important consideration in studies of various turbulence problems. For example, in the steady-state analyses of Kolmogorov [27] (velocity field) and Oboukhov [38] and Corrsin [6] (scalar field), it was assumed that the lengthscales at which energy entered the problem were very large compared with the lengthscales at which any significant dissipation occurred. This condition also held in the experimental velocity and scalar field studies of Grant,

Stewart and Moilliet [18] and Grant, Hughes, Vogel and Moilliet [19]. This results in turbulence spectra which span a large range of wavenumbers. By contrast, experiments conducted in most wind and water tunnels or other laboratory apparatus result in a relatively small range of wavenumbers due to the small size of the test section and the effects of dissipation/diffusion. For example, the (Puget sound) studies had spectral wavenumbers which spanned approximately four to six orders of magnitude. In contrast wind tunnel studies (e.g., Warhaft and Lumley [48]) spanned approximately three orders of magnitude. A general, nondimensional, quantitative way to characterize the wavenumber span of a given spectrum is to form the ratio of the integral lengthscale to the Taylor microscale, i.e., the ratio of the size of the energy containing eddies to that of the dissipation eddies. The larger this number, the flatter and broader the spectrum and small values indicate a more spikelike shape.

The location of the spectral peak in decaying turbulence may also affect the turbulence evolution. If a given spectral shape and normalized intensity peaks at a large lengthscale (small wavenumber), the initial dissipation of energy will differ from the same situation located at a smaller lengthscale (larger wavenumber). Thus the relative importance of the initial wavenumber ratio and the exact spectral shape will be investigated.

There is, however, one more problem which must be addressed before predictive simulation or modeling of laboratory experiments can take place. This concerns the rational normalization and coordination of time in the two techniques. Several different methods have been used in the past. One is to have time $t = 0$ in the computation coincide with the time the experimental flow passes through the turbulence producing grid and normalize all variables using initial known values. This corresponds to

$t = 0$ in the computations and $x/M = 40$–60 in experiments. This technique was used in Figures 4.1 through 4.3 and there are obvious problems with it. Although the R_λ curves may possibly be made to coincide, the energy and dissipation curves never will for at least the first several eddy circulation times since the computational and experimental results are at the same initial values (1.0 in the above figures) at distinctly different times. Physically, this is an unsatisfactory technique since the reference variable values come from different points during the evolution of the computation and experiment, indeed, at times when they are distinctly different and not dynamically similar.

A second technique is to initialize the computation to some initial spectra, R_λ, etc. and run the numerics for some length of time (e.g., 2–3 eddy circulation times) to allow the nonlinear energy transport to fully build up and give this mixing a chance to erase the "memory" of the initial conditions. This method has been used by Riley, Metcalfe, Weissman [41], Métais and Herring [36] among others. These workers compared numerical with experimental results and achieved satisfactory agreement. However, there are still two problems with this technique. The first is defining in a deterministic manner how long the numerics must run before comparing with experiment. The second is that previous studies, both DNS and DIA, show that even with the nonlinearities in full force, initial spectral characteristics can still exert a significant influence upon the subsequent problem evolution.

The technique used in the following work incorporated a hybrid of these ideas. The zero time of the computations was equivalenced to that time when the experimental flow passed through the turbulence producing grid. The experimental nondimensional eddy circulation time corresonding to the first measurement station was

determined using the variable values at that station. The numerical results were then searched for the point at which the numerical time, when nondimensionalized by the turbulence intensity and integral lengthscale at that time, was equal to the experimental nondimensional time of the first measurement station. This nondimensional time point in the numerical results was equated with that of the first experimental measurement station. The numerical field variable values at this point were then used for all other nondimensionalizations and became the basis for comparing the numerical results with those of the experiment.

In this study, the decay exponent of the normalized turbulence kinetic energy and the evolution of the microscale Reynolds number $R_\lambda(t)$ measured in experiments will be matched as closely as possible using the DIA by varying the initial values of R_λ and L_f as well as the initial energy spectral shape as measured by the lengthscale ratio. Then the evolution of such quantities as the integral lengthscale, Taylor microscale, dissipation of kinetic energy, etc. will be compared with experiment.

The Physics of Turbulent Passive Scalar Transport The physics driving the decaying passive scalar transport to approach an asymptotic state from varying initial scalar conditions are now investigated in more mathematical detail. The velocity fluctuations acting upon the scalar gradient generate scalar fluctuations in a manner spectrally similar to that of the driving velocity field. In addition, the nonlinear mixing of the scalar field by the velocity field acts in concert with scalar diffusion to tend to drive the scalar field into spectral similarity with the velocity field. It was noted during the course of this study that the initial scalar field intensity can strongly affect subsequent evolution of passive scalar transport in decaying isotropic

turbulence. For a given velocity field and mean scalar gradient, as the initial scalar intensity increased the effects of the transport became less apparent with the upper limit ($\lim[\vartheta/(a\lambda)]_o \rightarrow \infty$) being decaying isotropic scalar turbulence.

The governing equation for the scalar fluctuation field, with or without a uniform mean scalar gradient, is linear in the scalar fluctuation variable. This was noted by Hill [25] and used to analytically simplify the set of equations he solved in his study of the transport of a passive scalar in stationary turbulence. This linearity invites a question pertaining to the problem of scalar transport in decaying turbulence. Does the isotropic scalar transport problem with uniform mean scalar gradient consist of the sum of:

1) a decaying isotropic scalar turbulence problem with all the scalar field initial conditions of the complete scalar transport problem, and

2) a scalar transport problem with zero initial scalar field having a mean scalar gradient equal to that of the complete problem?

This question is now addressed.

The equations governing the fluctuating velocity and scalar fields are (with $n_m \equiv a_m/|bfa|$):

$$\left(\frac{d}{dt}+\frac{k^2}{R_\lambda}\right)u_i(\mathbf{k},t) = -\frac{i}{2}P_{imn}(\mathbf{k})\sum_{\Delta}u_m(\mathbf{p},t)u_n(\mathbf{q},t) \quad (4.3)$$

$$\left(\frac{d}{dt}+\frac{k^2}{PrR_\lambda}\right)\vartheta(\mathbf{k},t)+n_m u_m(\mathbf{k},t) = -ik_m\sum_{\Delta}u_m(\mathbf{p},t)\vartheta(\mathbf{q},t) \quad (4.4)$$

with initial conditions

$$u_i(\mathbf{k},t=0) = \textit{some specified spectrum} \quad (4.5)$$

$$\vartheta(\mathbf{k},t=0) = \textit{some specified spectrum} \quad (4.6)$$

Note that the scalar equation (equation (4.4)) is linear in ϑ. Consider two problems which may be viewed as special cases of that in equation (4.4): 1) A decaying isotropic scalar field with initial values identical to those of the scalar field in equation (4.4) and 2) A passive scalar transport problem with a uniform mean scalar gradient as in the above complete, general scalar transport field but with zero initial scalar field. Now express the complete scalar field in equation(4.4) as a sum of a decaying isotropic scalar turbulence field ($\theta_{iso.}(\mathbf{k},t)$) initialized as the initial field in the complete transport problem, a passive scalar transport field ($\theta_{trans.}(\mathbf{k},t)$) with zero initial scalar field and any remaining residual scalar field ($\theta_{res.}(\mathbf{k},t)$), i.e.:

$$\vartheta(\mathbf{k},t) \equiv \vartheta_{iso.}(\mathbf{k},t) + \vartheta_{tran.}(\mathbf{k},t) + \vartheta_{res.}(\mathbf{k},t) \tag{4.7}$$

The scalar fields in the isotropic and transport problems obey the following governing equations:

$$\left(\frac{d}{dt} + \frac{k^2}{PrR_\lambda}\right)\vartheta_{iso.}(\mathbf{k},t) = -ik_m \sum_{\Delta} u_m(\mathbf{p},t)\vartheta_{iso.}(\mathbf{q},t) \tag{4.8}$$

$$\left(\frac{d}{dt} + \frac{k^2}{PrR_\lambda}\right)\vartheta_{tran.}(\mathbf{k},t) + n_m u_m(\mathbf{k},t) = -ik_m \sum_{\Delta} u_m(\mathbf{p},t)\vartheta_{tran.}(\mathbf{q},t) \tag{4.9}$$

with initial conditions

$$\vartheta_{iso.}(\mathbf{k},t=0) = \vartheta(\mathbf{k},t=0) \tag{4.10}$$

$$\vartheta_{tran.}(\mathbf{k},t=0) = 0 \tag{4.11}$$

$$\Rightarrow \vartheta_{res.}(\mathbf{k},t=0) = 0 \tag{4.12}$$

Now substitute this scalar field decomposition into equation (4.4);

$$\left(\frac{d}{dt} + \frac{k^2}{PrR_\lambda}\right)[\vartheta_{iso.}(\mathbf{k},t) + \vartheta_{tran.}(\mathbf{k},t) + \vartheta_{res.}(\mathbf{k},t)] + n_m u_m(\mathbf{k},t) = \tag{4.13}$$

$$= -ik_m \sum_{\Delta} u_m(\mathbf{p},t)[\vartheta_{iso.}(\mathbf{q},t) + \vartheta_{tran}(\mathbf{q},t) + \vartheta_{res.}(\mathbf{q},t)] \tag{4.14}$$

and subtract equations (4.8) and (4.9) from equation (4.14) to obtain

$$\left(\frac{d}{dt}+\frac{k^2}{PrR_\lambda}\right)\vartheta_{res.}(\mathbf{k},t) = -ik_m\sum_{\Delta} u_m(\mathbf{p},t)\vartheta_{res.}(\mathbf{q},t) \tag{4.15}$$

Equation(4.15) governs the scalar fluctuations remaining in the passive scalar transport problem after the above specified isotropic scalar and passive scalar transport problems are subtracted. Note there are no linear forcing functions in this equation. Since $\vartheta_{res.}(\mathbf{k},t)$ is initially zero for all $\mathbf{k}$, the nonlinear and diffusive terms are zero, and thus the initial time derivative is also zero. Rewriting equation (4.15) as

$$\frac{d}{dt}\vartheta_{res.}(\mathbf{k},t) = -\frac{k^2}{PrR_\lambda}\vartheta_{res.}(\mathbf{k},t) - ik_m\sum_{\Delta} u_m(\mathbf{p},t)\vartheta_{res.}(\mathbf{q},t) \tag{4.16}$$

Taking the time derivative of equation (4.16) yields

$$\begin{aligned}\frac{d^2}{dt^2}\vartheta_{res.}(\mathbf{k},t) &= -\frac{k^2}{PrR_\lambda}\frac{d}{dt}\vartheta_{res.}(\mathbf{k},t) - ik_m\sum_{\Delta}\left[\frac{d}{dt}(u_m(\mathbf{p},t))\vartheta_{res.}(\mathbf{q},t)\right.\\ &\quad\left.+\, u_m(\mathbf{p},t)\frac{d}{dt}(\vartheta_{res.}(\mathbf{q},t))\right] \qquad (4.17)\\ \Rightarrow \frac{d^2}{dt^2}\vartheta_{res.}(\mathbf{k},t=0) &= 0 \qquad (4.18)\end{aligned}$$

as $\vartheta_{res.}(\mathbf{q},t=0)$ and $\frac{d}{dt}(\vartheta_{res.}(\mathbf{q},t=0))$ are both zero. Further, by induction

$$\begin{aligned}\frac{d^n}{dt^n}\vartheta_{res.}(\mathbf{k},t) &= -\frac{k^2}{PrR_\lambda}\frac{d^{n-1}}{dt^{n-1}}\vartheta_{res.}(\mathbf{k},t)\\ &= -ik_m\sum_{\Delta}\sum_{i=0}^{n-1}\frac{d^{n-i-1}}{dt^{n-i-1}}(u_m(\mathbf{p},t))\frac{d^i}{dt^i}\vartheta_{res.}(\mathbf{q},t)\\ \Rightarrow \frac{d^n}{dt^n}\vartheta_{res.}(\mathbf{k},t=0) &= 0 \qquad (4.19)\end{aligned}$$

since, starting with $n=2$, $\frac{d^{n-2}}{dt^{n-2}}\vartheta_{res.}(\mathbf{q},t=0)$ and $\frac{d^{n-1}}{dt^{n-1}}\vartheta_{res.}(\mathbf{q},t=0)$ are both zero. Since the initial value and all initial time derivatives are zero, $\vartheta_{res.}(\mathbf{k},t)$ remains zero for all time. Thus the scalar field in an isotropic passive transport problem consists

of two fields; a decaying isotropic scalar field and an initially zero passive scalar transport scalar field, i.e.,

$$\vartheta(\mathbf{k},t) \equiv \vartheta_{iso.}(\mathbf{k},t) + \vartheta_{tran.}(\mathbf{k},t) \tag{4.20}$$

Further, the general problem of the fluctuating fields in passive scalar transport is comprised of the sum of these two simpler problems.

We now turn to the statistical field equations. The complete two-point two-time velocity and scalar field variance and the velocity-scalar covariance equations are:

$$\left(\frac{d}{dt}+\frac{k^2}{R_\lambda}\right) < u_i(\mathbf{k},t)u_j(-\mathbf{k},t') >= \\ = -\frac{i}{2}P_{imn}(\mathbf{k})\sum_{\Delta} < u_m(\mathbf{p},t)u_n(\mathbf{q},t)u_j(-\mathbf{k},t') > \tag{4.21}$$

$$\left(\frac{d}{dt}+\frac{k^2}{R_\lambda}\right) < u_i(\mathbf{k},t)\vartheta(-\mathbf{k},t') >= \\ = -\frac{i}{2}P_{imn}(\mathbf{k})\sum_{\Delta} < u_m(\mathbf{p},t)u_n(\mathbf{q},t)\vartheta(-\mathbf{k},t') > \tag{4.22}$$

$$\left(\frac{d}{dt}+\frac{k^2}{PrR_\lambda}\right) < \vartheta(\mathbf{k},t)u_j(-\mathbf{k},t') > +n_m < u_m(\mathbf{k},t)u_j(-\mathbf{k},t') >= \\ = -ik_m\sum_{\Delta} < u_m(\mathbf{p},t)\vartheta(\mathbf{q},t)u_j(-\mathbf{k},t') > \tag{4.23}$$

$$\left(\frac{d}{dt}+\frac{k^2}{PrR_\lambda}\right) < \vartheta(\mathbf{k},t)\vartheta(-\mathbf{k},t') > +n_m < u_m(\mathbf{k},t)\vartheta(-\mathbf{k},t') >= \\ = -ik_m\sum_{\Delta} < u_m(\mathbf{p},t)\vartheta(\mathbf{q},t)\vartheta(-\mathbf{k},t') > \tag{4.24}$$

Equations (4.22) through (4.24) include the complete scalar field variable. Note that, by definition, the correlation between the velocity field and the isotropic scalar field is zero, or

$$< u_m(\mathbf{k},t)\vartheta_{iso.}(-\mathbf{k},t') > \equiv 0 \tag{4.25}$$

$$< \vartheta_{iso.}(\mathbf{k},t)u_m(-\mathbf{k},t') > \equiv 0 \tag{4.26}$$

The governing multi-point statistical equations for the isotropic scalar-scalar field and the transport covariance and scalar variance equations are:

$$\left(\frac{d}{dt}+\frac{k^2}{PrR_\lambda}\right) < \vartheta_{iso.}(\mathbf{k},t)\vartheta_{iso.}(-\mathbf{k},t') >=$$

$$= -ik_m \sum_{\Delta} < u_m(\mathbf{p},t)\vartheta_{iso.}(\mathbf{q},t)\vartheta_{iso.}(-\mathbf{k},t') > \qquad (4.27)$$

$$\left(\frac{d}{dt}+\frac{k^2}{R_\lambda}\right) < u_i(\mathbf{k},t)\vartheta_{tran.}(-\mathbf{k},t') >=$$

$$= -\frac{i}{2}P_{imn}(\mathbf{k}) \sum_{\Delta} < u_m(\mathbf{p},t)u_n(\mathbf{q},t)\vartheta_{tran.}(-\mathbf{k},t') > \qquad (4.28)$$

$$\left(\frac{d}{dt}+\frac{k^2}{PrR_\lambda}\right) < \vartheta_{tran.}(\mathbf{k},t)u_j(-\mathbf{k},t') > +n_m < u_m(\mathbf{k},t)u_j(-\mathbf{k},t') >=$$

$$= -ik_m \sum_{\Delta} < u_m(\mathbf{p},t)\vartheta_{tran.}(\mathbf{q},t)u_j(-\mathbf{k},t') > \qquad (4.29)$$

$$\left(\frac{d}{dt}+\frac{k^2}{PrR_\lambda}\right) < \vartheta_{tran.}(\mathbf{k},t)\vartheta_{tran.}(-\mathbf{k},t') > +n_m < u_m(\mathbf{k},t)\vartheta_{tran.}(-\mathbf{k},t') >=$$

$$= -ik_m \sum_{\Delta} < u_m(\mathbf{p},t)\vartheta_{tran.}(\mathbf{q},t)\vartheta_{tran.}(-\mathbf{k},t') > \qquad (4.30)$$

Substitute the decomposition for ϑ (equation (4.20)) for the complete scalar variable in equations (4.22), (4.23) and (4.24) and invoke equations (4.25) and (4.26):

$$\left(\frac{d}{dt}+\frac{k^2}{R_\lambda}\right) < u_i(\mathbf{k},t)\vartheta_{tran.}(-\mathbf{k},t') >=$$

$$= -\frac{i}{2}P_{imn}(\mathbf{k}) \sum_{\Delta} < u_m(\mathbf{p},t)u_n(\mathbf{q},t)\vartheta_{iso.}(-\mathbf{k},t') >$$

$$-\frac{i}{2}P_{imn}(\mathbf{k}) \sum_{\Delta} < u_m(\mathbf{p},t)u_n(\mathbf{q},t)\vartheta_{tran.}(-\mathbf{k},t') > \qquad (4.31)$$

$$\left(\frac{d}{dt}+\frac{k^2}{PrR_\lambda}\right) < \vartheta_{tran.}(\mathbf{k},t)u_j(-\mathbf{k},t') > +n_m < u_m(\mathbf{k},t)u_j(-\mathbf{k},t') >=$$

$$= -ik_m \sum_{\Delta} < u_m(\mathbf{p},t)\vartheta_{iso.}(\mathbf{q},t)u_j(-\mathbf{k},t') >$$

$$-ik_m \sum_{\Delta} < u_m(\mathbf{p},t)\vartheta_{tran.}(\mathbf{q},t)u_j(-\mathbf{k},t') > \qquad (4.32)$$

$$\left(\frac{d}{dt}+\frac{k^2}{PrR_\lambda}\right) [< \vartheta_{iso.}(\mathbf{k},t)\vartheta_{iso.}(-\mathbf{k},t') > + < \vartheta_{iso.}(\mathbf{k},t)\vartheta_{tran.}(-\mathbf{k},t') >$$

$$+ < \vartheta_{tran.}(\mathbf{k},t)\vartheta_{iso.}(-\mathbf{k},t') > + < \vartheta_{tran.}(\mathbf{k},t)\vartheta_{tran.}(-\mathbf{k},t') >]$$

$$+n_m < u_m(\mathbf{k},t)\vartheta_{tran.}(\mathbf{k},t) >=$$

$$\begin{aligned} &= -ik_m \sum_{\Delta} < u_m(\mathbf{p},t)\vartheta_{iso.}(\mathbf{q},t)\vartheta_{iso.}(-\mathbf{k},t') > \\ &\quad -ik_m \sum_{\Delta} < u_m(\mathbf{p},t)\vartheta_{iso.}(\mathbf{q},t)\vartheta_{tran.}(-\mathbf{k},t') > \\ &\quad -ik_m \sum_{\Delta} < u_m(\mathbf{p},t)\vartheta_{tran.}(\mathbf{q},t)\vartheta_{iso.}(-\mathbf{k},t') > \\ &\quad -ik_m \sum_{\Delta} < u_m(\mathbf{p},t)\vartheta_{tran.}(\mathbf{q},t)\vartheta_{tran.}(-\mathbf{k},t') > \end{aligned} \tag{4.33}$$

Now subtract equations (4.22) and (4.23) for the covariances from equations (4.31) and (4.32) and the isotropic and transport variance equations (equations (4.27) and (4.30)) from equation (4.33) to obtain

$$0 = -\frac{i}{2}P_{imn}(\mathbf{k}) \sum_{\Delta} < u_m(\mathbf{p},t)u_n(\mathbf{q},t)\vartheta_{iso.}(-\mathbf{k},t') > \tag{4.34}$$

$$0 = -ik_m \sum_{\Delta} < u_m(\mathbf{p},t)\vartheta_{iso.}(\mathbf{q},t)u_j(-\mathbf{k},t') > \tag{4.35}$$

$$\left(\frac{d}{dt} + \frac{k^2}{PrR_\lambda}\right)[< \vartheta_{iso.}(\mathbf{k},t)\vartheta_{tran.}(-\mathbf{k},t') > + < \vartheta_{tran.}(\mathbf{k},t)\vartheta_{iso.}(-\mathbf{k},t') >] =$$

$$\begin{aligned} &= [-ik_m \sum_{\Delta} < u_m(\mathbf{p},t)\vartheta_{iso.}(\mathbf{q},t)\vartheta_{tran.}(-\mathbf{k},t') > \\ &\quad -ik_m \sum_{\Delta} < u_m(\mathbf{p},t)\vartheta_{tran.}(\mathbf{q},t)\vartheta_{iso.}(-\mathbf{k},t') >] \end{aligned} \tag{4.36}$$

Equations (4.34) and (4.35) imply the governing equations for the complete covariances are

$$\left(\frac{d}{dt} + \frac{k^2}{R_\lambda}\right) < u_i(\mathbf{k},t)\vartheta(-\mathbf{k},t') >=$$

$$= -\frac{i}{2}P_{imn}(\mathbf{k}) \sum_{\Delta} < u_m(\mathbf{p},t)u_n(\mathbf{q},t)\vartheta_{tran.}(-\mathbf{k},t') > \tag{4.37}$$

$$\left(\frac{d}{dt} + \frac{k^2}{PrR_\lambda}\right) < \vartheta(\mathbf{k},t)u_j(-\mathbf{k},t') > +n_m < u_m(\mathbf{k},t)u_j(-\mathbf{k},t) >=$$

$$= -ik_m \sum_{\Delta} < u_m(\mathbf{p},t)\vartheta_{tran.}(\mathbf{q},t)u_j(-\mathbf{k},t') > \tag{4.38}$$

The governing equations for $< \vartheta_{iso.}(\mathbf{q},t)\vartheta_{tran.}(-\mathbf{k},t) >$ and $< \vartheta_{tran.}(\mathbf{q},t)\vartheta_{iso.}(-\mathbf{k},t) >$ may be formed from the isotropic scalar and transport scalar field equations:

$$\left[\frac{d}{dt}+\frac{k^2}{PrR_\lambda}\right] < \vartheta_{iso.}(\mathbf{k},t)\vartheta_{tran.}(-\mathbf{k},t') >=$$

$$= -ik_m \sum_{\Delta} < u_m(\mathbf{p},t)\vartheta_{iso.}(\mathbf{q},t)\vartheta_{tran.}(-\mathbf{k},t') > \tag{4.39}$$

$$\left[\frac{d}{dt}+\frac{k^2}{PrR_\lambda}\right] < \vartheta_{tran.}(\mathbf{k},t)\vartheta_{iso.}(-\mathbf{k},t') > + n_m < u_m(\mathbf{k},t)\vartheta_{iso.}(-\mathbf{k},t) >=$$

$$= -ik_m \sum_{\Delta} < u_m(\mathbf{p},t)\vartheta_{tran.}(\mathbf{q},t)\vartheta_{iso.}(-\mathbf{k},t') > \tag{4.40}$$

Since there is no correlation between the isotropic scalar field and the velocity field, equation (4.40) becomes

$$\left[\frac{d}{dt}+\frac{k^2}{PrR_\lambda}\right] < \vartheta_{tran.}(\mathbf{k},t)\vartheta_{iso.}(-\mathbf{k},t') >=$$

$$= -ik_m \sum_{\Delta} < u_m(\mathbf{p},t)\vartheta_{tran.}(\mathbf{q},t)\vartheta_{iso.}(-\mathbf{k},t') > \tag{4.41}$$

We may rewrite equations (4.39) and (4.41) as

$$\frac{d^n}{dt^n} < \vartheta_{iso.}(\mathbf{k},t)\vartheta_{tran.}(-\mathbf{k},t') >=$$

$$-\frac{k^2}{PrR_\lambda}\frac{d^{n-1}}{dt^{n-1}} < \vartheta_{iso.}(\mathbf{k},t)\vartheta_{tran.}(-\mathbf{k},t') >$$

$$-ik_m \sum_{\Delta} \sum_{i=0}^{n-1} \sum_{j=0}^{n-i-1} < \frac{d^{n-i-j-1}}{dt^{n-i-j-1}}(u_m(\mathbf{p},t))\frac{d^i}{dt^i}(\vartheta_{iso.}(\mathbf{q},t))\frac{d^j}{dt^j}(\vartheta_{tran.}(-\mathbf{k},t')) > \tag{4.42}$$

$$\frac{d^n}{dt^n} < \vartheta_{tran.}(\mathbf{k},t)\vartheta_{iso.}(-\mathbf{k},t') >=$$

$$-\frac{k^2}{PrR_\lambda}\frac{d^{n-1}}{dt^{n-1}} < \vartheta_{tran.}(\mathbf{k},t)\vartheta_{iso.}(-\mathbf{k},t') >$$

$$-ik_m \sum_{\Delta} \sum_{i=0}^{n-1} \sum_{j=0}^{n-i-1} < \frac{d^{n-i-j-1}}{dt^{n-i-j-1}}(u_m(\mathbf{p},t))\frac{d^i}{dt^i}(\vartheta_{tran.}(\mathbf{q},t))\frac{d^j}{dt^j}(\vartheta_{iso.}(-\mathbf{k},t')) > \tag{4.43}$$

and note that

$$\frac{d^n}{dt^n} < \vartheta_{iso.}(\mathbf{k},t)\vartheta_{tran.}(-\mathbf{k},t') >= 0 \tag{4.44}$$

$$\frac{d^n}{dt^n} < \vartheta_{tran.}(\mathbf{k},t)\vartheta_{iso.}(-\mathbf{k},t') >= 0 \tag{4.45}$$

since, for $n = 0$ and 1, $\frac{d^n}{dt^n} < \vartheta_{iso.}(\mathbf{k},t)\vartheta_{tran.}(-\mathbf{k},t') >= 0$ and $\frac{d^n}{dt^n} < \vartheta_{tran.}(\mathbf{k},t)\vartheta_{iso.}(-\mathbf{k},t') >= 0$ hold by initial conditions. With zero initial values, zero initial time derivatives of all orders, and no source terms, these covariances remain zero for all time. Thus the statistical problem of turbulent transport of a passive scalar is a linear superposition of the problems of decaying isotropic scalar turbulence with all initial scalar energy and passive scalar transport with zero initial conditions.

Figures 4.4, 4.5 and 4.6 compare the complete problem (with nonzero initial scalar field and passive scalar transport; the solid line) with the initally nonzero decaying isotropic scalar turbulent problem, the zero initial scalar field scalar transport problem, and their sum. The three Figures present the evolution of the scalar energy for three scenarios; Figure 4.4 illustrates the situation in which scalar transport is the dominant problem during the computational time, Figure 4.5 shows the situation in which the two problems are of approximately equal importance and Figure 4.6 presents the results for a dominant initial problem (at least for the first few eddy circulation times). These cases (all performed at Pr of 0.7) show excellent agreement between the results for the complete problem and the sum of the two subsidiary problems. Thus the integrated results of the DIA are consistent with the mathematical result that the scalar transport is the linear sum of a decaying isotropic scalar turbulence problem with all initial scalar energy and a zero initial scalar energy scalar transport problem.

Figures 4.4 through 4.6 illustrate the salient point that with time the scalar transport (illustrated by the zero initial scalar field problem) will tend to dominate the problem evolution. This occurs when the initial scalar field has decayed to a level of relative insignificance to that achieved by the transport problem. In Figure 4.4 this point occurs almost immediately, in Figure 4.5 it occurs at approximately 3–4 eddy circulation times and in Figure 4.6 that point occurs at approximately 6–8 circulation times. It should be noted that even before the transport problem dominates the isotropic scalar problem, it can strongly influence the behavior of the complete problem as is apparent in Figure 4.5 where, although the isotropic scalar problem strongly dominates the early part of the problem, the complete problem immediately deviates significantly from its evolution. The point here is that the asymptotic states noted in these studies result primarily from the velocity field acting upon the mean scalar gradient, not from the initial scalar field conditions. The initial isotropic scalar field may strongly affect the early evolution of passive scalar transport as seen in experiments and the numerical studies reported herein, but the exact nature of the problem's early behavior depends critically upon the evolution of the relative strengths of the two problems.

Figure 4.7 compares the spectra for the two subproblems, their sum and that for the complete problem. The agreement between the sum of the two subproblems and the complete problem is apparently exact. These results are typical of spectral comparisons made at different times and for the other problems. Thus the behavior of the DIA predicted scalar fields agrees well with the theoretical results.

Figure 4.8 compares the evolution of the eddy diffusivity ratio for the complete transport problem with that of the zero initial scalar field transport subproblem.

They are identical implying that the initial isotropic scalar field remains uncorrelated with the velocity field throughout the evolution of the problem. Thus if scalar fluctuations are generated rapidly relative to the initial scalar field intensity, the complete scalar field will become strongly correlated with the velocity field but if scalar transport is small relative to the initial scalar field, scalar–velocity correlation develops only slowly. This is illustrated by the evolution of the complete scalar transport correlation coefficients (lines labeled "Complete") seen in Figure 4.9 which shows situations progressing from scalar transport combined with a small initial scalar field through large initial scalar intensity. The former develop strong correlation between the scalar and velocity fields quite rapidly while the latter develop weaker correlation at a markedly slower pace. This Figure also compares the scalar transport correlation coefficients for the complete problem with the zero initial scalar field subproblem for $(\vartheta/a\lambda_g)_o^2 = 1.0$. Since the subproblem computes its correlation coefficients using only that scalar intensity attributable to scalar transport, these coefficients all have rather large magnitude with initial value of unity. The complete problem computes $\rho_{u\theta}(t)$ using the sum of the scalar intensities from both the scalar transport and isotropic subproblems. Comparison of the predictions of the combined subproblems with the complete problem requires a combination of the subproblem correlation coefficient as follows:

$$\rho_{u\theta\ comp.}(t) = \frac{< u\theta > (t)}{u'(t)\vartheta'_{comp.}(t)} \tag{4.46}$$

$$= \frac{< u\theta > (t)}{u'(t)\sqrt{\vartheta^2_{iso.}(t) + \vartheta^2_{tran.}(t)}} \tag{4.47}$$

The solid dots in Figure 4.9 represent the combined transport subproblem correlation coefficients which agree very closely with those for the complete problem in all three

cases.

The study of the dynamics of decaying turbulent passive scalar transport thus may be separated into the study of two simpler problems. The decay of isotropic scalar turbulence has been studied fairly extensively experimentally, theoretically and numerically. The problem of decaying turbulent passive scalar transport with zero initial scalar field has been studied explicitly using numerical methods in this paper and in the experimental study of Sirivat and Warhaft [45] when they produced the mean scalar gradient prior to the production of the turbulent velocity field by the air flowing through the turbulence producing grid. In addition to isolating effects due to the two separate subproblems, this separation may be useful in determining appropriate initial conditions for the modeling/simulation of passive turbulent scalar transport experiments.

The Isotropic Turbulent Scalar Field Equation (4.2) governs the scalar field in the presence of a uniform mean scalar gradient. If **a** is set to zero, the equation governing isotropic scalar turbulence is recovered. The addition of the uniform mean scalar gradient to the decaying isotropic scalar turbulence problem is a minor change to the governing equations and also constitutes a relatively minor change in algorithms such as DNS or LES. However, the presence of a nonzero scalar gradient produces dramatic changes in the equations necessary for statistical closure theories. The scalar gradient necessitates the inclusion of the scalar transport equations (i.e., the velocity–scalar and scalar–velocity correlation equations) and their response functions to create a closed set of statistical equations. These also must be correctly solved and their initial conditions properly handled in order to accurately model pas-

sive turbulent scalar transport. The problem of decaying isotropic scalar turbulence involves only the velocity–velocity and scalar–scalar quantities. By initially investigating this problem the interaction between the velocity and scalar fields may be studied without the complication of the scalar transport statistical equations. After successful modeling of decaying isotropic scalar turbulence, the transport problem and its accompanying additional equations may be examined. For this reason, this study will focus not only on the scalar transport problem but will also examine in some detail the decaying isotropic scalar problem.

The equation governing isotropic scalar turbulence is:

$$\left(\frac{d}{dt} + \frac{k^2}{PrR_\lambda}\right)\vartheta(\mathbf{k},t) \;=\; -\imath k_m \sum_{\Delta} u_m(\mathbf{p},t)\vartheta(\mathbf{q},t) \tag{4.48}$$

The velocity field is the dynamic driving force behind a decaying turbulent scalar field. Once the numerical technique correctly models the experimental velocity field, all parameters related to that field (e.g., R_λ, A_v, L_f) are fixed and only parameters related to the scalar field may be manipulated to alter the scalar field evolution. Thus the initial spectral shape, A_s and scalar integral lengthscale, $L_s = f(k_{s_o})$, may be varied to affect evolutionary behavior. Although these are valuable variables in their own right, their ratios with their velocity field counterparts are more useful in that they include the relationship between the two fields. Indeed the scalar to velocity integral lengthscale ratio, L_s/L_f, has been the basis for a number of experimental and numerical studies of the decay of the turbulent scalar field (e.g., the experiments of Warhaft and Lumley [48], the DNS computations of Mell, et al. [35], and the EDQNM computations of Eswaran and O'Brien [13]). Thus L_s/L_f and A_s/A_v will be varied in this DIA study. As all experimental data used for comparison in this paper were obtained in air, Pr is restricted to a value of 0.7.

The Problem of the Transport of a Passive Scalar The scalar transport problem is somewhat more complex than the isotropic scalar turbulence problem. The magnitudes of the initial scalar intensity and the magnitude of the scalar gradient, the initial level of scalar transport, and the time delay between the start of the velocity problem and the onset of scalar transport may all be varied as well as the other scalar field variables mentioned for the isotropic scalar turbulence problem. Most of these additional variables are self–explanatory but the time delay may not be. All experiments designed to study turbulent scalar transport generate the turbulence using a grid. Whether the mean scalar gradient is generated by appropriately heating the turbulence producing grid bars (c.f., Warhaft and Lumley [48]), by a grid of resistance wires downstream of the turbulence generating grid (c.f., Sirivat and Warhaft [45], Budwig, Tavoularis and Corrsin [4]), or upstream of the grid (c.f., Sirivat and Warhaft [45] for part of their study), the turbulence field immediately downstream of the turbulence generating grid consists of a number wakes which take some time to coalesce and form a decaying isotropic velocity field. In the case of the preexisting scalar gradient, the scalar field downstream of the grid includes wakes which will tend to mix the scalar concentrations existing across the width of the grid bar resulting in a more homogeneous scalar concentration across the wake than existed upstream of the grid. Thus, even if the scalar gradient at each opening is maintained across the resultant wake, the immediate downstream flow will not contain a smooth uniform gradient. In the case of heating grids, the gradient is created by initially discrete wakes of relatively uniform temperature. Both scenarios require some time to evolve into an homogeneous turbulent flow with uniform scalar gradient and homogeneous scalar fluctuations which may act to delay the onset of

turbulent scalar transport characteristic of the nominal mean scalar gradient (c.f. Pope [14], Mell, et al. [35]). The precise amount of time is unknown and, further, the corresponding magnitude of the transport time delay appropriate for the DIA using isotropic initial conditions is unknown.

This study will activate the scalar gradient at the beginning of the computation. Furthermore, the scalar transport (i.e., the scalar–velocity and velocity–scalar correlations) will be initially assumed to be zero. The scalar field variables, L_s/L_f and A_s/A_v and the relative initial scalar field strength, $[\vartheta/(a\lambda_{go})]^2$, will be varied to model the experiments of Sirivat and Warhaft [45].

The Velocity Fields

While the quality of experimentalists' isotropic velocity fields in wind/water tunnel test sections has been quite good for some time, the initial conditions just downstream of the turbulence producing grid are strongly inhomogeneous. However, the return to isotropy forces are sufficiently strong to reduce the anisotropies to relative insignificance by x/M positions of 40 to 60 in most experiments. The DNS and DIA codes used to numerically compute turbulence cannot (due to the implicit assumption of homogeneity in the use of Fourier transforms) be initialized to compute this early time flow and thus exact simulations of the experimental flows are not possible. Since these flows are strongly nonlinear, it should be possible to determine numerical initial conditions which lead to numerical problem evolution similar to the experiments.

As the velocity field is the driving force for the turbulent scalar field (with or without a mean scalar gradient) this is the first field to be studied. The governing

normalized equations for the isotropic turbulent velocity field are:

$$\left(\frac{d}{dt}+\frac{k^2}{R_\lambda}\right)u_i(\mathbf{k},t)=-\frac{\imath}{2}P_{imn}(\mathbf{k})\sum_{\Delta}u_m(\mathbf{p},t)u_n(\mathbf{q},t) \tag{4.49}$$

Dimensional analysis of this problem produces the initial microscale Reynolds number, R_λ, which appears explicitly in the above equation. However, past studies of evolving, decaying turbulence have shown that the shape of the initial energy spectrum can significantly affect the problem evolution. Figures 4.1 through 4.3 compare the evolution of the microscale Reynolds number, total kinetic energy and dissipation of kinetic energy as predicted by the DIA for initial conditions which are identical except for spectral shapes; Gaussian and exponential (note that the kinetic energy and dissipation curves are normalized with respect to their initial values). All three quantities show significant evolutionary differences due to the initial spectral shape, especially the Reynolds number. Since R_λ is an important modeling parameter, it is disconcerting to see such a large change due simply to changing the initial spectral shape, especially without any quantitative mathematical means for explanation. This effect will now be examined from a mathematical modeling point of view.

One of the noticeable differences between the Gaussian and exponential spectral shapes is the greater "peakedness" of the Gaussian spectrum. This results in a smaller difference in the magnitudes of the integral lengthscale and the Taylor microscale for the Gaussian spectrum compared with the exponential shape. As this lengthscale relationship is determined by the spectral shape, the ratio of the integral lengthscale and the Taylor microscale (a dimensionless number) might be used to quantitatively describe the geometrical shape of any spectrum, at the initial time as well as during

problem evolution. We define this dimensionless number as

$$A \equiv \frac{L_f}{\lambda_g} \tag{4.50}$$

A may be viewed as a spectral aspect ratio which describes the flatness (or peakedness) of the energy spectrum. It is also equal to the ratio of the integral lengthscale Reynolds number, R_L ($R_L \equiv (u'L_f/\nu)$ to the microscale Reynolds number, R_λ. While this quantity does not enter explicitly into the governing equations, it does appear in the nature of the initial conditions as well as the nature of the energy evolution. Kolmogorov [27] implicitly assumed a very large value for this parameter in his spectral analysis of the inertial range of the velocity field. Oboukhov [38] and Corrsin [6] also assumed large values of this parameter applied to the spectral field. Thus A has played an important role in past turbulence studies. Some past numerical studies have used initial spectral shapes of the Gaussian type ($E(k) \propto k^4 \exp^{-bk^2}$ or of the exponential type ($E(k) \propto k^n \exp^{-bk}$ where n varies from 1 to 3. Other initialization schemes have involved piecewise continuous initial spectra or running the velocity computations for 1 to 2 eddy turnover times starting from some arbitrary initial condition to allow the problem to fully generate the nonlinear convection. This field is then taken to be the initial velocity condition for further studies. The goal is to develop initial conditions which minimize the "startup" time, i.e., the time required to fully develop the field nonlinearities and, in the case of comparisons with experiment, maximize agreement with the measured data. This paper studies the effects of spectral aspect ratio, A, upon the evolution of decaying isotropic turbulence.

How A, R_λ, L_f Effect Velocity Field Evolution

In order to study the importance of initial spectral shape relative to the lengthscale ratio, several runs were made using the "Gaussian" and "exponential" types of spectra generalized to the forms $E(k, t = 0) = ak^n \exp^{-b(k/k_o)^2}$ and $ak^n \exp^{-b(k/k_o)}$, respectively. The proportionality constants a and b were determined so that k_o was the actual wavenumber peak and the initial turbulence intensity was unity. Table 4.1 lists the values of A using these spectral forms with a number of values of the wavenumber exponent, n. Three comments deserve mention. First, the exponential shape tends to have a higher lengthscale ratio for a given value of n than does the Gaussian. This reflects the flatter shape of the function $\exp^{-ax}$ compared with $\exp^{-ax^2}$. Second, both shapes appear to approach some asymptotic value as n increases. This is due to the increasingly spikelike nature of these spectra with increased n. Finally, in both shapes, the odd values of n result in a broader spectral shape (larger value of A) than do the even values. The reason for this is unknown.

Using Table 4.1 one may match (at least approximately) values of the lengthscale ratio between the two functional forms using the appropriate values of n. This allows the determination of the relative importance of initial spectral functional form and A in the subsequent evolution of the velocity field. The initial spectra resulting from selected values of A are illustrated in Figures 4.10 and 4.11 using the Gaussian and exponential functional forms, respectively. The exponential spectra exhibit a broader, flatter shape than do the Gaussian spectra due to the lower power on k in the exponent of the exponential term. However, both functional forms produce flatter spectra as the value of A increases. This illustrates the interpretation of A as the aspect ratio of the spectra; as it increases the spectra become flatter and more

Table 4.1: Lengthscale ratios for Gaussian and exponential spectral shapes with various wavenumber exponents.

	$A_o = L_f/\lambda_g$	
n	Gaussian	Exponential
2	1.45	1.80
3	1.72	2.25
4	1.25	1.44
5	1.32	1.57
6	1.19	1.31
7	1.21	1.37
8	1.15	1.25
9	1.17	1.28
10	1.13	1.21
11	1.14	1.23
12	1.12	1.17
13	1.13	1.20
14	1.11	1.17
15	1.11	1.17
16	1.10	1.15
17	1.11	1.16
18	1.10	1.14
19	1.10	1.15
20	1.09	1.13
25	1.09	1.12

elongated, just as a rectangle becomes more elongated as its aspect ratio increases. Figure 4.12 directly compares spectra of the two forms with a value of A of 1.25 at three different integral lengthscales. As can be seen, the peak wavenumbers are the same for both functional forms at each lengthscale and the spectra appear to be osculatory there. The spectra do have significant differences in the low and high wavenumber regimes.

Using the values in Table 4.1 a number of DIA computations were performed varying initial values of A, R_λ, and L_f to assess the dependency of the problem evolution upon these quantities. The runs are summarized in Table 4.2. These constitute a parametric study of the isotropic velocity field within the numerical limitations of gridsize, etc. Generally the decay exponents for exponential and Gaussian forms with the same (or similar) values of A are very close. As A increases, the decay exponent tends toward smaller magnitudes.

Figures 4.13, 4.14, and 4.15 compare the time evolution of the DIA microscale Reynolds number for runs with two initial values of R_λ and several initial values of L_f and A with that of the low and high speed runs of Sirivat and Warhaft. In Figure 4.13 it can be seen that the effect of initial spectral functional form is significantly less important to the subsequent evolution compared with the value of A. This is also true for all initial integral lengthscales shown (0.3359, 0.4950 and 0.7584). Figures 4.14 and 4.15 illustrate the effect of changing initial A while holding all other initial variables held constant. Figure 4.14 uses an initial R_λ of 60 which leads to Reynolds number evolutions which bound that of the low speed run of Sirivat and Warhaft while Figure 4.15 approximates their high speed run. The experimental data points are included for comparison. Both figures show close agreement of the exponential

Table 4.2: Summary of DIA run initial conditions, identification and kinetic energy decay exponents.

Name		A_o				n	
Exp.	Gau.	Exp.	Gau.	$R_{\lambda o}$	L_{fo}	Exp.	Gau.
E1	G1	1.25	1.25	60	0.3359	-1.60	-1.54
E2	G2	1.25	1.25	60	0.4590	-1.54	-1.50
E3	G3	1.25	1.25	60	0.7584	-1.60	-1.59
E4	G4	1.25	1.25	120	0.3359	-1.46	-1.41
E5	G5	1.25	1.25	120	0.4950	-1.50	-1.46
E6	G6	1.25	1.25	120	0.7584	-1.57	-1.56
E7	G7	1.44	1.45	60	0.3359	-1.40	-1.31
E8	G8	1.44	1.45	60	0.4590	-1.42	-1.39
E9	G9	1.44	1.45	60	0.7584	-1.53	-1.52
E10	G10	1.44	1.45	120	0.3359	-1.28	-1.19
E11	G11	1.44	1.45	120	0.4950	-1.37	-1.41
E12	G12	1.44	1.45	120	0.7584	-1.49	-1.56
E13	G13	1.72	1.80	60	0.3359	-1.21	-1.16
E14	G14	1.72	1.80	60	0.4590	-1.32	-1.29
E15	G15	1.72	1.80	60	0.7584	-1.45	-1.45
E16	G16	1.72	1.80	120	0.3359	-1.09	-1.04
E17	G17	1.72	1.80	120	0.4950	-1.25	-1.23
E18	G18	1.72	1.80	120	0.7584	-1.41	-1.41
E19	G19	2.25	1.11	60	0.4950	-1.23	-1.76
—	G20	—	1.19	60	0.4950	—	-1.59

and Gaussian initial spectral forms with identical initial A values. In the case of the curves which have exponential shape, $A_o = 1.80$, and Gaussian shape, $A_o = 1.72$, there exists more discrepancy than for the other cases. At least two potential explanations exist for the differences seen between these two curves. First is the significant difference in the A values (about 4%) caused by the discrete nature of the exponents used for the exponential wavenumber premultiplier. This difference may be sufficient to account for all the differences. Second is the fact that as A increases in value, the initial spectrum becomes flatter and broader, thus differences in the spectra at wavenumbers smaller and larger than the peak may have more effect in that they contain relatively more energy compared with the spectral peak region than is the case in the more peaked (smaller A) spectra. This, in turn, may amplify the effects of differences in the initial A.

Figures 4.16 through 4.21 show the dimensional velocity turbulence energy spectra at initial time and at just over 2 eddy turnover times for each of three different values of A. Each graph shows the results for three initial values of L_f. All initial spectra of the same A and L_f show significant differences in shape due to the "Gaussian" and exponential spectral forms. By the end of (1–2) eddy turnover times, those curves with the same initial integral lengthscales and similar initial values of A have evolved to very nearly coincide with each other in shape and magnitude although some slight differences remain at the lowest wavenumber or two. This similarity persists throughout the remainder of these computations. Although only curves for R_{λ_o} of 60 are shown, the same evolutionary behavior is observed at other values.

The spectra for the smallest initial integral lengthscale and largest value of A for $R_{\lambda o} = 60$ appear to flatten somewhat at high wavenumbers. This suggests that

the problem requires a wider wavenumber range for a complete description of the dissipation spectra than was available for these computations. Indeed, inspection of the corresponding dissipation spectra (Figures 4.22 through 4.27) show that, although the initial dissipation spectra are well contained within the numerics, the energy is advected to higher wavenumbers sufficiently rapidly that the problem grows larger than the numerical grid. While this problem generally disappears at later times, the inaccuracies incurred by this bandwidth limitation should not be ignored but cannot be quantified within the scope of this study. It is shown later that these conditions are not needed to best model the low speed Sirivat and Warhaft results.

Figures 4.22 through 4.27 that, for a given initial integral lengthscale, dissipation levels generally increase as A increases. This is consistent with the increased spreading of the spectra with increasing A leading to higher energy levels at the high wavenumbers and thus higher initial dissipation. Figure 4.13, however, indicates that it is the higher initial values of A which lead to higher late time values for R_λ. This seeming contradiction can be resolved by examining and comparing Figures 4.16 and 4.17 for $A = 1.25$ with Figures 4.20 and 4.21 for $A = 1.72/1.80$. Figures 4.16 and 4.17 have generally lower energy levels than are displayed in Figures 4.20 and 4.21 while Figure 4.16 shows higher initial energy levels in the low A spectra around the spectral peak than are shown in the high A spectra in Figure 4.20. Thus it appears that although initial dissipation levels in the low A problems is lower than in the high A cases, during the first 1–2 eddy circulation times dissipation occurs most rapidly in the low A cases, perhaps due to higher spectral energy gradients leading to higher rates of nonlinear energy convection into the higher wavenumbers. The later time ($t \geq 2.15$) higher dissipation levels in the high A cases is thus due to higher overall

energy levels while at early times (e.g., $t = 0$) are due more to specific energy distribution. All other initial conditions being equal, to induce higher levels of R_λ at late times, the initial spectral A should be increased.

We now turn attention to the evolution of the aspect ratio, A. Figures 4.30 and 4.31 show the evolution of A at the same initial R_λ and L_f but at several values of initial A and using Gaussian and exponential initial spectral shapes and compare them with those of the low and high speed runs of Sirivat and Warhaft. Note that in both of these Figures, A increases sharply during the first 2 eddy turnover times before gradually and monotonically decreasing (reminiscent of the evolution of the derivative skewnesses or scalar eddy diffusivity ratio in the passive scalar transport problem). This reflects the initial spectral redistribution of energy by the nonlinear convection which acts to move energy to the higher wavenumbers.

Figure 4.30 specifically compares the effect of initial spectral form with that of initial A. There are larger differences due to the Gaussian and exponential initial forms than were seen in the R_λ studies. However, these differences are of significantly less importance than those due to the original aspect ratio value. Varying A leads to significant evolutionary differences while varying the spectral form leads to relatively minor differences which tend to abate with time. The source of the differences due to spectral form (Gaussian or exponential) may be due to the persistent difference exhibited in the energy spectra at the lowest one or two wavenumbers between the Gaussian and exponential initial shapes. While this has a small effect upon the Taylor microscale and total energy, the integral lengthscale is sensitive to the character of the energy spectra in this range. Note the scattered nature of the experimental data compared with the smoothness of the computational data. This may be due to

measurement uncertainties or some anisotropies still present at the lowest wavenumbers of the experimental energy spectra at these wavenumbers, or a combination of these. In Figure 4.30 the curves for the lower initial values of A increase and peak at approximately 150% of the initial value while at higher initial values of A this increase is markedly less (roughly 133%). While this difference is remarkable, it may be pathological, due to the wavenumber bandwidth artificially constraining the evolution of the problem since these values of A result in very flat spectra. As noted above, the current wavenumber bandwidth does impose limitations on the range of appropriate computations, i.e., values of A, which may be used.

Figures 4.32 through 4.34 compare the evolution of A with initial R_λ of 60 at different initial integral lengthscales, each Figure using a constant initial A, while Figures 4.35 through 4.37 show analagous curves with initial R_λ of 120. In Figures 4.32 through 4.34, as the value of A_o increases, the spreading of the curves due to the variance of the initial integral lengthscale also increases. In Figure 4.32 the curves are reasonably convergent. As the initial spectra become more spread out (increasing A_o) the evolutionary behavior becomes more divergent with changes in the value of L_{f_o}.

At high R_λ (Figures 4.35 through 4.37) the convergence is noticeably poorer for any given A than at low R_λ but there is still reasonable convergence at A of 1.25 , worse for 1.45 and with virtually no similarity for A of 1.72/1.80. Thus the evolution of A appears to be considerably more sensitive to bandwidth limitations than is that of R_λ. Nonetheless, these Figures show the DIA can reasonably model the evolution of experimental A's in magnitude and, at least roughly, in evolutionary dynamics.

Figures 4.38 through 4.40 compare the evolution of the normalized kinetic energy

at initial values for R_λ and L_f of 60 and 0.4950, respectively. Figures 4.38 and 4.39 compare the relative effects of initial spectral form (Gaussian vs. exponential) and initial A. It is apparent that the initial spectral functional form has relatively small influence upon energy evolution while A has a pronounced effect. Although the initial energy spectra exhibit significant differences (as noted above in Figures 4.16, 4.18, etc.) the subsequent problem evolution is primarily determined by the nonlinear transport and it appears this is affected significantly by the initial value of A. The range of the effect of A_o upon energy decay is explored in Figure 4.40 in which the initial value of A ranges from 1.11 to 2.25, which is the maximum range available using the exponential and Gaussian initial spectral functions. As the initial spectral aspect ratio increases the turbulence energy decay rate decreases.

Figures 4.41 through 4.43 show the effects of changing the initial integral lengthscale holding initial R_λ at 60 and A constant while Figures 4.44 through 4.46 do the same for R_λ of 120. The data points from Sirivat and Warhaft's experiments are also shown in these figures for comparison. In these comparisons time and energy are normalized using initial values (t=0 for DIA and x/M=40 for experiment). In general, the initial lengthscale (which ranges from 0.3359 to 0.7584) has a more minor role in determining subsequent energy decay than does A. As noted above for A and R_λ, the more peaked initial spectra (smaller values of A_o) lead to energy evolution curves which collapse upon each other better than do the flatter spectra and decreasing R_λ improves this collapse. It appears from these initial comparisons that the energy decay rates measured experimentally agree best with the smaller values of A_o (i.e., more peaked initial spectra). Table 4.2 lists the energy decay exponents numerically for the runs illustrated in Figures 4.38 through 4.46.

Figure 4.47 illustrates the evolution of the velocity field derivative skewness for exponential and Gaussian initial spectral functions and initial values of A at $R_{\lambda o}$ of 60 and L_f of 0.4950. For a given A_o the skewness is relatively insensitive to the spectral shape and increasing A_o decreases the skewness. This may be seen as a consequence of the "flatness" or breadth of the initial spectrum. Increased flatness decreases the wavenumber spectral energy gradients, thus reducing the driving forces for nonlinear energy convection towards the dissipation range. The dissipation of total turbulence energy is thus reduced, reducing the decay rate for that problem over one with a smaller initial value of A. Note that the differences between the various runs, after large differences during the initial nonlinear buildup, decreases with time. While significant differences still exist after 9 eddy circulation times, the skewnesses do behave as if slowly approaching a single asymptotic value. Figure 4.48 illustrates the range of derivative skewness evolutionary behavior as initial A values vary from 1.11 to 2.25. Initial differences are twofold and, although they reduce to approximately 15% by t = 8–9. This Figure graphically shows the dramatic effect that the spectral aspect ratio has, long term as well as early time, upon the nonlinear turbulent energy transport.

Contrary to the results for the evolution of the turbulence energy, the velocity derivative skewnesses do not collapse at all as the initial integral lengthscale is changed. Rather they deviate from each other dramatically which is a requirement for the energy curves to collapse since varying the initial integral lengthscale affects the amount of energy initially in the dissipation range of the problem. Figures 4.49 through 4.54 illustrate how the skewnesses vary with L_{f_o}. As L_{f_o} decreases the skewness also decreases, at least for some initial period ranging from

about 5–10 eddy turnover times for R_{λ_o} of 60 to in excess 10 turnover times (for R_{λ_o} of 120). The geometric similarity of the curves coupled with the behavior seen in Figure fig:exdiavvskew3 through fig:exdiavvskew8 suggests that in time all the skewnesses approach some asymptotic value. For $R_{\lambda o}$ of 60 this value appears to be approximately 0.35. The $R_{\lambda o} = 120$ runs do not have as apparent an asymptotic behavior or value but do seem to be consistent with an asymptote of 0.35.

The energy in spectra with large initial L_f is concentrated relatively far (spectrally) from the dissipation range while that in spectra with small initial L_f is concentrated close to the dissipation range. The latter spectra rapidly evolve a spectral shape which is in "equilibrium" with the dissipation range while the former must convectively transport a large amount of energy up to a relatively broad range of wavenumbers before establishing any "equilibrium" with the dissipation range. The spectral energy gradients in the former case are larger for a longer period of time than are those of the latter case and thus nonlinear convection occurs at a higher rate. This is reflected in a higher derivative skewness. When the problem cannot be completely described within the confines of the numerical grid, this transport is distorted by a piling up of energy at the high wavenumber (ultraviolet) end and/or low wavenumber (infrared) end of the (truncated) spectrum. This can result in a turnup of the tail of the energy spectrum (due to insufficient characterization of the dissipation spectrum) or the same at the low end of the spectrum (due to insufficient characterization of the transport from that portion of the spectrum to the lower wavenumbers). The differences induced in the skewness due to the use of exponential or Gaussian initial spectral forms are negligible. Thus the nonlinear activity predicted by the DIA for isotropic velocity fields is primarily dependent upon the initial spectral aspect ratio,

A, and the initial integral lengthscale, L_f.

Simulating Experimental Decaying Isotropic Velocity Fields

The definition of the spectral aspect ratio, A provides a quantitative nondimensional modeling parameter which may be used with the Reynolds number, R_λ to model real flows using numerical techniques. The parameter A provides quantitative information useful in determining the similarity of the numerical and experimental spectra. Similarity in this regard helps provide for similarity in nonlinear energy convection along the spectrum.

The anticipated use of any theoretical/numerical turbulence prediction technique is to model the evolution of a given physical problem which has expected values of R_λ and A at some point in nondimensional time. The numerical goal is thus to determine appropriate initial conditions which allow the computation to achieve the specified physical "initial conditions" at the appropriate point in time. This was the approach used here to compare DIA results with those of experiment. Several runs were made with initial (t=0) values of R_λ and A which resulted in DIA predictions for the value of R_λ equal to that of Sirivat and Warhaft at the nondimensional time corresponding to their first measurement station, $x/M = 40$. The $t = 0$ initial conditions for the DIA runs are listed in Table 4.3. The Reynolds number results of this exercise for their low speed run are shown in Figure 4.55 and show all curves approximately intersecting at the first experimental point. Note that the best match between DIA and experiment occur for intermediate initial values of A, i.e., 1.45 and 1.57. The other two (1.13 and 2.25) exhibit significant deviation with the smaller initial A providing the worst match with experiment. Figure 4.56 compares the

evolution of A between the DIA runs and experiment. All DIA runs except the low initial A run (PZ) have at least some period of the computation when A is within the range of experimental values although run P3 drops to the very bottom of this range within 1.5 to 2 eddy turnover times. Runs P7 and P8 not only tend to remain within the experimental range throughout the run (after the first eddy turnover) but are also quite close to each other. The significance of these differences in run evolutions are seen in the next two Figures. Figure 4.57 compares the evolution of the normalized turbulence kinetic energy. The energy is normalized with respect to its value at the nondimensional time equal to the experimental nondimensional time corresponding to the first measurement station in the experiments of Sirivat and Warhaft. Somewhat surprisingly all four runs give reasonably good predictions of the decay of turbulence energy. However, as can be seen in Figure 4.58, the normalized dissipation rate predictions are more strongly dependent upon the initial conditions. (The dissipation is normalized by multiplication by the value of $\lambda^2/(\nu E_{vv}(t))$ at the time corresponding to the first measurement station of Sirivat and Warhaft.) All DIA runs with initial A above 1.45 agree satisfactorily with the experimental results while run PZ with initial A of 1.13 overpredicts the dissipation rate in the (self–similar) portion of the problem evolution.

Figures 4.59 through 4.62 illustrate the same situation relative to the high speed experimental run. In this case, Figure 4.59 shows reasonable agreement of all DIA R_λ evolutions with experiment although PL (with $A_o = 1.13$) is somewhat poorer than are the other three. Figure 4.60 shows that neither of the lower A_o runs (PK and PL) ever achieve A values within the range of experimental values for this high speed run but runs PC and PF do for a brief period of time before dropping below

Table 4.3: Summary of DIA run conditions for comparison with the experimental runs of Sirivat and Warhaft [45].

Name	A_o	$R_{\lambda o}$	L_{fo}	n_{E_v}	n_{ϵ_v}
P3	2.25	60	0.7584	-1.37	-2.01
P7	1.45	80	0.4950	-1.37	-2.26
P8	1.57	75	0.4950	-1.36	-2.21
PZ	1.13	75	0.7584	-1.66	-2.52
PC	1.80	140	0.7584	-1.40	-2.11
PF	2.25	125	0.7584	-1.33	-1.98
PK	1.25	155	0.7584	-1.55	-2.38
PL	1.13	145	0.7584	-1.64	-2.52
S/W Low	≈ 2.37	32.4	—	-1.29	-1.94
S/W High	≈ 2.77	50.4	—	-1.36	-1.91

experimental values. This might suggest that the experimental wavenumber bandwidth is larger than can be accommodated using the functional forms chosen for this study. Nonetheless it is instructive to further examine the results from these runs. Figure 4.61 compares the decay of turbulence energy for DIA and experiment. As seen with the low speed results, all DIA runs give nearly the same agreement with experiment. In this case the DIA runs appear to have decay rates somewhat reduced from that of experiment and in less agreement than in the low speed results. However, any of these would give about the same decay rate estimate. Again, as in the low speed case, the dissipation evolutions shown in Figure 4.62 exhibit a strong dependence upon initial A values with only the two highest (PC and PF) exhibiting behavior similar to that of experiment. As initial A values are reduced from 1.80, the disagreement with laboratory data increases.

The numerical decay exponents for turbulence energy and dissipation rates are

listed in Table 4.3 for the DIA runs as well as the experiments. In nearly every case, the DIA predicts exponents whose magnitudes are somewhat larger than those of experiment and these discrepancies increase with decreasing A_o. The DIA results with low A_o contained errors in the decay exponents as high as 20–30%. The runs with higher A_o include less than 10% error (approximately 6% for the low speed run and 3% for the high speed run) in the energy decay exponents. The dissipation decay exponents display more error (approximately 17% and 11% for the low and high speed runs, respectively). The normalized levels of energy are generally within 10% of measurements for all runs as are the dissipation predictions by runs with high A_o. In the runs with low A_o the dissipation predictions are in error by as much as 50%. These discrepancies may be the result of excessive nonlinear energy transport predicted by the DIA (in the inertial range this results in a spurious $k^{-3/2}$ inertial range spectral behavior rather than the proper $k^{-5/3}$). However, from the results presented here it might also be due, at least in part, to wavenumber bandwidth limitations or initial integral lengthscale values. Despite the errors, it appears plausible to obtain reasonable estimates of the behavior of isotropic turbulent velocity fields using the DIA if appropriate modeling of R_λ and A is ensured.

From the above results it may be said that simple agreement between the initial numerical and experimental microscale Reynolds numbers, or, perhaps, even their evolution is insufficient to guarantee correct modeling of the physics occurring in the physical problem. While energy decay may be appropriately modeled, only those runs which also appropriately modeled the wavenumber bandwidth could properly model the energy decay. When performing laboratory studies, the turbulence energy is generally the quantity concentrated upon to deduce the physics being observed.

However, in computational fluid dynamics (CFD) problems, the turbulence energy dissipation is a quantity of interest as this determines the effective eddy viscosity. The results presented here suggest that not only must R_λ be modeled correctly but also A. Since A consists of two lengthscales, it would appear from the results of this study that two lengthscales are required to properly model isotropic turbulent velocity fields.

Figures 4.63 through 4.66 summarize the two DIA runs which best fit the experimental data, one for the low and one for the high speed runs. The agreement between the numerical and experimental data is very satisfactory for the microscale Reynolds number, turbulence kinetic energy and dissipation of the kinetic energy. The agreement for the aspect ratio is not quite as good, in part due to the scatter of the experimental data and also due to the inadequacy of the numerical bandwidth to accurately compute the high speed run.

A brief summary of the velocity field results is now in order. The two modeling parameters used here for isotropic turbulent velocity fields are the microscale Reynolds number, R_λ and the spectral aspect ratio, A. It should be noted that these are not the only choices. The integral lengthscale Reynolds number, R_L, could be used instead of either R_λ or A since, as required by dimensional analysis, any product of two dimensionless numbers forms third, equally valid dimensionless parameter. We may form R_L by the product of A and R_λ, $A \times R_\lambda = R_L$. However, R_λ is the usual Reynolds number of choice for these types of studies while A possesses a reasonably direct geometric spectral interpretation not available with R_L and thus these two were selected for use in this study.

The Zero Transport Scalar Field

Although the primary interest of this paper is isotropic turbulent transport of a passive scalar with uniform mean gradient, it is appropriate to briefly investigate the behavior of the zero gradient isotropic turbulenct scalar field as predicted by the DIA. This is prompted by two reasons. First is the decomposition of the passive scalar transport problem into a decaying isotropic scalar field and a scalar transport problem with zero initial conditions as discussed above. Thus for those transport problems which have significant initial scalar fields not generated by the action of the turbulent velocity field upon the mean scalar gradient, it will be necessary to model a decaying isotropic scalar field.

Second, there exists a fundamental mathematical difference between DNS computations and those using statistical closure theories. The DNS algorithm involves the primitive velocity and scalar variables only. When a uniform mean scalar gradient is imposed upon the system, the only change is the addition of a linear source term to the scalar equation at each node. In the case of the statistical closure theory algorithms, not only is the additional source term added to the scalar equation but additional equations governing the scalar transport fields (i.e., the velocity–scalar covariance and scalar–velocity covariance equations and their associated response functions) are also derived and solved. These quantities also contribute to the nonlinear terms in the scalar equations. Thus the statistical closure theory algorithm adds some complexity merely by the addition of the scalar field and adds considerably more complexity when computing the scalar transport problem. A brief study of the zero gradient scalar problem and comparison with experiment thus gives some idea of the fidelity of the DIA in the simplest turbulent scalar problem.

The nondimensional equations governing the velocity and scalar variables in the problem of isotropic scalar turbulence are:

$$\left(\frac{d}{dt}+\frac{k^2}{R_\lambda}\right)u_i(\mathbf{k},t) = -\frac{\imath}{2}P_{imn}(\mathbf{k})\sum_{\Delta}u_m(\mathbf{p},t)u_n(\mathbf{q},t) \tag{4.51}$$

$$\left(\frac{d}{dt}+\frac{k^2}{PrR_\lambda}\right)\vartheta(\mathbf{k},t) = -\imath k_m\sum_{\Delta}u_m(\mathbf{p},t)\vartheta(\mathbf{q},t) \tag{4.52}$$

Here the scalar variable, $\vartheta(\mathbf{k},t)$ is nondimensionalized by its initial intensity, ϑ_o'. The nondimensional terms arising from a dimensional analysis of these equations and the isotropic scalar turbulence problem are the microscale Reynolds number, R_λ, the velocity spectrum aspect ratio, $A_v \equiv L_f/\lambda_g$, the Prandtl number, Pr, and the scalar–velocity integral lengthscale ratio, L_s/L_f. The scalar spectrum also possesses an aspect ratio, $A_s \equiv L_s/\lambda_s$. R_λ and A_v are determined by matching the DIA velocity field with that of the experiment of interest while the Prandtl number, Pr, is set by the experimental working fluid. Thus the only parameters which may be varied in the initial scalar field are A_s and L_s/L_f. The integral lengthscale ratio determines the relative position in wavenumber space of the initial spectra of the velocity and scalar fields. A_s determines the relative spectral flatness but what may be more important in determining the evolution of the scalar field is the flatness of the scalar spectrum compared with that of the velocity field. This ratio, $A_s/A_v \equiv (L_s/L_f)(\lambda_g/\lambda_s)$ could be replaced by λ_g/λ_s as the ratio of spectral aspect ratios contains the scalar/mechanical integral lengthscale ratio which could be divided out using the rules of dimensional analysis. However, the ratio of aspect ratios has a more meaningful physical interpretation in conjunction with the integral lengthscale ratio than does the Taylor microscale ratio. Thus in the following work, the ratio A_s/A_v will be the aspect ratio number of choice for describing the scalar spectral

shape characteristics.

Previous work has studied the relationship of the decay exponent of the scalar field variance with the initial mechanical to thermal lengthscale ratio and found significant dependence. Mell, Kosály and Riley [35] performed DNS computations investigating this relationship and found that for a range of lengthscale ratios spanning almost an order of magnitude (0.8–5.0) the decay exponent varied only from -2.23 to -2.76 (experiments have measured exponents from -0.87 to 3.20, cf. Warhaft and Lumley [48]). Mell, et al. initialized their velocity field using a Gaussian initial spectrum and allowing the DNS to run for sufficient time to fully establish the nonlinear interactions. The subsequent velocity field was then saved and used (with selected amplitude and wavenumber scaling to achieve an appropriate initial R_λ) as the initial velocity field for each of their scalar turbulence runs. This cannot be practically applied to a two time statistical closure theory such as the DIA. Thus none of the runs reported here are duplications of Mell et al.'s results.

Previous studies (including those of Mell, et al.) have used initial values for R_λ on the order of 40–50. While this is larger than or of the order of values experienced in most laboratory experiments, the R_λ evolution in time drops out of the range of the experimental values (e.g., see Mell, et al. [35]). As shown above, significantly higher initial R_λ's are required to obtain numerical DIA behavior similar to experiments. The question arises of what effect varying R_λ has upon the scalar decay rate. Although the Reynolds number will not be altered in the DIA runs reported here which compare directly with experiment, it is of interest to know how these results (run at higher initial Reynolds number than other computations) might be affected by reducing the initial Reynolds number. To this end, some brief comparisons are

Table 4.4: Dependency of decay exponents upon initial Reynolds number, integral lengthscale ratio and ratio of spectral aspect ratios. n is the decay exponent for the scalar energy and m is the decay exponent for the diffusion of scalar energy.

Run	L_s/L_f	A_s/A_v	R_λ	n	m
SU	0.50	0.48	30	-2.15	-3.24
SI	0.50	0.48	60	-2.20	-3.30
SM	0.50	0.48	90	-2.22	-3.33
SQ	0.50	0.48	120	-2.23	-3.32
ST	0.50	0.94	30	-1.06	-2.09
SH	0.50	0.94	60	-1.09	-2.20
SL	0.50	0.94	90	-1.10	-2.23
SP	0.50	0.94	120	-1.10	-2.21
SS	1.00	0.48	30	-1.93	-2.83
SC	1.00	0.48	60	-1.91	-2.82
SK	1.00	0.48	90	-1.90	-2.80
SO	1.00	0.48	120	-1.87	-2.76
SR	1.00	0.94	30	-0.95	-1.86
SB	1.00	0.94	60	-0.95	-1.94
SJ	1.00	0.94	90	-0.95	-1.95
SN	1.00	0.94	120	-0.94	-1.90
SE	2.00	0.94	60	-0.74	-1.47
SF	2.00	0.48	60	-1.19	-2.07

made at different $R_{\lambda o}$'s. Figure 4.67 compares the decay of scalar energy at two initial Reynolds numbers with different initial ratios of spectral aspect ratios, while Figure 4.68 shows the scalar variance diffusion for these runs and others involving different initial thermal to mechanical lengthscale ratios. The effect of initial R_λ upon scalar variance evolution is quite weak especially compared with those due to varying the integral lengthscale ratio or the ratio of the spectral aspect ratios. The scalar energy decay exponents for these runs are listed in Table 4.4. It is quite remarkable

that the decay exponents are so insensitive to initial R_λ; the maximum deviation exhibited in the table due to it is less than approximately 4% over a four–fold increase in initial R_λ. By contrast, changing the integral lengthscale ratio by a factor of two (0.5 to 1.0) results in a 15% decrease in the decay exponent while changing by a factor of four (0.5 to 2.0) results in a 25–50% decrease in decay exponent. Nearly doubling the ratio of initial aspect ratios (from 0.48 to 0.94) produces a 50% reduction in the decay exponent. These data show that the most influential variable in determining the behavior of the scalar energy decay, between R_λ, L_s/L_f, and A_s/A_v, is the latter one.

For the case of $L_s/L_f(t = 0)$ less than unity, the bulk of the scalar energy is initially situated in a stronger portion of the diffusive range than is the case for larger values of $L_s/L_f(t = 0)$. The former case results in more rapid scalar diffusion and a high magnitude decay exponent because the scalar energy does not need to be nonlinearly convected to the diffusive region which requires time to accomplish. In other words, the large $L_s/L_f(t = 0)$ case is a convection limited situation whereas the low $L_s/L_f(t = 0)$ case is primarily diffusion limited. Therefore the integral lengthscale ratio may be viewed as the parameter which determines the relative initial placement of the bulk of the scalar energy and affects the decay characteristics primarily by that location. (It should be emphasized that these comments are intended to apply to the current situation only. Altering Pr may change the behavior of the scalar field.)

Figure 4.69 compares the evolution of scalar energy with different initial values for both scalar to mechanical integral lengthscale and ratio of aspect ratios. Reducing the lengthscale ratio places more scalar energy at high wavenumbers, thus increasing initial dissipation rates and decreasing the total energy levels in a marked manner.

This also tends to increase the rate of decay (i.e., the magnitude of the decay exponent). Maintaining a constant initial integral lengthscale ratio but decreasing the ratio of aspect ratios also decreases somewhat the initial dissipation rates. However, the effects upon the final decay rates is more pronounced than occurs with the lengthscale ratio change. The decreased ratio of aspect ratios leads to greatly enhanced rates of decay of the scalar energy. Apparently, the reduced ratio of aspect ratios slows the initial rate of scalar energy decay due to reduced energy levels at high wavenumbers. However, this same characteristic eventually leads to enhanced rates of nonlinear convection and larger decay rates.

Figures 4.70 through 4.72 plot the time evolution of the mixed scalar skewness for initial values for A_s/A_v of 0.48, 0.58 and 0.94, respectively with each figure illustrating the effects of changing initial L_s/L_f from 0.5 to 2.0. Both $A_s/A_v(t=0)$ and $L_s/L_f(t=0)$ effect the short time ($t <$ 2–4 eddy circulation times) evolution of the skewness significantly. As the lengthscale ratio increases the initial surge in skewness increases dramatically. At later times, these differences decrease but never disappear as the curves appear to approach a common asymptote during the computations. Thus the relative wavenumber location of the energy distribution acts to affect the convective transport and diffusion rates. As $L_s/L_f(t=0)$ decreases, the scalar energy is concentrated increasingly in the strongly diffusive region of the problem and away from the wavenumber region in which the strongest convection effects act. This increases the total rate of diffusion while decreasing the nonlinear convection.

Altering A_s/A_v has a pronounced effect upon the scalar field evolution. This occurs due to the difference in spectral shapes between the two fields. At low values of A_s/A_v (e.g., 0.48) the velocity spectrum is relatively flat compared with that of

the scalar field; the scalar spectrum more resembles a spike of scalar energy. Thus the convection by the velocity field can act upon a large concentration of scalar variance and rapidly transport it (due to the high scalar spectral gradient) to high wavenumbers and subsequent diffusion at early times. At higher values of A_s/A_v the spectral shape of the scalar field is flatter relative to the velocity field, the scalar spectral gradients are lower, the concentration of scalar energy at the peak of the spectrum is lower and the nonlinear convection of scalar variance is subsequently lower, leading to lower initial diffusion rates. After a time, the nonlinear convection (skewness) increases to a value actually somewhat higher than that for lower A_s/A_v cases. However, it is insufficiently high to make up for the large initial convection in these latter cases and this leads to lower diffusion rates (and decay exponents). This can be seen in Figures 4.73, 4.74 and 4.75 which compare the mixed scalar skewnesses for various values of A_s/A_v at a given value of L_s/L_f. As A_s/A_v decreases, the initial convective transport (and thus the skewness) increases due to the enhanced scalar spectral gradients. Although this effect lasts only approximately two or four eddy turnover times, examination of Figure 4.67 shows that this is the time during which the decay characteristics are determined. After this time the skewness evolutions show a reversal, i.e., the skewness (transport) increases with increasing A_s/A_v which reflects primarily the significantly higher energy levels in these problems due to their reduced early time diffusion.

Thus both L_s/L_v and A_s/A_v play important roles in determining the nonlinear scalar convection. Choosing an initial value for L_s/L_v serves to place the scalar energy either in a region subject to strong nonlinear convection (large values) or relatively isolated from it (small L_s/L_v). This has the physical interpretation that large initial

L_s/L_v indicates the scalar fluctuations are predominantly of scales much larger than those of the velocity field. The velocity fluctuations strongly distort these large scale scalar fluctuations, straining them into ever smaller scales. A small initial L_s/L_v indicates that variations in the scalar field are primarily of scales small relative to those in the velocity field. Thus velocity fluctuations are more apt to simply convect the scalar fluctuations in their entirety without significant straining or distortion. Small initial A_s/A_v indicates the scalar fluctuations tend to be close to the scales characteristic of the peak wavenumber and velocity fluctuations of scales smaller than these will strain the scalar field. Large initial A_s/A_v indicates a wide range of scalar variation sizes, the large ones susceptible to nonlinear convective straining while the small ones tend to be convected whole, with little straining. These two ratios also interact as a large initial L_s/L_v will indicate a situation in which all scalar fluctuations, even if there is a wide range of scales, will be subject to straining by the velocity field and the scalar convection will be strong for all initial values of A_s/A_v. This can be seen in Figure 4.73 in which L_s/L_v has an initial value of 2.0. Not only is the skewness large but varying A_s/A_v from 0.48 to 0.94 has little effect upon the nonlinearities. As the initial lengthscale ratio is reduced to 1.0 (Figure 4.74) and 0.5 (Figure 4.75), the initial spike and subsequent minima in the skewness decrease as the relative scales of the scalar field become smaller than those of the velocity field and more scalar fluctuations are simply convected without significant straining. Furthermore, as L_s/L_v is reduced, the initial A_s/A_v has a stronger effect upon the nonlinear behavior of the scalar field. Smaller initial A_s/A_v concentrates scalar fluctuation scales closer to the spectral peak, subjecting a higher percentage of them to nonlinear straining and leading to higher skewness values. It is interesting

to note that all cases shown in Figures 4.71 through 4.75 have achieved values of approximately 0.30 by the end of the computations (approximately 9 eddy turnover times) although the scalar energy levels at this time are approximately 1–5% of their original values. While this may not be a condition of final stages of decay, the bulk of decay has occurred.

The energy spectra (Figures 4.76 through 4.79 for the case of initial integral lengthscale ratio of unity) reflect this in the great change in the spectra for runs with low $A_s/A_v(t=0)$ which initially have spectra that differ radically at high wavenumbers from those with high $A_s/A_v(t=0)$. Within two eddy turnover times, they achieve spectral shapes very similar to the high $A_s/A_v(t=0)$ runs at all wavenumbers but the lowest ones. Thus the value of $A_s/A_v(t=0)$ acts to determine the initial scalar spectral gradients which in turn determines the initial rates of nonlinear scalar convection. Note that the low $A_s/A_v(t=0)$ spectra in these figures maintain higher levels at high wavenumbers than do the high $A_s/A_v(t=0)$ spectra after the initial time. This is what maintains the more rapid energy decay rate of the low $A_s/A_v(t=0)$ runs. It is only at the lowest one or two wavenumbers where the high $A_s/A_v(t=0)$ spectra are higher than the low ones. This is, however, sufficient to maintain a higher total (integrated) energy level in the high $A_s/A_v(t=0)$ runs than the low $A_s/A_v(t=0)$ runs after approximately 2.5 eddy turnover times. Figures 4.80 through 4.83 show the same spectra but in Cartesian coordinates. In these figures it is easier to see why the high $A_s/A_v(t=0)$ runs have more total energy due to the significantly higher spectral levels at the low wavenumbers.

Figures 4.84 through 4.87 show the spectra at the same times as before but for an initial integral lengthscale ratio of 0.5. Here the same comments apply as

for the $L_s/L_f(t = 0) = 1.0$ case. In addition, it should be noted that, while the low $A_s/A_v(t = 0)$ runs do convect sufficiently at early times to have higher high wavenumber spectral levels than the high $A_s/A_v(t = 0)$ runs (see Figure 4.85), by 4–5 eddy turnover times these levels are approximately equal (Figure 4.86) and by 6.5 eddy turnover times (Figure 4.87) the low $A_s/A_v(t = 0)$ runs once more have lower spectral levels than do the corresponding high $A_s/A_v(t = 0)$ runs at all wavenumbers. This is due to the effects of placing the spectra higher in the wavenumber range relative to the velocity field than was the case for the $L_s/L_f(t = 0) = 1.0$ runs. The lower initial A_s/A_v has a higher scalar energy level at the spectral peak which leads to enhanced convection. In Figures 4.76 through 4.79 this peak remains higher than that for the high initial A_s/A_v runs, although in Figure 4.79 they have become comparable. In Figures 4.84 through 4.87, the lower initial value of L_s/L_v places the scalar spectral peaks in a region of stronger diffusion and this reduces the low A_s/A_v spectral peak at a more rapid pace than was the case for L_s/L_v of unity.

Figures 4.88 through 4.91 illustrate the time progression of the spectra for $L_s/L_f(t = 0)$ values of 0.5 and 1.0 at $A_s/A_v(t = 0)$ of 0.94 while Figures 4.92 through 4.95 show similar runs for $A_s/A_v(t = 0) = 0.48$. Note that the initial value of R_λ was determined by adjusting the viscosity so for given initial values of L_s/L_v and A_s/A_v, the initial energy spectra did not change with R_λ. These figures show that while the high $L_s/L_f(t = 0)$ runs possess initially low spectral energy levels at high wavenumbers, over time the nonlinear transport raises these above those of the low $L_s/L_f(t = 0)$ such that the low $L_s/L_f(t = 0)$ runs are uniformly lower over the wavenumber range of the problem. It may also be noted that reverse nonlinear convection occurs at a higher rate for the low $L_s/L_f(t = 0)$ runs than the high

$L_s/L_f(t=0)$ runs. The former increase their low wavenumber levels by nearly three orders of magnitude while the latter by only one. This reverse cascade is sufficient to bring the spectral shapes into approximate similarity but not to equality. Even by 6.5 eddy turnover times, the high $L_s/L_f(t=0)$ runs have a sharper rolloff at high k than the low ones, thus yielding a somewhat lower energy decay rate.

The differences between the high and low $A_s/A_v(t=0)$ runs lies primarily in energy distribution about the spectral peak. High $A_s/A_v(t=0)$ initial conditions lead to a flat spectrum which spreads energy broadly about the peak while a low $A_s/A_v(t=0)$ concentrates it near the peak. The former produces relatively more rapid energy decay during the early part of the run (see Figure 4.67), roughly the first 2 to 3 eddy turnover times, but this achieves a "steady state" condition dominated by nonlinear convection down a scalar spectrum which descends gradually from a low wavenumber peak (Figure 4.91). The low $A_s/A_v(t=0)$ runs have relatively lower initial decay due to the very low initial energy levels in the high wavenumber diffusion range. The sharply peaked initial spectra lead to strong convection into the diffusion range where scalar energy is diffused at a "steady state" rate more rapid than that of the high $A_s/A_v(t=0)$ runs. Comparison of Figure 4.91 with Figure 4.95 shows how even after 6.5 eddy turnover times the low $A_s/A_v(t=0)$ runs have spectra with more pronounced peaks and, although the total energy at these late times is lower in the low than the high $A_s/A_v(t=0)$ runs, the scalar energy levels at the higher wavenumbers is comparable or higher, thus leading to significantly higher normalized decay rates. From this evidence, it appears reasonable to conclude that nonlinear convection of the scalar energy from low to high wavenumbers is stronger under conditions in which the scalar spectrum is sharply peaked (i.e., low $A_s/A_v(t=0)$)

than if it is broad (i.e., high $A_s/A_v(t=0)$).

The unexpected aspect of this is that A_s/A_v values are more effective than are L_s/L_f values in changing the physics of isotropic scalar turbulence behavior. One explanation for this is that changing the initial value of $L_s/L_f(t=0)$ changes only the wavenumber position of the spectrum. The spectral gradients remain the same so the scalar convection will be initially similar in all these cases. The changes in nonlinear convection (due to changes in the spectral gradients) is induced by the enhanced diffusion which occurs in the low $L_s/L_f(t=0)$ due to the higher wavenumber location of the spectrum. When $A_s/A_v(t=0)$ is varied at a given $L_s/L_f(t=0)$, the spectral wavenumber peaks are similar but the initial scalar spectral gradients are dramatically changed, which can dramatically alter the initial convection characteristics and subsequent decay of scalar energy.

When $L_s/L_f(t=0)$ is less than unity, this indicates that the scalar field "energy containing eddies" are smaller than are those for the velocity field. Figure 4.96 shows the evolution of this ratio for two different initial values of A_s/A_v, two of L_s/L_v, and three of R_λ. While R_λ can have a noticable effect upon the evolution of L_s/L_f the most interesting effect is due to varying A_s/A_v. The runs with $A_s/A_v = 0.94$ show significant growth of L_s/L_f while those with $A_s/A_v = 0.48$ show significant decline or modest growth depending upon the initial value of L_s/L_f. Runs with either initial value of L_s/L_f (0.5 or 1.0) appear to approach roughly similar asymptotic values in the range 0.6–0.7 and 1.2–1.4, respectively, and these asymptotic values are dependent upon the initial value, not of L_s/L_f, but of A_s/A_v. As shown above the inverse cascade of energy is not as efficient as the forward cascade. Thus the low wavenumber shape of the spectra tends to be more strongly dominated by the

initial spectral shape. Since this is important in the determination of the integral lengthscale, the initial A_s/A_v is apparently more important in the long term than initial L_s/L_f in determining later time values for the latter ratio.

Figure 4.97 shows the evolution of A_s for these initial conditions and, without exception, this ratio grows to some extent and then begins declining. The magnitude of the peak increases with the initial R_λ and inversely with initial L_s/L_f. The effects of L_s/L_f tend to disappear at long time (5–7 eddy turnover times) but the R_λ and A_s/A_v effects do not. It would be expected that, given sufficient time, the velocity field would generally act, through the nonlinear convection, to reform the scalar spectrum into a shape related to its own. Indeed, under conditions of steady state, the scalar spectral shape would depend heavily upon that of the velocity field (as well as any sources of scalar fluctuations).

Comparison of DIA with Experiments

Figures 4.99–4.104 compare the DIA results which best agreed with those of Warhaft and Lumley for the scalar energy and scalar diffusion. It should be noted that the experimental results were at conditions analogous to those of the high speed experiments of Sirivat and Warhaft. Thus the DIA computations were made with an excessively small bandwidth resulting in an ultraviolet buildup of energy at the higher wavenumbers for a period of time. Thus these computations should be viewed strictly as approximate models of the experiments with the inherent deficiencies due to the faults of the theory (lack of Galilean invariance) plus numerical deficiencies due to the bandwidth problems. The conditions used to achieve these DIA results are not expected to be appropriate for a proper numerical evaluation of the DIA for

this problem. Given these caveats, it is surprising that the DIA implemented here is capable of such close agreement with experiment.

The experimental values for the scalar energy are measured values, but the scalar diffusion values were not reported by Warhaft and Lumley. What is shown are the diffusion values predicted by the experimentally determined scalar energy decay rate. The scalar diffusion evolution equation, integrated over all k is derived as follows:

$$\frac{d}{dt}E_\theta(t) = -\varepsilon_\theta(t) \tag{4.53}$$

$$E_\theta(x/M) = B\left(\frac{x}{M}\right)^{-n} \tag{4.54}$$

$$\begin{aligned}
\varepsilon_\theta(t) &= -\frac{d}{dt}E_\theta(t) \\
&= -\frac{d}{dt}E_\theta(x/M) \\
&= -\frac{d}{d(x/M)}E_\theta(x/M)\frac{d(x/M)}{dt} \\
&= -\frac{1}{M}\frac{d}{d(x/M)}\left[B\left(\frac{x}{M}\right)^{-n}\right]\frac{dx}{dt} \\
&= \frac{-B}{M}\left[-n\left(\frac{x}{M}\right)^{-(n+1)}\right]\overline{U} \\
\Rightarrow \varepsilon_\theta(t) &= \frac{nB\overline{U}}{M}\left(\frac{x}{M}\right)^{-(n+1)}
\end{aligned} \tag{4.55}$$

where $\overline{U}$ is the mean tunnel velocity. The quantities $\overline{U}$, M and $\frac{x}{M}$ are determined by the laboratory windtunnel setup while n and B were determined from the measured decay of the scalar energy for each experiment. Equation (4.55) was used to compute the experimental values for the diffusion of the scalar energy for comparison with the DIA results.

Summary of Results

While previous studies (experimental and numerical) have determined that the initial relationship between the integral lengthscales of the velocity and scalar fields can have significant effects upon the evolution of decaying isotropic scalar turbulence, this study shows that the initial ratio of the spectral aspect ratios of the two fields exerts an even more profound influence. Initial Reynolds number effects are generally fairly minimal relative to these other two. Using various combinations of initial L_s/L_f and A_s/A_v in a series of DIA runs, this study has shown that nearly as wide a range of scalar variance decay exponents may be achieved as that seen in various experimental studies, and much wider than that reported by Mell, et al. [35]. The largest magnitude decay exponents measured in laboratory studies were not attained in this study, perhaps due to the inability to model a lower initial A_s/A_v using the specific spectral forms chosen. Future work could expand these possibilities by further generalizing the available initial spectral functional forms (e.g., arbitrary powers in the exponent of the exponential).

The results of this study indicate that the role of the initial L_s/L_f is to place the scalar spectrum relative to the velocity spectrum in wavenumber space. Thus, using the same spectral shapes and changing L_s/L_f acts to affect the initial scalar diffusion rates. Also, due to the varying effect of diffusion upon the scalar field depending upon its initial wavenumber placement, the "self-similar" decay rate may be varied. This occurs because the diffusion affects the scalar spectral gradients differently as L_s/L_f varies. These spectral gradients are profoundly affected by the choice of initial A_s/A_v and, since these shapes tend to persist, especially at the low wavenumbers, A_s/A_v has a stronger effect upon the decay exponent than does L_s/L_f. In terms of the

spectral gradients, as the initial R_λ increases, it tends only to broaden the scalar spectrum which has a minimal effect upon overall scalar decay. Therefore, in studies of decaying isotropic scalar turbulence, as in decaying isotropic velocity turbulence, the value of A_s/A_v chosen for the initial conditions has a significant impact upon the evolution of the system and must be taken into account in any attempt to model real physical turbulence. Further, the DIA shows promise as a useful tool for the prediction of the behavior of isotropic scalar turbulence.

The Passive Scalar Transport Problem

Once the appropriate initial conditions have been determine to model the velocity field, the next step is to determine the appropriate initial scalar conditions to properly predict the evolution of the scalar field. As the velocity field conditions are now fixed, this task consists of determining an appropriate initial scalar field (just as in the isotropic decaying scalar problem), and appropriate transport characteristics. This section studies the effects of these upon the evolution of the scalar field.

The Scalar Field

Previous experimental studies of passive scalar transport have examined the effects of varying the mean scalar gradient, initial integral lengthscales, initial integral lengthscale ratios and initial scalar field intensity. These variables will also be studied here using the DIA closure theory. Figure 4.105 illustrates the effects of changes in the mean scalar gradient. Note that runs TB and TK (with zero initial conditions) yield identical growth of the scalar energy field. This is a consequence of the normalization of the scalar variable using the magnitude of the scalar gradient. Since the scalar

governing equations are linear in the scalar variable and the scalar gradient only multiplies the (linear) velocity term this normalization reduces the scalar gradient term to a vector of unity magnitude. Thus this result is mathematically consistent and predictable and the DIA computations reflect this. Experimental results, such as those of Sirivat and Warhaft [45], are consistent with this.

Figures 4.106 and 4.107 show the results of changing initial scalar intensity on scalar field evolution at two different initial integral lengthscale ratios (0.25 and 0.50). Both Figures use run TB (with zero initial scalar field) as a reference. Clearly changing the initial scalar intensity or lengthscale ratio significantly influence the early time behavior of the scalar field. However, all runs asymptotically approach run TB. This is a graphic numerical confirmation of the trends observed by Sirivat and Warhaft. This asymptotic behavior as determined by the zero initial scalar field transport problem plus the linearity of the scalar field governing equations prompted the investigation into the viability of using linear superposition of a problem of decaying isotropic scalar turbulence incorporating all nonzero initial scalar conditions with a passive scalar transport problem incorporating all transport characteristics but zero initial scalar field and mathematically, this superposition principle holds for homogeneous passive scalar transport with uniform mean scalar gradient.

Figure 4.108 compares the scalar field evolution for problems with identical initial (normalized) scalar intensities but different initial integral lengthscale ratios (L_s/L_v). As this ratio varies from 0.00 to 1.50 the scalar field behaves quite differently. Low nonzero initial lengthscale ratios represent situations in which most of the scalar energy resides at higher wavenumbers than the velocity peak spectral wavenumber, in the dissipation region of the velocity spectrum. As L_s/L_v increases, the scalar energy

increasingly shifts from wavenumbers high in the velocity spectrum to wavenumbers below the velocity peak, thus placing a decreasing fraction of scalar variance in this dissipation region. This is reflected in the Figure by decreasing scalar diffusion rates at early times (actually initial scalar growth for L_s/L_v of 1.50). This has the additional effect of delaying the time and rate of approach to the asymptotic state represented by run TB. Thus, as seen experimentally, the initial value of L_s/L_v can significantly affect the initial evolution of a passive scalar transport problem.

The next few Figures compare the evolution of the DIA scalar energy with that measured by Sirivat and Warhaft. Figure 4.109 compares the DIA results for zero initial scalar field (i.e., the asymptotic state for DIA runs with nonzero initial scalar conditions) with several low speed runs reported by Sirivat and Warhaft. These were preferentially selected as they appear to have minimal initial scalar field values. The velocity field was that found to best agree with the low speed turbulence velocity fields and thus the value of the Taylor microscale used to normalize the DIA scalar field was that at the nondimensional time corresponding to the experimental $x/M = 40$ measurement station. Two differences are notable. The first is that, although the DIA results are quite close to those of experiment at early times, it is at the low end and remains there up to about 4 eddy circulation times. The growth rate of the DIA scalar field is close to, although also somewhat lower than, the measured results. More dramatic, and more troubling, is that, after 4 circulation times, all three experimental runs exhibit a significant increase (roughly a doubling) in the growth rate while the DIA results experience a slow but steady decrease of its growth rate. Figure 4.110 shows the low speed Sirivat and Warhaft results which appear to have a significant initial scalar energy field since these two runs have scalar diffusion

dominating the scalar transport. These are compared with DIA runs having various initial levels of scalar intensity. All DIA runs exceed the experimental results over much of the measurement regime. By varying the combination of initial values of scalar intensity and L_s/L_v the DIA results can be manipulated to yield a wide range of behavior during the first roughly 3 eddy circulation times. The scalar variance minima occur in the 2.6–3.0 circulation time region while those for the DIA generally occur before that. Run TJ is the sole DIA run which hits a minimum in this time region but it does not possess sufficient curvature or a small enough magnitude to accurately model the experiments. Finally, when the experimental results do begin growing, the growth rate is again significantly higher than that of the DIA results.

While the proximity of the DIA and experimental results in magnitude is encouraging, the qualitative differences indicate that there are still differences of some significance. The shapes of the two curves in Figure 4.110 relative to those of the DIA results suggest two possibilities, both related to the low growth rates exhibited by the runs until nearly 4 eddy cycles. One is that the initial scalar fields may be quite large to account for the broad and rather significant minima displayed. DIA runs such as TD and TF appear to account for the scalar energy drop exhibited in the experimental run "S/W Low; 2.24" while run TJ exhibits the broad minimum and approximately correct timing of the minimum point of "S/W Low; 1.78". It might be possible, with the correct combination of initial scalar field and initial value for L_s/L_v to correctly model these two runs. A second possibility is that, with a moderate (or negligible) initial scalar field, the generation of the scalar gradient may have produced some initial net counter–gradient scalar transport between the wakes of the mandoline wires prior to the final establishment of the mean scalar field. While

this would serve to establish a growing scalar field early in the flow, it would take some time after the mean field was well established to reorient the scalar flux in the down gradient direction, during which scalar fluctuation production would be reduced allowing diffusion to reduce its intensity. Numerically this could be simulated by initializing the scalar transport fields to some positive value which, in time, would be reoriented to a negative value by the action of the velocity field upon the mean scalar gradient. All runs in this study were initialized with zero initial scalar transport.

A final possible explanation for the discrepancies between the numerical and experimental results arises from bandwidth limitations in the computations. At later times in the DIA runs, the spectral peaks are at the low end of the spectral grid, typically residing close to the second to lowest wavenumber grid. This might introduce error into the computations of the nonlinear convection terms.

Figures 4.111–4.115 compare a range of DIA runs with all the low speed experimental data. While the various initial conditions for the DIA runs provide for varying degrees of agreement with experiment at early and intermediate times, all tend to converge to the same asymptotic behavior which differs from that of the final experimental points.

Figure 4.116 compares a number of DIA runs, differing in the initial scalar field conditions, with the high speed experimental "toaster" runs of Sirivat and Warhaft. As was mentioned in the discussion of the modeling of the high speed velocity field, the spectral bandwidth of the DIA computations was inadequate at the high end, yielding an accumulation of kinetic turbulence energy at the higher wavenumbers during a portion of the runs. This did not seem to harm the isotropic decaying scalar

turbulence simulations but here it results in a significant overprediction of the scalar field growth. As in the low speed results, the different initial conditions significantly alter the early time behavior but the tendency towards similar asymptotic states is also present.

Figures 4.117–4.119 compare the evolution of the scalar spectral ratio, A_s, as predicted by the DIA and measured experimentally. It is not surprising that, in time, all runs approach similar asymptotic states since the velocity field is the same in all cases and it (through the scalar transport) dominates the problem with time. Note, however, that the reduction of the mean scalar gradient magnitude from 1.0 to 0.5 significantly affects A_s throughout the run in both Figures 4.117 and 4.118. This does not appear to affect the total scalar field. In all cases with unity mean scalar gradient, both for the low and high speed problems, the DIA and measured spectral aspect ratios are quite close in evolution and magnitude. Although this is gratifying, it is not unexpected as the DIA velocity fields were matched to those of the experiments as closely as possible.

The behavior of the scalar/mechanical integral lengthscale ratio is more perplexing. This is shown in Figures 4.120 through 4.122. Again the value of the mean scalar gradient significantly affects the evolution of this quantity although it still appears that the final asymptotic value is unchanged. In all low speed cases, the DIA ratio peaks at 1–2 eddy circulation times and then decreases to some asymptotic value. The experimental values, with the exception of the "S/W Low: 2.24" run, tend to hover around the 0.8–1.0 range. The low speed DIA values appear to tend towards unity, with the runs with mean scalar gradient of 0.5 being significantly slower in their approach. The high speed DIA runs are significantly higher than experimental

values, probably because the bandwidth of the computations was too narrow for this vigorous a flow.

The Scalar Transport Field

The eddy diffusivity ratios are presented in Figures 4.123 through 4.125. All scalar transport fields were initialized at zero, the velocity fields were identical for all the low speed and all the high speed runs and the only scalar field terms entering into the computation of the scalar transport nonlinear terms are the response functions. Thus the DIA predicted diffusivity ratios for a given initial velocity field are essentially identical, being independent of the initial scalar energy fields. The low speed DIA results lie in the middle of the experimental range of results and their time evolutionary behavior is very similar to that of the experiments which appeared not to have significant initial scalar energy or counter-gradient diffusion. The two runs which did appear to have these initial conditions ("S/W Low; 1.78" and especially "S/W Low; 2.24") display a different evolution with sustained growth of the eddy diffusivity.

While the high speed DIA diffusivity ratio evolution (Figure 4.125) appears to decay in a manner consistent with that of experiment, it achieves too high a peak value due to the inadequate modeling of the velocity field. Nevertheless, the DIA results are surprisingly close in magnitude to measured values so correction of the bandwidth appears to be the solution for correcting the DIA errors.

Figures 4.126 and 4.127 compare the DIA low speed scalar transport correlation coefficients with those measured by Sirivat and Warhaft while Figure 4.128 compares the high speed results. In Figures 4.126 and 4.127 it can be seen that the low ini-

tial scalar/mechanical lengthscale ratios result in a too rapid buildup of $\rho_{u\theta}$ and the asymptotic value has somewhat too high a magnitude. Initial values of L_s/L_v of 0.5 to 1.5 (in Figure 4.127) better simulate the behavior of the experiments. The two experimental runs labeled "S/W Low; 2.24" behave in a manner consistent with an initially positive correlation coefficient (corresponding to an initial countergradient transport of scalar) while the mean scalar field is establishing itself. This cannot be positively verified. Although the high speed DIA results must be viewed with skepticism due to the insufficiently wide bandwidth, the experimental data does appear consistent with a small initial L_s/L_v. The DIA results are comparable in value to measurements because the increased DIA scalar transport is normalized and compensated by the increased scalar field magnitude.

The final point of comparison between the DIA and experiment is the mechanical/thermal timescale, r, shown in Figures 4.129–4.131. The DIA results generally achieve values at the high end or higher than those measured in both low and high speed experiments. The low speed experimental values appear to asymptote to values in the range of 1.4–1.8 while the numerical asymptote appears to be somewhat less than 2.

Conclusions

In this study the DIA was used to study and model decaying isotropic turbulent velocity fields of two strengths, several decaying isotropic turbulent scalar fields of different decay behavior, and several problems involving isotropic turbulence transporting a passive scalar in the presence of a uniform mean scalar gradient. DIA runs were designed to model the experimental velocity and passive scalar transport results

of Sirivat and Warhaft and the decaying isotropic scalar experiments of Warhaft and Lumley.

The study of the decaying isotropic turbulent velocity field showed that the most important modeling parameters were the Reynolds number (R_λ) of the turbulence (based upon the Taylor microscale) and the spectral aspect ratio, $A_v \equiv L_v/\lambda_g$. This aspect ratio was shown to explain the different dynamic behavior of computations initialized with exponential and Gaussian initial spectral shapes in that they have different spectral geometries. "Exponential" and "Gaussian" spectra which were designed to have similar initial values of the aspect ratio (by varying the exponent (n) of the k^n multiplying the exponential term) led to velocity fields which evolved similarly. Matching the evolutionary behavior of both R_λ and A_v between the DIA computations and experiments was shown to yield accurate modeling of the evolution of the turbulence kinetic energy and its dissipation.

To accurately model the decaying isotropic scalar field requires first the accurate modeling of the dynamics of its velocity field. This was done as outlined above. This study found that, in addition to the initial scalar/mechanical integral lengthscale ratio (L_s/L_v), the initial scalar/mechanical aspect ratio (A_s/A_v) plays a very important role in determining the time behavior of the scalar field. Employment of the proper combination of initial values of these two modeling parameters allowed accurate computation of the behavior of several decaying isotropic scalar fields reported by Warhaft and Lumley. Both scalar energy and scalar diffusion were accurately computed.

The turbulent transport of the passive scalar reported by Sirivat and Warhaft were also modeled using the DIA and the velocity conditions found to accurately

compute their velocity fields. Due to the linearity of the governing equation for the scalar fluctuation variable it was shown that this problem was a linear superposition of a decaying isotropic turbulent scalar field with all the initial scalar field conditions and a passive transport problem with zero initial scalar field. This allows the decoupling of their effects. A number of runs were made using various initial scalar fields and it was shown that, except for a couple of lengthscale quantities, the magnitude of the mean scalar gradient did not influence the problem (normalized as it was). While highly accurate modeling of these problems was not accomplished, the DIA was able to reasonably predict the magnitude and temporal behavior of the scalar and scalar transport fields. It appeared that some of the experimental results were consistent with either very large initial scalar fields and/or initially counter-gradient scalar transport. This was not investigated in detail by this study.

In summary, this study shows the DIA may be of value in modeling the behavior of isotropic velocity fields and their associated scalar fields, with and without uniform mean scalar gradient transport.

Acknowledgements

The authors gratefully acknowledge the computer facilities provided by APTEK, Inc. and the first author is very grateful for the support, encouragement and conversations with Mr. Thomas Meagher and Dr. Eugene Fitzgerald, both of APTEK.

References

[1] Alexopoulos, C.C. and Keffer, J.F.; Turbulent wake in a passively stratified field. Phys. Fluids, **14**, pp. 216–224, 1971.

[2] Batchelor, G.K.; Small-scale variation of convected quantities like temperature in turbulent fluid. Part 1. General discussion and the case of small conductivity. J. Fluid Mech., **5**, pp. 113–133, 1959.

[3] Batchelor, G.K., Howells, I.D. and Townsend, A.A.; Small-scale variation of convected quantities like temperature in turbulent fluid. Part 2. The case of large conductivity. J. Fluid Mech., **5**, pp. 134–139, 1959.

[4] Budwig, R., Tavoularis, S. and Corrsin, S.; Temperature fluctuations and heat flux in grid generated isotropic turbulence. J. Fluid Mech., **153**, pp. 441–460, 1985.

[5] Cambon, C., Jeandel, D. and Mathieu, J. Spectral modelling of homogeneous non-isotropic turbulence. J. Fluid Mech., **104**, pp. 247–262, 1981.

[6] Corrsin, S.; On the spectrum of isotropic temperature fluctuations in an isotropic turbulence. J. Appl. Phys., **22**, pp. 469–473, 1951.

[7] Corrsin, S.; Heat transfer in isotropic turbulence. J. Appl. Phys. **23**, pp. 113–118, 1952.

[8] Chakrabarti, M. Numerical studies of chemical selectivity and heat transfer in decaying homogeneous turbulence. Ph.D. Thesis, Iowa State University, Ames, Ia., 1991.

[9] Chasnov, J.R.; Similarity states of passive scalar transport in isotropic turbulence. Phys. Fluids, 6, pp. 1036–1051, 1994.

[10] Craya, A. *Contribution a l'Analyse de la Turbulence a des Vitesse Moyennes*, P.S.T. Ministere de l'Air (Fr.), 1958.

[11] Dannevik, W.P., Yakhot, V. and Orszag, S.A.; Analytical theories of turbulence and the ϵ-expansion, Phys. Fluids, **30**, pp. 2021–2029, 1987.

[12] Durbin, P.A.; Analysis of the decay of temperature fluctuations in isotropic turbulence. Phys. Fluids, **25**, pp. 1328–1332, 1982.

[13] Eswaran, V. and O'Brien, E.E.; Simulations of scalar mixing in grid turbulence using an eddy-damped closure model. Phys. Fluids A, **1**, pp. 537–548, 1989.

[14] Eswaran, V. and Pope, S.B.; Direct numerical simulations of the turbulent mixing of a passive scalar. Phys. Fluids, **31**, pp. 506–520, 1988.

[15] Gibson, C.H.; Fine structure of scalar fields mixed by turbulence. I. Zero-gradient points and minimal gradient surfaces. Phys. Fluids, **11**, pp. 2305–2315, 1968.

[16] Gibson, C.H.; Fine structure of scalar fields mixed by turbulence. II. Spectral theory. Phys. Fluids, **11**, pp. 2316–2327, 1968.

[17] Gibson, M.M. and Dakos, T.; Production of temperature fluctuations in grid turbulence: Wiskind's experiment revisited. Exp. in Fluids, **16**, pp. 146–154, 1993.

[18] Grant, H.L., Stewart, R.W. and Moilliet, A.; Turbulence spectra from a tidal channel. J. Fluid Mech., **12**, pp. 241–268, 1962.

[19] Grant, H.L., Hughes, B.A., Vogel, W.M. and Moilliet, A.; The spectrum of temperature fluctuations in turbulent flow. J. Fluid Mech., **34**, pp.423–442, 1968.

[20] Herring, J.R.; Approach of axisymmetric turbulence to isotropy. Phys. Fluids **17**, pp. 859–872, 1974.

[21] Herring, J.R., Schertzer, D., Lesieur, M., Newman, G.R., Chollet, J.P. and Larcheveque, M.; A comparative assessment of spectral closures as applied to passive scalar diffusion. J. Fluid Mech., **124**, pp. 411–437, 1982.

[22] Métais, O. and Herring, J.R.; Numerical simulations of freely evolvoing turbulence in stably stratified fluids. J. Fluid Mech., **202**, pp. 117–148, 1989.

[23] Herring, J.R. and Métais, O.; Numerical experiments in forced stably stratified turbulence. J. Fluid Mech., **202**, pp. 97–115, 1989.

[24] Herring, J.R. and Kerr, R.M.; Comparison of direct numerical simulations with predictions of two-point closures for isotropic turbulence convecting a passive scalar. J. Fluid Mech., **118**, pp. 205–219, 1982.

[25] Hill, J.C.; Heat transfer in isotropic turbulence.; Chem. Eng. Commun., **12**, pp. 69–96, 1981.

[26] Hinze, J.O. *Turbulence,* 2^{nd} *edition.* McGraw–Hill Book Co., New York, N.Y., 1975.

[27] Kolmogorov, A.N.; The local structure of turbulence in incompressible viscous fluid for very large Reynolds numbers. Compte. rendu. Acad. Sci. URSS, **30**, pp. 301, 1941.

[28] Kraichnan, R.H.; The structure of turbulence at very high Reynolds numbers, J. of Fluid Mech., **5**, pp. 497–543, 1959.

[29] Kraichnan, R.H.; Decay of isotropic turbulence in the direct–interaction approximation. Phys. Fluids, **7**, pp. 1030–1048, 1964.

[30] Kraichnan, R.H.; The direct interaction approximation for shear and thermally driven turbulence. Phys. Fluids., **7**, pp. 1048–1062 ,1964.

[31] Kraichnan, R.H.; Convergents to turbulence functions. J. Fluid Mech., **41**, pp. 189–217, 1970.

[32] Kraichnan, R.H.; Small–scale structure of a scalar field convected by turbulence. Phys. Fluids, **11**, pp. 945–953, 1968.

[33] Kraichnan, R.H.; An almost markovian Galilean–invariant turbulence model. J. Fluid Mech., **47**, pp. 513–524, 1971.

[34] Leslie, D.C.; *Developments in the theory of turbulence*, Oxford University Press; Oxford, England, 1973.

[35] Mell, W.E., Kosály, G. and Riley, J.J.; The length–scale dependence of scalar mixing. Phys. Fluids A, **3**, pp. 2474–2476, 1991.

[36] Métais, O. and Herring, J.R.,; Numerical simulations of freely evolving turbulence in stably stratified fluids. J. Fluid Mech., **202**, pp. 117–148, 1989.

[37] Newman, G.R. and Herring, J.R.; A test field model study of a passive scalar in isotropic turbulence. J. Fluid Mech., **94**, pp. 163–194, 1979.

[38] Oboukhov, A.M.;Isotropic scalar turbulence in infinite turbulence. Compte Rendu Acad. Sci. URSS, 1947.

[39] Orszag, S.A.; Analytical theories of turbulence. J. Fluid Mech., **41**, pp. 363–386, 1970.

[40] Orszag, S.A. and Patterson, G.S.; in *Statistical Models and Turbulence.* Springer–Verlag, New York, 1972.

[41] Riley, J.J., Metcalfe, R.W. and Weissman, M.A.; Direct numerical simulations of homogeneous turbulence in density–stratified fluids. pp. 79–112, 1981.

[42] Sanderson, R.C., Hill, J.C. and Herring, J.R.; Transient behavior of a stably stratified homogeneous turbulent flow. in Advances in Turbulence, G. Comte–Bellot and J. Mathieu, eds., 1987.

[43] Sanderson, R.C. and Hill, J.C.; Dynamics of decaying stably stratified turbulent flow, Presented at the Geophysical Turbulence Symposium of the American Meteorological Society, San Diego, Ca., 1988.

[44] Sanderson, R.C., Leonard, A.D., Herring, J.R. and Hill, J.C.; Fossil and active turbulence. In *Turbulence and Coherent Structures*, M. Lesieur and O. Métais, eds., Kluwer Academic Press, 1989.

[45] Sirivat, A. and Warhaft, Z.; The effect of a passive cross–stream temperature gradient on the evolution of temperature variance and heat flux in grid turbulence. J. Fluid Mech., **128**, pp. 323–346, 1983.

[46] Smith, L.M. and Reynolds, W.C.; On the Yakhot–Orszag renormalization group method for deriving turbulence statistics and models. Phys. Fluids A, **4**, pp 364–390, 1992.

[47] Venkataramani, K.S. and Chevray, R.; Statirtical features of heat transfer in grid–generated turbulence: constant–gradient case. J. Fluid Mech., **86**, pp. 513–543, 1978.

[48] Warhaft, Z. and Lumley, J.L.; An experimental study of the decay of temperature fluctuations in grid–generated turbulence. J. Fluid Mech., **88**, pp. 659–684, 1978.

[49] Wiskind, H.K.; A uniform gradient turbulent transport experiment. J. Geophys. Res., **67**, pp. 3033–3048, 1962.

[50] Yakhot, V. and Orszag, S.A.; Renormalization group analysis of turbulence. I. Basic Theory, J. Sci. Comp., **1**, pp. 3–51, 1986.

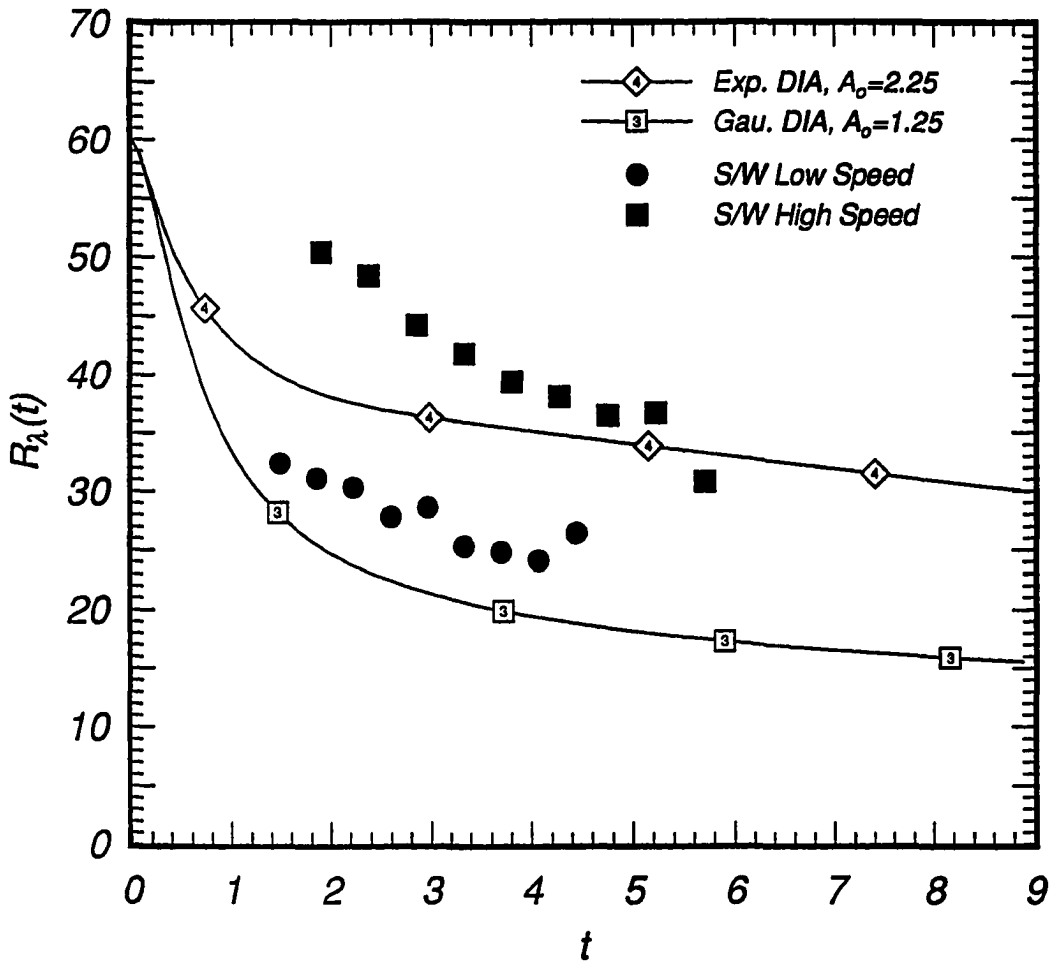

Figure 4.1: Evolution of DIA R_λ for Gaussian and exponential initial spectra, $L_{vo} = 0.495$.

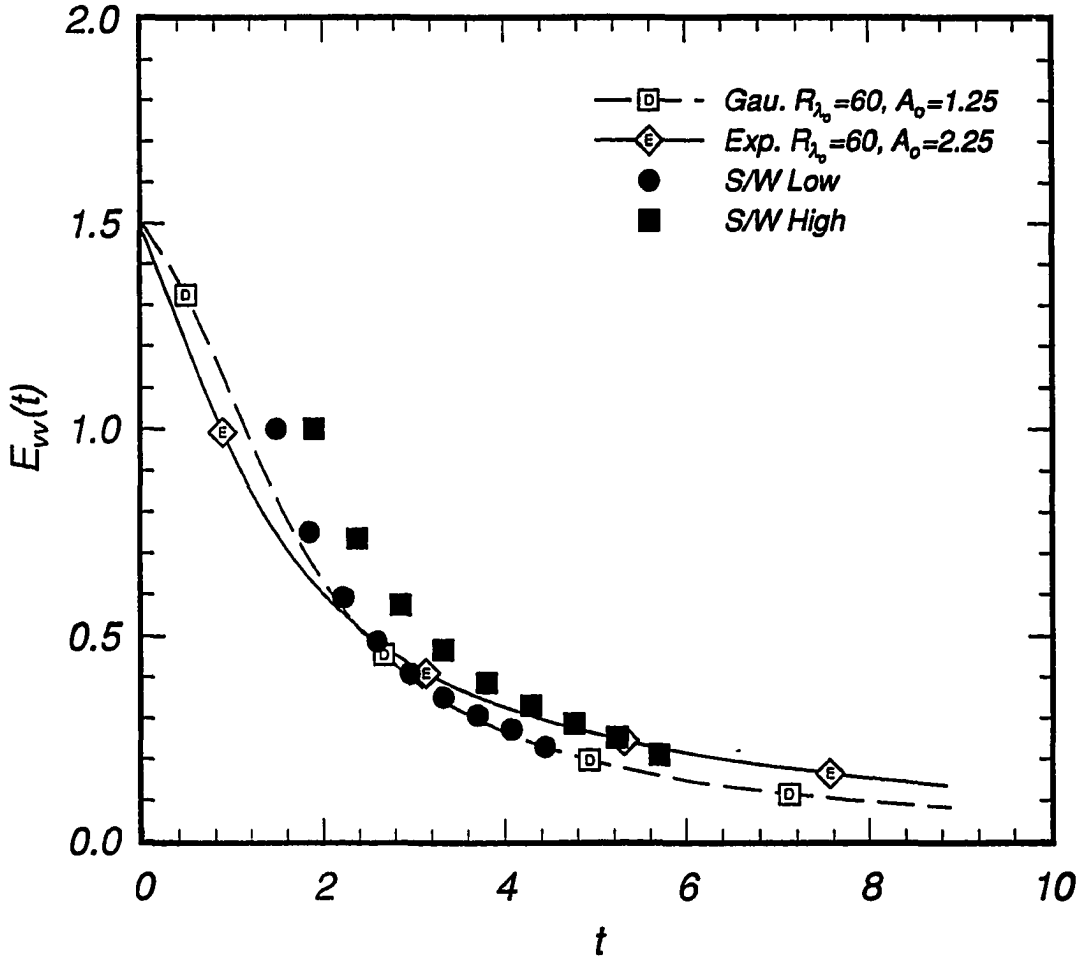

Figure 4.2: Evolution of DIA kinetic energy for Gaussian and exponential initial spectra, $L_{vo} = 0.495$.

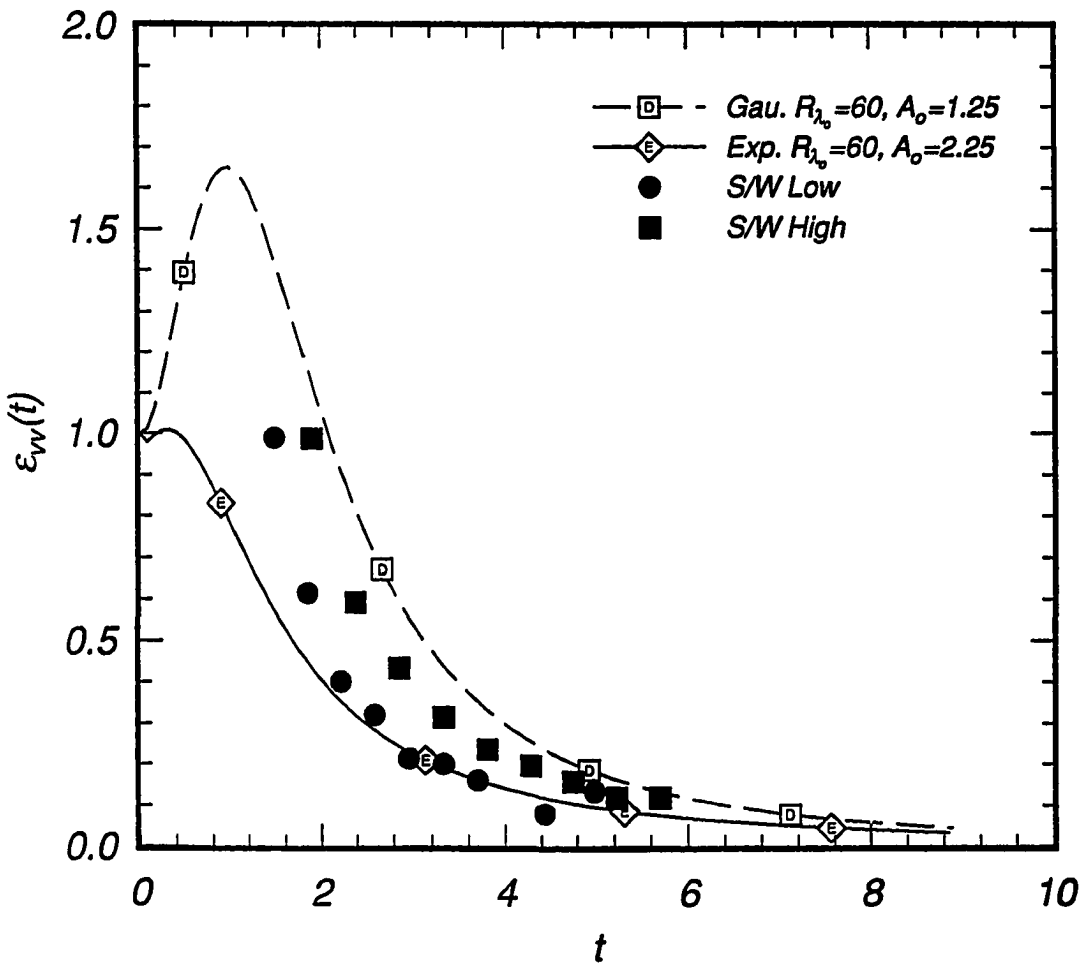

Figure 4.3: Evolution of DIA energy dissipation for Gaussian and exponential initial spectra, $L_{vo} = 0.495$.

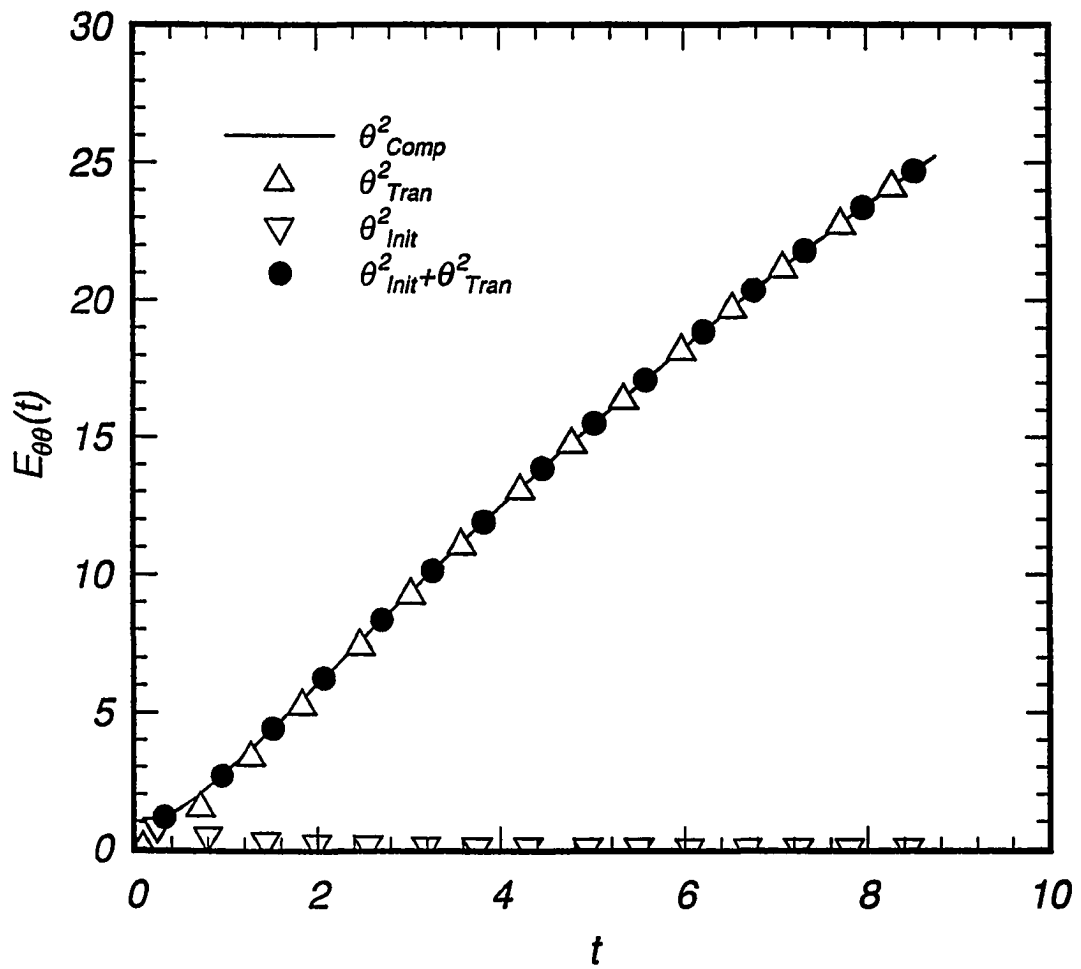

Figure 4.4: Comparison of complete scalar problem, θ^2_{Comp}, with the isotropic initial problem, θ^2_{Init}, the initially zero scalar transport problem, θ^2_{Tran}, and their sum, $\theta^2_{Init} + \theta^2_{Tran}$.

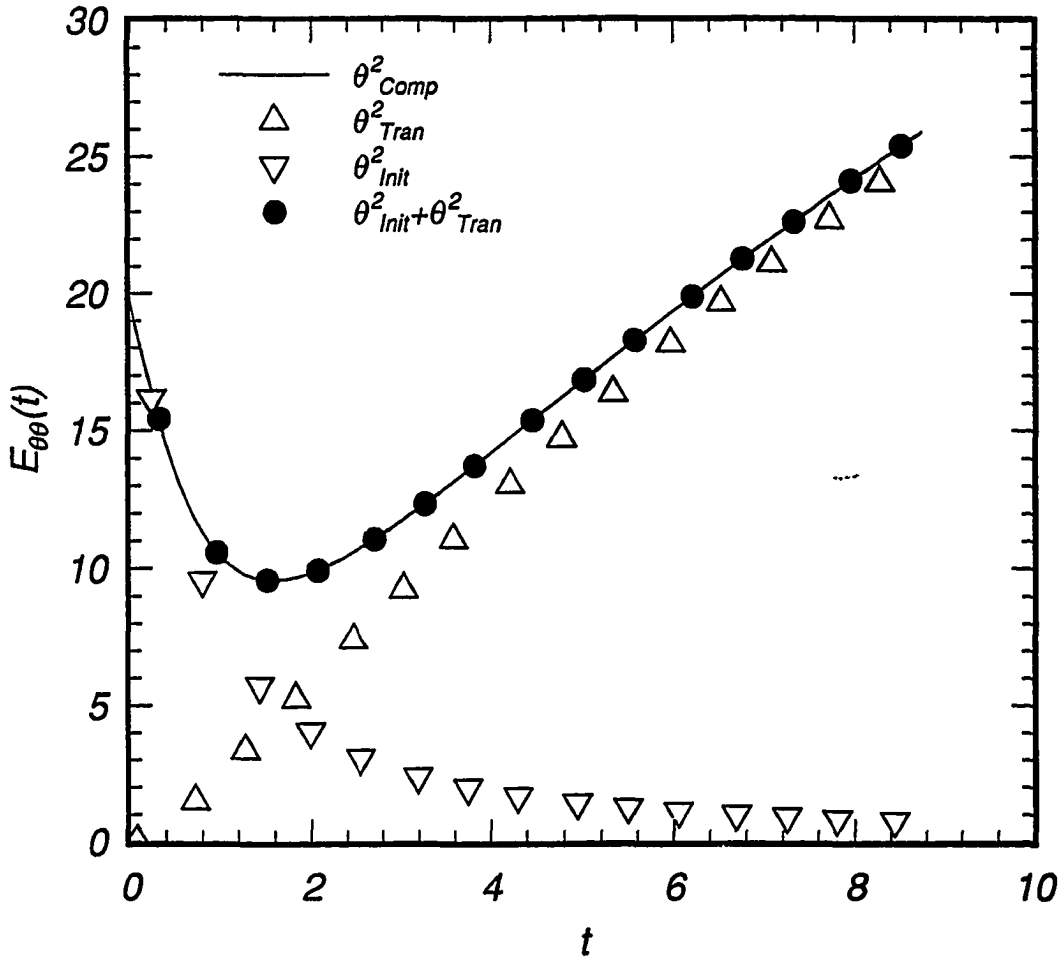

Figure 4.5: Comparison of complete scalar problem, θ^2_{Comp}, with the isotropic initial problem, θ^2_{Init}, the initially zero scalar transport problem, θ^2_{Tran}, and their sum, $\theta^2_{Init} + \theta^2_{Tran}$.

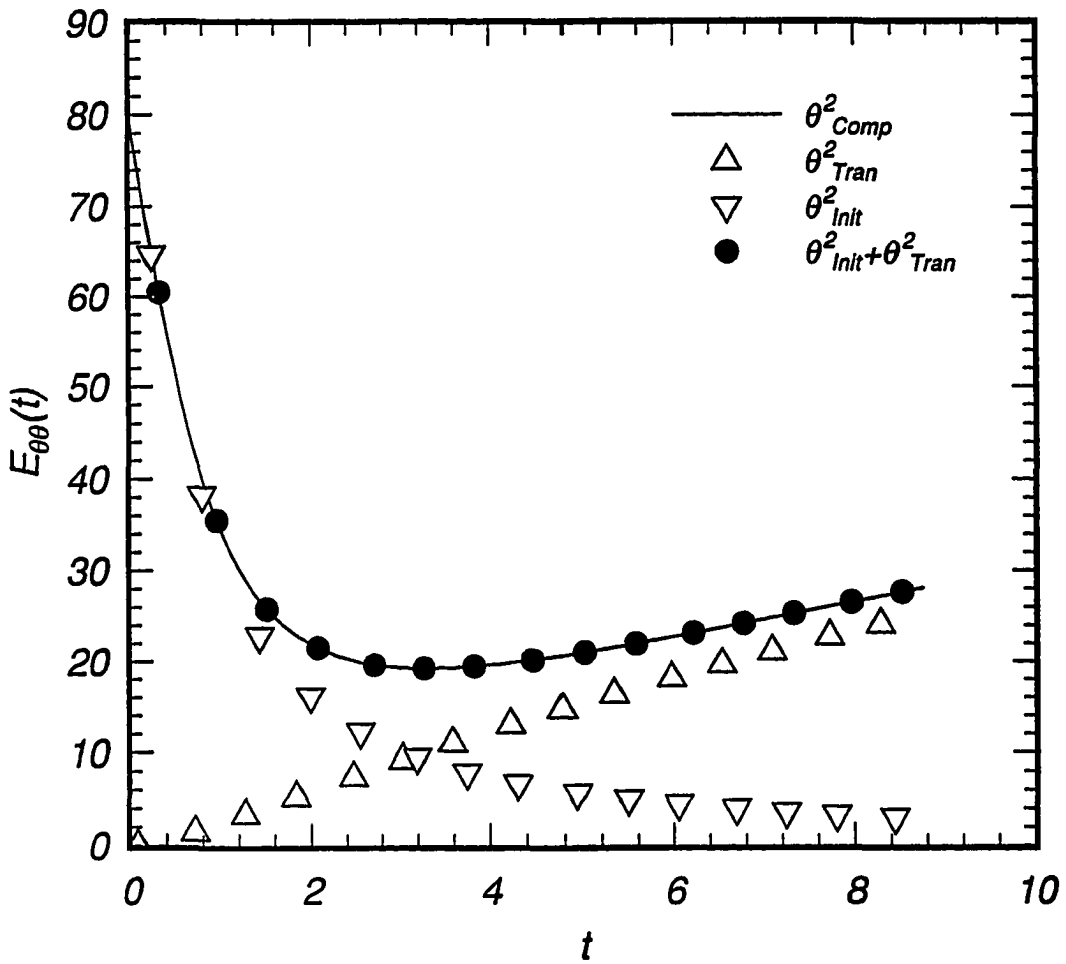

Figure 4.6: Comparison of spectra for the complete scalar problem, $\theta^2_{Comp}(k)$, with the isotropic problem, $\theta^2_{Init}(k)$, the initially zero scalar transport problem, $\theta^2_{Tran}(k)$, and their sum, $\theta^2_{Init}(k) + \theta^2_{Tran}(k)$, $t = 2.13$.

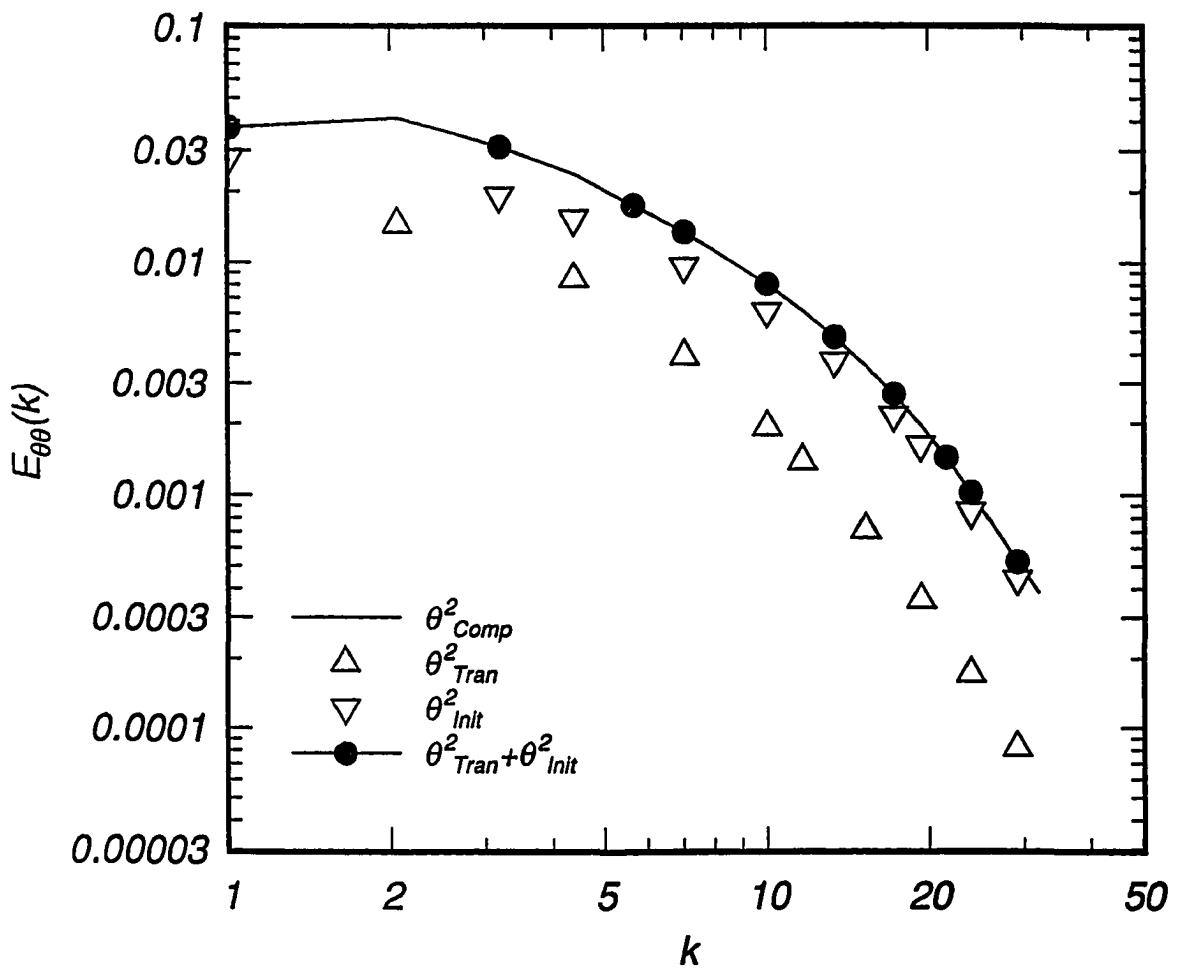

Figure 4.7: Comparison of spectra for the complete scalar problem, $\theta^2_{Comp}(k)$, with the isotropic problem, $\theta^2_{Init}(k)$, the initially zero scalar transport problem, $\theta^2_{Tran}(k)$, and their sum, $\theta^2_{Init}(k) + \theta^2_{Tran}(k)$.

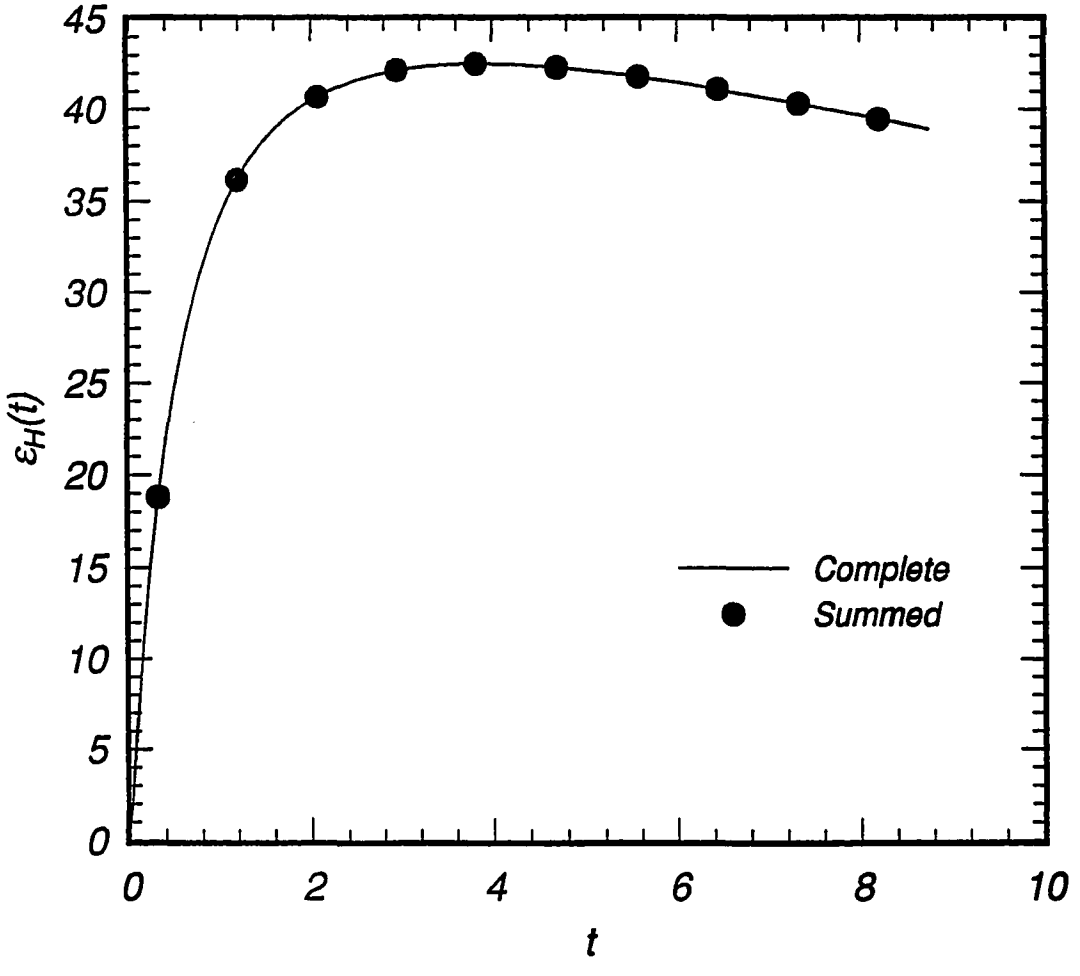

Figure 4.8: Comparison of eddy diffusivity ratios for complete and zero initial scalar field scalar transport problems.

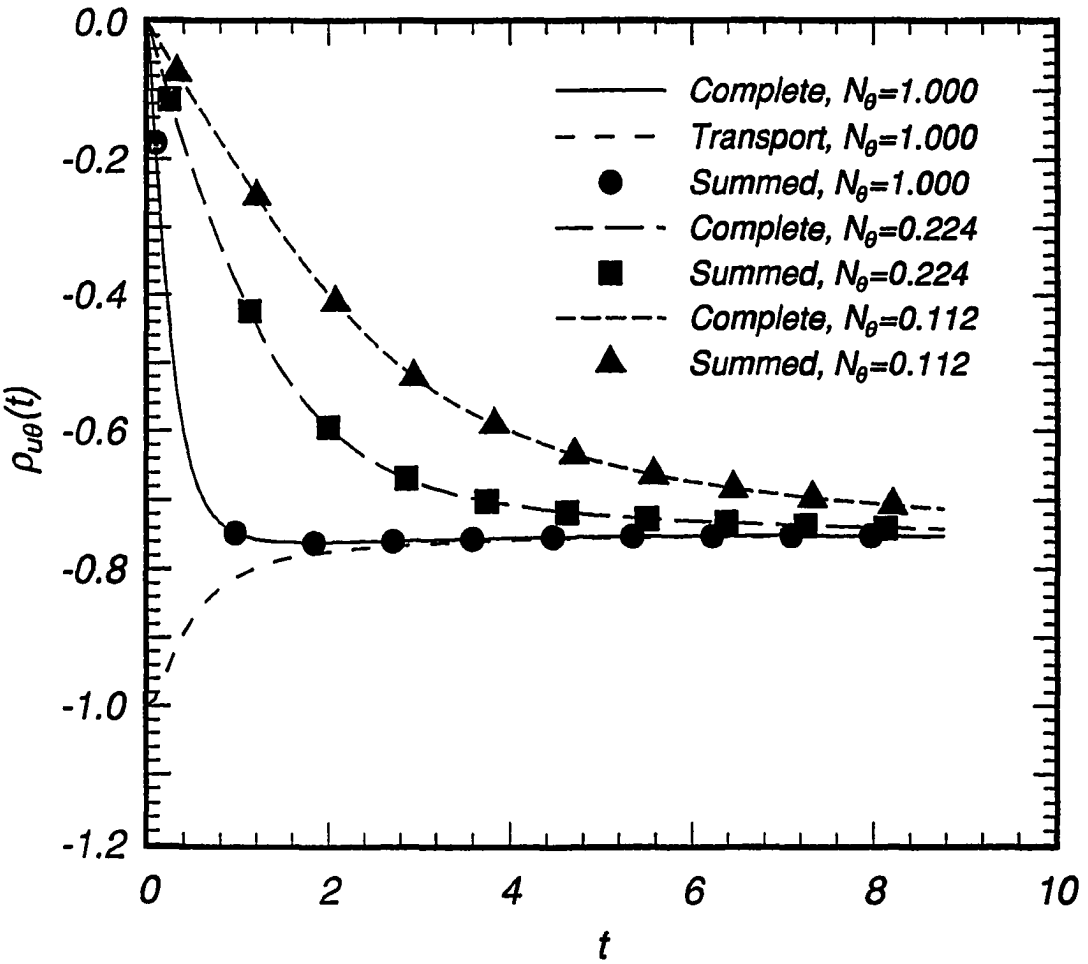

Figure 4.9: Comparison of scalar transport correlation coefficients for the complete problem with isotropic initial problem, initially zero scalar transport problem and their sum.

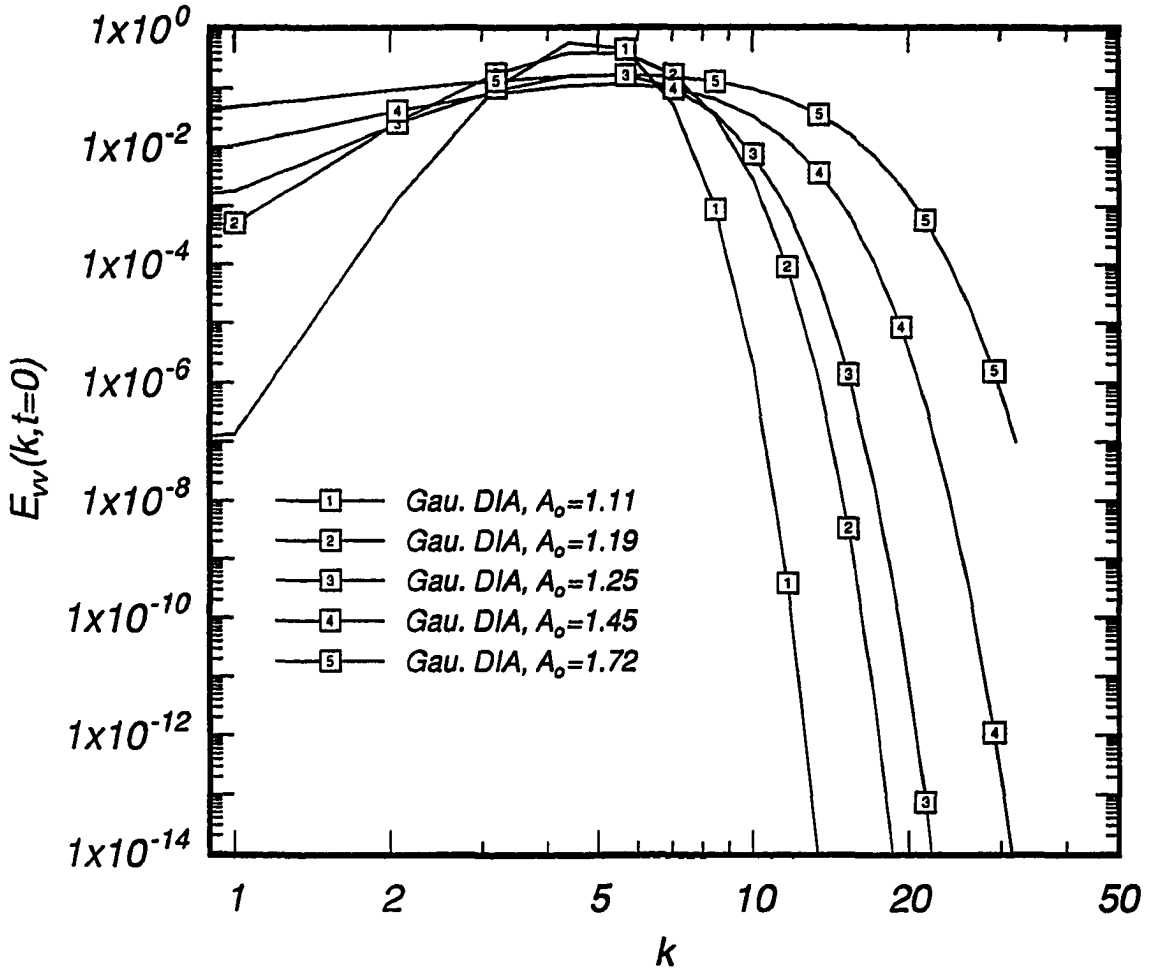

Figure 4.10: Initial exponential spectra for different values of A, $L_{vo} = 0.495$.

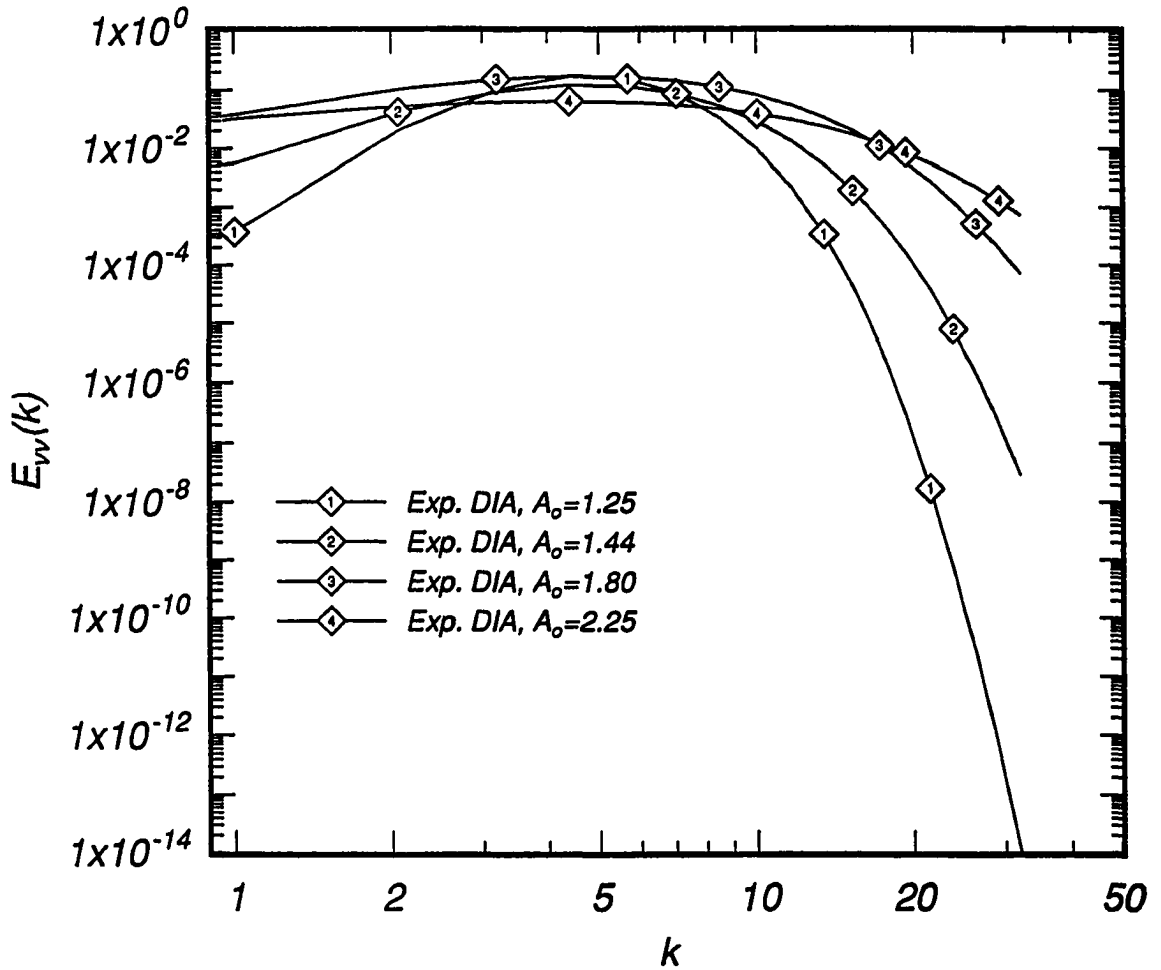

Figure 4.11: Initial Gaussian spectra for different values of A, $L_{vo} = 0.495$.

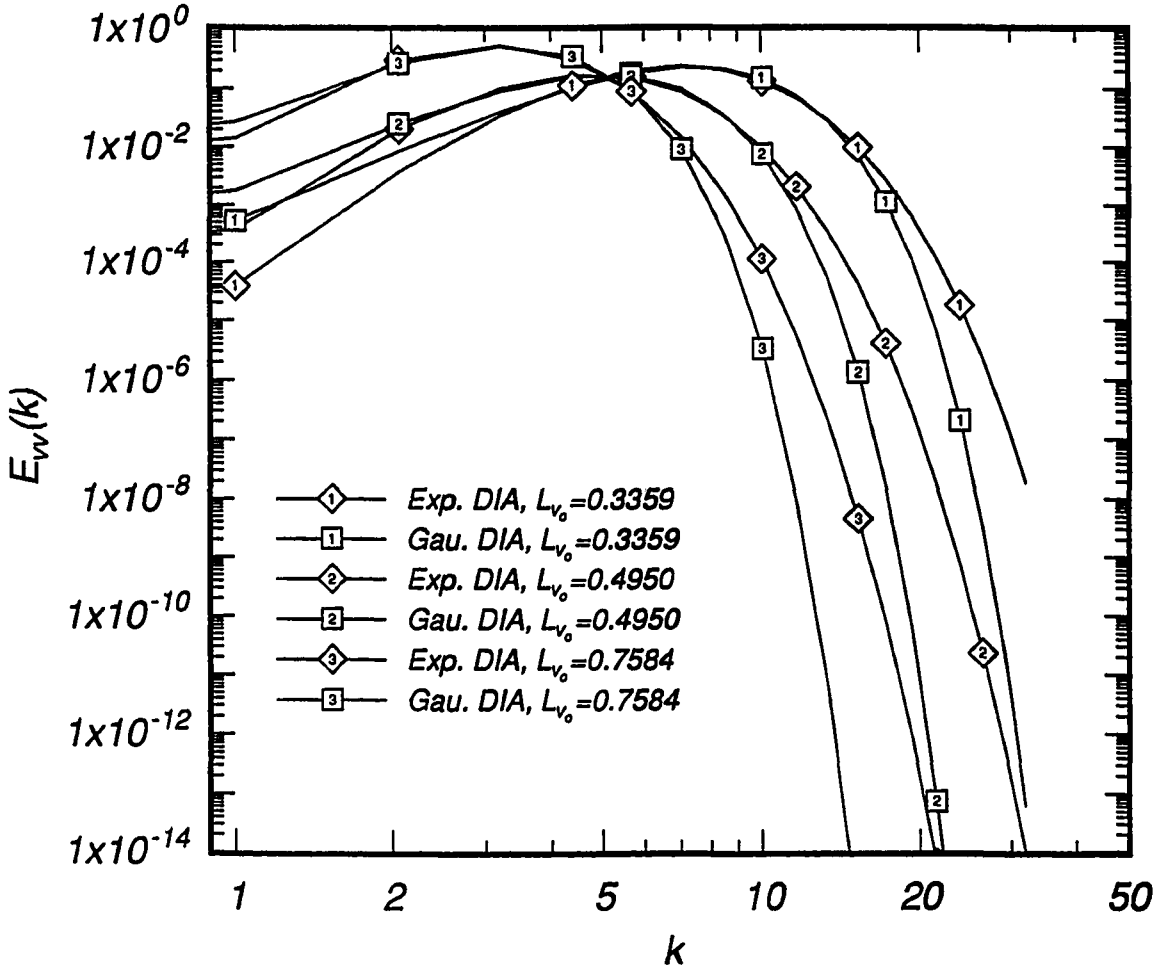

Figure 4.12: Initial Gaussian and exponential spectra for different values of L_{v_o}, $A_o = 1.25$, $R_{\lambda_o} = 60$.

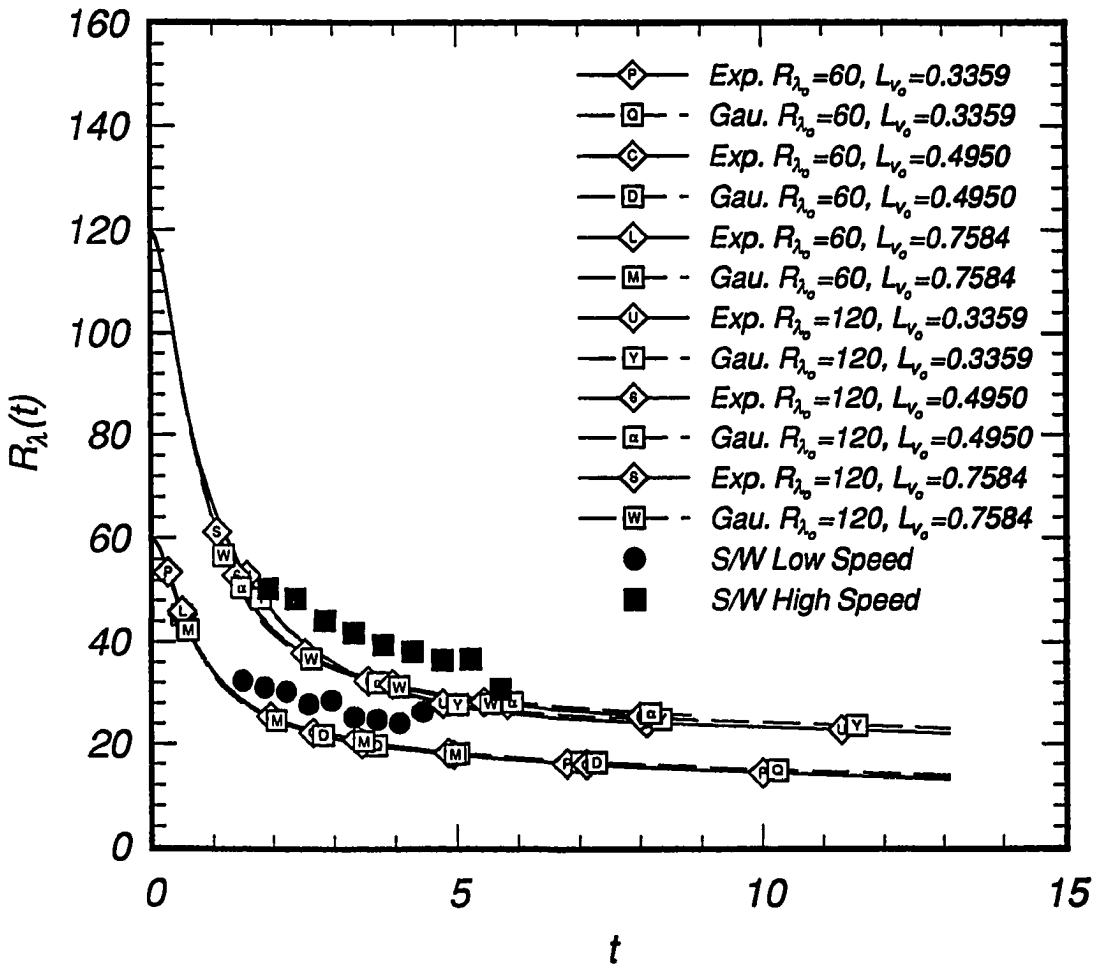

Figure 4.13: Evolution of Reynolds number for experiment and Gaussian and exponential initial DIA velocity field spectra and $A = 1.25$.

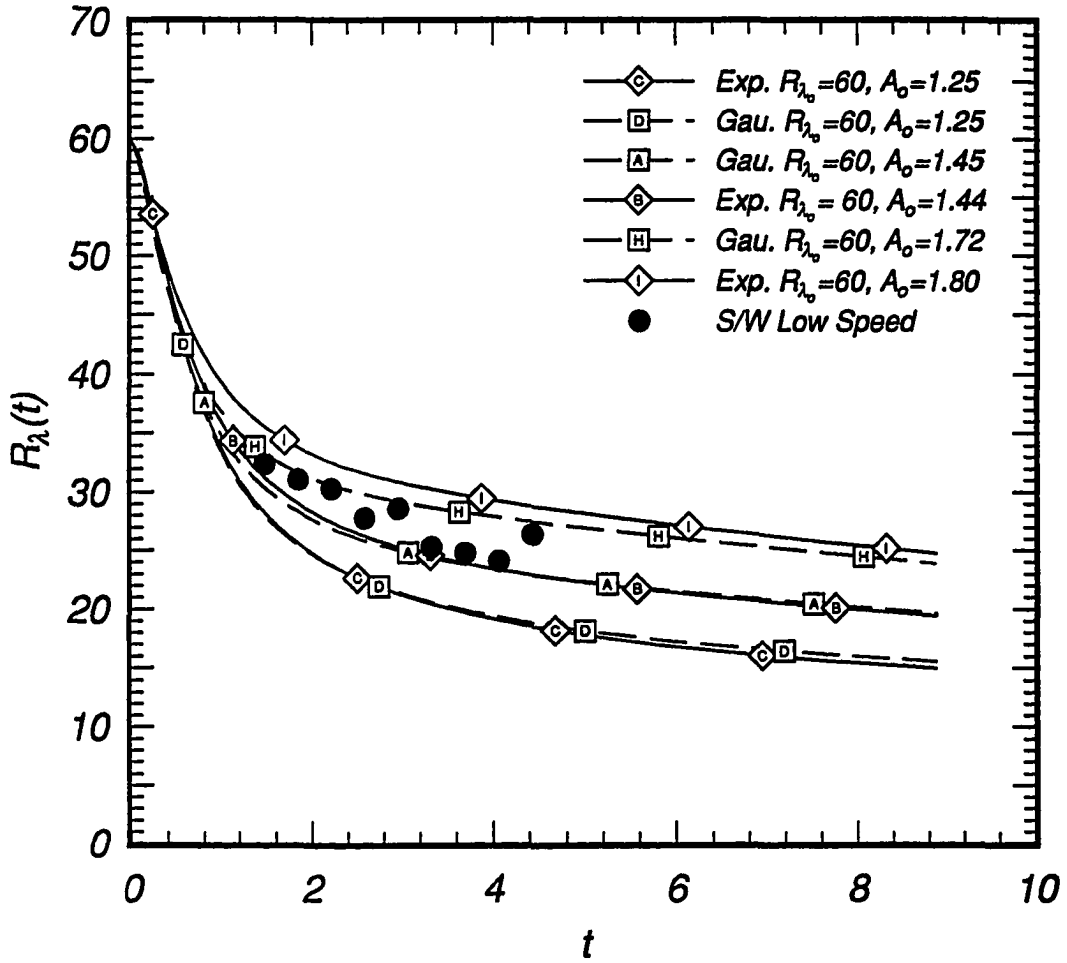

Figure 4.14: Evolution of Reynolds number for experiment and DIA with different initial values of A and $L_{v_o} = 0.495$.

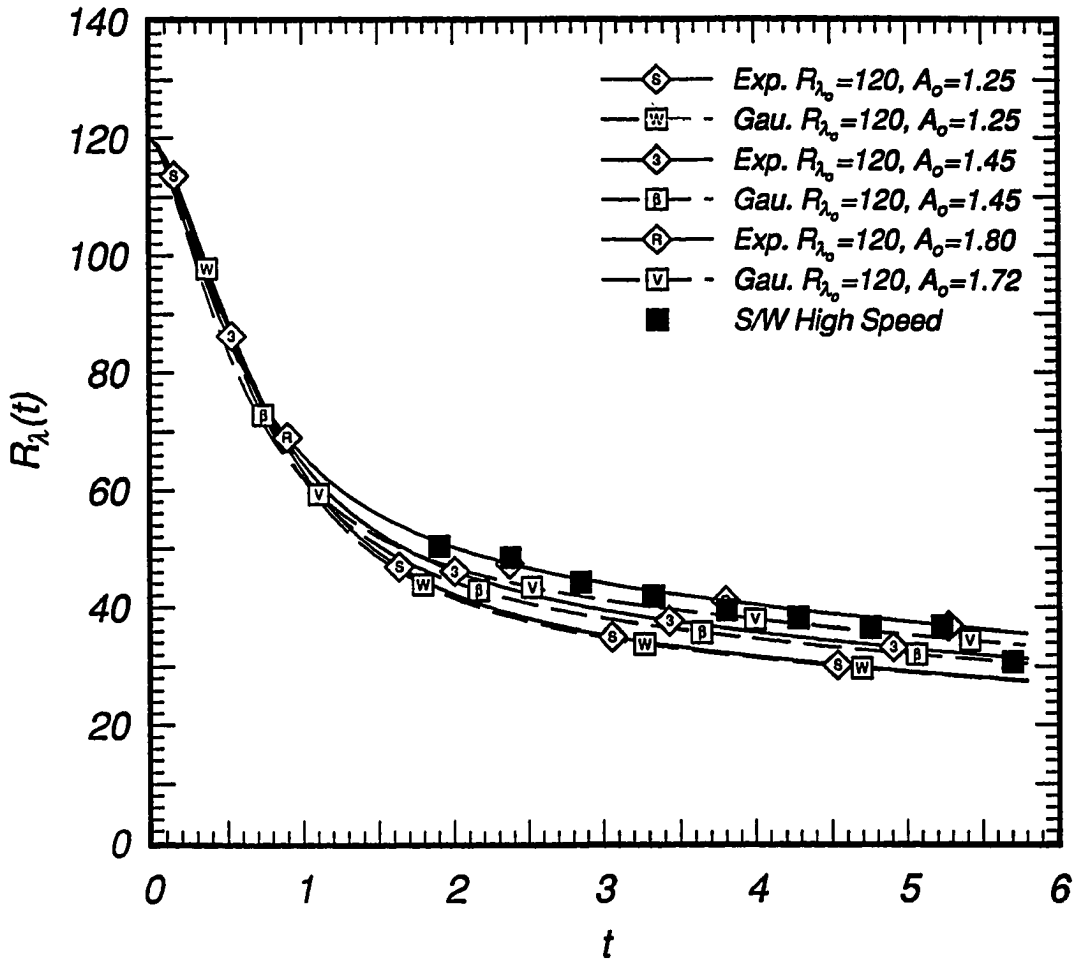

Figure 4.15: Evolution of Reynolds number for experiment and DIA with different initial values of A and $L_{v_o} = 0.7584$.

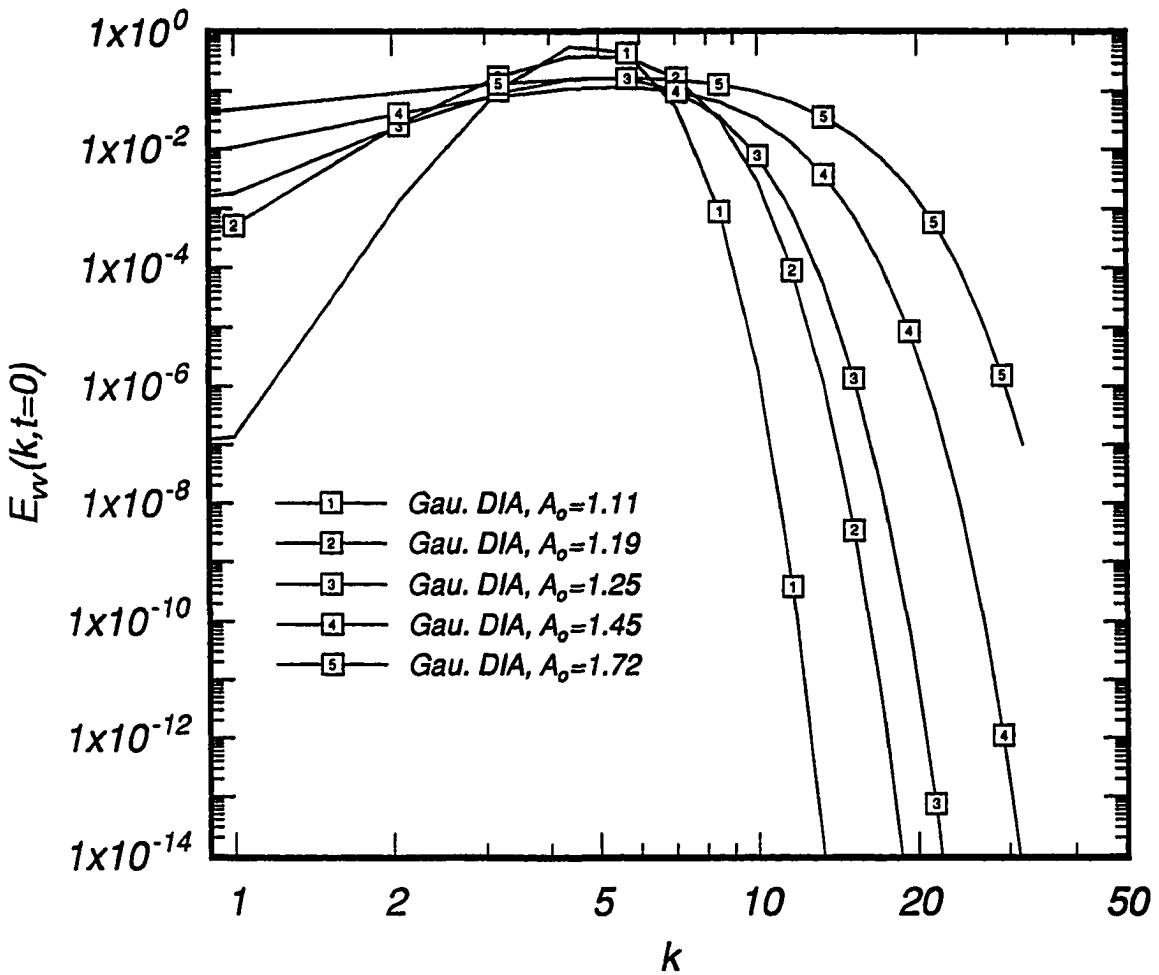

Figure 4.16: Initial DIA velocity field spectra for R_λ=60, A=1.25, L_{v_o}=0.495.

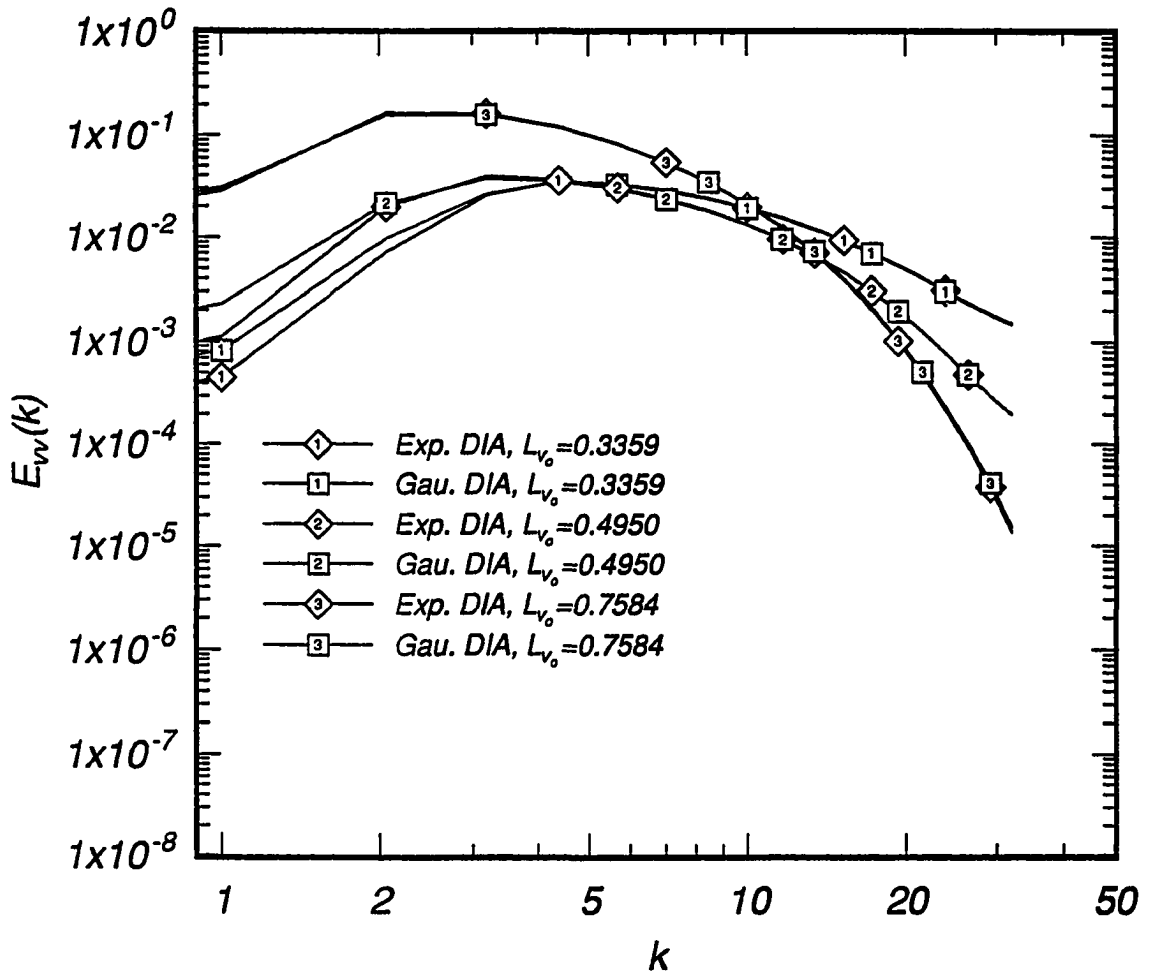

Figure 4.17: DIA velocity field spectra for R_λ=60, A=1.25, t=2.15.

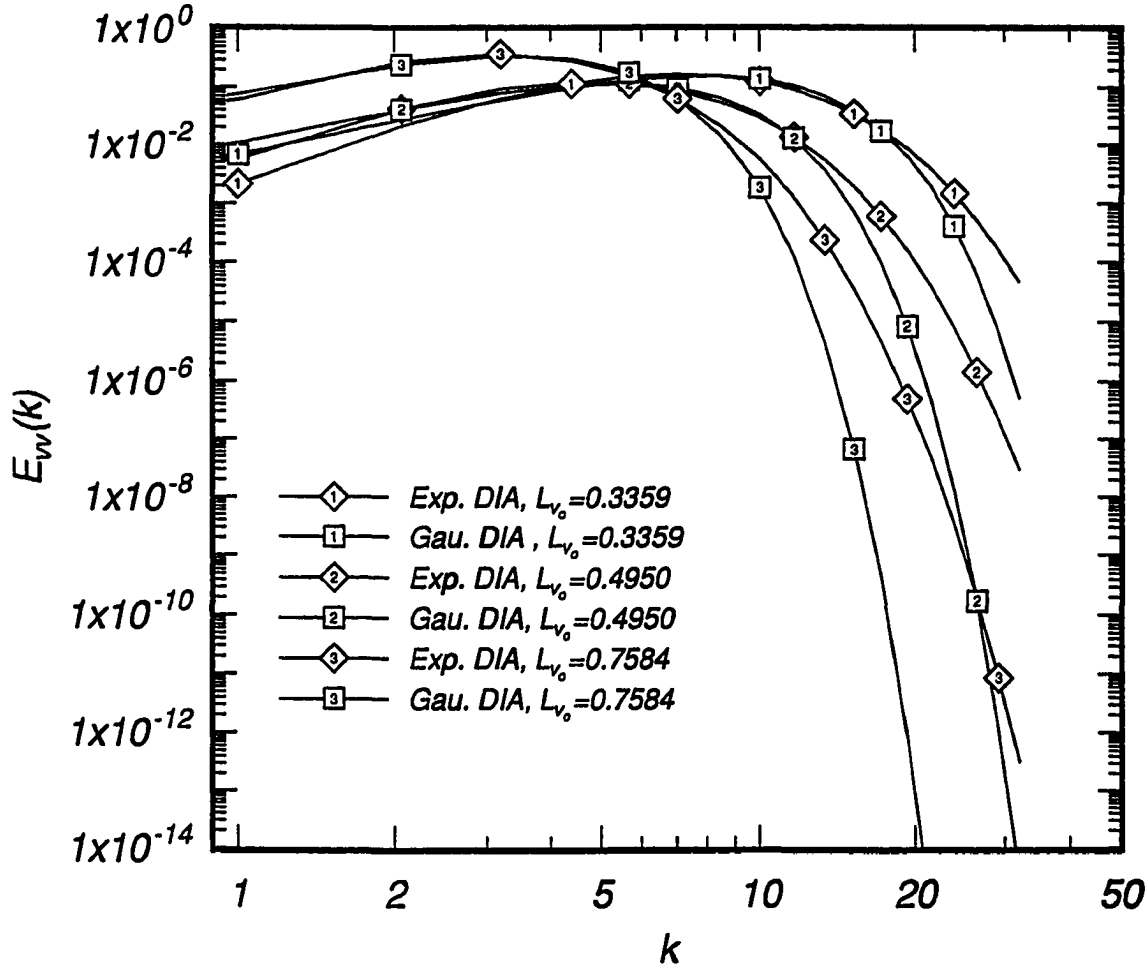

Figure 4.18: Initial DIA velocity field spectra for R_λ=60, A=1.45.

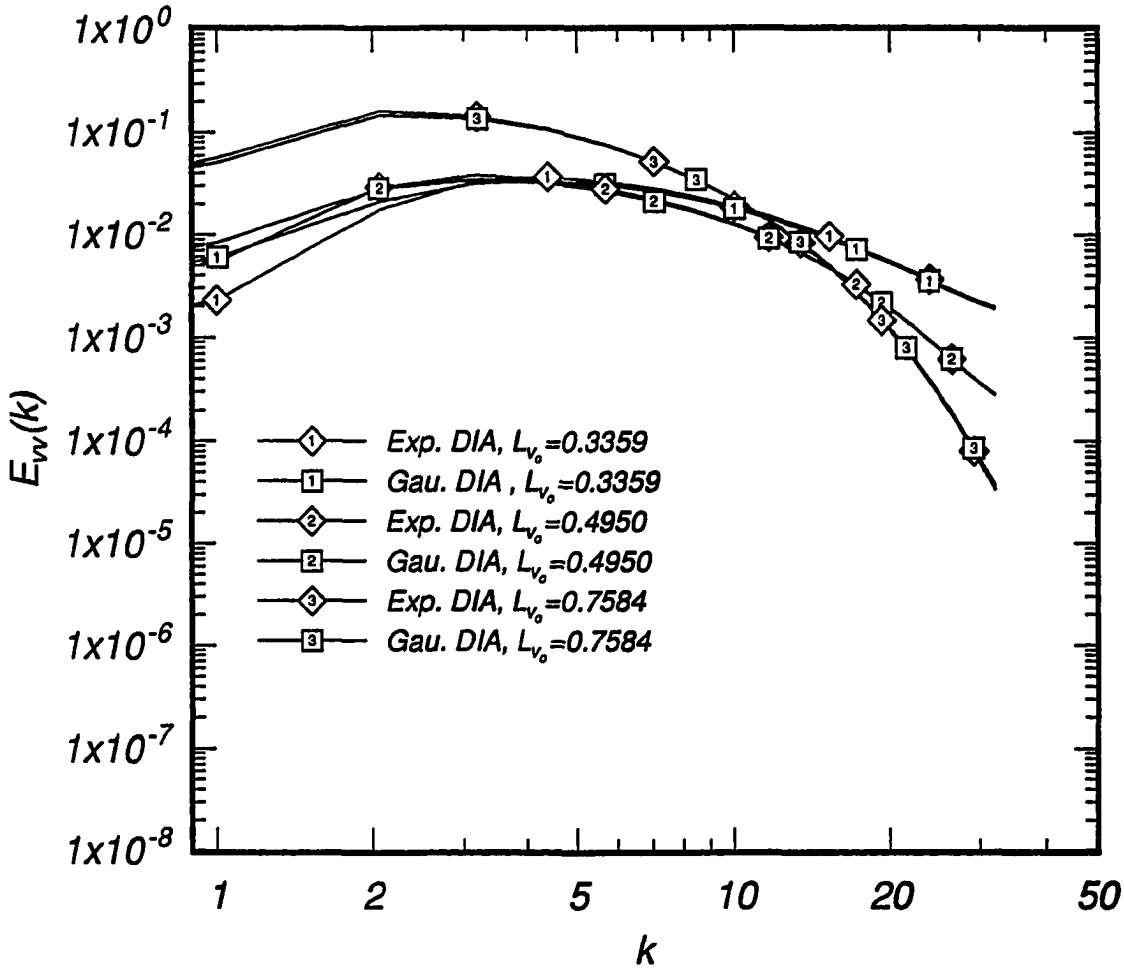

Figure 4.19: DIA velocity field spectra for R_λ=60, A=1.45, t=2.15.

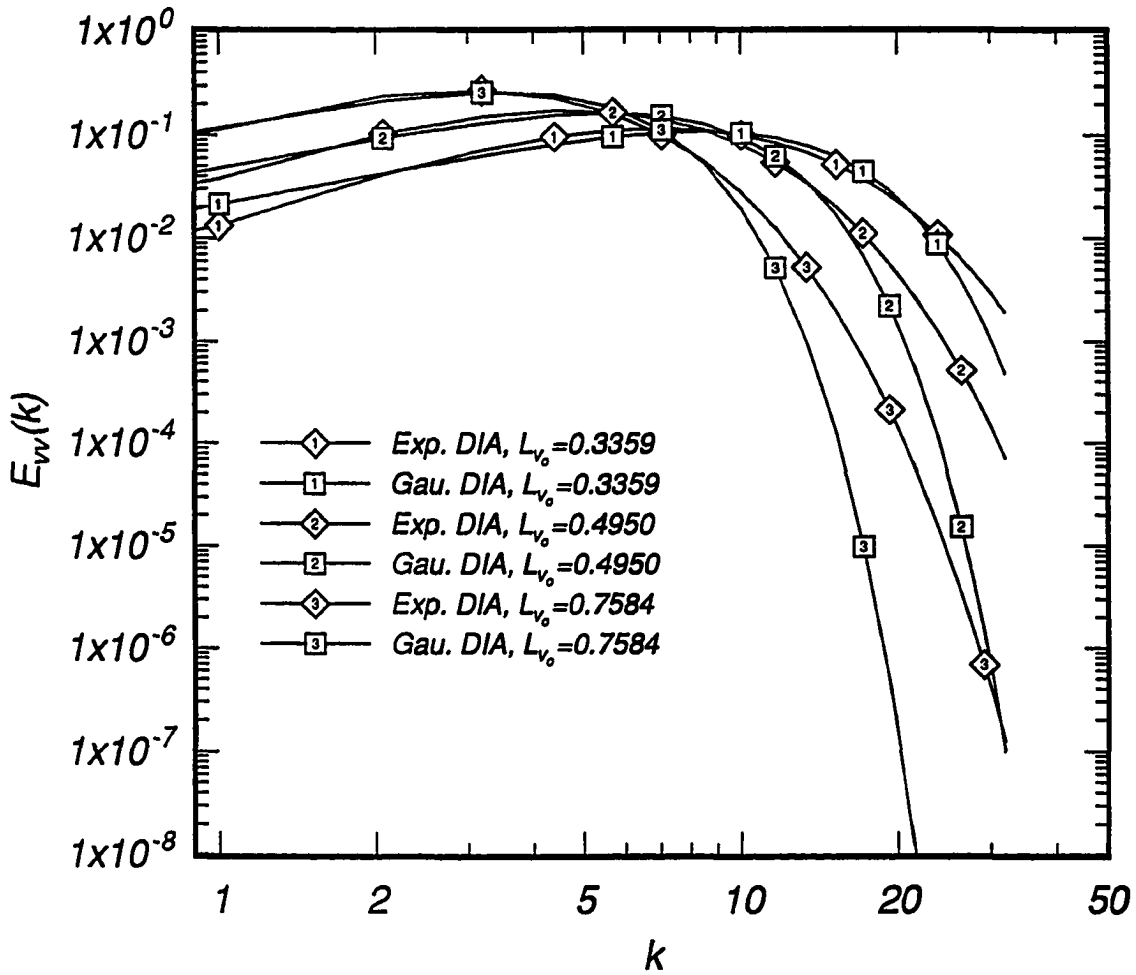

Figure 4.20: Initial DIA velocity field spectra for R_λ=60, A=1.72/1.80.

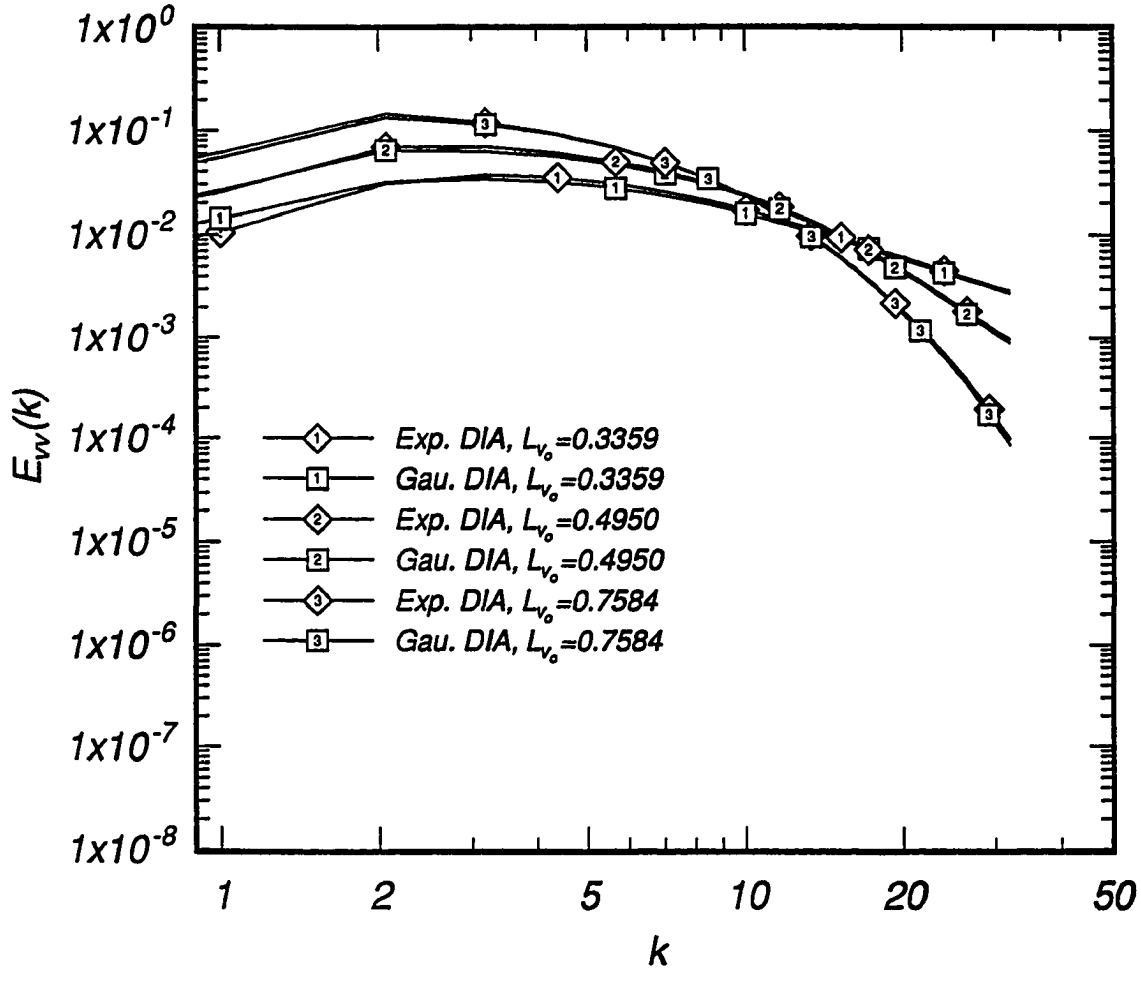

Figure 4.21: DIA velocity field spectra for R_λ=60, A=1.72/1.80, t=2.15.

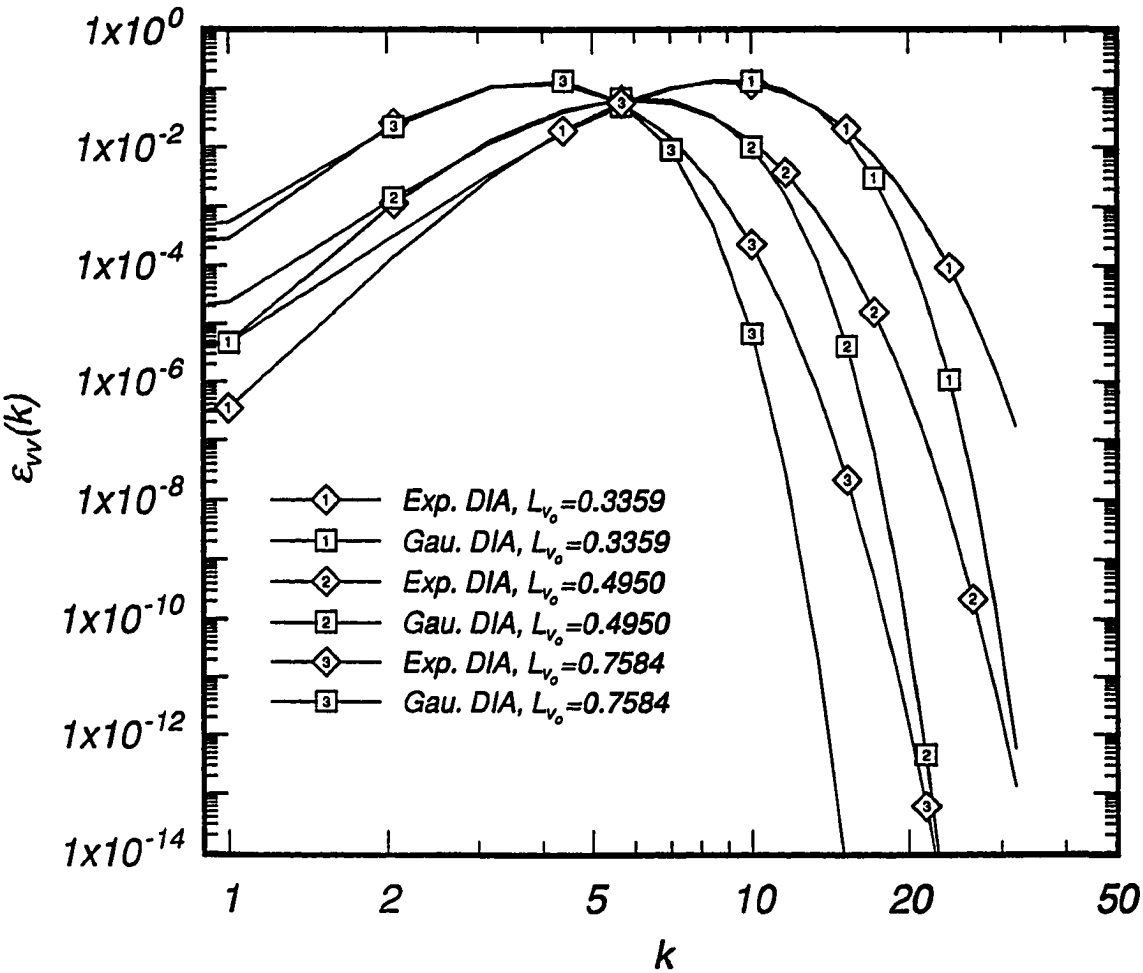

Figure 4.22: DIA velocity field dissipation spectra for R_λ=60, A=1.25, t=0.00.

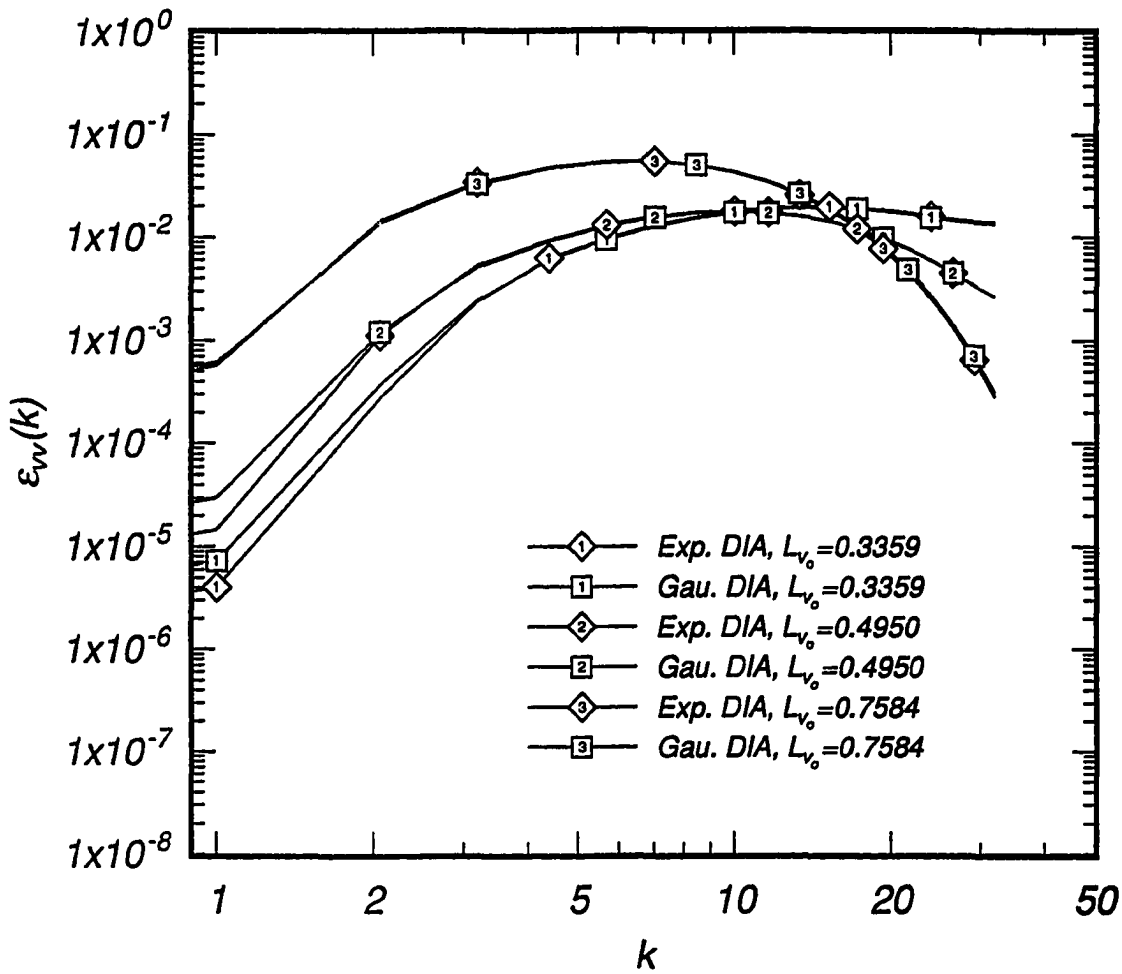

Figure 4.23: DIA velocity field dissipation spectra for R_λ=60, A=1.25, t=2.15.

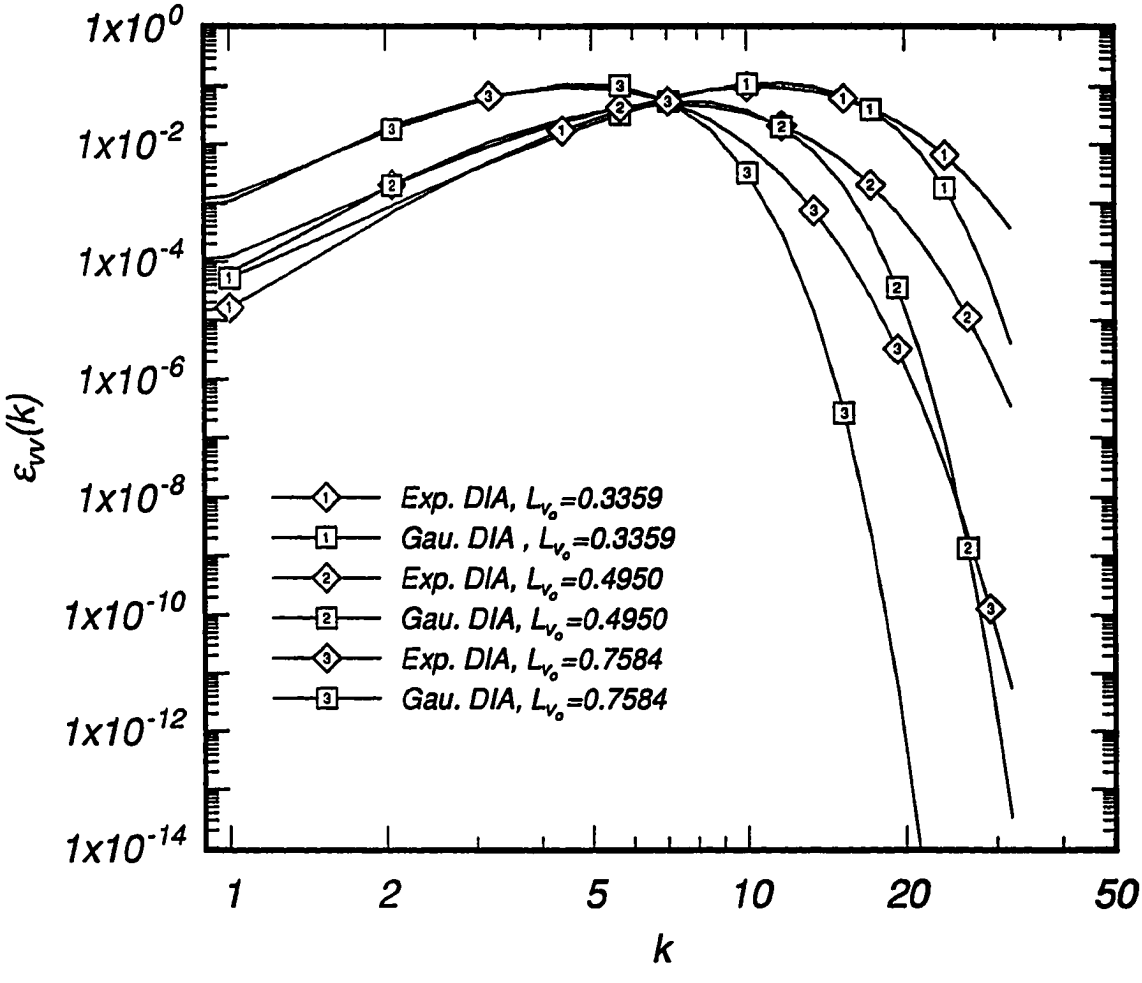

Figure 4.24: DIA velocity field dissipation spectra for R_λ=60, A=1.45, t=0.00.

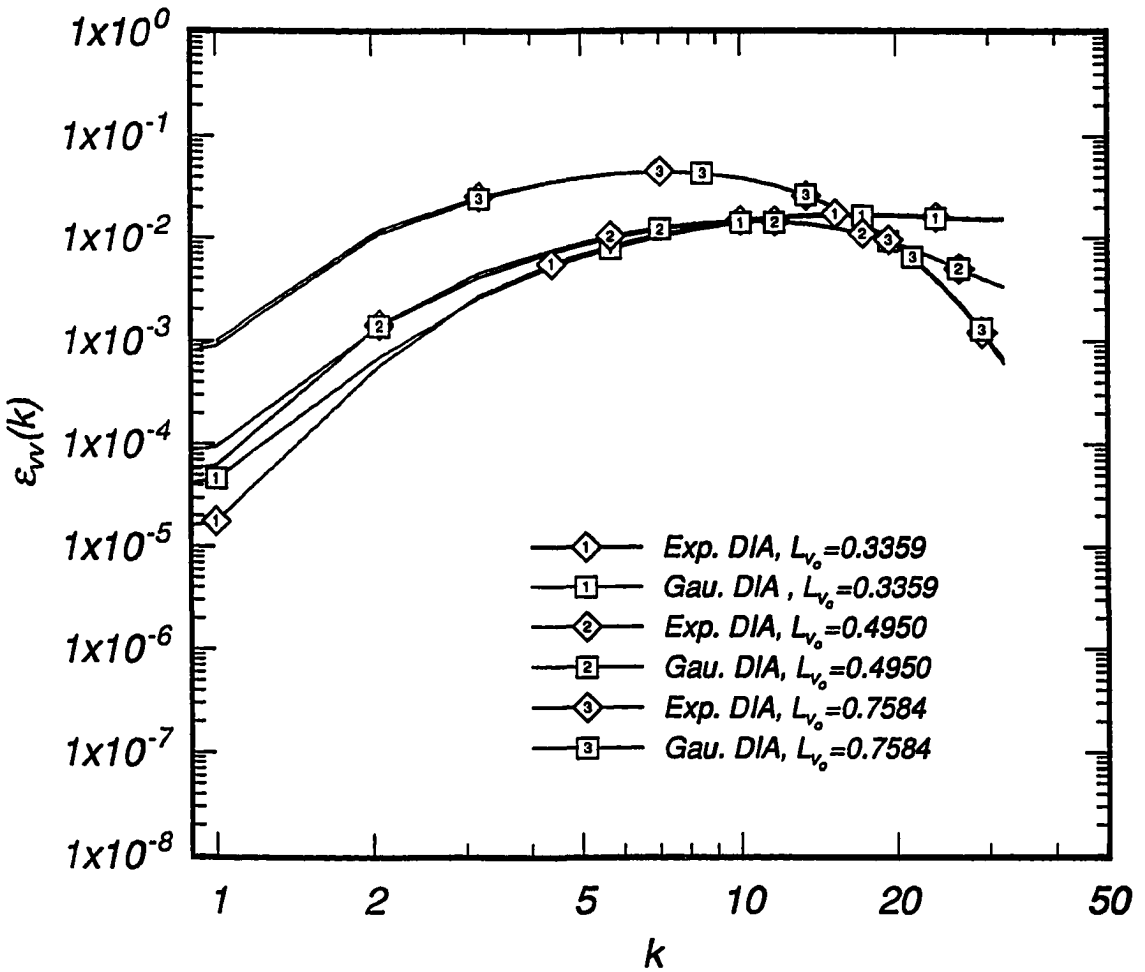

Figure 4.25: DIA velocity field dissipation spectra for R_λ=60, A=1.45, t=2.15.

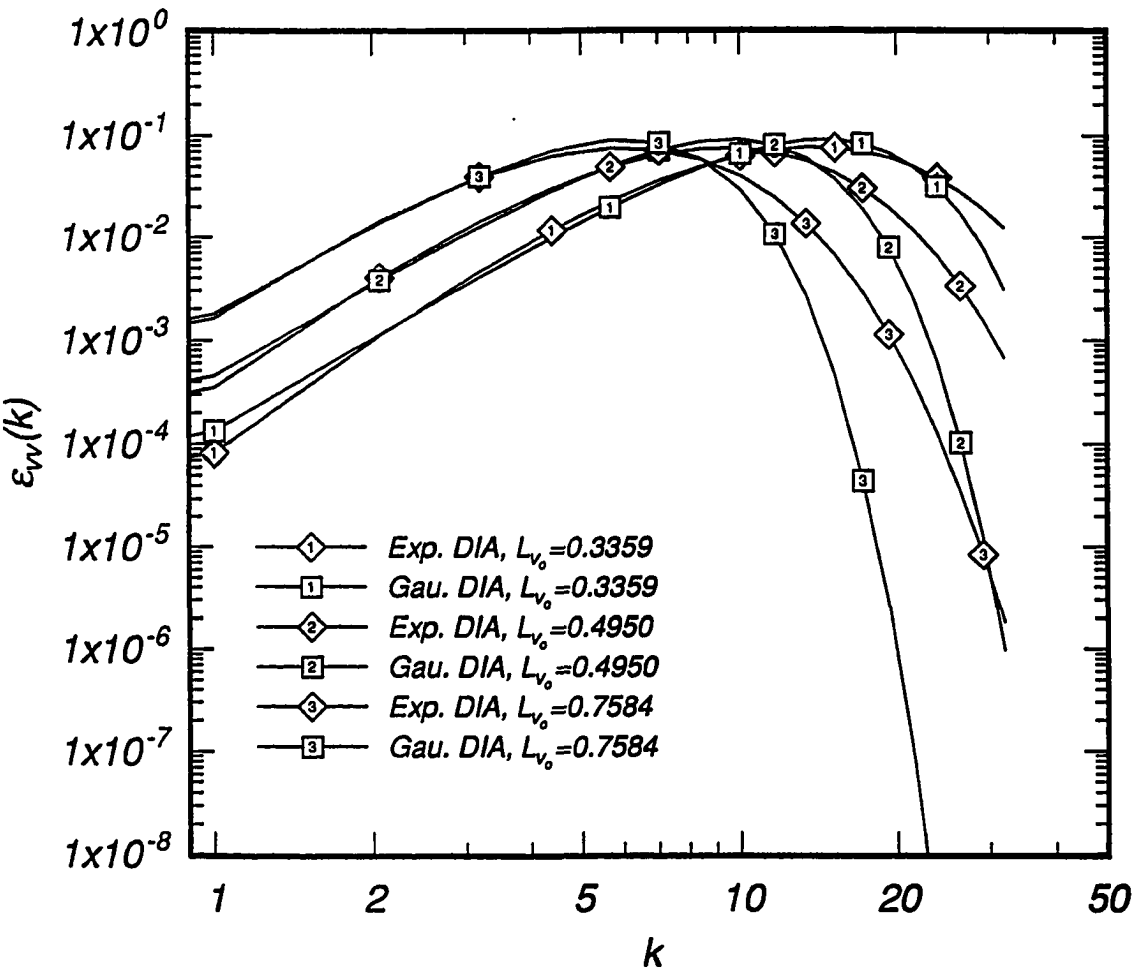

Figure 4.26: DIA velocity field dissipation spectra for R_λ=60, A=1.72/1.80, t=0.00.

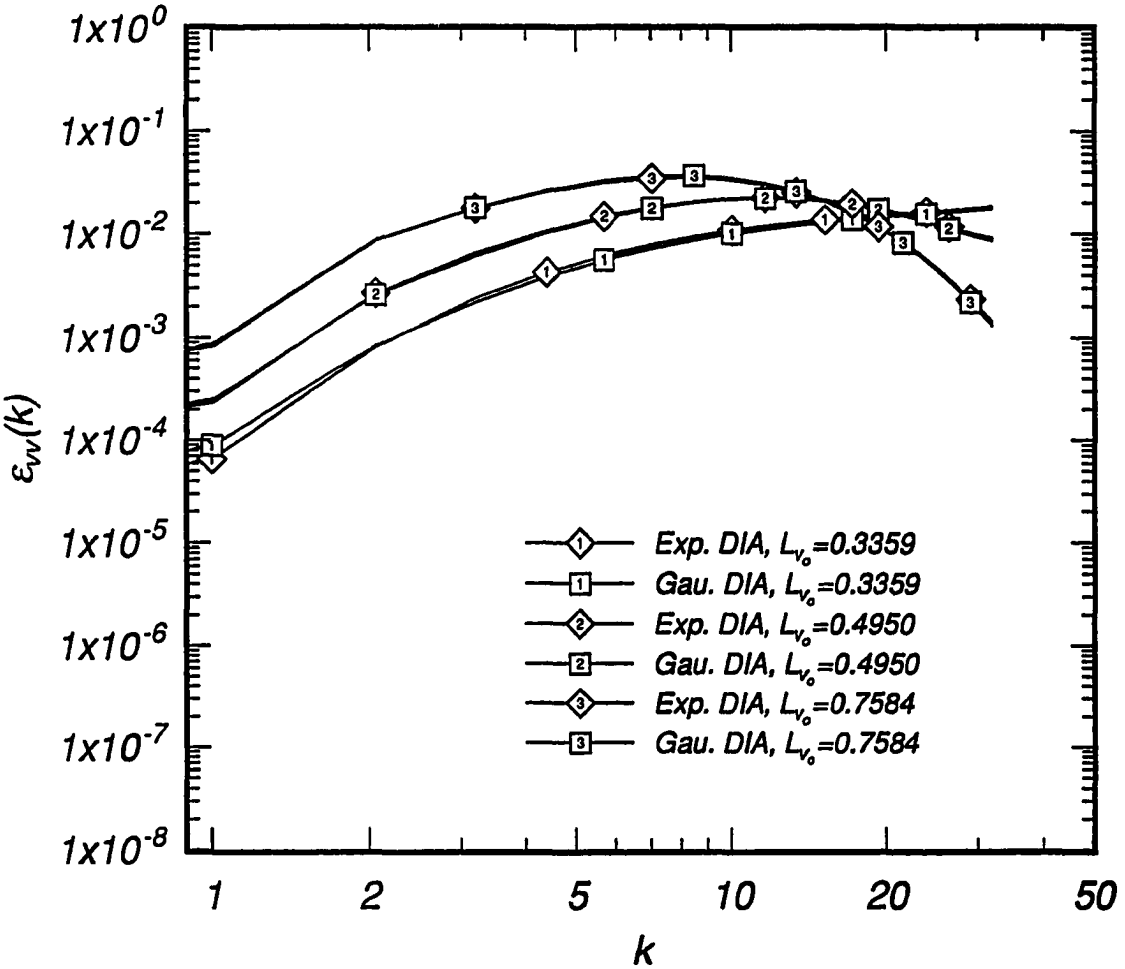

Figure 4.27: DIA velocity field dissipation spectra for R_λ=60, A=1.72/1.80, t=2.15.

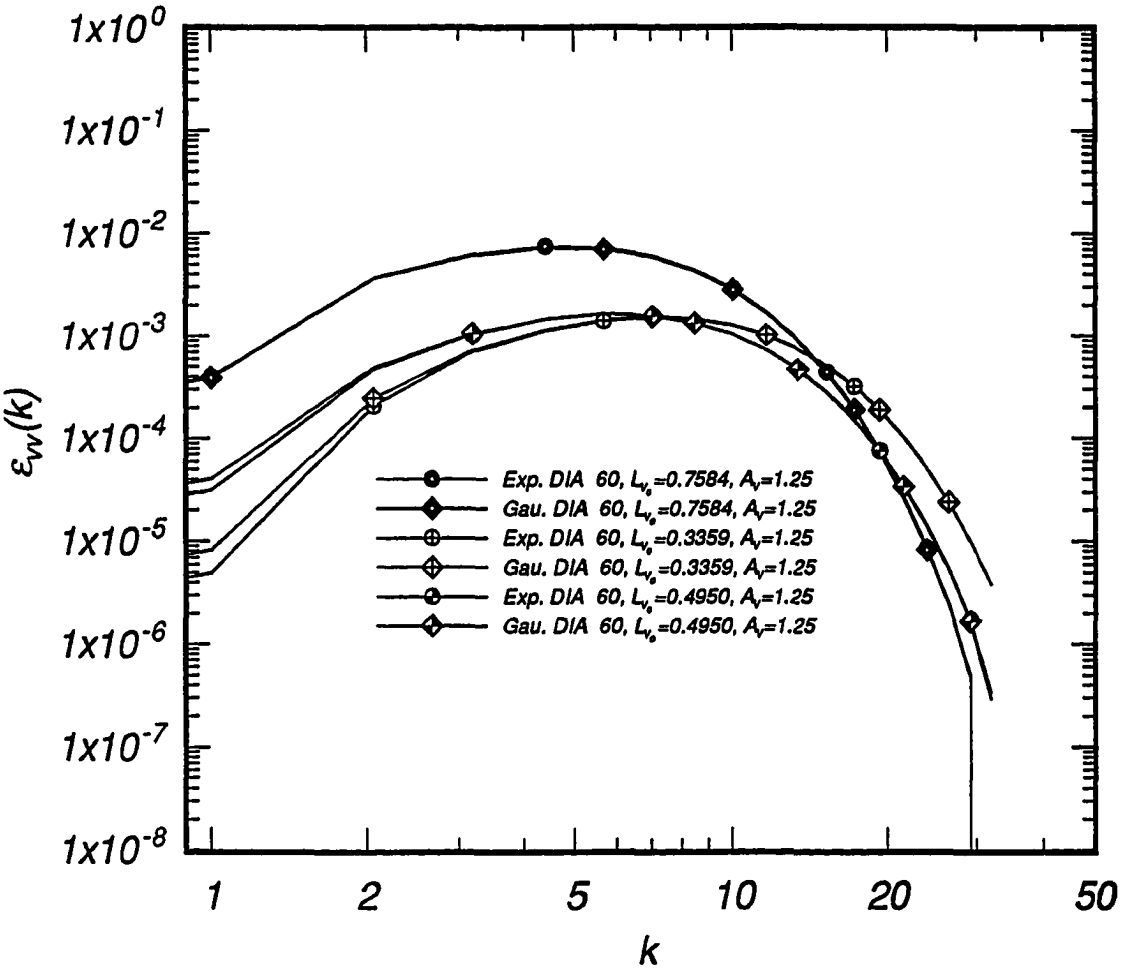

Figure 4.28: DIA velocity field dissipation spectra for R_λ=60, A=1.25, t=8.61.

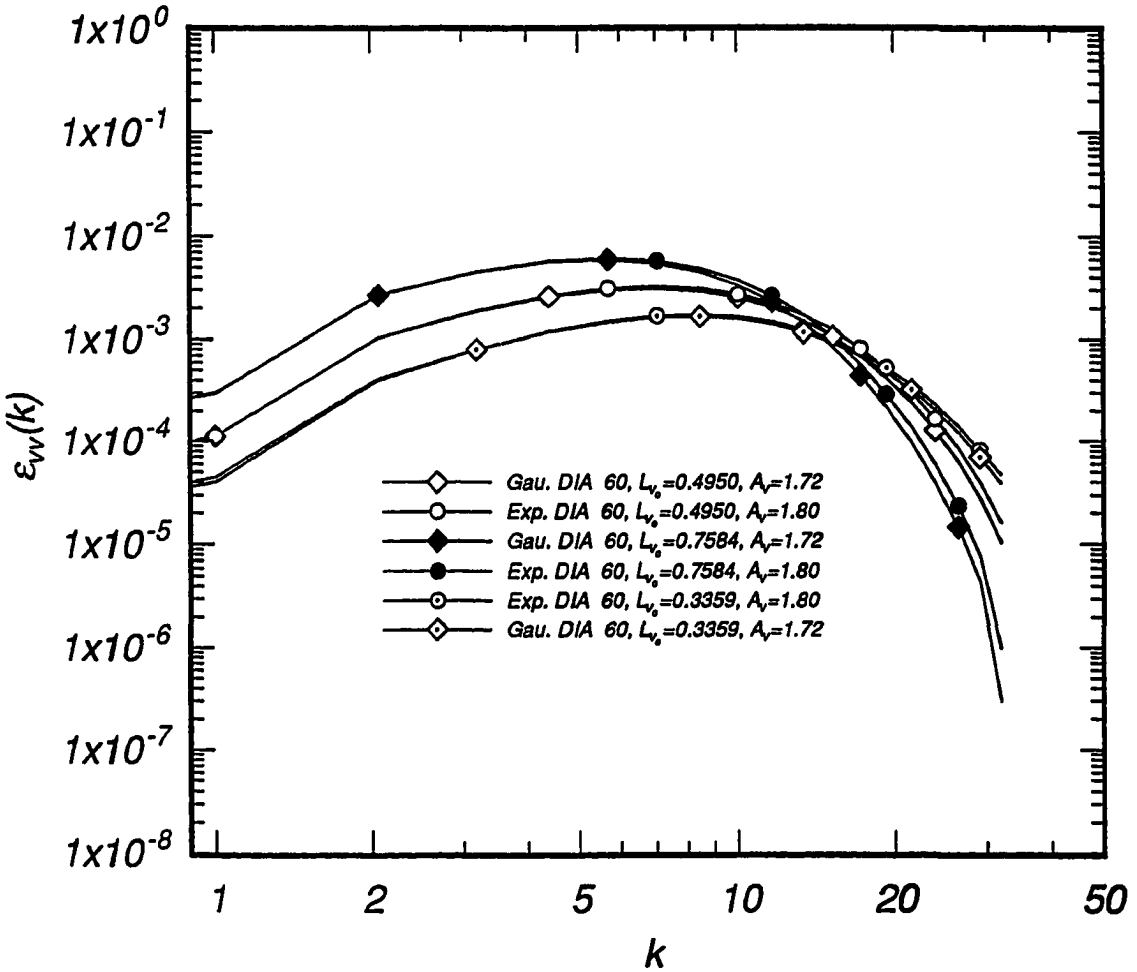

Figure 4.29: DIA velocity field dissipation spectra for R_λ=60, A=1.72/1.80, t=8.61.

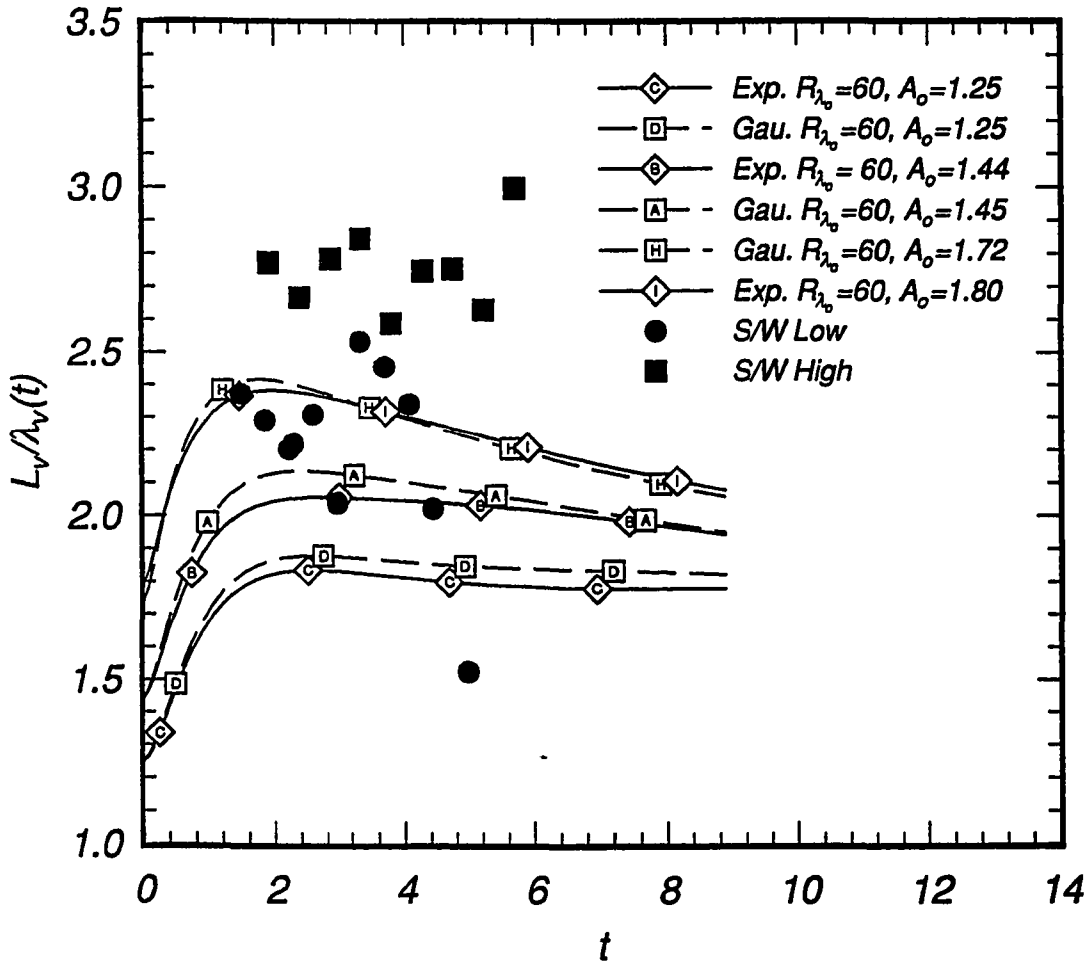

Figure 4.30: Evolution of A for experiment and DIA with $L_{vo} = 0.4950$, $R_{\lambda o} = 60$ comparing exponential and Gaussian spectral shapes.

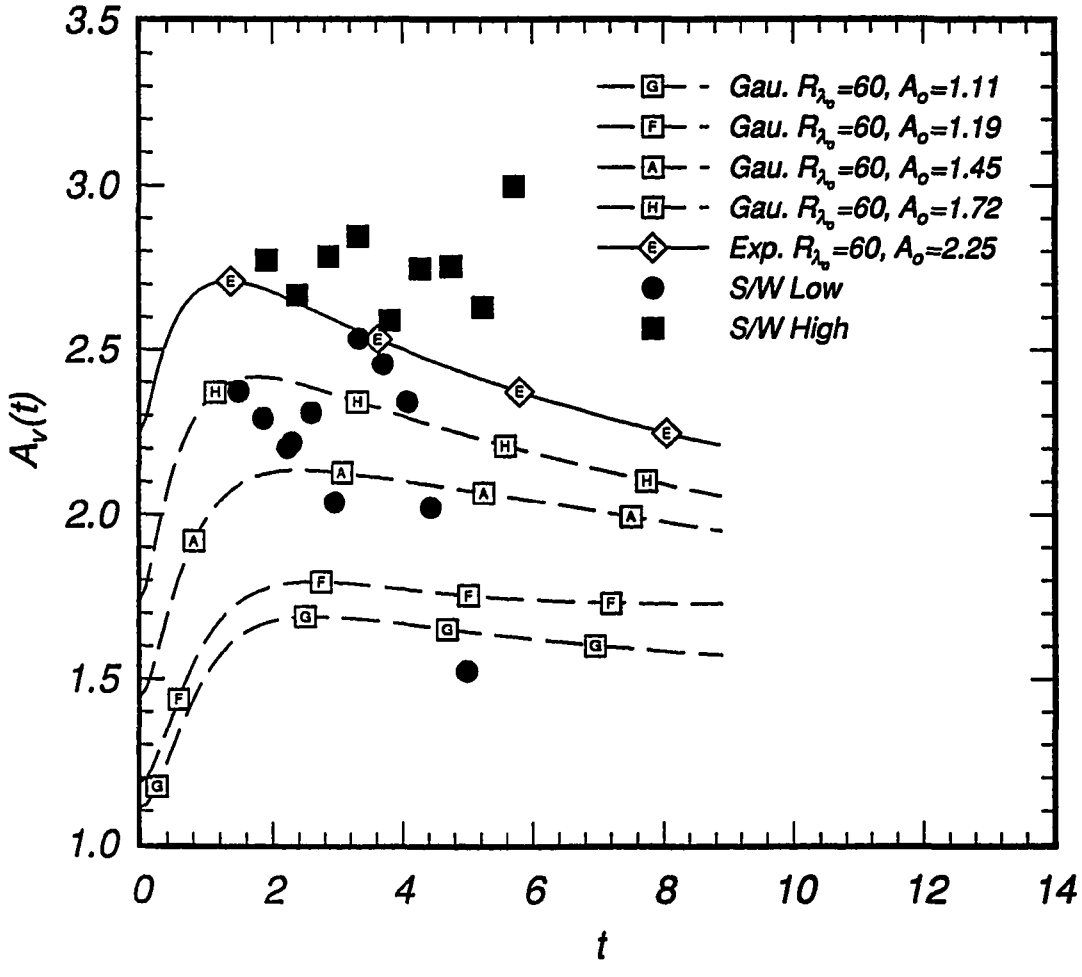

Figure 4.31: Evolution of A for experiment and DIA with $L_{vo} = 0.4950$ $R_{\lambda o} = 60$.

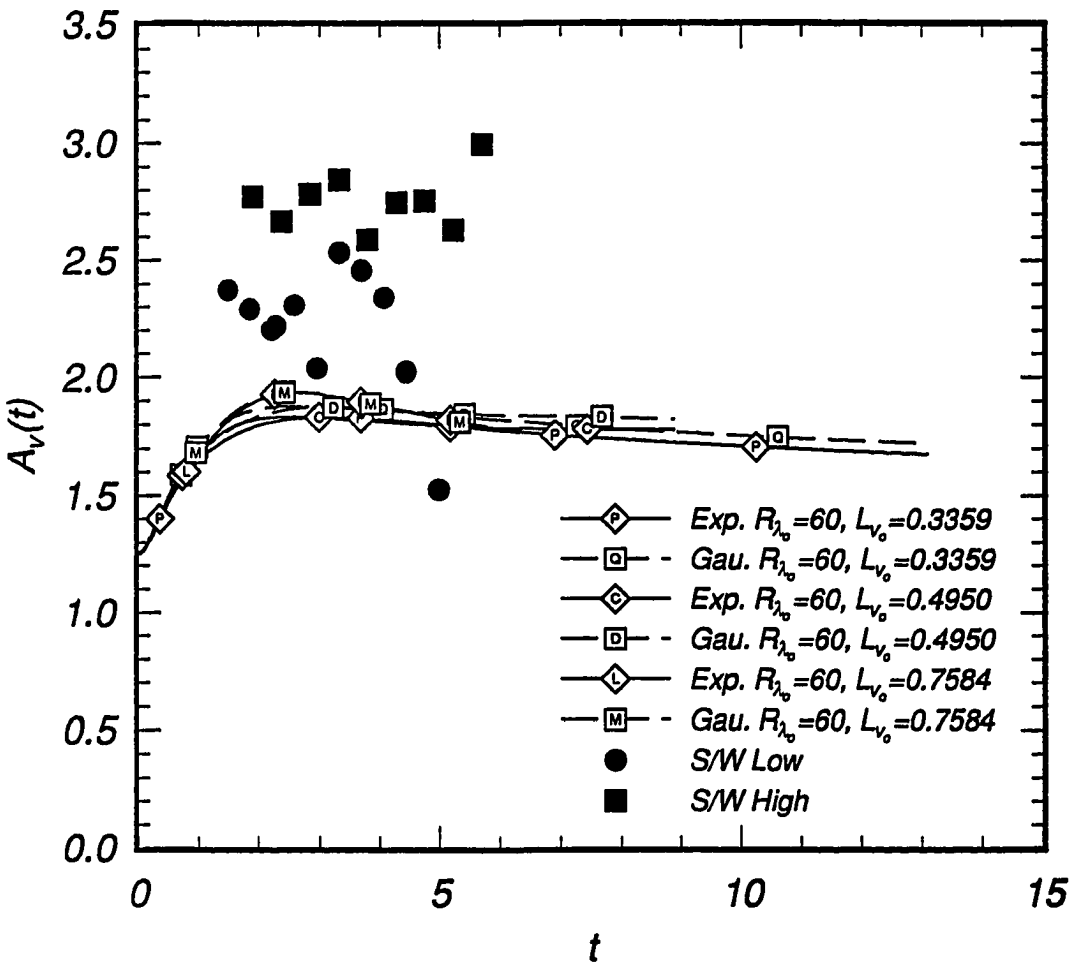

Figure 4.32: Evolution of A for experiment and DIA with $A_o = 1.25$ $R_{\lambda o} = 60$.

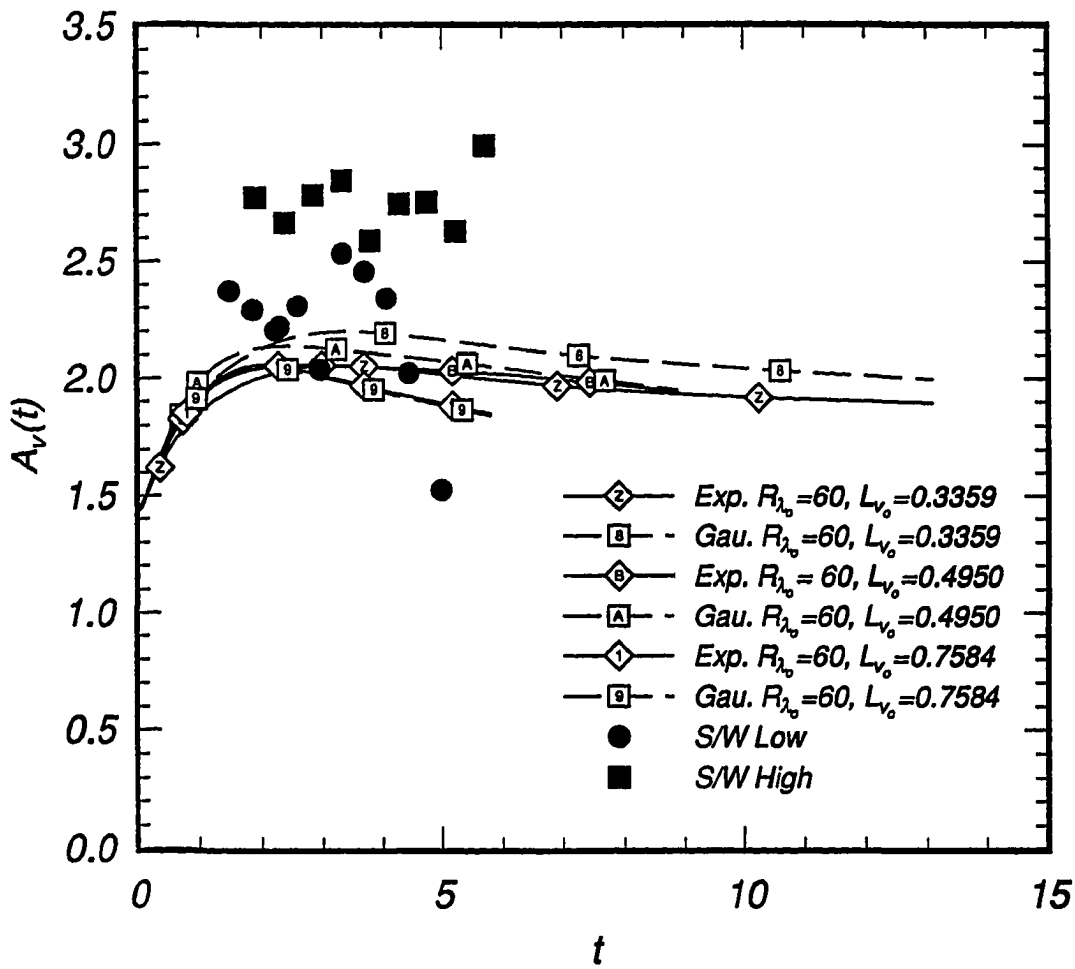

Figure 4.33: Evolution of A for experiment and DIA with $A_o = 1.45/1.44$ $R_{\lambda o} = 60$.

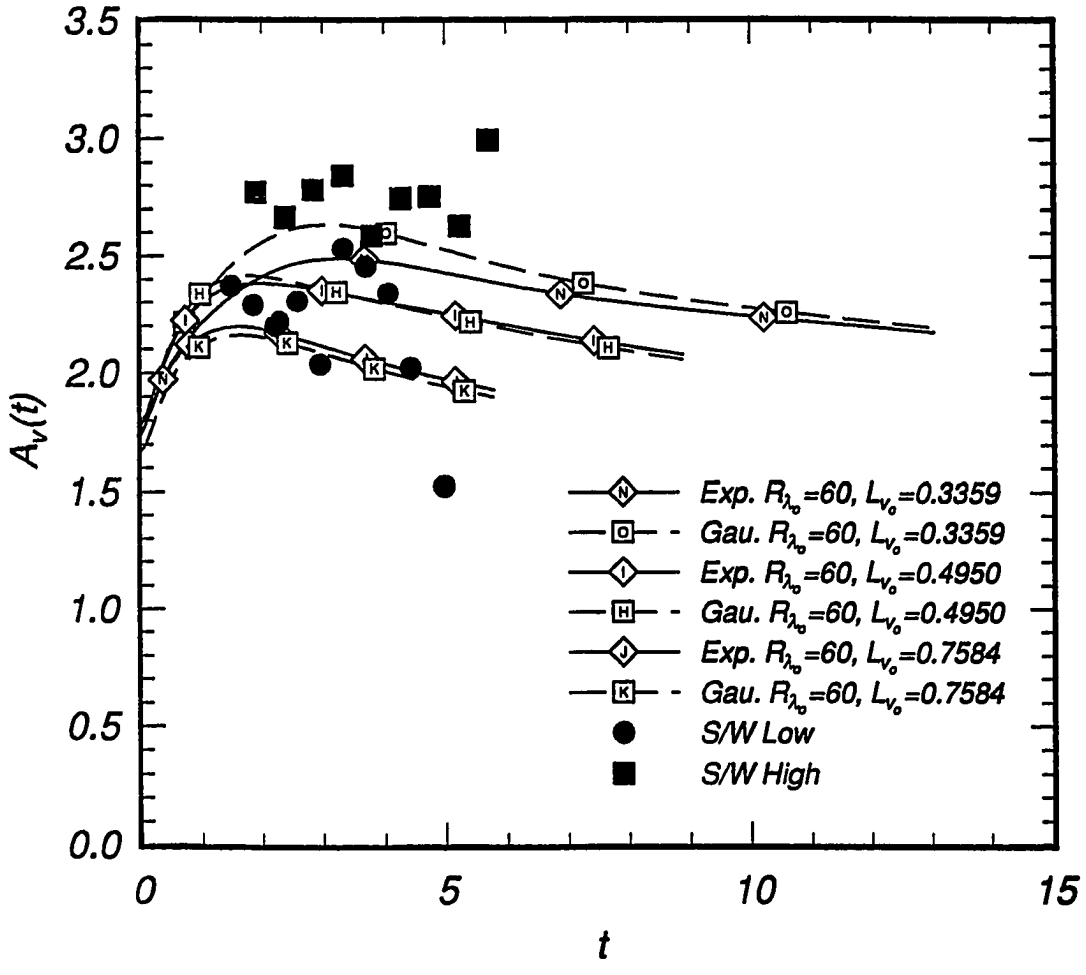

Figure 4.34: Evolution of A for experiment and DIA with $A_o = 1.72/1.80$ $R_{\lambda o} = 60$.

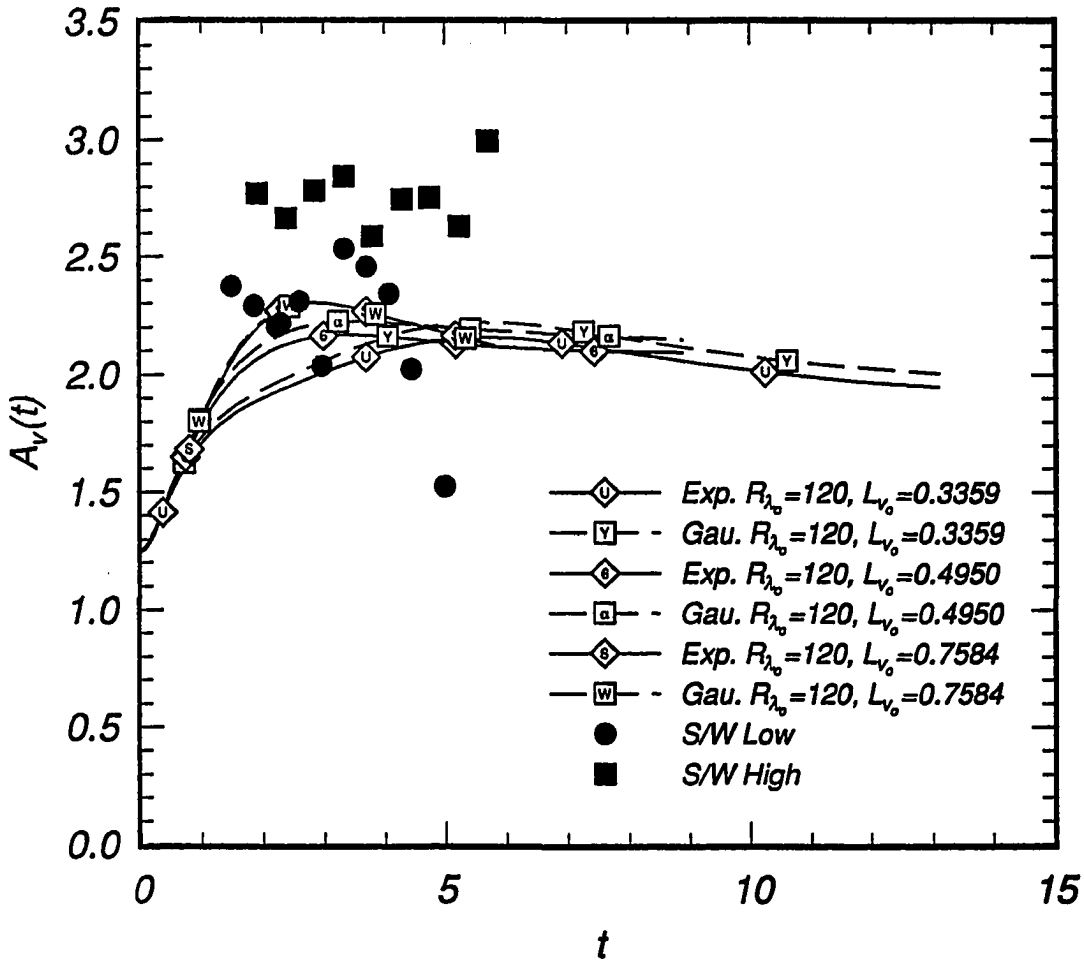

Figure 4.35: Evolution of A for experiment and DIA with $A_o = 1.25$, $R_{\lambda o} = 120$.

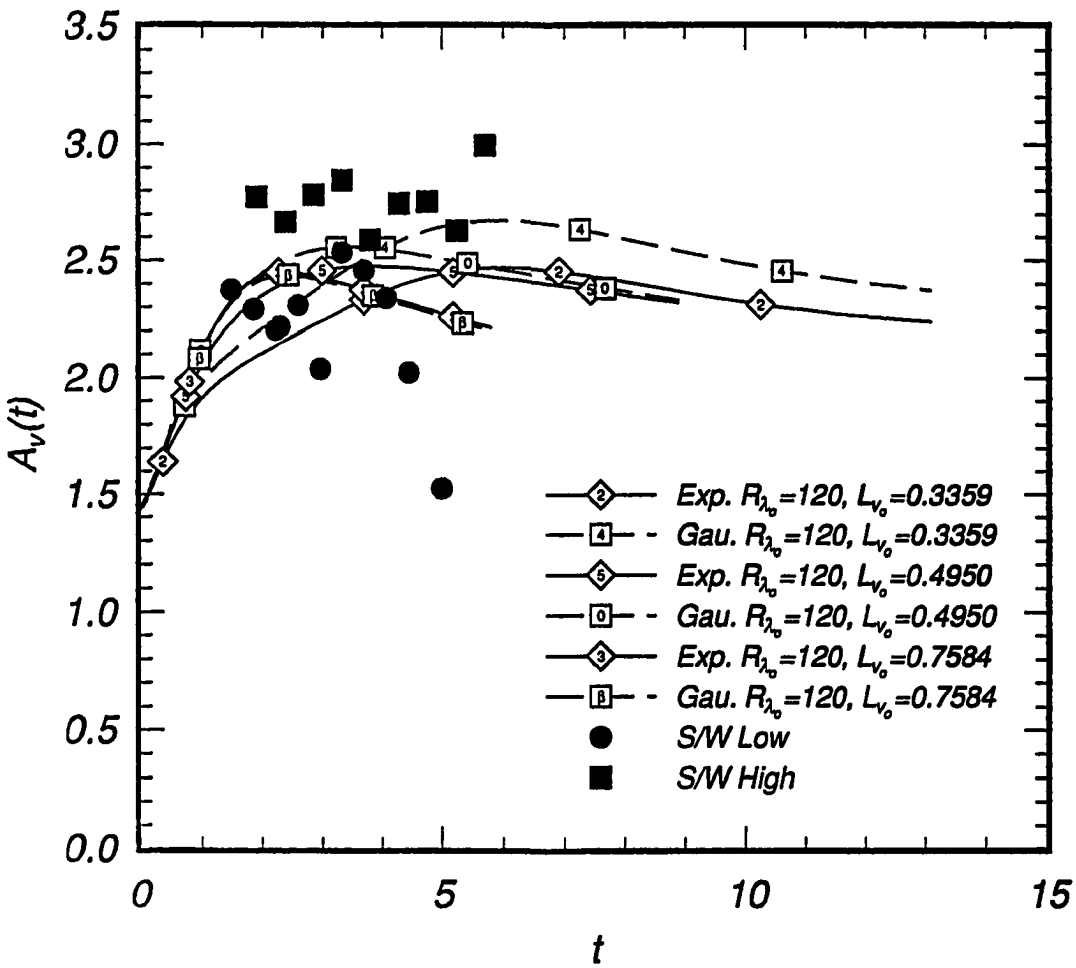

Figure 4.36: Evolution of A for experiment and DIA with $A_o = 1.45/1.44$, $R_{\lambda o} = 120$.

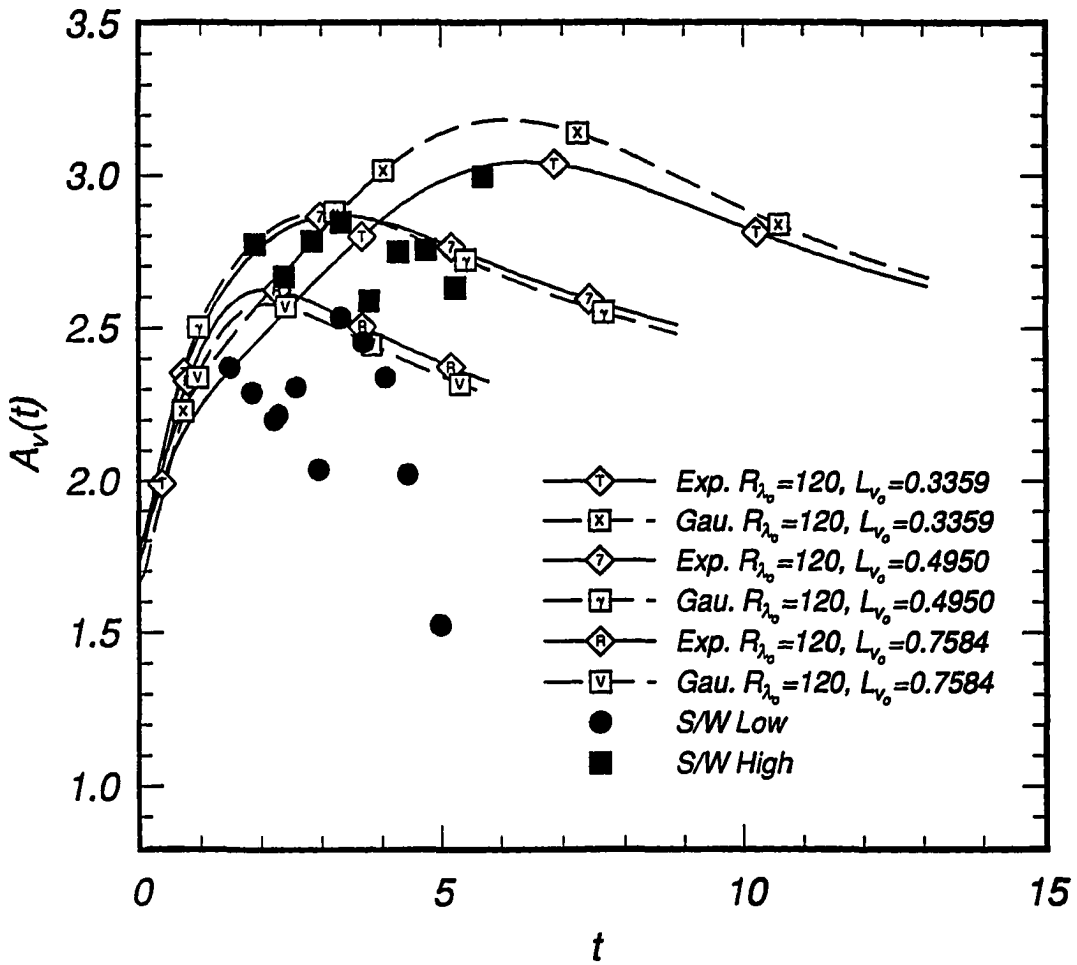

Figure 4.37: Evolution of A for experiment and DIA with $A_o = 1.72/1.80$, $R_{\lambda o} = 120$.

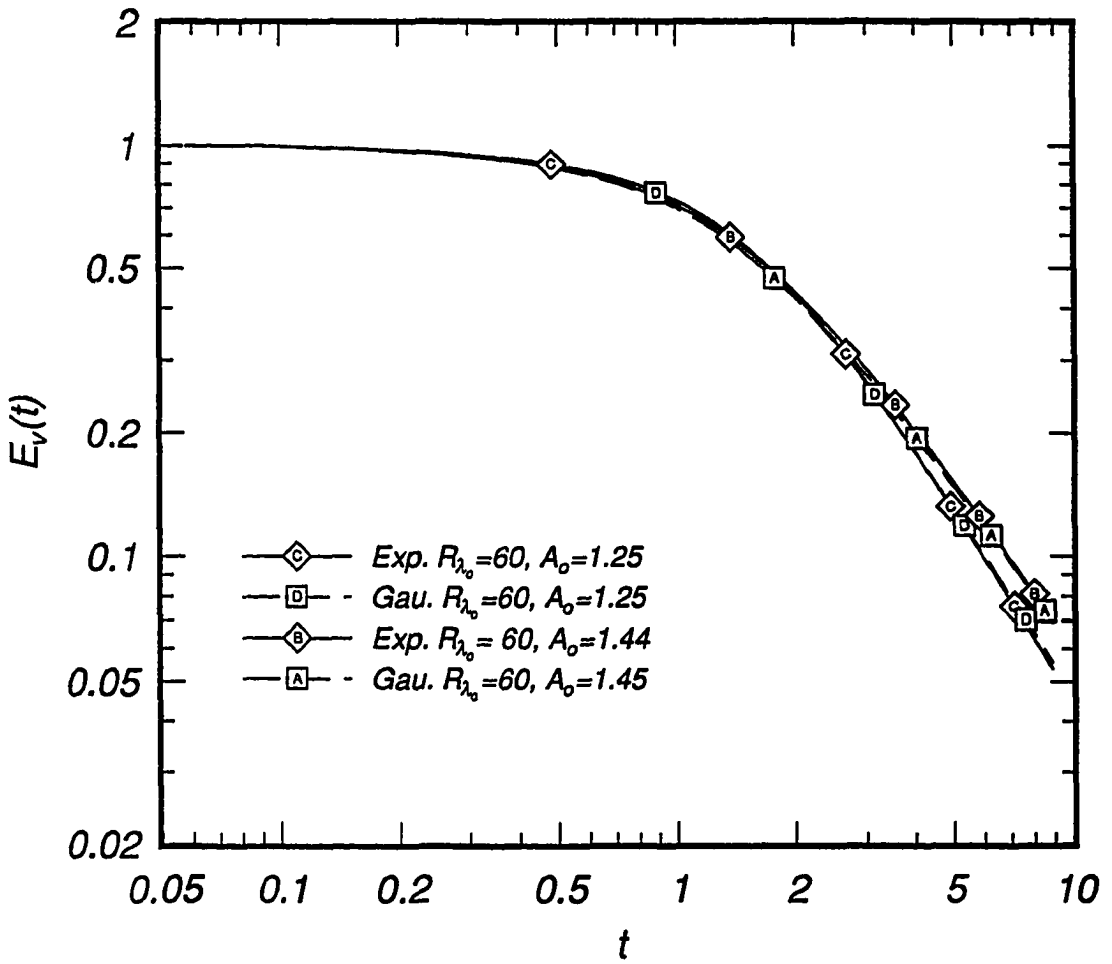

Figure 4.38: Evolution of turbulence energy with $A_o = 1.25, 1.44/1.45$, $R_{\lambda o}$ =60 and $L_{vo} = 0.4950$ using Gaussian and exponential initial spectral shapes.

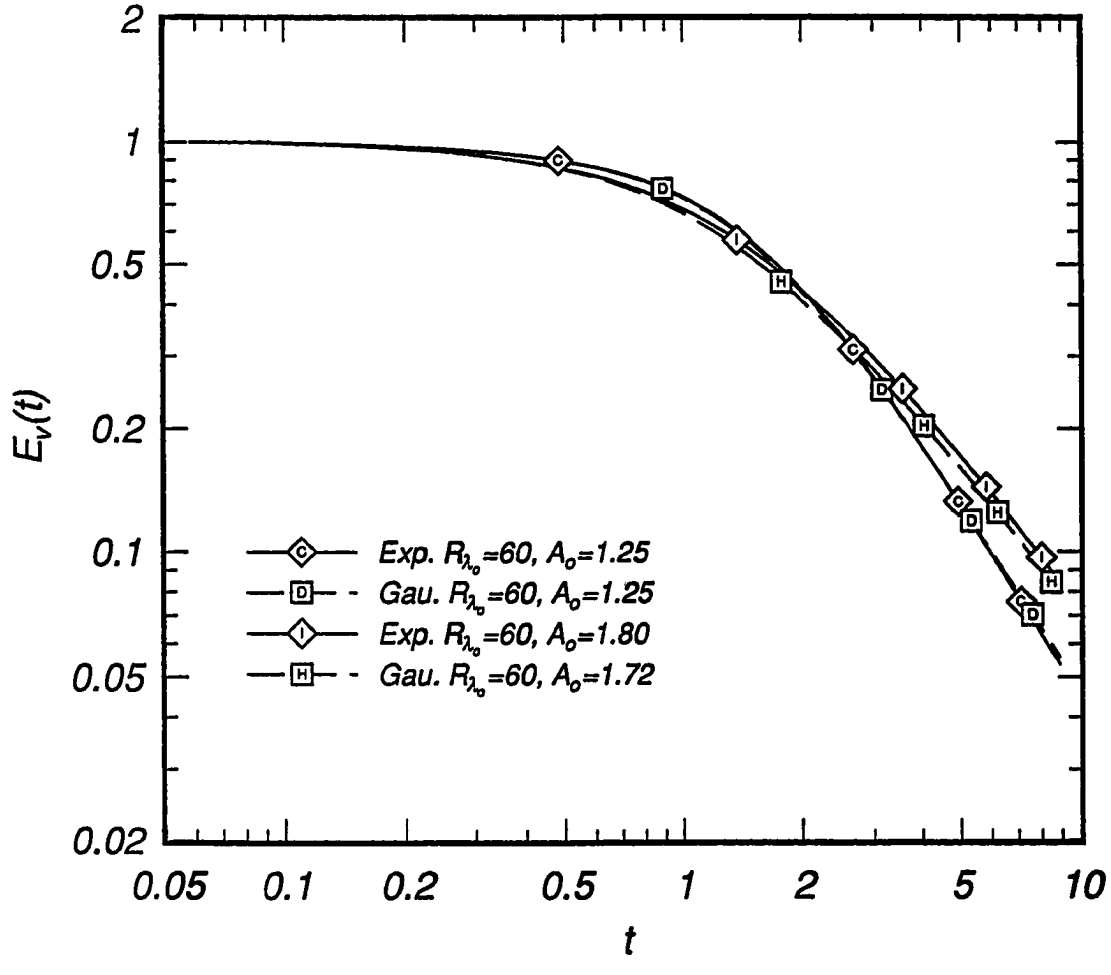

Figure 4.39: Evolution of turbulence energy with $A_o = 1.25$, 1.72/1.80, $R_{\lambda o}$ =60 and $L_{vo} = 0.4950$ using Gaussian and exponential initial spectral shapes.

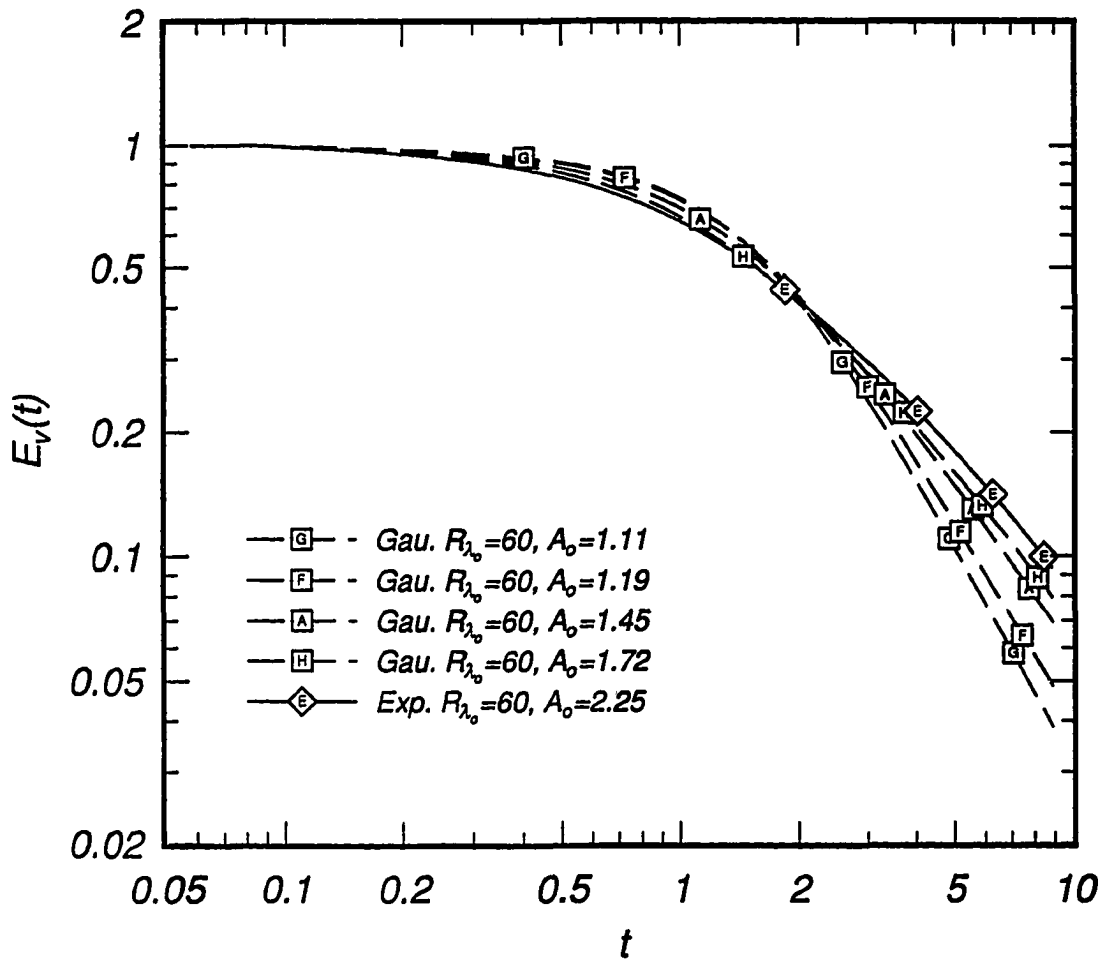

Figure 4.40: Evolution of turbulence energy as a function of A using $R_{\lambda o}$ =60 and L_{vo} = 0.4950.

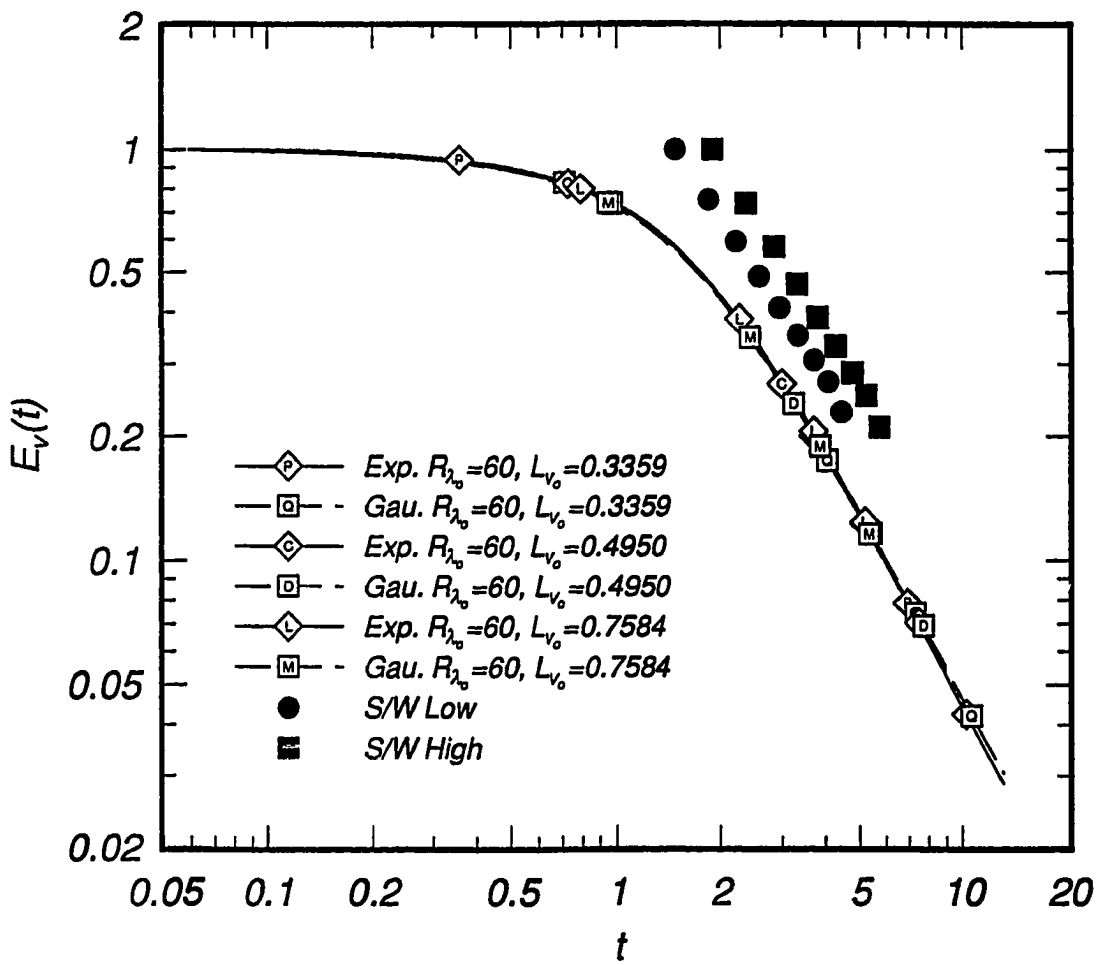

Figure 4.41: Evolution of turbulence energy as a function of L_{vo} with $A_o = 1.25$ and $R_{\lambda o} = 60$ using Gaussian and exponential initial spectral shapes.

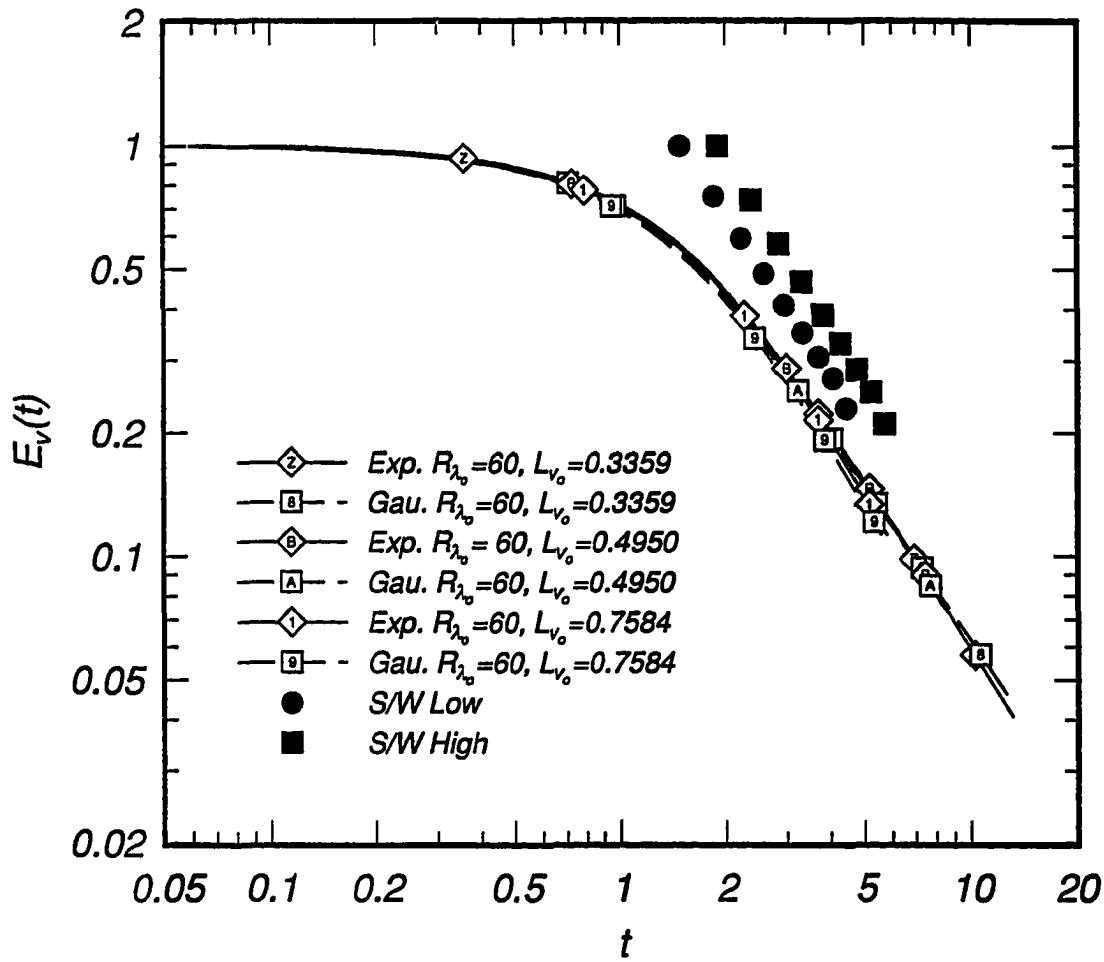

Figure 4.42: Evolution of turbulence energy as a function of L_{vo} with $A_o = 1.45/1.45$ and $R_{\lambda o} = 60$ using Gaussian and exponential initial spectral shapes.

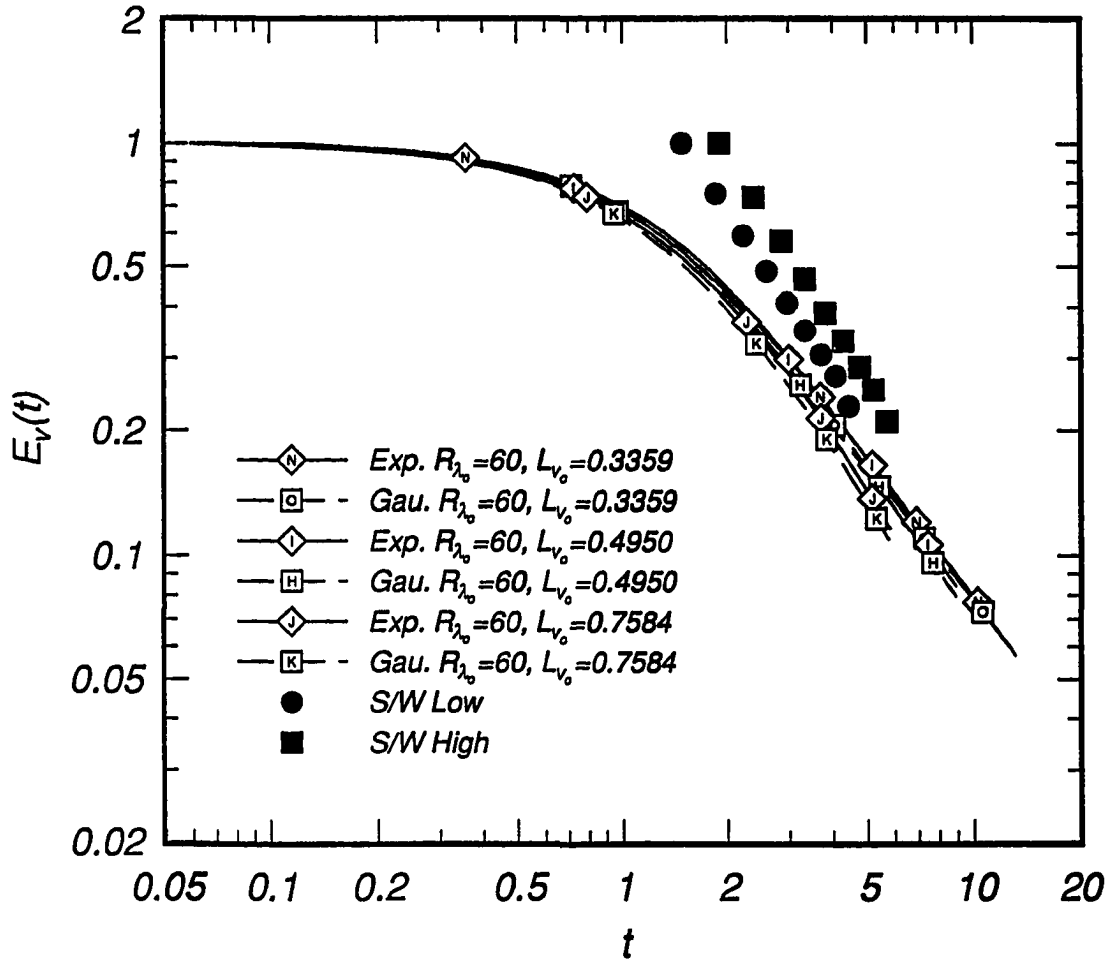

Figure 4.43: Evolution of turbulence energy as a function of L_{vo} with $A_o = 1.72/1.80$ and $R_{\lambda o} = 60$ using Gaussian and exponential initial spectral shapes.

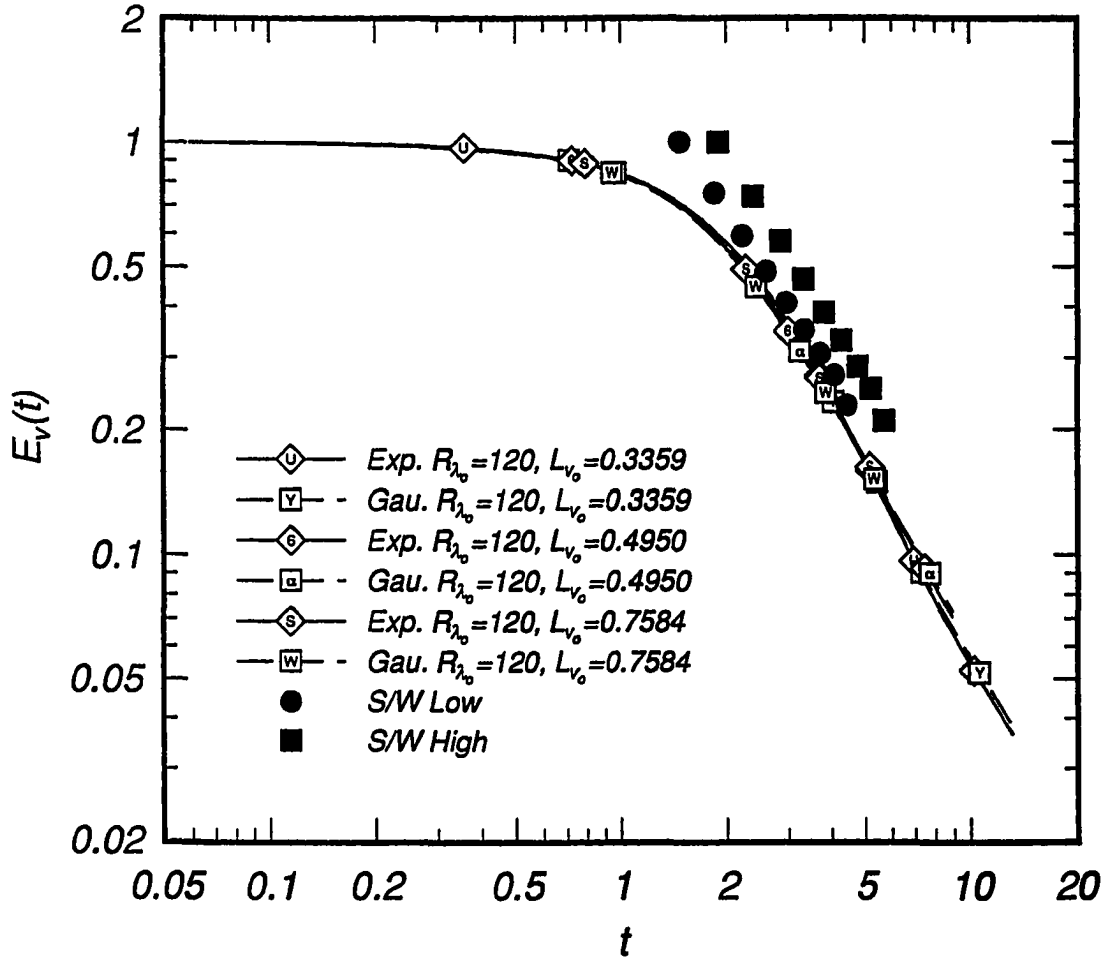

Figure 4.44: Evolution of turbulence energy as a function of L_{vo} with $A_o = 1.25$ and $R_{\lambda o} = 120$ using Gaussian and exponential initial spectral shapes.

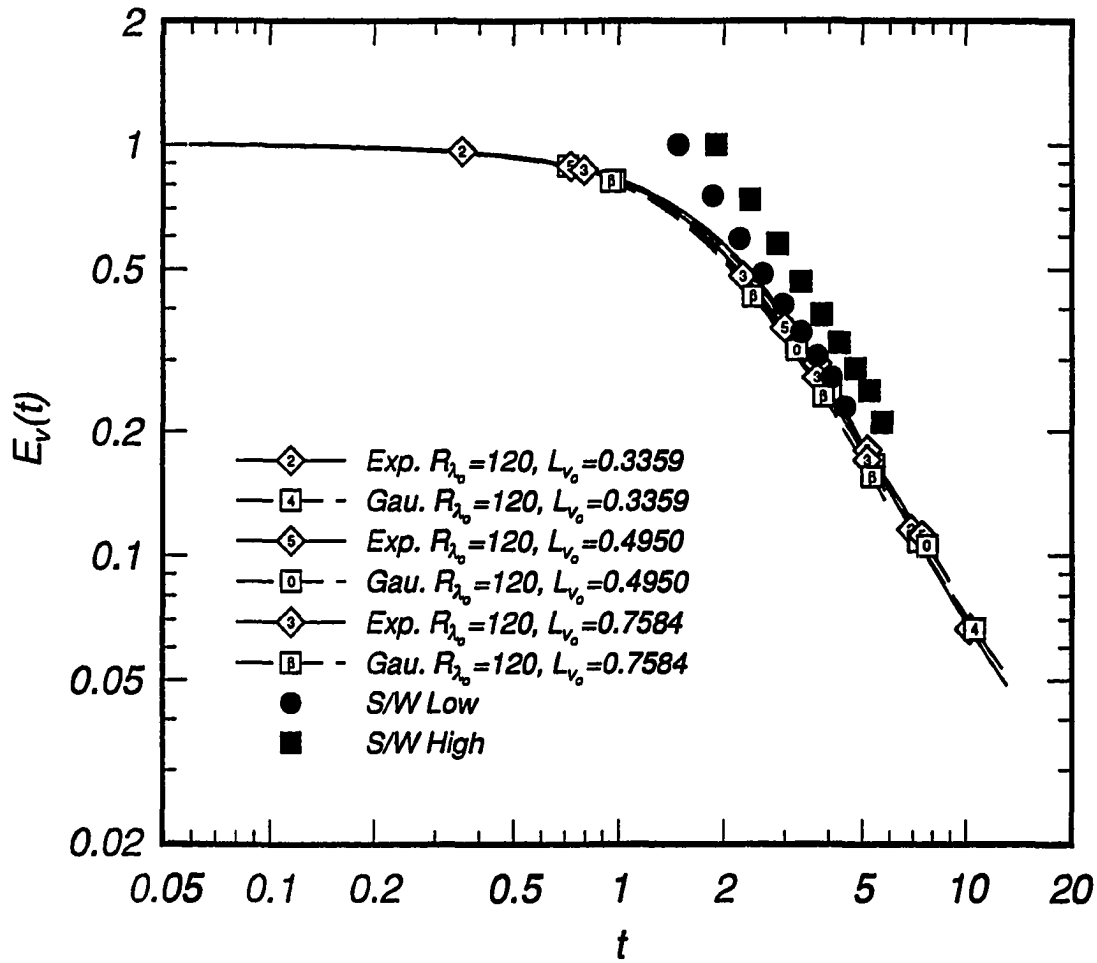

Figure 4.45: Evolution of turbulence energy as a function of L_{vo} with $A_o = 1.44/1.45$ and $R_{\lambda o} = 120$ using Gaussian and exponential initial spectral shapes.

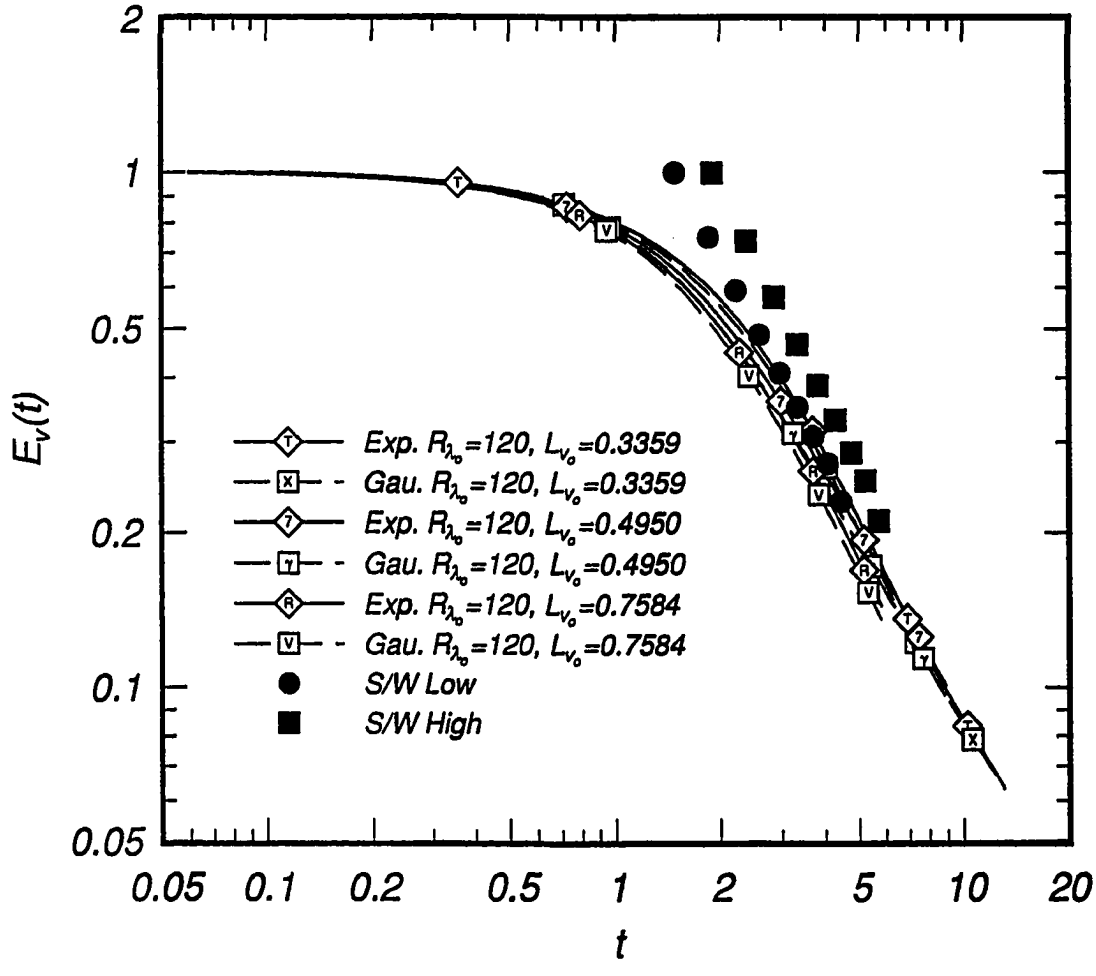

Figure 4.46: Evolution of turbulence energy as a function of L_{vo} with $A_o = 1.72/1.80$ and $R_{\lambda o} = 120$ using Gaussian and exponential initial spectral shapes.

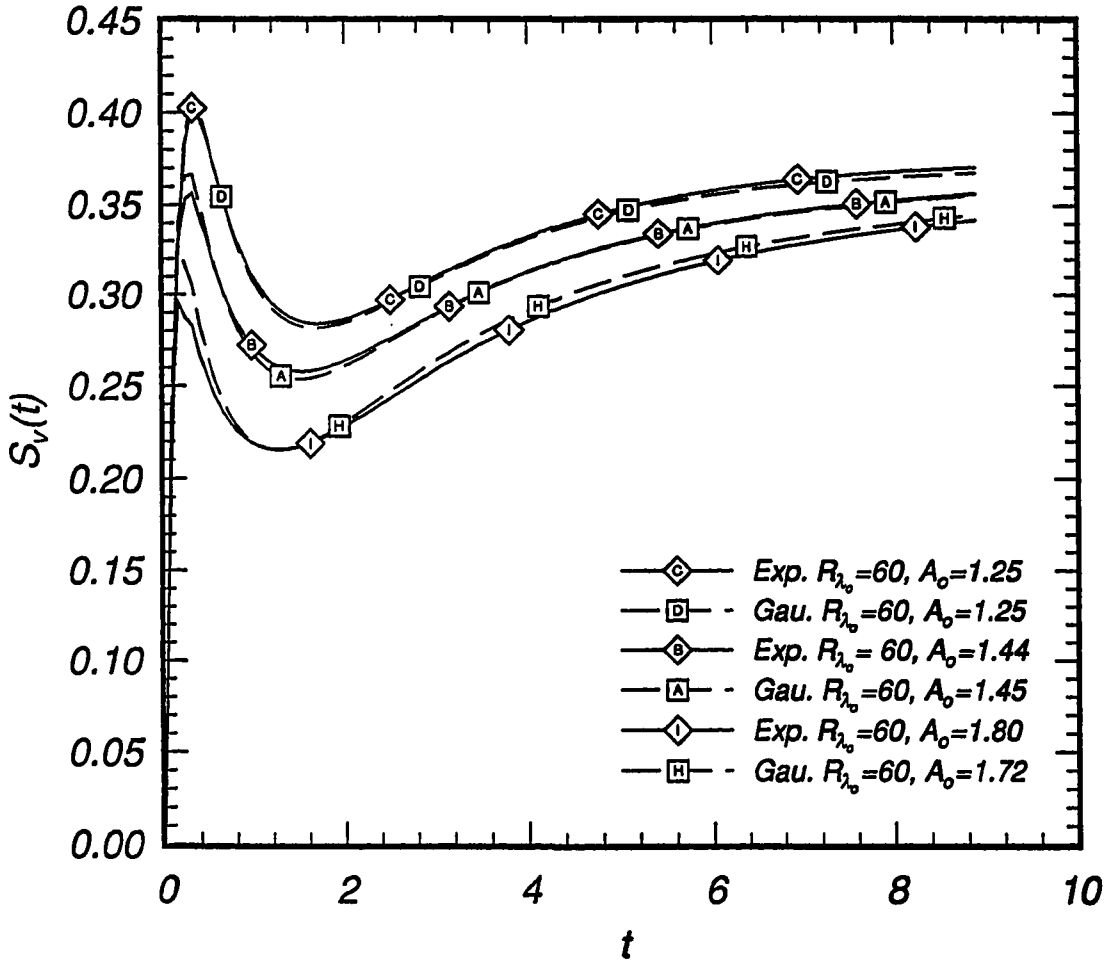

Figure 4.47: Evolution of the derivative skewness with A_o = 1.25, 1.44/1.45, 1.72/1.80, $R_{\lambda o}$ =60 and L_{vo} = 0.4950 using Gaussian and exponential initial spectral shapes.

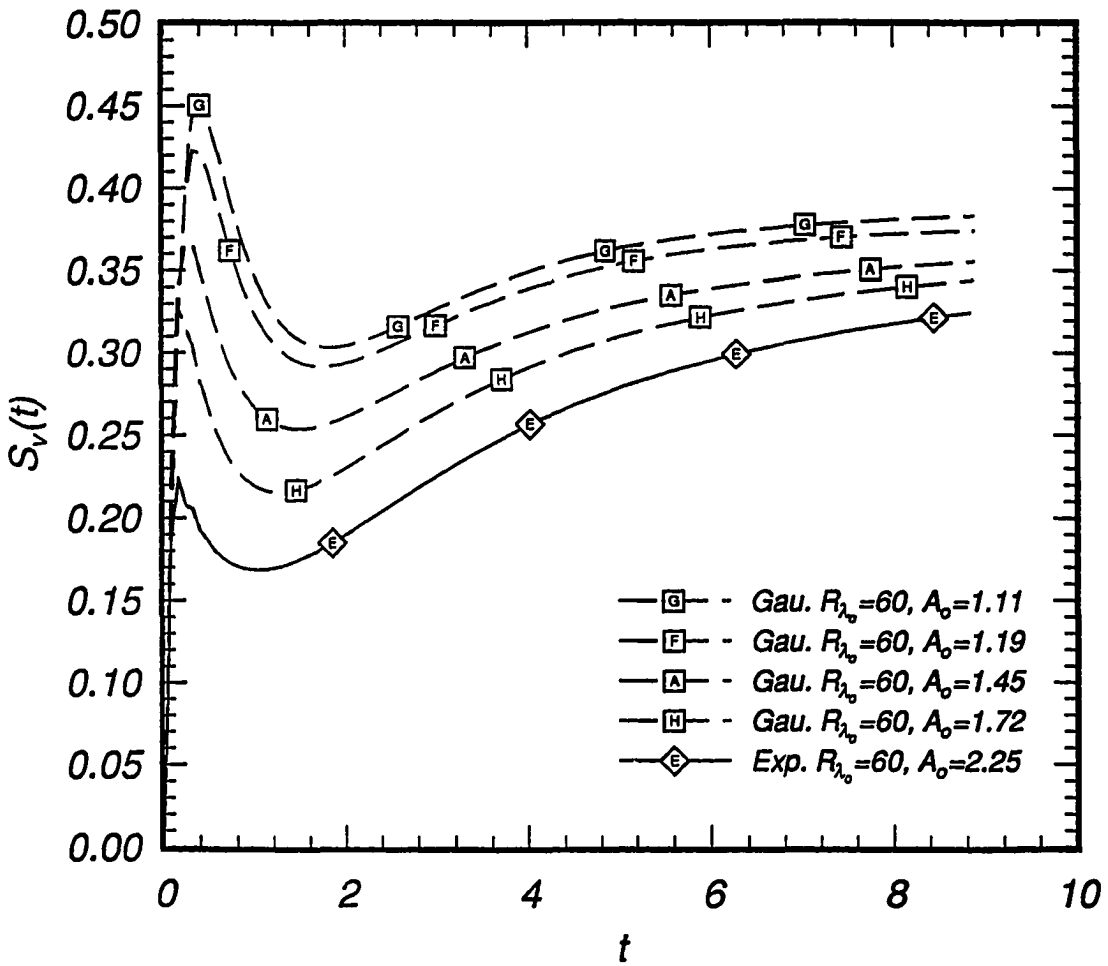

Figure 4.48: Evolution of the derivative skewness as a function of A using $R_{\lambda o} = 60$ and $L_{vo} = 0.4950$.

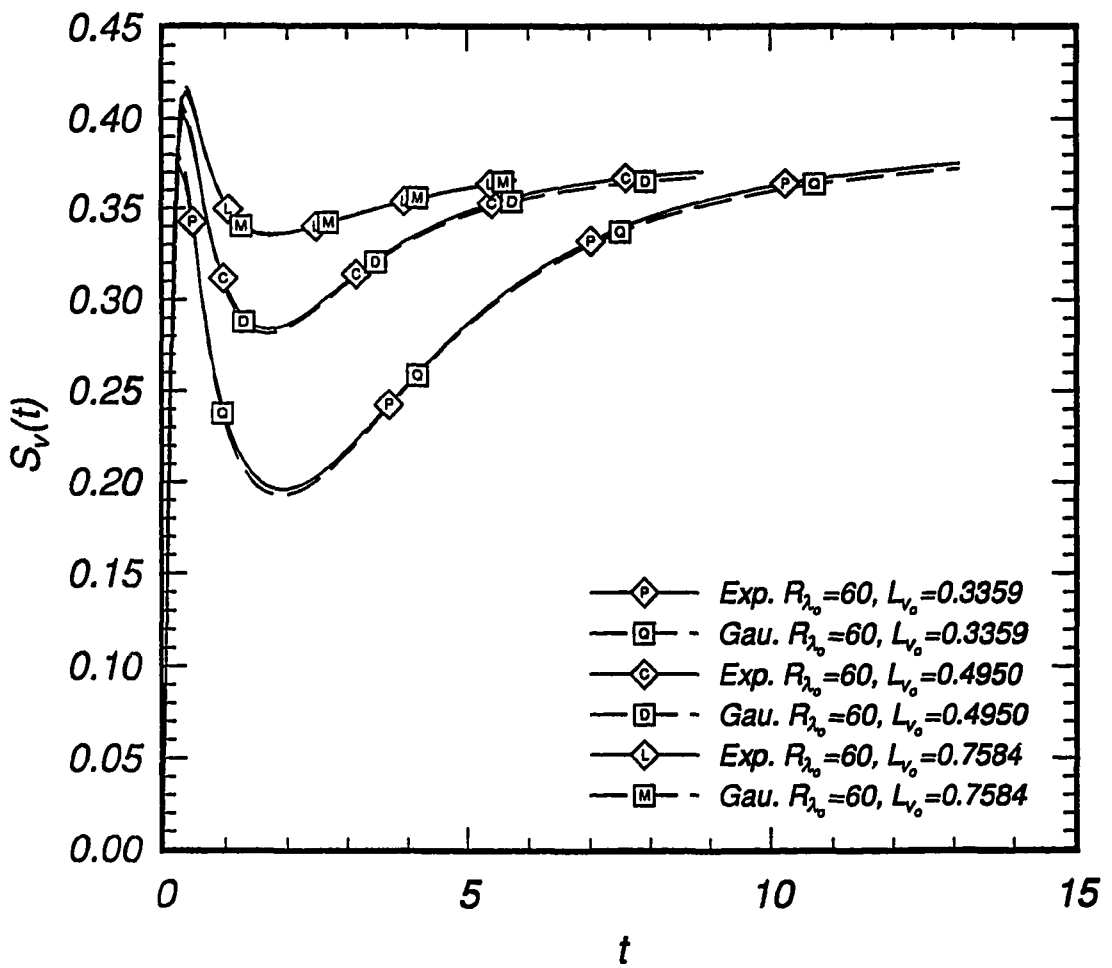

Figure 4.49: Evolution of derivative skewnesses as functions of L_v using $A_o = 1.25$ and $R_{\lambda o} = 60$.

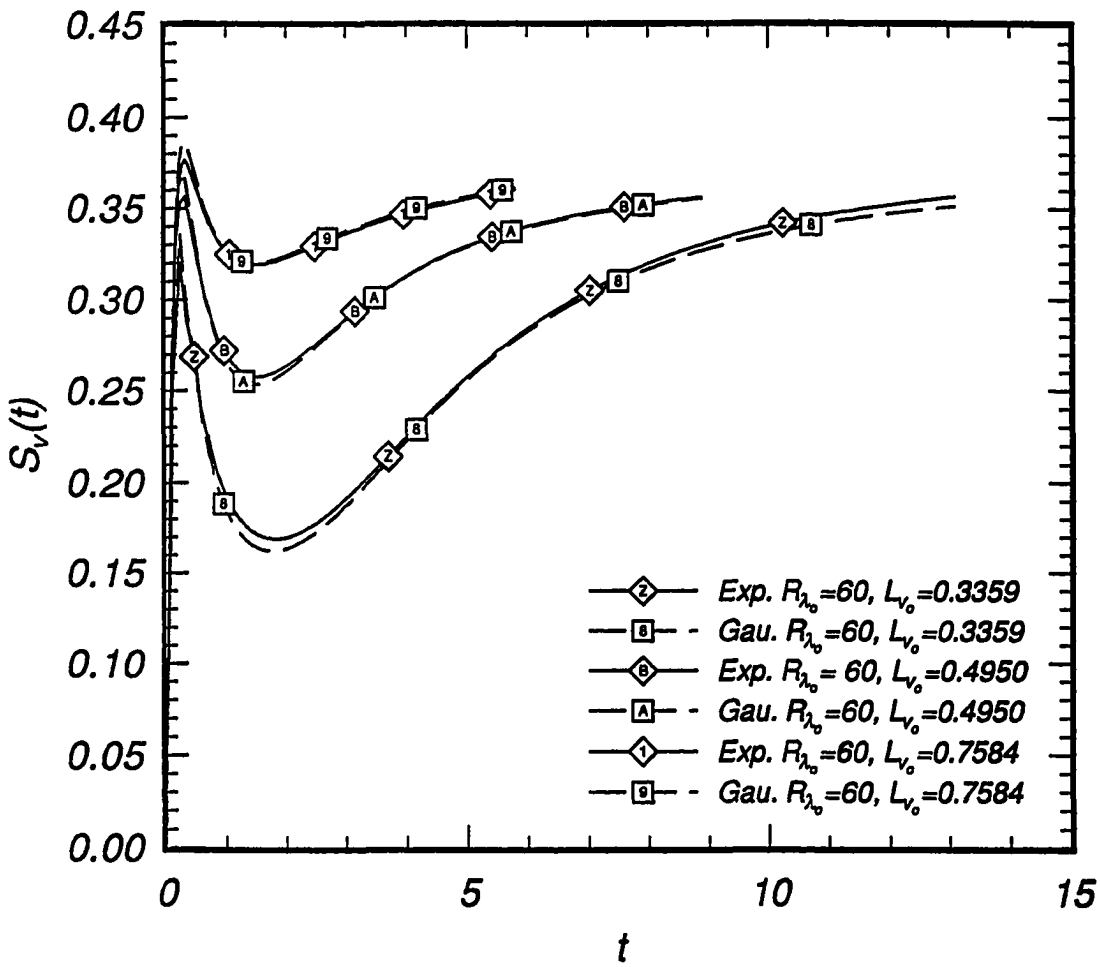

Figure 4.50: Evolution of derivative skewnesses as functions of L_v using $A_o = 1.45$ and $R_{\lambda o} = 60$.

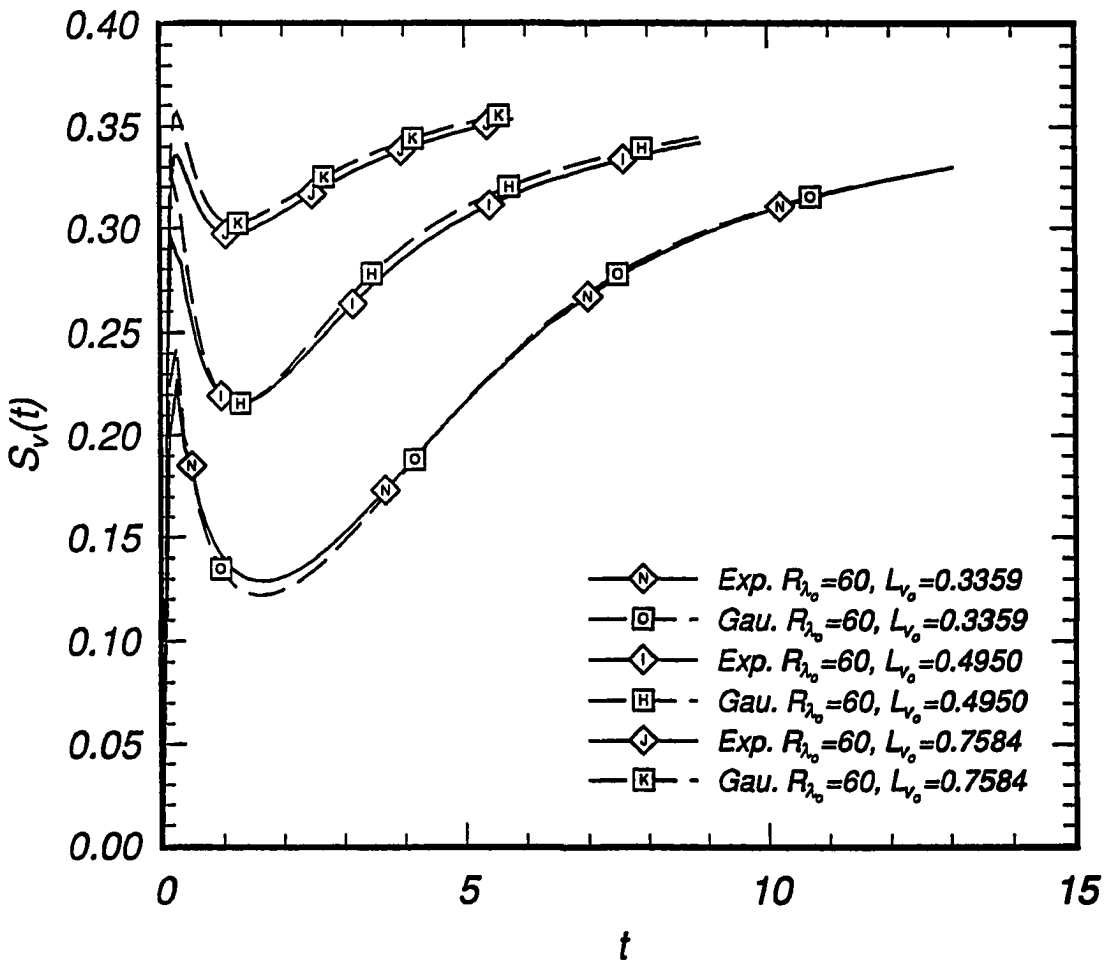

Figure 4.51: Evolution of derivative skewnesses as functions of L_v using A_o = 1.72/1.80 and $R_{\lambda o} = 60$.

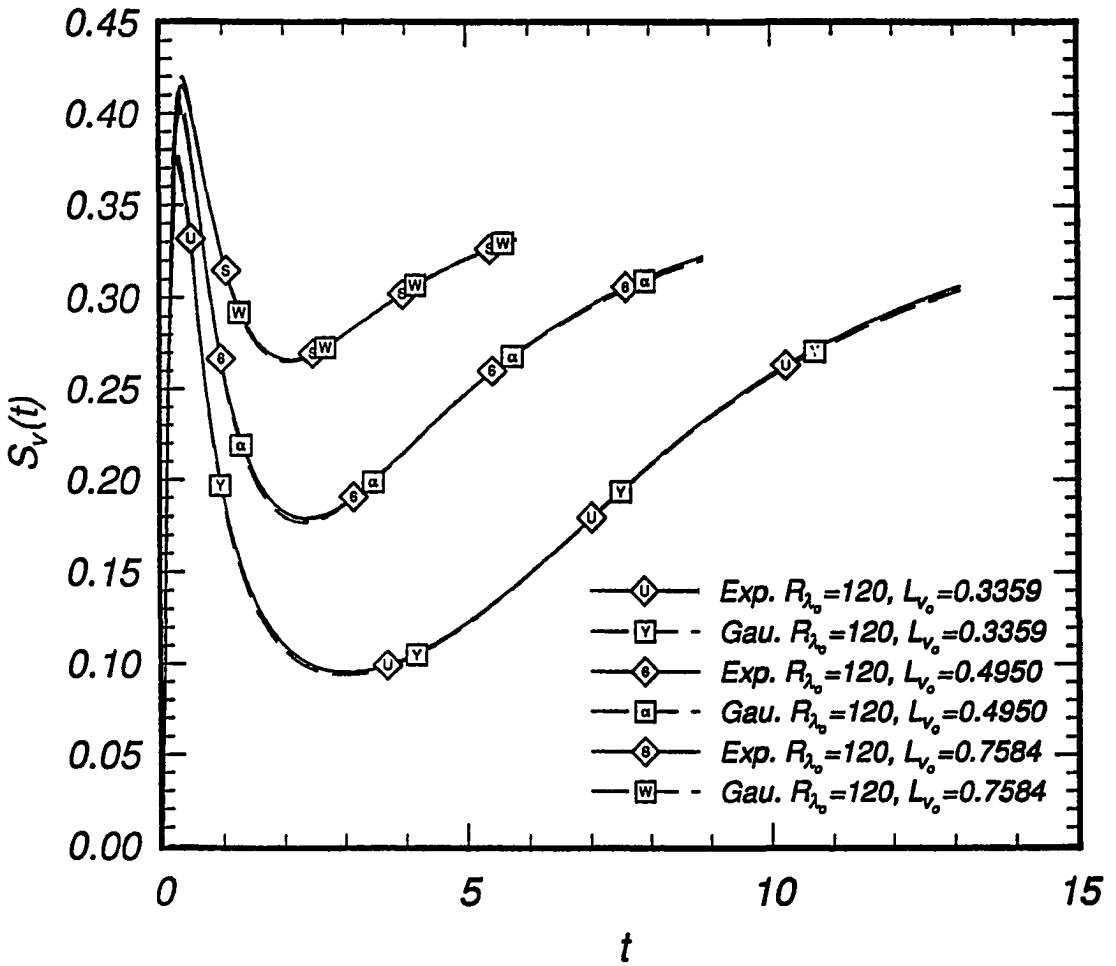

Figure 4.52: Evolution of derivative skewnesses as functions of L_v using $A_o = 1.25$ and $R_{\lambda o} = 120$.

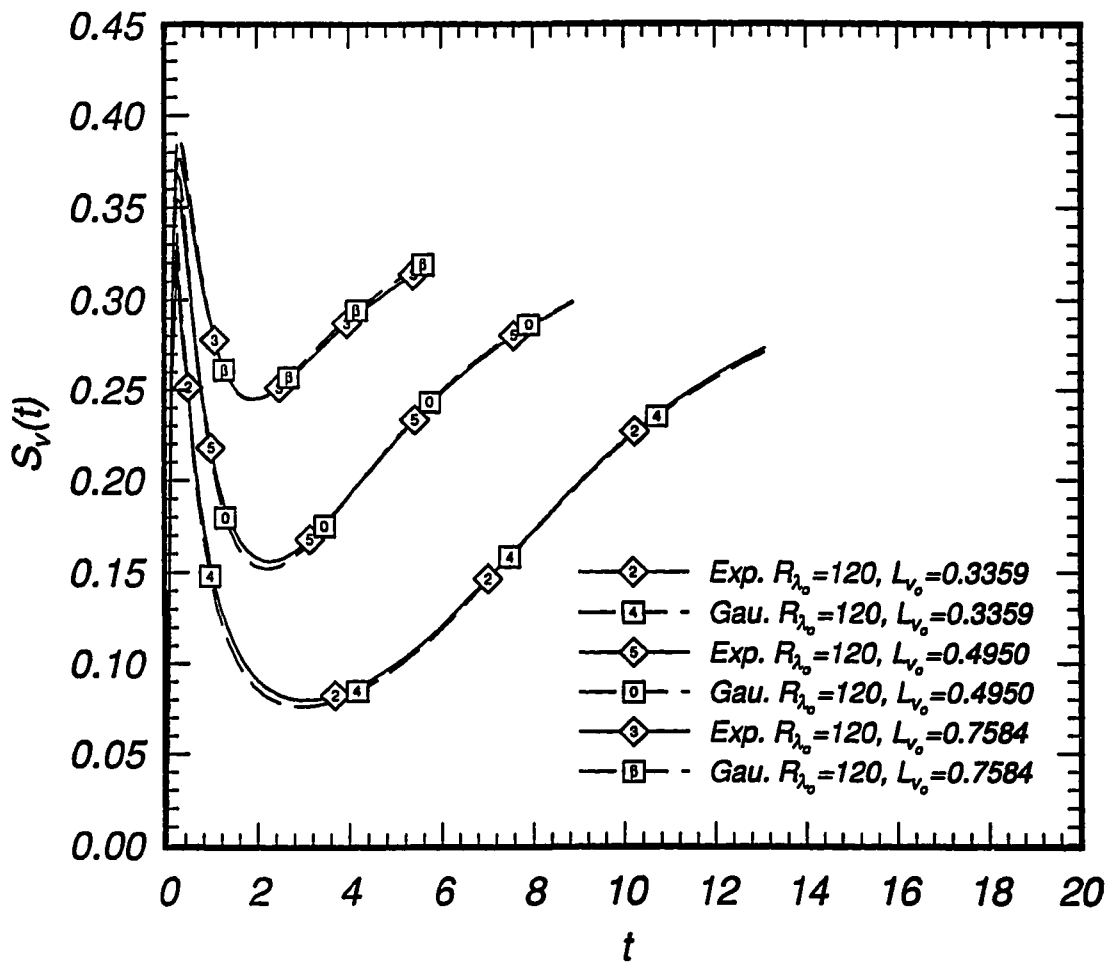

Figure 4.53: Evolution of derivative skewnesses as functions of L_v using A_o = 1.44/1.45 and $R_{\lambda o} = 120$.

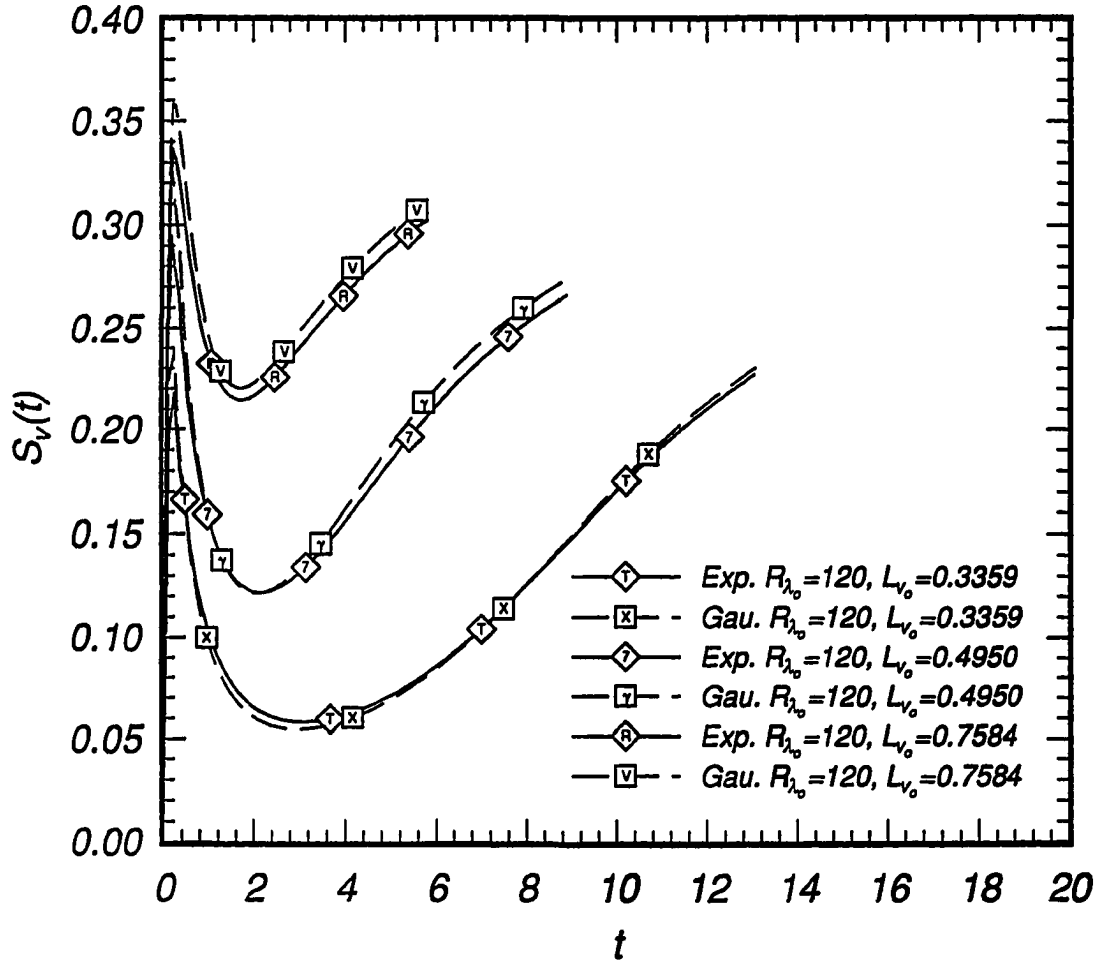

Figure 4.54: Evolution of derivative skewnesses as functions of L_v using A_o = 1.72/1.80 and $R_{\lambda o} = 120$.

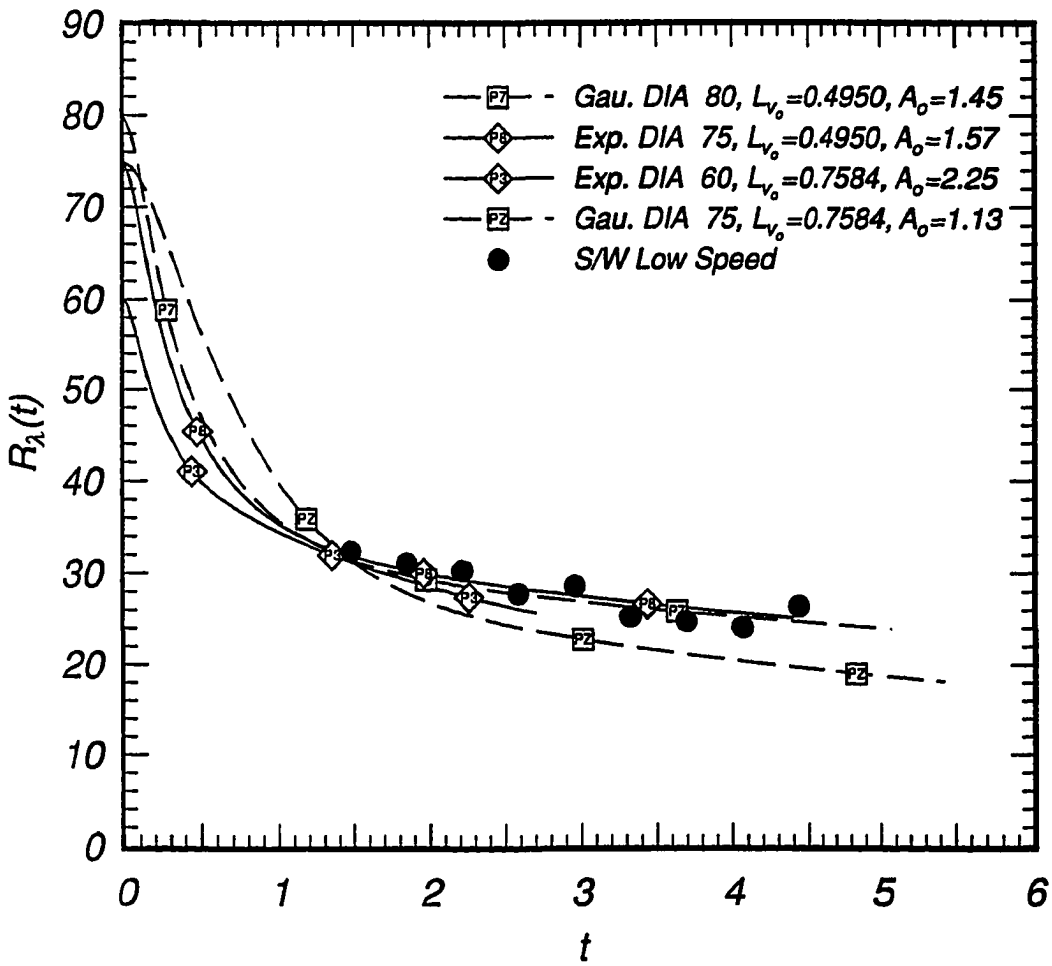

Figure 4.55: Evolution of DIA microscale Reynolds numbers as functions of A_o and $R_{\lambda o}$ compared with low speed experimental results of Sirivat and Warhaft.

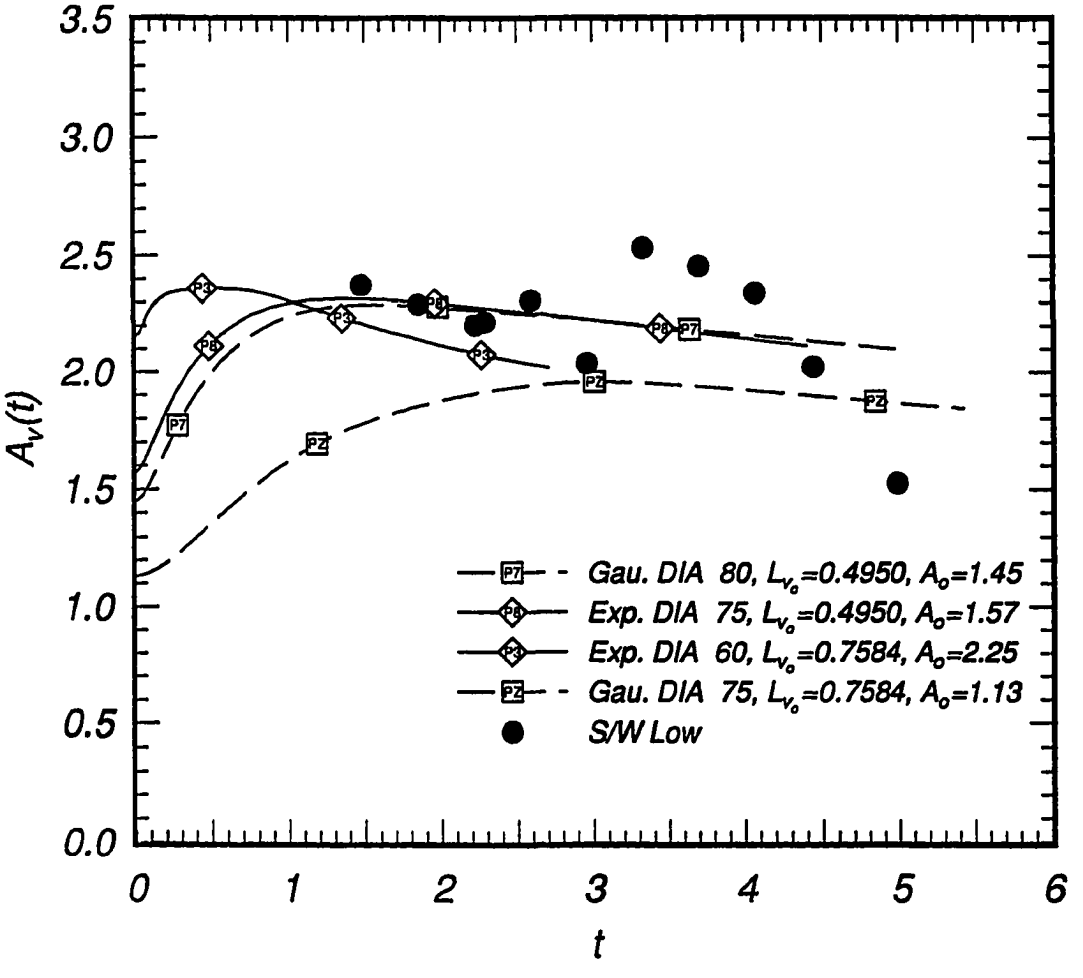

Figure 4.56: Evolution of DIA aspect ratios, A, as functions of A_o and $R_{\lambda o}$ compared with low speed experimental results of Sirivat and Warhaft.

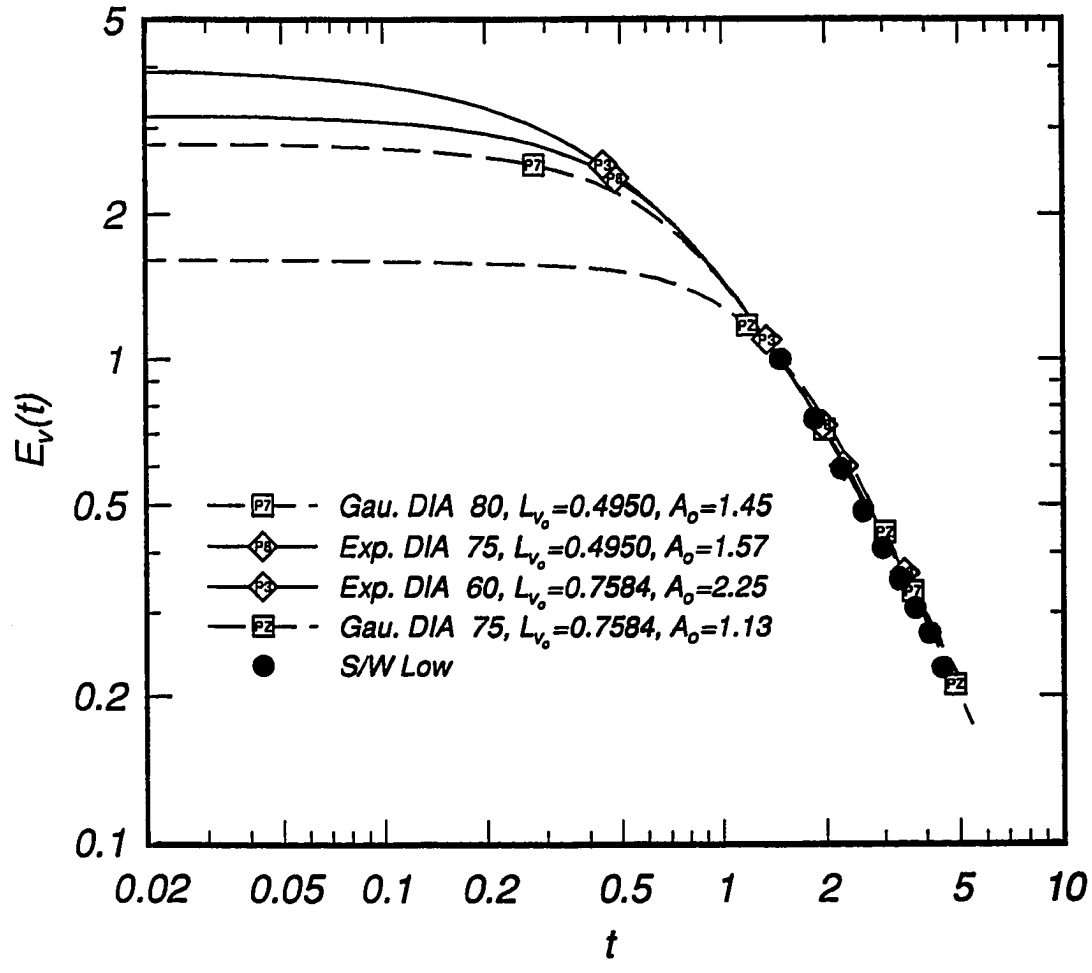

Figure 4.57: Evolution of DIA turbulence energy, E_{vv}, as functions of A_o and $R_{\lambda o}$ compared with low speed experimental results of Sirivat and Warhaft, (L_{v_o}=0.495).

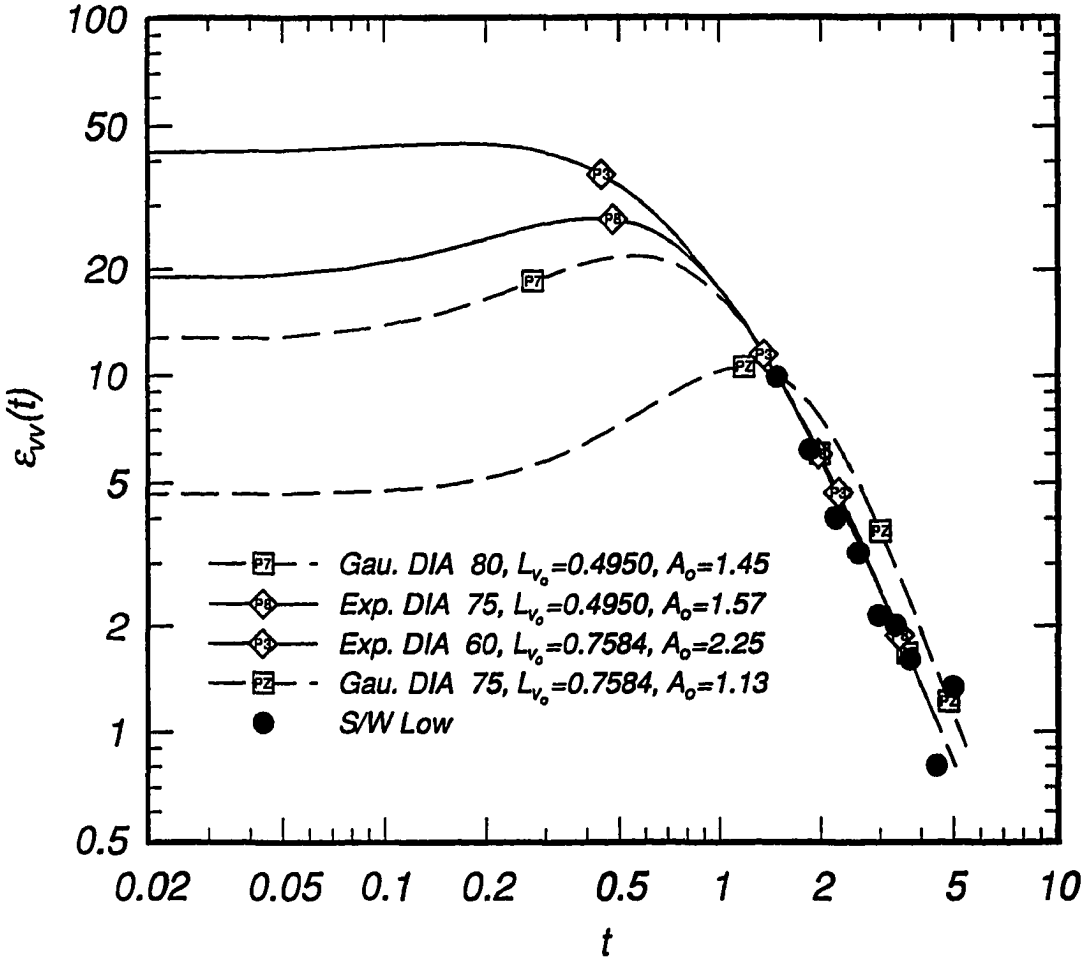

Figure 4.58: Evolution of DIA turbulence energy dissipation, ϵ_{vv}, as functions of A_o and $R_{\lambda o}$ compared with low speed experimental results of Sirivat and Warhaft.

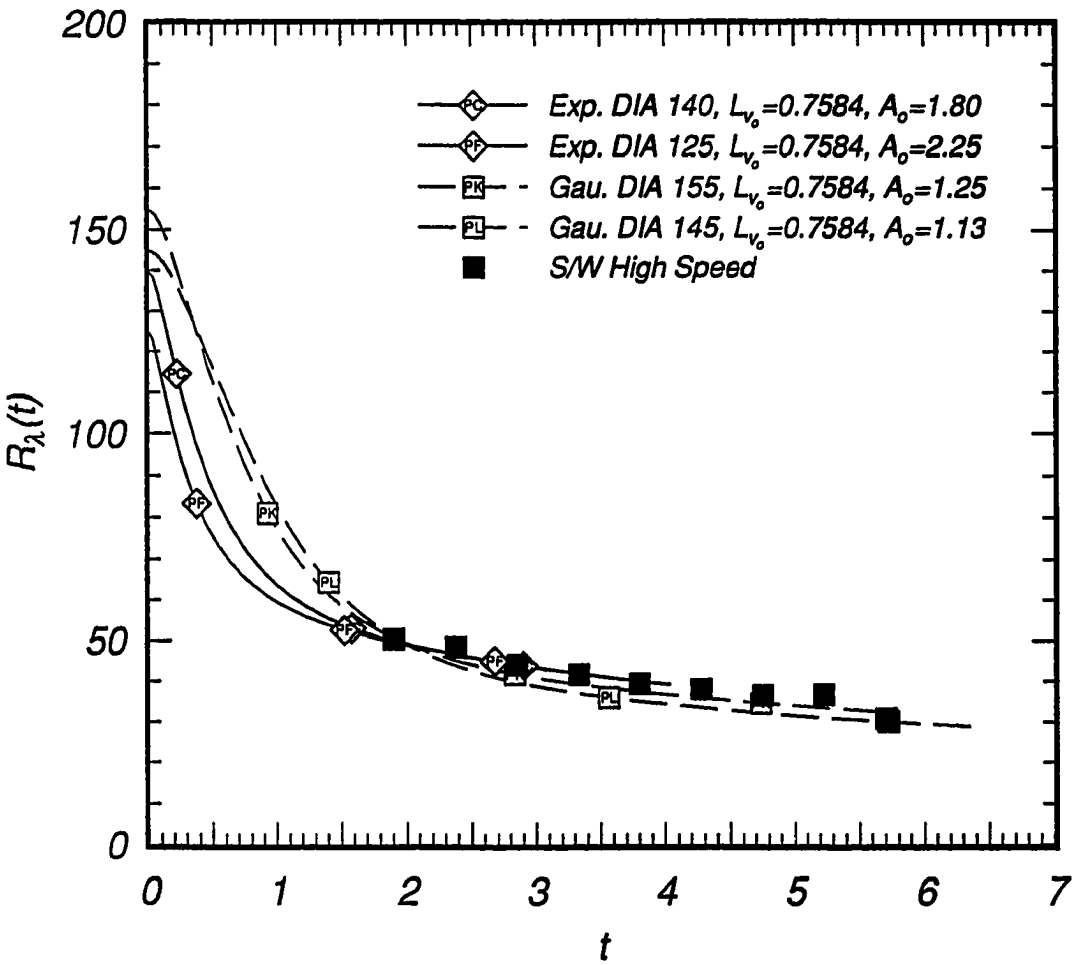

Figure 4.59: Evolution of DIA microscale Reynolds numbers as functions of A_o and $R_{\lambda o}$ compared with high speed experimental results of Sirivat and Warhaft.

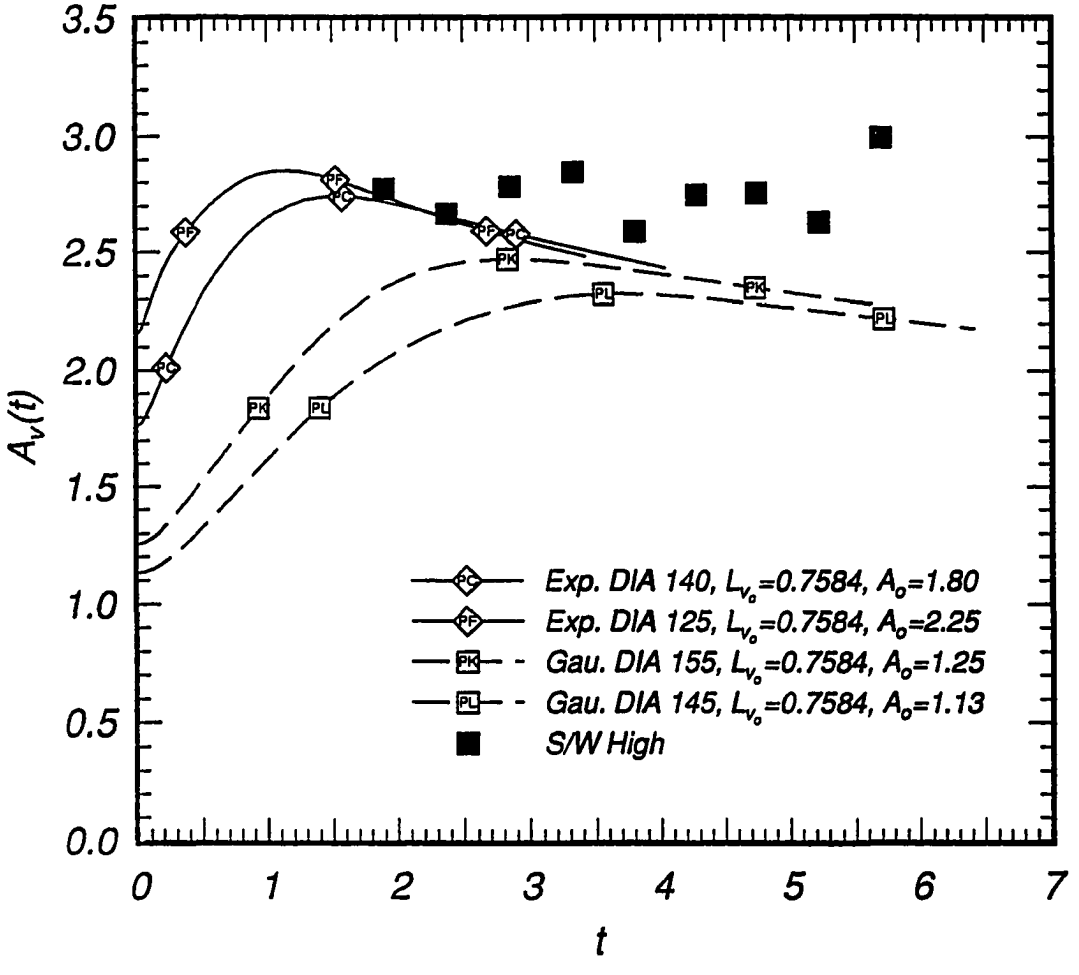

Figure 4.60: Evolution of DIA aspect ratios, A, as functions of A_o and $R_{\lambda o}$ compared with high speed experimental results of Sirivat and Warhaft.

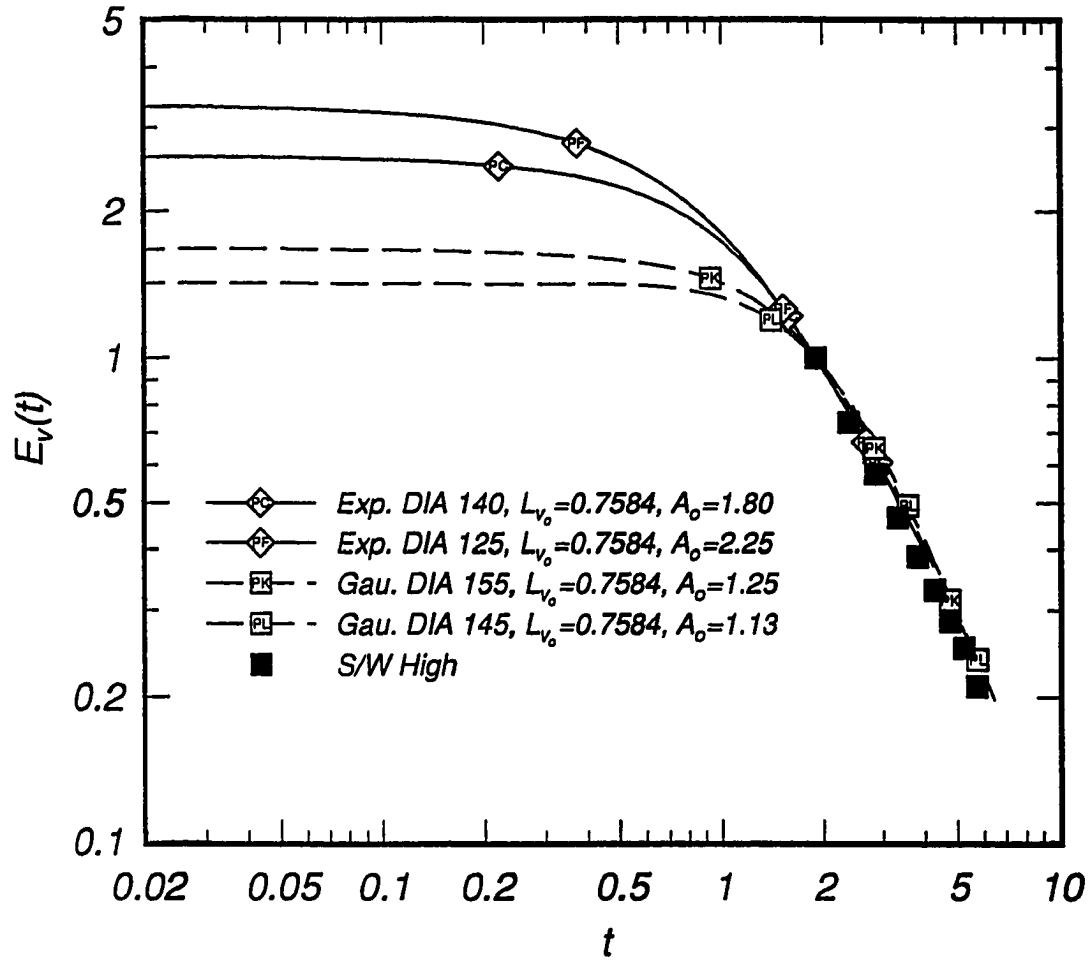

Figure 4.61: Evolution of DIA turbulence energy, E_{vv}, as functions of A_o and $R_{\lambda o}$ compared with high speed experimental results of Sirivat and Warhaft.

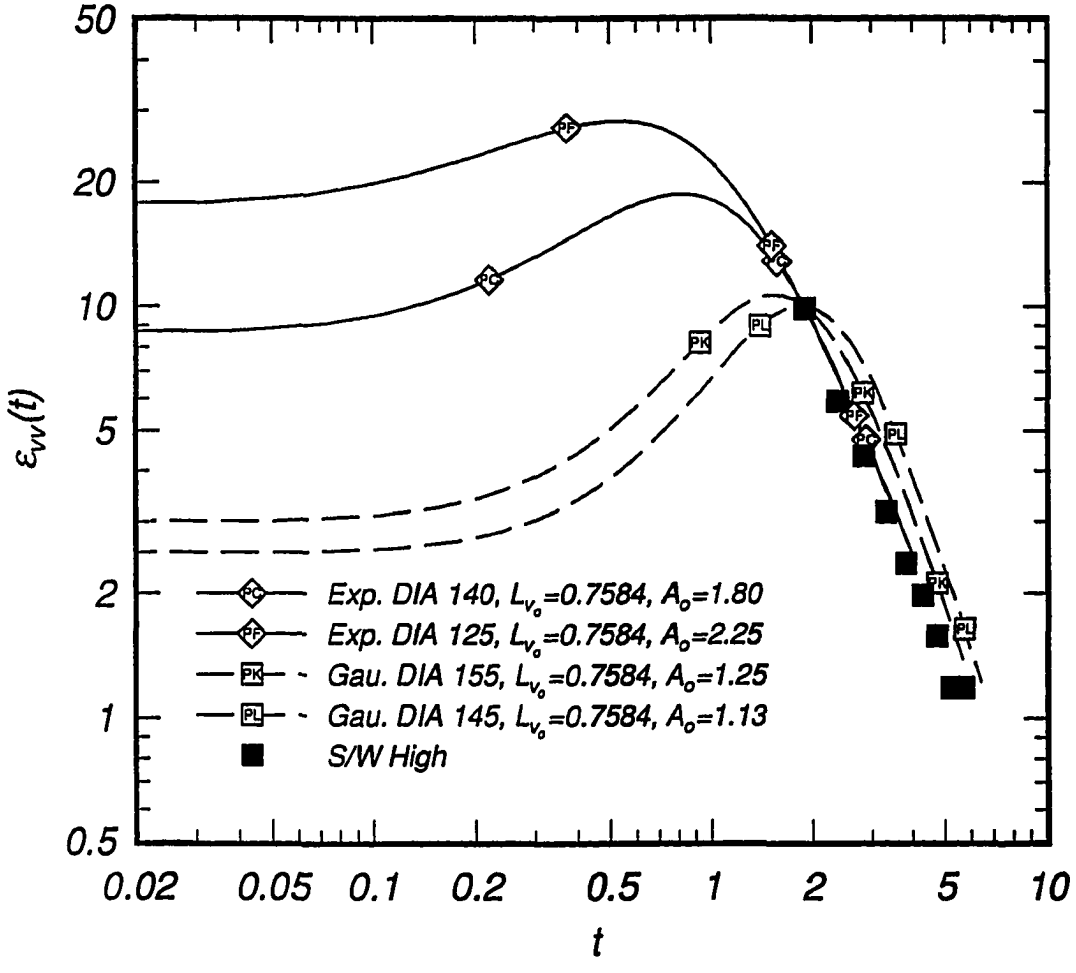

Figure 4.62: Evolution of DIA turbulence energy dissipation, ϵ_{vv}, as functions of A_o and $R_{\lambda o}$ compared with high speed experimental results of Sirivat and Warhaft.

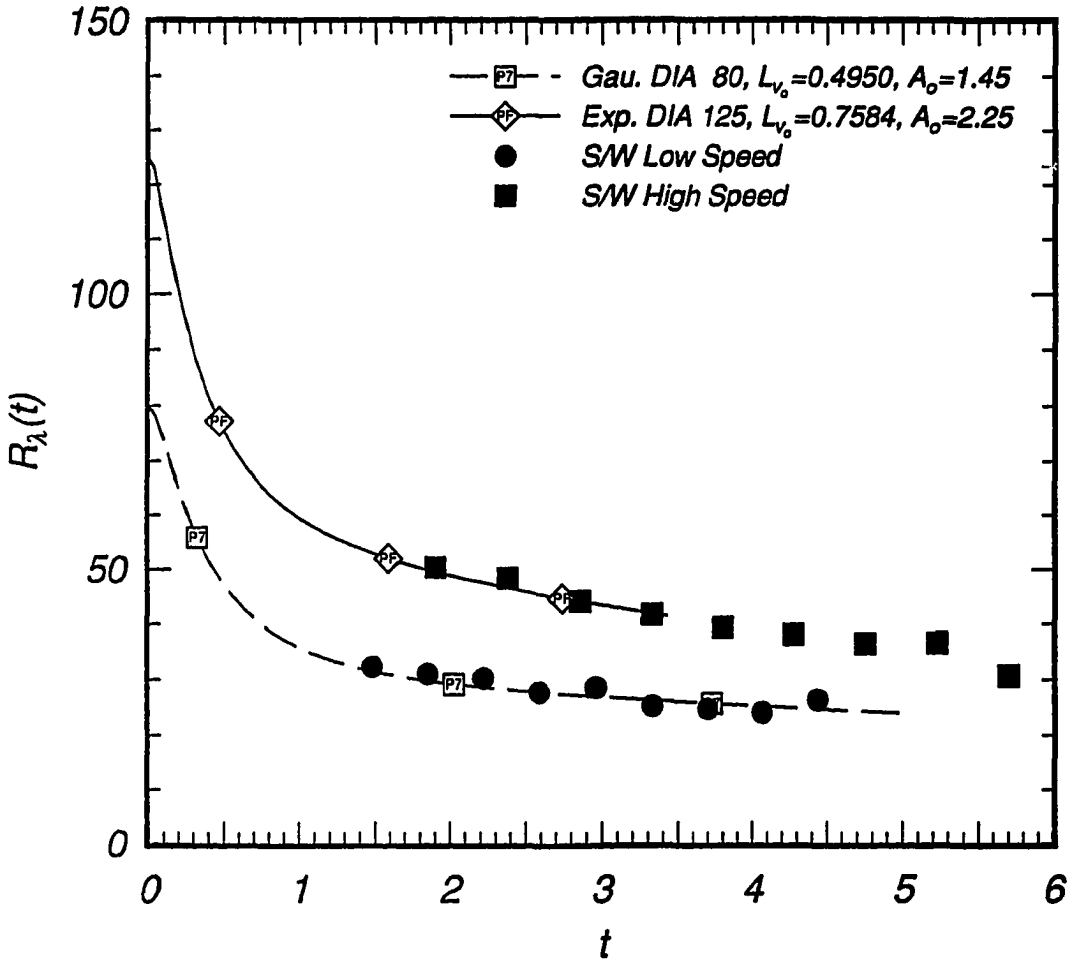

Figure 4.63: Evolution of best fit DIA microscale Reynolds numbers compared with the experimental results of Sirivat and Warhaft.

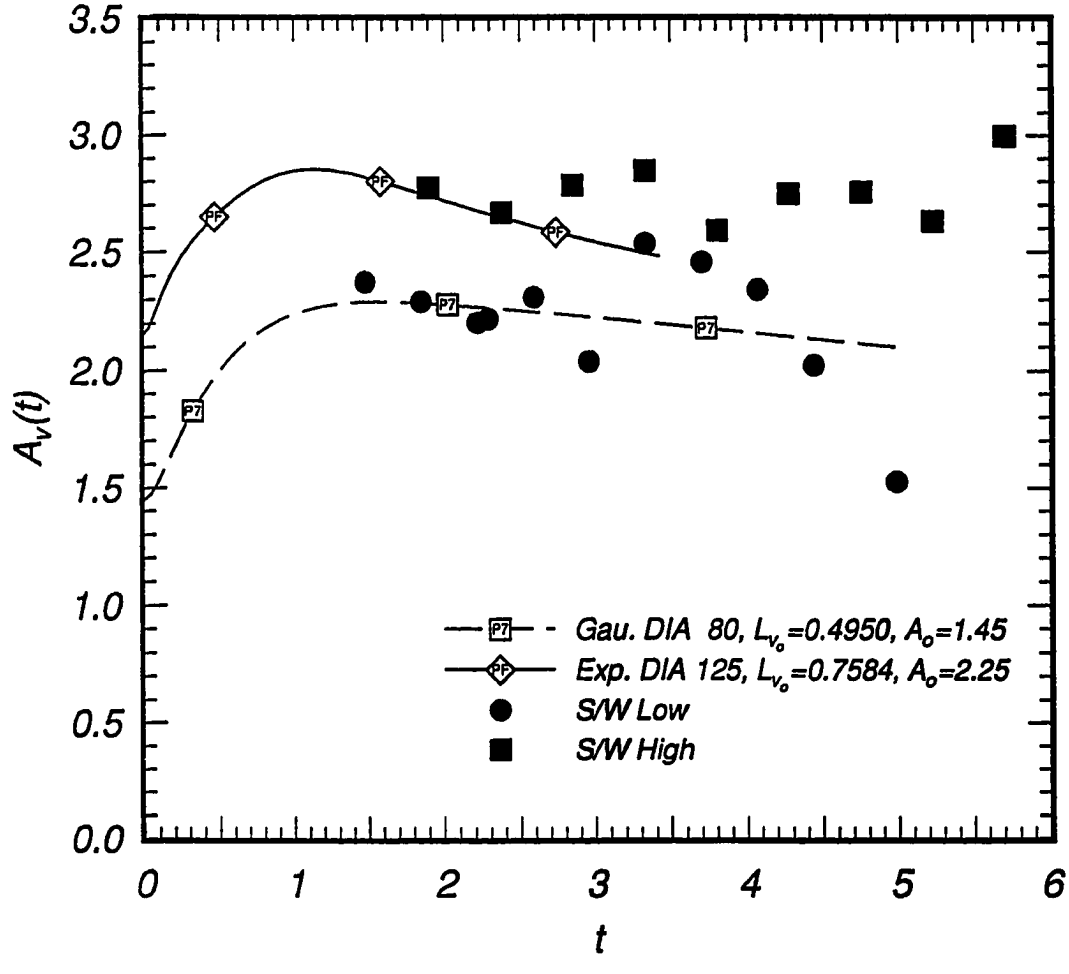

Figure 4.64: Evolution of best fit DIA aspect ratios, A, as compared with the experimental results of Sirivat and Warhaft.

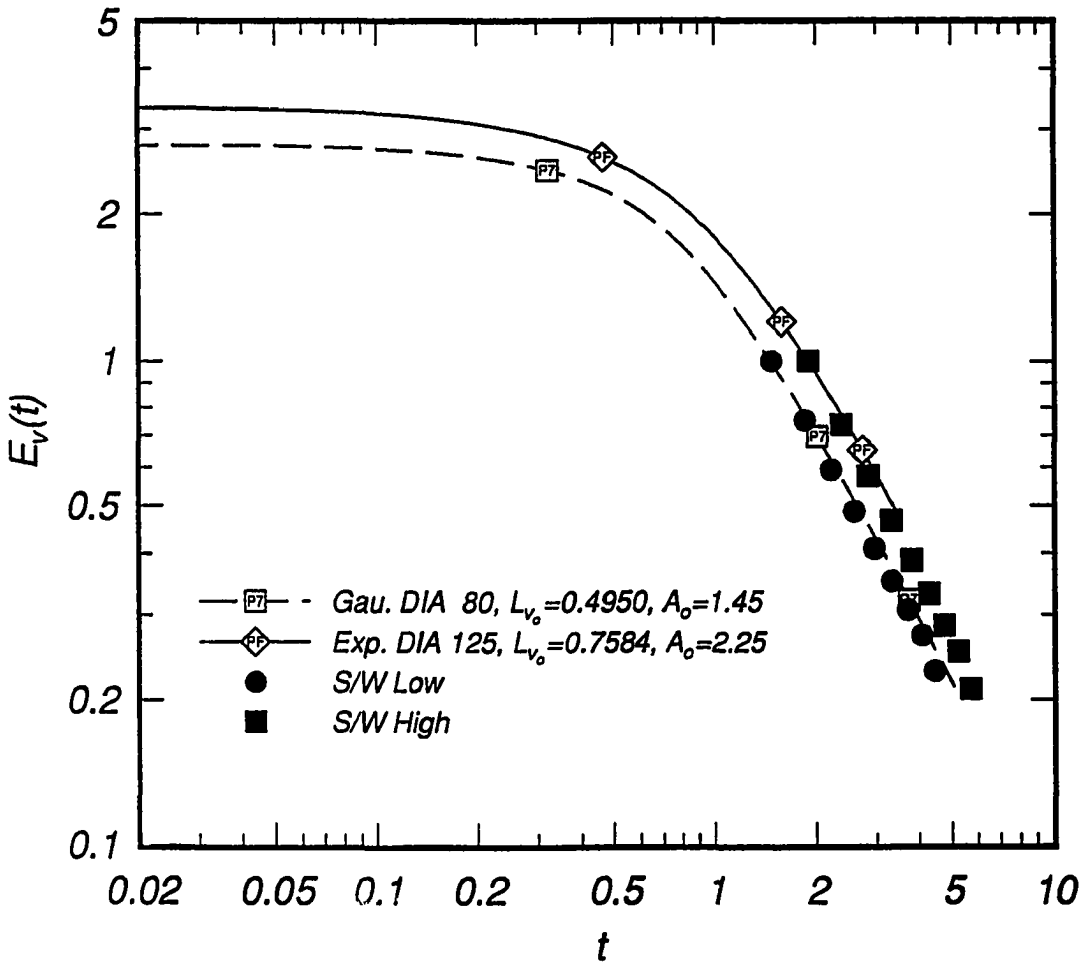

Figure 4.65: Evolution of best fit DIA turbulence energy, E_{vv}, as compared with the experimental results of Sirivat and Warhaft.

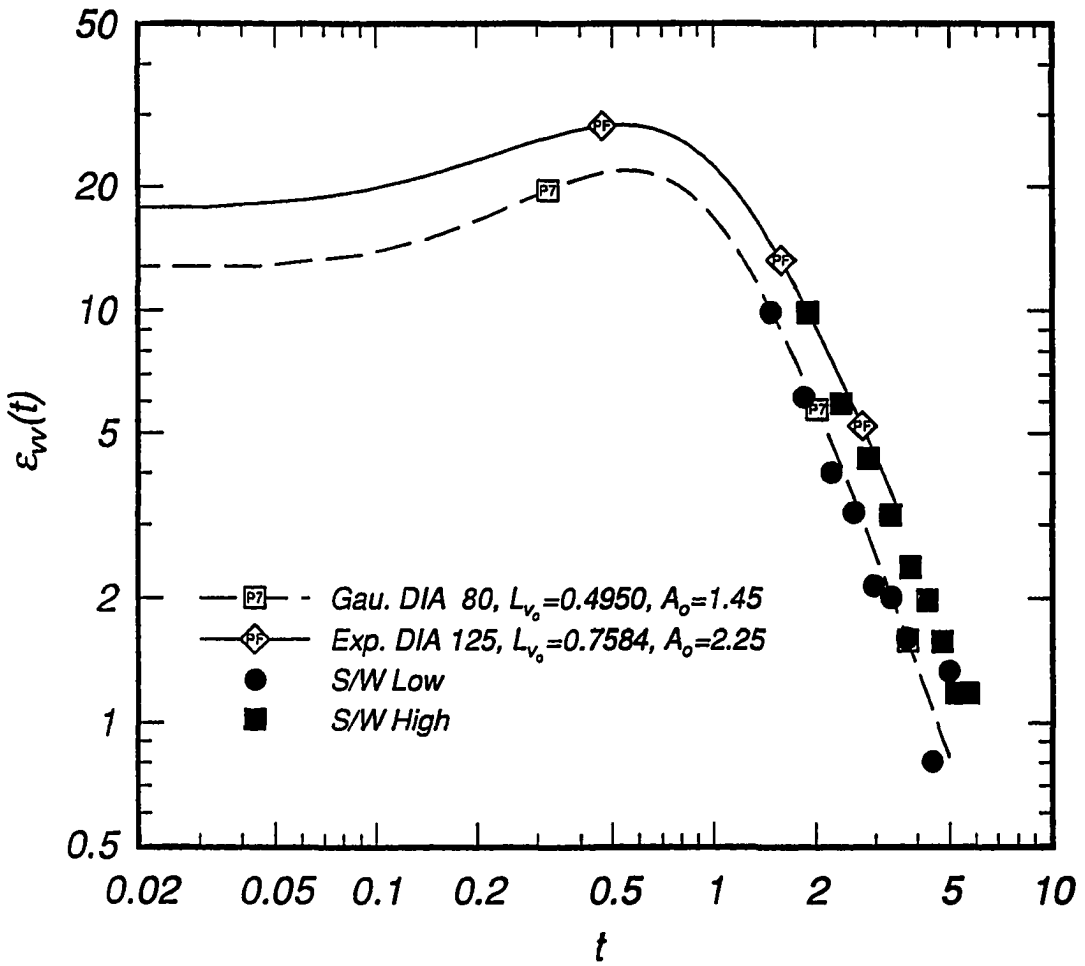

Figure 4.66: Evolution of best fit DIA turbulence energy dissipation, ϵ_{vv}, as compared with the experimental results of Sirivat and Warhaft.

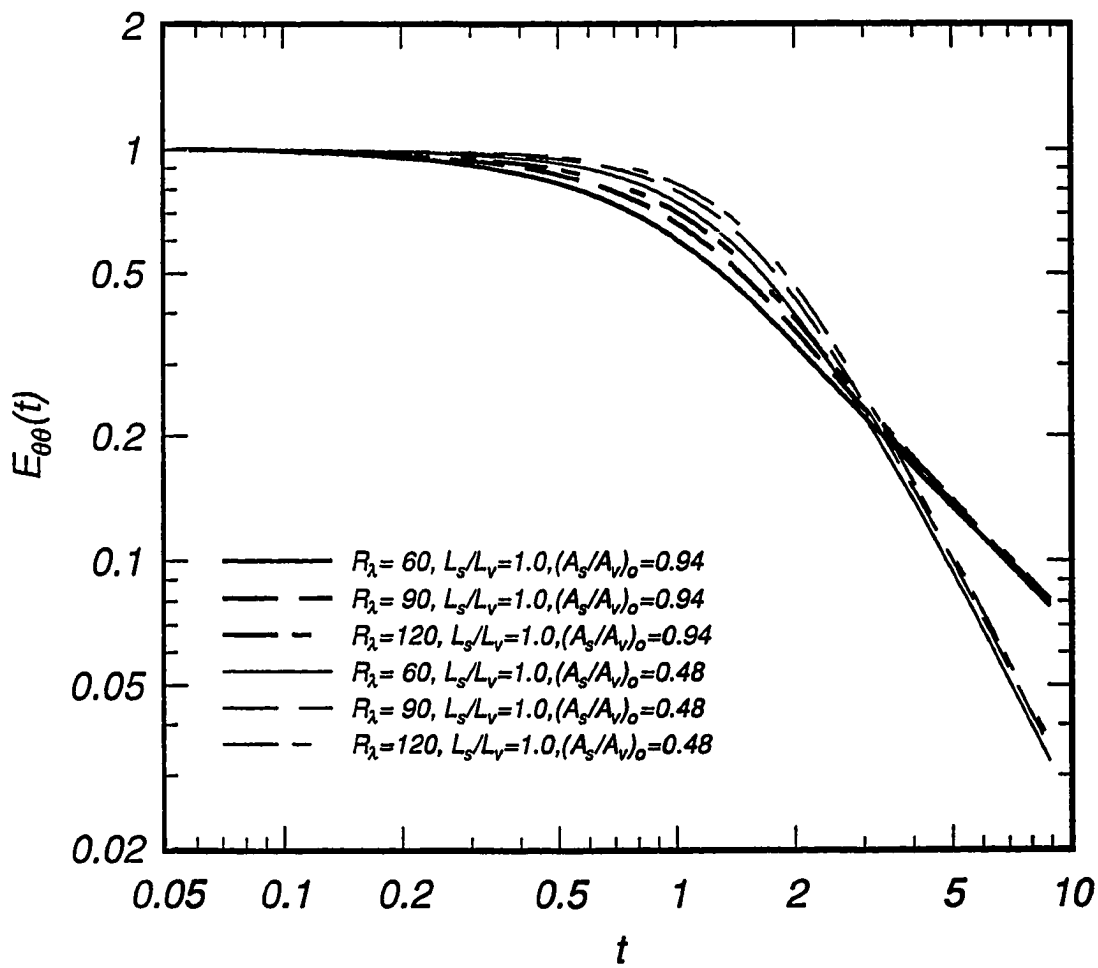

Figure 4.67: Evolution of scalar energy at different spectral aspect ratios.

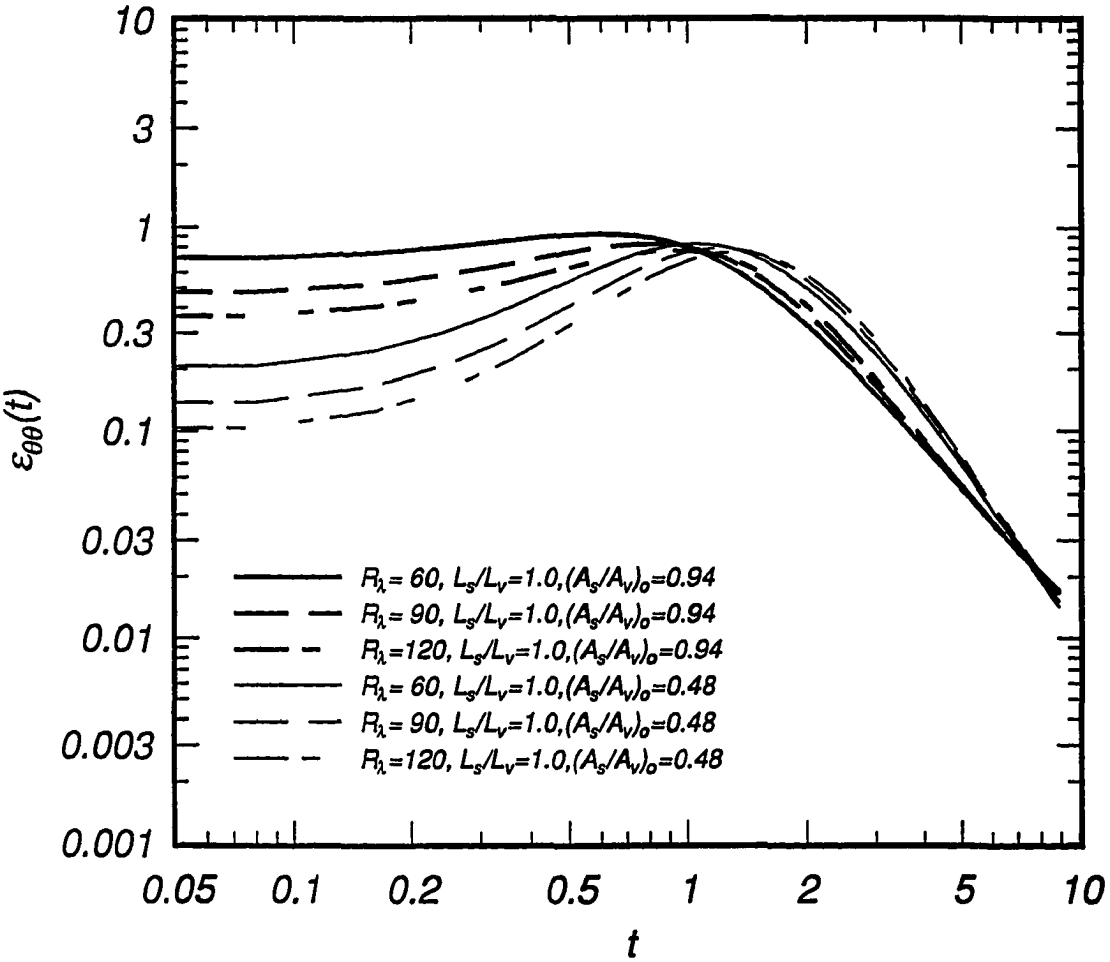

Figure 4.68: Evolution of scalar energy diffusion for different spectral aspect ratios.

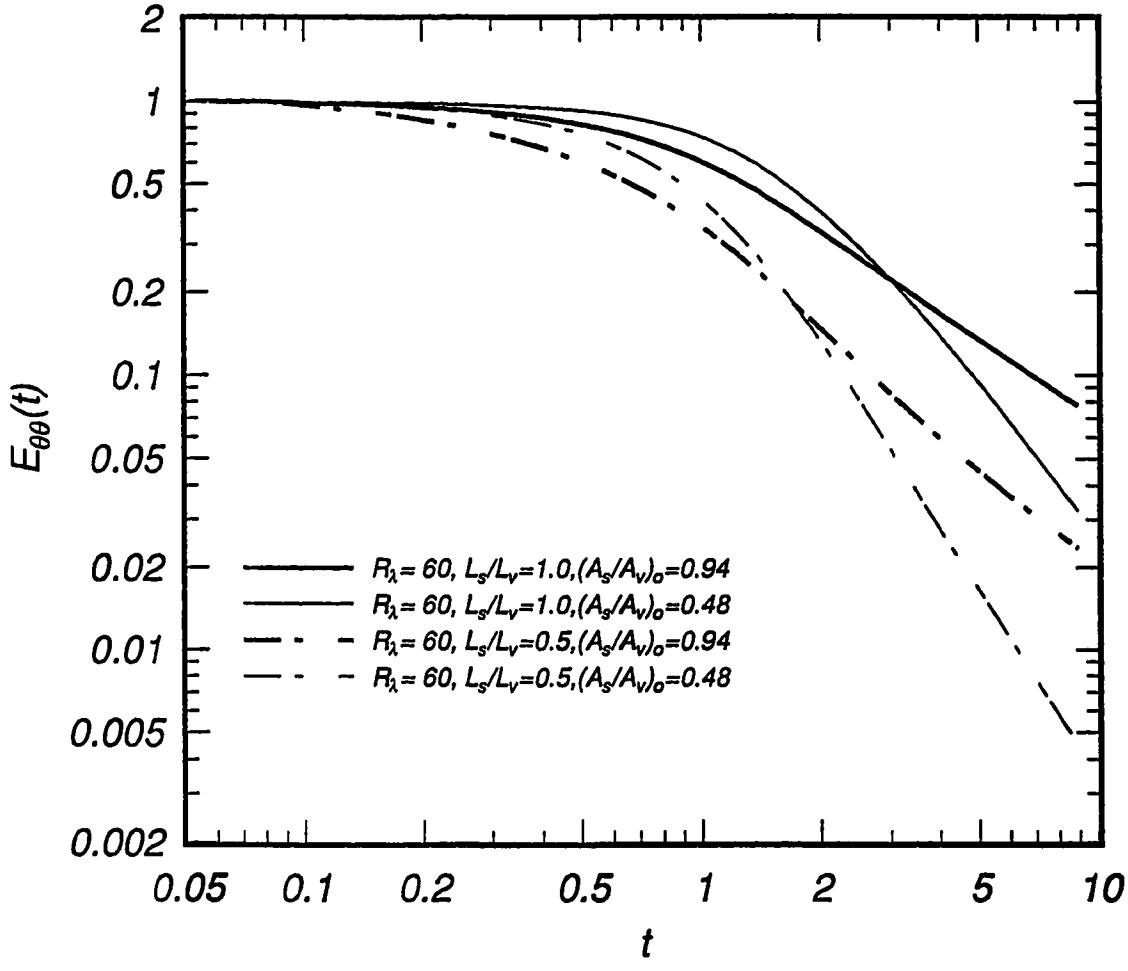

Figure 4.69: Evolution of scalar energy for different initial integral lengthscales and spectral aspect ratios.

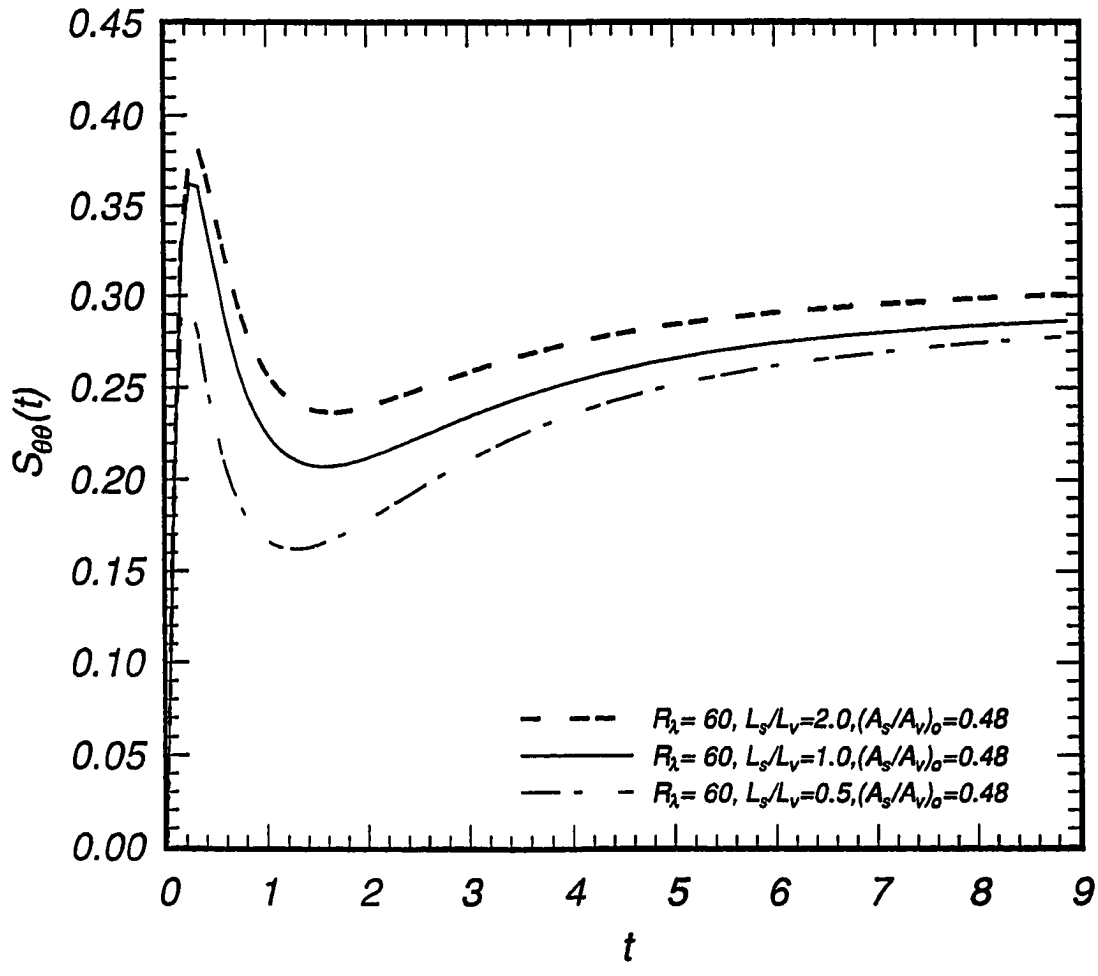

Figure 4.70: Evolution of scalar mixed derivative skewness at different initial integral lengthscales, $A_s/A_v = 0.48$.

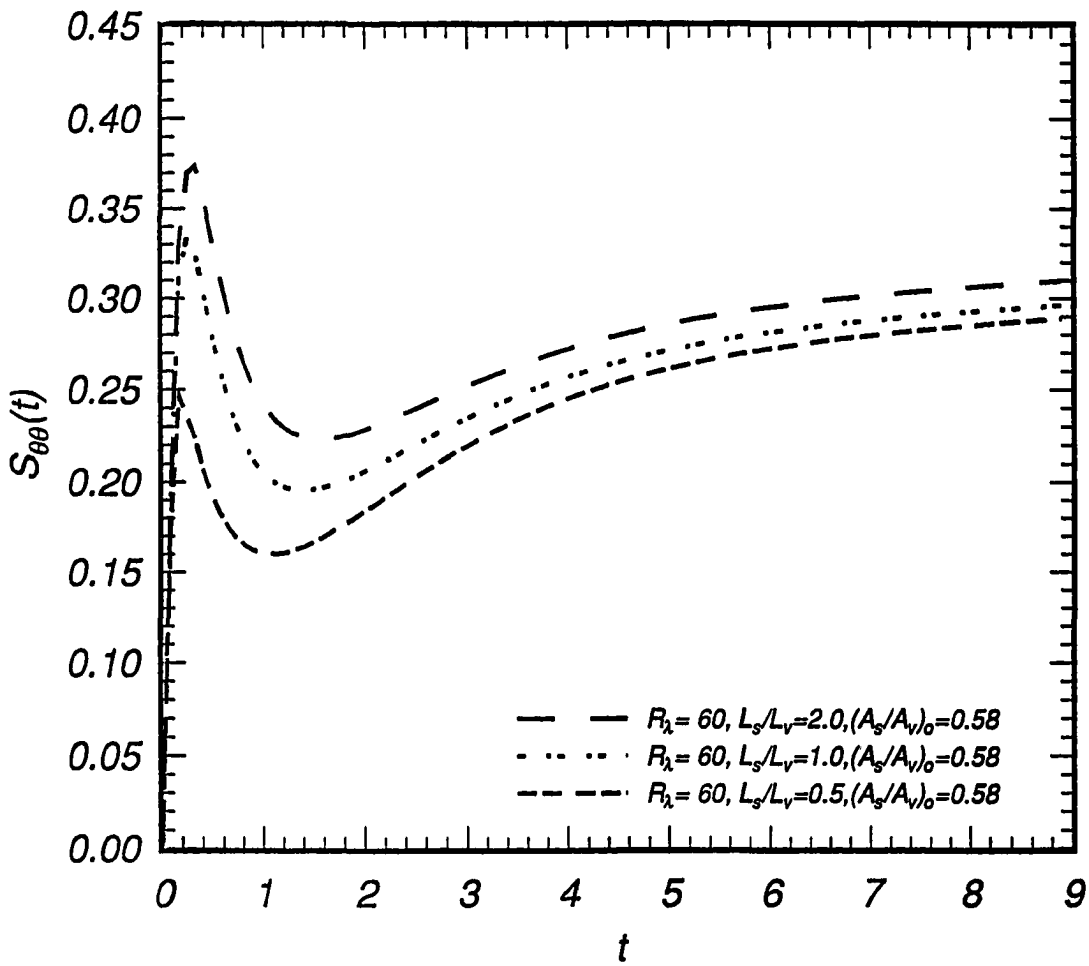

Figure 4.71: Evolution of scalar mixed derivative skewness at different initial integral lengthscales, $A_s/A_v = 0.58$.

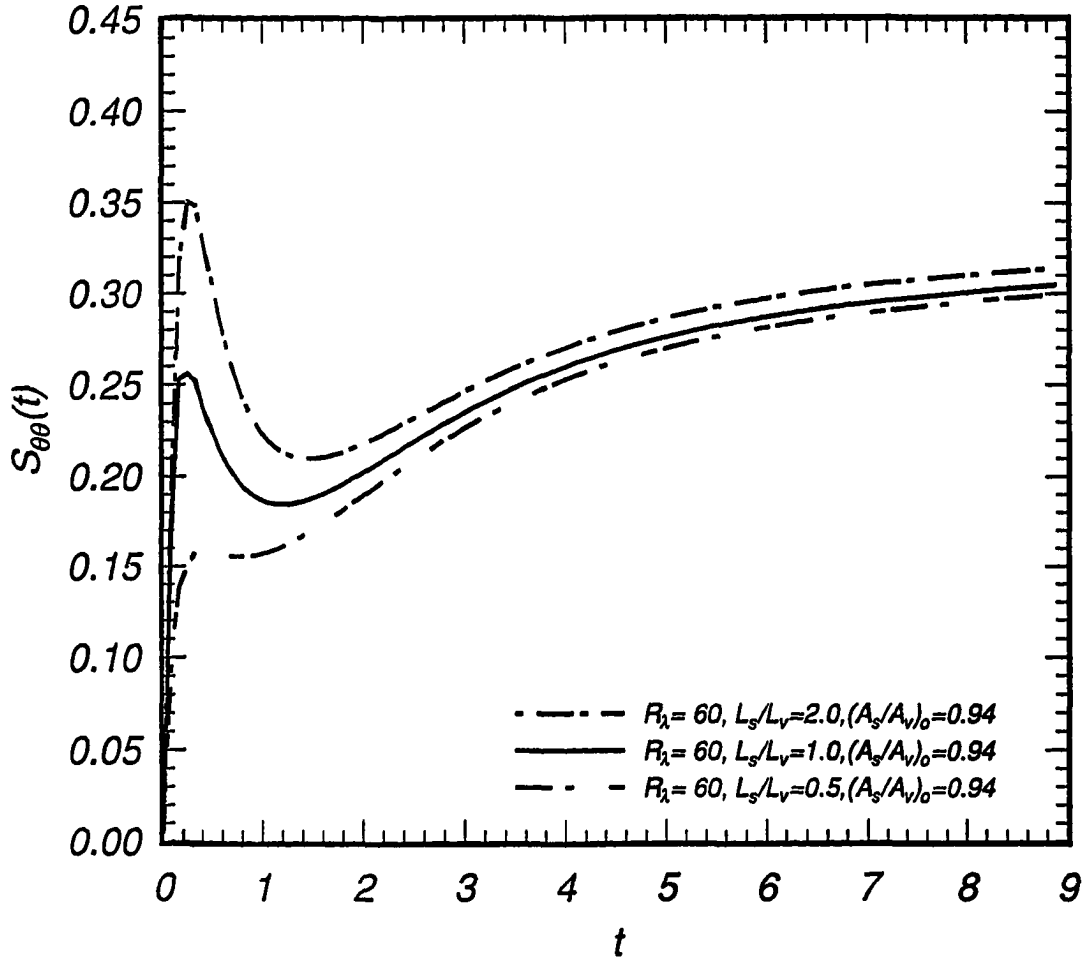

Figure 4.72: Evolution of scalar mixed derivative skewness at different initial integral lengthscales, $A_s/A_v = 0.94$.

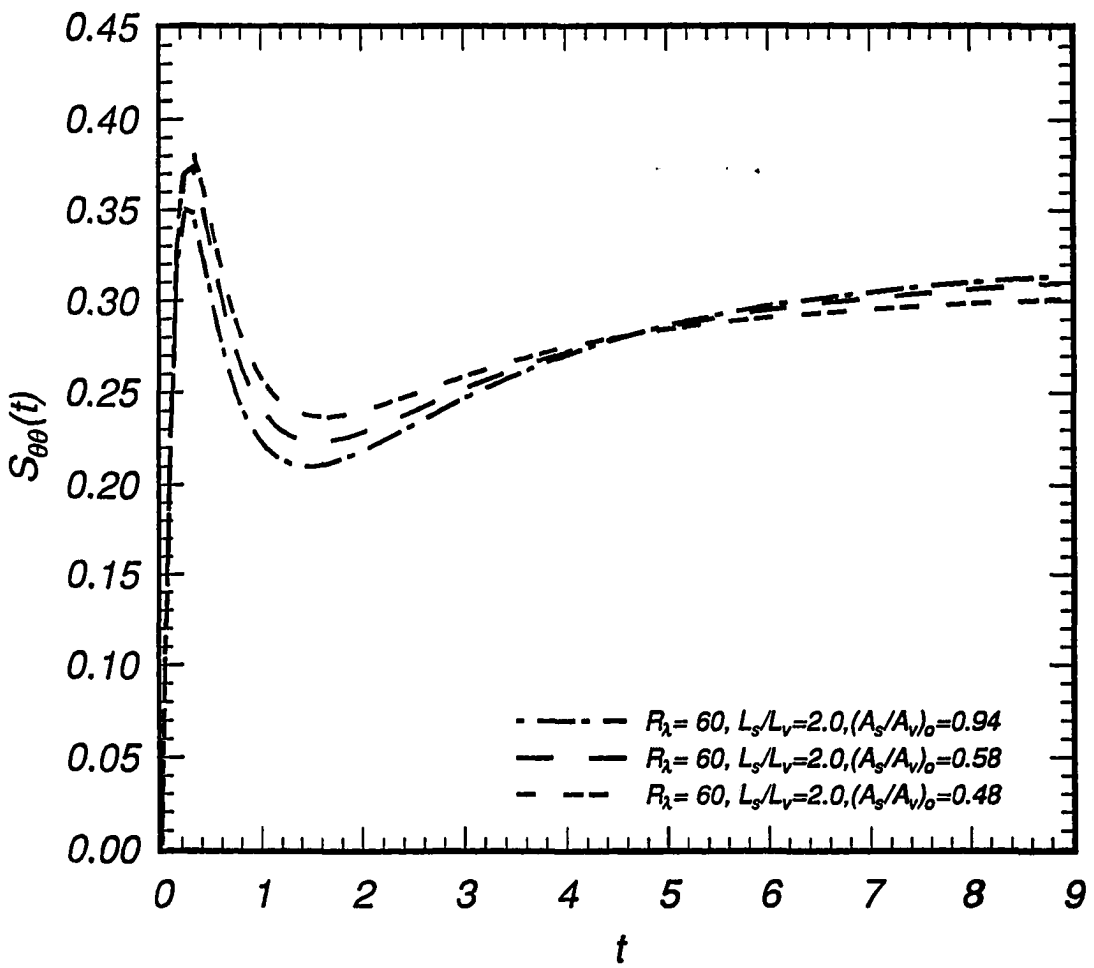

Figure 4.73: Evolution of scalar mixed derivative skewness at different initial spectral aspect ratios, $L_s/L_v = 2.0$.

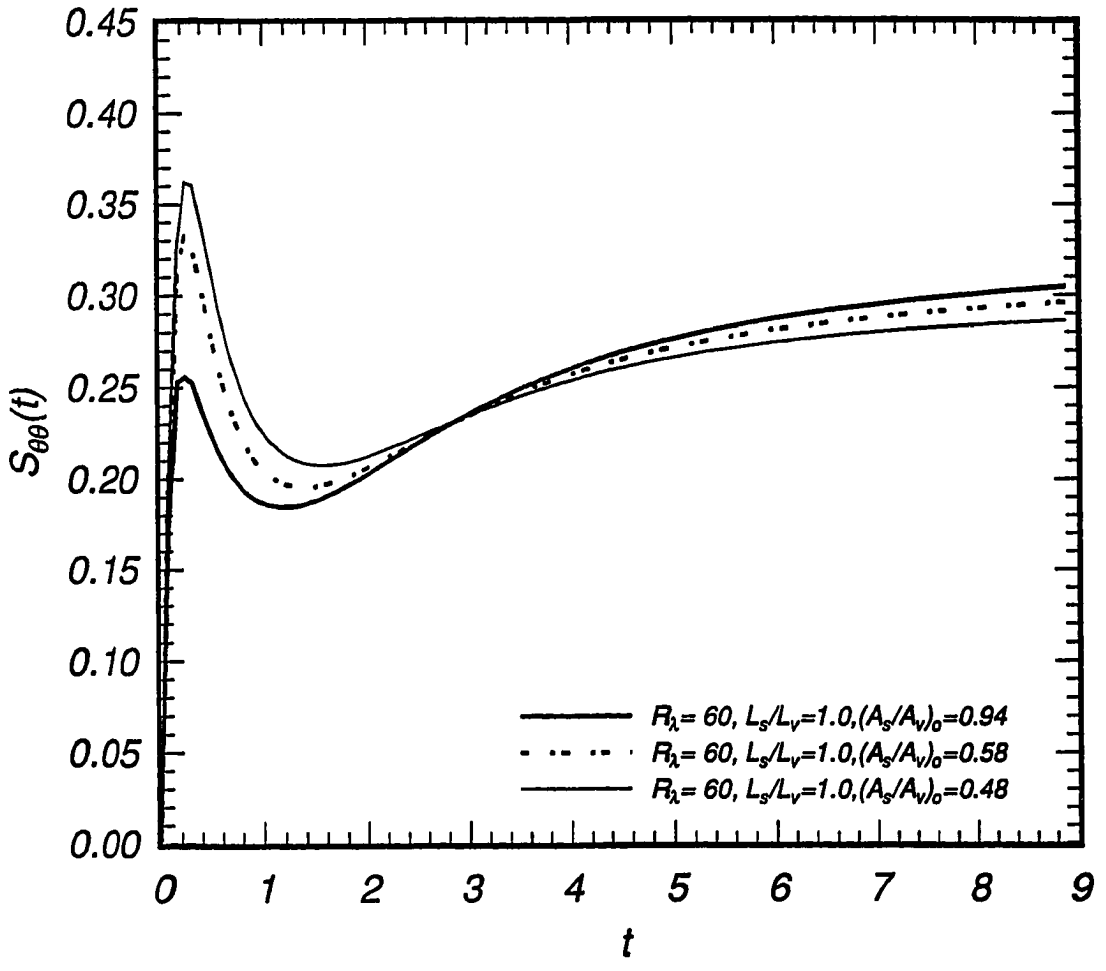

Figure 4.74: Evolution of scalar mixed derivative skewness at different initial spectral aspect ratios, $L_s/L_v = 1.0$.

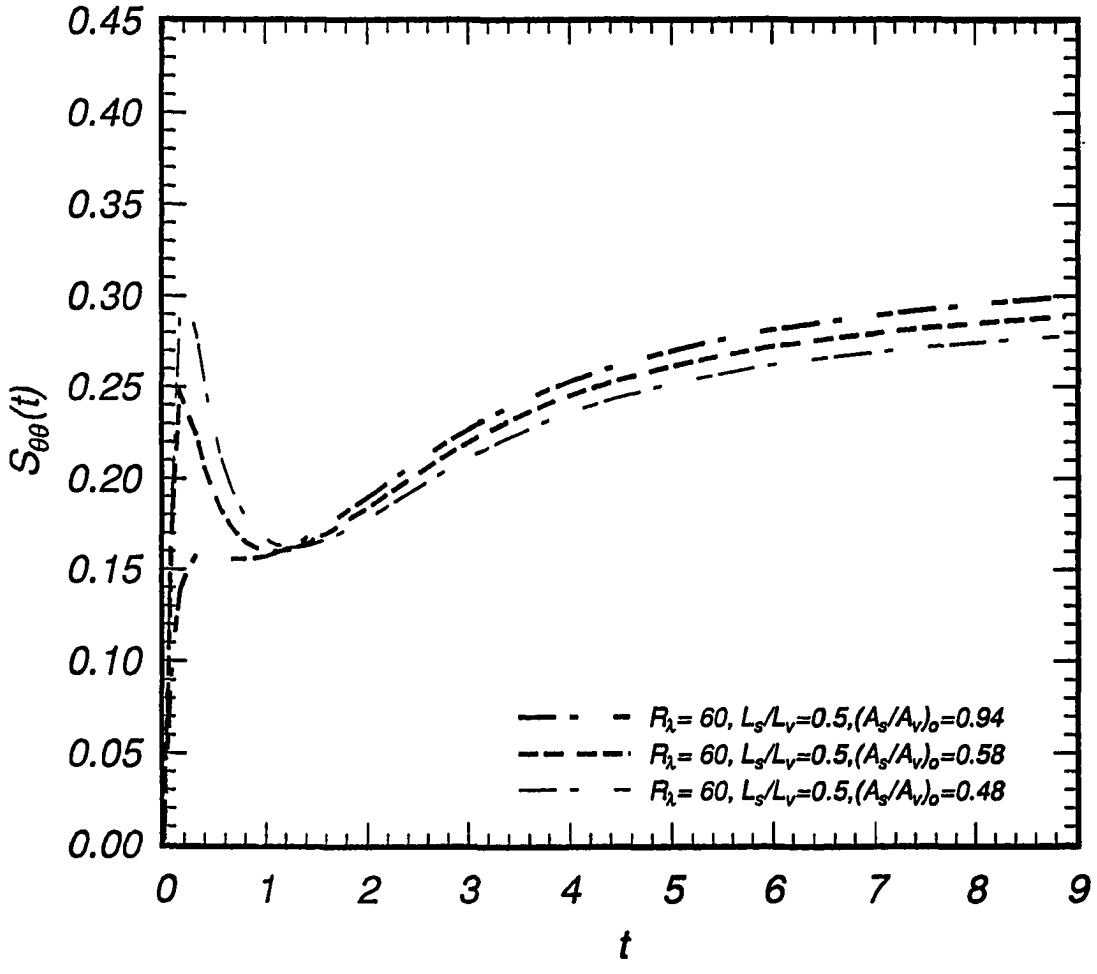

Figure 4.75: Evolution of scalar mixed derivative skewness at different initial spectral aspect ratios, $L_s/L_v = 0.5$.

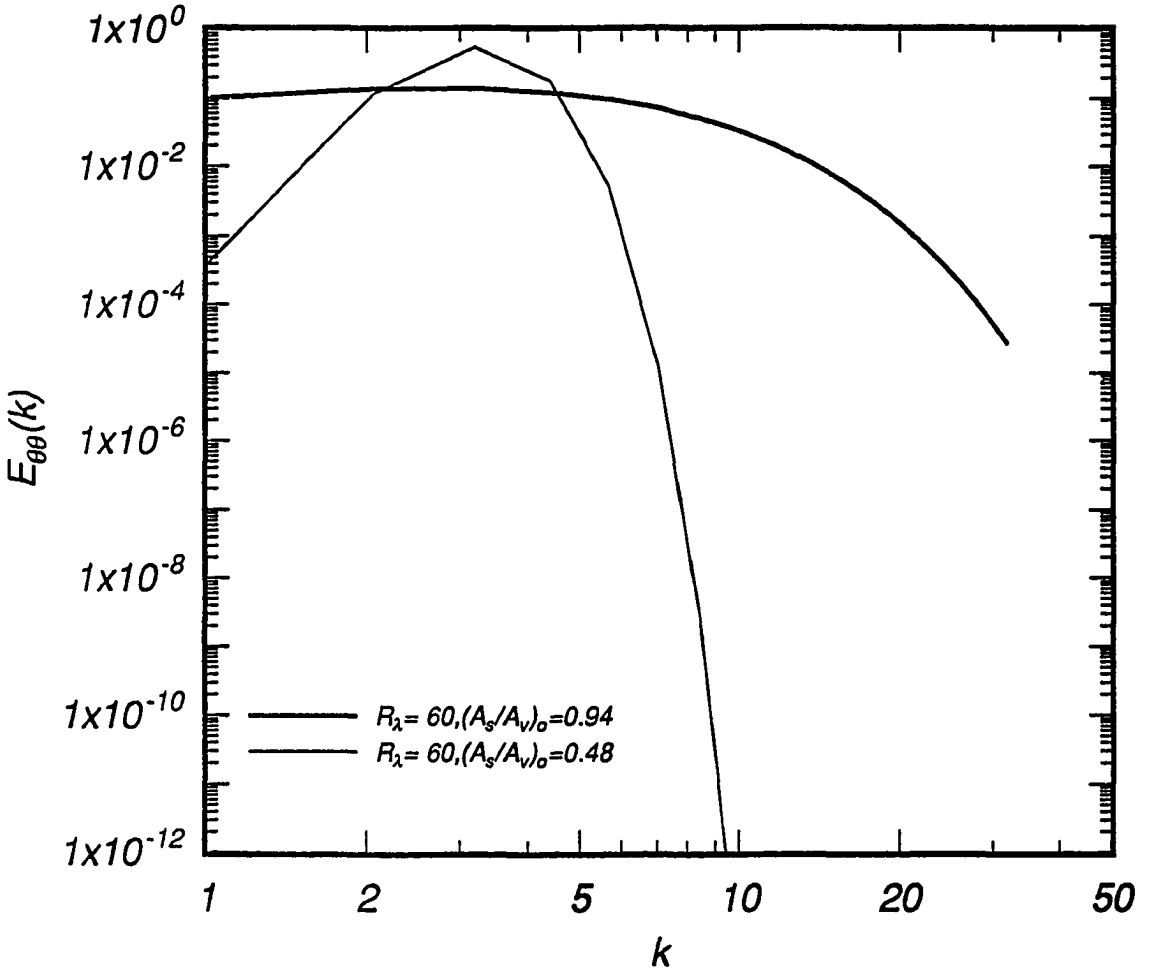

Figure 4.76: Scalar energy spectra at different initial R_λ and spectral aspect ratios, $L_s/L_v = 1.0$, $t = 0.00$.

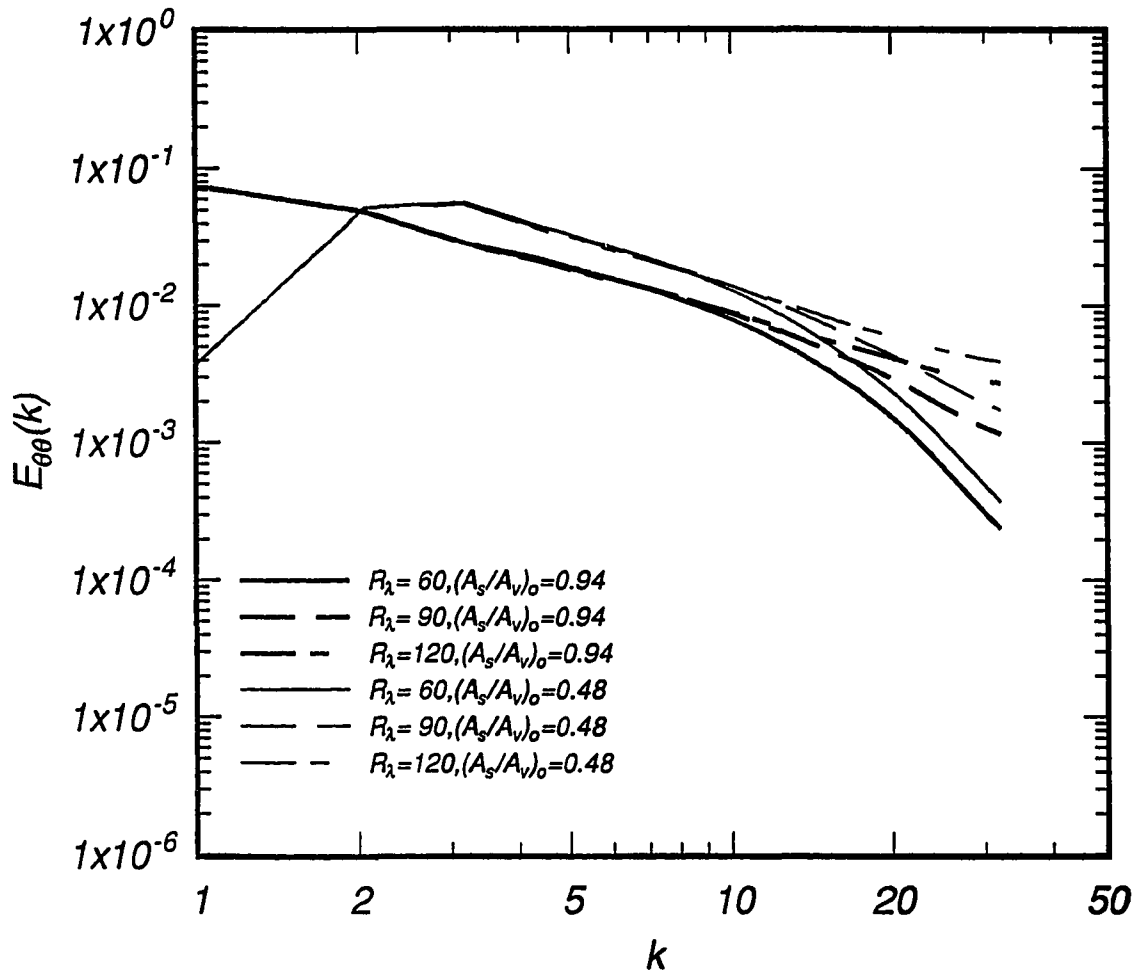

Figure 4.77: Scalar energy spectra at different initial R_λ and spectral aspect ratios, $L_s/L_v = 1.0$, $t = 2.16$.

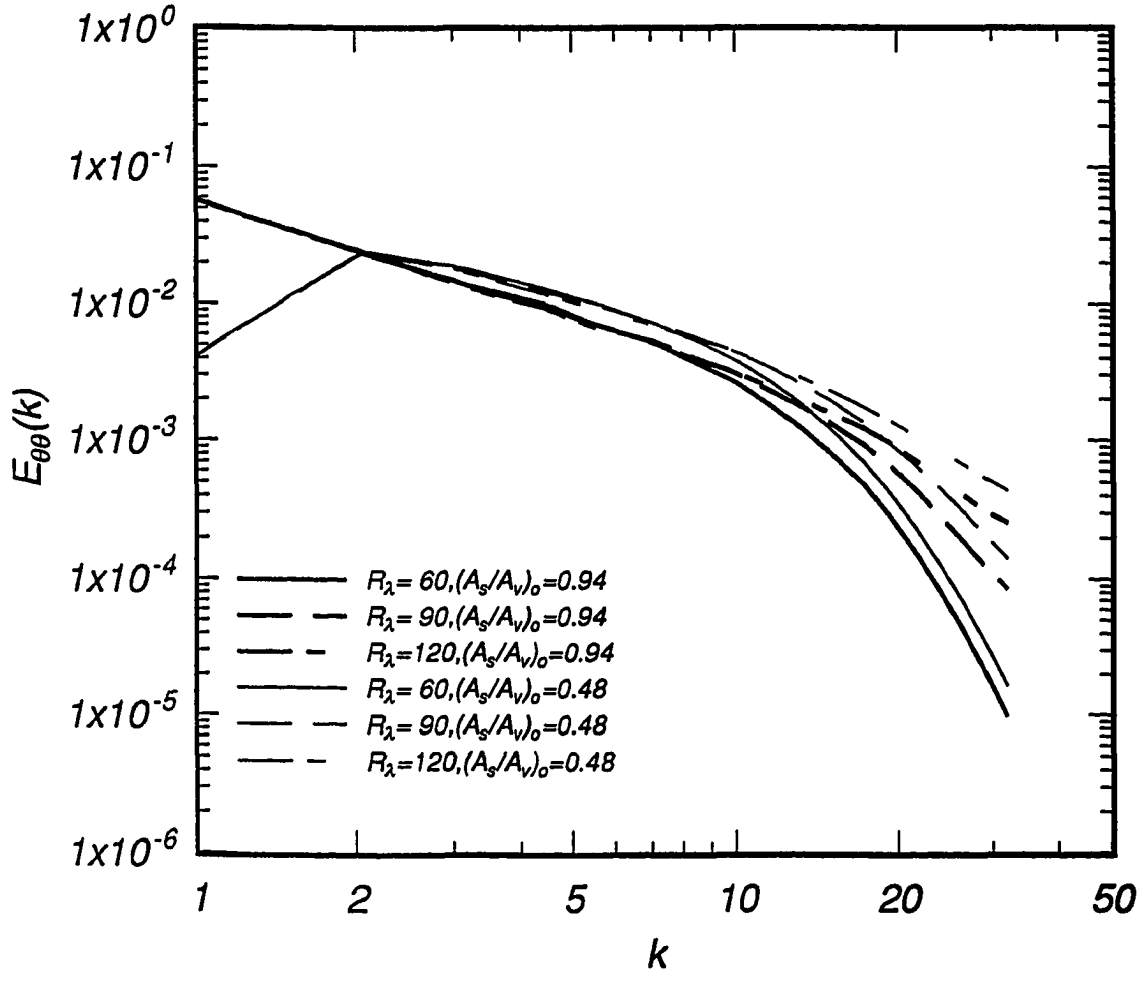

Figure 4.78: Scalar energy spectra at different initial R_λ and spectral aspect ratios, $L_s/L_v = 1.0$, $t = 4.32$.

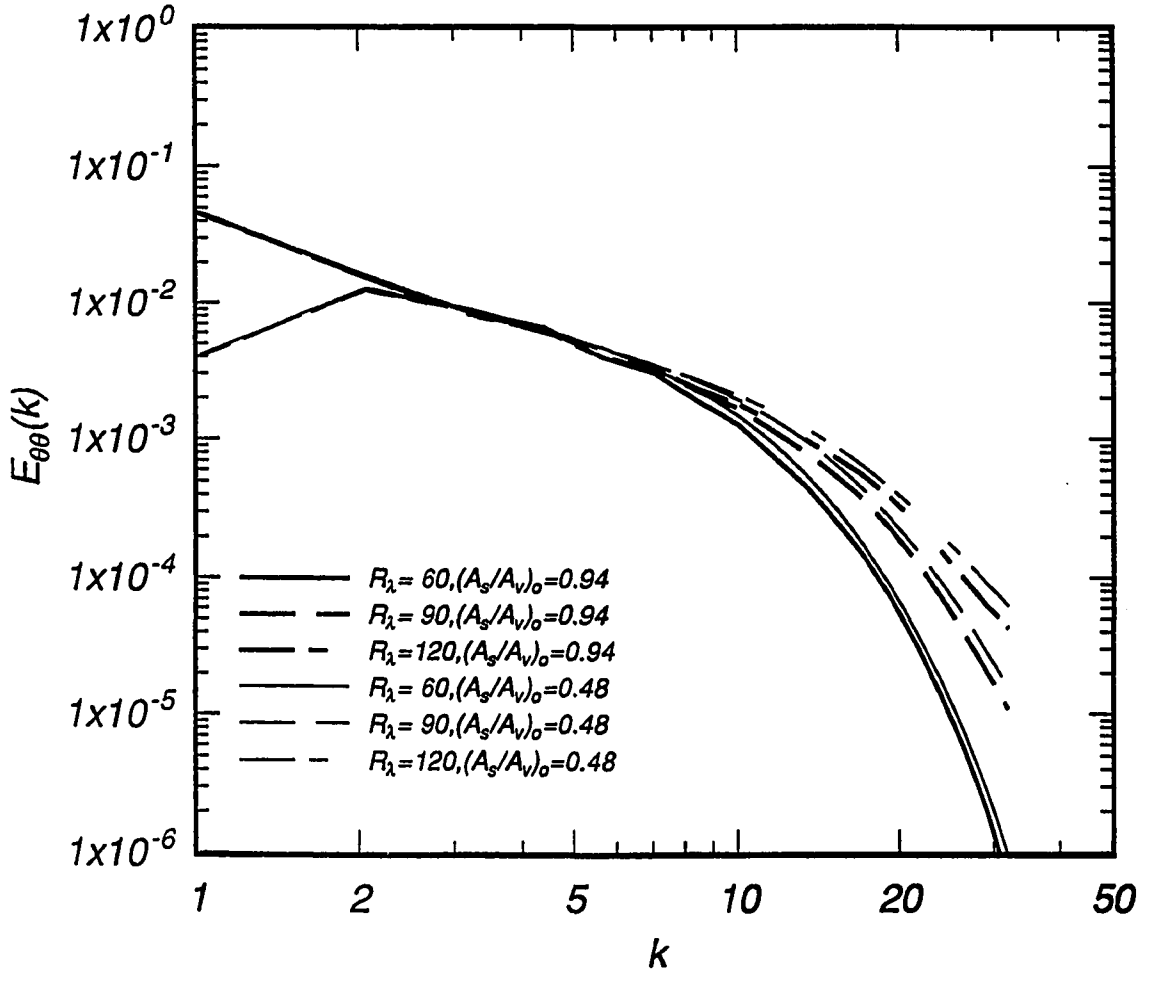

Figure 4.79: Scalar energy spectra at different initial R_λ and spectral aspect ratios, $L_s/L_v = 1.0$, $t = 6.49$.

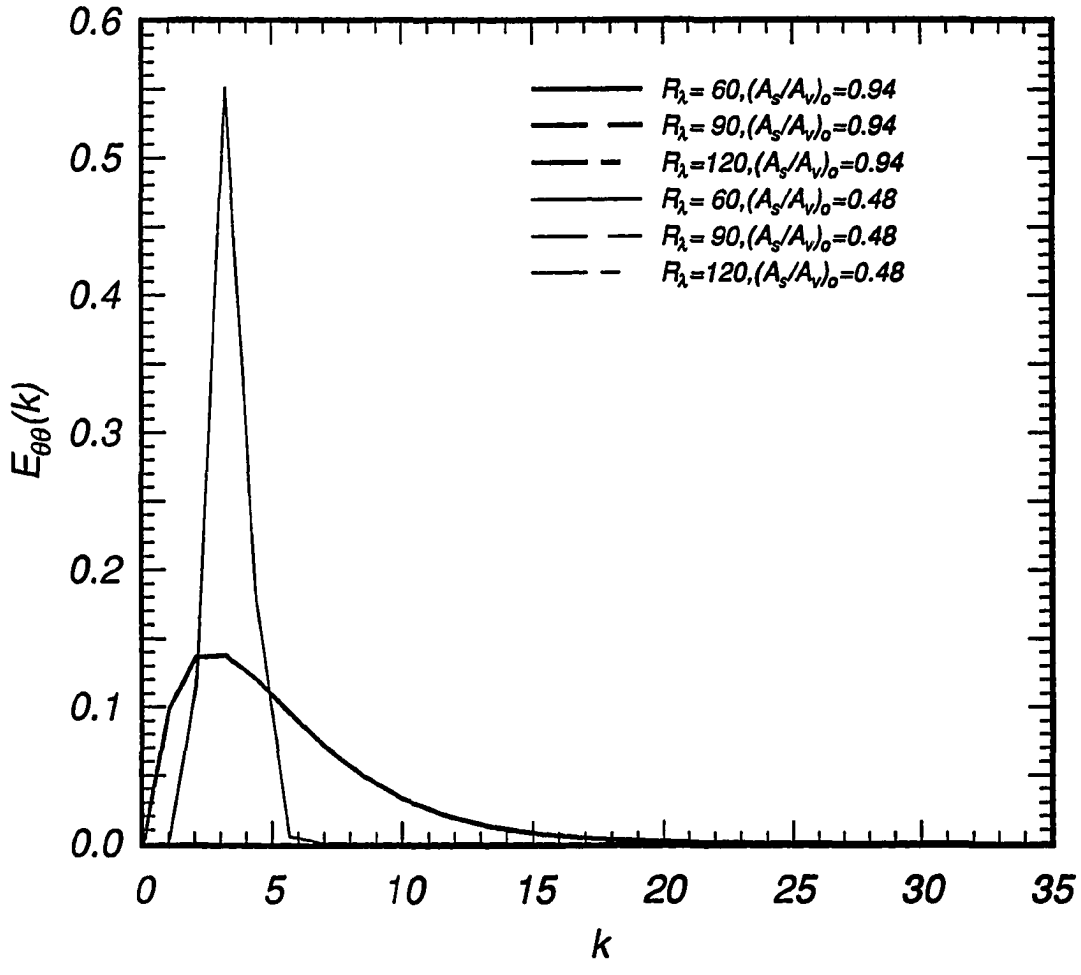

Figure 4.80: Scalar energy spectra at different initial R_λ and spectral aspect ratios, $L_s/L_v = 1.0$, $t = 0.00$.

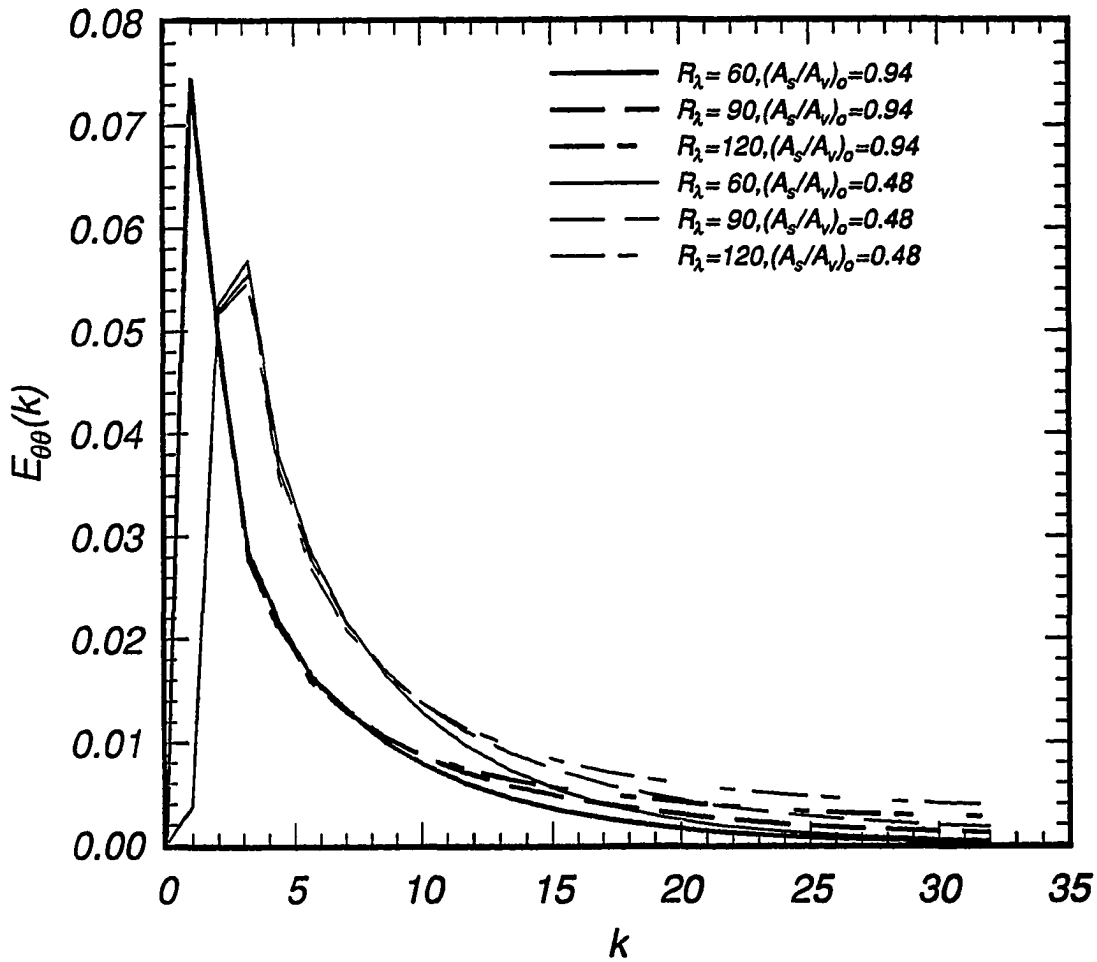

Figure 4.81: Scalar energy spectra at different initial R_λ and spectral aspect ratios, $L_s/L_v = 1.0$, $t = 2.16$.

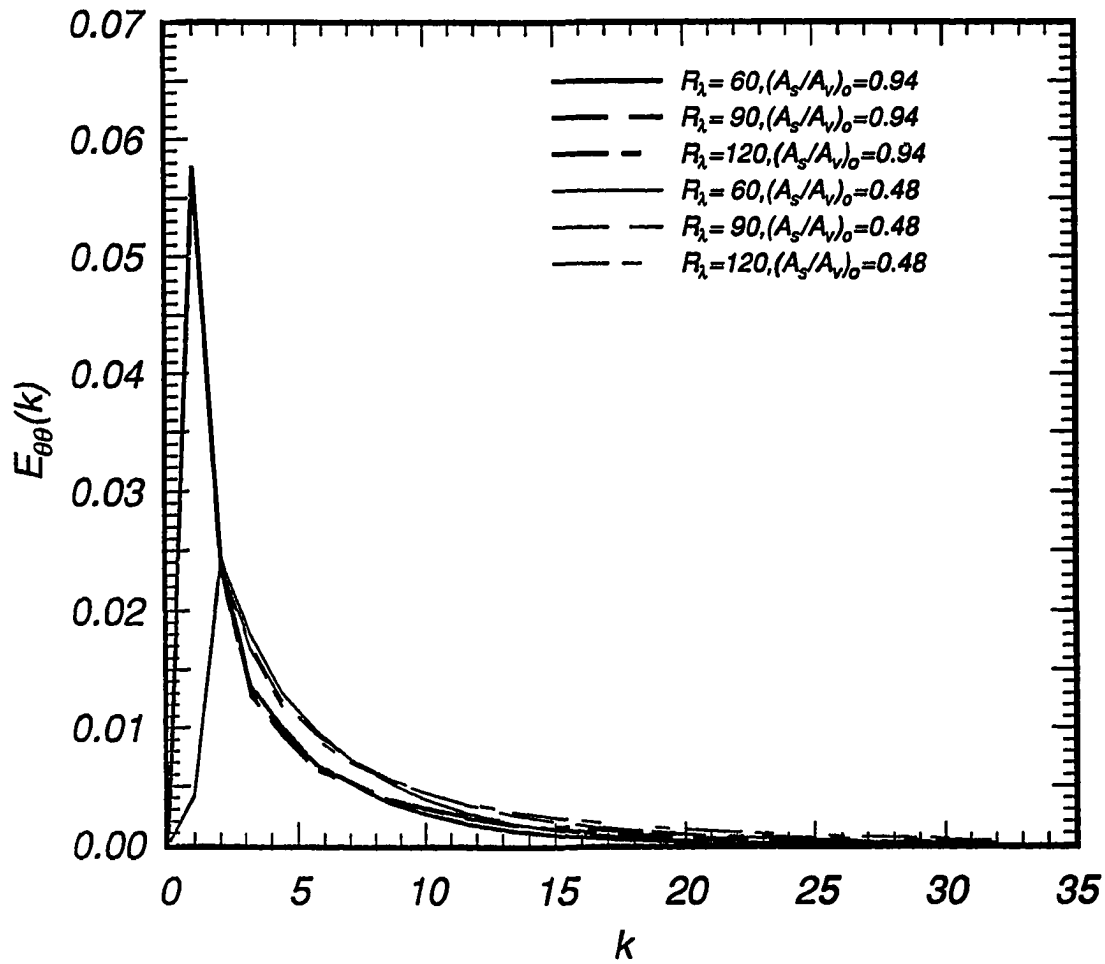

Figure 4.82: Scalar energy spectra at different initial R_λ and spectral aspect ratios, $L_s/L_v = 1.0$, $t = 4.32$.

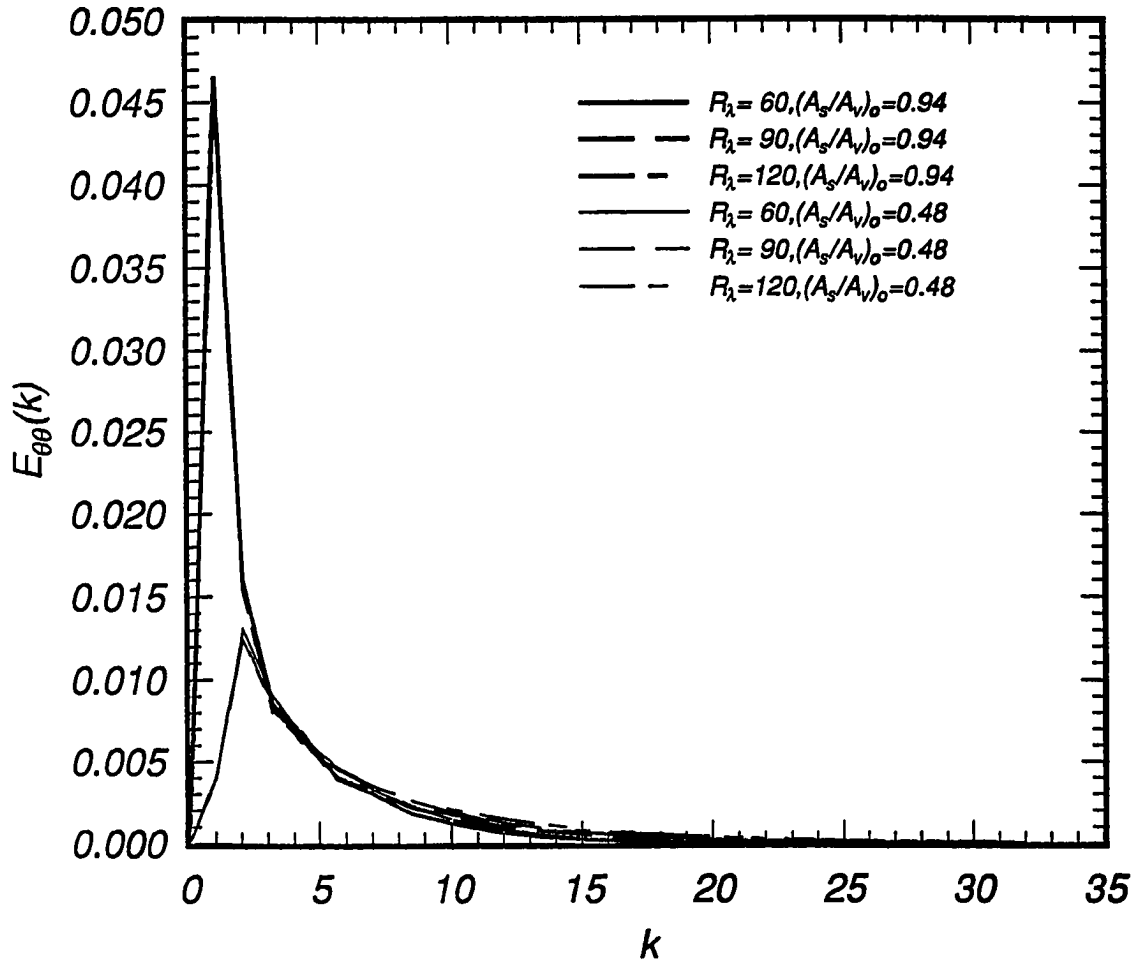

Figure 4.83: Scalar energy spectra at different initial R_λ and spectral aspect ratios, $L_s/L_v = 1.0$, $t = 6.49$.

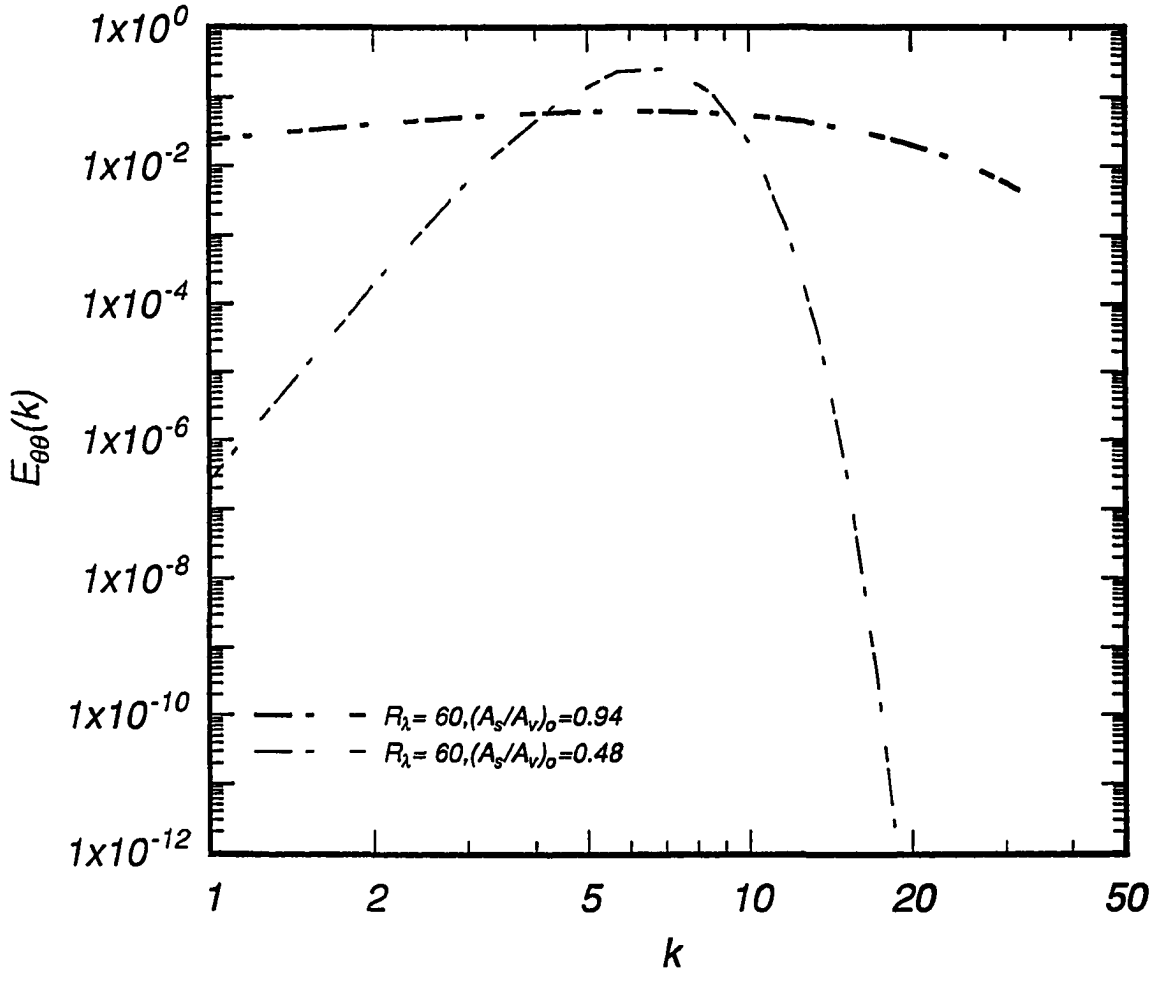

Figure 4.84: Scalar energy spectra at different initial R_λ and spectral aspect ratios, $L_s/L_v = 0.5$, $t = 0.00$.

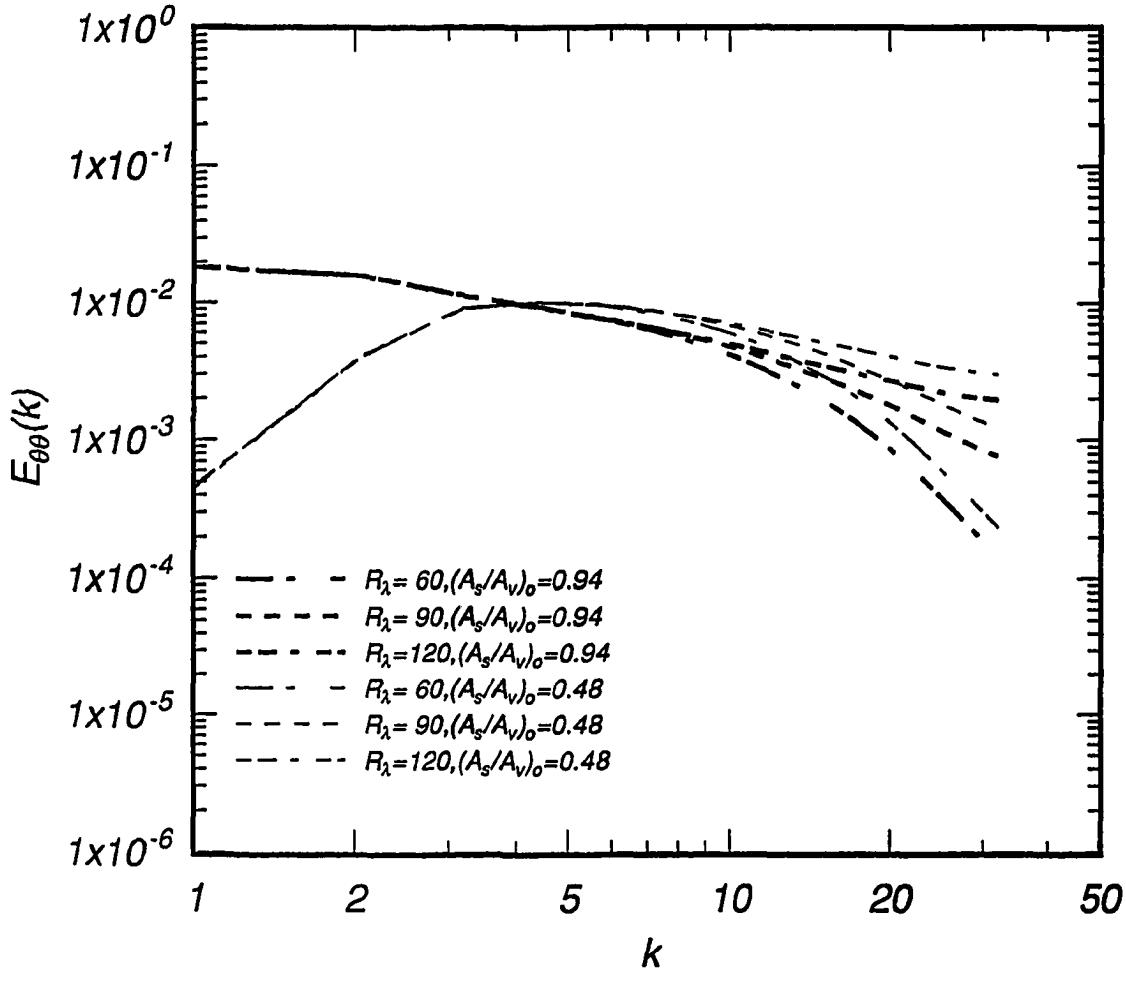

Figure 4.85: Scalar energy spectra at different initial R_λ and spectral aspect ratios, $L_s/L_v = 0.5$, $t = 2.16$.

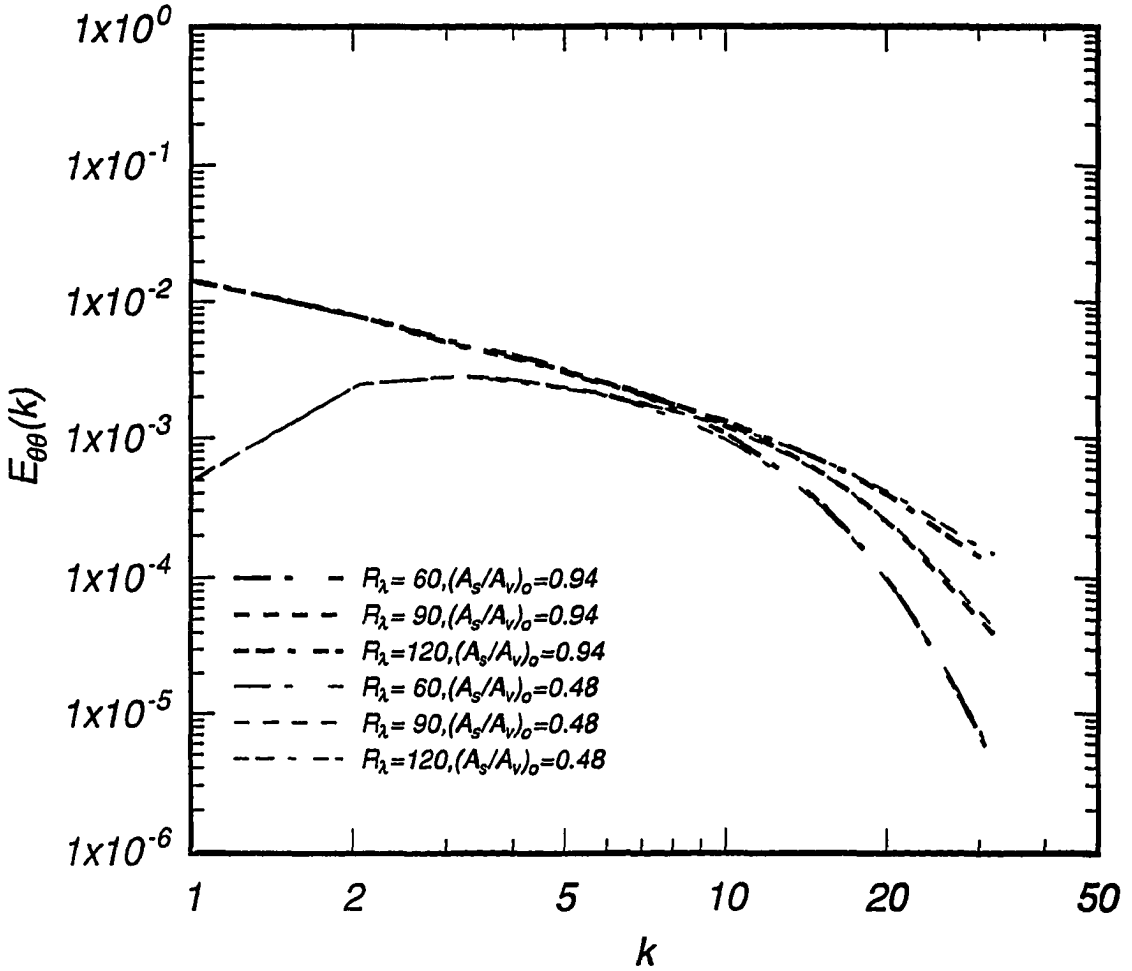

Figure 4.86: Scalar energy spectra at different initial R_λ and spectral aspect ratios, $L_s/L_v = 0.5$, $t = 4.32$.

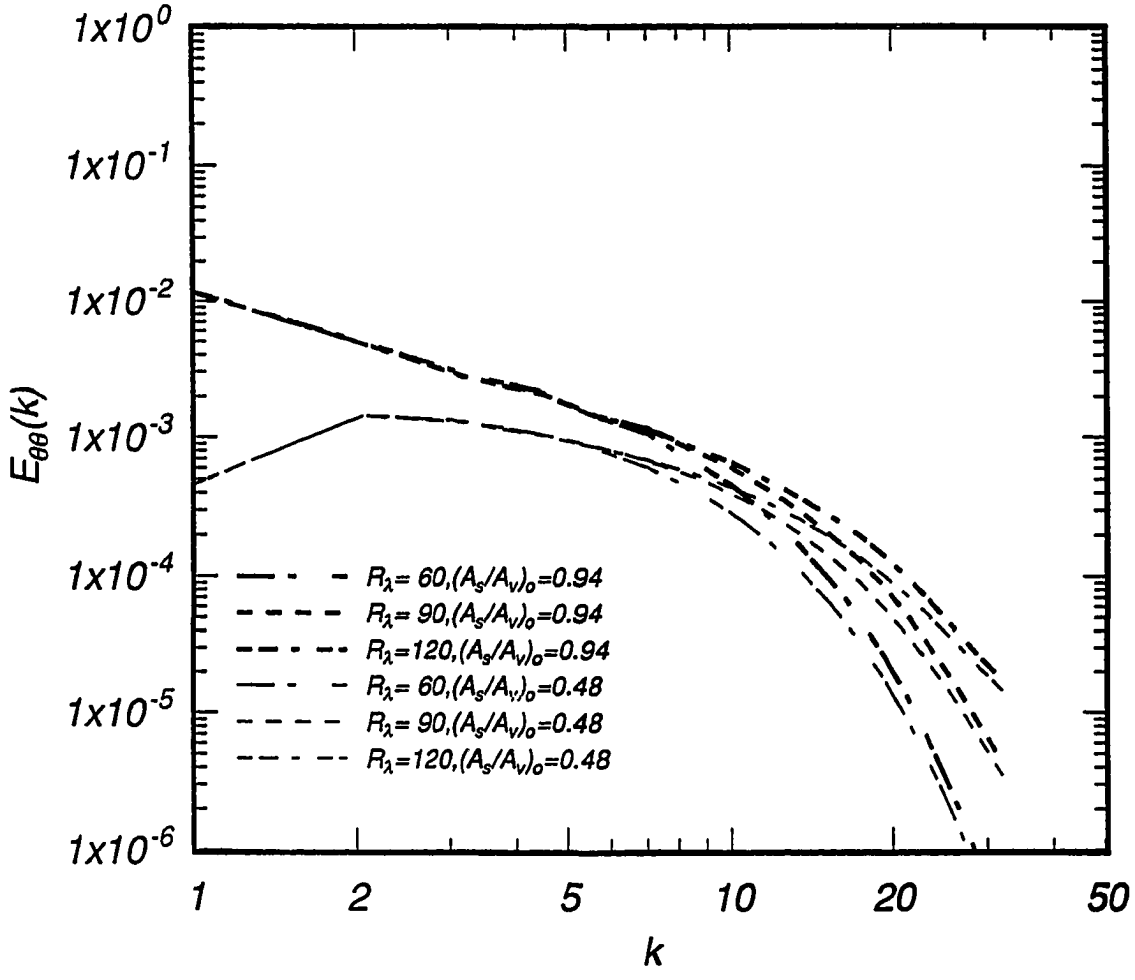

Figure 4.87: Scalar energy spectra at different initial R_λ and spectral aspect ratios, $L_s/L_v = 0.5$, $t = 6.49$.

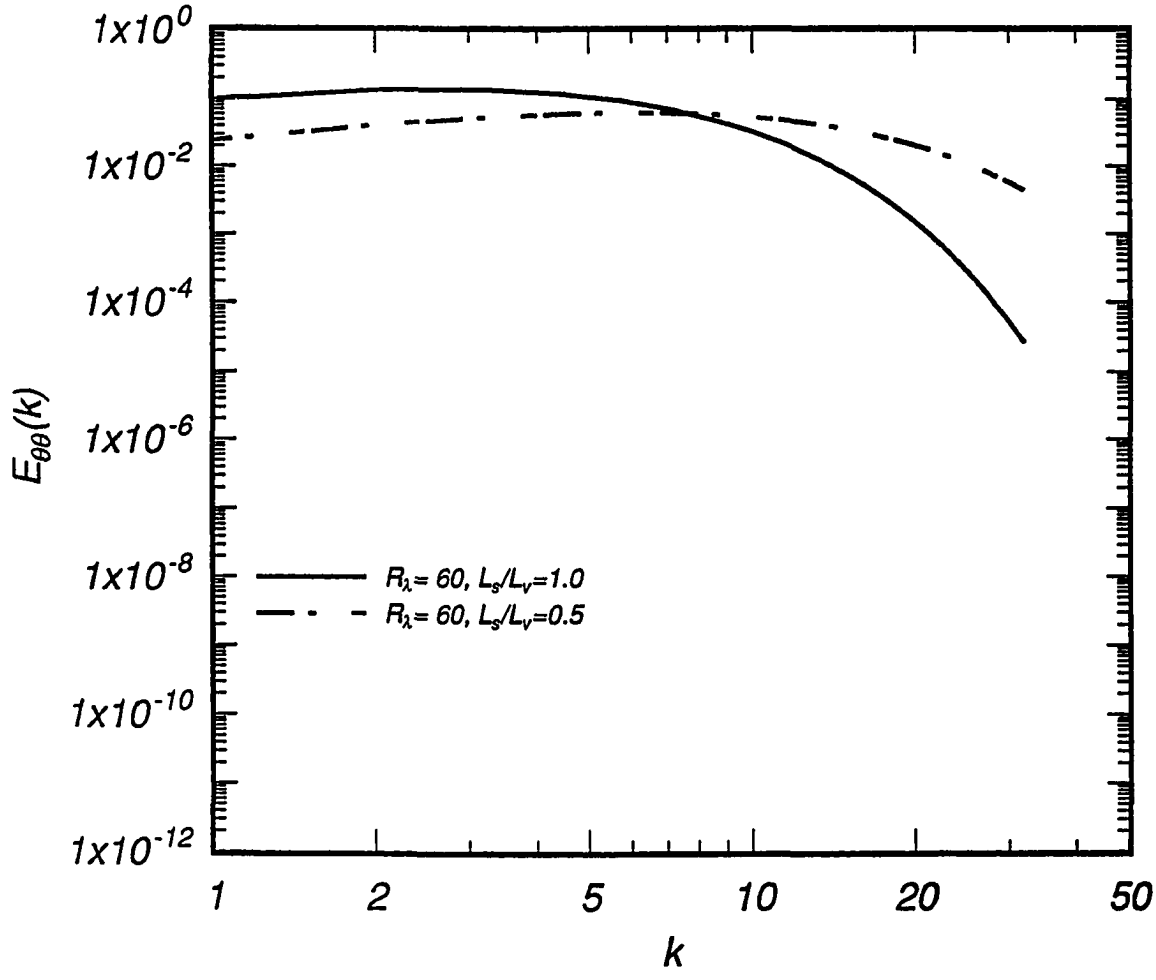

Figure 4.88: Scalar energy spectra at different initial R_λ and spectral lengthscale ratios, $A_s/A_v = 0.94$, $t = 0.00$.

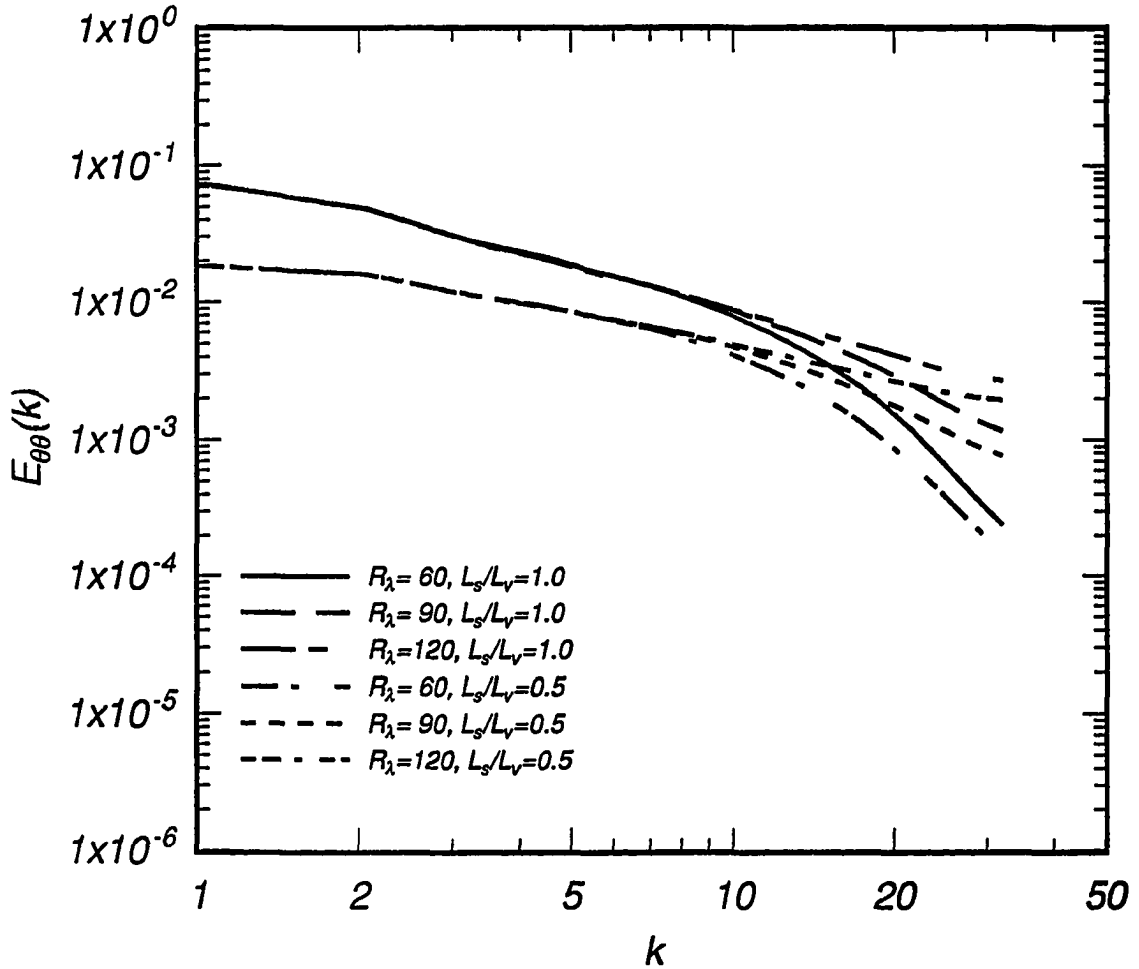

Figure 4.89: Scalar energy spectra at different initial R_λ and spectral lengthscale ratios, $A_s/A_v = 0.94$, $t = 2.16$.

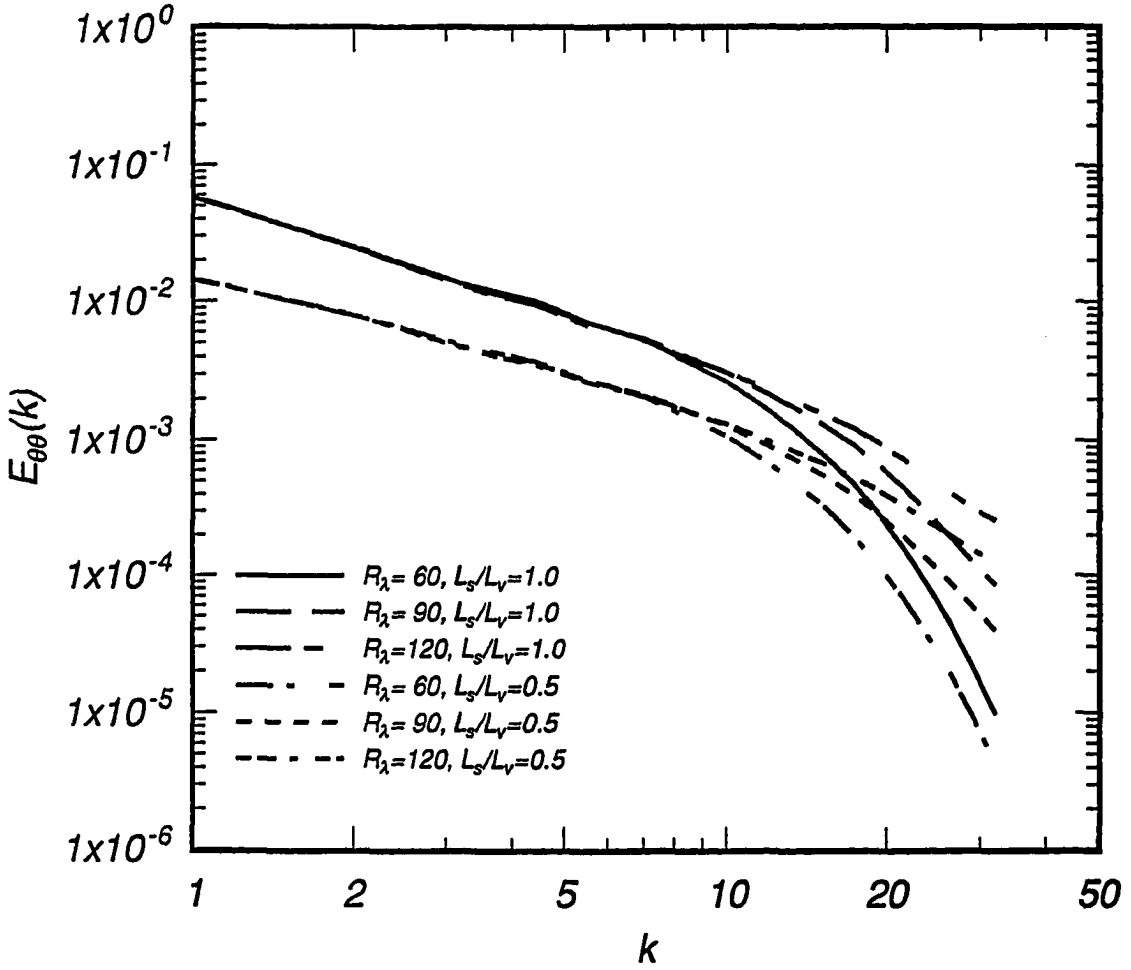

Figure 4.90: Scalar energy spectra at different initial R_λ and spectral lengthscale ratios, $A_s/A_v = 0.94$, $t = 4.32$.

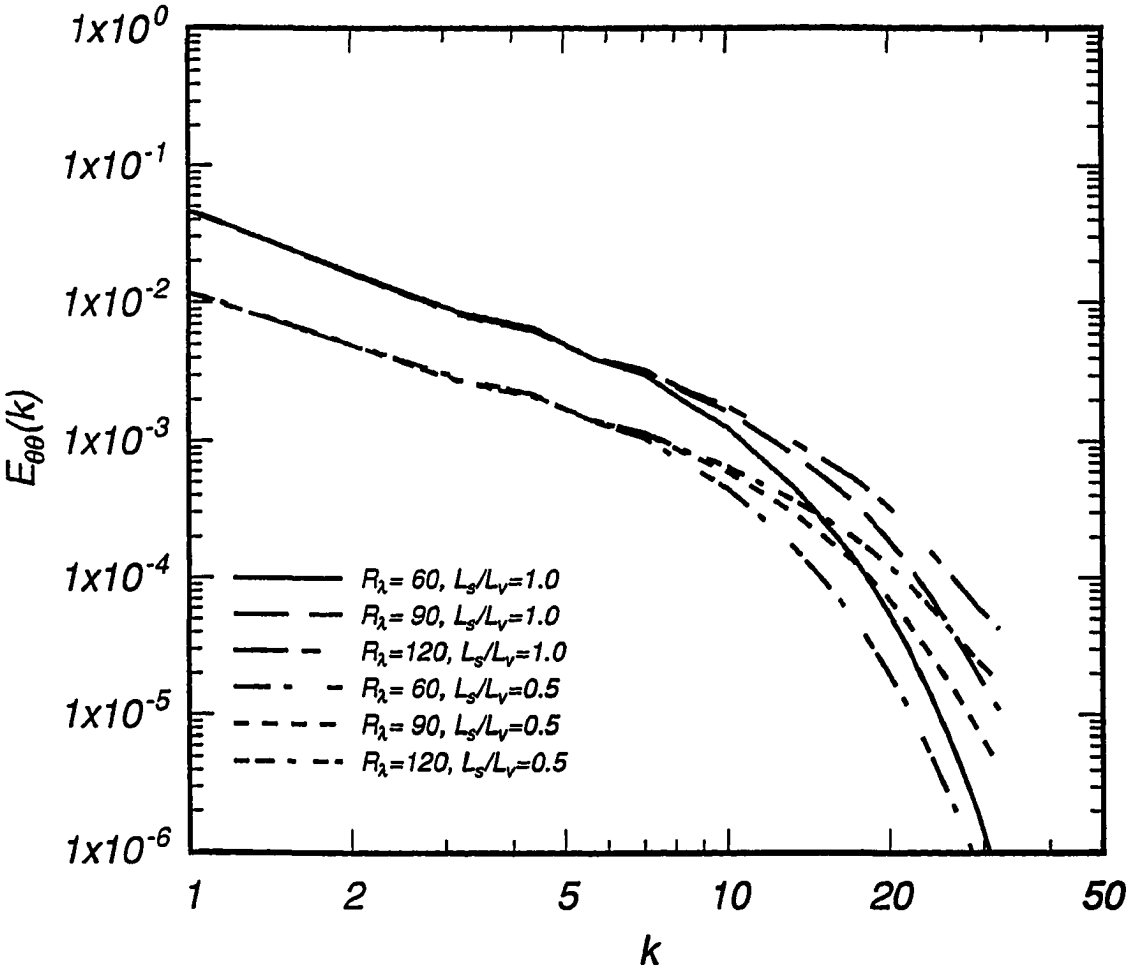

Figure 4.91: Scalar energy spectra at different initial R_λ and spectral lengthscale ratios, $A_s/A_v = 0.94$, $t = 6.49$.

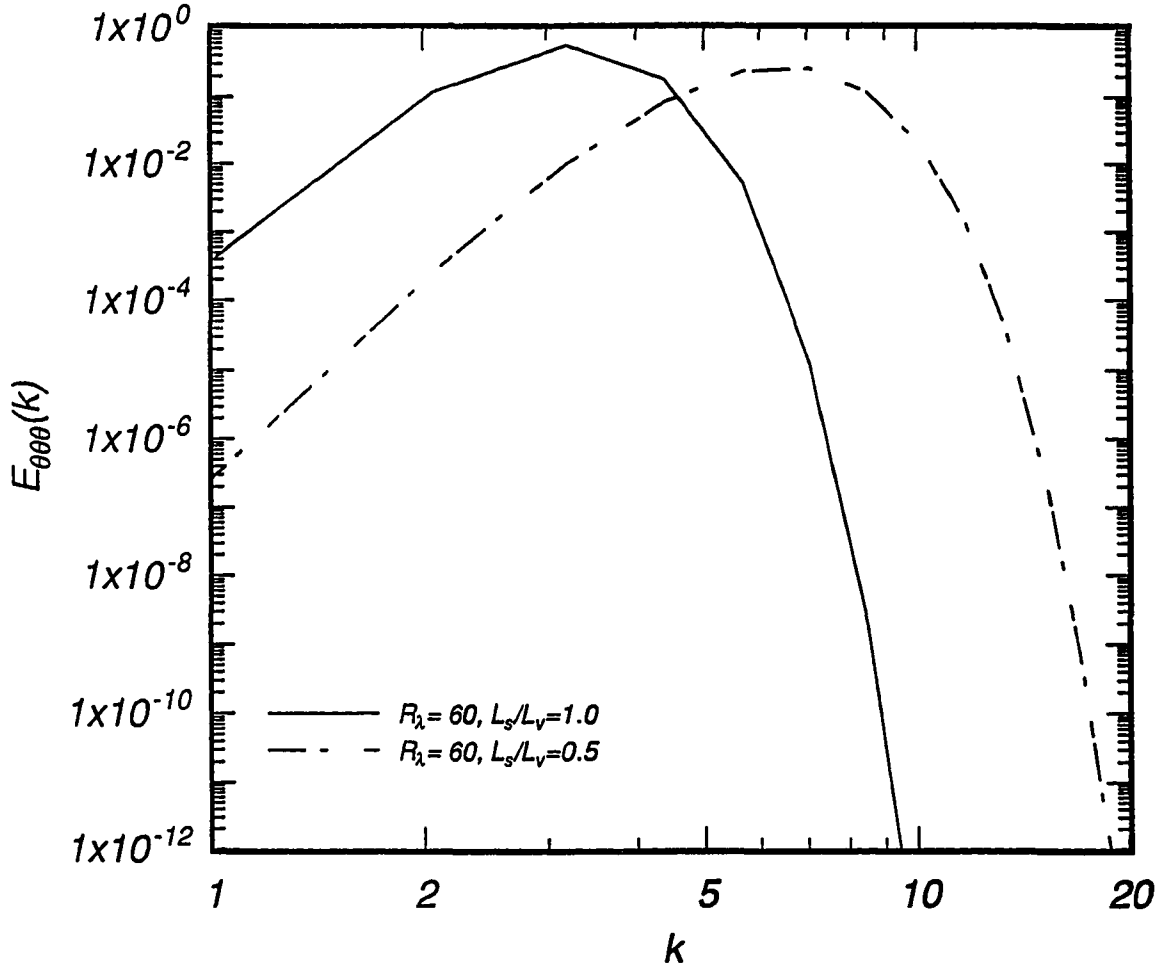

Figure 4.92: Scalar energy spectra at different initial R_λ and spectral lengthscale ratios, $A_s/A_v = 0.48$, $t = 0.00$.

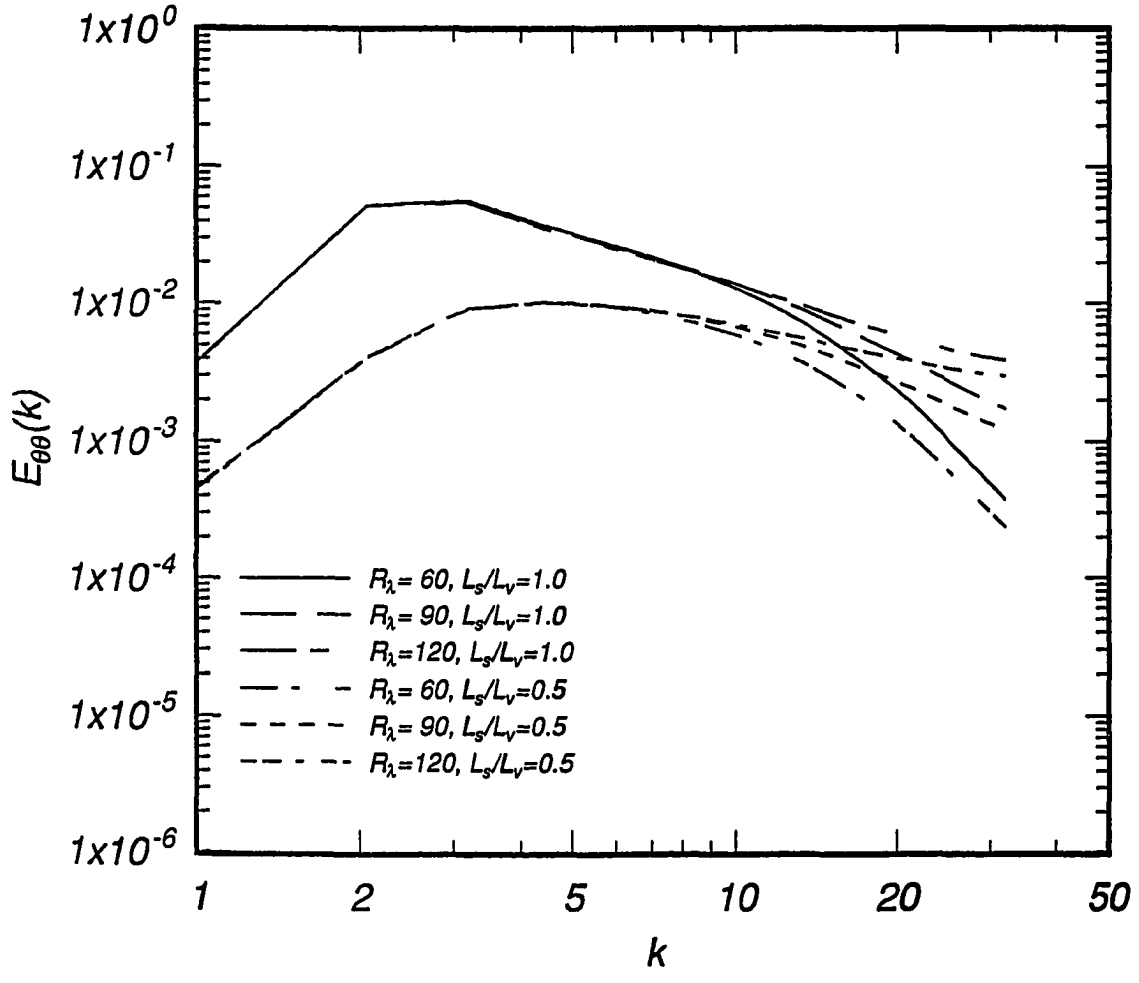

Figure 4.93: Scalar energy spectra at different initial R_λ and spectral lengthscale ratios, $A_s/A_v = 0.48$, $t = 2.16$.

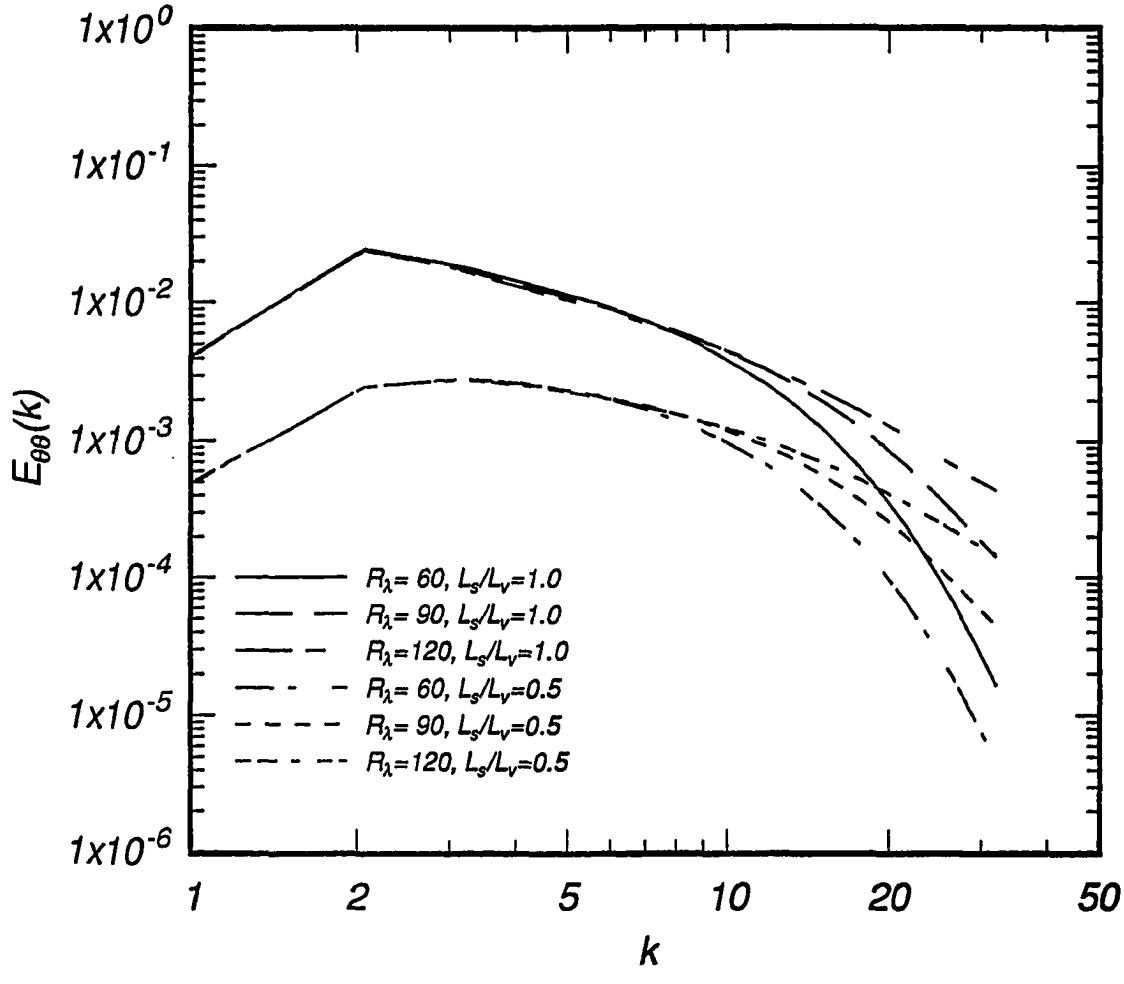

Figure 4.94: Scalar energy spectra at different initial R_λ and spectral lengthscale ratios, $A_s/A_v = 0.48$, $t = 4.32$.

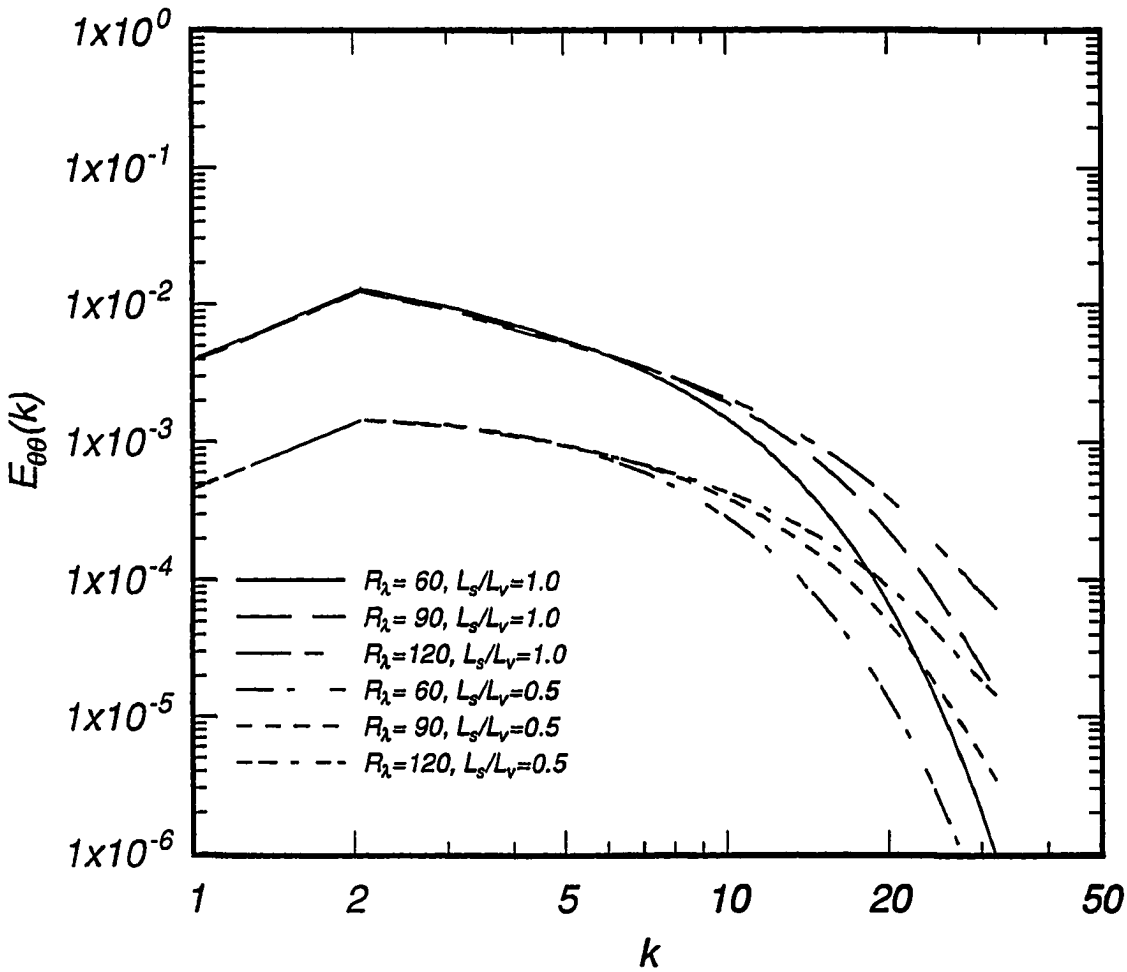

Figure 4.95: Scalar energy spectra at different initial R_λ and spectral lengthscale ratios, $A_s/A_v = 0.48$, $t = 6.49$.

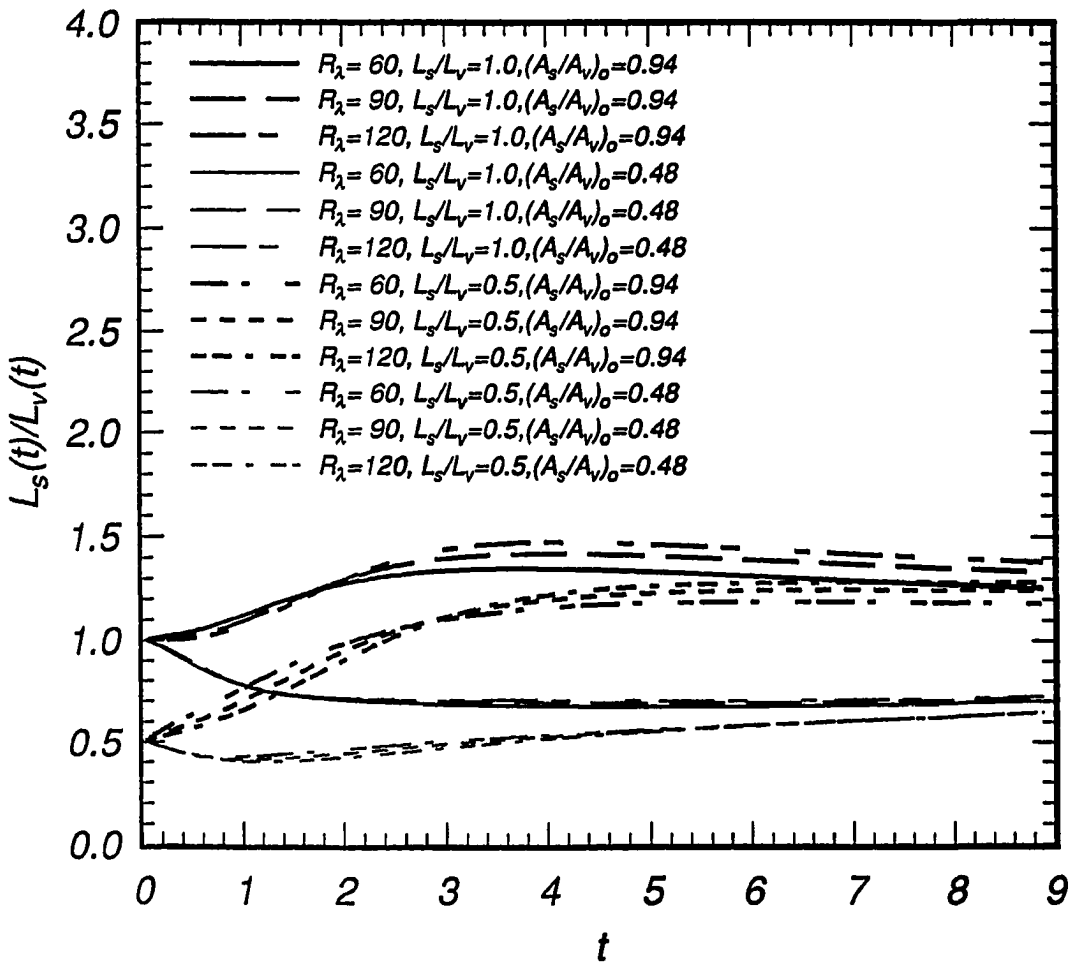

Figure 4.96: Evolution of scalar to velocity integral lengthscale ratios.

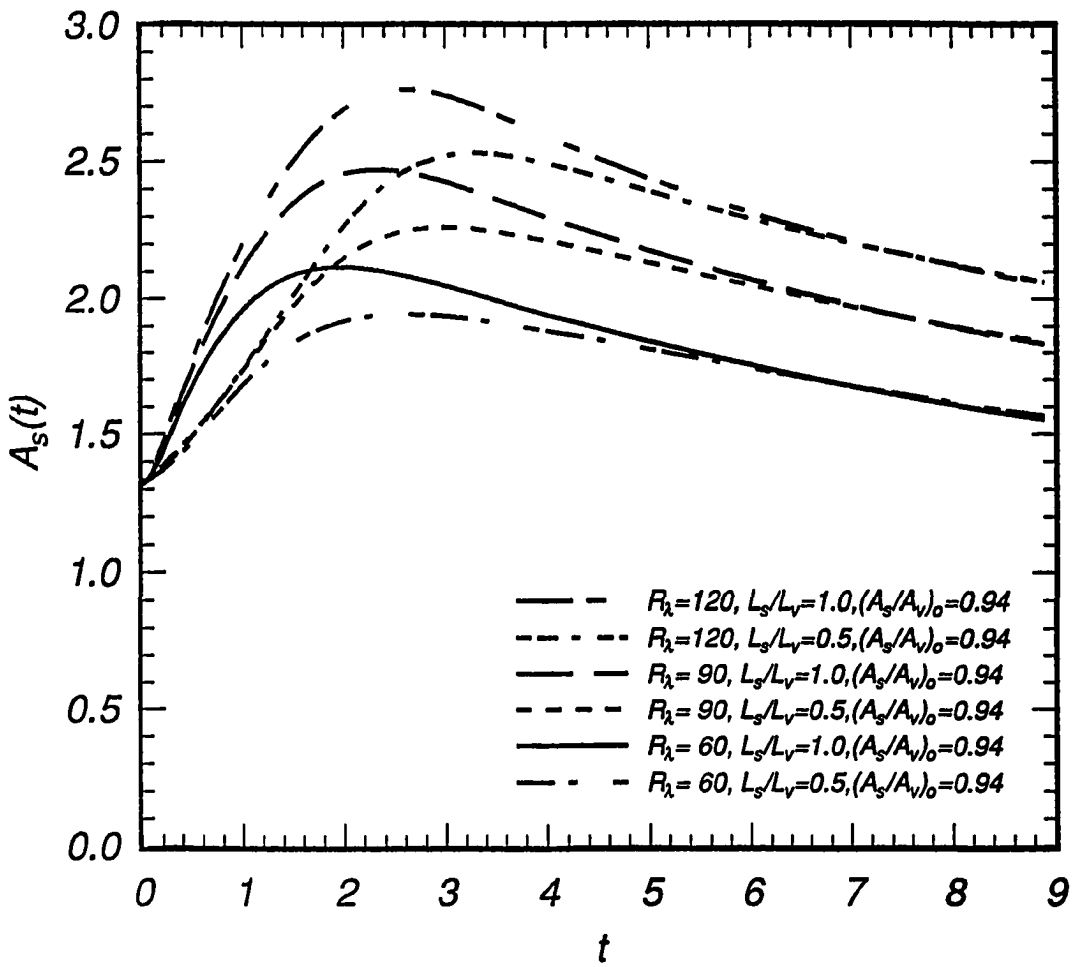

Figure 4.97: Evolution of scalar spectral aspect ratios.

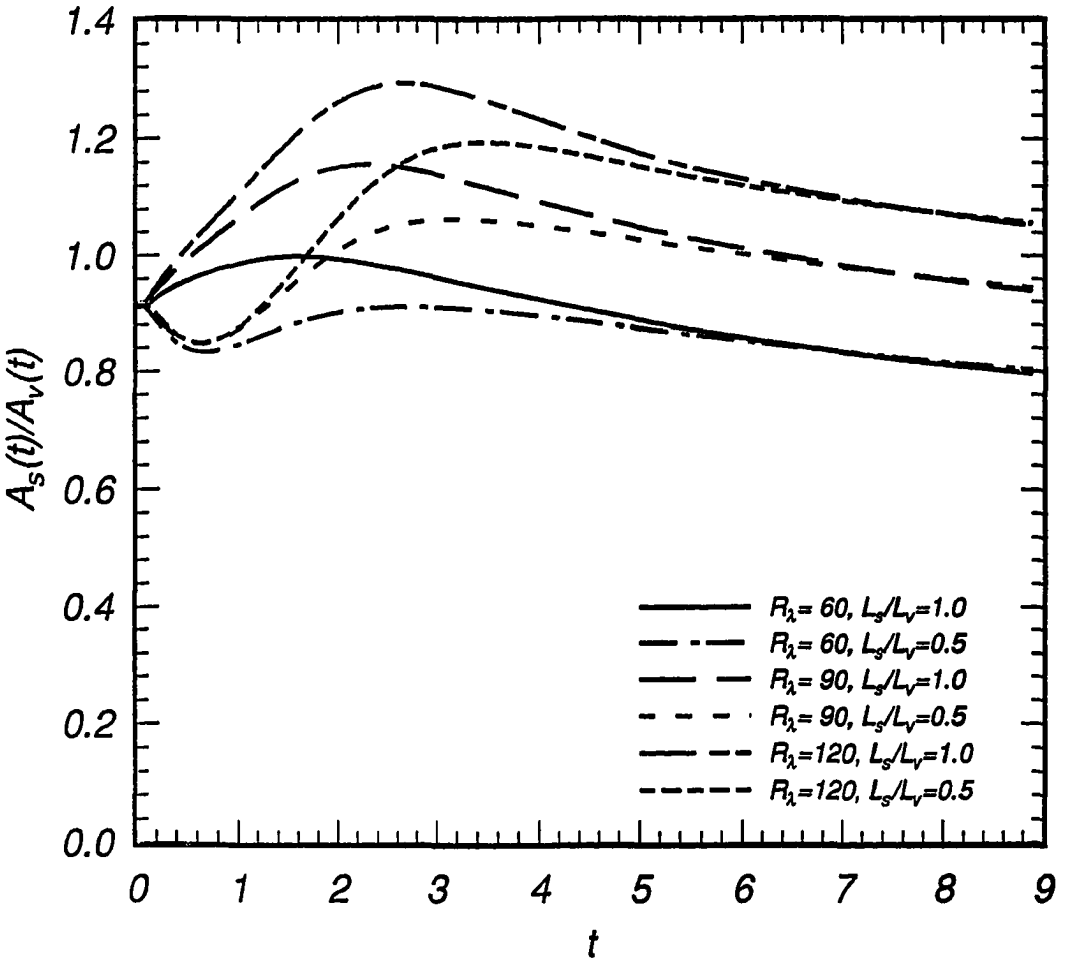

Figure 4.98: Evolution of ratio scalar to velocity spectral aspect ratios.

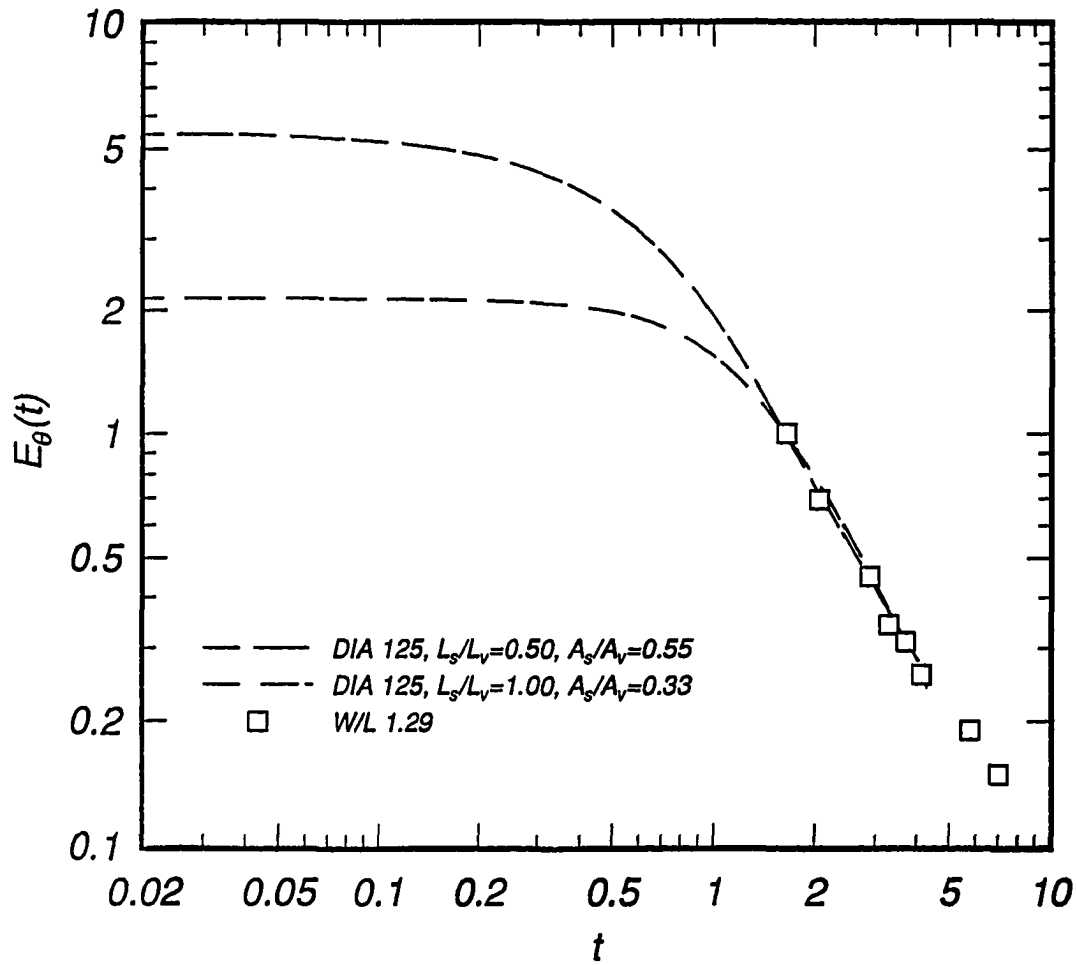

Figure 4.99: Best fit of DIA to scalar energy evolution reported by Warhaft and Lumley.

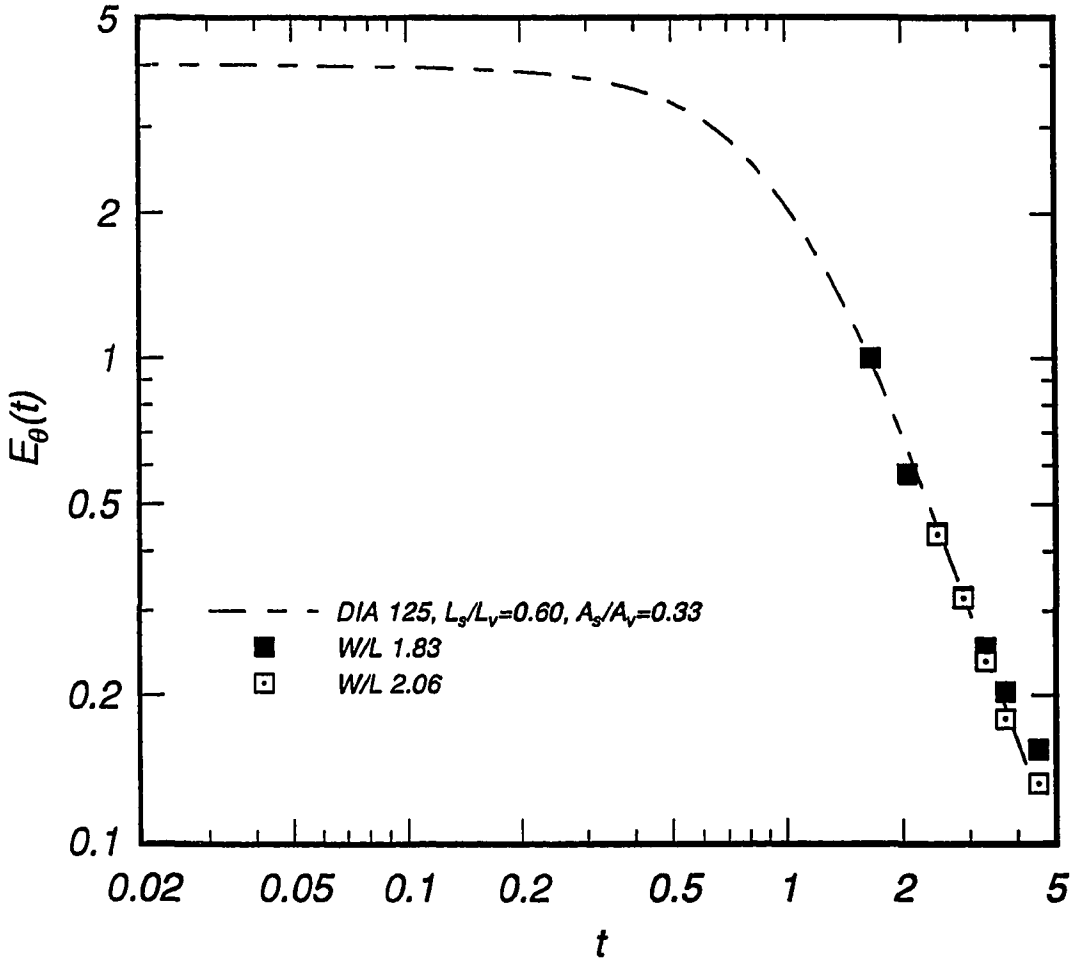

Figure 4.100: Best fit of DIA to scalar energy evolution reported by Warhaft and Lumley.

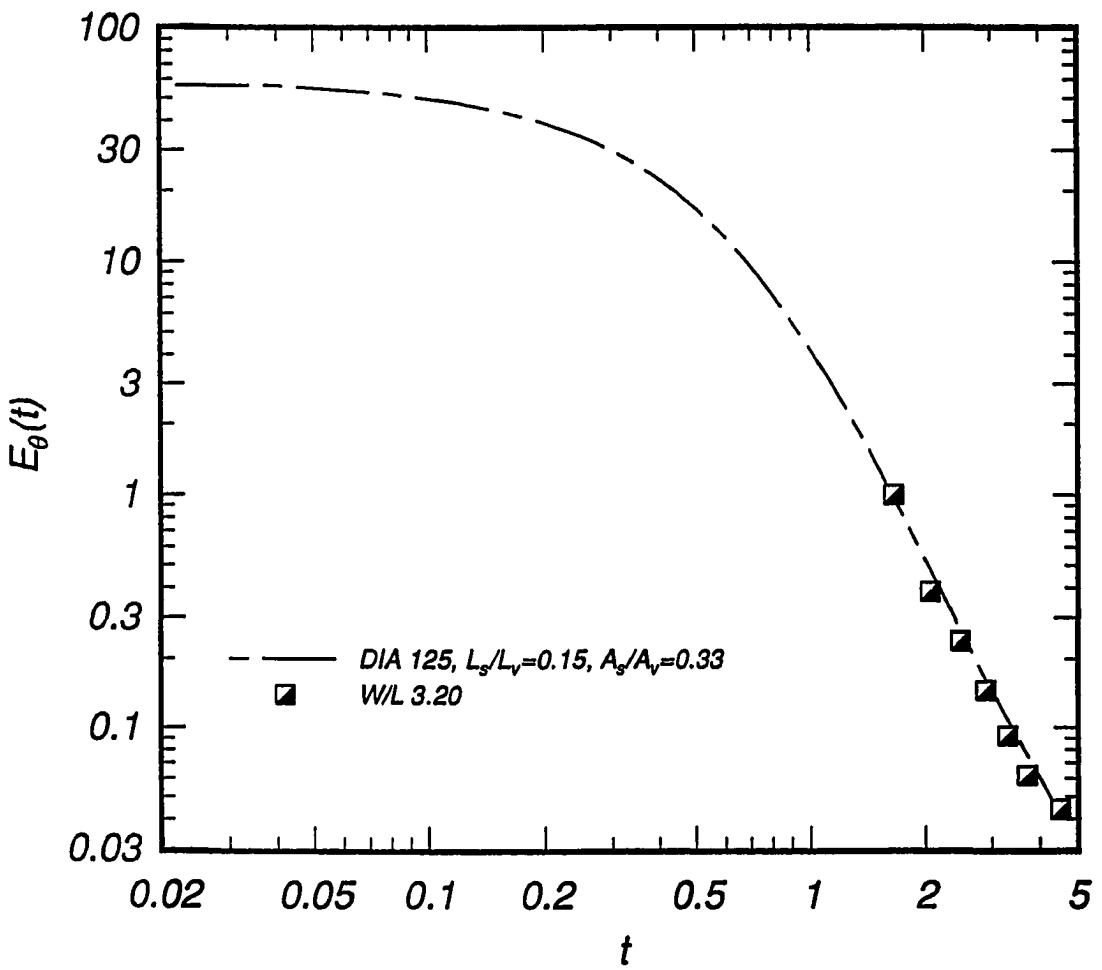

Figure 4.101: Best fit of DIA to scalar energy evolution reported by Warhaft and Lumley.

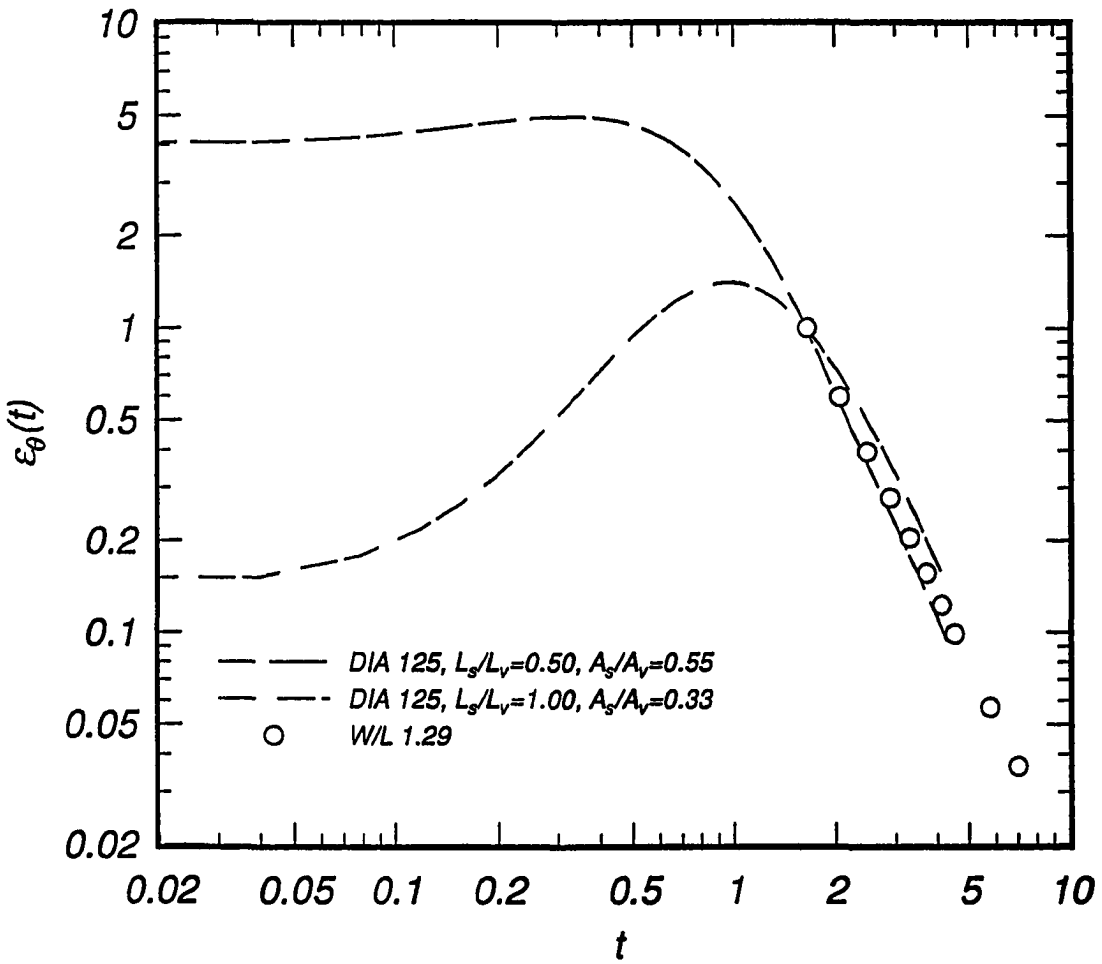

Figure 4.102: Comparison of DIA to scalar diffusion evolution reported by Warhaft and Lumley.

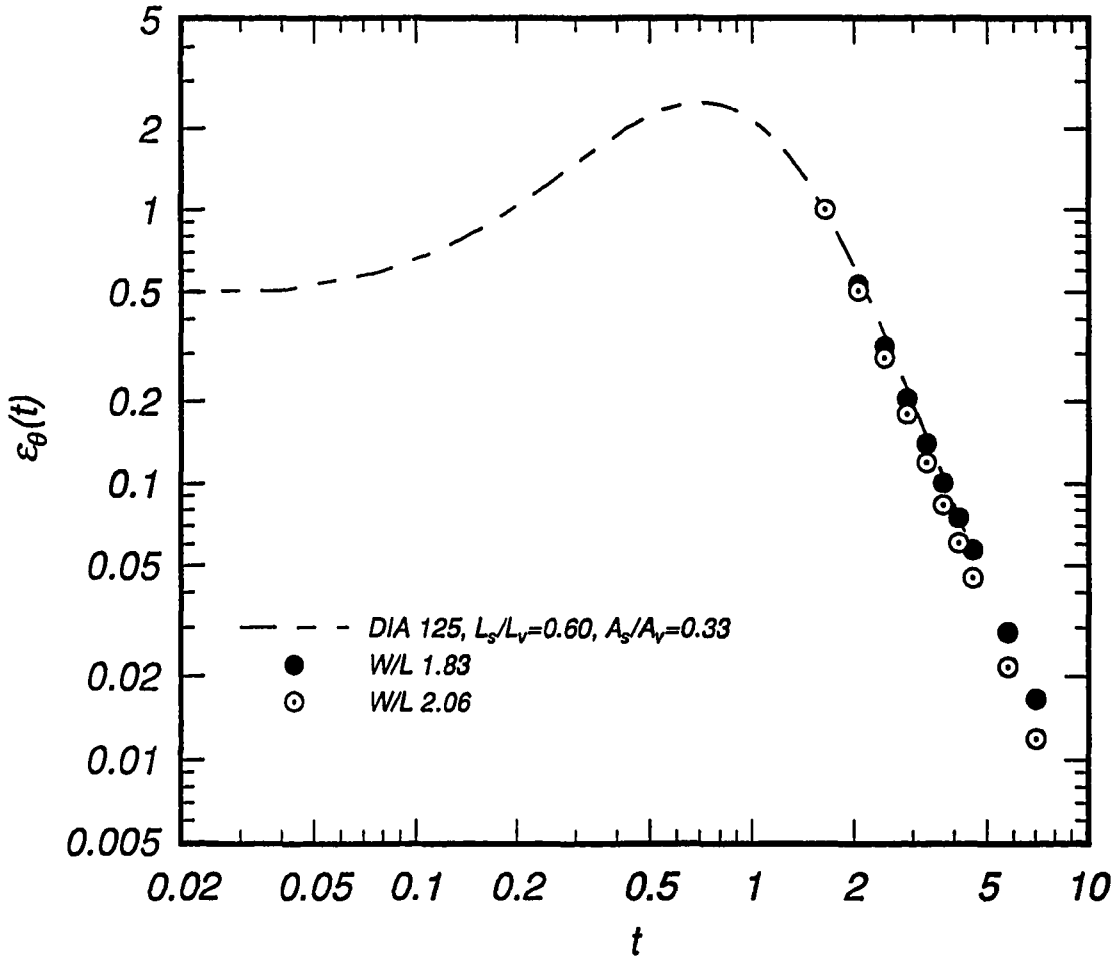

Figure 4.103: Comparison of DIA to scalar diffusion evolution reported by Warhaft and Lumley.

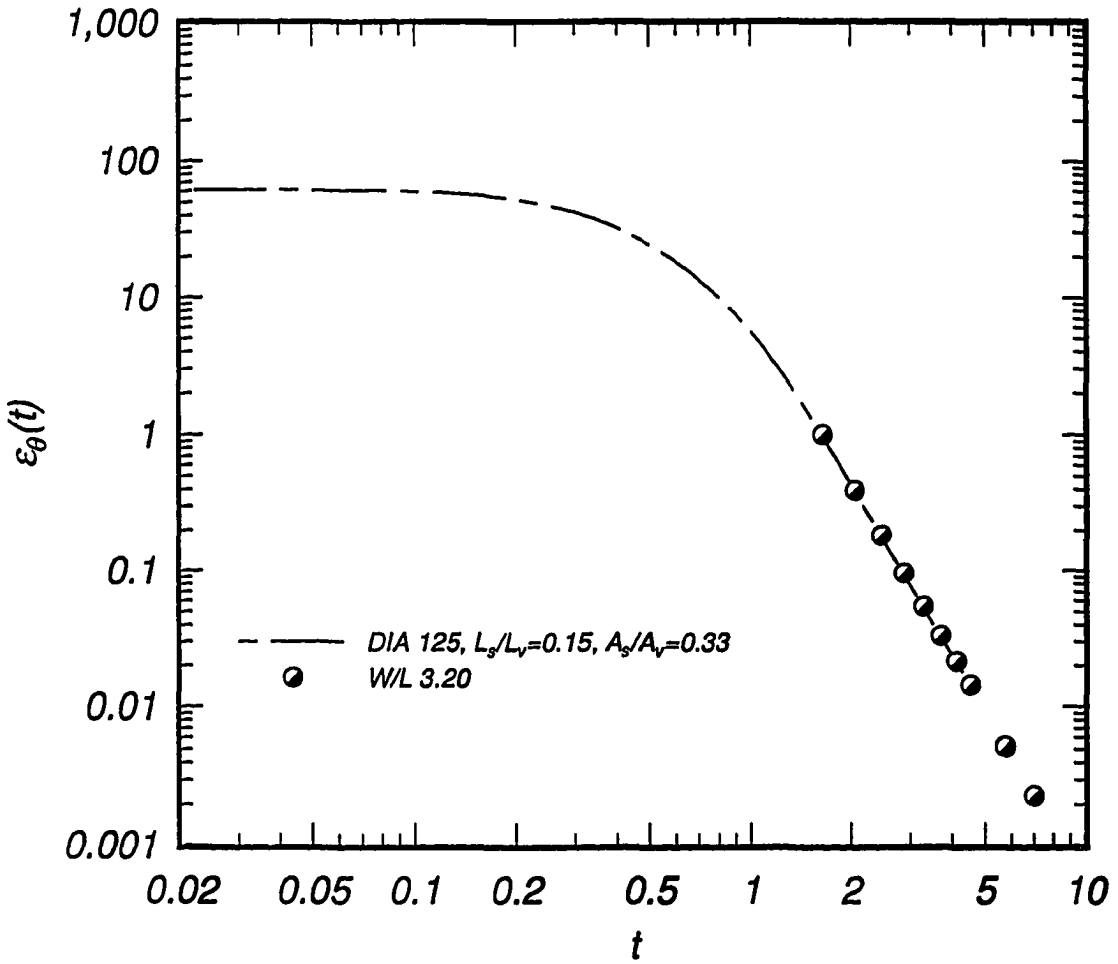

Figure 4.104: Comparison of DIA to scalar diffusion evolution reported by Warhaft and Lumley.

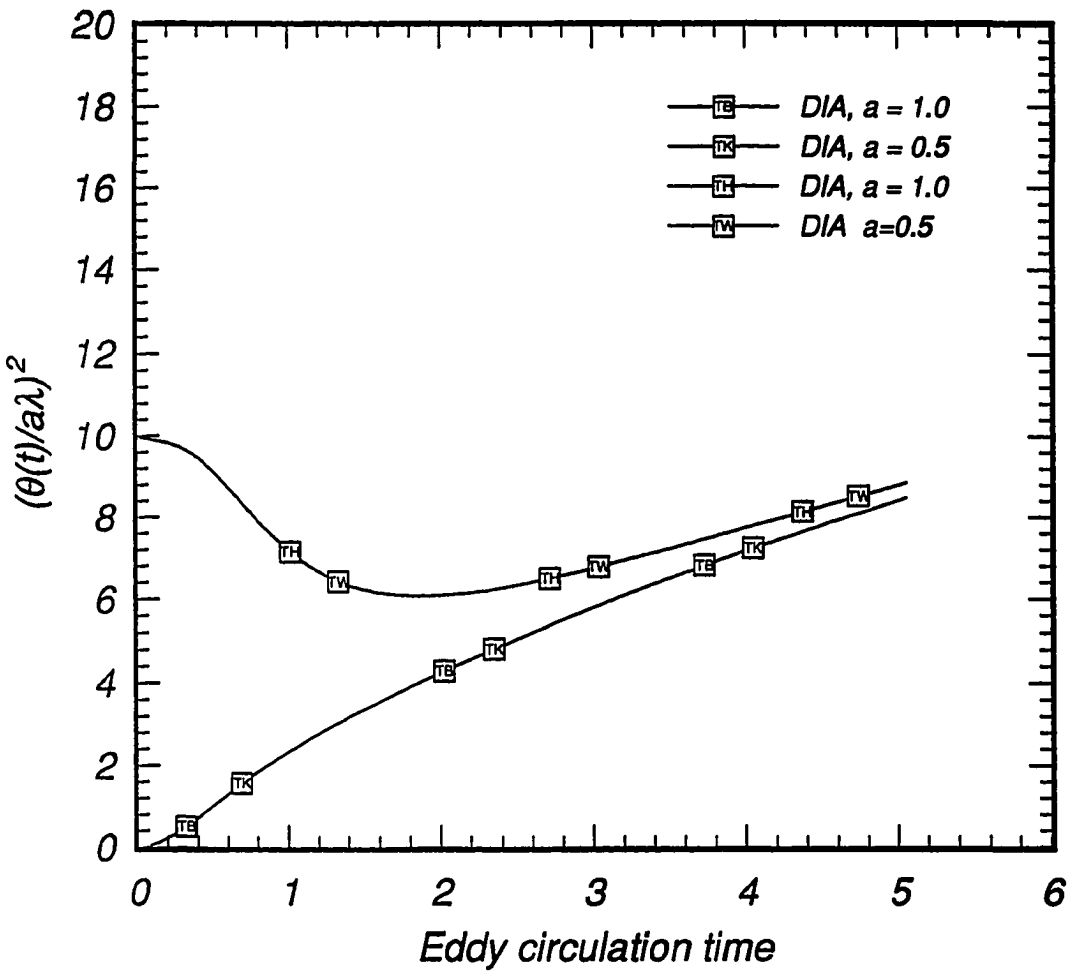

Figure 4.105: Evolution of DIA scalar variance for different initial variances and scalar gradient magnitudes ($R_{\lambda_o} = 80, L_{v_o} = 0.50$).

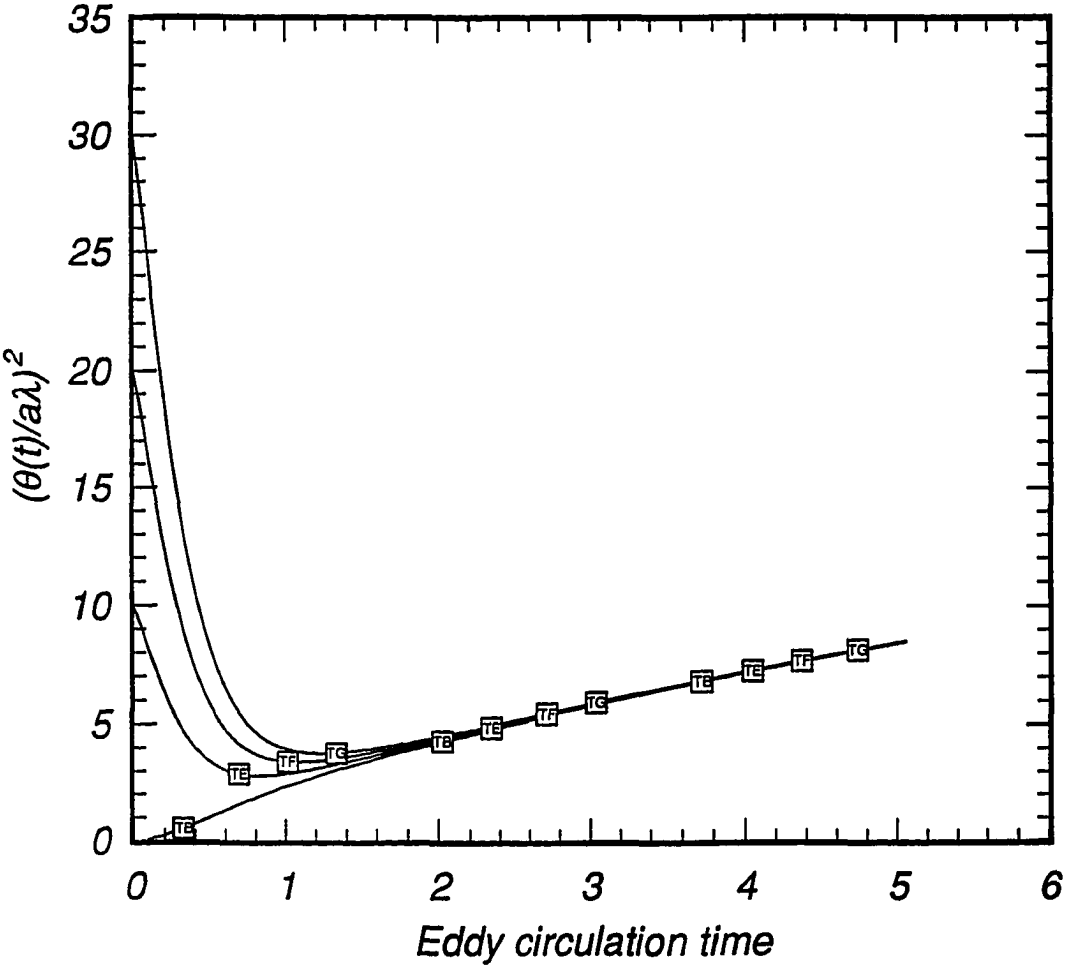

Figure 4.106: Evolution of DIA scalar variance for various initial variances and ($R_{\lambda_o} = 80, L_s/L_{v_o} = 0.25$).

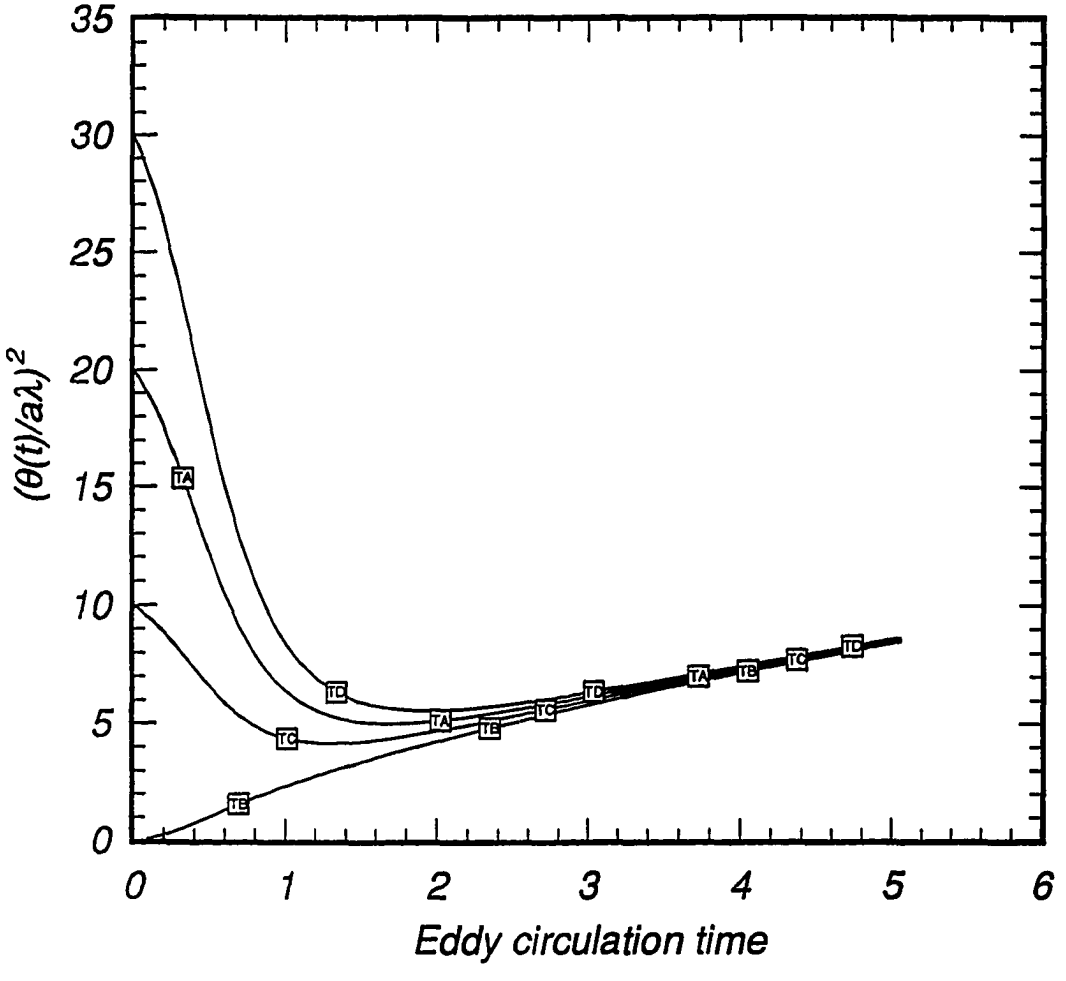

Figure 4.107: Evolution of DIA scalar variance for various initial variances and $(R_{\lambda_o} = 80, L_s/L_{v_o} = 0.50)$.

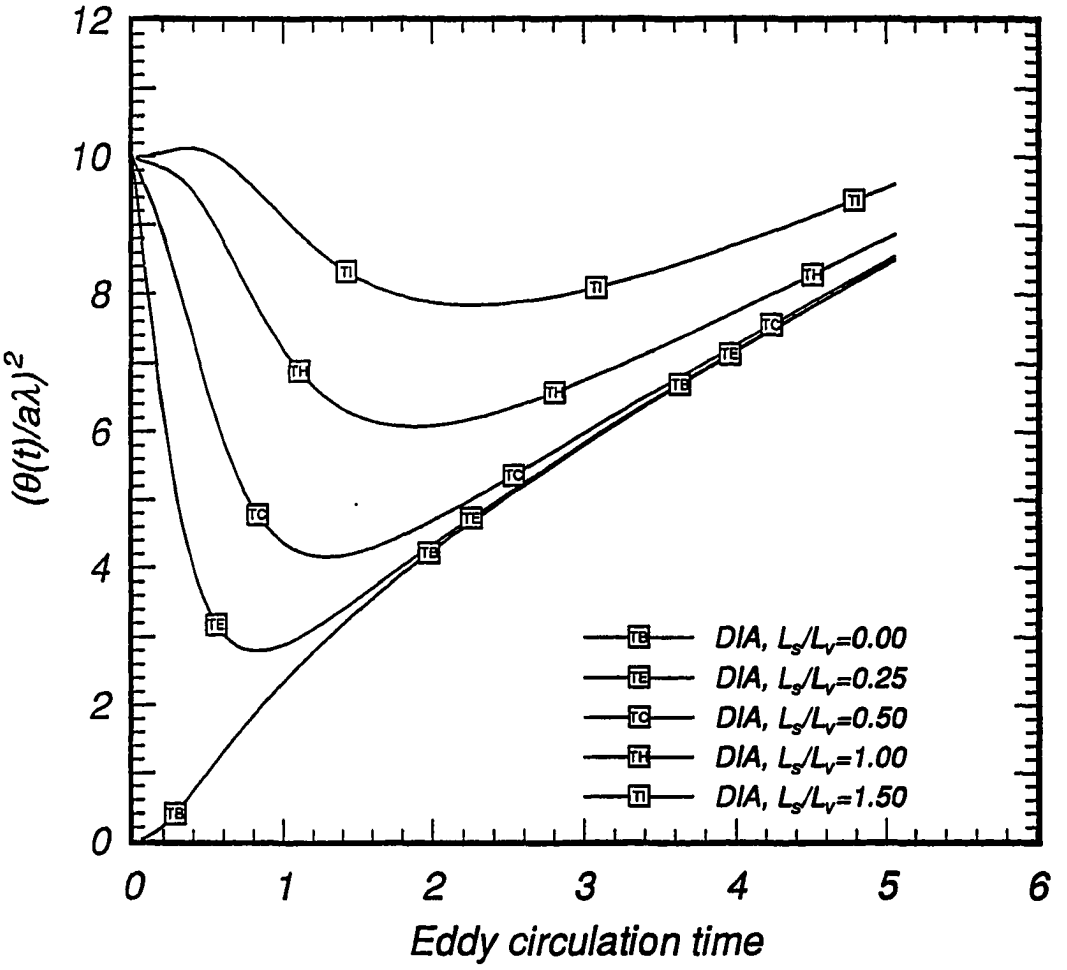

Figure 4.108: Evolution of DIA scalar variance for various initial variances and initial L_s/L_v's ($R_{\lambda_o} = 80, L_{v_o} = 0.50$).

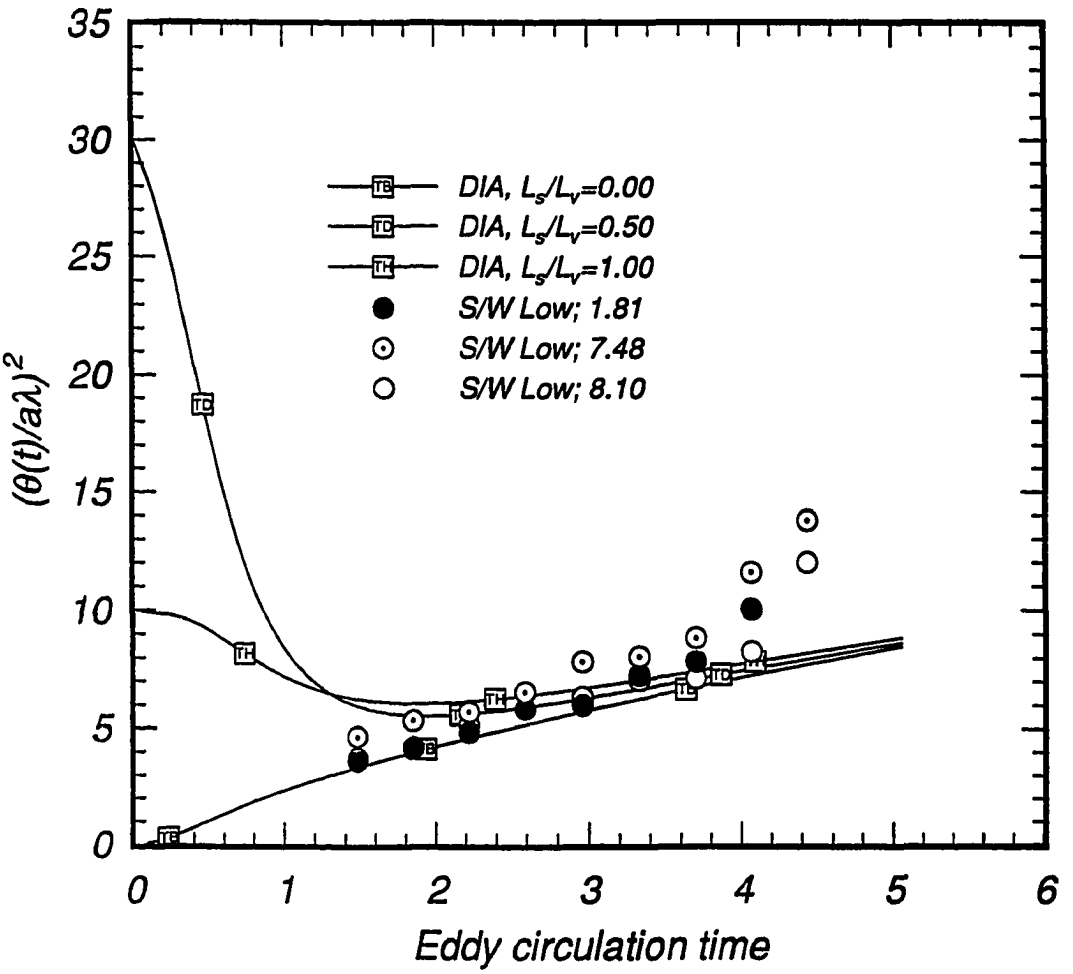

Figure 4.109: Comparison of experimental and DIA scalar variance for the low speed runs of Sirivat and Warhaft ($R_{\lambda_o} = 80, L_{v_o} = 0.50$).

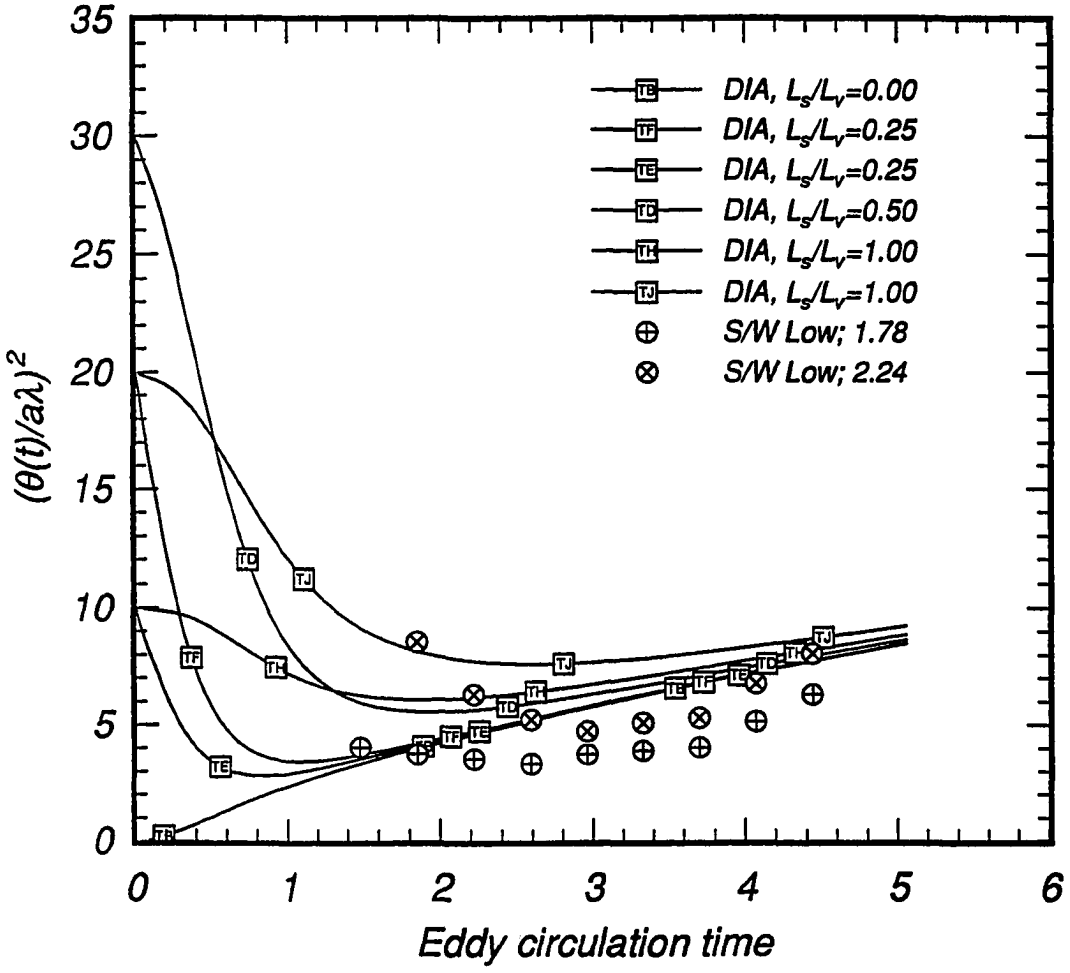

Figure 4.110: Comparison of experimental and DIA scalar variance for the low speed runs of Sirivat and Warhaft ($R_{\lambda_o} = 80, L_{v_o} = 0.50$).

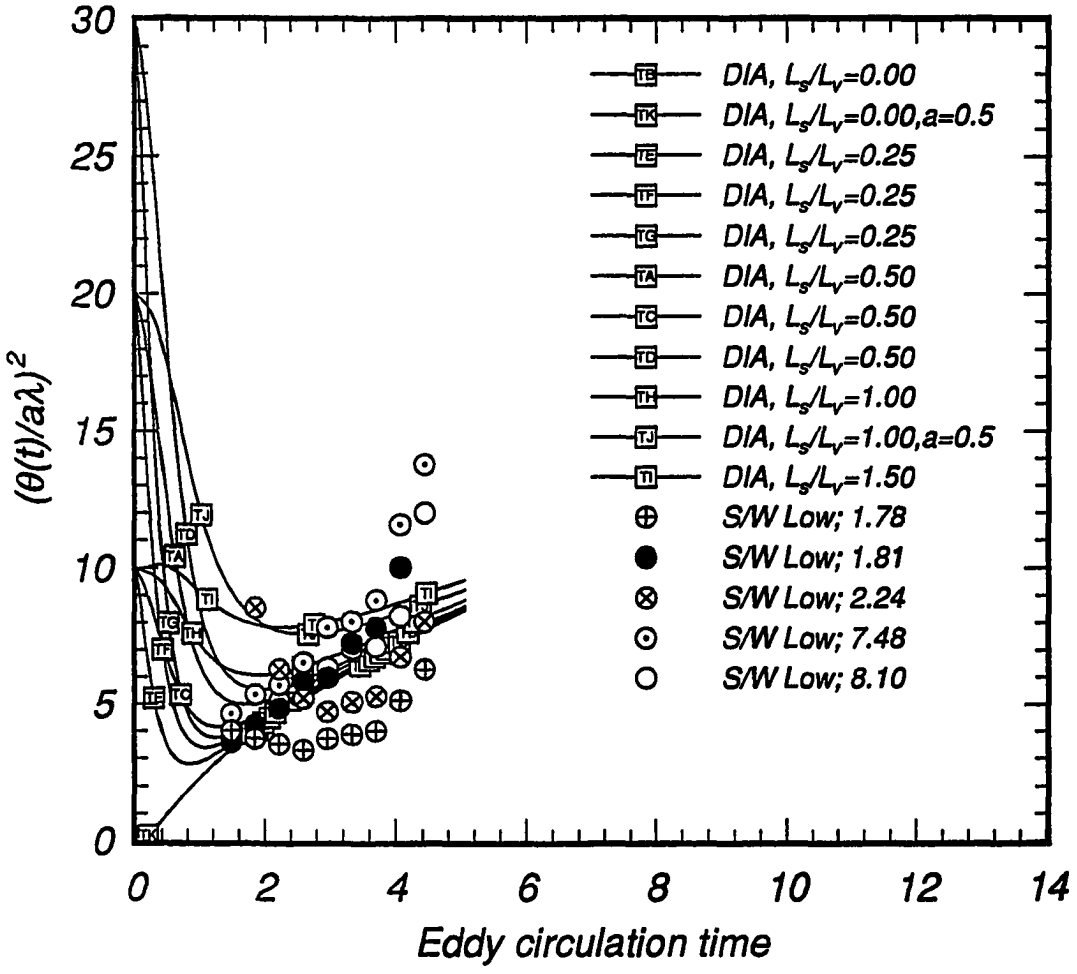

Figure 4.111: Comparison of experimental and DIA scalar variance for the low speed runs of Sirivat and Warhaft ($R_{\lambda_o} = 80$, a=1.0 or as noted).

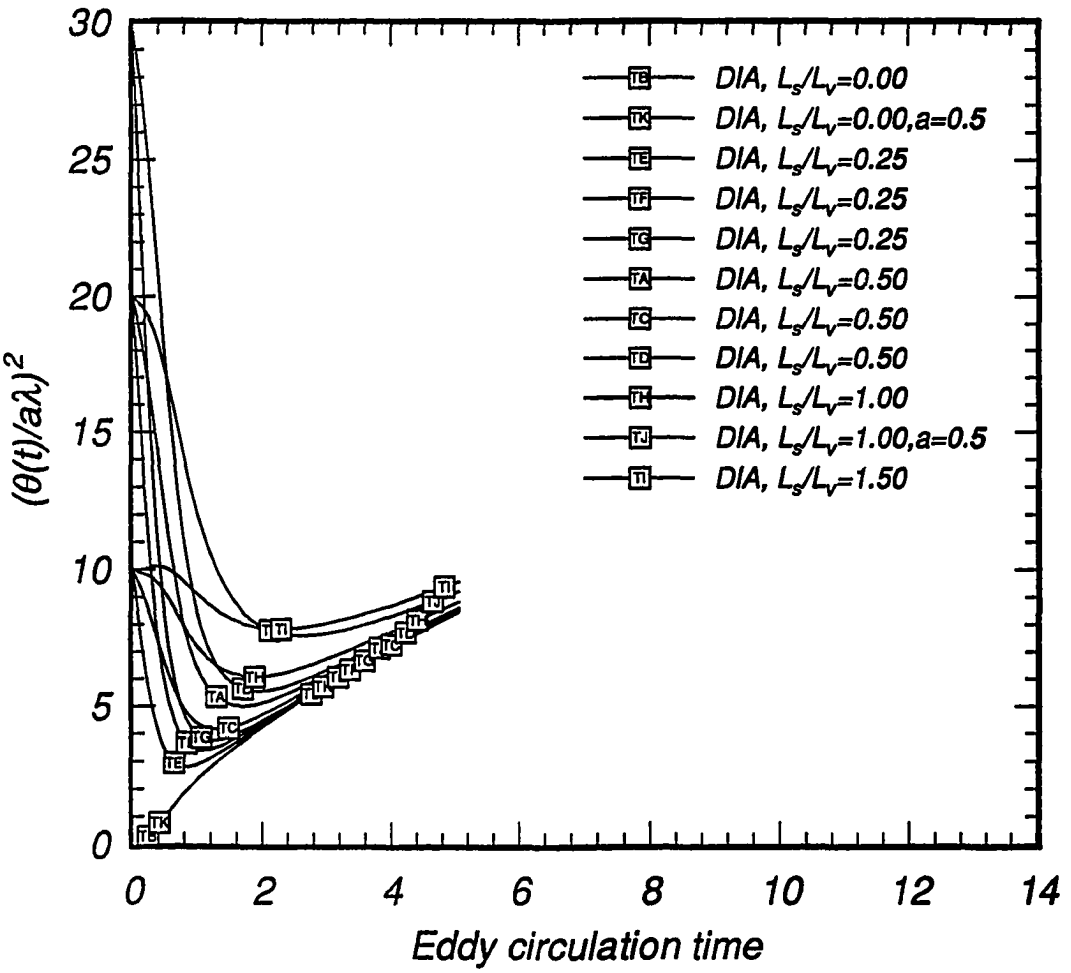

Figure 4.112: Comparison of DIA scalar variances for various initial conditions and scalar gradients ($R_{\lambda_o} = 80$, a=1.0 or as noted).

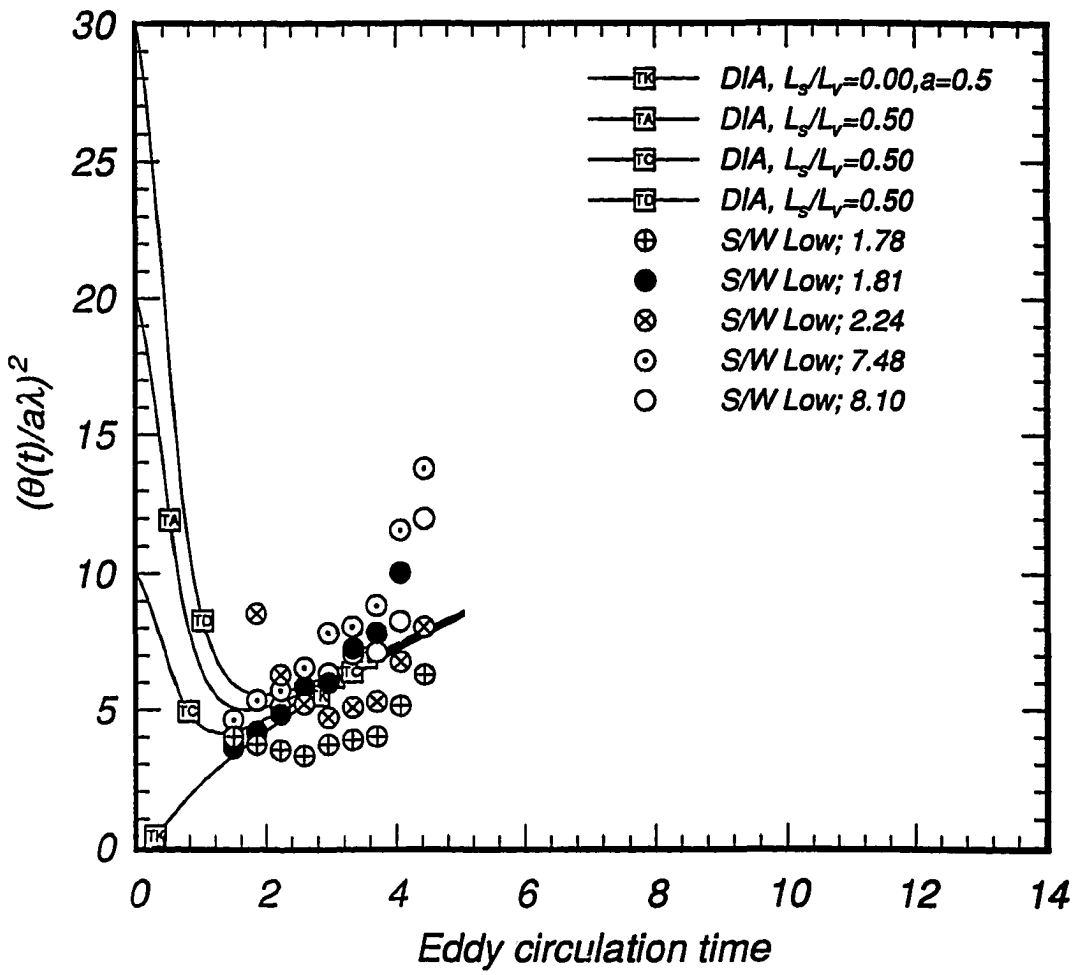

Figure 4.113: Comparison of experimental and DIA scalar variance for the low speed runs of Sirivat and Warhaft (initial DIA L_s/L_v of 0.50, a=1.0 or as noted).

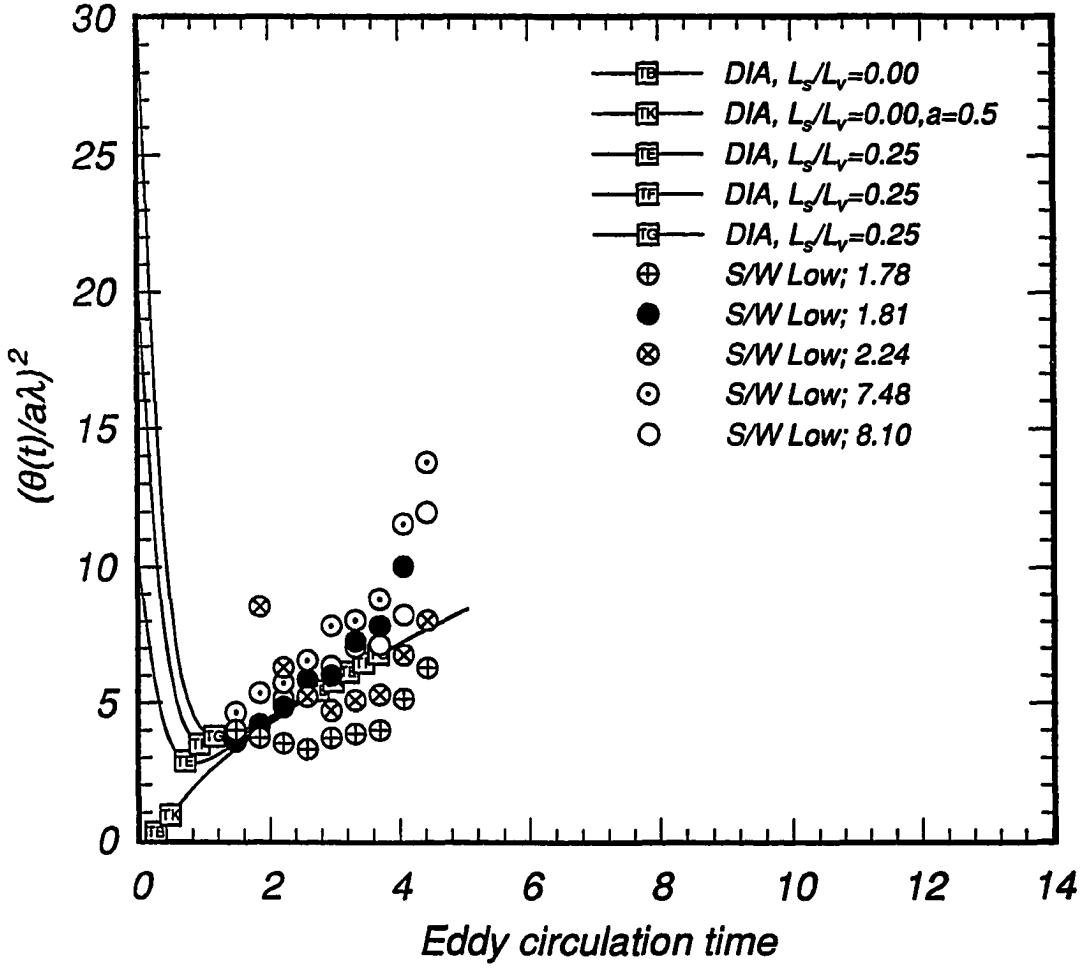

Figure 4.114: Comparison of experimental and DIA scalar variance for the low speed runs of Sirivat and Warhaft (initial DIA L_s/L_v of 0.25, a=1.0 or as noted).

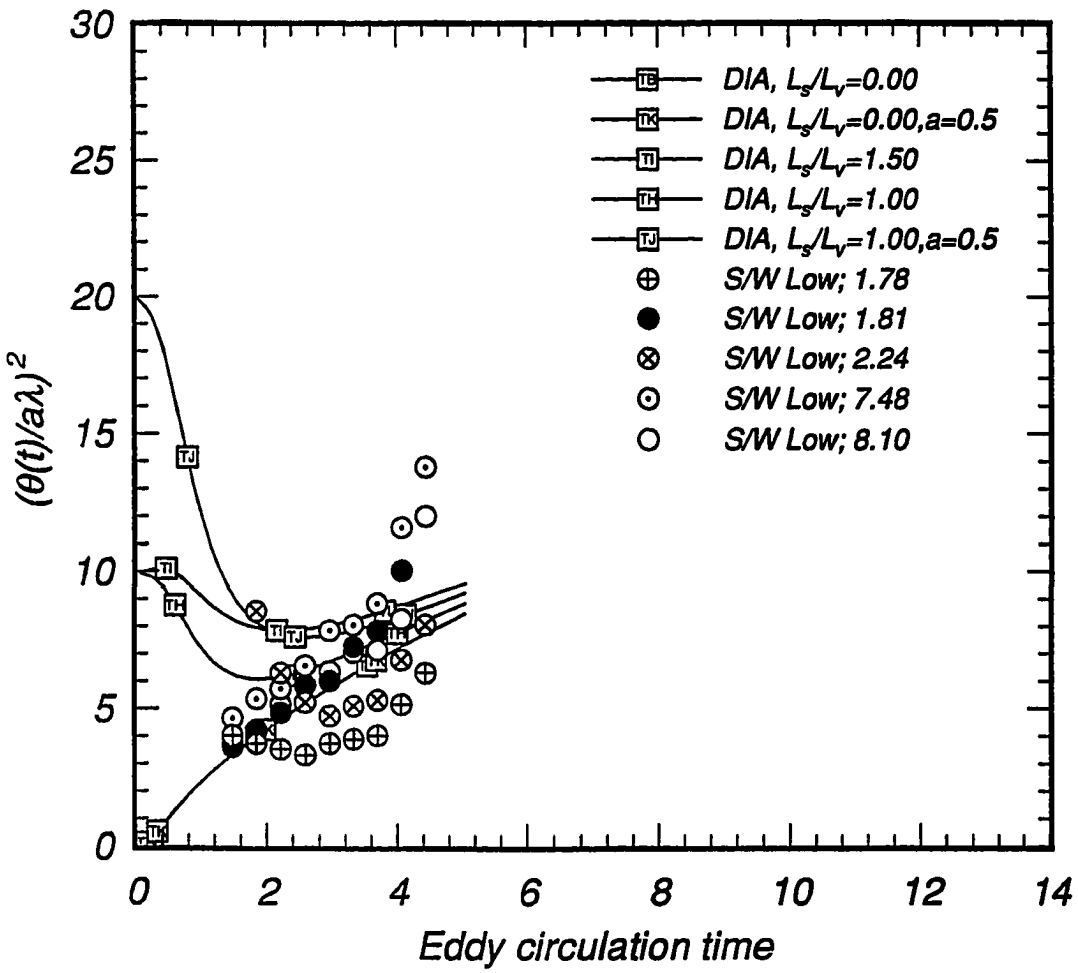

Figure 4.115: Comparison of experimental and DIA scalar variance for the low speed runs of Sirivat and Warhaft (initial DIA L_s/L_v of 1.0 or 1.5.

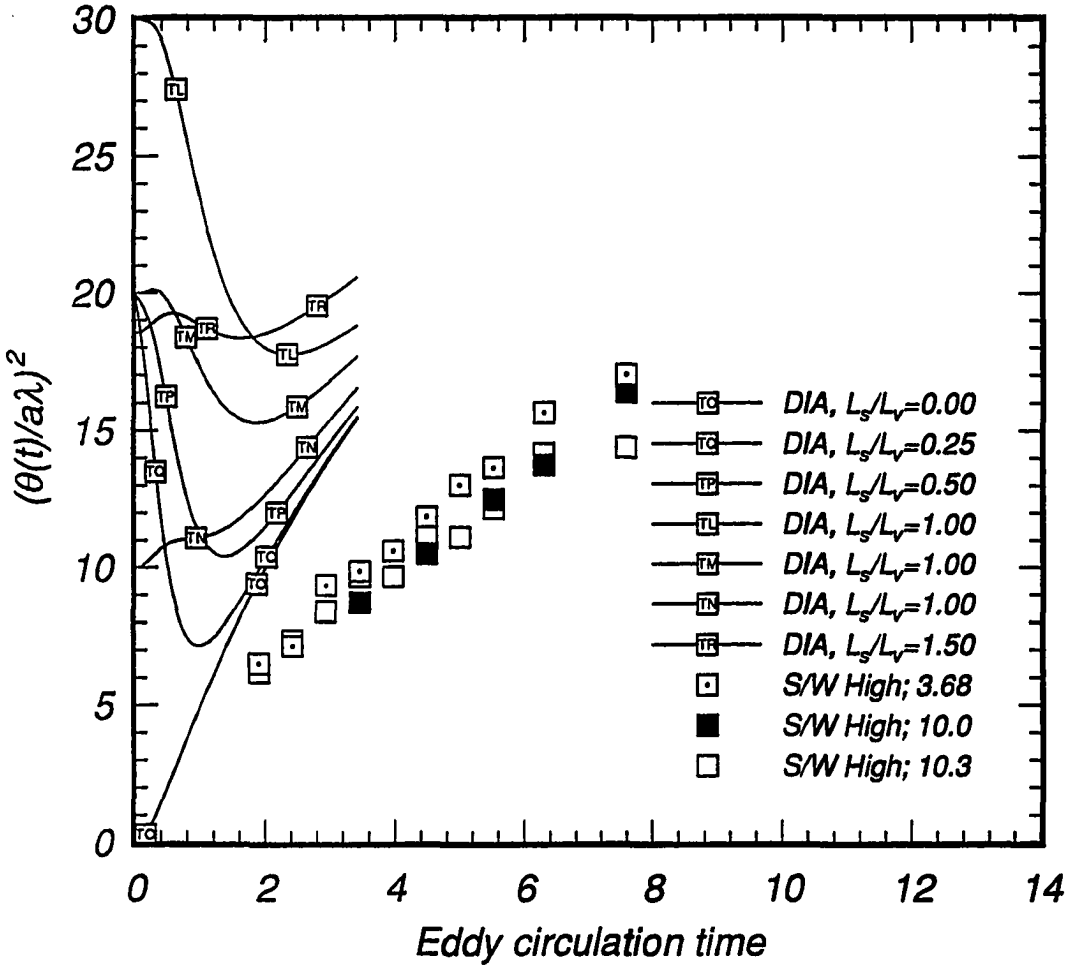

Figure 4.116: Comparison of experimental and DIA scalar variance for the high speed runs of Sirivat and Warhaft (DIA a=1.0 or as noted).

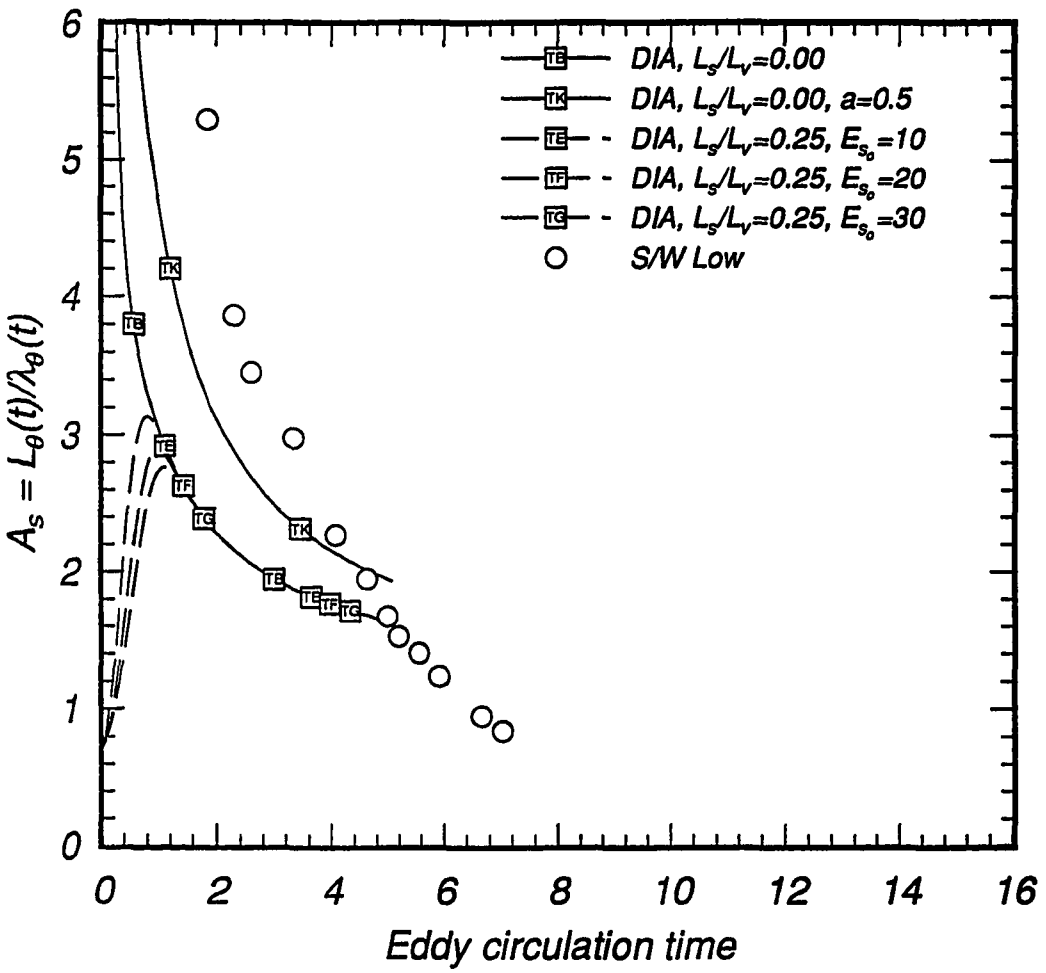

Figure 4.117: Evolution of scalar field A_s (integral lengthscale/Taylor microscale ratio) for low speed experiment and DIA (DIA a=1.0 or as noted).

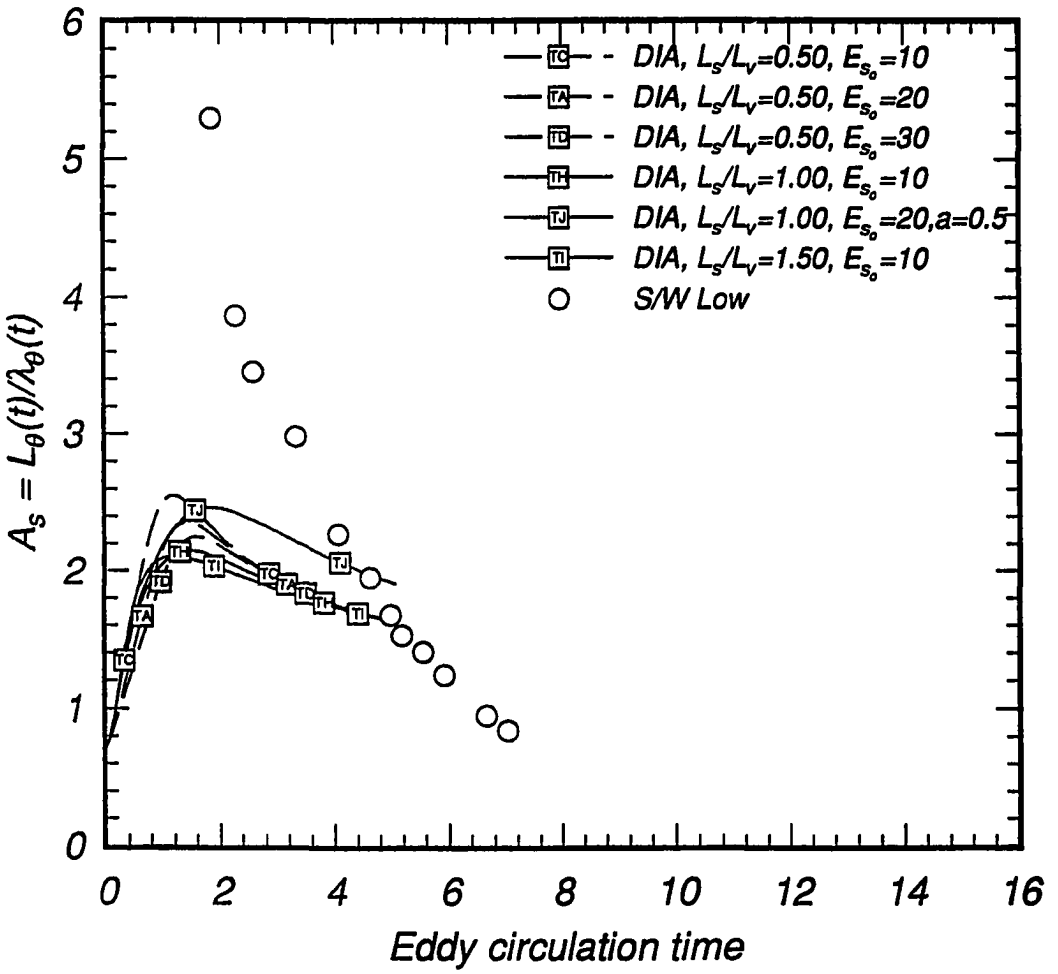

Figure 4.118: Evolution of scalar field A_s (integral lengthscale/Taylor microscale ratio) for low speed experiment and DIA (DIA a=1.0 or as noted).

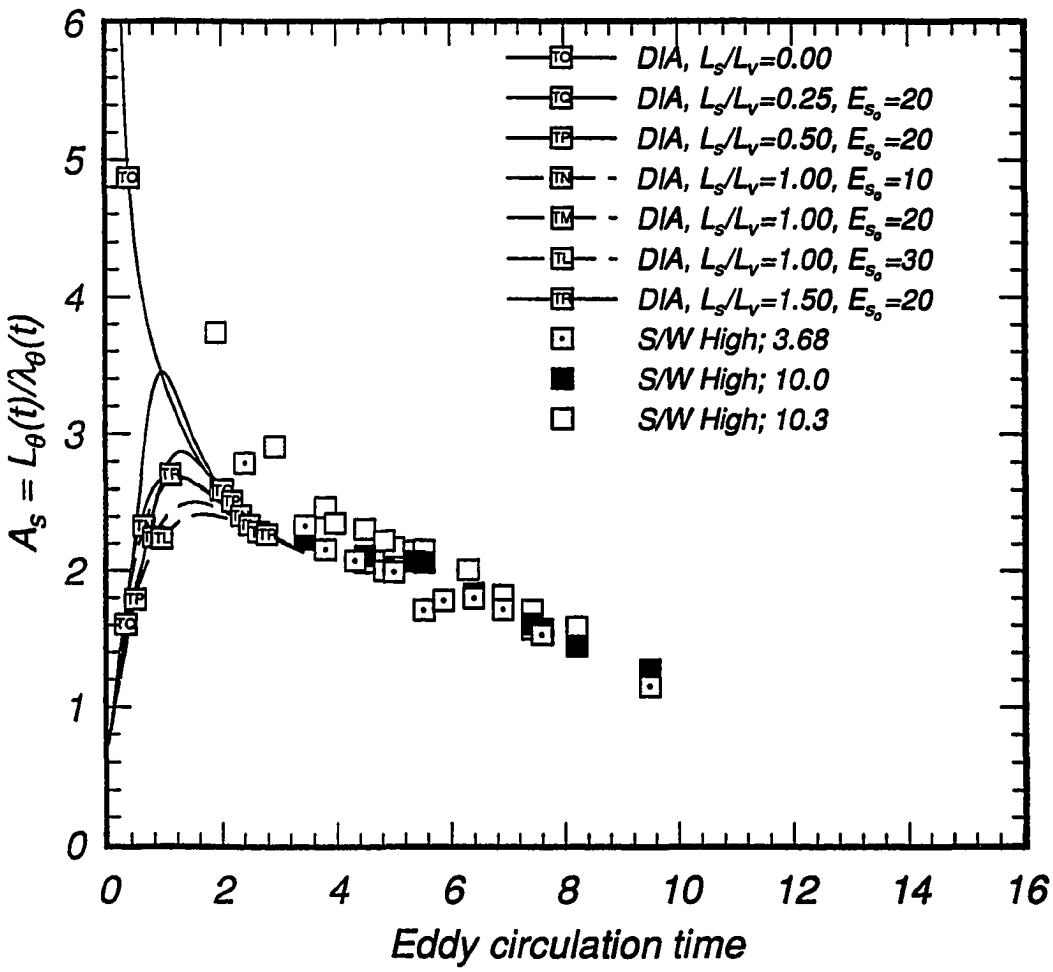

Figure 4.119: Evolution of scalar field A_s (integral lengthscale/Taylor microscale ratio) for high speed experiment and DIA.

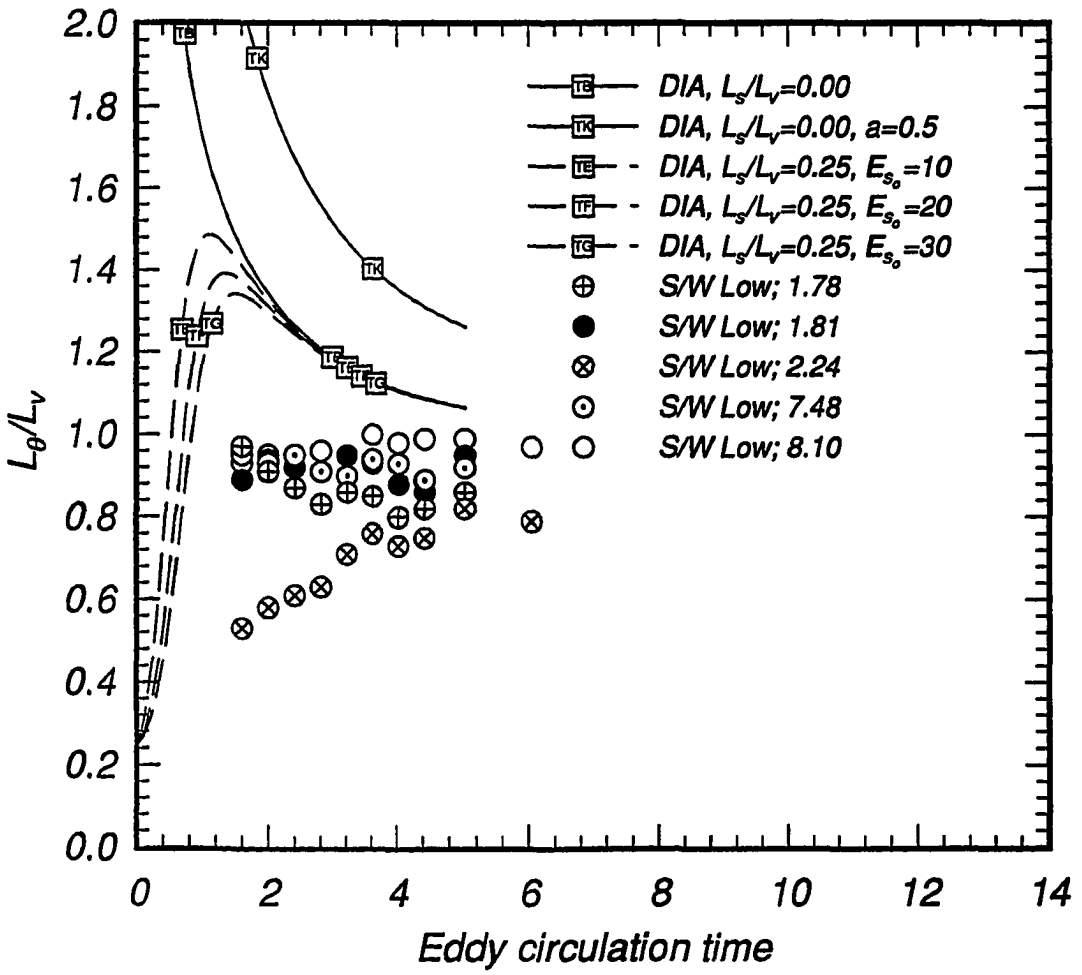

Figure 4.120: Evolution of scalar to velocity field integral lengthscale ratio for low speed experiment and DIA.

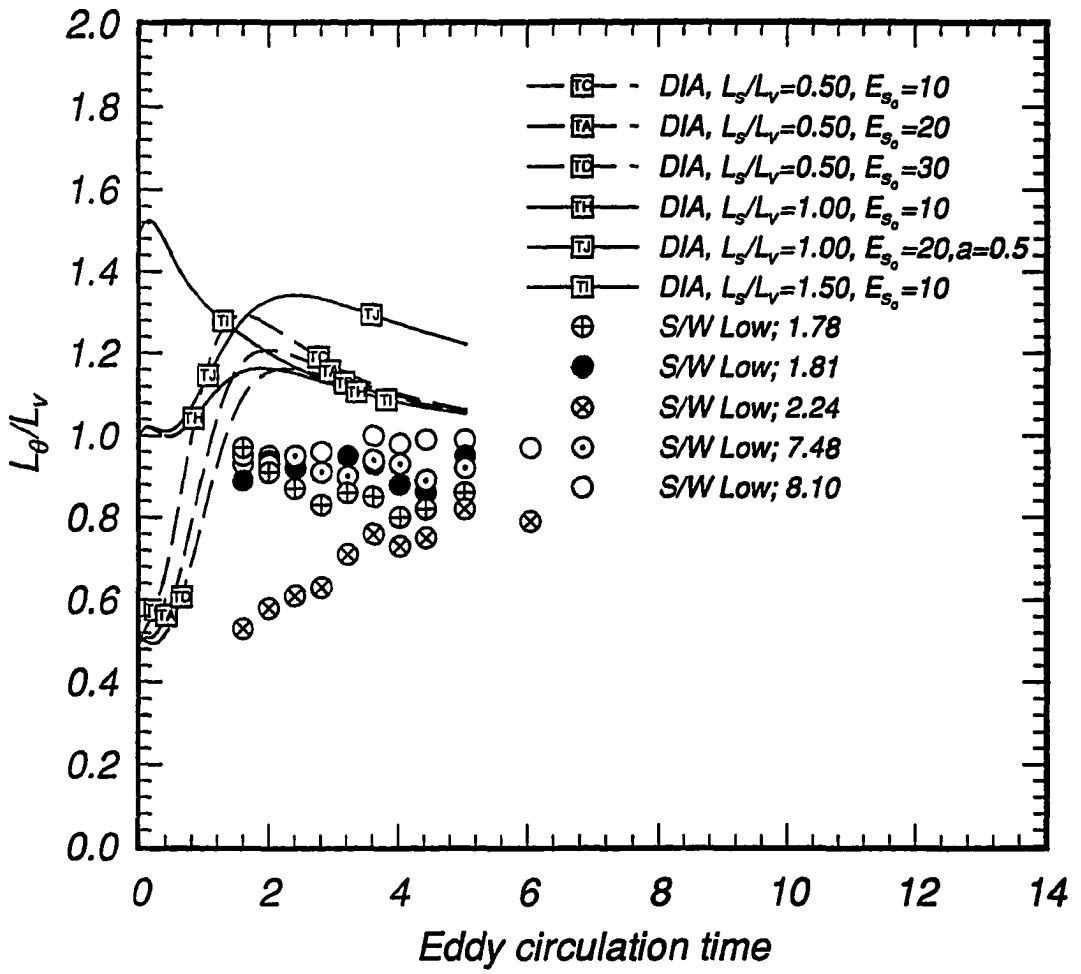

Figure 4.121: Evolution of scalar to velocity field integral lengthscale ratio for low speed experiment and DIA (DIA a=1.0 or as noted).

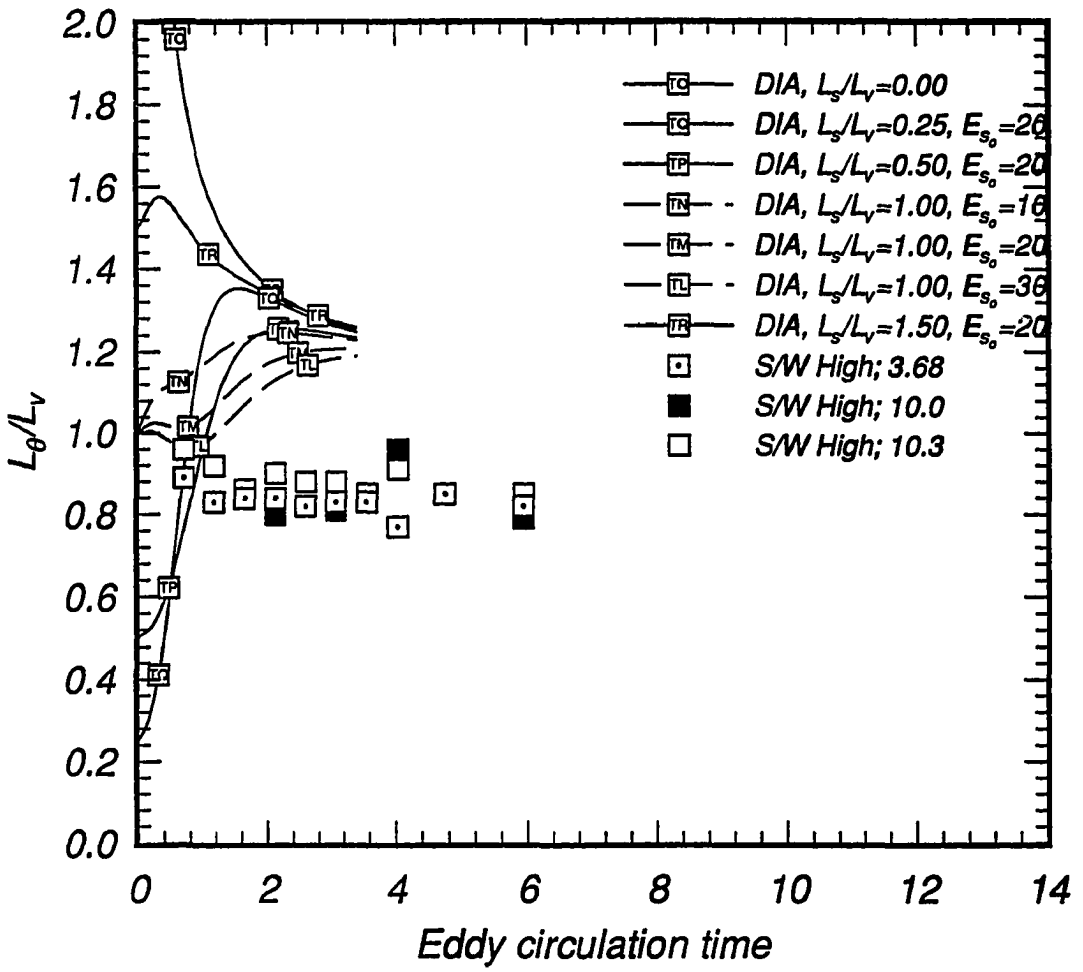

Figure 4.122: Evolution of scalar to velocity field integral lengthscale ratio for high speed experiment and DIA (DIA a=1.0 or as noted).

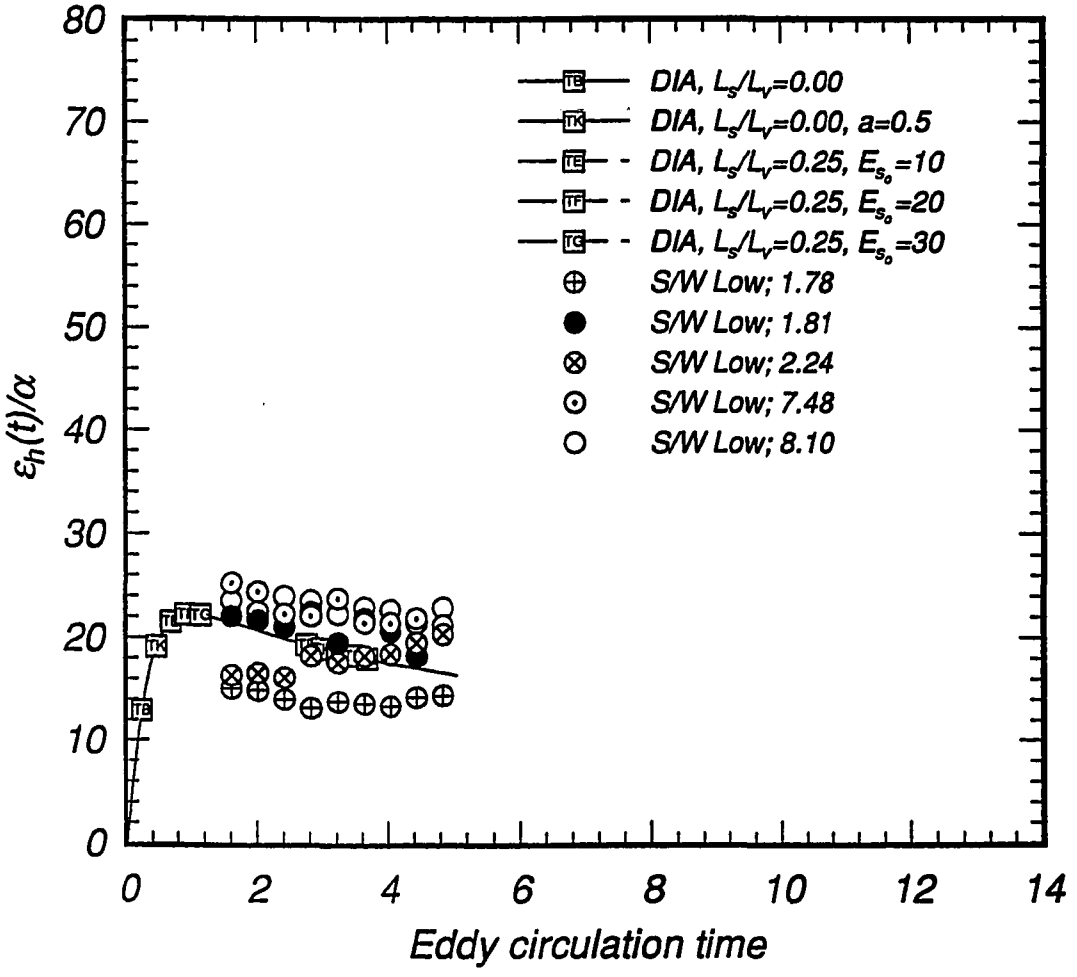

Figure 4.123: Evolution of eddy diffusivity ratios for low speed experiments and DIA (DIA a=1.0 or as noted).

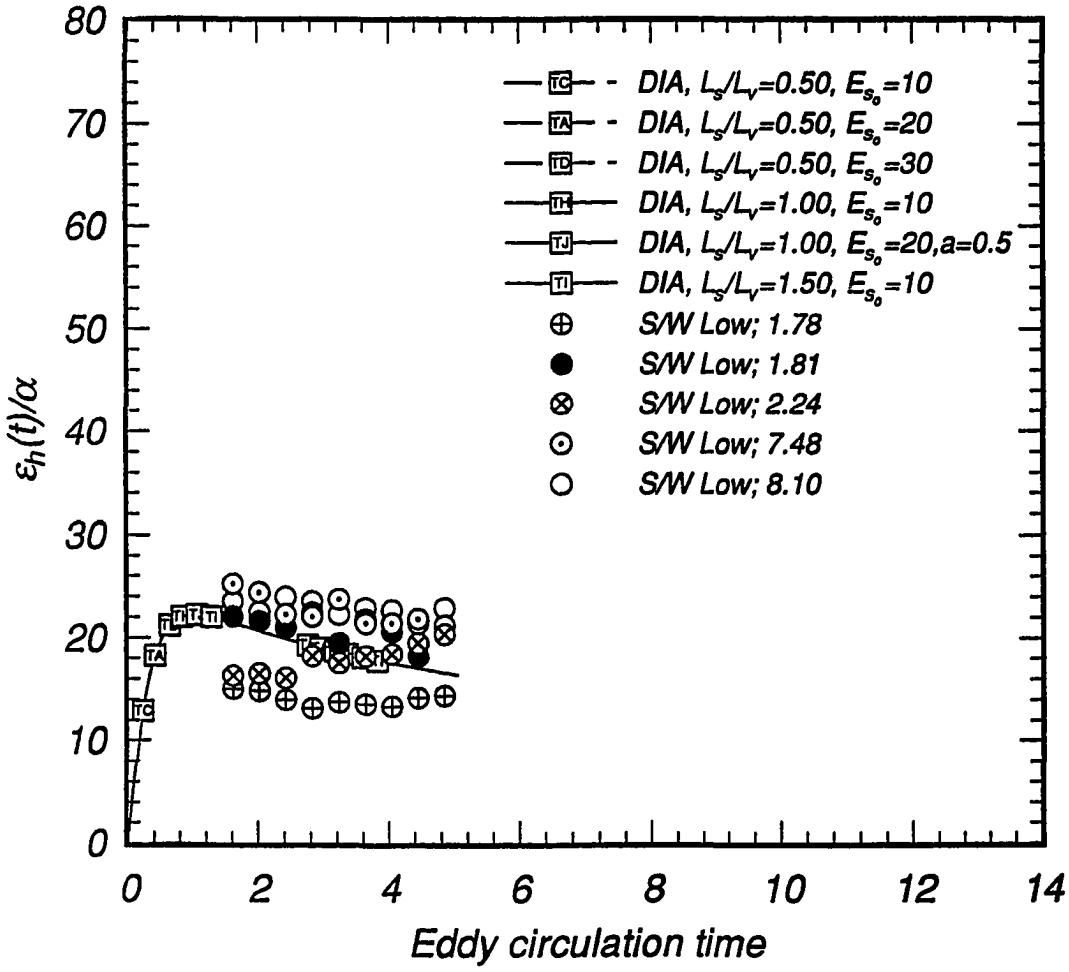

Figure 4.124: Evolution of eddy diffusivity ratios for low speed experiments and DIA (DIA a=1.0 or as noted).

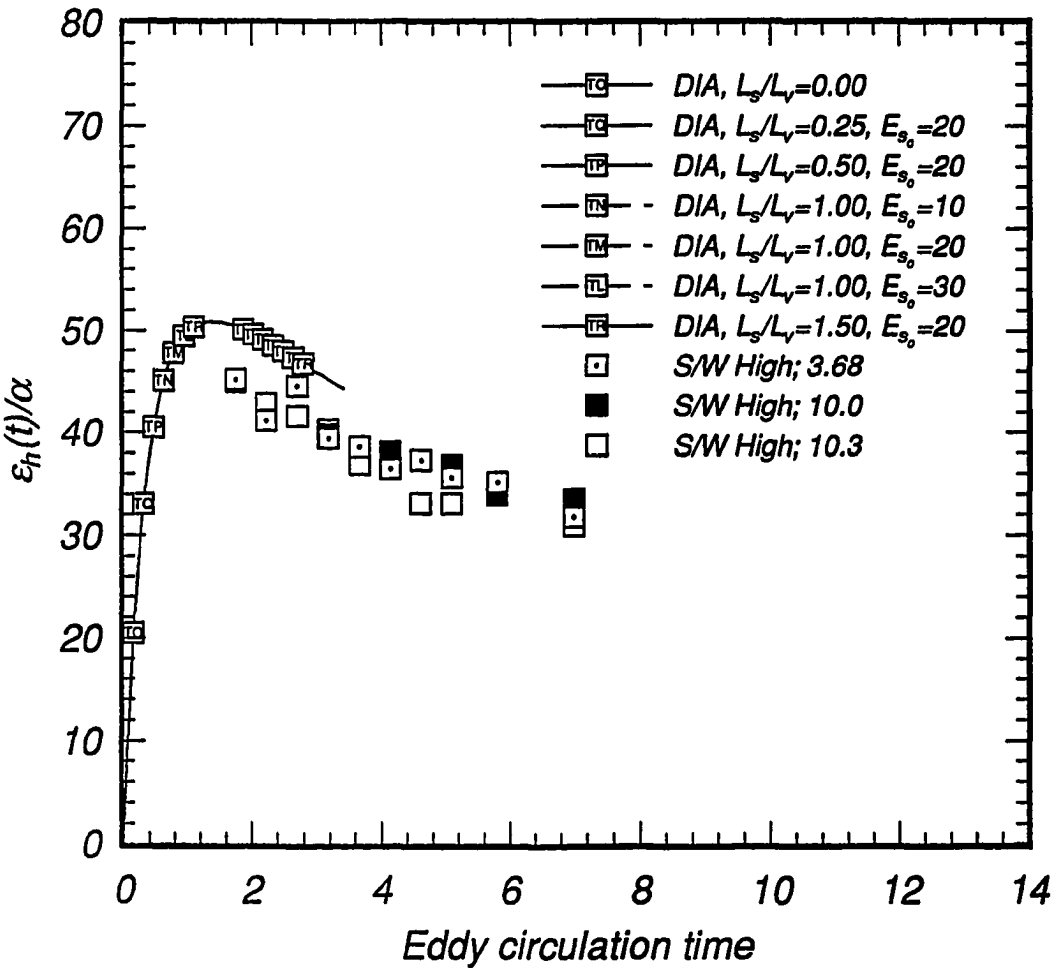

Figure 4.125: Evolution of eddy diffusivity ratios for high speed experiments and DIA (DIA a=1.0 or as noted).

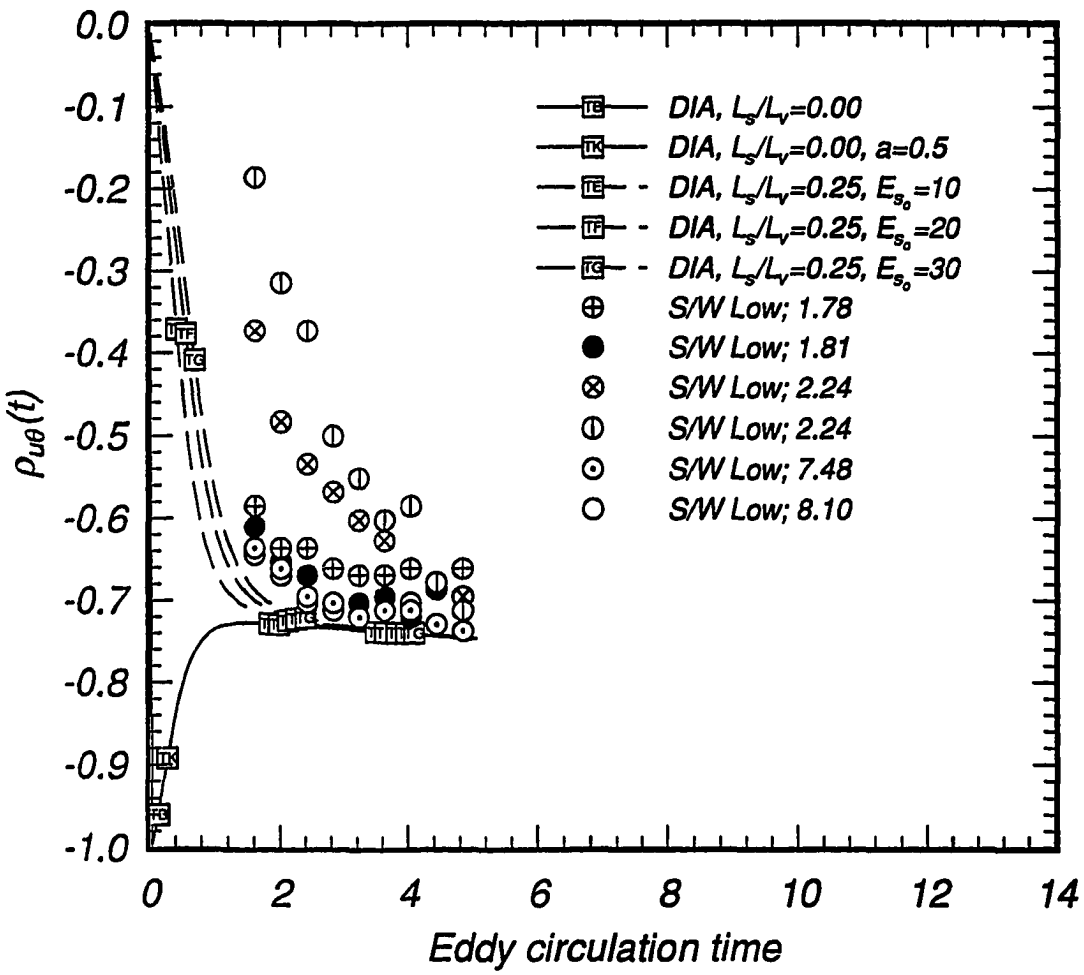

Figure 4.126: Evolution of scalar transport correlation coefficients for low speed experiments and DIA (DIA a=1.0 or as noted).

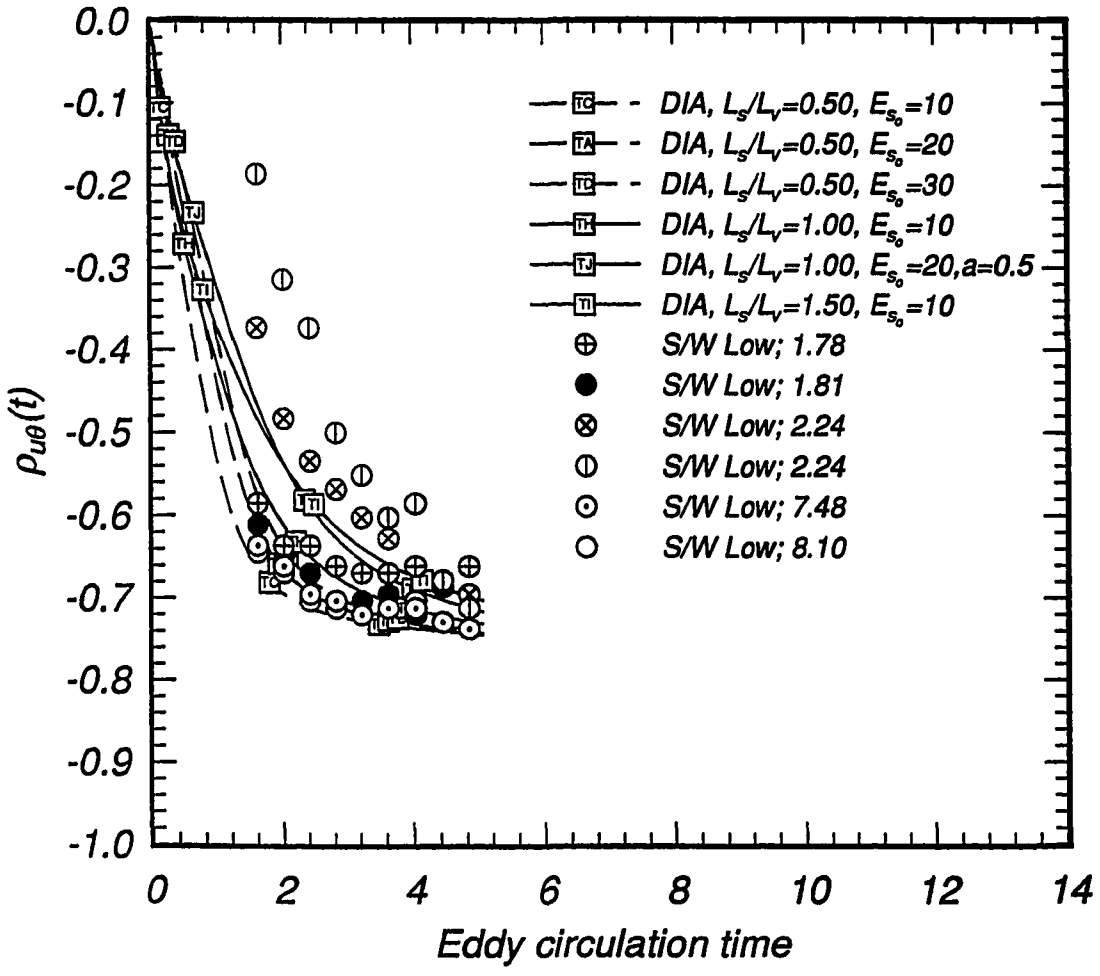

Figure 4.127: Evolution of scalar transport correlation coefficients for low speed experiments and DIA (DIA a=1.0 or as noted).

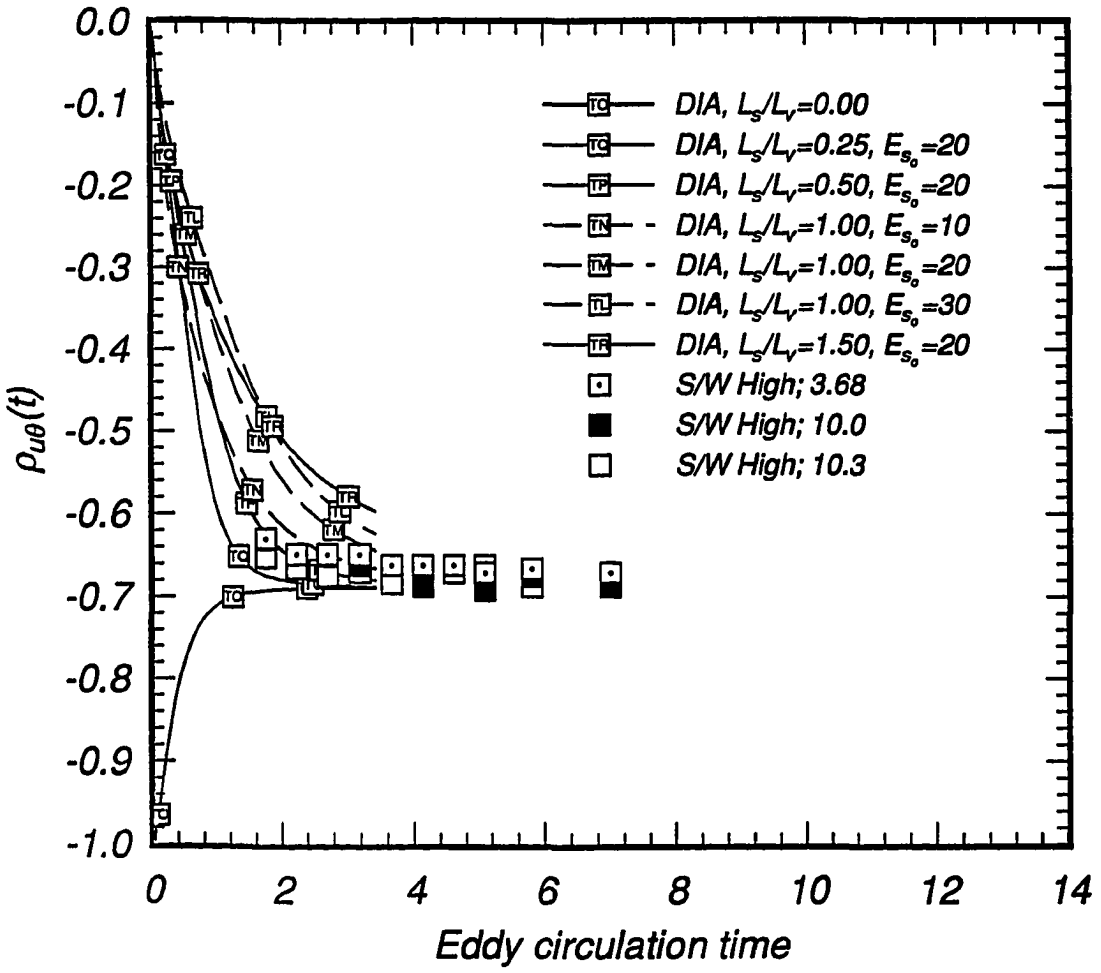

Figure 4.128: Evolution of scalar transport correlation coefficients for high speed experiments and DIA (DIA a=1.0 or as noted).

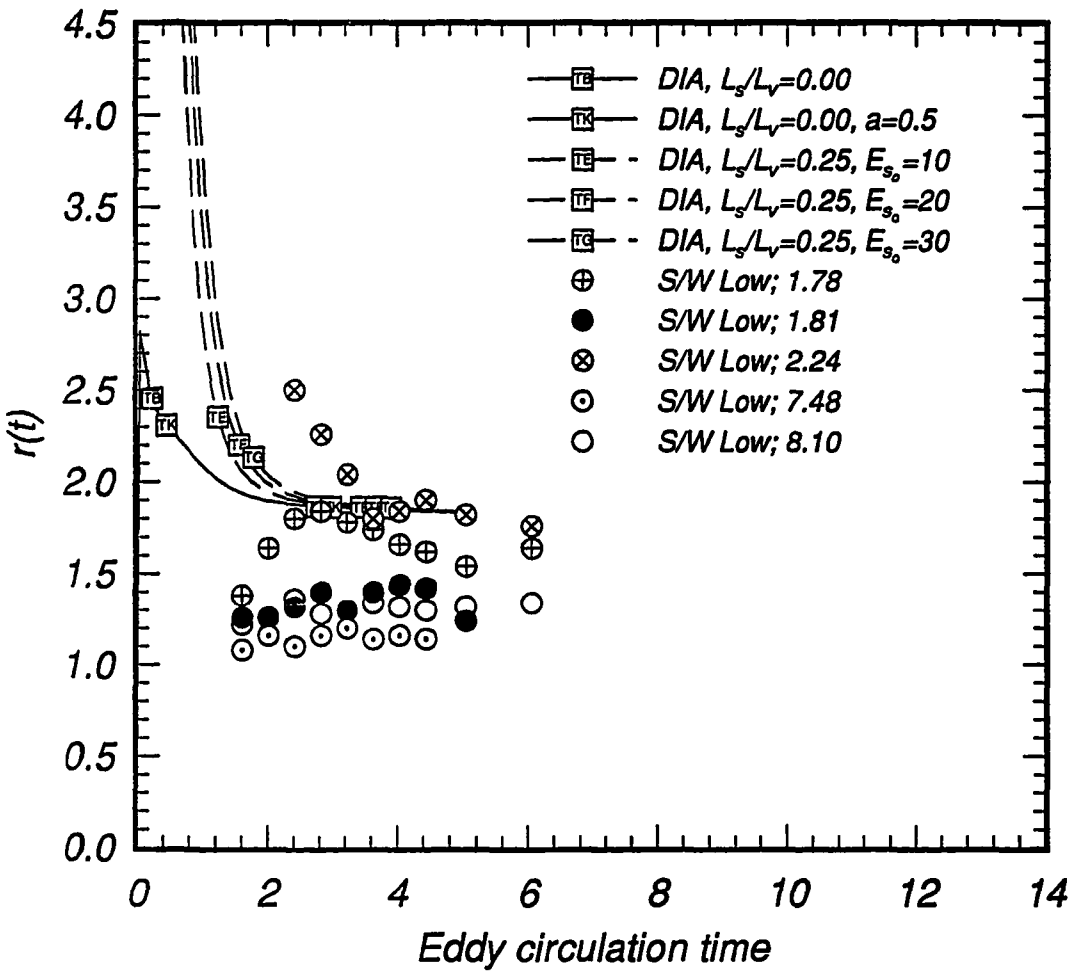

Figure 4.129: Evolution of mechanical/thermal timescale ratios for low speed experiments and DIA (DIA a=1.0 or as noted).

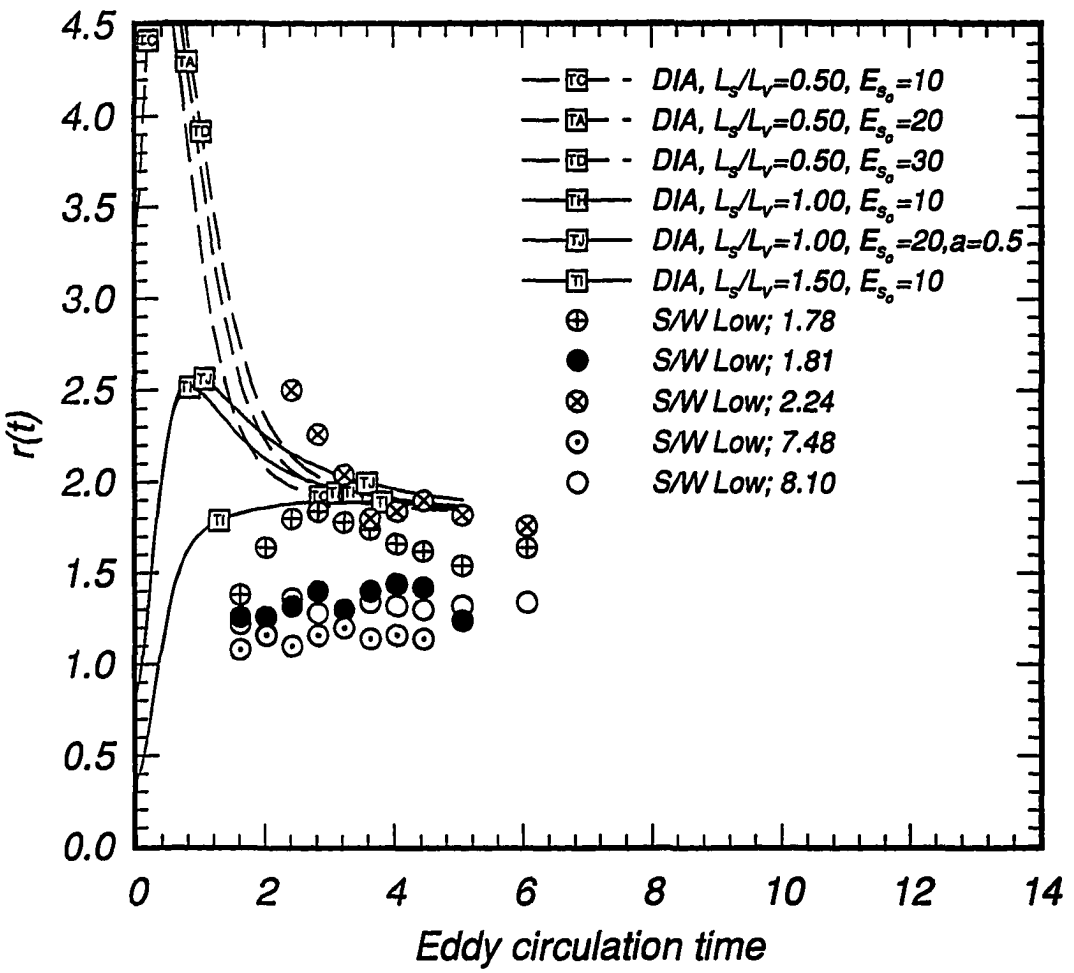

Figure 4.130: Evolution of mechanical/thermal timescale ratios for low speed experiments and DIA (DIA a=1.0 or as noted).

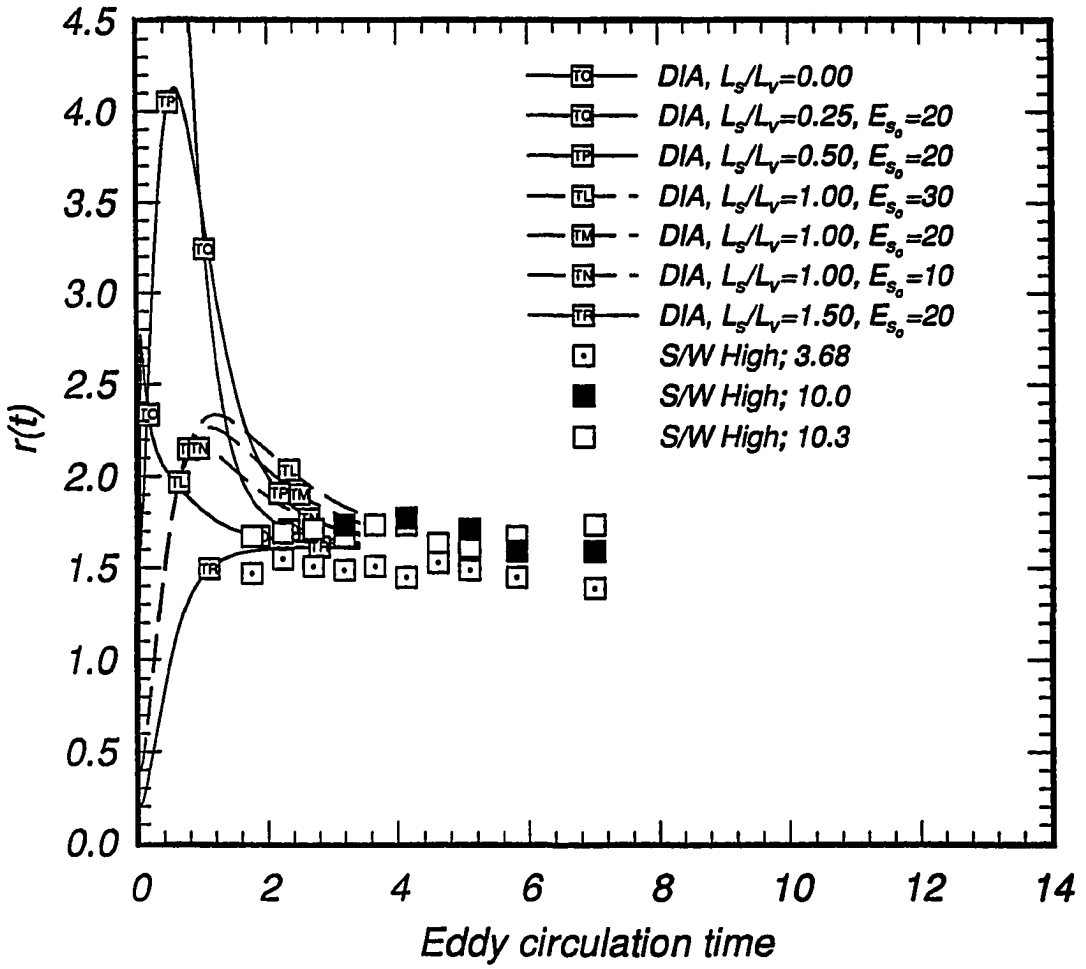

Figure 4.131: Evolution of mechanical/thermal timescale ratios for high speed experiments and DIA (DIA a=1.0 or as noted).

CHAPTER 5. SUMMARY

The DIA was used to study homogeneous turbulent scalar transport, with and without buoyancy effects, and compare with the results of DNS computations and of experiments. The DIA was also used independently to study some aspects additional aspects of isotropic scalar turbulence and to simulate results of some experimental studies of isotropic decaying velocity fields, decaying isotropic scalar fields and isotropic passive scalar turbulent transport.

Comparisons of DIA and DNS for decaying, low Reynolds number isotropic velocity and scalar fields indicated reasonable agreement. The study of active and fossil stably stratified turbulence showed reasonably good qualitative agreement between the DIA and DNS results. However, using only the first Legendre coefficients resulted in degraded quantitative accuracy of the DIA results. The initiation of zero energy in the vertical kinetic energy field resulted in a significantly more strongly anisotropic velocity field than with nonzero initial conditions. When all initial energy was invested in the potential energy field (e.g., a "blob" of higher density fluid placed in lower density ambient fluid) all velocity fields experienced very strong oscillations. In the more conventional situation (a substantial or all of the energy initialized in the velocity field) the half–horizontal energy experienced relatively minor oscillations.

It was shown that for the case of isotropic transport of a passive scalar the change

from one Legendre coefficient to two coefficient computations altered the angular behavior of only the scalar field but did not affect the behavior of the integrated scalar field or the scalar transport field. It was further shown numerically that the addition of the second Legendre coefficient did affect the integrated scalar field and scalar transport results in the case of a anisotropic velocity field and for buoyant scalar problems.

The nonlinear two-point two–time passive scalar transport problem was shown, both in the exact problem and numerically using the DIA, to be equivalent to the linear superposition of the isotropic passive scalar turbulence problem with all nonzero initial scalar conditions plus the isotropic passive scalar transport problem. This was due to the linearity of the formally nonlinear scalar fluctuation equation in the scalar fluctuation variable and the isotropy of the velocity field. Although this result may be expected to hold in the fluctuation equations, it was not obvious for the statistical equations due to the introduction of cross–correlations between the two scalar fields by the decomposition which need not be necessarily zero.

In addition, the direct comparison of DIA with experiment also showed reasonable agreement using a comparison paradigm developed by the author. This technique involves the assumption that the initial (dimensional) time for experiment is the moment the flow passes through the turbulence producing grid while the initial time for the numerical computations is $t = 0$. The normalization for the experiments can be accomplished by using data no earlier than at the first measurement station (typically at $x/M = 40$). Using this point as the basis for normalization of measured data, a straightforward way to put computational results on a rational comparison basis with measured data is to find that time in the computation at which the nondi-

mensional time coincides with that at the first experimental measurement and use that numerical point as the analog of that experimental point. Further, it was shown that the initial spectral shapes, as described by the spectral aspect ratios A_v or A_s, could exert a profound effect upon the evolution of the decaying turbulence fields. Good agreement between DIA and experiment was achieved for the isotropic velocity fields and the decaying isotropic scalar fields. The scalar transport problem proved more troublesome, although reasonable agreement in behavior and magnitudes were achievable for the eddy diffusivity ratio (for the low speed runs), scalar transport correlation coefficient, lengthscale ratios, timescale ratios. The scalar energy was of the correct magnitude for the low speed runs but differences in the evolutionary trends were noted. For the high speed runs, scalar transport was considerably too high (the computations experienced ultraviolet buildup of turbulence energy at high wavenumbers during the first 2 to 3 eddy turnover times due to insufficient numerical wavenumber bandwidth for this high R_λ run) leading to excessive growth of the scalar energy. Surprizingly, the isotropic decaying scalar runs were accurate using the same velocity field conditions. This remains an area for future work.

ACKNOWLEDGEMENTS

I would like to thank my major professor, Dr. James Hill, for his help, guidance, stimulating conversations and advice with the physics, math, and theory involved in turbulent flows and their associated scalar fields as well as bringing me up to speed on numerical, Fortran coding, and debugging techniques. I would also like to thank the members of my committee, Dr. William Abraham, Dr. Howard Levine, Dr. Richard Seagrave, Dr. Richard Pletcher as well as Dr. Alric Rothmeyer and Dr. R. Dennis Vigil who substituted for Drs. Abraham and Levine for my final examination. I also wish to thank Dr. Seagrave and Dr. Maurice Larson for their help, both financially through the Department of Chemical Engineering and for their advice on many subjects throughout my tenure as a graduate student. I also want to acknowledge the Iowa State University Computation Center and its staff for the use of its facilities and the many questions they answered. Finally, this entire project would not have been possible without the financial assistance of the Exxon Foundation through their three year Exxon Teaching Fellowship, for which I am very grateful.

I also owe many thanks to Dr. Jackson Herring and the National Center for Atmospheric Research. Dr. Herring provided me with access to the computational facilities and staff at NCAR for performing the stably stratified flow work. I had many insightful conversations with him over this and other subjects in the general area of turbulence.

I want to thank my parents, Dr. Donald Sanderson and the late Carol Sanderson, whose help and encouragement, not only during my degree program but throughout my life, made this achievement possible. I only regret that my mother did not live to see the completion of my degree.

I owe a large debt of gratitude to APTEK, Inc., its president and owner, Thomas Meagher, and its vice–president, Dr. Eugene Fitzgerald, for providing complete and full access to and use of their computing and graphical facilities for the passive scalar transport work. This work, especially the DIA modelling of the experiments, would not have been possible without this access.

Finally, I cannot express the depth of gratitude I feel for my family; my wife, Nancy Sanderson, and my children, Jamie, Karl and David. Their willing sacrifices of time, income and attention and their continuing support while I spent countless hours away from home working on my degree cannot be understated or overappreciated. Without their support, especially that of my wife, this degree program could not and would not have been completed. I thank you and salute you.

APPENDIX A. THE DIRECT INTERACTION EQUATIONS FOR PASSIVE SCALAR TRANSPORT

The DIA equations used in this study were derived for the case of a nonzero vertical mean scalar gradient with no buoyancy effects consistent with the derivation by Kraichnan [43] for shear and thermally driven turbulence. The correlation and response functions were reexpressed in terms of their eigenfunctions following Herring [32], i.e.:

$$\begin{aligned} U_{ij}(\mathbf{k},t,t') &= \sum_{\lambda=1}^{2} \varphi_{vv}^{\lambda}(\mathbf{k},t,t') e_i^{\lambda}(\mathbf{k}) e_j^{\lambda}(\mathbf{k}) \\ U_{i\theta}(\mathbf{k},t,t') &= \sum_{\lambda=1}^{2} \varphi_{vs}^{\lambda}(\mathbf{k},t,t') e_i^{\lambda}(\mathbf{k}) \\ U_{\theta j}(\mathbf{k},t,t') &= \sum_{\lambda=1}^{2} \varphi_{sv}^{\lambda}(\mathbf{k},t,t') e_j^{\lambda}(\mathbf{k}) \\ U_{\theta\theta}(\mathbf{k},t,t') &= \varphi_{ss}(\mathbf{k},t,t') \end{aligned}$$

These eigenfunctions are substituted into the DIA equations and the equations solved for the eigenfunctions. The response function equations are treated in the same manner. The resulting equations form the DIA closure to the passive homogeneous turbulent scalar transport problem and are:

$$(\text{Define}) \sum_{DIA} \equiv \sum_{l,m,n=0}^{\infty} \sum_{\mu,\nu=1}^{2} \tag{A.1}$$

$$\left(\frac{d}{dt} + \frac{k^2}{R_{\lambda o}}\right) \varphi_{vv_l}^{\lambda}(k,t,t') =$$

$$= \sum_{DIA} \iint_{\Delta} A1^{\lambda\mu\nu}_{lll'mn}(k,p,q) \int_0^{t'} g^{\lambda}_{vv\,ll'}(k,t',s)\varphi^{\mu}_{vv_m}(p,t,s)\varphi^{\nu}_{vv_n}(q,t,s)\,ds\,dp\,dq +$$

$$- \sum_{DIA} \iint_{\Delta} B1^{\lambda\mu\nu}_{lll'mn}(k,p,q) \int_0^{t} g^{\mu}_{vv_m}(p,t,s)\varphi^{\nu}_{vv_n}(q,t,s)\varphi^{\lambda}_{vv\,ll'}(k,t',s)\,ds\,dp\,dq \qquad \text{(A.2)}$$

$$\left(\frac{d}{dt} + \frac{k^2}{R_{\lambda o}}\right) \varphi^{\lambda}_{vs_l}(k,t,t') =$$

$$= \sum_{DIA} \iint_{\Delta} A1^{\lambda\mu\nu}_{lll'mn}(k,p,q) \int_0^{t'} g^{\lambda}_{sv\,ll'}(k,t',s)\varphi^{\mu}_{vv_m}(p,t,s)\varphi^{\nu}_{vv_n}(q,t,s)\,ds\,dp\,dq +$$

$$+ \sum_{DIA} \iint_{\Delta} A2^{\lambda\mu\nu}_{lll'mn}(k,p,q) \int_0^{t'} g_{ss\,ll'}(k,t',s)\varphi^{\mu}_{vv_m}(p,t,s)\varphi^{\nu}_{vs_n}(q,t,s)\,ds\,dp\,dq +$$

$$- \sum_{DIA} \iint_{\Delta} B1^{\lambda\mu\nu}_{lll'mn}(k,p,q) \int_0^{t} g^{\mu}_{vv_m}(p,t,s)\varphi^{\nu}_{vv_n}(q,t,s)\varphi^{\lambda}_{vs\,ll'}(k,t',s)\,ds\,dp\,dq \qquad \text{(A.3)}$$

$$\left(\frac{d}{dt} + \frac{k^2}{PrR_{\lambda o}}\right) \varphi_{sv_l}(k,t,t') - \sum_{ll'=1}^{\infty} BB^{\lambda}_{ll'}(k)\varphi^{\lambda}_{vv\,ll'}(k,t,t') =$$

$$= \sum_{DIA} \iint_{\Delta} AS3^{\lambda\mu\nu}_{lll'mn}(k,p,q) \int_0^{t'} g^{\lambda}_{vv\,ll'}(k,t',s)\varphi^{\mu}_{sv_m}(p,t,s)\varphi^{\nu}_{vv_n}(q,t,s)\,ds\,dp\,dq +$$

$$- \sum_{DIA} \iint_{\Delta} BS1^{\lambda\mu\nu}_{lll'mn}(k,p,q) \int_0^{t} g^{\mu}_{vv_m}(p,t,s)\varphi^{\nu}_{sv_n}(q,t,s)\varphi^{\lambda}_{vv\,ll'}(k,t',s)\,ds\,dp\,dq +$$

$$- \sum_{DIA} \iint_{\Delta} BS2^{\lambda\mu\nu}_{lll'mn}(k,p,q) \int_0^{t} g_{ss_m}(p,t,s)\varphi^{\nu}_{vv_n}(q,t,s)\varphi^{\lambda}_{vs\,ll'}(k,t',s)\,ds\,dp\,dq +$$

$$- \sum_{DIA} \iint_{\Delta} BS3^{\lambda\mu\nu}_{lll'mn}(k,p,q) \int_0^{t} g^{\mu}_{sv_m}(p,t,s)\varphi^{\nu}_{vv_n}(q,t,s)\varphi^{\lambda}_{vv\,ll'}(k,t',s)\,ds\,dp\,dq$$

$$- \sum_{DIA} \iint_{\Delta} BS4^{\lambda\mu\nu}_{lll'mn}(k,p,q) \int_0^{t} g_{ss_m}(p,t,s)\varphi^{\nu}_{vs_n}(q,t,s)\varphi^{\lambda}_{vv\,ll'}(k,t',s)\,ds\,dp\,dq \qquad \text{(A.4)}$$

$$\left(\frac{d}{dt} + \frac{k^2}{PrR_{\lambda o}}\right) \varphi_{ss_l}(k,t,t') - \sum_{ll'=1}^{\infty} BB^{\lambda}_{ll'}(k)\varphi^{\lambda}_{vs\,ll'}(k,t,t') =$$

$$= \sum_{DIA} \iint_{\Delta} AS1^{\lambda\mu\nu}_{lll'mn}(k,p,q) \int_0^{t'} g_{ss\,ll'}(k,t',s)\varphi_{ss_m}(p,t,s)\varphi^{\nu}_{vv_n}(q,t,s)\,ds\,dp\,dq +$$

$$+ \sum_{DIA} \iint_{\Delta} AS2^{\lambda\mu\nu}_{lll'mn}(k,p,q) \int_0^{t'} g_{ss\,ll'}(k,t',s)\varphi^{\mu}_{vs_m}(p,t,s)\varphi^{\nu}_{sv_n}(q,t,s)\,ds\,dp\,dq +$$

$$+ \sum_{DIA} \iint_{\Delta} AS3^{\lambda\mu\nu}_{lll'mn}(k,p,q) \int_0^{t'} g^{\lambda}_{sv\,ll'}(k,t',s)\varphi^{\mu}_{sv_m}(p,t,s)\varphi^{\nu}_{vv_n}(q,t,s)\,ds\,dp\,dq +$$

$$-\sum_{DIA}\int\int_{\Delta} BS1^{\lambda\mu\nu}_{lll'm'n}(k,p,q)\int_0^t g^{\mu}_{vv_m}(p,t,s)\varphi^{\nu}_{sv_n}(q,t,s)\varphi^{\lambda}_{sv\,l'}(k,t',s)\,ds\,dp\,dq+$$

$$-\sum_{DIA}\int\int_{\Delta} BS2^{\lambda\mu\nu}_{lll'm'n}(k,p,q)\int_0^t g_{ss_m}(p,t,s)\varphi^{\nu}_{vv_n}(q,t,s)\varphi_{ss\,l'}(k,t',s)\,ds\,dp\,dq+$$

$$-\sum_{DIA}\int\int_{\Delta} BS3^{\lambda\mu\nu}_{lll'm'n}(k,p,q)\int_0^t g^{\mu}_{sv_m}(p,t,s)\varphi^{\nu}_{vv_n}(q,t,s)\varphi^{\lambda}_{sv\,l'}(k,t',s)\,ds\,dp\,dq$$

$$-\sum_{DIA}\int\int_{\Delta} BS4^{\lambda\mu\nu}_{lll'm'n}(k,p,q)\int_0^t g_{ss_m}(p,t,s)\varphi^{\nu}_{vs_n}(q,t,s)\varphi^{\lambda}_{sv\,l'}(k,t',s)\,ds\,dp\,dq \qquad \text{(A.5)}$$

The equations governing the response functions for all four fields are now given.

$$\left(\frac{d}{dt}+\frac{k^2}{R_{\lambda o}}\right)g^{\lambda}_{vv_l}(k,t,t') =$$

$$=-\sum_{DIA}\int\int_{\Delta} B1^{\lambda\mu\nu}_{lll'm'n}(k,p,q)\int_{t'}^t g^{\mu}_{vv_m}(p,t,s)\varphi^{\nu}_{vv_n}(q,t,s)g^{\lambda}_{vv\,l'}(k,s,t')\,ds\,dp\,dq \qquad \text{(A.6)}$$

$$\left(\frac{d}{dt}+\frac{k^2}{R_{\lambda o}}\right)g_{ss_l}(k,t,t') =$$

$$=-\sum_{DIA}\int\int_{\Delta} BS2^{\lambda\mu\nu}_{lll'm'n}(k,p,q)\int_{t'}^t g_{ss_m}(p,t,s)\varphi^{\nu}_{vv_n}(q,t,s)g_{ss\,l'}(k,s,t')\,ds\,dp\,dq \qquad \text{(A.7)}$$

$$\left(\frac{d}{dt}+\frac{k^2}{R_{\lambda o}}\right)g^{\lambda}_{sv_l}(k,t,t')-\sum_{l'=1}^{\infty}\sum_{\lambda=1}^{2}BB^{\lambda}_{l'}(k)g^{\lambda}_{vv\,l'}(k,t,t') =$$

$$=-\sum_{DIA}\int\int_{\Delta} BS1^{\lambda\mu\nu}_{lll'm'n}(k,p,q)\int_{t'}^t g^{\lambda}_{vv_m}(p,t,s)\varphi^{\nu}_{sv_n}(q,t,s)g^{\lambda}_{vv\,l'}(k,s,t')\,ds\,dp\,dq+$$

$$-\sum_{DIA}\int\int_{\Delta} BS2^{\lambda\mu\nu}_{lll'm'n}(k,p,q)\int_{t'}^t g_{ss_m}(p,t,s)\varphi^{\nu}_{vv_n}(q,t,s)g^{\lambda}_{sv\,l'}(k,s,t')\,ds\,dp\,dq+$$

$$-\sum_{DIA}\int\int_{\Delta} BS3^{\lambda\mu\nu}_{lll'm'n}(k,p,q)\int_{t'}^t g^{\mu}_{sv_m}(p,t,s)\varphi^{\nu}_{vv_n}(q,t,s)g^{\lambda}_{vv\,l'}(k,s,t')\,ds\,dp\,dq$$

$$-\sum_{DIA}\int\int_{\Delta} BS4^{\lambda\mu\nu}_{lll'm'n}(k,p,q)\int_{t'}^t g_{ss_m}(p,t,s)\varphi^{\nu}_{vs_n}(q,t,s)g^{\lambda}_{vv\,l'}(k,s,t')\,ds\,dp\,dq \qquad \text{(A.8)}$$

$$g^{\mu}_{vs_l}(k,t,t')\equiv 0 \qquad \text{(A.9)}$$

The single time DIA equations are formed from exact single time equations in the same manner as the two time DIA equations are and will not be listed here.

The geometric coefficients for the velocity–velocity and velocity–scalar equations are now listed.

$$A1^{\lambda\mu\nu}(\mathbf{k},\mathbf{p},\mathbf{q}) = \frac{1}{2}F^{\lambda\mu\nu}(\mathbf{k},\mathbf{p},\mathbf{q})F^{\lambda\mu\nu}(\mathbf{k},\mathbf{p},\mathbf{q}) \quad \text{(A.10)}$$

$$A2^{\lambda\mu\nu}(\mathbf{k},\mathbf{p},\mathbf{q}) = F^{\lambda\mu\nu}(\mathbf{k},\mathbf{p},\mathbf{q})(\mathbf{k}\cdot\mathbf{e}^{\mu}(\mathbf{p})) \quad \text{(A.11)}$$

$$B1^{\lambda\mu\nu}(\mathbf{k},\mathbf{p},\mathbf{q}) = A1^{\lambda\mu\nu}(\mathbf{k},\mathbf{p},\mathbf{q}) \quad \text{(A.12)}$$

The above equations make use of the following definitions:

$$F^{\lambda\mu\nu}(\mathbf{k},\mathbf{p},\mathbf{q}) \equiv (\mathbf{k}\cdot\mathbf{e}^{\nu}(\mathbf{q}))(\mathbf{e}^{\lambda}(\mathbf{k})\cdot\mathbf{e}^{\mu}(\mathbf{p})) + (\mathbf{k}\cdot\mathbf{e}^{\mu}(\mathbf{p}))(\mathbf{e}^{\lambda}(\mathbf{k})\cdot\mathbf{e}^{\nu}(\mathbf{q}))$$

$$L^{\lambda\mu\nu}(\mathbf{k},\mathbf{p},\mathbf{q}) \equiv (\mathbf{q}\cdot\mathbf{e}^{\lambda}(\mathbf{k}))(\mathbf{e}^{\mu}(\mathbf{p})\cdot\mathbf{e}^{\nu}(\mathbf{q})) - (\mathbf{k}\cdot\mathbf{e}^{\nu}(\mathbf{q}))(\mathbf{e}^{\lambda}(\mathbf{k})\cdot\mathbf{e}^{\mu}(\mathbf{p}))$$

The corresponding coefficients for the scalar–scalar and scalar–velocity equations are:

$$AS1^{\lambda\mu\nu}(\mathbf{k},\mathbf{p},\mathbf{q}) = (\mathbf{k}\cdot\mathbf{e}^{\nu}(\mathbf{q}))(\mathbf{k}\cdot\mathbf{e}^{\nu}(\mathbf{q})) \quad \text{(A.13)}$$

$$AS2^{\lambda\mu\nu}(\mathbf{k},\mathbf{p},\mathbf{q}) = (\mathbf{k}\cdot\mathbf{e}^{\mu}(\mathbf{p}))(\mathbf{k}\cdot\mathbf{e}^{\nu}(\mathbf{q})) \quad \text{(A.14)}$$

$$AS3^{\lambda\mu\nu}(\mathbf{k},\mathbf{p},\mathbf{q}) = (\mathbf{k}\cdot\mathbf{e}^{\mu}(\mathbf{p}))F^{\lambda\mu\nu}(\mathbf{k},\mathbf{p},\mathbf{q}) \quad \text{(A.15)}$$

$$BS1^{\lambda\mu\nu}(\mathbf{k},\mathbf{p},\mathbf{q}) = (\mathbf{k}\cdot\mathbf{e}^{\nu}(\mathbf{q}))L^{\lambda\mu\nu}(\mathbf{k},\mathbf{p},\mathbf{q}) \quad \text{(A.16)}$$

$$BS2^{\lambda\mu\nu}(\mathbf{k},\mathbf{p},\mathbf{q}) = AS1^{\lambda\mu\nu}(\mathbf{k},\mathbf{p},\mathbf{q}) \quad \text{(A.17)}$$

$$BS3^{\lambda\mu\nu}(\mathbf{k},\mathbf{p},\mathbf{q}) = (\mathbf{k}\cdot\mathbf{e}^{\nu}(\mathbf{q}))L^{\lambda\mu\nu}(\mathbf{k},\mathbf{p},\mathbf{q}) \quad \text{(A.18)}$$

$$BS4^{\lambda\mu\nu}(\mathbf{k},\mathbf{p},\mathbf{q}) = (\mathbf{k}\cdot\mathbf{e}^{\nu}(\mathbf{q}))(\mathbf{p}\cdot\mathbf{e}^{\lambda}(\mathbf{k})) \quad \text{(A.19)}$$

The final forms for the coefficients are obtained by representing the eigenfunctions in terms of Legendre function series and solving for the Legendre coefficients. The resulting DIA geometric coefficients, (used in the actual numerical computations) are now listed. The coefficients for the velocity field are:

$$A1^{\lambda\mu\nu}_{l,l'mn}(k,p,q) = \int_0^{2\pi}\int_{-1}^{1}\frac{1}{2}F^{\lambda\mu\nu}(\mathbf{k},\mathbf{p},\mathbf{q})F^{\lambda\mu\nu}(\mathbf{k},\mathbf{p},\mathbf{q})P^{0000}_{l'lmn}(\mu_{k,p,q})\,d\mu_k\,d\phi \quad \text{(A.20)}$$

$$B1^{\lambda\mu\nu}_{l,l'mn}(k,p,q) = \int_0^{2\pi}\int_{-1}^{1} \frac{1}{2} F^{\lambda\mu\nu}(\mathbf{k},\mathbf{p},\mathbf{q}) F^{\lambda\mu\nu}(\mathbf{k},\mathbf{p},\mathbf{q}) P^{0000}_{l'lmn}(\mu_{k,p,q})\, d\mu_k\, d\phi \quad \text{(A.21)}$$

The coefficients to be used in the velocity–scalar field equations are

$$A1^{\lambda\mu\nu}_{l,l'mn}(k,p,q) = \int_0^{2\pi}\int_{-1}^{1} \frac{1}{2} F^{\lambda\mu\nu}(\mathbf{k},\mathbf{p},\mathbf{q}) F^{\lambda\mu\nu}(\mathbf{k},\mathbf{p},\mathbf{q}) P^{1100}_{l'lmn}(\mu_{k,p,q})\, d\mu_k\, d\phi \quad \text{(A.22)}$$

$$A2^{\lambda\mu\nu}_{l,l'mn}(k,p,q) = \int_0^{2\pi}\int_{-1}^{1} F^{\lambda\mu\nu}(\mathbf{k},\mathbf{p},\mathbf{q})(\mathbf{k}\cdot\mathbf{e}^{\nu}(-\mathbf{q})) P^{1001}_{l'lmn}(\mu_{k,p,q})\, d\mu_k\, d\phi \quad \text{(A.23)}$$

$$B1^{\lambda\mu\nu}_{l,l'mn}(k,p,q) = \int_0^{2\pi}\int_{-1}^{1} \frac{1}{2} F^{\lambda\mu\nu}(\mathbf{k},\mathbf{p},\mathbf{q}) F^{\lambda\mu\nu}(\mathbf{k},\mathbf{p},\mathbf{q}) P^{1001}_{l'lmn}(\mu_{k,p,q})\, d\mu_k\, d\phi \quad \text{(A.24)}$$

The coefficients for the scalar–scalar equations are:

$$AS1^{\lambda\mu\nu}_{l,l'mn}(k,p,q) = \int_0^{2\pi}\int_{-1}^{1} (\mathbf{k}\cdot\mathbf{e}^{\nu}(\mathbf{q}))(\mathbf{k}\cdot\mathbf{e}^{\nu}(\mathbf{q})) P^{0000}_{l'lmn}(\mu_{k,p,q})\, d\mu_k\, d\phi \quad \text{(A.25)}$$

$$AS2^{\lambda\mu\nu}_{l,l'mn}(k,p,q) = \int_0^{2\pi}\int_{-1}^{1} (\mathbf{k}\cdot\mathbf{e}^{\mu}(\mathbf{p}))(\mathbf{k}\cdot\mathbf{e}^{\nu}(\mathbf{q})) P^{0011}_{l'lmn}(\mu_{k,p,q})\, d\mu_k\, d\phi \quad \text{(A.26)}$$

$$AS3^{\lambda\mu\nu}_{l,l'mn}(k,p,q) = \int_0^{2\pi}\int_{-1}^{1} F^{\lambda\mu\nu}(\mathbf{k},\mathbf{p},\mathbf{q})(\mathbf{k}\cdot\mathbf{e}^{\mu}(\mathbf{p})) P^{0110}_{l'lmn}(\mu_{k,p,q})\, d\mu_k\, d\phi \quad \text{(A.27)}$$

$$BS1^{\lambda\mu\nu}_{l,l'mn}(k,p,q) = \int_0^{2\pi}\int_{-1}^{1} (\mathbf{k}\cdot\mathbf{e}^{\nu}(\mathbf{q})) L^{\lambda\mu\nu}(\mathbf{k},\mathbf{p},\mathbf{q}) P^{0101}_{l'lmn}(\mu_{k,p,q})\, d\mu_k\, d\phi \quad \text{(A.28)}$$

$$BS2^{\lambda\mu\nu}_{l,l'mn}(k,p,q) = \int_0^{2\pi}\int_{-1}^{1} (\mathbf{k}\cdot\mathbf{e}^{\nu}(\mathbf{q}))(\mathbf{k}\cdot\mathbf{e}^{\nu}(\mathbf{q})) P^{0000}_{l'lmn}(\mu_{k,p,q})\, d\mu_k\, d\phi \quad \text{(A.29)}$$

$$BS3^{\lambda\mu\nu}_{l,l'mn}(k,p,q) = \int_0^{2\pi}\int_{-1}^{1} L^{\lambda\mu\nu}(\mathbf{k},\mathbf{p},\mathbf{q})(\mathbf{k}\cdot\mathbf{e}^{\nu}(\mathbf{q})) P^{0110}_{l'lmn}(\mu_{k,p,q})\, d\mu_k\, d\phi \quad \text{(A.30)}$$

$$BS4^{\lambda\mu\nu}_{l,l'mn}(k,p,q) = \int_0^{2\pi}\int_{-1}^{1} L^{\lambda\mu\nu}(\mathbf{k},\mathbf{p},\mathbf{q})(\mathbf{k}\cdot\mathbf{e}^{\nu}(\mathbf{q})) P^{0101}_{l'lmn}(\mu_{k,p,q})\, d\mu_k\, d\phi \quad \text{(A.31)}$$

The coefficients to be used in the scalar–velocity field equations are

$$AS3^{\lambda\mu\nu}_{l,l'mn}(k,p,q) = \int_0^{2\pi}\int_{-1}^{1} F^{\lambda\mu\nu}(\mathbf{k},\mathbf{p},\mathbf{q})(\mathbf{k}\cdot\mathbf{e}^{\mu}(\mathbf{p})) P^{1010}_{l'lmn}(\mu_{k,p,q})\, d\mu_k\, d\phi \quad \text{(A.32)}$$

$$BS1^{\lambda\mu\nu}_{l,l'mn}(k,p,q) = \int_0^{2\pi}\int_{-1}^{1} (\mathbf{k}\cdot\mathbf{e}^{\nu}(\mathbf{q})) L^{\lambda\mu\nu}(\mathbf{k},\mathbf{p},\mathbf{q}) P^{1001}_{l'lmn}(\mu_{k,p,q})\, d\mu_k\, d\phi \quad \text{(A.33)}$$

$$BS2^{\lambda\mu\nu}_{l,l'mn}(k,p,q) = \int_0^{2\pi}\int_{-1}^{1} (\mathbf{k}\cdot\mathbf{e}^{\nu}(\mathbf{q}))(\mathbf{k}\cdot\mathbf{e}^{\nu}(\mathbf{q})) P^{1100}_{l'lmn}(\mu_{k,p,q})\, d\mu_k\, d\phi \quad \text{(A.34)}$$

$$BS3^{\lambda\mu\nu}_{l,l'mn}(k,p,q) = \int_0^{2\pi}\int_{-1}^{1} L^{\lambda\mu\nu}(\mathbf{k},\mathbf{p},\mathbf{q})(\mathbf{k}\cdot\mathbf{e}^{\nu}(\mathbf{q})) P^{1010}_{l'lmn}(\mu_{k,p,q})\, d\mu_k\, d\phi \quad \text{(A.35)}$$

$$BS4^{\lambda\mu\nu}_{l,l'mn}(k,p,q) = \int_0^{2\pi}\int_{-1}^{1} L^{\lambda\mu\nu}(\mathbf{k},\mathbf{p},\mathbf{q})(\mathbf{k}\cdot\mathbf{e}^{\nu}(\mathbf{q}))(\mathbf{p}\cdot\mathbf{e}^{\lambda}(\mathbf{k})) P^{1010}_{l'lmn}(\mu_{k,p,q})\, d\mu_k\, d\phi \quad \text{(A.36)}$$

where

$$\mu_k \equiv \frac{\mathbf{k}\cdot\mathbf{n}}{\sqrt{\mathbf{k}\cdot\mathbf{k}}} \;;\; \mu_p \equiv \frac{\mathbf{p}\cdot\mathbf{n}}{\sqrt{\mathbf{p}\cdot\mathbf{p}}} \;;\; \mu_q \equiv \frac{\mathbf{q}\cdot\mathbf{n}}{\sqrt{\mathbf{q}\cdot\mathbf{q}}} \tag{A.37}$$

and

$$P^{abcd}_{l'lmn}(\mu_{k,p,q}) \equiv P^a_{l'}(\mu_k)P^b_l(\mu_k)P^c_m(\mu_p)P^d_n(\mu_q) \tag{A.38}$$

where the superscripts take the values 0 or 1 depending upon whether the appropriate Legendre function is a polynomial (0) or associated Legendre function of the first kind (1). $P^1_l(\mu_k)$ represents an associated Legendre function of the first kind which are used in the series representation of the velocity–scalar and scalar–velocity functions.

Linear Forcing Terms and Their Coefficients

The velocity–velocity and velocity–scalar correlation and the velocity–velocity response functions are the only functions involved in the linear (mean scalar gradient) forcing terms. Since the velocity–velocity field is isotropic it has only one non–zero Legendre polynomial coefficient; the zeroth one. This is also true of the velocity–velocity response function. The two sets of coefficients we are studying here are given as follows:

$$ALS1^{\lambda}_{l,l'}(k) \equiv \frac{2l+1}{2}\int_{-1}^{1} P_l(\mu_k)P^1_{l'}(\mu_k)[\mathbf{e}^{\lambda}(\mathbf{k})\cdot\mathbf{n}]\,d\mu_k \tag{A.39}$$

$$ALHTS1^{\lambda}_{l,l'}(k) \equiv \frac{2l+1}{2l(l+1)}\int_{-1}^{1} P^1_l(\mu_k)P_{l'}(\mu_k)[\mathbf{e}^{\lambda}(\mathbf{k})\cdot\mathbf{n}]\,d\mu_k \tag{A.40}$$

Note that these coefficients are nonzero only for $\lambda = 2$ as the $\lambda = 1$ eigenvector is perpendicular to the mean scalar gradient (which has direction $\mathbf{n}$) since $\mathbf{e}^{\lambda=1}(\mathbf{k}) \equiv \mathbf{k}\wedge\mathbf{n}/(k\sin\theta_k)$. Thus the dot product of $\mathbf{n}$ and $\mathbf{e}^{\lambda=1}(\mathbf{k})$ is identically zero. The dot product $n_i e_i^{\lambda=2}(\mathbf{k})$ can be shown to be $-\sin\theta_k$ so we are thus interested in

$$ALS1^{\lambda}_{l,l'}(k) \equiv -\frac{2l+1}{2}\int_{-1}^{1} P_l(\mu_k)P^1(\mu_k)\sin\theta_k\,dx \tag{A.41}$$

$$ALHTS1^{\lambda}_{l,l'}(k) \equiv -\frac{2l+1}{2l(l+1)}\int_{-1}^{1} P_l^1(\mu_k)P(\mu_k)\sin\theta_k\, dx \qquad (A.42)$$

The definition of $P_l^1(x)$ (where $x \equiv \mu_k$) is

$$P_l^1(x) \equiv \left(1-x^2\right)^{\frac{1}{2}}\frac{d}{dx}P_l(x) \qquad (A.43)$$

At this point the most important piece of information needed is under what conditions the integral in equations (A.41) and (A.42) is zero. We now show that this integral may be expressed entirely in terms of (constant) coefficients and Legendre polynomials from which it may easily be deduced under what conditions it will have nonzero values.

Now we have (concentrating only upon the scalar-scalar coefficient for the moment; the scalar–velocity coefficient is easily deduced from this one), substituting x for μ_k and noting that $(1-x^2)^{\frac{1}{2}} \equiv \sin\theta_k$:

$$\begin{aligned} ALS1^{\lambda}_{l,l'}(k) &\equiv -\frac{2l+1}{2}\int_{-1}^{1} P_l(x)P^{1'}(x)(1-x^2)^{\frac{1}{2}}\, dx \\ &\equiv -\frac{2l+1}{2}\int_{-1}^{1} P_l(x)(1-x^2)^{\frac{1}{2}}P'_{l'}(x)(1-x^2)^{\frac{1}{2}}\, dx \qquad (A.44) \end{aligned}$$

where $P'_{l'}(x) \equiv \frac{d}{dx}P_{l'}(x)$. Two more useful identities for Legendre polynomials are

$$(1-x^2)P'_n(x) = nP_{n-1}(x) - nxP_n(x) \qquad (A.45)$$

$$(2n+1)xP_n(x) = (n+1)P_{n+1}(x) + nP_{n-1}(x) \qquad (A.46)$$

$$\Rightarrow xP_n(x) = \left[\frac{n+1}{2n+1}\right]P_{n+1}(x) + \left[\frac{n}{2n+1}\right]P_{n-1}(x) \qquad (A.47)$$

$$\begin{aligned} \Rightarrow (1-x^2)P'_n(x) &= nP_{n-1}(x) - n\left\{\left[\frac{n+1}{2n+1}\right]P_{n+1}(x) + \left[\frac{n}{2n+1}\right]P_{n-1}(x)\right\} \\ &= nP_{n-1}(x) - \left[\frac{n(n+1)}{2n+1}\right]P_{n+1}(x) - \left[\frac{n^2}{2n+1}\right]P_{n-1}(x) \\ &= -\left[\frac{n(n+1)}{2n+1}\right][P_{n+1}(x) - P_{n-1}(x)] \qquad (A.48) \end{aligned}$$

Using equation (A.48) in (A.44) yields

$$\begin{aligned} ALS1^{\lambda}_{l,l'}(k) &\equiv -\frac{2l+1}{2}\int_{-1}^{1} P_l(x)(1-x^2)P'_{l'}(x)\,dx \\ &\equiv \frac{2l+1}{2}\int_{-1}^{1} P_l(x)\left[\frac{l'(l'+1)}{2l'+1}\right][P_{l'+1}(x)-P_{l'-1}(x)]\,dx \\ &\equiv \frac{2l+1}{2}\int_{-1}^{1}\left[\frac{l'(l'+1)}{2l'+1}\right][P_l(x)P_{l'+1}(x)-P_l(x)P_{l'-1}(x)]\,dx \\ &\equiv \frac{2l+1}{2}\left[\frac{l'(l'+1)}{2l'+1}\right]\left[\int_{-1}^{1} P_l(x)P_{l'+1}(x)\,dx-\int_{-1}^{1} P_l(x)P_{l'-1}(x)\,dx\right] \\ &\equiv \frac{2l+1}{2}\left[\frac{l'(l'+1)}{2l'+1}\right]\left[\delta_{l,l'+1}\frac{2}{2(l'+1)+1}-\delta_{l,l'-1}\frac{2}{2(l'-1)+1}\right] \quad \text{(A.49)} \end{aligned}$$

Due to the evenness of the velocity–velocity and scalar–scalar functions, only the even Legendre polynomials and odd associated Legendre functions will be used.

As can be clearly seen in equation (A.49) the only times $ALS1^{\lambda}_{l,l'}(k)$ will be nonzero is for $l = l'-1, l'+1$, or in words, only associated Legendre functions of order adjacent to that of the Legendre polynomial (numerically above or below the order of the Legendre polynomial) may interact in a nonzero manner. However, at the lower end of the series, even these interactions are limited. For example, for $l = 0$ (the lowest Legendre polynomial for the scalar–scalar correlation) there exists no $l' = -1$ associated Legendre functions for this problem and thus, only one scalar–velocity coefficient ($l' = 1$) may interact with the $l = 0$ scalar–scalar coefficient. In practical terms for the current problem this implies that the scalar–velocity correlation and response functions develop only the first coefficient as a result of interaction with the isotropic velocity field since it has only one coefficient ($l = 0$) although it is possible for an anisotropic velocity field with nonzero $l = 2$ coefficient to influence the first coefficient of the scalar–velocity functions. The scalar–scalar correlation function may develop two coefficients due to $l = 0, l' = 1$ and $l = 2, l' = 1/l = 2, l' = 3$

Table A.1: Illustration of location of the linear coefficients' zeros.

	$l=0$	$l=2$	$l=4$	$l=6$	$l=8$	$l=10$	$l=12$
$l'=1$			0	0	0	0	0
$l'=3$	0			0	0	0	0
$l'=5$	0	0			0	0	0
$l'=7$	0	0	0			0	0
$l'=9$	0	0	0	0			0
$l'=11$	0	0	0	0	0		
$l'=13$	0	0	0	0	0	0	

interactions but no linear $l=0, l'=3$ interactions are possible due to the structure of the linear coefficients.

A table showing the l, l' combinations which produce nonzero values for the coefficient integral is instructive:

APPENDIX B. DERIVATION OF HOMOGENEOUS DIA COEFFICIENTS

Here we list the DIA geometric coefficients for the case of homogeneous anisotropic turbulence and passive scalar field with uniform mean scalar gradient oriented in the direction of gravity.

Velocity–Velocity Equation Coefficients

The velocity field (or velocity–velocity equation) coefficients are here derived by expressing the tensors in the velocity–velocity equation in terms of the eigenfunctions and corresponding eigenvectors.

$$A1^{\lambda\mu\nu}(\mathbf{k},\mathbf{p},\mathbf{q}) \equiv \frac{1}{2}P_{imn}(\mathbf{k})P_{abc}(\mathbf{k})e_a^\lambda(\mathbf{k})e_i^\lambda(\mathbf{k})e_m^\mu(\mathbf{p})e_b^\mu(\mathbf{p})e_n^\nu(\mathbf{q})e_c^\nu(\mathbf{q}) \quad \text{(B.1)}$$

$$A2^{\lambda\mu\nu}(\mathbf{k},\mathbf{p},\mathbf{q}) \equiv P_{imn}(\mathbf{k})k_b e_i^\lambda(\mathbf{k})e_m^\mu(\mathbf{p})e_b^\mu(\mathbf{p})e_n^\nu(\mathbf{q}) \quad \text{(B.2)}$$

$$B1^{\lambda\mu\nu}(\mathbf{k},\mathbf{p},\mathbf{q}) \equiv -P_{imn}(\mathbf{k})P_{abc}(\mathbf{p})e_b^\lambda(\mathbf{k})e_i^\lambda(\mathbf{k})e_m^\mu(\mathbf{p})e_a^\mu(\mathbf{p})e_n^\nu(\mathbf{q})e_c^\nu(\mathbf{q}) \quad \text{(B.3)}$$

$$B2^{\lambda\mu\nu}(\mathbf{k},\mathbf{p},\mathbf{q}) \equiv -P_{imn}(\mathbf{k})p_b e_b^\lambda(\mathbf{k})e_i^\lambda(\mathbf{k})e_m^\mu(\mathbf{p})e_n^\nu(\mathbf{q}) \quad \text{(B.4)}$$

$$B3^{\lambda\mu\nu}(\mathbf{k},\mathbf{p},\mathbf{q}) \equiv -P_{imn}(\mathbf{k})p_b e_i^\lambda(\mathbf{k})e_m^\mu(\mathbf{p})e_n^\nu(\mathbf{q})e_b^\nu(\mathbf{q}) \quad \text{(B.5)}$$

Now define

$$F^{\lambda\mu\nu}(\mathrm{k},\mathrm{p},\mathrm{q}) \equiv P_{imn}(\mathbf{k})e_i^\lambda(\mathbf{k})e_m^\mu(\mathbf{p})e_n^\nu(\mathbf{q}) \quad \text{(B.6)}$$

$$L^{\lambda\mu\nu}(\mathrm{k},\mathrm{p},\mathrm{q}) \equiv -P_{abc}(\mathbf{p})e_a^\mu(\mathbf{p})e_b^\lambda(\mathbf{k})e_c^\nu(\mathbf{q}) \quad \text{(B.7)}$$

Employing these definitions and rewriting the products of quantities with summed indices as dot products, the coefficients may be reexpressed as follows:

$$A1^{\lambda\mu\nu}(\mathbf{k},\mathbf{p},\mathbf{q}) \equiv \frac{1}{2}F^{\lambda\mu\nu}(\mathbf{k},\mathbf{p},\mathbf{q})F^{\lambda\mu\nu}(\mathbf{k},\mathbf{p},\mathbf{q}) \quad \text{(B.8)}$$

$$A2^{\lambda\mu\nu}(\mathbf{k},\mathbf{p},\mathbf{q}) \equiv F^{\lambda\mu\nu}(\mathbf{k},\mathbf{p},\mathbf{q})\left[\mathbf{k}\cdot\mathbf{e}^{\mu}(\mathbf{p})\right] \quad \text{(B.9)}$$

$$B1^{\lambda\mu\nu}(\mathbf{k},\mathbf{p},\mathbf{q}) \equiv F^{\lambda\mu\nu}(\mathbf{k},\mathbf{p},\mathbf{q})L^{\lambda\mu\nu}(\mathbf{k},\mathbf{p},\mathbf{q}) \quad \text{(B.10)}$$

$$B2^{\lambda\mu\nu}(\mathbf{k},\mathbf{p},\mathbf{q}) \equiv F^{\lambda\mu\nu}(\mathbf{k},\mathbf{p},\mathbf{q})\left[\mathbf{q}\cdot\mathbf{e}^{\lambda}(\mathbf{k})\right] \quad \text{(B.11)}$$

$$B3^{\lambda\mu\nu}(\mathbf{k},\mathbf{p},\mathbf{q}) \equiv -F^{\lambda\mu\nu}(\mathbf{k},\mathbf{p},\mathbf{q})\left[\mathbf{p}\cdot\mathbf{e}^{\nu}(\mathbf{q})\right] \quad \text{(B.12)}$$

In order to complete the evaluation of these coefficients it is only necessary to derive the dot product expressions for $F^{\lambda\mu\nu}(\mathbf{k},\mathbf{p},\mathbf{q})$ and $L^{\lambda\mu\nu}(\mathbf{k},\mathbf{p},\mathbf{q})$.

$$F^{\lambda\mu\nu}(\mathbf{k},\mathbf{p},\mathbf{q}) \equiv \left[\mathbf{k}\cdot\mathbf{e}^{\mu}(\mathbf{p})\right]\left[\mathbf{e}^{\lambda}(\mathbf{k})\cdot\mathbf{e}^{\nu}(\mathbf{q})\right] + \left[\mathbf{k}\cdot\mathbf{e}^{\nu}(\mathbf{q})\right]\left[\mathbf{e}^{\lambda}(\mathbf{k})\cdot\mathbf{e}^{\mu}(\mathbf{p})\right] \quad \text{(B.13)}$$

$$L^{\lambda\mu\nu}(\mathbf{k},\mathbf{p},\mathbf{q}) \equiv \left[\mathbf{q}\cdot\mathbf{e}^{\lambda}(\mathbf{k})\right]\left[\mathbf{e}^{\mu}(\mathbf{p})\cdot\mathbf{e}^{\nu}(\mathbf{q})\right] - \left[\mathbf{p}\cdot\mathbf{e}^{\nu}(\mathbf{q})\right]\left[\mathbf{e}^{\mu}(\mathbf{p})\cdot\mathbf{e}^{\lambda}(\mathbf{k})\right] \quad \text{(B.14)}$$

Now the velocity–velocity equation's coefficients may be easily evaluated for any specified wave vector arguments $(\mathbf{k},\mathbf{p},\mathbf{q})$.

Scalar–Scalar Equation Coefficients

The scalar field (or scalar–scalar equation) coefficients are here derived by expressing the tensors in terms of the eigenfunctions and corresponding eigenvectors. Rewriting these coefficients in terms of dot products and the F and L functions defined earlier for the velocity–velocity coefficients we obtain:

$$AS1^{\lambda\mu\nu}(\mathbf{k},\mathbf{p},\mathbf{q}) \equiv \left[\mathbf{k}\cdot\mathbf{e}^{\mu}(\mathbf{p})\right]\left[\mathbf{k}\cdot\mathbf{e}^{\mu}(\mathbf{p})\right] \quad \text{(B.15)}$$

$$AS2^{\lambda\mu\nu}(\mathbf{k},\mathbf{p},\mathbf{q}) \equiv \left[\mathbf{k}\cdot\mathbf{e}^{\mu}(\mathbf{p})\right]\left[\mathbf{k}\cdot\mathbf{e}^{\nu}(\mathbf{q})\right] \quad \text{(B.16)}$$

$$AS3^{\lambda\mu\nu}(\mathbf{k},\mathbf{p},\mathbf{q}) \equiv F^{\lambda\mu\nu}(\mathbf{k},\mathbf{p},\mathbf{q})\left[\mathbf{k}\cdot\mathbf{e}^{\mu}(\mathbf{p})\right] \quad \text{(B.17)}$$

$$BS1^{\lambda\mu\nu}(\mathbf{k},\mathbf{p},\mathbf{q}) \equiv L^{\lambda\mu\nu}(\mathbf{k},\mathbf{p},\mathbf{q})\,[\mathbf{k}\cdot\mathbf{e}^{\mu}(\mathbf{p})] \tag{B.18}$$

$$BS2^{\lambda\mu\nu}(\mathbf{k},\mathbf{p},\mathbf{q}) \equiv [\mathbf{k}\cdot\mathbf{e}^{\mu}(\mathbf{p})]\left[\mathbf{q}\cdot\mathbf{e}^{\lambda}(\mathbf{k})\right] \tag{B.19}$$

$$BS3^{\lambda\mu\nu}(\mathbf{k},\mathbf{p},\mathbf{q}) \equiv -[\mathbf{k}\cdot\mathbf{e}^{\mu}(\mathbf{p})]\,[\mathbf{p}\cdot\mathbf{e}^{\nu}(\mathbf{q})] \tag{B.20}$$

$$BS4^{\lambda\mu\nu}(\mathbf{k},\mathbf{p},\mathbf{q}) \equiv [\mathbf{k}\cdot\mathbf{e}^{\nu}(\mathbf{q})]\left[\mathbf{q}\cdot\mathbf{e}^{\lambda}(\mathbf{k})\right] \tag{B.21}$$

$$BS5^{\lambda\mu\nu}(\mathbf{k},\mathbf{p},\mathbf{q}) \equiv -[\mathbf{k}\cdot\mathbf{e}^{\nu}(\mathbf{q})]\,[\mathbf{p}\cdot\mathbf{e}^{\nu}(\mathbf{q})] \tag{B.22}$$

$$BS6^{\lambda\mu\nu}(\mathbf{k},\mathbf{p},\mathbf{q}) \equiv L^{\lambda\mu\nu}(\mathbf{k},\mathbf{p},\mathbf{q})\,[\mathbf{k}\cdot\mathbf{e}^{\nu}(\mathbf{q})] \tag{B.23}$$

$$\tag{B.24}$$

Some Comments and Observations Concerning the Various DIA Coefficients

By inspection we can discern some relationships between the various coefficients. For example

$$A1^{\lambda\mu\nu}(\mathbf{k},\mathbf{p},\mathbf{q}) = -\left[B1^{\lambda\mu\nu}(\mathbf{k},\mathbf{p},\mathbf{q}) + B1^{\lambda\nu\mu}(\mathbf{k},\mathbf{q},\mathbf{p})\right] \tag{B.25}$$

$$A2^{\lambda\mu\nu}(\mathbf{k},\mathbf{p},\mathbf{q}) = -B3^{\lambda\nu\mu}(\mathbf{k},\mathbf{q},\mathbf{p}) \tag{B.26}$$

$$AS1^{\lambda\mu\nu}(\mathbf{k},\mathbf{p},\mathbf{q}) = BS5^{\lambda\nu\mu}(\mathbf{k},\mathbf{q},\mathbf{p}) \tag{B.27}$$

$$AS2^{\lambda\mu\nu}(\mathbf{k},\mathbf{p},\mathbf{q}) = -BS3^{\lambda\mu\nu}(\mathbf{k},\mathbf{p},\mathbf{q}) \tag{B.28}$$

$$BS2^{\lambda\mu\nu}(\mathbf{k},\mathbf{p},\mathbf{q}) = -BS4^{\lambda\nu\mu}(\mathbf{k},\mathbf{q},\mathbf{p}) \tag{B.29}$$

$$AS3^{\lambda\mu\nu}(\mathbf{k},\mathbf{p},\mathbf{q}) = A2^{\lambda\mu\nu}(\mathbf{k},\mathbf{p},\mathbf{q}) \tag{B.30}$$

$$= -\left[BS1^{\lambda\mu\nu}(\mathbf{k},\mathbf{p},\mathbf{q}) + BS6^{\lambda\nu\mu}(\mathbf{k},\mathbf{q},\mathbf{p})\right] \tag{B.31}$$

These relationships may be used to reduce the numerical computation required for evaluation of these coefficients.

APPENDIX C. ANALYSIS OF DIA COEFFICIENTS

In order for an isotropic velocity field to induce no additional anisotropy into the scalar field in passive homogeneous turbulent scalar transport than is produced by the linear forcing term, there must be some special relationships between certain coefficients to allow the cancellation of nonlinear anisotropic contributions but allow these to be significant in the case of an anisotropic velocity field. This appendix strives to discover these relationships and explain this phenomenon.

The DIA equations are here reiterated in the Legendre representation format to allow easy access and reference. We define

$$\sum_{DIA} \equiv \sum_{l',m,n} \sum_{\mu,\nu=1}^{2} . \tag{C.1}$$

$$\left(\frac{d}{dt} + \frac{k^2}{R_\lambda}\right) \varphi^{\lambda}_{vv_{l'}}(k,t,t') = \tag{C.2}$$

$$= \sum_{DIA} \int\int_{\Delta} AV1^{\lambda\mu\nu}_{l,l',m,n}(k,p,q) \int_0^{t'} g^{\lambda}_{vv_{l'}}(k,t',s) \varphi^{\mu}_{vv_m}(p,t,s) \varphi^{\nu}_{vv_n}(q,t,s) ds\, dp\, dq$$

$$+ \sum_{DIA} \int\int_{\Delta} BV1^{\lambda\mu\nu}_{l,l',m,n}(k,p,q) \int_0^{t} g^{\mu}_{vv_m}(p,t,s) \varphi^{\nu}_{vv_n}(q,t,s) \varphi^{\lambda}_{vv_{l'}}(k,s,t') ds\, dp\, dq \tag{C.3}$$

$$\left(\frac{d}{dt} + \frac{k^2}{R_\lambda}\right) \varphi^{\lambda}_{vs_l}(k,t,t') =$$

$$= \sum_{DIA} \int\int_{\Delta} AVHT1^{\lambda\mu\nu}_{l,l',m,n}(k,p,q) \int_0^{t'} g^{\lambda}_{sv_{l'}}(-k,t',s) \varphi^{\mu}_{vv_m}(p,t,s) \varphi^{\nu}_{vv_n}(q,t,s) ds\, dp\, dq$$

$$+ \sum_{DIA} \int\int_{\Delta} AVHT2^{\lambda\mu\nu}_{l,l',m,n}(k,p,q) \int_0^{t'} g_{ss_{l'}}(k,t',s) \varphi^{\mu}_{vv_m}(p,t,s) \varphi^{\nu}_{vs_n}(q,t,s) ds\, dp\, dq$$

$$+ \sum_{DIA} \int\int_{\Delta} BVHT1^{\lambda\mu\nu}_{l,l',m,n}(k,p,q) \int_0^t g^{\mu}_{vv_m}(p,t,s)\varphi^{\nu}_{vv_n}(q,t,s)\varphi^{\lambda}_{vs_{l'}}(k,s,t')ds\ dp\ dq \tag{C.4}$$

$$\left(\frac{d}{dt} + \frac{k^2}{R_\lambda}\right)\varphi^{\lambda}_{sv_l}(k,t,t') + \sum_{l'} n_i e^{\lambda}_i(\mathbf{k})\varphi^{\lambda}_{vv_{l'}}(k,t,t') =$$

$$= \sum_{DIA} \int\int_{\Delta} ASHT3^{\lambda\mu\nu}_{l,l',m,n}(k,p,q) \int_0^{t'} g^{\lambda}_{vv_{l'}}(k,t',s)\varphi^{\mu}_{vv_m}(p,t,s)\varphi^{\nu}_{sv_n}(q,t,s)ds\ dp\ dq$$

$$+ \sum_{DIA} \int\int_{\Delta} BSHT1^{\lambda\mu\nu}_{l,l',m,n}(k,p,q) \int_0^{t} g^{\mu}_{vv_m}(p,t,s)\varphi^{\nu}_{sv_n}(q,t,s)\varphi^{\lambda}_{vv_{l'}}(k,s,t')ds\ dp\ dq$$

$$+ \sum_{DIA} \int\int_{\Delta} BSHT4^{\lambda\mu\nu}_{l,l',m,n}(k,p,q) \int_0^{t} g_{ss_m}(p,t,s)\varphi^{\nu}_{vs_n}(q,t,s)\varphi^{\lambda}_{vv_{l'}}(k,s,t')ds\ dp\ dq$$

$$+ \sum_{DIA} \int\int_{\Delta} BSHT5^{\lambda\mu\nu}_{l,l',m,n}(k,p,q) \int_0^{t} g_{ss_m}(p,t,s)\varphi^{\nu}_{vv_n}(q,t,s)\varphi^{\lambda}_{sv_{l'}}(k,s,t')ds\ dp\ dq$$

$$+ \sum_{DIA} \int\int_{\Delta} BSHT6^{\lambda\mu\nu}_{l,l',m,n}(k,p,q) \int_0^{t} g^{\mu}_{sv_m}(p,t,s)\varphi^{\nu}_{vv_n}(q,t,s)\varphi^{\lambda}_{vv_{l'}}(k,s,t')ds\ dp\ dq \tag{C.5}$$

$$\left(\frac{d}{dt} + \frac{k^2}{R_\lambda}\right)\varphi_{ss_l}(k,t,t') + \sum_{l'} n_i e^{\lambda}_i(\mathbf{k})\varphi^{\lambda}_{vs_{l'}}(k,t,t') =$$

$$= \sum_{DIA} \int\int_{\Delta} AS1^{\lambda\mu\nu}_{l,l',m,n}(k,p,q) \int_0^{t'} g_{ss_{l'}}(k,t',s)\varphi^{\mu}_{vv_m}(p,t,s)\varphi_{ss_n}(q,t,s)ds\ dp\ dq$$

$$+ \sum_{DIA} \int\int_{\Delta} AS2^{\lambda\mu\nu}_{l,l',m,n}(k,p,q) \int_0^{t'} g_{ss_{l'}}(k,t',s)\varphi^{\mu}_{vs_m}(p,t,s)\varphi^{\nu}_{sv_n}(q,t,s)ds\ dp\ dq$$

$$+ \sum_{DIA} \int\int_{\Delta} AS3^{\lambda\mu\nu}_{l,l',m,n}(k,p,q) \int_0^{t'} g^{\lambda}_{sv_{l'}}(-k,t',s)\varphi^{\mu}_{vv_m}(p,t,s)\varphi^{\nu}_{sv_n}(q,t,s)ds\ dp\ dq$$

$$+ \sum_{DIA} \int\int_{\Delta} BS1^{\lambda\mu\nu}_{l,l',m,n}(k,p,q) \int_0^{t} g^{\mu}_{vv_m}(p,t,s)\varphi^{\nu}_{sv_n}(q,t,s)\varphi^{\lambda}_{vs_{l'}}(k,s,t')ds\ dp\ dq$$

$$+ \sum_{DIA} \int\int_{\Delta} BS4^{\lambda\mu\nu}_{l,l',m,n}(k,p,q) \int_0^{t} g_{ss_m}(p,t,s)\varphi^{\nu}_{vs_n}(q,t,s)\varphi^{\lambda}_{vs_{l'}}(k,s,t')ds\ dp\ dq$$

$$+ \sum_{DIA} \int\int_{\Delta} BS5^{\lambda\mu\nu}_{l,l',m,n}(k,p,q) \int_0^{t} g_{ss_m}(p,t,s)\varphi^{\nu}_{vv_n}(q,t,s)\varphi_{ss_{l'}}(k,s,t')ds\ dp\ dq$$

$$+ \sum_{DIA} \int\int_{\Delta} BS6^{\lambda\mu\nu}_{l,l',m,n}(k,p,q) \int_0^{t} g^{\mu}_{sv_m}(p,t,s)\varphi^{\nu}_{vv_n}(q,t,s)\varphi^{\lambda}_{vs_{l'}}(k,s,t')ds\ dp\ dq \tag{C.6}$$

The geometric coefficients are now defined in the form used in the DIA computations.

Those for the velocity and scalar variance equations are:

$$AV1^{\lambda\mu\nu}_{ll'mn}(k,p,q) \equiv C_l^{kpq}\int_0^{2\pi}\int_{-1}^{1} P^{0000}_{ll'mn}(\mu_{k,p,q})AV1^{\lambda\mu\nu}(\mathbf{k},\mathbf{p},\mathbf{q})d\mu_k\, d\phi_k \quad \text{(C.7)}$$

$$BV1^{\lambda\mu\nu}_{ll'mn}(k,p,q) \equiv C_l^{kpq}\int_0^{2\pi}\int_{-1}^{1} P^{0000}_{ll'mn}(\mu_{k,p,q})BV1^{\lambda\mu\nu}(\mathbf{k},\mathbf{p},\mathbf{q})d\mu_k\, d\phi_k \quad \text{(C.8)}$$

$$AS1^{\lambda\mu\nu}_{ll'mn}(k,p,q) \equiv C_l^{kpq}\int_0^{2\pi}\int_{-1}^{1} P^{0000}_{ll'mn}(\mu_{k,p,q})AS1^{\lambda\mu\nu}(\mathbf{k},\mathbf{p},\mathbf{q})d\mu_k\, d\phi_k \quad \text{(C.9)}$$

$$AS2^{\lambda\mu\nu}_{ll'mn}(k,p,q) \equiv C_l^{kpq}\int_0^{2\pi}\int_{-1}^{1} P^{0011}_{ll'mn}(\mu_{k,p,q})AS2^{\lambda\mu\nu}(\mathbf{k},\mathbf{p},\mathbf{q})d\mu_k\, d\phi_k \quad \text{(C.10)}$$

$$AS3^{\lambda\mu\nu}_{ll'mn}(k,p,q) \equiv C_l^{kpq}\int_0^{2\pi}\int_{-1}^{1} P^{0101}_{ll'mn}(\mu_{k,p,q})AS3^{\lambda\mu\nu}(\mathbf{k},\mathbf{p},\mathbf{q})d\mu_k\, d\phi_k \quad \text{(C.11)}$$

$$BS1^{\lambda\mu\nu}_{ll'mn}(k,p,q) \equiv C_l^{kpq}\int_0^{2\pi}\int_{-1}^{1} P^{0101}_{ll'mn}(\mu_{k,p,q})BS1^{\lambda\mu\nu}(\mathbf{k},\mathbf{p},\mathbf{q})d\mu_k\, d\phi_k \quad \text{(C.12)}$$

$$BS4^{\lambda\mu\nu}_{ll'mn}(k,p,q) \equiv C_l^{kpq}\int_0^{2\pi}\int_{-1}^{1} P^{0110}_{ll'mn}(\mu_{k,p,q})BS4^{\lambda\mu\nu}(\mathbf{k},\mathbf{p},\mathbf{q})d\mu_k\, d\phi_k \quad \text{(C.13)}$$

$$BS5^{\lambda\mu\nu}_{ll'mn}(k,p,q) \equiv C_l^{kpq}\int_0^{2\pi}\int_{-1}^{1} P^{0000}_{ll'mn}(\mu_{k,p,q})BS5^{\lambda\mu\nu}(\mathbf{k},\mathbf{p},\mathbf{q})d\mu_k\, d\phi_k \quad \text{(C.14)}$$

$$BS6^{\lambda\mu\nu}_{ll'mn}(k,p,q) \equiv C_l^{kpq}\int_0^{2\pi}\int_{-1}^{1} P^{0101}_{ll'mn}(\mu_{k,p,q})BS6^{\lambda\mu\nu}(\mathbf{k},\mathbf{p},\mathbf{q})d\mu_k\, d\phi_k \quad \text{(C.15)}$$

$$\text{where } C_l^{kpq} \equiv \frac{2l+1}{2}\frac{pq}{k} \quad \text{(C.16)}$$

$$\text{and } P^{abcd}_{ll'mn}(\mu_{k,p,q}) = P_l^a(\mu_k)P_{l'}^b(\mu_k)P_m^c(\mu_p)P_n^d(\mu_q) \quad \text{(C.17)}$$

and those for the velocity–scalar covariance equations are:

$$AVHT1^{\lambda\mu\nu}_{ll'mn}(k,p,q) \equiv D_l^{kpq}\int_0^{2\pi}\int_{-1}^{1} P^{1100}_{ll'mn}(\mu_{k,p,q})AV1^{\lambda\mu\nu}(\mathbf{k},\mathbf{p},\mathbf{q})d\mu_k\, d\phi_k \quad \text{(C.18)}$$

$$AVHT2^{\lambda\mu\nu}_{ll'mn}(k,p,q) \equiv D_l^{kpq}\int_0^{2\pi}\int_{-1}^{1} P^{1001}_{ll'mn}(\mu_{k,p,q})AV2^{\lambda\mu\nu}(\mathbf{k},\mathbf{p},\mathbf{q})d\mu_k\, d\phi_k \quad \text{(C.19)}$$

$$BVHT1^{\lambda\mu\nu}_{ll'mn}(k,p,q) \equiv D_l^{kpq}\int_0^{2\pi}\int_{-1}^{1} P^{1100}_{ll'mn}(\mu_{k,p,q})BV1^{\lambda\mu\nu}(\mathbf{k},\mathbf{p},\mathbf{q})d\mu_k\, d\phi_k \quad \text{(C.20)}$$

$$ASHT3^{\lambda\mu\nu}_{ll'mn}(k,p,q) \equiv D_l^{kpq}\int_0^{2\pi}\int_{-1}^{1} P^{1001}_{ll'mn}(\mu_{k,p,q})AS3^{\lambda\mu\nu}(\mathbf{k},\mathbf{p},\mathbf{q})d\mu_k\, d\phi_k \quad \text{(C.21)}$$

$$BSHT1^{\lambda\mu\nu}_{ll'mn}(k,p,q) \equiv D_l^{kpq}\int_0^{2\pi}\int_{-1}^{1} P^{1001}_{ll'mn}(\mu_{k,p,q})BS1^{\lambda\mu\nu}(\mathbf{k},\mathbf{p},\mathbf{q})d\mu_k\, d\phi_k \quad \text{(C.22)}$$

$$BSHT4^{\lambda\mu\nu}_{ll'mn}(k,p,q) \equiv D_l^{kpq}\int_0^{2\pi}\int_{-1}^{1} P^{1001}_{ll'mn}(\mu_{k,p,q})BS4^{\lambda\mu\nu}(\mathbf{k},\mathbf{p},\mathbf{q})d\mu_k\, d\phi_k \quad \text{(C.23)}$$

$$BSHT5^{\lambda\mu\nu}_{ll'mn}(k,p,q) \equiv D_l^{kpq}\int_0^{2\pi}\int_{-1}^{1} P^{1100}_{ll'mn}(\mu_{k,p,q})BS5^{\lambda\mu\nu}(\mathbf{k},\mathbf{p},\mathbf{q})d\mu_k\, d\phi_k \quad \text{(C.24)}$$

$$BSHT6^{\lambda\mu\nu}_{ll'mn}(k,p,q) \equiv D_l^{kpq}\int_0^{2\pi}\int_{-1}^{1} P^{1010}_{ll'mn}(\mu_{k,p,q})BS6^{\lambda\mu\nu}(\mathbf{k},\mathbf{p},\mathbf{q})d\mu_k\, d\phi_k \quad \text{(C.25)}$$

$$\text{where } D_l^{kpq} \equiv \frac{2l+1}{2l(l+1)}\frac{pq}{k} \quad \text{(C.26)}$$

It should be noted here that of the statistical functions here used, the velocity variance and response functions are isotropic as is the scalar response function. Thus these functions will have only the first terms in their Legendre representations possessing nonzero coefficients. It will be further assumed that the scalar transport and scalar fields will be initialized at zero levels. This implies that all anisotropy in these fields will be due to the action of the velocity field upon the mean scalar gradient and nonlinear interactions, not to any initial conditions which are not of interest in this study. In addition, the two-time equations will be the only ones studies here at this point as the single time equations should behave in a similar manner.

A general comment is appropriate here. As can be seen in equations (C.4) and (C.5), the scalar–scalar correlation function does not appear in any of the nonlinear integrals. Thus the only way that nonzero Legendre coefficients beyond the first may be induced is by the nonlinear interaction of the first terms of the velocity field (correlation and response function), the scalar field response function and the scalar transport functions.

The Velocity–Scalar Functions

We will first investigate the velocity–scalar correlation equation. The velocity–scalar equations are the following:

$$\left(\frac{d}{dt}+\frac{k^2}{R_\lambda}\right)\varphi^{\lambda}_{vs_l}(k,t,t') =$$

$$= \sum_{DIA} \iint_{\Delta} AVHT1^{\lambda\mu\nu}_{l,l',m,n}(k,p,q) \int_0^{t'} g^{\lambda}_{sv_{l'}}(-k,t',s)\varphi^{\mu}_{vv_m}(p,t,s)\varphi^{\nu}_{vv_n}(q,t,s)ds\,dp\,dq$$

$$+ \sum_{DIA} \iint_{\Delta} AVHT2^{\lambda\mu\nu}_{l,l',m,n}(k,p,q) \int_0^{t'} g_{ss_{l'}}(k,t',s)\varphi^{\mu}_{vv_m}(p,t,s)\varphi^{\nu}_{vs_n}(q,t,s)ds\,dp\,dq$$

$$+ \sum_{DIA} \iint_{\Delta} BVHT1^{\lambda\mu\nu}_{l,l',m,n}(k,p,q) \int_0^{t} g^{\mu}_{vv_m}(p,t,s)\varphi^{\nu}_{vv_n}(q,t,s)\varphi^{\lambda}_{vs_{l'}}(k,s,t')ds\,dp\,dq \tag{C.27}$$

$$\left(\frac{d}{dt} + \frac{k^2}{R_\lambda}\right) g^{\lambda}_{vs_l}(k,t,t') = 0 \tag{C.28}$$

The first and third terms on the right hand side of this equation contain all velocity–velocity functions with **p** and **q** arguments with the coefficients $AVHT1^{\lambda\mu\nu}_{l,l',m,n}(k,p,q)$ and $BVHT1^{\lambda\mu\nu}_{l,l',m,n}(k,p,q)$. Thus, due to the isotropy of the velocity field, if, for a given $g^{\lambda}_{vs_{l'}}(k,s,t')$ or $\varphi^{\lambda}_{vs_{l'}}(k,s,t')$, the coefficients possess the property that

$$\sum_{\mu,\nu=1}^{2} AVHT1^{\lambda\mu\nu}_{2,1,1,1}(k,p,q) = 0 \tag{C.29}$$

$$\sum_{\mu,\nu=1}^{2} BVHT1^{\lambda\mu\nu}_{2,1,1,1}(k,p,q) = 0 \tag{C.30}$$

these nonlinear terms will not contribute to the second Legendre term of the velocity–scalar correlation representation. The second term on the right hand side would need a coefficient relationship of

$$\sum_{\mu=1}^{2} AVHT1^{\lambda\mu\nu}_{2,1,1,1}(k,p,q) = 0 \tag{C.31}$$

Tables C.1 and C.2 list these coefficients for two different $\mathbf{k}-\mathbf{p}-\mathbf{q}$ combinations.

Table C.1: Example numerical values for the coefficients used in the velocity–scalar two–time equations for $k = 1.0000, p = 0.7500, q = 0.6614$.

λ	μ	ν	AVHT1	AVHT2	BVHT1
1	1	1	2.42565E-02	1.29190E-01	-2.42565E-02
1	1	2	-6.42075E-02	0.00000E-00	6.42075E-02
1	2	1	-4.99392E-02	-1.29190E-01	4.99392E-02
1	2	2	8.98902E-02	0.00000E-00	-8.98902E-02
2	1	1	1.07928E-01	0.00000E-00	-1.07928E-01
2	1	2	-6.80191E-03	-2.34159E-01	6.80191E-03
2	2	1	-2.12265E-01	0.00000E-00	2.12265E-01
2	2	2	1.11139E-01	2.34159E-01	-1.11139E-01

Table C.2: Example numerical values for the coefficients used in the velocity–scalar two–time equations for $k = 1.0000, p = 0.6614, q = 0.7500$.

λ	μ	ν	AVHT1	AVHT2	BVHT1
1	1	1	1.25402E-01	-8.56100E-02	-1.25402E-01
1	1	2	-8.54512E-02	0.00000E-00	8.54512E-02
1	2	1	-1.09866E-01	8.56100E-02	1.09866E-01
1	2	2	6.99147E-02	0.00000E-00	-6.99147E-02
2	1	1	9.70990E-02	0.00000E-00	-9.70990E-02
2	1	2	-3.59236E-02	2.55402E-01	3.59236E-02
2	2	1	-1.60216E-01	0.00000E-00	1.60216E-01
2	2	2	9.90411E-02	-2.55402E-01	-9.90411E-02

Summing up $AVHT1^{\lambda\mu\nu}_{2,1,1,1,1}(k,p,q)$ or $BVHT1^{\lambda\mu\nu}_{2,1,1,1,1}(k,p,q)$ over μ and ν and $AVHT2^{\lambda\mu\nu}_{2,1,1,1,1}(k,p,q)$ over μ all result in a zero result. Thus the first coefficients cannot contribute to any second coefficient growth through nonlinear interaction and for a situation with zero initial second coefficient for the velocity–scalar correlation this equation will contribute nothing to that second coefficient.

The Scalar–Velocity Functions

The governing equations for the scalar–velocity correlation and response function are:

$$\left(\frac{d}{dt}+\frac{k^2}{R_\lambda}\right)\varphi^\lambda_{sv_l}(k,t,t')+\sum_{l'} n_i e^\lambda_i(\mathbf{k})\varphi^\lambda_{vv_{l'}}(k,t,t') =$$
$$= \sum_{DIA}\int\!\!\int_\Delta ASHT3^{\lambda\mu\nu}_{l,l',m,n}(k,p,q)\int_0^{t'} g^\lambda_{vv_{l'}}(k,t',s)\varphi^\mu_{vv_m}(p,t,s)\varphi^\nu_{sv_n}(q,t,s)ds\,dp\,dq$$
$$+ \sum_{DIA}\int\!\!\int_\Delta BSHT1^{\lambda\mu\nu}_{l,l',m,n}(k,p,q)\int_0^{t} g^\mu_{vv_m}(p,t,s)\varphi^\nu_{sv_n}(q,t,s)\varphi^\lambda_{vv_{l'}}(k,s,t')ds\,dp\,dq$$
$$+ \sum_{DIA}\int\!\!\int_\Delta BSHT4^{\lambda\mu\nu}_{l,l',m,n}(k,p,q)\int_0^{t} g_{ss_m}(p,t,s)\varphi^\nu_{vs_n}(q,t,s)\varphi^\lambda_{vv_{l'}}(k,s,t')ds\,dp\,dq$$
$$+ \sum_{DIA}\int\!\!\int_\Delta BSHT5^{\lambda\mu\nu}_{l,l',m,n}(k,p,q)\int_0^{t} g_{ss_m}(p,t,s)\varphi^\nu_{vv_n}(q,t,s)\varphi^\lambda_{sv_{l'}}(k,s,t')ds\,dp\,dq$$
$$+ \sum_{DIA}\int\!\!\int_\Delta BSHT6^{\lambda\mu\nu}_{l,l',m,n}(k,p,q)\int_0^{t} g^\mu_{sv_m}(p,t,s)\varphi^\nu_{vv_n}(q,t,s)\varphi^\lambda_{vv_{l'}}(k,s,t')ds\,dp\,dq \tag{C.32}$$

$$\left(\frac{d}{dt}+\frac{k^2}{R_\lambda}\right)g^\lambda_{sv_l}(k,t,t')+\sum_{l'} n_i e^\lambda_i(\mathbf{k})g^\lambda_{vv_{l'}}(k,t,t') =$$
$$= \sum_{DIA}\int\!\!\int_\Delta BSHT1^{\lambda\mu\nu}_{l,l',m,n}(k,p,q)\int_0^{t} g^\mu_{vv_m}(p,t,s)\varphi^\nu_{sv_n}(q,t,s)g^\lambda_{vv_{l'}}(k,s,t')ds\,dp\,dq$$
$$+ \sum_{DIA}\int\!\!\int_\Delta BSHT4^{\lambda\mu\nu}_{l,l',m,n}(k,p,q)\int_0^{t} g_{ss_m}(p,t,s)\varphi^\nu_{vs_n}(q,t,s)g^\lambda_{vv_{l'}}(k,s,t')ds\,dp\,dq$$
$$+ \sum_{DIA}\int\!\!\int_\Delta BSHT5^{\lambda\mu\nu}_{l,l',m,n}(k,p,q)\int_0^{t} g_{ss_m}(p,t,s)\varphi^\nu_{vv_n}(q,t,s)g^\lambda_{sv_{l'}}(k,s,t')ds\,dp\,dq$$
$$+ \sum_{DIA}\int\!\!\int_\Delta BSHT6^{\lambda\mu\nu}_{l,l',m,n}(k,p,q)\int_0^{t} g^\mu_{sv_m}(p,t,s)\varphi^\nu_{vv_n}(q,t,s)g^\lambda_{vv_{l'}}(k,s,t')ds\,dp\,dq$$

Table C.3: Example numerical values for the coefficients used in the scalar–velocity two–time equations for $k = 1.0000, p = 0.7500, q = 0.6614$.

λ	μ	ν	ASHT3	BSHT1	BSHT4	BSHT5	BSHT6
1	1	1	1.29190E-01	-2.11402E-01	-5.41478E-03	1.15573E-01	1.54097E-01
1	1	2	0.00000E-00	0.00000E-00	0.00000E-00	-1.15573E-01	-1.54097E-01
1	2	1	-1.29190E-02	2.11402E-01	0.00000E-00	0.00000E-00	0.00000E-00
1	2	2	0.00000E-00	0.00000E-00	0.00000E-00	0.00000E-00	0.00000E-00
2	1	1	0.00000E-00	0.00000E-00	0.00000E-00	1.15573E-01	0.00000E-00
2	1	2	-2.34159E-01	2.49695E-01	1.80386E-01	-1.15573E-01	0.00000E-00
2	2	1	0.00000E-00	0.00000E-00	0.00000E-00	0.00000E-00	2.56828E-02
2	2	2	2.34159E-01	-2.49695E-01	0.00000E-00	0.00000E-00	-2.56827E-02

(C.33)

Here are written, in tabular form, these coefficients for two different $\mathbf{k-p-q}$ combinations for the $(2,1,1,1)$ Legendre coefficient combinations.

Table C.4: Example numerical values for the coefficients used in the scalar–velocity two–time equations for $k = 1.0000, p = 0.6614, q = 0.7500$.

λ	μ	ν	ASHT3	BSHT1	BSHT4	BSHT5	BSHT6
1	1	1	8.56100E-02	-2.39707E-01	-3.38404E-02	5.43782E-02	8.22121E-02
1	1	2	0.00000E-00	0.00000E-00	0.00000E-00	-5.43782E-02	-8.22120E-02
1	2	1	-8.56100E-02	2.39707E-01	0.00000E-00	0.00000E-00	0.00000E-00
1	2	2	0.00000E-00	0.00000E-00	0.00000E-00	0.00000E-00	0.00000E-00
2	1	1	0.00000E-00	0.00000E-00	0.00000E-00	5.43782E-02	0.00000E-00
2	1	2	-2.55402E-01	2.29720E-01	1.11093E-01	-5.43782E-02	0.00000E-00
2	2	1	0.00000E-00	0.00000E-00	0.00000E-00	0.00000E-00	-1.55365E-02
2	2	2	2.55402E-01	-2.29720E-01	0.00000E-00	0.00000E-00	1.55365E-02

From Tables C.3 and C.4 we have

$$\sum_{\mu=1}^{2} ASHT3^{\lambda\mu\nu}_{2,1,1,1}(k,p,q) = 0 \tag{C.34}$$

$$\sum_{\mu=1}^{2} BSHT1^{\lambda\mu\nu}_{2,1,1,1}(k,p,q) = 0 \tag{C.35}$$

$$\sum_{\nu=1}^{2} BSHT5^{\lambda\mu\nu}_{2,1,1,1}(k,p,q) = 0 \tag{C.36}$$

$$\sum_{\nu=1}^{2} BSHT6^{\lambda\mu\nu}_{2,1,1,1}(k,p,q) = 0 \tag{C.37}$$

and from inspection of equation (C.32) we see that the relationships of equations (C.34) through (C.37) guarantee no nonlinear contributions to the second coefficients from the first coefficients. However, $BSHT6^{\lambda\mu\nu}_{2,1,1,1}(k,p,q)$ does not sum to zero in any way and thus may contribute to the second coefficient for this two–time scalar–velocity correlation. As the scalar–velocity response function also contains a nonlinear term incorporating the coefficient $BSHT4^{\lambda\mu\nu}_{l,l',m,n}(k,p,q)$ it may also develop some nonzero second coefficient as will the single time velocity–scalar/scalar–velocity correlation. However, each of these functions receives input from only one of the five (or four for the response function) which may thus be expected to be small. The two–time velocity–scalar correlation retains zero second coefficient for this problem and its corresponding response function is identically zero for this passive scalar problem.

The Scalar–Scalar Functions

The governing equation for the scalar–scalar correlation is:

$$\left(\frac{d}{dt}+\frac{k^2}{R_\lambda}\right)\varphi_{ss_l}(k,t,t') + \sum_{l'} n_i e_i^\lambda(\mathrm{k})\varphi^\lambda_{vs_{l'}}(k,t,t') =$$

$$= \sum_{DIA}\iint_\Delta AS1^{\lambda\mu\nu}_{l,l',m,n}(k,p,q)\int_0^{t'} g_{ss_{l'}}(k,t',s)\varphi^\mu_{vv_m}(p,t,s)\varphi_{ss_n}(q,t,s)ds\,dp\,dq$$

$$+ \sum_{DIA} \iint_{\Delta} AS2^{\lambda\mu\nu}_{l,l',m,n}(k,p,q) \int_0^{t'} g_{ss_{l'}}(k,t',s)\varphi^{\mu}_{vs_m}(p,t,s)\varphi^{\nu}_{sv_n}(q,t,s)ds\ dp\ dq$$

$$+ \sum_{DIA} \iint_{\Delta} AS3^{\lambda\mu\nu}_{l,l',m,n}(k,p,q) \int_0^{t'} g^{\lambda}_{sv_{l'}}(-k,t',s)\varphi^{\mu}_{vv_m}(p,t,s)\varphi^{\nu}_{sv_n}(q,t,s)ds\ dp\ dq$$

$$+ \sum_{DIA} \iint_{\Delta} BS1^{\lambda\mu\nu}_{l,l',m,n}(k,p,q) \int_0^{t} g^{\mu}_{vv_m}(p,t,s)\varphi^{\nu}_{sv_n}(q,t,s)\varphi^{\lambda}_{vs_{l'}}(k,s,t')ds\ dp\ dq$$

$$+ \sum_{DIA} \iint_{\Delta} BS4^{\lambda\mu\nu}_{l,l',m,n}(k,p,q) \int_0^{t} g_{ss_m}(p,t,s)\varphi^{\nu}_{vs_n}(q,t,s)\varphi^{\lambda}_{vs_{l'}}(k,s,t')ds\ dp\ dq$$

$$+ \sum_{DIA} \iint_{\Delta} BS5^{\lambda\mu\nu}_{l,l',m,n}(k,p,q) \int_0^{t} g_{ss_m}(p,t,s)\varphi^{\nu}_{vv_n}(q,t,s)\varphi_{ss_{l'}}(k,s,t')ds\ dp\ dq$$

$$+ \sum_{DIA} \iint_{\Delta} BS6^{\lambda\mu\nu}_{l,l',m,n}(k,p,q) \int_0^{t} g^{\mu}_{sv_m}(p,t,s)\varphi^{\nu}_{vv_n}(q,t,s)\varphi^{\lambda}_{vs_{l'}}(k,s,t')ds\ dp\ dq \tag{C.38}$$

$$\left(\frac{d}{dt} + \frac{k^2}{R_\lambda}\right) g_{ss_l}(k,t,t') =$$

$$= \sum_{DIA} \iint_{\Delta} BS5^{\lambda\mu\nu}_{l,l',m,n}(k,p,q) \int_0^{t} g_{ss_m}(p,t,s)\varphi^{\nu}_{vv_n}(q,t,s)g_{ss_{l'}}(k,s,t')ds\ dp\ dq \tag{C.39}$$

Here are written, in tabular form, these coefficients for two different $\mathbf{k} - \mathbf{p} - \mathbf{q}$ combinations.

Table C.5: Example numerical values for the coefficients used in the scalar–scalar two–time equations for $k = 1.0000, p = 0.7500, q = 0.6614$.

λ	μ	ν	AS3	BS1	BS4	BS5	BS6
1	1	1	-1.55028E-01	-2.53683E-01	6.49774E-03	1.23278E-01	1.84917E-01
1	1	2	0.00000E-00	0.00000E-00	0.00000E-00	-1.23278E-01	-1.84917E-01
1	2	1	1.55028E-01	2.53683E-01	0.00000E-00	0.00000E-00	0.00000E-00
1	2	2	0.00000E-00	0.00000E-00	0.00000E-00	0.00000E-00	0.00000E-00
2	1	1	0.00000E-00	0.00000E-00	0.00000E-00	1.23278E-01	0.00000E-00
2	1	2	2.80990E-01	2.99634E-01	-2.16463E-01	-1.23278E-01	0.00000E-00
2	2	1	0.00000E-00	0.00000E-00	0.00000E-00	0.00000E-00	3.08193E-02
2	2	2	-2.80990E-01	-2.99634E-01	0.00000E-00	0.00000E-00	-3.08192E-02

Table C.6: Example numerical values for the coefficients used in the scalar–scalar two–time equations for $k = 1.0000, p = 0.6614, q = 0.7500$.

λ	μ	ν	AS3	BS1	BS4	BS5	BS6
1	1	1	1.02732E-01	-2.87649E-01	4.06085E-02	7.45757E-02	9.86545E-02
1	1	2	0.00000E-00	0.00000E-00	0.00000E-00	-7.45757E-02	-9.86545E-02
1	2	1	-1.02732E-01	2.87649E-01	0.00000E-00	0.00000E-00	0.00000E-00
1	2	2	0.00000E-00	0.00000E-00	0.00000E-00	0.00000E-00	0.00000E-00
2	1	1	0.00000E-00	0.00000E-00	0.00000E-00	7.45757E-02	0.00000E-00
2	1	2	-3.06483E-01	2.75664E-01	-1.33311E-01	-7.45757E-02	0.00000E-00
2	2	1	0.00000E-00	0.00000E-00	0.00000E-00	0.00000E-00	-1.86438E-02
2	2	2	3.06483E-01	-2.75664E-01	0.00000E-00	0.00000E-00	1.86438E-02

Table C.7: Example numerical values for some of the coefficients used in the scalar–scalar two–time equations for $k = 1.0000, p = 0.7500, q = 0.6614$.

λ	μ	ν	AS1	BS5
1	1	1	-1.62253E-08	6.16389E-01
1	1	2	2.20967E-08	-6.16389E-01
1	2	1	0.00000E-00	0.00000E-00
1	2	2	0.00000E-00	0.00000E-00
2	1	1	-1.62253E-08	6.16389E-01
2	1	2	2.20967E-08	-6.16389E-01
2	2	1	0.00000E-00	0.00000E-00
2	2	2	0.00000E-00	0.00000E-00

Let us assume that the scalar transport field has only one Legendre functional representation (for either the correlations or the response function). We know this to be true for the isotropic velocity field correlation and response function and the scalar field response function. In order for the second Legendre function of the scalar field to affect the integrated scalar field quantities requires some special relationships for the coefficients $AS1^{\lambda\mu\nu}_{1112}(\mathbf{k},\mathbf{p},\mathbf{q})$ and $BS5^{\lambda\mu\nu}_{1211}(\mathbf{k},\mathbf{p},\mathbf{q})$. We now list their values in Tables C.7 and C.8.

Table C.8: Example numerical values for some of the coefficients used in the scalar–scalar two–time equations for $k = 1.0000, p = 0.6614, q = 0.7500$.

λ	μ	ν	AS1	BS5
1	1	1	-1.22773E-08	3.72879E-01
1	1	2	1.24644E-08	-3.72879E-01
1	2	1	0.00000E-00	0.00000E-00
1	2	2	0.00000E-00	0.00000E-00
2	1	1	-1.22773E-08	3.72879E-01
2	1	2	1.24644E-08	-3.72879E-01
2	2	1	0.00000E-00	0.00000E-00
2	2	2	0.00000E-00	0.00000E-00

The coefficient $BS5^{\lambda\mu\nu}_{1211}(\mathbf{k},\mathbf{p},\mathbf{q})$ is antisymmetric with respect to ν and thus will contribute nothing to the first Legendre coefficient of the scalar–scalar correlation. The coefficient $AS1^{\lambda\mu\nu}_{1112}(\mathbf{k},\mathbf{p},\mathbf{q})$ is not antisymmetric, although the two entries are opposite in sign. Most importantly, these values are numerically very small so that any contribution from this term to the first coefficient equation will be correspondingly small.

Another concern is the effect of the second coefficient of the scalar–velocity correlation and response functions. These may affect the first coefficient equation through the coefficients $AS2^{\lambda\mu\nu}_{1112}(\mathbf{k},\mathbf{p},\mathbf{q})$, $AS3^{\lambda\mu\nu}_{1112}(\mathbf{k},\mathbf{p},\mathbf{q})$, $AS3^{\lambda\mu\nu}_{1211}(\mathbf{k},\mathbf{p},\mathbf{q})$, $AS3^{\lambda\mu\nu}_{1212}(\mathbf{k},\mathbf{p},\mathbf{q})$, $BS1^{\lambda\mu\nu}_{1112}(\mathbf{k},\mathbf{p},\mathbf{q})$, and $BS6^{\lambda\mu\nu}_{1121}(\mathbf{k},\mathbf{p},\mathbf{q})$.

Table C.9: Example numerical values for the coefficients used in the scalar–scalar two–time equations for $k = 1.0000, p = 0.7500, q = 0.6614$.

λ	μ	ν	$AS2_{1112}$	$AS3_{1112}$	$AS3_{1211}$	$AS3_{1212}$
1	1	1	1.41459E-08	-2.25496E-01	1.55028E-01	-3.51725E-01
1	1	2	0.00000E-00	0.00000E-00	0.00000E-00	0.00000E-00
1	2	1	0.00000E-00	2.25496E-01	-1.55028E-01	-5.71540E-01
1	2	2	-3.05347E-08	0.00000E-00	0.00000E-00	0.00000E-00
2	1	1	1.41459E-08	0.00000E-00	0.00000E-00	0.00000E-00
2	1	2	0.00000E-00	-1.49151E-01	-2.80990E-01	8.90342E-02
2	2	1	0.00000E-00	0.00000E-00	0.00000E-00	0.00000E-00
2	2	2	-3.05347E-08	1.49151E-01	2.80990E-01	4.20058E-01

Table C.10: Example numerical values for the coefficients used in the scalar–scalar two–time equations for $k = 1.0000, p = 0.7500, q = 0.6614$.

λ	μ	ν	$BS1_{1112}$	$BS6_{1121}$
1	1	1	-5.44771E-09	3.28741E-01
1	1	2	0.00000E-00	-3.28741E-01
1	2	1	-5.16173E-09	0.00000E-00
1	2	2	0.00000E-00	0.00000E-00
2	1	1	0.00000E-00	0.00000E-00
2	1	2	-1.91766E-01	0.00000E-00
2	2	1	0.00000E-00	4.38322E-01
2	2	2	1.91766E-01	-4.38322E-01

Table C.11: Example numerical values for the coefficients used in the scalar–scalar two–time equations for $k = 1.0000, p = 0.6614, q = 0.7500$.

λ	μ	ν	$AS2_{1112}$	$AS3_{1112}$	$AS3_{1211}$	$AS3_{1212}$
1	1	1	2.17148E-08	-3.28741E-01	1.02732E-01	-2.61844E-01
1	1	2	0.00000E-00	0.00000E-00	0.00000E-00	0.00000E-00
1	2	1	0.00000E-00	3.28741E-01	-1.02732E-01	-3.46721E-01
1	2	2	-1.20924E-08	0.00000E-00	0.00000E-00	0.00000E-00
2	1	1	2.17148E-08	0.00000E-00	0.00000E-00	0.00000E-00
2	1	2	0.00000E-00	-2.46556E-01	-3.06483E-01	1.70241E-02
2	2	1	0.00000E-00	0.00000E-00	0.00000E-00	0.00000E-00
2	2	2	-1.20924E-08	2.46556E-01	3.06483E-01	3.90380E-01

Table C.12: Example numerical values for the coefficients used in the scalar–scalar two–time equations for $k = 1.0000, p = 0.6614, q = 0.7500$.

λ	μ	ν	$BS1_{1112}$	$BS6_{1121}$
1	1	1	-1.50856E-08	2.25496E-01
1	1	2	0.00000E-00	-2.25496E-01
1	2	1	7.22600E-10	0.00000E-00
1	2	2	0.00000E-00	0.00000E-00
2	1	1	0.00000E-00	0.00000E-00
2	1	2	-1.91766E-01	0.00000E-00
2	2	1	0.00000E-00	3.40917E-01
2	2	2	1.91766E-01	-3.40917E-01

APPENDIX D. MATHEMATICAL TREATMENT OF DIA COEFFICIENTS

The antisymmetry of the DIA coefficients is apparently responsible for the lack of effect upon the single time quantities of including the second Legendre coefficients in computations of passive homogeneous turbulent scalar transport. Numerical evaluation of these coefficients for selected $k-p-q$ triples have pointed out this antisymmetry but mathematical analysis and proof of this property would be more general, acceptable and potentially more revealing of the mathematics of this phenomenon. To this end we will first examine the simplest of all the coefficients.

"Isotropic Scalar" Coefficient

The simplest of the DIA coefficients for the scalar–velocity correlation is:

$$BS5^{\lambda\mu\nu}_{ll'mn}(k,p,q) \equiv \int_0^{2\pi}\int_{-1}^{1}[\mathbf{k}\cdot\mathbf{e}^{\mu}(\mathbf{p})]^2 P_l^1(x)P_{l'}^1(x)P_m(\mu_p)P_n(\mu_q)\,dx\,d\phi \qquad \text{(D.1)}$$

The case of interest is that in which all functions of the integrand are the lowest order coefficients while the coefficient being computed by the equation is the second order one. Thus the specific coefficient to be studied is

$$\begin{aligned} BS5^{\lambda\mu\nu}_{ll'mn}(k,p,q) &\equiv \int_0^{2\pi}\int_{-1}^{1}[\mathbf{k}\cdot\mathbf{e}^{\mu}(\mathbf{p})]^2 P_{l=3}^1(x)P_{l'=1}^1(x)P_{m=0}(\mu_p)P_{n=0}(\mu_q)\,dx\,d\phi \\ &\equiv \int_0^{2\pi}\int_{-1}^{1}[\mathbf{k}\cdot\mathbf{e}^{\mu}(\mathbf{p})]^2\left[\frac{3}{2}\sin\theta_k(5\cos^2\theta_k-1)\right]\sin\theta_k\,dx\,d\phi \end{aligned}$$

$$\equiv \int_0^{2\pi}\int_{-1}^{1}[\mathbf{k}\cdot\mathbf{e}^{\mu}(\mathbf{p})]^2\left[\frac{3}{2}\sin^2\theta_k(5\cos^2\theta_k-1)\right]\,dx\,d\phi$$
$$\equiv \int_0^{2\pi}\int_{-1}^{1}[\mathbf{k}\cdot\mathbf{e}^{\mu}(\mathbf{p})]^2\left[\frac{3}{2}(1-x^2)(5x^2-1)\right]\,dx\,d\phi \qquad \text{(D.2)}$$

Obviously the dot product term is always nonnegative since it is a real quantity which is squared. Since $-1 \le x \le 1$ the term $\frac{3}{2}(1-x^2)$ is always nonnegative. The final term in the integrand, $(5x^2-1)$, may be either positive or negative. Since this coefficient has only one eigenfunction, μ, the antisymmetry must occur between $\mu = 1$ and $\mu = 2$ and these must be studied to infer and/or prove what occurs as this eigenfunction number is changed. Specifically we have

$$BS5^{\lambda\mu=1\nu}_{ll'mn}(k,p,q) \equiv \int_0^{2\pi}\int_{-1}^{1}[\mathbf{k}\cdot\mathbf{e}^{\mu=1}(\mathbf{p})]^2\left[\frac{3}{2}(1-x^2)(5x^2-1)\right]\,dx\,d\phi$$
$$\equiv \int_0^{2\pi}\int_{-1}^{1}\left[\frac{-k\sqrt{1-x^2}\sin\phi\sin\gamma}{\sin\theta_p}\right]^2\times$$
$$\times\left[\frac{3}{2}(1-x^2)(5x^2-1)\right]\,dx\,d\phi \qquad \text{(D.3)}$$

$$BS5^{\lambda\mu=2\nu}_{ll'mn}(k,p,q) \equiv \int_0^{2\pi}\int_{-1}^{1}[\mathbf{k}\cdot\mathbf{e}^{\mu=2}(\mathbf{p})]^2\left[\frac{3}{2}(1-x^2)(5x^2-1)\right]\,dx\,d\phi$$
$$\equiv \int_0^{2\pi}\int_{-1}^{1}\left[\frac{k(\cos\theta_p\cos\gamma-x)}{\sin\theta_p}\right]^2\times$$
$$\times\left[\frac{3}{2}(1-x^2)(5x^2-1)\right]\,dx\,d\phi \qquad \text{(D.4)}$$

The terms $\cos\alpha$, $\cos\beta$ and $\cos\gamma$ and the corresponding sin terms depend upon the angles prescribed by the triangle formed by $\mathbf{k}$, $\mathbf{p}$ and $\mathbf{q}$ and are thus constants for given lengths of these vectors. The terms $\cos\theta_p$ and $\cos\theta_q$ may be reexpressed as follows:

$$\cos\theta_p \equiv x\cos\gamma - \sqrt{1-x^2}\cos\phi\sin\gamma \qquad \text{(D.5)}$$

$$\sin\theta_p \equiv \sqrt{1-\cos^2\theta_p} \qquad \text{(D.6)}$$

$$\cos\theta_q \equiv \cos\beta x + \cos\phi \sin\beta\sqrt{1-x^2} \tag{D.7}$$

$$\sin\theta_q \equiv \sqrt{1-\cos^2\theta_q} \tag{D.8}$$

Thus we may rewrite the coefficients as

$$BS5^{\lambda\mu=1\nu}_{ll'mn}(k,p,q) \equiv \int_0^{2\pi}\int_{-1}^{1}\left[\frac{-k\sqrt{1-x^2}\sin\phi\sin\gamma}{\sin\theta_p}\right]^2 \times \times\left[\frac{3}{2}(1-x^2)(5x^2-1)\right]\,dx\,d\phi \tag{D.9}$$

$$BS5^{\lambda\mu=2\nu}_{ll'mn}(k,p,q) \equiv \int_0^{2\pi}\int_{-1}^{1}\left[\frac{k([x\cos\gamma-\sqrt{1-x^2}\cos\phi\sin\gamma]\cos\gamma-x)}{\sin\theta_p}\right]^2 \times\left[\frac{3}{2}(1-x^2)(5x^2-1)\right]\,dx\,d\phi \tag{D.10}$$

For the first associated Legendre functions of the scalar–velocity function, in determining the evolution of the higher order coefficients from the first coefficients of the integrand we have the Legendre product (where $\mu_k = x$)

$$\begin{aligned} P^1_l(x)P^1_{l'=1}(x)P_{m=0}(\mu_p)P_{n=0}(\mu_q) = \\ &= P^1_l(x)\sqrt{1-x^2}(1)(1) \\ &= \sqrt{1-x^2}P'_l(x)\sqrt{1-x^2} \\ &= (1-x^2)P'_l(x) \\ &= -\left[\frac{l(l+1)}{2l+1}\right][P_{l+1}(x)-P_{l-1}(x)] \end{aligned} \tag{D.11}$$

where the last identity was shown in Appendix C.

The generalized form for the four term product of Legendre functions is

$$\begin{aligned} P^1_l(x)P^1_{l'}(x)P_m(\mu_p)P_n(\mu_q) = \\ &= \sqrt{1-x^2}P'_l(x)\sqrt{1-x^2}P'_{l'}(x)P_m(\mu_p)P_n(\mu_q) \\ &= (1-x^2)P'_l(x)P'_{l'}(x)P_m(\mu_p)P_n(\mu_q) \end{aligned} \tag{D.12}$$

Using these results in the expression for the coefficient yields

$$
\begin{aligned}
BS5^{\lambda\mu=1\nu}_{ll'mn}(k,p,q) &\equiv \int_0^{2\pi}\int_{-1}^{1}[\mathbf{k}\cdot\mathbf{e}^{\mu=1}(\mathbf{p})]^2\left[-\frac{l(l+1)}{2l+1}\right][P_{l+1}(x)-P_{l-1}(x)]\;dx\;d\phi \\
&\equiv \int_0^{2\pi}\int_{-1}^{1}\left[\frac{-k\sqrt{1-x^2}\sin\phi\sin\gamma}{\sin\theta_p}\right]^2\times \\
&\quad\times[P_{l+1}(x)-P_{l-1}(x)]\;dx\;d\phi\left[-\frac{l(l+1)}{2l+1}\right] \\
&\equiv \int_0^{2\pi}\int_{-1}^{1}\left[\frac{-k\sqrt{1-x^2}\sin\phi\sin\gamma}{\sqrt{1-\left[x\cos\gamma-\sqrt{1-x^2}\cos\phi\sin\gamma\right]^2}}\right]^2 \\
&\quad\times[P_{l+1}(x)-P_{l-1}(x)]\;dx\;d\phi\left[-\frac{l(l+1)}{2l+1}\right] \\
&\equiv \int_0^{2\pi}\int_{-1}^{1}\left[\frac{k^2(1-x^2)\sin^2\phi\sin^2\gamma}{1-\left[x\cos\gamma-\sqrt{1-x^2}\cos\phi\sin\gamma\right]^2}\right] \\
&\quad\times[P_{l+1}(x)-P_{l-1}(x)]\;dx\;d\phi\left[-\frac{l(l+1)}{2l+1}\right] \qquad \text{(D.13)} \\
BS5^{\lambda\mu=2\nu}_{ll'mn}(k,p,q) &\equiv \int_0^{2\pi}\int_{-1}^{1}[\mathbf{k}\cdot\mathbf{e}^{\mu=2}(\mathbf{p})]^2\left[-\frac{l(l+1)}{2l+1}\right][P_{l+1}(x)-P_{l-1}(x)]\;dx\;d\phi \\
&\equiv \int_0^{2\pi}\int_{-1}^{1}\left[\frac{k([x\cos\gamma-\sqrt{1-x^2}\cos\phi\sin\gamma]\cos\gamma-x)}{\sqrt{1-\left[x\cos\gamma-\sqrt{1-x^2}\cos\phi\sin\gamma\right]^2}}\right]^2 \\
&\quad\times[P_{l+1}(x)-P_{l-1}(x)]\;dx\;d\phi\left[-\frac{l(l+1)}{2l+1}\right] \\
&\equiv \int_0^{2\pi}\int_{-1}^{1}\left[\frac{k([x\cos\gamma-\sqrt{1-x^2}\cos\phi\sin\gamma]\cos\gamma-x)}{\sqrt{1-\left[x\cos\gamma-\sqrt{1-x^2}\cos\phi\sin\gamma\right]^2}}\right]^2 \\
&\quad\times[P_{l+1}(x)-P_{l-1}(x)]\;dx\;d\phi\left[-\frac{l(l+1)}{2l+1}\right] \\
&\equiv \int_0^{2\pi}\int_{-1}^{1}\frac{\left[k([x\cos\gamma-\sqrt{1-x^2}\cos\phi\sin\gamma]\cos\gamma-x)\right]^2}{1-\left[x\cos\gamma-\sqrt{1-x^2}\cos\phi\sin\gamma\right]^2}
\end{aligned}
$$

$$\times [P_{l+1}(x) - P_{l-1}(x)]\ dx\ d\phi \left[-\frac{l(l+1)}{2l+1}\right] \tag{D.14}$$

At this point it is instructive to examine the relationship between the two coefficients $\mathbf{k}\cdot\mathbf{e}^1(\mathbf{p})$ and $\mathbf{k}\cdot\mathbf{e}^2(\mathbf{p})$. We have

$$\mathbf{k}\cdot\mathbf{e}^1(\mathbf{p}) = \frac{-k\sin\phi\sin\gamma\sqrt{1-x^2}}{\sin\theta_p} \tag{D.15}$$

$$\begin{aligned}
\mathbf{k}\cdot\mathbf{e}^2(\mathbf{p}) &= \frac{k(\cos\theta_p\cos\gamma - x)}{\sin\theta_p} \\
&= \frac{k\sqrt{[\cos\theta_p\cos\gamma - x]^2}}{\sin\theta_p} \\
&= \frac{k\sqrt{\cos^2\theta_p\cos^2\gamma - 2x\cos\theta_p\cos\gamma + x^2}}{\sin\theta_p} \\
&= \frac{k\sqrt{\cos^2\gamma - \sin^2\theta_p + \sin^2\theta_p\sin^2\gamma - 2x\cos\theta_p\cos\gamma + x^2}}{\sin\theta_p} \\
&= \frac{k\sqrt{\sin^2\theta_p\sin^2\gamma + x^2 - \sin^2\gamma + \cos^2\theta_p - 2x\cos\theta_p\cos\gamma}}{\sin\theta_p} \\
&= \frac{k\left\{\sin^2\theta_p\sin^2\gamma + x^2 - \sin^2\gamma + x^2\cos^2\gamma - 2\cos\phi\sin\gamma\cos\gamma x\sqrt{1-x^2}\right.}{\sin\theta_p} \\
&\quad + \frac{\left. + \cos^2\phi\sin^2\gamma(1-x^2) - 2x^2\cos^2\gamma + 2\cos\phi\sin\gamma\cos\gamma x\sqrt{1-x^2}\right\}^{\frac{1}{2}}}{\sin\theta_p} \\
&= \frac{k\sqrt{\sin^2\theta_p\sin^2\gamma - \sin^2\gamma + x^2(1-\cos^2\gamma) + \cos^2\phi\sin^2\gamma(1-x^2)}}{\sin\theta_p} \\
&= \frac{k\sqrt{\sin^2\theta_p\sin^2\gamma - \sin^2\gamma + x^2\sin^2\gamma + \cos^2\phi\sin^2\gamma(1-x^2)}}{\sin\theta_p} \\
&= \frac{k\sqrt{\sin^2\theta_p\sin^2\gamma + (x^2-1)\sin^2\gamma + \cos^2\phi\sin^2\gamma(1-x^2)}}{\sin\theta_p} \\
&= \frac{k\sqrt{\sin^2\theta_p\sin^2\gamma + (\cos^2\phi - 1)\sin^2\gamma(1-x^2)}}{\sin\theta_p} \\
&= \frac{k\sqrt{\sin^2\theta_p\sin^2\gamma - \sin^2\phi\sin^2\gamma(1-x^2)}}{\sin\theta_p}
\end{aligned}$$

$$= \frac{\sqrt{k^2\sin^2\theta_p\sin^2\gamma - k^2\sin^2\phi\sin^2\gamma(1-x^2)}}{\sin\theta_p}$$
$$= \frac{\sqrt{k^2\sin^2\theta_p\sin^2\gamma - \sin^2\theta_p[\mathbf{k}\cdot\mathbf{e}^1(\mathbf{p})]^2}}{\sin\theta_p}$$
$$= \sqrt{k^2\sin^2\gamma - [\mathbf{k}\cdot\mathbf{e}^1(\mathbf{p})]^2} \qquad \text{(D.16)}$$

Employing analagous analyses we may show that

$$\mathbf{k}\cdot\mathbf{e}^1(\mathbf{q}) = \frac{-k\sin\phi\sin\beta\sqrt{1-x^2}}{\sin\theta_q} \qquad \text{(D.17)}$$
$$\mathbf{k}\cdot\mathbf{e}^2(\mathbf{q}) = \sqrt{\left[k^2\sin^2\beta - [\mathbf{k}\cdot\mathbf{e}^1(\mathbf{q})]^2\right]} \qquad \text{(D.18)}$$

and

$$\mathbf{p}\cdot\mathbf{e}^1(\mathbf{k}) = p\sin\phi\sin\gamma \qquad \text{(D.19)}$$
$$\mathbf{p}\cdot\mathbf{e}^2(\mathbf{k}) = \sqrt{p^2\sin^2\gamma - [\mathbf{p}\cdot\mathbf{e}^1(\mathbf{k})]^2} \qquad \text{(D.20)}$$

and

$$\mathbf{q}\cdot\mathbf{e}^1(\mathbf{k}) = -q\sin\phi\sin\beta \qquad \text{(D.21)}$$
$$\mathbf{q}\cdot\mathbf{e}^2(\mathbf{k}) = \sqrt{q^2\sin^2\beta - [\mathbf{q}\cdot\mathbf{e}^1(\mathbf{k})]^2} \qquad \text{(D.22)}$$

Thus, using equation (D.16) we find that

$$BS5^{\lambda\mu=2\nu}_{ll'mn}(k,p,q) \equiv \int_0^{2\pi}\int_{-1}^{1}[\mathbf{k}\cdot\mathbf{e}^{\mu=2}(\mathbf{p})]^2\left[-\frac{l(l+1)}{2l+1}\right][P_{l+1}(x)-P_{l-1}(x)]\,dx\,d\phi$$
$$\equiv \left[-\frac{l(l+1)}{2l+1}\right]\int_0^{2\pi}\int_{-1}^{1}\left[k^2\sin^2\gamma - [\mathbf{k}\cdot\mathbf{e}^1(\mathbf{p})]^2\right]\times$$
$$\times[P_{l+1}(x)-P_{l-1}(x)]\,dx\,d\phi$$
$$\equiv \left[-\frac{l(l+1)}{2l+1}\right]\left[k^2\sin^2\gamma\right]\int_0^{2\pi}\int_{-1}^{1}[P_{l+1}(x)-P_{l-1}(x)]\,dx\,d\phi$$
$$+ \left[-\frac{l(l+1)}{2l+1}\right]\int_0^{2\pi}\int_{-1}^{1}\left[\mathbf{k}\cdot\mathbf{e}^1(\mathbf{p})\right]^2[P_{l+1}(x)-P_{l-1}(x)]\,dx\,d\phi$$

$$\equiv \left[-\frac{l(l+1)}{2l+1}\right]\left[k^2\sin^2\gamma\right]\int_0^{2\pi}\int_{-1}^{1}\left[P_{l+1}(x)-P_{l-1}(x)\right]\,dx\,d\phi$$
$$+ \quad -BS5_{ll'mn}^{\lambda\mu=1\nu}(k,p,q) \qquad \text{(D.23)}$$

For $l \geq 2$ the first integral in equation (D.23) is zero as the Legendre polynomial integral in x is $P_0(x)$ multiplied by higher order polynomials. Thus the two coefficients are equal in magnitude and opposite in sign which means that lowest order velocity field and scalar field quantities cannot contribute to the evolution of any higher order scalar transport coefficients in the nonlinear terms containing this coefficient.

APPENDIX E. $P-Q$ WAVENUMBER INTEGRATION TECHNIQUE

Herein are described the details of the wavenumber integration used in the evaluation of the DIA geometric coefficients. This is a two–dimensional integration over the magnitudes of wavevectors $\mathbf{p}$ and $\mathbf{q}$ which form the vectoral sum $\mathbf{p} + \mathbf{q} = \mathbf{k}$. Examples of the domains of integration are illustrated in Figure E.1. Although each is of relatively simple shape, its geometrical orientation and position with respect to the p and q axes renders the integration difficult due to the nonconstancy of the limits of integration for the first integral(s). Beginning with the point on the q axis and proceeding clockwise, the equations for the sides of the integration domain corresponding to k are

$$q - p = k \tag{E.1}$$

$$q = k_{max} \tag{E.2}$$

$$p = k_{max} \tag{E.3}$$

$$p - q = k \tag{E.4}$$

$$p + q = k. \tag{E.5}$$

For the case of $k = k_{max}$, equations E.1 and E.4 do not apply.

Since all quantities in the DIA coefficients are represented in terms of cubic

B–splines in the p and q directions, appropriate geometric transformations of the integrand can render the integration easier. The transformations to be described rotate the domain of integration so that its centerline lies on the p axis and then transform the original pentagonal shape into a rectangle. These two transformations are illustrated in Figures E.2 and E.3.

The first variable transformation rotated the domain by $\pi/4$ in the clockwise direction and expanded the domain. It consisted of

$$u_1 = p + k \tag{E.6}$$

$$v_1 = p - k \tag{E.7}$$

The second change of variables tranformed the pentagonal shape into a rectangle and consisted of

$$u = u' \frac{u'_{max}}{u'_{max} - v'}, v' \geq 0 \tag{E.8}$$

$$u = u' \frac{u'_{max}}{u'_{max} + v'}, v' < 0 \tag{E.9}$$

$$v = v', \forall u' \tag{E.10}$$

The final integral was of the form

$$\int_{-v_{max}}^{v_{max}} \int_{2}^{2*k_{max}-1} A(k,p,q) J(u,v|u',v') J(u',v'|p,q) du\, dv \tag{E.11}$$

The numerical work necessary to compute the DIA geometric coefficients using the above outlined transformations can be reduced still further. The geometric DIA coefficients as derived for the tensor DIA equations scale with uniform scaling of the (k,p,q) arguments as the scaling constant cubed, i.e., for G constant

$$A^{\lambda\mu\nu}_{abc}(G\mathbf{k}, G\mathbf{p}, G\mathbf{q}) = G^3 A^{\lambda\mu\nu}_{abc}(\mathbf{k}, \mathbf{p}, \mathbf{q}) \tag{E.12}$$

Furthermore, the domains for all k greater than the minimum k are merely scaled subsets of that for the minimum k as shown in Figure E.4. If the data points for the approximation of the geometric coefficients (less the Legendre functions) are chosen to characterize these coefficients with a minimum of error for the case of the minimum k and then computed numerically, these same coefficients may be used for the domains of all the other k's merely by scaling them by a factor of $(k/k_{min})^3$. This feature allows, with a minimum of computations, the highly accurate approximation of the geometric coefficients for the domains of all values of k while paying the computational cost only for accurate representation of the domain of k_{min}. To simplify the integrations, DIA coefficients were computed along the outer boundaries of the integration domain (i.e., those corresponding to $p = k$ and $q = k$ in the $p-q$ domain) with a sufficient additional number to allow accurate interpolation by the B–splines between data points.

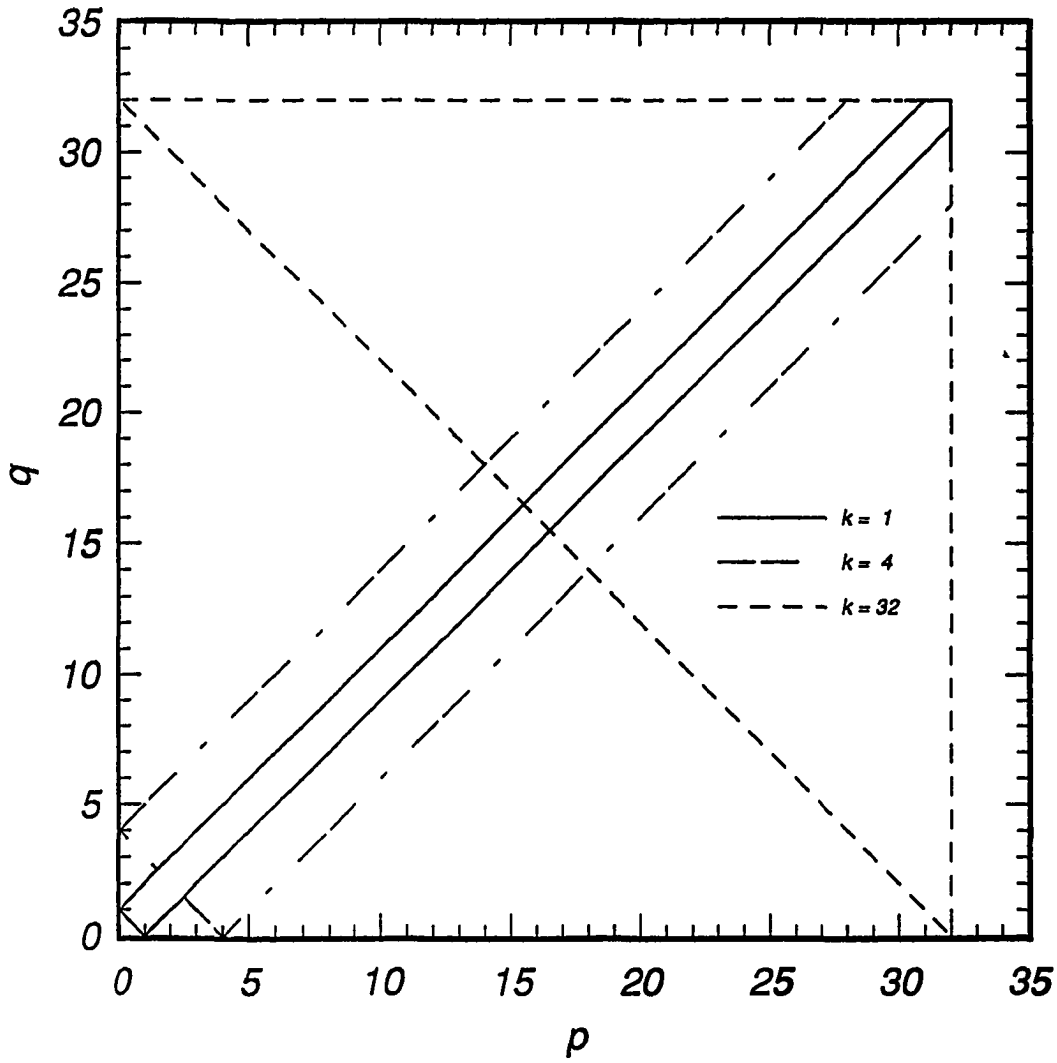

Figure E.1: Domains of $p - q$ integration for k values of 1, 4 and 32.

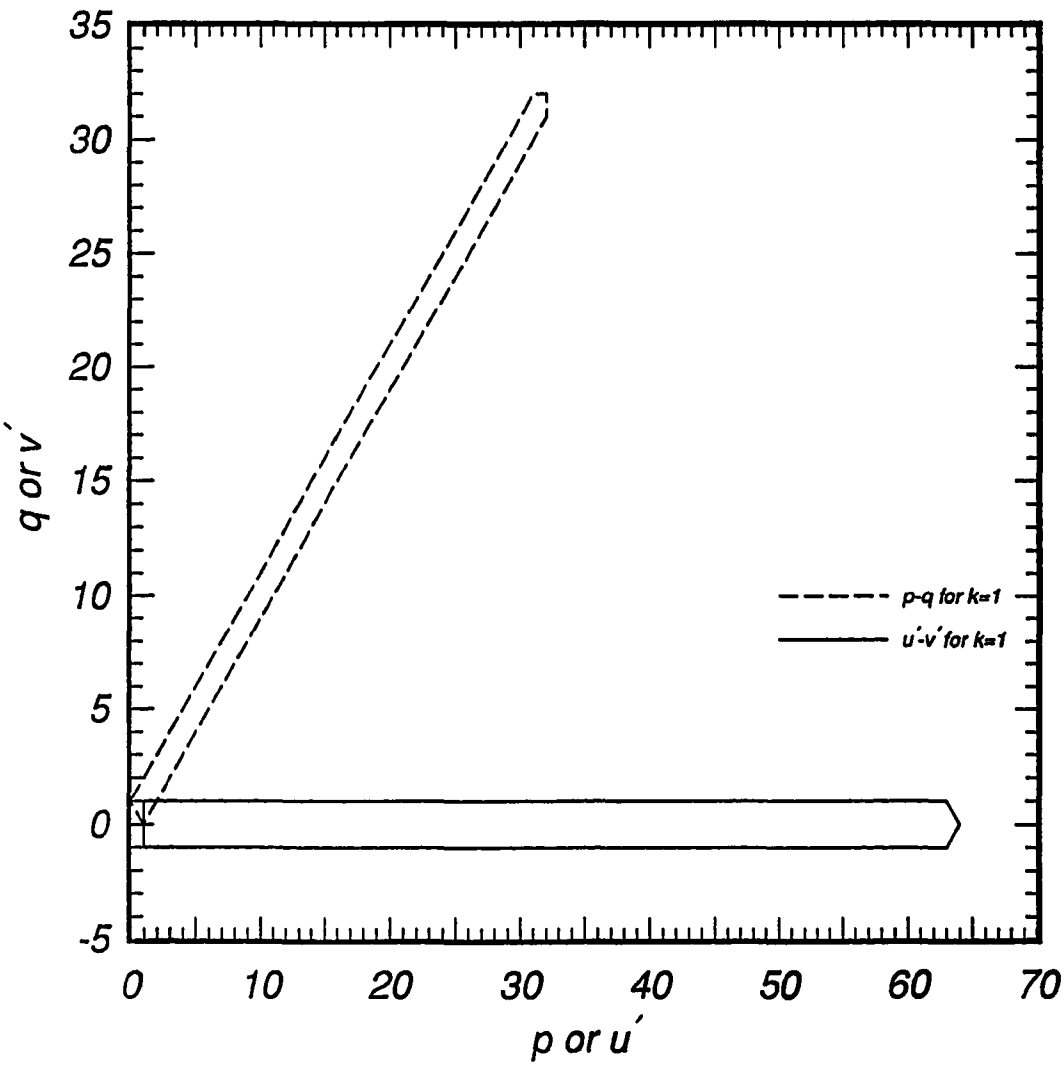

Figure E.2: Domain of $p - q$ integration rotated to the horizontal and expanded.

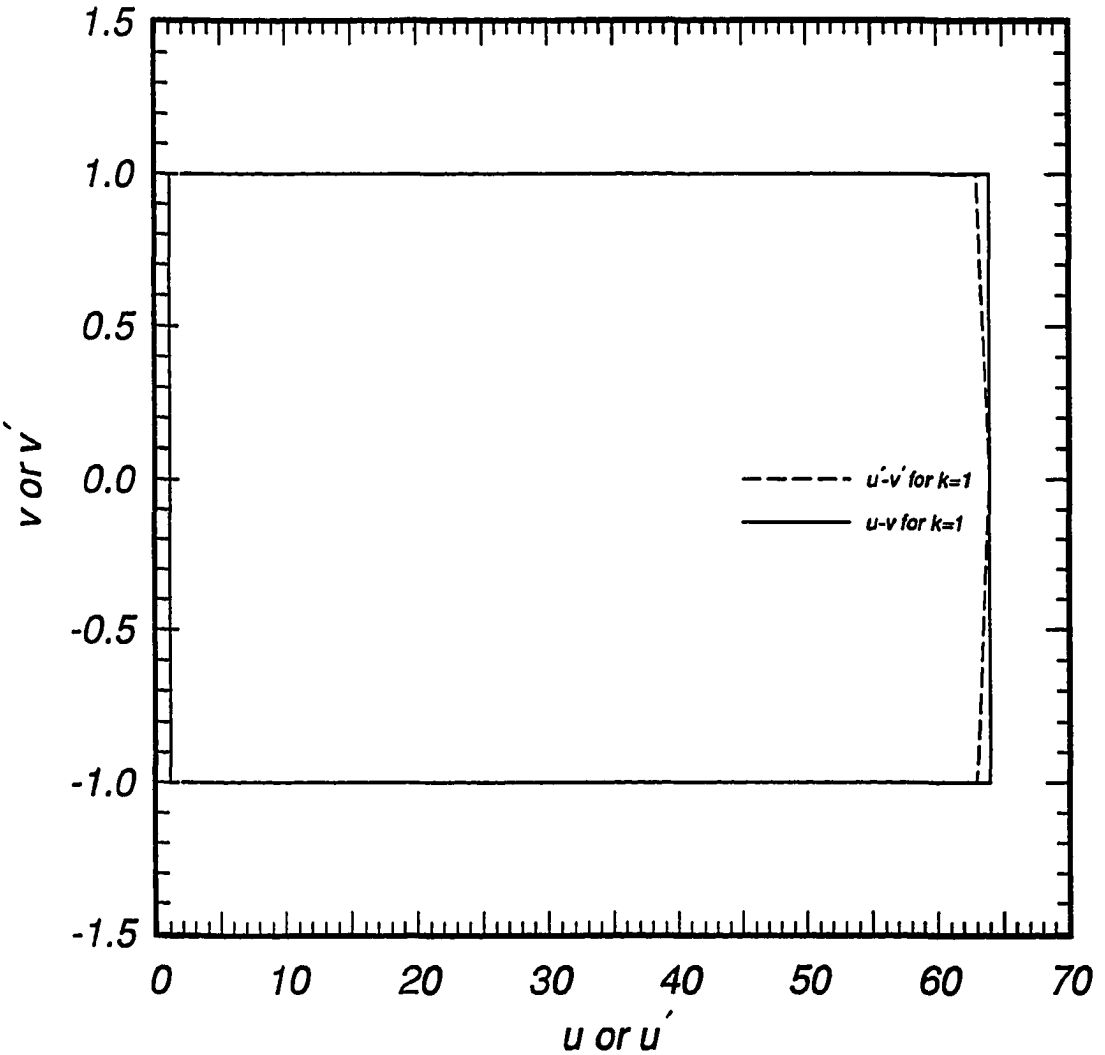

Figure E.3: Domain of the $p - q$ integration transformed into a rectangle.

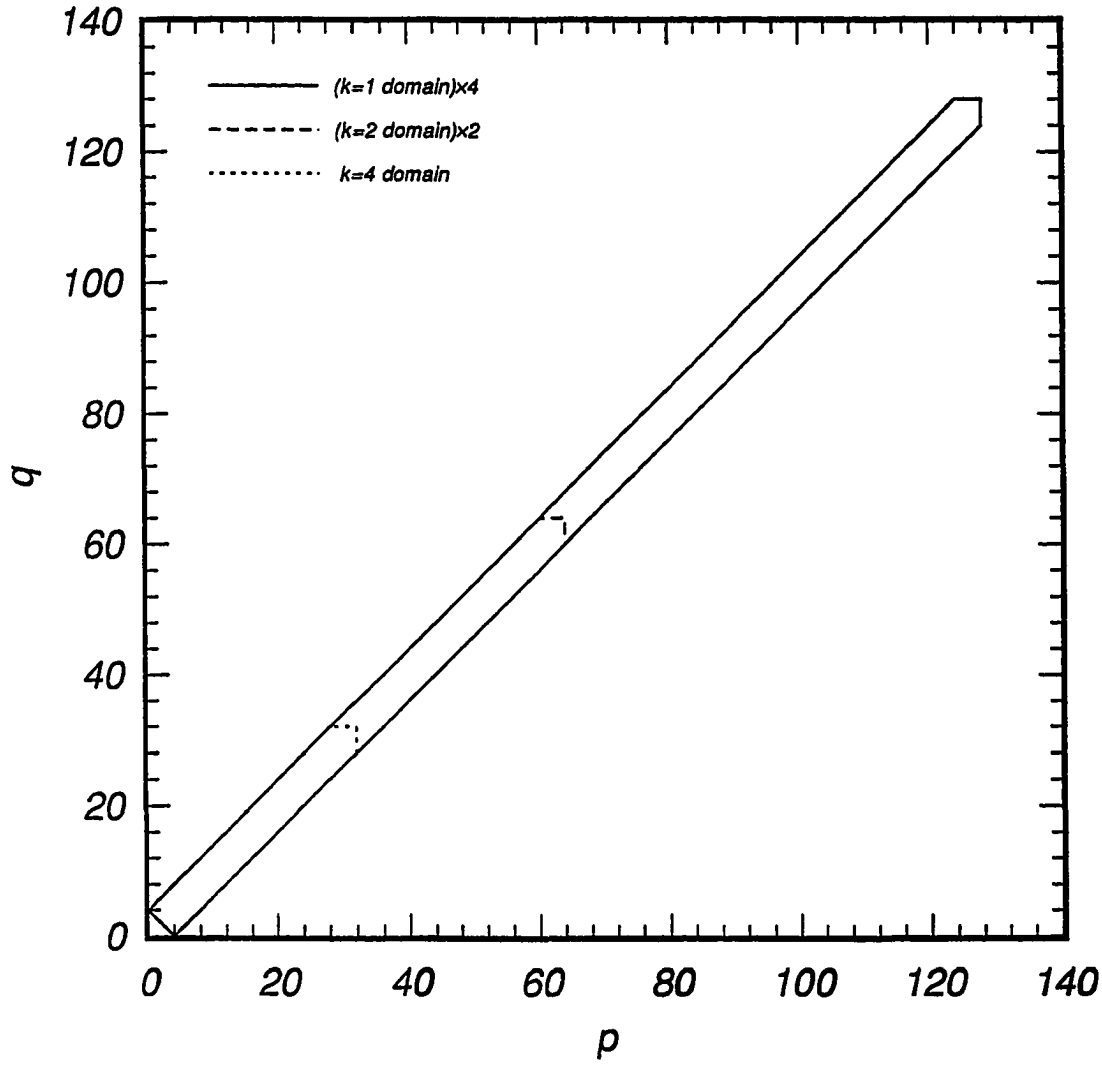

Figure E.4: Comparison of scaled domains of integration for k values of 1, 2, and 4.